Universidad de Valladolid

Escuela de Doctorado Universidad de Valladolid

PROGRAMA DE DOCTORADO EN INVESTIGACIÓN BIOMÉDICA

TESIS DOCTORAL:

DEVELOPMENT OF NOVEL WOUND DRESSING BASED ON ELASTIN-LIKE RECOMBINAMERS FOR SKIN REGENERATION

Presentada por Diana Juanes Gusano
para optar al grado de
Doctora por la Universidad de Valladolid

Dirigida por:
Dr. José Carlos Rodríguez Cabello
Dra. Mercedes Santos García

2024

A mi familia

Nuestra mayor debilidad es
rendirse, la única manera de
tener éxito es intentarlo
siempre una vez más
-Thomas A. Edison-

INDEX

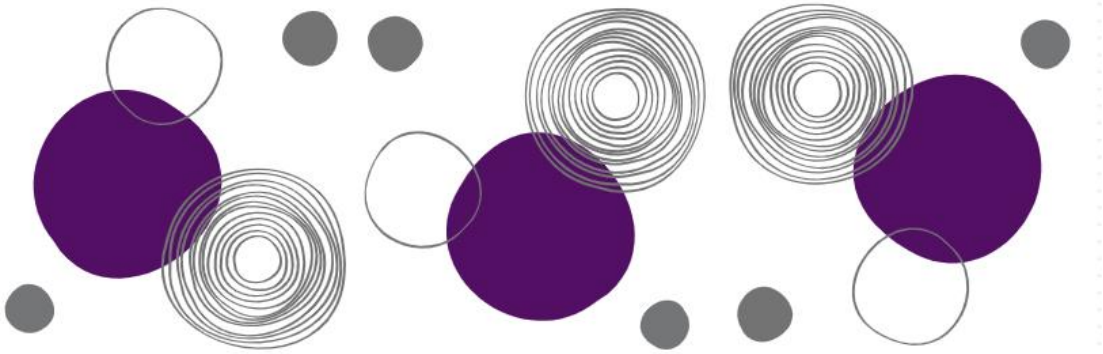

Index

ABSTRACT

Abstract/Resumen

Abstract

Tissue engineering is an interdisciplinary field that combines principles from engineering, biology and medicine to develop innovative solutions for the repair, replacement or enhancement of tissues and organs within the human body. One of the key factors in the success of tissue engineering is the development of biomaterials that are not only biocompatible but also functional, capable of effectively interacting with target tissue cells and promoting their regeneration. These biomaterials can be three-dimensional scaffolds, biodegradable matrices or bioactive products that mimic the properties of natural tissues and provide a favourable environment for cell growth and differentiation. Furthermore, the development of biomaterials that are specific to different tissue types and clinical applications may facilitate the creation of more effective and personalised treatments for patients, thereby improving their quality of life and accelerating their recovery.

In particular, the treatment of chronic wounds represents a significant challenge in healthcare, as these wounds can persist for weeks, months or even years, affecting the quality of life of patients and generating considerable treatment costs. In response to this pressing need, the development of biomaterials that facilitate and accelerate the healing process of chronic wounds has become a crucial area of research. Biomaterials utilised in wound dressings must provide a suitable environment for tissue regeneration, promoting cell migration, proliferation and extracellular matrix synthesis. Furthermore, in order to be considered optimal, these materials must meet a number of requirements including the provision of a temporary protective physical barrier against external agents or pathogens, the ease of application, the maintenance of the correct level of moisture to promote re-epithelialisation and the absorption of exudate. In addition, they must also demonstrate good bioadhesion to the wound surface, elasticity, mechanical strength, ease of sterilisation and biodegradability without toxic or antigenic residues. Consequently, recombinant proteins are emerging as promising alternatives in the field of regenerative medicine, thanks to their ability to be engineered at the genetic level, which offers meticulous control over their physicochemical and bioactive characteristics. This enables precise adaptations for skin regeneration. Elastin-like recombinamers (ELRs) permit the incorporation of specific epitopes, such as cell adhesion sequences, proteolytics, or biologically active growth factors.

Therefore, the ELRs that are the subject of this thesis are based on the Val-Pro-Gly-X-Gly pentapeptide repeat, which is found in natural elastin. The X residue (host residue) can be any amino acid, with the exception of L-proline, which allows the physicochemical properties of these ELRs to be modulated by simply choosing one amino acid or another as host, thereby varying the polarity of the chain.

Moreover, if this residue contains functional groups, it can also be used for further chemical modifications to achieve, for example, covalently cross-linked hydrogels, using fast, orthogonal and cell-compatible reactions. The sequence of hydrophobic domains confers to ELRs a smart thermo-responsive behaviour in aqueous media, defined by the inverse temperature transition (ITT), which occurs above the transition temperature (T_t), leading to a change in protein conformation. This thermal response enables the economical purification of these materials by means of heating and cooling cycles, a process known as the inverse transition cycle (ITC).

The objective of this thesis is to develop novel wound healing wound dressings by obtaining elastin-based scaffolds, either membranes or hydrogels. These will be employed to incorporate enhanced bioactivities that meet all the requirements to be considered as an ideal dressing to induce and improve skin regeneration. In particular, a detailed physicochemical and biological characterisation of ELR membranes will be carried out in order to determine their suitability as dressings for the improvement of difficult-to-heal wounds. Furthermore, the development of novel multifunctional elastin-based hydrogels with a high degree of selectivity and bioactivity is proposed by the inclusion of laminin sequences that significantly improve keratinocyte adhesion, thus conferring a benefit in wound healing.

The initial chapter of this thesis assesses the physicochemical properties of ELR membranes in terms of surface roughness, wettability and degradation as these factors are crucial for the dressing to possess adequate properties for its intended function and proper adhesion to the wound. Furthermore, they influence cell behaviour in terms of adhesion capacity, proliferation, morphology and viability. Subsequently, the biocompatibility and non-cytotoxicity of the membranes are analysed using a range of methods in order to determine their suitability for tissue engineering applications. *In vitro* cytocompatibility is evaluated by culturing fibroblasts and keratinocytes on ELR substrates, showing optimal proliferation up to 21 days. In addition, the ability of the cells to grow, migrate, and mature in the presence of the membranes is analysed using diverse methodologies, including qPCR and scratch assay. The regenerative capacity of these membranes is evaluated with an *ex vivo* human skin model, which demonstrates good re-epithelialisation without shrinkage, which is the main factor leading to visible scarring. Regarding *in vivo* cytocompatibility, cells colonise the material, and ELR membranes remain stable for at least seven weeks following subcutaneous implantation. Furthermore, no rejection or foreign body effect is observed after macroscopic and histological evaluation, as no fibrotic tissue is observed. Finally, ELR membranes are implanted in a healing study involving a full-thickness excision model in mouse skin, demonstrating a beneficial effect on defect regeneration. Consequently, this membrane system demonstrates significant potential in wound regeneration, promoting self-regeneration by the surrounding tissue without the need for the addition of stem cells or external growth factors.

Having established the beneficial effect of ELR membranes, new ELRs are designed to enhance this advantage effect and promote skin regeneration in chronic

wounds. Two approaches are proposed to achieve this goal: the chemical synthesis of laminin mimetic peptides (KAASIKVAVSADR and KPPFLMLLKGSTR) and their anchoring by click chemistry to the main chain of the ELR polymer; and the use of genetic engineering techniques and recombinant expression in *Escherichia coli* to enable the biosynthesis of polymers encoding the desired complementary bioactivities in their backbone. Subsequently, chemically cross-linked hydrogels are obtained and a comprehensive characterisation is conducted, encompassing macroscopic properties, internal morphology, water content and mechanical properties. Furthermore, the biomimetic hydrogels, both with the chemically grafted peptides and the sequences within their polypeptide chain, demonstrate excellent biocompatibility *in vitro*. Additionally, it has been confirmed that the presence of the PPFLMLLLKGSTR sequence induces an improvement in keratinocyte cell adhesion.

In summary, this thesis encompasses all stages, from the design of ELR genes specific for skin regeneration to their analysis, both *in vitro* and *in vivo*. This includes their efficient, clean, sustainable and economical production in genetically modified organisms, as well as their purification and further chemical modification. Furthermore, innovative membranes and hydrogels, characterised by their physico-chemical and biological properties, have been developed using these polymers, demonstrating the biocompatibility of both types of scaffolds based on these ELRs. Moreover, it has been demonstrated that the utilisation of ELR-based membranes can facilitate skin regeneration by enabling the incorporation of sequences of interest, which can result in the development of innovative properties or bioactivities that are tailored to the desired tissue.

Resumen

La ingeniería de tejidos es una disciplina interdisciplinaria que combina principios de la ingeniería, la biología y la medicina para diseñar soluciones innovadoras que reparen, reemplacen o mejoren tejidos y órganos en el cuerpo humano. Una de las claves para el éxito de la ingeniería de tejidos es el desarrollo de biomateriales que sean no solo biocompatibles, sino también funcionales, capaces de interactuar de manera efectiva con las células del tejido objetivo y promover su regeneración. Estos biomateriales pueden ser andamios tridimensionales, matrices biodegradables o productos bioactivos que imitan las propiedades de los tejidos naturales y proporcionan un entorno favorable para el crecimiento y la diferenciación celular. Además, el desarrollo de biomateriales a la carta y específicos para diferentes tipos de tejidos y aplicaciones clínicas puede abrir la puerta a tratamientos más eficaces y personalizados para los pacientes, mejorando su calidad de vida y acelerando su recuperación.

Más concretamente, la cicatrización de heridas crónicas de la piel representa un desafío significativo en el ámbito de la atención médica, ya que estas heridas pueden persistir durante semanas, meses o incluso años, afectando la calidad de vida de los pacientes y generando costos de tratamiento considerablemente altos. En respuesta a esta necesidad apremiante, el desarrollo de biomateriales que

faciliten y aceleren el proceso de cicatrización de heridas crónicas se ha convertido en un área de investigación crucial. Los biomateriales empleados en apósitos deben proporcionar un entorno adecuado para la regeneración tisular, promoviendo la migración celular, la proliferación y la síntesis de matriz extracelular. Además, para ser considerados óptimos, estos materiales deben cumplir una serie de requisitos como proporcionar una barrera física protectora temporal frente a agentes externos o patógenos, ser fáciles de aplicar, mantener el nivel adecuado de humedad para favorecer la re-epitelización y absorción del exudado. Asimismo, deben poseer una buena bioadhesión a la superficie de la herida, elasticidad, resistencia mecánica, facilidad de esterilización y biodegradabilidad sin residuos tóxicos o antigénicos. Así, las proteínas recombinantes están surgiendo como alternativas prometedoras en la actualidad, gracias a su habilidad para ser diseñados a nivel genético ofreciendo un control meticuloso sobre sus características físico-químicas y bioactivas, permitiendo adaptaciones precisas para la regeneración de la piel. Los ELR permiten la inclusión de epítopos específicos, como secuencias de adhesión celular, proteolíticas o factores de crecimiento biológicamente activos.

Por lo tanto, los materiales ELRs con los que trabajamos en esta tesis se basan en la repetición del pentapéptido Val-Pro-Gly-X-Gly que se encuentra en la elastina natural, donde X (residuo huésped) puede ser cualquier aminoácido excepto la L-prolina, de tal manera que se pueden modular las propiedades físico-químicas de estos ELR simplemente eligiendo un aminoácido u otro como huésped al variar la polaridad de la cadena. Además, si este residuo contiene grupos funcionales, también se puede utilizar para modificaciones químicas adicionales con el fin de lograr, por ejemplo, hidrogeles reticulados covalentemente, empleando reacciones rápidas, ortogonales y compatibles con las células. Esta secuencia de dominios hidrófobos confiere a los ELR un comportamiento inteligente de termorespuesta en medio acuoso definido por la denominada transición de temperatura inversa (ITT), que ocurre por encima de la denominada temperatura de transición (T_t) que conlleva un cambio en la conformación de las proteínas. Esta respuesta térmica facilita su purificación económica mediante ciclos de calentamiento y enfriamiento, un proceso conocido como ciclo de transición inversa (ITC).

El objetivo de esta tesis es desarrollar nuevos apósitos que favorezcan la cicatrización de heridas mediante la obtención de andamios basados en elastina, ya sean membranas o hidrogeles aprovechando su versatilidad para incorporar nuevas bioactividades mejoradas que cumplan con todos los requisitos para ser considerado un apósito ideal que induzca y mejore la regeneración de la piel. En particular, se lleva a cabo una caracterización fisicoquímica y biológica detallada de las membranas ELR con el fin de determinar su idoneidad como apósitos para la mejora de heridas difíciles de curar. Además, se propone el desarrollo de novedosos hidrogeles multifuncionales a base de elastina con un alto grado de selectividad y bioactividad, lo que se consigue mediante la inclusión de secuencias de laminina que mejoran significativamente la adhesión de los queratinocitos, confiriéndose así un beneficio en la cicatrización de heridas.

En el primer capítulo de esta tesis se evalúan las propiedades físico-químicas de las membranas ELR, obtenidas mediante una metodología novedosa que permite que tengan espesores variables entre 5 y 25 µm dependiendo de la concentración y altamente porosas, en términos de rugosidad de la superficie, humectabilidad y degradación, ya que estos factores son indispensables para que el apósito tenga unas propiedades adecuadas para su función y para su correcta adhesión a la herida, además, de ejercer un efecto sobre el comportamiento celular en cuanto a su capacidad de adhesión, proliferación, morfología y viabilidad. A continuación, se analiza la biocompatibilidad y la no citotoxicidad de las membranas mediante una amplia variedad de métodos para determinar si son adecuadas para aplicaciones ingeniería tisular. Para ello, se estudia la citocompatibilidad *in vitro* mediante el cultivo de células fibroblastos y queratinocitos sobre sustratos ELR, mostrando una proliferación óptima hasta los 21 días. Además, se analiza la capacidad que tienen las células en crecer, migrar y madurar en presencia de las membranas usando diferentes métodos como qPCR o ensayos de rasgados. La capacidad regenerativa de estas membranas se evalúa con un modelo *ex vivo* de piel humana comprobando una buena re-epitelización sin contracción, que es el principal factor que induce la generación de cicatrices visibles. Con respecto a la citocompatibilidad *in vivo*, las células colonizan el material y las membranas ELR permanecen estables durante al menos 7 semanas tras la implantación subcutánea. Además, se comprueba que no hay rechazo ni efecto de cuerpo extraño tras la evaluación macroscópica e histológica al no observarse tejido fibrótico. Por último, las membranas ELR se implantan en un estudio de cicatrización que involucra un modelo de escisión de espesor total en la piel de ratones, mostrando un efecto beneficioso en la regeneración del defecto. Por consiguiente, este sistema de membrana demuestra un importante potencial en la regeneración de heridas, promoviendo la autorregeneración por parte del tejido circundante sin requerir la adición de células madre ni factores de crecimiento externos.

Una vez confirmado el efecto beneficioso de las membranas ELR, se procede al diseño de nuevos ELR con el fin de potenciar este efecto ventajoso y promover la regeneración de piel en heridas crónicas. Para alcanzar este objetivo se plantean dos enfoques: la síntesis química de péptidos miméticos de la lámina (KAASIKVAVSADR y KPPFLMLLKGSTR) y su anclaje mediante química click a la cadena principal del polímero ELR; y el uso de técnicas de ingeniería genética y expresión recombinante en *Escherichia coli* para permitir la biosíntesis de polímeros que codifican las bioactividades complementarias deseadas en su columna vertebral. A continuación, se obtienen hidrogeles entrecruzados químicamente y se lleva a cabo una caracterización exhaustiva que abarca propiedades macroscópicas, morfología interna, contenido de agua y propiedades mecánicas. Además, los hidrogeles biomiméticos, tanto con los péptidos injertados químicamente como con las secuencias en el interior de su cadena polipeptídica, demuestran una excelente biocompatibilidad *in vitro*, y se confirma que la presencia la secuencia PPFLMLLKGSTR induce una notable mejora de la adhesión celular de queratinocitos.

En resumen, esta tesis abarca todas las etapas desde el diseño de los genes de los ELRs específicos para la regeneración de piel hasta su análisis tanto *in vitro* como *in vivo*. Esto incluye su producción eficiente, limpia, sostenible y económica en organismos genéticamente modificados, así como su purificación y posterior modificación química. Además, utilizando estos polímeros se han desarrollado membranas e hidrogeles innovadores, caracterizados por sus propiedades físico-químicas y biológicas, demostrando la biocompatibilidad de ambos tipos de andamios basados en estos ELR. Por último, se ha evidenciado que el uso de membranas basadas en ELR puede beneficiar la regeneración de piel al permitir ajustes en el diseño mediante la incorporación de secuencias de interés, lo que puede conducir a propiedades innovadoras o bioactividades adaptadas al tejido deseado.

HYPOTHESIS

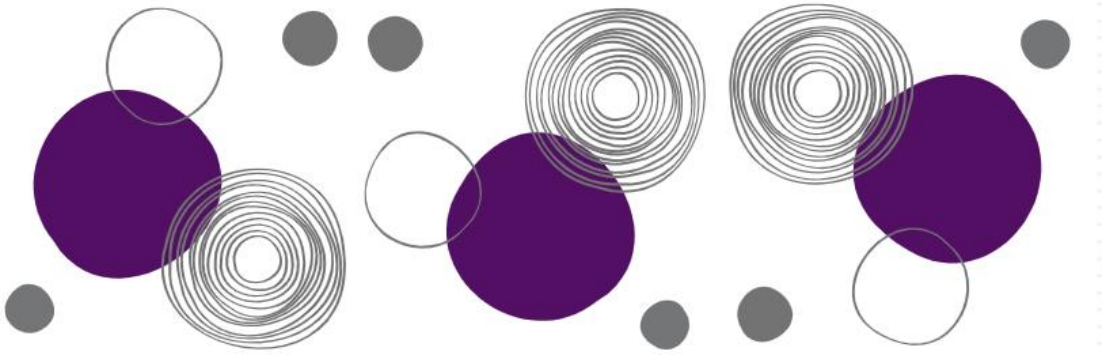

Context and motivation for the work

In developed countries, it is estimated that between 1 and 2 % of the population will experience chronic wounds to the skin at some point in their lives [1]. A recent study conducted in Spain investigated the prevalence of chronic wounds and skin lesions, revealing that venous ulcers are the most prevalent, followed by pressure sores and diabetic foot ulcers. Moreover, 51.21 % of individuals with wounds are women [2]. The increase in the incidence of chronic wounds globally in recent years can be attributed to two primary factors: the ageing population and the increase in diseases and comorbidities that affect wound healing, including diabetes, obesity, venous hypertension and vascular diseases [1]. In addition, skin cancer is one of the most prevalent cancers in humans, with surgical removal of the affected area being a common treatment. This can result in the formation of lesions that resemble chronic wounds in appearance and healing process [3].

A variety of approaches are employed in the treatment of different types of chronic wounds, with skin graft transplantation being the most common method. This process involves the transfer of healthy skin from one area of the body to the wound site [4], [5]. Skin grafts can be autografts (derived from the own skin of the patient), allografts (obtained from a deceased human donor) or xenografts (derived from another species). Autografts are the preferred option due to a lower likelihood of rejection, although they may cause additional wounds in the donor area that could become chronic [5]. Furthermore, there may be a shortage of suitable donor tissue or the patient may have diseases that render them unfit for this treatment. Additionally, skin grafts may not be completely effective in some lesions due to bacterial resistance or persistent infection [6].

Consequently, these therapies represent a significant economic and clinical burden on the healthcare system, as well as being a painful process for affected patients. Therefore, it is crucial to identify effective solutions that not only address the lesions in the short term, but also reduce the overall economic and clinical burden associated with current treatments. In this context, novel skin regeneration therapies are focusing on tissue engineering (TE) solutions, which leverage available technology to develop regenerative models tailored to the individual patient [7]. Therefore, elastin, a crucial protein within the extracellular matrix (ECM) of the skin, and its mimetic materials, such as elastin-like recombinamers (ELRs), present a significant opportunity for the fabrication of support structures. These structures combine the inherent properties of natural polymers with the adaptability of recombinant proteins. Furthermore, ELRs exhibit excellent biocompatibility, as they are based on the natural sequence of elastin, thereby enabling the host immune system to not distinguish between endogenous elastin and ELRs [8]. The adjustable properties of ELRs allow them to be easily modified according to the specific application required [9]. One of the proposed models for skin regeneration is the use of thin membranes prepared by a method developed by Bioforge research group that requires the formation of a lattice by chemical cross-

linking of ELRs. These membranes would act as bioactive structural supports, facilitating the healing of chronic wounds or burns.

Hypothesis

The development of a wound dressing based on elastin-like recombinamer (ELR) polymer has the potential to effectively induce skin regeneration and improve the healing process of difficult-to-heal wounds, such as chronic wounds or burns. This enhancement can be attributed to the intrinsic properties of ELRs, including thermosensitivity, biocompatibility, bioactivity, and mechanical strength. Furthermore, the incorporation of laminin sequences into innovative multifunctional elastin-based hydrogels will markedly accelerate wound healing by providing specific bioactivities. The proposed study will employ two approaches: the chemical synthesis of peptides that will be subsequently conjugated to the ELR polymer chain via click chemistry, and the biosynthesis of polymers with encoded complementary bioactivities using genetic engineering techniques coupled with recombinant expression in *Escherichia coli*. These approaches will further amplify the biological responses observed, ultimately leading to the development of an optimal wound dressing for skin regeneration.

Objectives

The general objective of this research is the development and validation of novel scaffolds based on ELRs as models for skin regeneration. In order to achieve this aim, we will prepare ELRs with specific bioactivity in the context of skin regeneration, form membranes and hydrogels, and then assess their suitability in terms of mechanical properties, biocompatibility and bioactivity, which are essential for effective tissue regeneration.

To this purpose, we will employ two distinct approaches:

1.- The first objective is the production of highly porous, thin elastin membranes through the utilisation of two ELRs (specifically VKV and SKS), which are dissolved in two immiscible aqueous and organic phases. It is hypothesised that the serine amino acids in one ELR polymer provide a high transition temperature for solubility in the aqueous phase at room temperature, while the RGD tripeptide in the other ELR polymer enhances cell adhesiveness. The aforementioned ELRs will be modified with complementary click cross-linkable groups in order to form porous, highly hydrated, interconnected networks with properties that can be modulated depending on the initial concentrations of the polymers.

- A comprehensive characterisation of ELR membranes will be presented, with a particular focus on the structural composition, thermal behaviour, and surface topography of the membranes. Additionally, the self-healing behaviour of the membranes will be also analysed, as well as an evaluation of their wettability, swelling ratio, and enzymatic degradation under physiological conditions. The ultimate goal is to ascertain that these

membranes possess the requisite physico-chemical characteristics for efficacious wound dressings.

- The biocompatibility and cytotoxicity of ELR membranes will be evaluated through cell culture experiments utilising fibroblasts and keratinocytes. The incorporation of bioactive domains, such as the RGD sequence, is intended to enhance cell-material interactions and promote a favourable cellular response for tissue regeneration. Moreover, the growth of cells and the expression of specific genes will be examined, as well as the capacity of cell migration.

- The assessment of the regenerative ability of ELR membranes using an *ex vivo* human skin wound model will also be described. Furthermore, the interaction between ELR-based membranes and living tissues must be elucidated using animal models. Consequently, mice will be employed for the *in vivo* evaluation of the biocompatibility and long-term stability of these membranes through subcutaneous implantation. Subsequently, the capacity of elastin membranes to promote wound regeneration will be evaluated through the use of a murine full-thickness excisional skin model, including daily observation with fluorescent staining and histopathology.

2.- The second objective is the production of novel elastin-based hydrogels with specific functionalities for the regeneration of skin wounds. The biofunctionalized hydrogel will contain laminin peptide sequences, which will enhance keratinocytes adhesion, thereby facilitating wound healing. In order to achieve the aforementioned goals, the following partial objectives have been met:

- The chemical synthesis of novel peptides displaying laminin domains will be accomplished through the utilisation of the solid phase peptide synthesis (SPPS) technique. The peptides, designed with azide groups in terminal amino acid for subsequent binding to an ELR polymer, will be characterised in order to ensure the correct synthesis before use.

- In-depth characterisation will be employed to ensure the correct anchoring of laminin peptides to the ELR polymer via a click reaction between the azide groups in the peptides and the cyclooctyne groups in the polymer. A variety of physicochemical techniques will be employed, including high performance liquid chromatography (HPLC) for amino acid analysis, nuclear magnetic resonance spectroscopy (NMR) for peptide fingerprint data, matrix-assisted laser desorption/ionization time-of-flight (MALDI-TOF) mass spectrometry for purity and molecular weight assessment, and attenuated total reflectance Fourier-transform infrared (ATR-FTIR) spectroscopy.

- The development of a new tricomponent hydrogel will be explored using catalyst-free click chemistry. Furthermore, a comprehensive characterisation of this novel hydrogel will be conducted, encompassing macroscopic properties, internal morphology, water content, and

mechanical properties to assess the feasibility of creating injectable hydrogels, which can facilitate the optimally placement of the wound dressing by adapting to the dimensions and contour of the wound, while a hydrogel is generated *in situ* at the site of injury.

- The biological characterisation of the new tricomponent ELR hydrogels will demonstrate specific functionalities, including the presence of cell adhesion motifs (RGD) in their main peptide chain and the incorporation of keratinocyte-specific adhesion domains through the mimetic peptides. The aforementioned functionalities are designed to enhance biocompatibility, support skin regeneration, and provide an effective scaffold for cell adhesion, growth, and proliferation, thereby facilitating the formation of functional new tissue.

- An alternative methodology would be to employ the techniques of molecular biology and recombinant DNA technology to synthesise three genes encoding elastin-type polymers with the keratinocyte-specific sequences within their structure. The objective of this approach is to optimize the production efficiency and enhance the functionality of the elastin-based polymers.

- Consequently, the aforementioned genes encoding bioactive ELRs will be incorporated into a plasmid vector pDrive All. By employing iterative-recursive technology in conjunction with restriction enzymes, the final construct of interest will be generated and subsequently transfected into a plasmid for expression. The novel bioactive ELRs will then be bioproduced using *Escherichia coli*, purified and characterised for further utilisation.

- The production of new chemically cross-linked bioactive ELR hydrogels with laminin-specific cell adhesion motifs will be explored. Furthermore, a comprehensive characterisation of this novel hydrogel will be conducted, encompassing macroscopic attributes, internal structure, water content, and mechanical properties.

- An *in vitro* evaluation of the impact of novel adhesive domains integrated into the main ELR polymer chain on keratinocytes and fibroblasts will also be conducted. These domains are expected to enhance the adhesion capacity of the cells, facilitating a more rapid and efficient cell invasion, leading to the gradual replacement of the synthetic matrix by the new functional tissue.

Thesis outline

This thesis is comprised of four chapters, which are displayed in the following order:

Chapter 1 includes an introduction to the thesis, detailing the anatomy, physiology, functions and biomechanics of the skin, as well as a detailed description of the stages of the wound healing process and the complications encountered in chronic wounds. The characteristics of an optimal wound dressing and the types and materials available for this purpose are outlined, with a particular focus on elastin-based materials.

Chapter 2 provides a comprehensive overview of the materials and methods employed throughout the course of this thesis, encompassing a range of techniques, including molecular biology techniques, chemical synthesis of peptides, physicochemical and biological characterisation conducted *in vitro, ex vivo* and *in vivo*.

Chapter 3 presents the obtained results in this thesis. This chapter is divided into two main sections. The first section concerns the development of ELR membranes, while the second addresses the creation of advanced biomaterials functionalised with laminin mimetic peptides. In regard to the ELR membranes, the results of the physico-chemical characterisation of the ELR membranes are presented, as well as their biological characterisation. Furthermore, the findings related to the evaluation of the wound regeneration capacity of ELR membranes using a human *ex vivo* wound culture model are exhibited, as well as the evaluation of the *in vivo* biocompatibility and long-term stability of ELR membranes by subcutaneous implantation. Finally, the results of the evaluation of the wound regeneration capacity of ELR membranes using a murine full-thickness excision wound model are also discussed. With regard to the development of advanced biomaterials functionalised with laminin mimetic peptides to improve the wound healing process, the results of this novel hydrogel are presented. This encompasses the chemical anchoring of the peptides and the incorporation of the sequence into the backbone of the ELR. In both cases, an exhaustive characterisation of their properties is conducted, including transparency, water content, and mechanical properties. Additionally, an *in vitro* assessment of the enhanced cell adhesion observed when the cell adhesion sequences of laminin are incorporated into the elastin hydrogels is performed.

Finally, **Chapter 4** proposes the principal conclusions and future perspectives of the work developed in this thesis.

INTRODUCTION

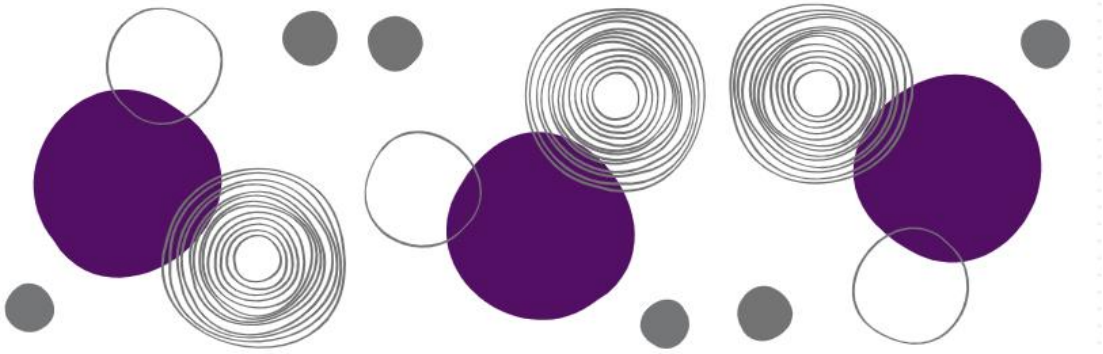

1.- Introduction

1.1.- The human skin

The skin is the largest organ of the body and performs vital functions serving as an efficient and protective barrier that defends the organism against external stress factors such as environmental factors (temperature or humidity), microorganisms, UV radiation, and chemical, biological, and physical agents [10]. In addition to its protective function, the skin plays an important role in neuroendocrine and immune processes that contribute to the maintenance of body homeostasis by preventing dehydration and regulating body temperature, as well as playing a metabolic role in synthesizing vitamin D [11], [12]. As a sensory organ and due to the presence of independent nerve endings and special receptors, the skin enables the perception and localization of mechanical stimuli such as pressure, friction and vibration as well as temperature and pain [11].

Human skin is composed of three distinct layers that are very different in anatomy and function, but with complex interrelationships, namely epidermis, dermis and hypodermis, as illustrated in Figure 1A. The epidermis, the outermost layer of the skin, is a highly specialized multi-layered cellular epithelium. The dermis, situated beneath the epidermis, is a thicker underlying layer of connective tissues. Finally, the innermost layer of skin, the hypodermis, is a layer of subcutaneous fat that is separated from the rest of the body by a vestigial layer of striated muscle. Inseparably, human skin also contains appendages or cutaneous annexes. In addition to hair and nails (keratinised annexes), which are external and evident, there are also other types of cutaneous appendages produced by invaginations of the epidermis including hair follicles, sebaceous and sweat glands [13], [14]. Table 1 provides an overview of all cells present in the skin, their location and their main functions.

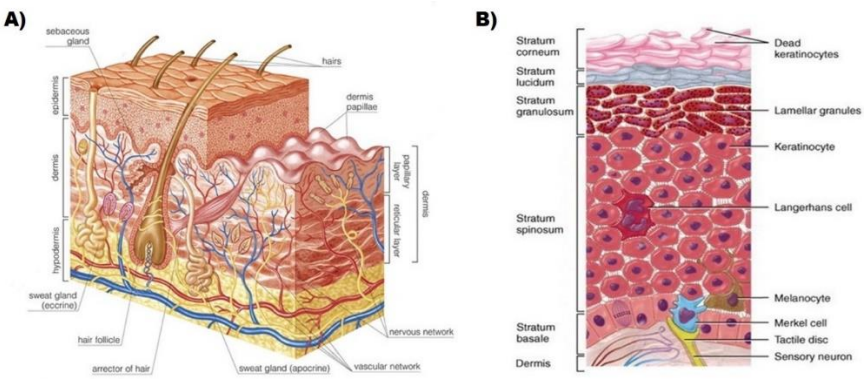

Figure 1: ***Anatomy of skin and epidermal architecture. A)*** *The skin is composed of three main layers: the epidermis, dermis, and hypodermis. The epidermal barrier layer, which is approximately 0.1–0.2 mm in thickness, is firmly attached to the dermis by a specialized basement membrane zone, which can be observed under an electron microscope. The dermis, which exhibits considerable variation in thickness, is primarily composed of collagen I and contains hair shafts and sweat glands. It is well vascularised and contains receptors for touch, temperature, and pain. The epidermal keratinocytes rely on diffusion from the dermal capillaries and differentiate from the basal layer, forming a keratinised layer that provides a barrier against bacteria and prevents fluid loss. The skin also comprises appendages such as hair, nails, hair follicles, sebaceous and sweat glands. Image from Sciencephoto.* ***B)*** *The epidermis is composed of four main stratified layers: the stratum basale, the stratum spinosum, the stratum granulosum, and the stratum corneum. Each of these layers undergoes programmed differentiation in order to facilitate the constant renewal of the skin. The basal layer is connected to the dermis via*

hemidesmosomes and integrin-based adhesions, thereby anchoring it to the extracellular matrix. During differentiation, keratinocytes form unique structures in each layer with specific cytoskeleton and cell junction types, including adherent junctions, tight junctions, desmosomes, and gap junctions. These changes facilitate tissue morphogenesis and the specific functions of each layer, from regeneration in the stratum basale to shedding in the stratum corneum. Image from Earthslab.

1.1.1.- The epidermis

The epidermis is a highly specialized, poly-stratified and keratinized epithelium that covers the entire body surface and has evolved to achieve vital protective functions, including preventing water loss, participating in immune responses, excluding toxins and resisting mechanical stress. The epidermis is avascular, and its care and maintenance are dependent on the diffusion of nutrients from the capillary network of the dermis. In order to establish a barrier between the organism and its environment, the epidermis is predominantly composed of keratinocytes (approximately 95 %), which are in progressive stages of differentiation. As they divide and proliferate, these keratinocytes move from the deepest layer to the most superficial layer. The epidermal layers are categorized based on the cellular morphology, taking into account the differentiation states of the keratinocytes. They can be divided into the following layers: *stratum basale, stratum spinosum, stratum granulosum, stratum lucidum* (which is only present in the thicker skin of the palms and soles), and *stratum corneum* [15], [16], as shown in Figure 1B. In terms of function, three distinct regions can be identified within the epidermis, which are continuously renewed from the base. These regions are: a) the proliferative zone (*stratum basale*), which is responsible for cell renewal (also known as epidermopoiesis); b) the differentiation zone (*stratum spinosum* and *stratum granulosum*), which is responsible for cellular differentiation and maturation; and c) the functional zone (*stratum corneum*), which is responsible for the formation of a protective *stratum corneum* and cell elimination [14].

The *stratum basale* is the innermost layer of the epidermis and is composed of a continuous single-cell-thick layer of keratinocytes that are separated from the dermis by the basement membrane and anchored to it via hemidesmosomes [15]. The proliferative keratinocytes, which are responsible for regenerating the different layers of the epidermis, have a cylindrical or cuboidal shape with a large nucleus and a very dense cytoplasm with numerous ribosomes, and express keratins 5 and 14 (KRT5/KRT14) [17]–[20].

Upon the commencement of the differentiation process, keratinocytes undergo a replacement of keratins 5 and 14 (KRT5 / KRT14) with 1 and 10 (KRT1 / KRT10), resulting in a loss of adhesiveness, detachment from the basement membrane, and upward movement to form the *stratum spinosum*. This zone contains up to six layers of polyhedral and irregularly spiny cells, which establish strong and robust connections with neighbouring cells by spine-like projections of the cytoplasm and intercellular junctions called desmosomes [19].

Subsequent differentiation gives rise to the *stratum granulosum*, which initiates a gradual cornification process. This zone comprises three to five layers of elongated, rhomboidal, and flattened cells, which are characterized by intracellular keratohyalin granules and lamellar bodies that discharge phospholipids, ceramides, and glycolipids that are important for holding cells together and forming the lipid barrier, which serves to maintain the protective function and waterproofing of the skin [15]. Granular keratinocytes exhibit an increase in protein synthesis and express differentiation markers such as filaggrin (FLG), involucrin (IVL), and

loricrin (LOR) [21]. As one ascends through the layers of this stratum, the cells lose their cytoplasmic organelles, leaving only the desmosomes, which assemble an impermeable cornified envelope [14], [22]. The influence of filaggrin results in the aggregation of keratin filaments and the formation of cross-linked macrofibres, which gradually replace the plasma membrane of the keratinocyte with a lipidic cornified envelope. This process occurs when keratinocytes have undergone the complete differentiation programme and have formed the *stratum corneum* [23].

The outermost layer of the epidermis is the *stratum corneum*, which comprises approximately 15 to 20 layers of dead, flattened, and keratinized cells, devoid of nuclei and cytosolic organelles and now referred to as corneocytes. They are arranged on top of each other in a shingles-like pattern and develop a highly insoluble cornified envelope [24]. Typical markers of terminally differentiated cells are loricrin (LOR) and filaggrin (FLG). Nevertheless, despite this apparent cellular inactivity, numerous chemical processes persist, pre-programmed in the living layers, that play an essential role in the constant renewal process of this layer through the desquamation of superficial corneocytes that are continually shed through the rupture of desmosomes to maintain epidermal homeostasis [25]. This layer plays a crucial role in the maintenance of the epidermal barrier, preventing water loss, protecting against microbial invasion, and shielding other cells and structures from the harmful effects of ultraviolet radiation [26].

The *stratum lucidum* is situated between the stratum granulosum and the stratum corneum and is only observed in specific areas of the body where the epidermis is thicker, such as the palms of the hands or the soles of the feet. This layer is formed by two to three layers of flattened, diaphanous, anucleated keratinocytes, with a cytoplasm filled with a gelatinous substance called eleidin, which is a precursor of keratin. The intermediate keratin filaments are intimately aggregated and oriented parallel to the surface, thereby preventing the entry or exit of water [22].

Although the epidermis is mainly composed of keratinocytes, it also contains other cells that perform essential functions, including melanocytes, Langerhans cells, and Merkel cells [27]. Melanocytes are located in the basal layer and transfer melanin to numerous keratinocytes, which are essential for determining skin colour and providing photoprotection to skin cells [28]. Additionally, Merkel cells are found in the basal layer, where they possess a high density of touch-sensitive areas, including the fingertips and tips. They function as mechanical transducers, converting signals into sensory neurons [29]. Finally, Langerhans cells are found in the spinous layer, where they are involved in antigen presentation and therefore contribute to the immune system of skin [30].

1.1.1.1.- Basement membrane

The basement membrane (BM) is a very thin (approximately 200 nm) [31], and highly specialized and homogeneous extracellular matrix sheet found in various types of tissues, including the skin. The BM in skin is located precisely at the interface between the epidermis and dermis, providing structural support and orchestrating cell behaviour by serving as a platform for intricate signalling between different cell types [32]. BM affects cell signalling not only through direct binding of cell surface receptors, but also via the presentation of growth factors such as [33] fibroblast growth factor 2 (FGF2), transforming growth factor beta 1 (TGFb1),

heparin-binding epidermal growth factor (HB-EGF) and vascular endothelial growth factor (VEGF) [34], [35].

The basement membrane displays a tissue- and organ-specific molecular composition, which is essential for the support of their specific biological functions [33], [36]. In general, BM is a complex structure composed mostly of a mixture of extracellular matrix proteins, including collagen-rich fibres (particularly types IV and XVII) and laminins [37] as is illustrated in Figure 2. In addition to other components, such as proteoglycans (e.g., perlecan) and glycoproteins (e.g., nidogen or fibronectin), among many others [36]. Laminins constitute a family of large heterotrimeric glycoproteins that serve as the central structural component of basement membranes, anchoring cells to the matrix and facilitating signalling between cells and the extracellular environment. Collagens are fibrous proteins that provide tensile strength and elasticity to the matrix. Proteoglycans are large, highly glycosylated molecules that interact with other components of the matrix and regulate the diffusion of nutrients and waste products. Finally, glycoproteins are involved in the processes of cell adhesion and matrix assembly [38].

The BM of the skin is organised into two main layers, the *basal lamina* and the *lamina reticularis* or *dense sublamina* [39]. The underlying connective tissue is attached to the *basal lamina* by collagen VII anchoring fibrils and fibrillin microfibrils [40]. The *basal lamina* layer is further subdivided into two layers, designated the *lamina lucida* and the *lamina densa*. The basal cells are attached to the *lamina densa* by filaments, which are predominantly composed of laminin 5 and BP180. The *lamina densa* is the thickest layer of the BM and consists of an underlying network of collagen IV reticular fibrils, laminins and perlecan heparan sulphate-rich proteoglycans [41]. This lamina provides mechanical stability to the matrix and forms a selective barrier that prevents the diffusion of large molecules and cells. The *lamina lucida* is the outermost layer of the BM, adjacent to the epidermis and consists of laminins, integrins, entactins and dystroglycans. Integrins represent a pivotal component of the hemidesmosomes, which serve to anchor the epithelium to the underlying basement membrane. The *lamina reticularis,* or *dense sublamina,* is a region of the dermis immediately adjacent to the basement membrane that contains connective tissue fibres composed of type III collagen, which are secreted by reticular cells and fibroblasts. These fibres then cross-link to form a fine meshwork, known as reticulin. The *dense sublamina* provides additional support to the basement membrane and is involved in the regulation of cell behaviour and tissue homeostasis [42].

Therefore, disruption of the basement membrane can lead to the development of a number of dermatological conditions, including epidermolysis bullosa, pemphigus and psoriasis.

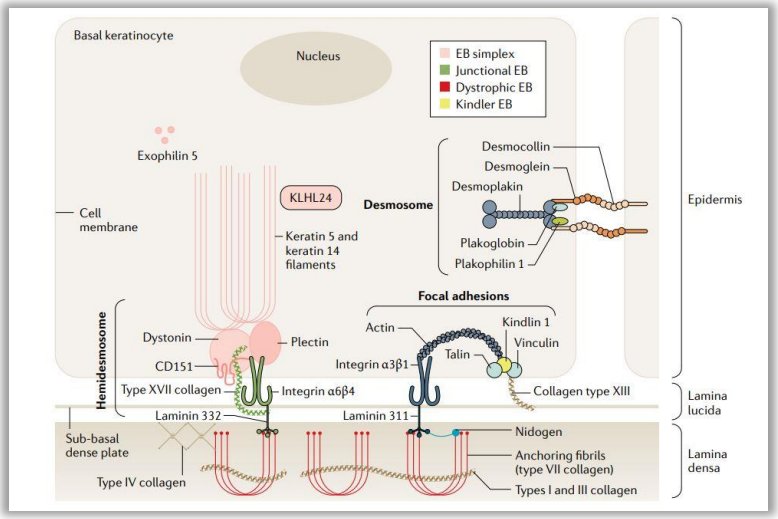

Figure 2: ***Basement membrane and the cutaneous dermal-epidermal junction.*** *Keratins 5 and 14 are produced in basal keratinocytes, which form heterodimers compacted into intermediate filaments that confer resistance through a cytoskeletal network. The intermediate filaments connect to hemidesmosomes, which are asymmetrically located on the basal surface of the keratinocyte, consist of internal and external plaques with various components, including dystonin, plectin, α6β4 integrin and type XVII collagen. KLHL24 is involved in the degradation of keratins. Laminins are glycoproteins composed of α, β and γ chains that bind to integrins in the lamina lucida and lamina densa. Laminin 332 is the principal component of the anchoring filaments of the lamina lucida, binding to integrin α6β4 and integrin α3β1. Type VII collagen forms anchoring fibrils that interact with type IV collagen and further interact with laminins and integrins, integrating into the dermal extracellular matrix. Furthermore, dermal keratinocytes and fibroblasts secrete type VII collagen as a procollagen molecule. Kindlin 1 is a focal adhesion protein that activates integrins. Finally, desmosomes facilitate intercellular junctions, signalling and differentiation. They are composed of cadherins, armadillo proteins and desmoplakin. Reproduced from* [43].

1.1.2.- The dermis

The dermis is the primary structural component of the skin, providing strength, flexibility, elasticity, and adaptability to movement and changes in volume. It is a vascularised connective tissue with a high density of nerve endings that lies between the epidermis and the subcutaneous tissue. The dermis is attached to the epidermis via the basement membrane [15]. This layer is primarily constituted of extracellular matrix (ECM), fibro-elastic content (collagen and elastic fibres), and a multitude of appendages [44]. The extracellular matrix, which contains a high proportion of proteoglycans, due to their great capacity for absorbing water, provides hydration to the skin and influences cell migration, cell adhesion, and cell differentiation. Elastic fibres provide skin elasticity, while collagen provides resistance to skin traction against trauma (mechanical properties). The principal cell of the connective tissue is represented by fibroblasts, which synthesize and release precursors of collagen, elastin, and proteoglycans to construct the extracellular matrix and also link to each other to form a three-dimensional network [45]. Fibroblasts perform a variety of functions, including cell proliferation, cell differentiation, ECM production, and the secretion of cytokines and growth factors [44].

The dermis can be divided according to the arrangement of fibroelastic tissue, dermal cells and extracellular matrix into upper papillary dermis and underlying reticular dermis. The papillary dermis is the layer that connects to the epidermis. It is composed of cell-rich, lax connective tissue, poorly organised collagen type III bundles and blood vessels, and also contains dermal papillae, which are projections into the avascularised epidermis that nourish it. The reticular dermis

is located deeper within the dermis and is thicker than the papillary dermis. It contains less cellular material and consists of very dense connective tissue, where type I collagen fibres form thick bundles interconnected with elastic fibres. The reticular layer also contains the cutaneous appendages, blood and lymphatic vessels and mesh-like bundles of nerves [46], [47].

In addition, the dermis also contains other motile cells with important properties and functions, such as histiocytes (macrophages), dermal dendritic cells (DCs), mast cells, and adipocytes. Table 1 provides a synopsis of the most crucial cells in the various regions of the skin. Histiocytes are a type of macrophages that plays a role in the immune system. Mast cells are inflammatory cells located in the perivascular areas of the dermis that secrete vasoactive and pro-inflammatory mediators, which are involved in the inflammatory response, collagen remodelling, and wound healing. Dermal adipocytes are distinct from those found in the subcutaneous adipose tissue and are responsible for dermal structure insulation, energy storage, hair follicle regeneration, and wound healing [14], [48], [49].

Table 1: Main functions of the different cell types in the skin.

Main functions of the different cell types in the skin			
Cell	**Location(s)**	**Function(s)**	**Activating factors**
Keratinocyte	Epidermis	Mechanical barrier, keratin production, immune function, innate immunity	IFN-γ, infections
Langerhans cell	Epidermis	Antigen-presenting cell, migration and recruitment to the secondary lymphoid organs, and antigenic presentation to T lymphocytes	Infectious and noninfectious antigens
Dermal dendrocyte	Dermis	Antigen-presenting cell, phagocytosis, regulation of collagen synthesis, and homeostasis of the dermis	Infectious and noninfectious antigens
Inflammatory dendritic cell	Dermis Epidermis	Antigen-presenting cell	Microbial and endogenous antigens
Plasma	Dermis	Synthesis and release of antibodies	IL-4, IL-6, IL-10, IFN-γ, BAFF
M1 macrophage	Dermis	Phagocytosis, antigen presentation, bactericidal action	IFN-γ
M2 macrophage	Dermis	Phagocytosis, antigen presentation, regenerative effects	IL-4, IL-13
Mast Cell	Dermis around the vessels	Hypersensitivity reaction, vasodilation, chemotaxis, inflammation	IL-3, IL-5, IL-13
Endothelial cell	Dermis	Inflammation, immune response, infections	IL-1, IL-6, TNF-α
Fibroblast	Dermis	Inflammation, immune response, infections	IL-1, TNF-α

1.1.3.- The hypodermis

The hypodermis, the deepest layer of the skin, is situated between the dermis and the underlying organs. Its thickness varies depending on location, body weight, sex, and age. It is composed of lax connective tissue, and a significant proportion of its fibres are anchored to the dermis, forming attachment points that fix the skin to the underlying structures (*fascia, periosteum, or perichondrium*). Additionally, the hypodermis serves as a conduit for blood vessels and sensory nerves that pass from the underlying tissues to the dermis. It is also the site of origin of hair follicles and sweat glands. Almost the entire hypodermis is capable of storing adipose tissue, which is composed of adipose cells or adipocytes, which perform a number of functions, including protection, isolation, storage, and energy production [50]. Indeed, current studies demonstrate that adipose-derived stem cells facilitate skin

wound healing and immune response, thereby promoting tissue repair and regeneration [51], [52].

1.2.- Relevant skin proteins

In this thesis, we will focus on two proteins found in the different layers of the skin: laminin and elastin. These proteins will be used as the basis for the development of biomaterials with specific functionalities.

1.2.1.- Laminin

Laminin is the most abundant multidomain glycoprotein in the BM and plays a pivotal role in the assembly and maintenance of the BM of skin. It is a heterotrimeric complex, arranged in cross-shaped structure, composed of three different laminin chains, designated α, β and γ. To date, 16 different laminin isoforms have been identified in mammals, which are formed by different combinations of these subunits. Each isoform enables cell-type-specific functions, including adhesion, differentiation, migration and maintenance of phenotype [53], [54].

The N-terminal region of the α-chain comprises three globular domains, separated by three EGF-like repeats while the C-terminal region contains five globular domains, designated the G-domain. In contrast, the N-terminal region of the β- and γ-chains consists of only two globular domains, separated by two EGF-repeats, with no G-domain present in the C-terminal region [54]. The assembly of the α-, β- and γ-chain heterotrimer is cross-linked by covalent disulfide bonds at the centre of the chains and at the C-terminal region. Additionally, non-covalent interactions, such as electrostatic interactions, hydrogen bonds and hydrophobic interactions, leave the three N-terminal regions free resulting in three short arms as is shown in Figure 3A [54]–[56].

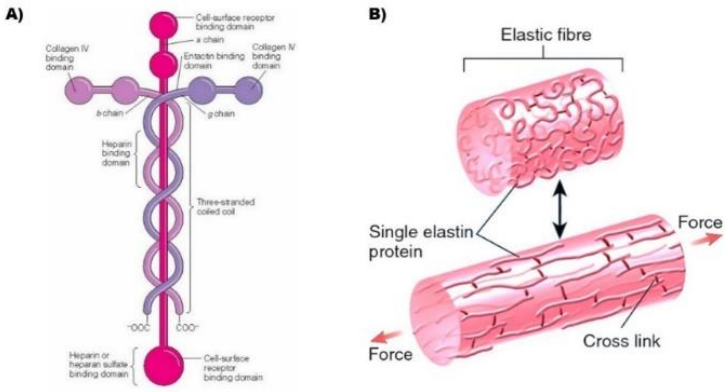

*Figure 3: **Structure of relevant skin proteins**. **A)** General structure of laminin, which is a heterotrimeric complex, arranged in a cross-shaped structure, composed of three different laminin chains, designated α, β and γ. **B)** General structure of elastin. In the absence of a tensile force, the elastin proteins exist in a compact conformation. However, when subjected to a stretching force, the elastin proteins elongate but remain attached to each other via cross-links. Reproduced from Pearson Education 2005.*

In this way, laminins have binding sites for other extracellular matrix molecules, such as collagen IV and heparan sulphate proteoglycans, in the N-terminal region forming a network of cross-linked filaments, and in turn can bind to

cellular transmembrane receptors, such as integrins and dystroglycan, through the G domain of the C-terminal region, anchoring the basement membrane to the underlying tissue and triggering signalling pathways that regulate cell adhesion, migration and proliferation. Consequently, the binding of laminin to these molecules and receptors is of critical importance for the assembly, signalling and maintenance of the skin basement membrane [55], [56].

In the basement membrane of the skin, the laminin-332 isoform (formerly known as laminin-5) is of particular importance as the main component of the anchoring filaments that bind the epidermis to the dermis. Laminin-332 is produced by basal keratinocytes and secreted into the extracellular space, where it binds to cell surface receptors, such as integrins and dystroglycans, on adjacent cells. It forms a network of cross-linked filaments that interconnect with type IV collagen and other extracellular matrix molecules, thereby providing a stable and elastic scaffold for the skin. Laminin-332 also promotes cell adhesion, migration and proliferation by activating various signalling pathways and interacts with growth factors, such as epidermal growth factor (EGF) and hepatocyte growth factor (HGF) [54], [55].

Biologically active regions of laminin have been identified based on the activity of synthetic peptides corresponding to sequences of the protein that promote cell adhesion, migration and angiogenesis. Some of these active peptides recognized various cellular receptors, including integrins and syndecans, and have the potential to serve as bioadhesives or as biomaterials for tissue engineering. In this thesis, laminin mimetic peptides, AASIKVAVSADR and PPFMLLKGSTR, were selected for use as peptides that support the wound healing process. On the one hand, the AASIKVAVSADR peptide is present in the globular region of the long alpha chain of laminin 1. This sequence has been shown to promote diverse functions, including cell adhesion, neurite outgrowth, angiogenesis, collagenase IV production (a key enzyme in basement membrane degradation) and tumour metastasis. These mimetic peptides form a β-sheet and assemble into amyloid-like fibrils. Fibril formation is essential for the biological activities of these peptides, including the promotion of cell adhesion and neurite outgrowth [57], [58]. The IKVAV sequence displays an integrin-specific response and binds with α3β1, α4β1 and α6β1 integrins to assist cell propagation, differentiation and migration [59], [60]. The activity of the IKVAV sequence is dependent on the peptide conformation and the inversion of the sequence (VAVKI) results in the loss of IKVAV activity [61]. This AASIKVAVSADR peptide has been demonstrated to enhance endothelial cell motility, capillary branching and vessel formation, thereby promoting angiogenesis, a process essential for tissue healing [62]. Covertly, the peptide PPFMLLKGSTR is present in the globular domain of the α3 chain of laminin 5. This sequence regulates a number of cellular functions including cell adhesion, spreading and motility [63]. Laminin-5 regulates the stable adhesion of epithelium to underlying connective tissue [64], as well as influencing cell behaviour through interactions with cell surface receptors such as α3β1 and α6β4 integrins [64]–[66]. Among the integrins expressed in normal human keratinocytes, integrin α3β1 is involved in the formation of focal adhesions, which are associated with actin-containing stress fibres and the mediation of keratinocyte motility, thereby promoting wound healing by accelerating re-epithelialisation [67], [68]. The α6β4 integrin forms the structure of the hemidesmosome of epithelial cells, mediating epithelial cell adhesion,

migration and wound healing, and is also involved in carcinoma cell invasion [69], [70]. The active peptide PPFLMLLKGSTR has been tested on full-thickness wounds in rats and rabbits, and it was observed that its use significantly promoted wound healing by accelerating re-epithelialisation, markedly reducing inflammatory cell infiltration and enhancing fibroblast proliferation [71].

1.2.2.- Elastin

Elastin is a structurally and functionally significant component of the extracellular matrix. It is a fibrous, insoluble, hydrophobic and extensively cross-linked protein of approximately 66 kDa, found in vertebrate tissues. Elastin fulfils a number of functions, including providing elasticity and strength to tissues and organs, and it is particularly abundant in those that require repetitive and reversible deformation, such as blood vessels, ligaments, lungs and skin [72]–[76]. The abundance of elastin in the ECM is tailored to the specific tissue type and biomechanical requirements of each tissue. Furthermore, the distribution of elastin within a single organ can be heterogeneous [73].

The functionality of elastin within the body is governed by several biophysical properties, including glass transition [77], coacervation [78] and most significantly, elasticity [79], [80]. In fact, this elasticity is due to the predominantly composed of hydrophobic domains with valine, glycine and proline residues, which have the ability to deform without rupture in response to mechanical stresses and return to their original state once the force has disappeared. This elastic stretching process occurs without any loss of energy, which means that it is entropic [81], considering that all the energy required by the backbone can be recovered upon relaxation [82].

Elastic fibres are mainly composed by elastin, which confers upon the skin the capacity to stretch, resilience and elasticity [83], [84] as is illustrated in Figure 3B. However, other components are also required for the formation of functional fibres, including microfibrillar proteins (fibrillins), binding proteins (fibulins, elastin microfibril interfaces (EMILIN), microfibril-associated glycoproteins (MAGPs)) and soluble factors (e.g., transforming growth factor (β-TFG) [85], [86]. Furthermore, a fibronectin network is required for the assembly of fibrillins and, consequently, microfibrils, which provides a microenvironment that controls tropoelastin/elastin arrangement and cross-linking processes [87]. In addition, the interweaving of collagen fibrils with the elastin fibres is also necessary to limit the amount of deformation and thus prevent laceration or plastic and irreparable deformation of the tissue. This mechanism of producing functional elastic fibres is a complex process that requires a defined number of controlled spatio-temporal steps. This process is referred to as elastogenesis [86], [88]–[91]. Elastic fibres are present in the dermal layer, oriented both perpendicular and parallel to the skin surface, forming an intricate network and playing a key role in maintaining skin homeostasis [92]. Furthermore, the composition of elastic fibres differs in different layers of the skin, varying in thickness, orientation and relative composition of elastin, fibrin and other molecules [83].

Elastin production declines with age and is not easily regenerated when a tissue is damaged. For this reason, strategies to regenerate tissue often involve the use of exogenous elastin or the promotion of endogenous elastin production with the aim of replicating the composition, architecture and function of native tissues [93].

Loss or damage to the elastic fibre network has a negative effect on the wound healing process and can worsen the structure and appearance of scars and stretch marks by developing atrophic (depressed), hypertrophic (raised) and keloid (overgrown) scars. The result of these processes is the formation of scar tissue, which is characterised by the deposition of large amounts of collagen in abnormally arranged, often large bundles, making this new tissue less elastic than the original tissue. It is therefore of great importance to identify methods of restoring elastic fibres and elastin, as this could lead to improvements in the appearance, texture, elasticity and healing ability of injured skin. A plethora of treatments have been developed to enhance collagen and hyaluronic acid levels in damaged skin. However, there are only a few established treatments that aim to increase elastin production[94]–[97].

1.2.3.- Tropoelastin

The formation of native human elastin is a complex process involving the interaction of several molecules of its soluble precursor, tropoelastin. This process culminates in the formation of the amorphous component of elastic fibres. Tropoelastin is one of the most elastic proteins known, with a molecular weight of approximately 60-70 kDa, and is secreted by a variety of cells, including smooth muscle cells, endothelial cells, fibroblasts and chondrocytes [98]–[100]. In addition, it can exist as a monomer in solution in two different arrangements: an open globular molecule and a distended polypeptide [101]. It is composed of alternating repetitive hydrophobic domains of variable length (elastomeric domains) and hydrophilic domains for cross-linking [86], [102], [103]. These hydrophobic domains are composed of the repetition of non-polar amino acids such as valine (V), glycine (G) and proline (P) arranged in repetitive motifs, such as VPG, VPGG, VPGVG, IPGVG, VAPGVG, being the pentapeptide VPGVG the most commonly found. Alternatively, hydrophilic regions, which are well characterised by their high lysine and alanine content, have been identified [86], [102].

Tropoelastin formation is characterized by both intramolecular and intermolecular cross-linking, with mechanical deformation of the elastin network storing energy, thereby conferring elastomeric properties. The process of elastogenesis occurs when elastogenic cells, such as fibroblasts, secrete tropoelastin into the extracellular space. This tropoelastin then undergoes self-aggregation at the cell surface interstice through a colloidal phase separation called coacervation [90], [91], [104], [105]. During this process, hydrophobic regions of tropoelastin begin to interact, giving rise to non-covalent associations, which then form insoluble three-dimensional spherules that facilitate the subsequent cross-linking process [106]. Subsequently, these globular aggregates of tropoelastin are then transferred to the

aligned microfibrillar templates found in the intercellular space [88], [107]. Finally, these molecules are covalently cross-linked by the action of the lysyl oxidase (LOX) enzyme [108]. The entire process is summarised in Figure 4. The consolidation of this structure is achieved by the repetition of these steps, which culminates in the maturation of the elastic fibres [82], [109].

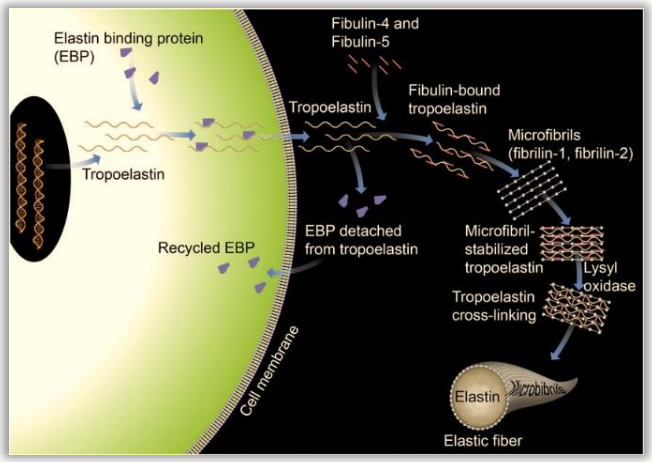

*Figure 4: **Elastogenesis**. Tropoelastin synthesis, binding with elastin-binding protein (EBP), transport, release of EBP, assembly with fibulins, binding to microfibrils, lysyl oxidase-mediated cross-linking, and final formation of an elastic fibre with microfibrils. Reproduced from* [110].

Although the normal tendency of physical systems is for order states to increase with decreasing temperature, tropoelastin coacervation functions in a completely opposite manner, and can be explained by the effect of water on the tropoelastin molecule [104].

At temperatures below the physiological range, tropoelastin remains unfolded in aqueous solutions, exhibiting a disordered conformation with extended random coils, where the hydrophobic side chains are fully hydrated, surrounded by ordered water molecules called clathrate-like water structures that solvate them by hydrophobic hydration, preventing their self-aggregation and making the protein soluble in aqueous solvents [111]. Although the hydrophobic regions remain preferentially hidden from the aqueous phase and the number of non-polar interactions is tripled in the coacervate, the formation of water-excluding cores and secondary structures is prevented by the characteristic glycine and proline content. The rigid proline residues confer conformational restrictions that prevent the formation of stable secondary structures such as β-turns and β-sheets. Conversely, glycine residues introduce flexibility and facilitate hydrogen bond interactions with water. These characteristics lead to the classification of tropoelastin as an intrinsically disordered protein (IDP), which is responsible for conferring the elasticity and high flexibility observed at the supramolecular scale [112].

However, as the temperature increases towards the physiological range, the clathrate configuration is destroyed, releasing the hydrophobic domains to interact with each other, forming aggregates and giving rise to a cloudy solution at the macroscale level. A change in the conformation of the tropoelastin from random coils to β-spiral structures is observed. This process is thermodynamically

controlled and can be reversed by cooling the solution [113]. The observed behaviour of full-length tropoelastin is therefore transferred to smaller elastin mimetic proteins when they are designed to follow the same hydrophobic assembly. Consequently, the reverse transition is known as Inverse Temperature Transition (ITT) [114], [115], and the temperature at which it occurs is referred to as the transition temperature (T_t). Upon exceeding the T_t, a phase transition from a soluble, water-rich phase to an insoluble, polypeptide-rich phase is observed [115].

Skin injury can trigger a rapid reactivation of tropoelastin production, which is influenced by a variety of soluble factors, in particular insulin-like growth factor-1, tumour necrosis factor-α, interleukin-1β and TGF-β, and is important for wound healing [78], [86], [116]. Elastin fragments generated during the process of injury and wound healing are released into the ECM by proteases and act as biologically active ligands, supporting the induction of biological responses in a variety of cell types [117]. These biological responses include monocyte chemotaxis [118], keratinocyte migration [119], fibroblast proliferation and migration, smooth muscle proliferation [120], promotion of an angiogenic phenotype in endothelial cells [121] and regulation of protease release [117], [122]. Furthermore, elastin peptides may also influence calcium transport [123], ECM production [124] and cell survival [125]. Given that elastin regulates and modifies cellular activity, its involvement in the later stages of adult wound healing is particularly important. Thus, dermal fibroblasts bind to tropoelastin and interact with elastin peptides, thereby influencing their cellular behaviour [84], [126]. In addition, although elastin is not present in the epidermal BM, it influences the differentiation and migration of keratinocytes, which is essential for the stratified re-epithelialisation of the epidermis [84], [119]. Furthermore, elastin also influences the process of angiogenesis by promoting endothelial migration and the expression of MMP-1, a vital process in the reparative phase of granulation tissue and cell migration and proliferation [127].

Despite the increased expression of elastin at the onset of injury, it is not detected in the dermis until many months after the initial stages of the healing process. Indeed, elastic fibres are the last to form in reduced quantities within the extracellular matrix [128], [129]. Elastin plays a crucial role in the process of wound healing, not only providing mechanical elasticity but also exerting a regulatory influence on cells, thereby gradually reducing wound contraction and facilitating dermal regeneration [84]. The production of elastin during the healing process indicates that it plays an important role in the formation of scar tissue and the flexibility of newly formed skin. However, the exact mechanisms of these processes remain to be fully elucidated. On the one hand, elastin contributes to scar-free recovery during the healing of fetal wounds from mid-gestation onwards, when the elastic fibre network is still developing. This fully restores skin architecture and tissue integrity, suggesting the importance of elastin in this process [84], [130]. Conversely, in the case of adult healing, scars exhibit reduced elastin content and a fragmented elastic fibre network, as well as disorganised collagen bundles, which contribute to the reduced physical properties of scars compared to uninjured skin [94]. Elastin has inherent properties that are beneficial in adult wound healing, such

as its capacity to regress and resist, induce cellular activity (including cell migration and proliferation), extracellular matrix synthesis and protease production, making it a desirable substance in this process. The effects of elastin, both in terms of its physical properties and cell signalling, are analogous to the innate non-scarring properties of fetal wound healing, hence its importance in the development of elastin-based biomaterials for use in skin regeneration to enable scarless healing [131].

1.3.- The physiology of normal skin wound healing process

As the skin is the most important protective barrier in the body and performs critical functions, any loss in its integrity due to injury or disease can result in a major physiological imbalance and ultimately in significant disability or even death. In such cases, rapid and effective restoration is required, but often results in scar formation [132]. For this reason, wound healing is one of the most complex and vital biological processes in the human body, consisting of the correct repair of wounds, which allows the reconstruction of the stratified epithelium (the epidermis), the dermoepidermal junction, the dermis and its vascularisation. This dynamic process involves many different cell types that must work in coordination to achieve healing [133]. The cell types and biological processes most relevant to each stage are depicted in Figure 5 and will be elucidated in more detail in this section.

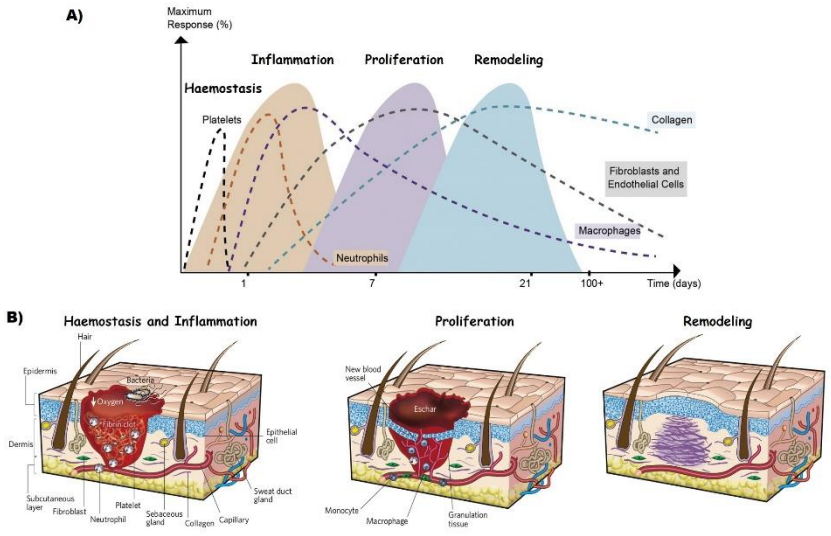

Figure 5: ***Physiology of normal skin wound healing process. A)*** *Schematic diagram of the normal wound healing process, indicating the timing of each stage and the predominant cells in each phase. Adapted from* [134]. ***B)*** *The four stages of wound repair are haemostasis and inflammation, new tissue formation (proliferation) and remodelling. The inflammatory phase, which lasts up to 48 hours, features a hypoxic environment with a fibrin clot, bacteria, neutrophils and platelets. The proliferative phase, which lasts between two and ten days, is characterised by the formation of an eschar, cell migration and the formation of new blood vessels. The final stage of wound repair, remodelling, occurs over a period of 1-12 months. This stage involves fibroblasts laying disorganized collagen, wound contraction, and a re-epithelialized surface lacking normal skin appendages. Adapted from* [135].

In healthy people, surgical wounds, traumatic injuries or burns typically heal in a timely manner [136]. The normal wound healing process is characterised by four sequential but overlapping stages: (1) haemostasis or immediate response, (2) inflammation, (3) proliferation for the formation of new tissue, and (4) remodelling [133], [137], [138].

1.3.1.- The haemostatic phase

In the event of a skin injury that damages the epidermal and dermal layers of the skin, the underlying tissue where the blood vessels are located is exposed, resulting in an outflow of blood from the tissue. Following the injury, haemostasis occurs within several minutes, whereby vascular smooth muscle cells contract rapidly to reduce blood flow and a clot rich in fibrin, vitronectin and fibronectin is formed from platelets and clotting cascade factors to temporarily close the wound and stop bleeding [137], [139]. The fibrin clot also serves as a temporary migration scaffold for other cells and as a source of chemotactic signals by releasing growth factors and other signalling molecules [140], [141]. During the process of haemostasis activated platelets release a wide range of cytokines and growth factors, including platelet-derived growth factor (PDGF), epidermal growth factor (EGF) and transforming growth factor-β (TGF-β) that act as signalling molecules to recruit neutrophils, macrophages, endothelial cells and fibroblasts [142]–[144]. Consequently, the sequence of events that occur during platelet activation and clot formation provides the transition to the subsequent phase of healing.

1.3.2.- The inflammatory phase

The inflammatory stage, which is initiated within hours of the wound being inflicted, is characterised by the arrival of neutrophils, the first immune cells to reach the wound site following haemostasis. Several chemokines produced during the coagulation process attract neutrophils from the circulation by inducing the expression of adhesion molecules on endothelial cells [145]. Neutrophils play a key role in the protection of the wound from external factors such as bacteria and foreign bodies. This is achieved through the phagocytosis of these agents by neutrophils, which releases toxic granules containing specific antimicrobial agents, including proteases, matrix metalloproteinases (MMPs) and collagenases. Furthermore, they degrade damaged matrix proteins and release secretory vesicles that express integrins, growth factors and cytokines, which amplify the inflammatory response [142], [146]. Thus, approximately three to five days after the neutrophils have performed their functions, they undergo apoptosis, and monocytes arrive at the wound site, eliminating tissue debris and destroying the remaining neutrophils [145], [147]. Monocytes differentiate into macrophages. During the initial stages of healing, macrophages exhibit a pro-inflammatory M1 phenotype and express tumour necrosis factor alpha (TNF-α), interleukin 1-beta (IL-1β) and interleukin-6 (IL-6). M1 macrophages are also microbicidal and secrete MMPs, which enable them to digest ECM and assist in cell migration [148]. With the removal of neutrophils and a reduction in inflammation, macrophages turn to an anti-

inflammatory M2 phenotype [149]. M2 macrophages secrete a range of growth factors, including endothelial growth factors (VEGF), which are important for the promotion of neovascularisation, re-epithelialisation and fibroblast migration [150], [151].

Consequently, the inflammatory phase is absolutely beneficial for the healing process. However, a lack of adequate levels of immune response or prolonged activation of the inflammatory phase could impede the progression to the next proliferation phase thereby affecting the wound healing process [145]. Thus, persistent hyperinflammation represents a distinctive pathophysiological characteristic of chronic wounds, and macrophage malfunction is considered an important contributor to it [152], [153].

1.3.3.- The growth phase

Approximately three to ten days following the injury, healing process enters the proliferative phase. During this phase, cellular activity is predominant to initiate wound regeneration. This is characterised by re-epithelialisation, restoration of the vascular system (angiogenesis) and formation of granulation tissue (fibroplasia) [142], [154].

1.3.3.1.- Angiogenesis

The restoration of the blood vessel network is crucial for supplying nutrients and oxygen to the damaged area and for the efficient healing of wounds. Angiogenesis refers to the growth of new vessels by the budding of pre-existing vessels adjacent to the wound. In response to injury, microvascular endothelial cells initiate an angiogenic process that involves the activation of endothelial cells (ECs) lining the blood vessels that receive signals from the hypoxic wound environment, including PDGF, VEGF, TGF-β and fibroblast growth factor-2 (FGF2) [144]. Once activated, ECs degrade the ECM and basement membrane, proliferate, migrate and form new cell-cell junctions before branching to form new capillaries. The newly formed vessels participate in the development of granulation tissue and provide nutrition and oxygen to emerging tissues. During angiogenesis, endothelial cells also secrete and release growth factors and cytokines useful for the wound healing process [155]–[157].

1.3.3.2.- Fibroplasia

Dermal reconstitution is initiated approximately three to four days after injury. This stage is characterised by the formation of granulation tissue, which is a wound-specific connective tissue that collectively includes macrophages, dermal fibroblasts, nascent endothelium, as well as collagen matrix, fibrinogen and fibronectin, all referred to as fibroplasia [158]. The provisional extracellular matrix formed by the fibrin clot during the homeostatic phase is replaced by the formation of granulation tissue, which provides scaffolding and contact guidance for cells to migrate into the internal spaces of the wound and for angiogenesis to occur.

Fibroplasia is an effort to replace wounded dermal tissue and is described as a process of fibroblast proliferation, migration to the wound fibrin clot and production of new collagen and other matrix proteins, which contribute to the formation of granulation tissue. The migration and proliferation of dermal fibroblasts are facilitated by several growth factors, such as PDGF secreted by inflammatory cells [136].

1.3.3.3.- Re-epithelialisation

Re-epithelialisation is the process of restoration of the broken epidermis after injury to the skin. In this third phase, following extrinsic signals from the ECM, growth factors and surrounding cells, the epidermal keratinocytes commence migration from the wound edges inwards and subsequently proliferate to invade the wound. In order for this to occur, integrins and actin filaments must be reorganised beforehand. Migrating keratinocytes secrete high levels of MMPs, which facilitate their migration through the fibrin plug and the granulation tissue. Subsequently, the basement membrane zone, which connects the epidermis to the underlying dermis, have to be restored. Finally, the neoepithelium must to differentiate into a stratified epidermis [133]. In the initial stages of the growth phase, keratinocytes produce IL-1 and TNF-α, which stimulate fibroblasts to release factors, such as TGF, EGF, FGF and connective tissue growth factor (CTGF), needed for keratinocyte migration and proliferation. In the later stages of repair, activated fibroblasts provide the TGF-β necessary for the reversion of keratinocytes to a basal state and the cessation of proliferation. These findings have reinforced the idea that an efficient communication between keratinocytes and fibroblasts is important for a balanced wound closure [159].

1.3.3.4.- Wound contraction

Upon reaching the wound site, dermal fibroblasts, in the presence of transforming growth factor-β (TGF-β), bind to fibrous proteins in the extracellular matrix, thereby undergoing a differentiation process that results in the formation of contractile myofibroblasts. The principal source of myofibroblasts originates from local fibroblasts in the uninjured dermis and subcutaneous tissue, which migrate to the centre of the wound [160]. From day 6 onwards, activated myofibroblasts overexpress markers of smooth muscle differentiation such as β- and γ-cytoplasmic actins, as well as α-smooth muscle actin (α-SMA) or smooth muscle myosin and desmin to establish a contractile force that pulls the wound margins together until reaching a maximum on day 15, after which it starts to progressively recede [161]. The extracellular matrix (comprising collagen, hyaluronan, proteoglycans, etc.) produced by fibroblasts replaces the provisional matrix formed by platelets. This collagen matrix serves as the foundation for the migration of additional fibroblasts and contributes to the contraction of the wound by attempting to pull the wound edges together [158], [162]. As the new collagen matrix accumulates, neovascularisation is reduced, and as healing progresses, granulation tissue matures to form a scar [163], [164].

By contraction, the surface area of the wound is diminished, thereby reducing the efforts required for re-epithelialization. Wound contraction commences shortly after wounding and reaches a maximum peak at two weeks, after which it will continue until the final stages of the remodelling phase. The degree of wound contraction depends mainly on the depth of the wound. In the case of full-thickness wounds, contraction can result in a reduction of up to 40 % in wound size [165].

1.3.4.- The remodelling phase

The final stage of the healing process is remodelling, also referred to as the maturation phase, which aims to restore the epidermis, dermis and extracellular matrix to the original functionality of the tissue. Due to the complexity of the process, this stage can last for extended periods of time, ranging from months to years, depending on the size and type of wound [139].

At the end of the proliferation phase, angiogenesis and cell proliferation exhibit a gradual decline, ultimately reaching a plateau and finally ceasing [139]. Provisional granulation tissue synthesized in the proliferative phase, which is rich in type III collagen and blood vessels, is gradually degraded by metalloproteinases and subsequently replaced by a collagen scar predominantly of type I collagen, the major component of the ECM prior to injury. The newly secreted collagen I has a higher tensile strength than the initially secreted collagen III and thus helps to retain the hardness and texture of the wound after healing [145], [166], [167]. Macrophages participate in this phase by removing dead cells and ECM debris [168]. Consequently, during this period, the granulation tissue is gradually reduced, while the epidermis, dermal vasculature and myofibres are remodelled into fully functional tissue. Therefore, it is essential to maintain a precise equilibrium between the degradation and synthesis of matrix components for the successful remodelling of wounds. As the wound heals, excess fibroblasts, macrophages and endothelial cells undergo apoptosis followed by a decrease in blood flow to the wound. The remaining granulation tissue eventually matures into scar tissue, thereby completing the wound healing process. It is important that all these processes are precisely regulated to prevent the proliferation of cells and the overproduction of tissue, which could result in the formation of fibrotic scars, hypertrophic scars, or keloids [133], [169].

1.4.- Complications of skin wound repair - Chronic wounds -

1.4.1.- Scar formation

The process of skin regeneration is intricate, yet despite the involvement of a multitude of cell types in the wound healing cascade, skin injuries frequently result in the formation of scar tissue that is deficient in functionality and fails to restore all components. The aforementioned scar tissue is characterised by an excess of ECM

and the absence of skin appendages, such as hair follicles, sweat glands, and skin fat [170]. In addition, scar tissue shows altered biomechanical properties, such as reduced elasticity [171]. The main producers of scar tissue are myofibroblasts which, given their rapid proliferation and willingness to produce ECM, are able to produce a large amount of tissue in a short time, although this tissue is not of adequate quality similar to intact skin. Therefore, it is important during the final phase of wound healing that the ECM is remodelled, i.e., type III collagen is replaced by type I collagen and elastin, which confers elasticity to the skin and that myofibroblasts undergo apoptosis in due time. Delayed myofibroblast apoptosis may be one of the driving factors for excessive scarring to occur [172], [173].

1.4.2.- Chronic wounds

The healing of acute wounds occurs within a period of 8 to 12 weeks following the initial injury. However, any disruption in the normal wound healing process will result in the formation of chronic wounds. Difficult-to-heal wounds or chronic wounds are characterised as skin wounds that do not heal completely within a reasonable period of time (usually more than 12 weeks), as illustrated in Figure 6A. Furthermore, these injuries do not undergo an orderly and timely progression through the different phases of the normal regeneration process to regain full structure and function [174]–[176].

The development of chronic wounds can be attributed to a multitude of factors, including chronic diseases, advanced age, an unhealthy lifestyle, repeated trauma to the same area, and medications or infections. However, the three most significant and prevalent factors are diabetes mellitus (diabetic ulcer, DU), vascular insufficiency (venous/arterial ulcer, VU/AU), and local mechanical pressure (pressure ulcer, PU), which is caused by an inadequate blood supply due to prolonged pressure on the skin, often occurring in wheelchair-bound or bedridden elderly individuals [177]. Table 2 provides a comprehensive overview of the most prevalent chronic wounds, accompanied by a detailed description of their associated symptoms and risk factors. Figure 6C offers a visual representation of various types of impaired chronic wounds. The incidence of chronic wounds has increased as a consequence of an ageing population, changes in lifestyle and dietary habits, and the prevalence of diabetes and cardiovascular disease [178]. The lack of effective treatment for chronic wounds results in a significant healthcare and economic burden. These wounds can result in chronic pain, recurrent infections, or disability, which in turn leads to a decrease in the quality of life of patients. The high rate of amputation and even mortality associated with these wounds is a further concern [179].

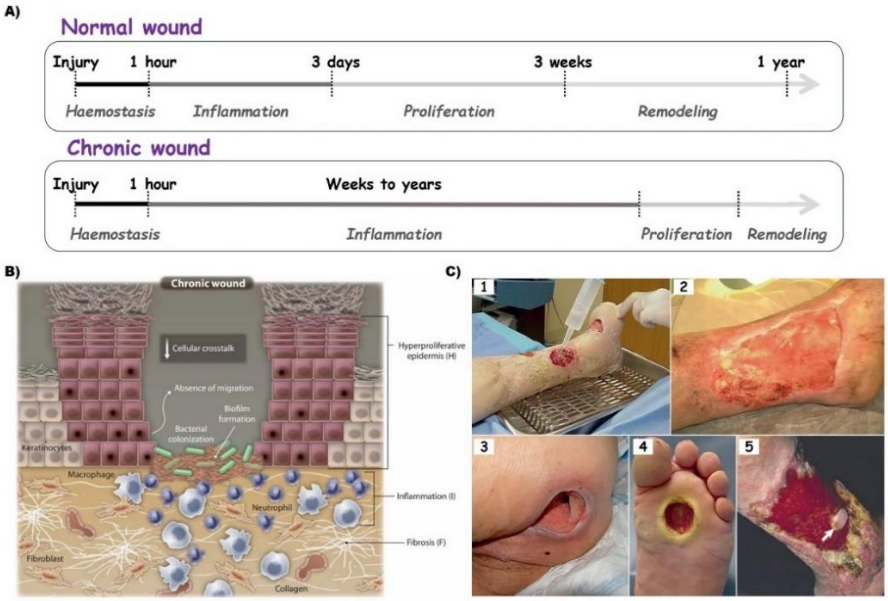

Figure 6: ***Chronic wounds****.* ***A)*** *Phases and timing of healing in a normal wound and in a chronic wound.* ***B)*** *The impairment of molecular and cellular mechanisms in chronic wounds. Chronic wounds exhibit hyperproliferative and nonmigratory epidermis, unresolved inflammation, infection, and biofilm formation. Inflammatory cells (neutrophils and macrophages) are increased but dysfunctional, with uncontrolled proteases interfering with the repair mechanisms. There is reduced angiogenesis, stem cell recruitment, and ECM remodelling compared to normal wound healing. Reproduced from* [180]. ***C)*** *Representative clinical photographs of typical chronic wounds:* ***1)*** *Diabetic ulceration due to both neuropathy and arterial insufficiency,* ***2)*** *Venous ulcer,* ***3)*** *Deep pressure (decubitus) ulcer in the sacral area,* ***4)*** *Neuropathic diabetic ulcer on the sole of a patient with diabetes, and* ***5)*** *Extensive ulceration of the lower leg due to combined venous and lymphatic disease. Adapted from* [181].

Table 2: The most prevalent chronic wounds encountered in clinical wound therapy. Adapted from [181].

The most prevalent chronic wounds			
Type of ulcer	**Description**	**Risks factors**	**Symptoms**
Diabetic ulcers	Diabetic foot ulcers represent a major complication of diabetes mellitus. The most common cause is uncontrolled blood glucose (sugar) over a prolonged period of time. Two other disorders, diabetic neuropathy and peripheral vascular disease, can also contribute to the formation of ulcers.	• Uncontrolled blood sugar levels • Diabetic peripheral neuropathy • Peripheral vascular disease	Diabetic ulcers typically manifest on the foot in areas subjected to trauma or bearing weight. The wound bed is frequently characterised by a lack of moisture and the presence of necrotic tissue or an unpleasant odour. This kind of ulcer may be a small wound area on the surface, but it can also be an underlying abscess. The surrounding skin is frequently characterised by hyperkeratosis. These ulcers are generally painless due to altered sensation or neuropathy.
Venous ulcers	Venous ulcers are a consequence of venous insufficiency. Damaged valves permit blood to accumulate in the vein, and as the vein becomes overfilled, blood may leak out into the surrounding tissue, resulting in a tissue breakdown and the development of a skin ulcer. Venous ulcers are most commonly observed on the lateral aspects of the lower extremity, extending from the ankle to the knee.	• Deep vein thrombosis • Obesity or poor nutrition • Pregnancies • A family history of varicose veins • Smoking and excessive alcohol use • The lack of physical activity • Aging • Work that requires prolonged standing	The initial indication of a venous skin ulcer is the appearance of skin that has turned dark red or purple in colour over the area where blood is leaking from the vein. The wound bed is often characterized by a pronounced redness and may exhibit a tendency to bleed. It is possible that the ulcer may be painful. Additionally, necrotic tissue, slough (yellow, tan, grey, green, or black), and/or eschar (tan, brown, or black) may be present. Additionally, the skin may become thick, dry, and itchy. Venous ulcers are frequently slow to heal and often necessitate lifelong modifications to prevent re-development.
Arterial ulcers	Arterial ulcers are the result of a complete or partial blockage in the arteries. Atherosclerosis is almost invariably the underlying cause. In this pathological process, cholesterol or other fatty plaques accumulate within the arteries, resulting in the obstruction that impair blood circulation. This inadequate blood flow results in tissue necrosis and the formation of ulcers.	• Trauma • Limited joint mobility • Increased age • Diabetes mellitus • High blood pressure • Arteriosclerosis • Peripheral vascular disease	Wounds frequently exhibit minimal drainage and are often associated with considerable pain. The sensation of pain is alleviated by the application of dangling legs, and is intensified when the legs are elevated.
Pressure ulcers	Pressure ulcers occur in individuals with conditions that limit or inhibit the movement of body parts that are commonly subjected to pressure, such as the sacrum and heels. A pressure ulcer is defined as an area of skin that deteriorates when the skin is exposed to prolonged pressure. This prolonged and unrelieved pressure impairs blood flow to the area, resulting in tissue damage or death.	• Patients confined to wheelchair or bed • Increased age • Mental or physical deficits that affect their ability to move • Chronic conditions that prevent areas of the body from receiving proper blood flow • Fragile skin (patient under steroidal therapy), urinary or faecal incontinence • Malnutrition	A pressure ulcer typically begins as a reddened area of the skin. If the underlying pressure is not relieved, the ulcer will progress to a blister, then an open sore, and finally a deep crater. This deterioration may occur with considerable rapidity. The most common locations for pressure ulcers to develop are over bones in close proximity to the skin, including the sacrum, heels, elbows, hips, ankles, shoulders, back, and the back of the head. Pressure sores are categorized from stage I (earliest signs) to stage IV (most severe) according to their severity and the treatments depend on the wound stage.

1.4.3.- Pathophysiology of chronic wounds

The pathophysiology of chronic wounds is highly intricate and the underlying mechanisms remain poorly understood. Chronic wound healing can be impaired at any stage, exhibiting a non-linear progression of the normal stages of healing and thus impeding the recovery of anatomical integrity and functionality [177]. A number of factors have been identified that can affect normal wound healing and may promote the development of chronic wounds such as persistent inflammation [182], infection by pathogenic bacteria, the existence of hyperproliferative but non-migratory keratinocytes and senescent fibroblasts, decreased growth factors, altered angiogenesis, excess proteolytic enzymes and reactive oxygen species (ROS) leading to oxidative stress [183].

1.4.3.1.- Persistent and excessive inflammation

A wound that remains in the inflammatory phase and does not progress to the other phases becomes a chronic wound [184], [185]. Chronic inflammation, a defining feature of non-healing wounds, can lead to a number of other potential complications, including infection, necrosis or sepsis, as illustrated in Figure 6B. Furthermore, it predisposes the affected tissue to develop cancer [170], [186], [187]. During the inflammation phase, an immune response is initiated to facilitate the clearance of microorganisms and damaged tissues from the injured area. In chronic wounds, the excessive and exaggerated cellular infiltration of neutrophils and M1 macrophages results in a delayed healing process as they release persistent inflammatory chemicals such as pro-inflammatory cytokines (TNF-α and IL1β) that delay normal healing. Indeed, it has been demonstrated that an inflammatory phase that is excessively prolonged not only restricts regenerative potential but also increases scar formation [182]. Similarly, the absence of transition from M1 to M2 macrophages is a significant factor in the pathogenesis of chronic wounds, as M2 macrophages are essential for the killing of neutrophils, the resolution of inflammation and the initiation of the subsequent proliferative phase [145]. Finally, elevated levels of MMPs result in the continuous ECM degradation, impairing cell migration and releasing oxygen free radicals that further damage tissue [148].

1.4.3.2.- Infection

Open wounds are frequently colonised by microorganisms, including bacteria, viruses and fungi. However, such colonisation rarely results in a serious infection. The polymicrobial presence in chronic wounds has been the subject of extensive study and it has been demonstrated that the bioburden, including microbial diversity, microbial load and the presence of pathogenic microorganisms, plays a key role in poor wound healing even in the absence of clinical infection [188]. The most common bacteria that colonise and reproduce within the wound bed are *Staphylococcus aureus*, *Pseudomonas aeruginosa* and *Enterococcus faecalis*. In addition, an elevated bacterial load contributes to the accumulation of pro-inflammatory cells, thereby prolonging inflammation and impairing wound healing. During the inflammatory phase, microbes are expected to be eliminated through the

immune response. However, pathogenic bacteria aggregate into thick biofilms, which promotes their adherence to the wound and hinders the immune response of the host or antibiotic treatment, leading to chronic inflammation. Furthermore, some bacteria are capable of producing chemicals agents that inhibit collagen production and wound re-epithelialisation [189], [190].

1.4.3.3.- Impaired angiogenesis

The majority of chronic wounds (VU, AU, UP, DU) are associated with peripheral vascular disease, which results in an inadequate supply of oxygen and nutrients to the injured area. Insufficient angiogenesis is therefore a significant contributor to impaired healing, as a lack of oxygen can inhibit collagen production and wound re-epithelialisation. A reduction in vascularisation may be attributed to elevated levels of anti-angiogenic proteins, such as myeloperoxidase, and a deficiency in angiogenic stimulators, such as superoxide dismutase, which together can lead to ECM damage and apoptosis. Another crucial pro-angiogenic factor, VEGF, has been demonstrated to undergo proteolytic degradation and inactivation within the hypoxic and hostile microenvironment of the diabetic wound [191].

1.4.3.4.- Senescence

During the proliferation stage, cells initiate the process of reproduction and migration to the injured area, where they rebuild tissue. In chronic wounds, cells at the wound site enter a state of premature senescence due to their constant exposure to inflammation and stress. When fibroblasts become senescent, they are unable to fulfil their normal functions, which can result in a reduction in the production of collagen and other components of the extracellular matrix, as well as alterations to the microenvironment and the impact on neighbouring cells. This can contribute to a decrease in the elasticity and strength of connective tissue, which may lead to the formation of scars and a decline in the ability to heal of tissue [192]. Furthermore, it has also been shown that prematurely aged fibroblasts exhibit a diminished capacity to migrate and are unresponsive to growth factors [193]. These senescent cells produce fewer growth factors and secrete more pro-inflammatory cytokines and proteases that inhibit proliferation, angiogenesis and induce uncontrolled tissue degradation [140], [194].

1.4.3.5.- Proteases

In chronic wounds, the abnormal activity of certain proteases and their inhibitors also plays an important role. For instance, certain proteins designated as MMPs, such as collagenase and gelatinases A and B, are overexpressed in chronic wounds. Similarly, an excessive increase in serine proteases is observed, which results in the breakdown of fibronectin, ECM and multiple key growth factors, thereby impairing the proper wound healing process [195], [196].

1.4.3.6.- Ageing and other pathological factors

Advanced age is a common and readily apparent feature of patients presenting with chronic wounds. Hormonal changes that occur during the aging process, particularly estrogens and androgens, are the primary factors that contribute to compromised wound healing in the context of aging *per se* [197]. The reduced number and function of stem/progenitor cells, as well as the irreversible ageing of cells with limited proliferative potential and an altered response to stress, also predispose older people to the development of chronic wounds [192]. Finally, numerous additional risk factors have been associated with poor wound healing, including alcoholism, obesity, smoking, stress, illness such as jaundice and uremia, and medications such as glucocorticoid steroids and chemotherapy [186].

In summary, chronic wounds are generally characterised by a prolonged inflammatory response and impaired healing due to a number of factors, such as the presence of infection, dysfunction of the cells responsible for healing, lack of oxygen and nutrients to the injured area, and advanced age. Consequently, the management of chronic wounds is frequently intricate and requires an individualised assessment of each patient to address underlying factors that may delay healing and contribute to the chronicity of the wound, including diabetes, poor nutrition and oxidative stress. Furthermore, prevention is of paramount importance in order to avoid wounds from becoming chronic. This may entail instructing patients on the significance of hygiene and skin care, as well as fostering an awareness of the importance of early recognition of wounds and prompt treatment of acute wounds.

A number of approaches may be employed to address the issue of chronic wounds, including the treatment of infection, improvement of blood circulation, removal of necrotic tissue and the use of specialised wound dressings.

1.5.- Wound dressing

As previously discussed, chronic wounds affect a significant proportion of patients, resulting in suffering, diminished quality of life and increased healthcare costs. Currently, there are no effective and efficient treatments that can cure chronic wounds due to the lack of knowledge of the exact processes involved in the pathology, the high cost of developing therapies that require highly specialised personnel and laboratories and the poor design of clinical trials, as well as the heterogeneity of wounds and patients [198]. Consequently, a comprehensive evaluation of the general health of patient and nutritional status, medication use, and vascular status is essential to identify an optimal and individualized treatment plan for each patient.

A number of studies have shown that early and rapid wound closure improves epidermal-dermal interactions and reduces the probability of a chronic wound. In this way, the possibility of developing excessive scarring problems and fibrotic conditions, such as keloids or hypertrophic scars, is reduced [184], [199].

Tissue engineering (TE) is a multidisciplinary field that attempts to emulate organogenesis and produce replacements for dysfunctional tissues by combining biology, materials science, engineering and surgery [200], [201]. In general, TE techniques involve the combination of cells, biologically active molecules and biomaterials in such a way that, while the material is resorbed and disappears, the cells proliferate and generate an innate ECM that performs tissue regeneration and restores the initial and original functionality of the damaged tissue. Tissue engineering is now widely applied in numerous areas of medicine, including the regeneration of cartilage, bone and heart tissue, as well as skin, particularly in the context of chronic wounds and burns [202].

Conventional treatments of chronic wounds currently include mechanical techniques to prepare the wound bed, extensive surgical debridement to remove residual exudate and devitalised tissue from the wound edge to achieve a well-vascularised wound bed, surgical drainage of abscesses and essential antimicrobial therapy to eliminate pathogens [203], [204]. In these treatments, it is essential to minimise skin irritation or friction, protect the wounds from contaminants and maintain the correct humidity and temperature conditions. To achieve this, different wound dressings have been developed, including semipermeable films, hydrogels and foams [203]–[206], where the use of biomaterials plays a crucial role in the healing process by interacting with biological systems. A number of wound dressings have been developed with the intention of counteracting the underlying cause of chronicity and dampening the inflammatory response, thus allowing the wound to resume healing [207].

A wound dressing is a material applied directly to a wound that is designed to provide structural support, promote cell adhesion and migration, modulate the local microenvironment to enhance healing and prevent further tissue damage. Furthermore, an optimal dressing should also aim to achieve other objectives, such as providing a temporary protective physical barrier against external agents or pathogens, ease of application, providing the correct level of moisture to promote re-epithelialisation and absorb wound exudate, good bioadhesion to the wound surface, elasticity and high mechanical strength, ease of sterilisation and good biodegradability without toxic or antigenic residues [208], [209]. In addition, the novel dressings offer additional benefits, including enzyme or growth factor supplementation, inhibition of microbial invasion, thermal insulation, gas exchange permeability and protection of free nerve endings for pain relief [210], [211]. Consequently, biomaterials employed in dressings are essential in the context of standard wound care.

A moist environment promotes wound healing, particularly in chronic wounds, with healing rates three to five times faster than in a dry environment [212]. This is due to the increased moisture allowing for more uniform re-epithelialisation of the wound bed. In contrast, in a dry wound, migrating epithelial cells follow the ridges of moisture, resulting in inefficient and uneven regeneration. In addition, moist wounds secrete an exudate produced during the vasodilatation of the inflammatory phase, which is rich in leukocytes, cytokines and proteins that

promote proper healing. In dry wounds, the absence of exudate in the wound bed delays healing. However, an excess of exudate, and therefore moisture, also impedes healing by maceration and damage to the surrounding skin. In addition, it can also promote the growth of bacteria. It is therefore essential that the moisture levels are perfectly controlled for normal wound healing to occur [213], [214].

The selection of dressing depends on the pathophysiological and anatomical characteristics of the wound, in addition to the medical history of the patient, the location, size and type/depth of the wound, the cost of the product, the ease of application and dressing changes, the frequency of dressing changes or the need for additional antibiotics. For instance, it is essential to determine whether the wound is acute or chronic, whether it is infected or not, and its depth and shape. Furthermore, if the wound is not infected, it is important to determine whether it is draining or not and whether it is healing properly (i.e. granularly) or necrotically. Similarly, infected wounds require frequent dressing changes to avoid fluid accumulation and occlusive dressings are not recommended [215]. The present of bacteria in high numbers results in a reduction in the availability of oxygen and nutrients to the wound cells, thereby impeding the healing process. In such instances, the use of antimicrobial dressings may be considered [216]. In the case of wounds that are excessively moist, it is necessary to use a dressing that is capable of absorbing the excess exudate, thus maintaining a balanced wound surface without completely drying out the wound. Finally, in dry wounds, it is essential to use moist wound dressings to facilitate cell migration and nutrient diffusion, thus facilitating faster healing [213], [217].

The existing literature suggests that wound healing is considerably accelerated when a dressing is employed. This is due to the ability of the dressing to facilitate re-epithelialisation, collagen synthesis, angiogenesis, and redaction in pH, all of which contribute to a reduction in wound infection. It is important to monitor the wound throughout the healing process, noting any known dressing complications such as lateral absorption or excessive exudate accumulation. If wound healing is not progressing properly in a timely manner or if the wound deteriorates, it is necessary to change the chosen dressing type [218]–[220].

1.5.1.- Types of wound dressing

Wound dressings are typically categorised according to their mode of action as: (a) passive products, (b) interactive products and (c) bioactive products [221]. A passive wound dressing, such as traditional gauze, is a non-occlusive material that merely covers the wound without participating in the wound healing process. Interactive products, such as polymeric films, are usually transparent, permeable to water vapour and oxygen, but impermeable to bacteria and suitable for use on low-exudate wounds. Finally, a bioactive dressing is capable of actively contributing to the healing process, either independently or through the delivery of active substances. Table 3 provides a summary of the different dressings used for different types of wounds and their respective characteristics. In chronic wounds, where patients often undergo prolonged treatment with frequent dressing changes, the

selection of a dressing that can deliver drugs to the wound site in a controlled manner can enhance the therapeutic outcome.

1.5.1.1.- Passive products

1.5.1.1.1.- Gauze: Traditional gauze dressings remain the most commonly used for the treatment of wounds and burns [222], particularly in the short-term during the initial procedure to prevent wound contact with the external environment and bleeding. However, gauze are unsuitable for long-term treatment due to their tendency to dry the wound surface rapidly, permit bacterial penetration and adhere to granulation tissue, which may result in damage to the newly formed epithelium upon removal [223], [224]. A plethora of gauze dressings are available, comprising both synthetic and cotton varieties, with different fibre densities and pore sizes, and impregnated with compounds to reduce adhesion and prevent pain. Despite being economical and versatile, gauze can cause injury during dressing changes, increase the risk of infection and potentially lead to granuloma formation from residual material [225], [226].

Table 3: Properties of dressing materials.

Type	Actions	Indications/Use	Precautions/Contraindications	Papers
Passive products				
Gauze	Rapidly absorbs fluid and stops bleeding	Use as primary dressing over superficially infected or non-infected wounds	May dry out the wound bed if used on dry or very lightly exuding wounds. Adhesive nature may injure the wound during dressing changes. Risk of infection	[222][223][224] [225] [226]
Interative products				
Films	Allows visualization of wounds during healing. Provides bacterial protection. Adheres to wounds in mobile areas	Used as a primary dressing over superficial dry or low exuding wounds. Can be used as a secondary dressing over hydrogel alginate to rehydrate the wound bed	Do not use on patients with fragile or compromised periwound skin, skin sensitive to adhesives, or infected wounds	[217][226]
Bioactive products				
Hydrogel	Rehydrates wounds, balances moisture, and provides a cooling sensation on wounds	For use on dry to moderately exuding wounds. Can be combined with silver for antimicrobial activity	Do not use on infected wounds or heavily exuding wounds. May cause maceration with fluid accumulation	[207] [217] [227] [228]
Foams	Rapidly absorbs fluid and balances moisture in the wound bed. Protects the wound bed from further damage. Does not adhere to the wound	For use on moderate to heavily exuding wounds. Can be found in rope or ribbon presentation for required cases. Can be combined with silver for antimicrobial activity	Do not use on dry/necrotic wounds or wounds with minimal exudate. Low-adhesion versions are available for patients with fragile skin	[213]
Hydrocolloids	Absorbs liquid in the inner layer to balance moisture. Can be left on for several days	For use on dry to moderately exuding wounds. Can be combined with silver for antimicrobial activity	Do not use on infected wounds or heavily exuding wounds. May cause hypersensitivity reaction, or maceration with fluid accumulation. May promote overgranulation	[213] [2017] [229]
Composites	Absorbs and retains moisture. Protects against bacteria. Semi-adhesive form for use on mobile wounds sites and non-adhesive for optimal wound healing	For use on superficial, light to moderately exuding wounds	Do not use semi-adhesive form if patient is sensitive to adhesives. May dry out thr wound bed if used on dry or very lightly exuding wounds.	[2013]

1.5.1.2.- Interactive products

1.5.1.2.1.- Films: Films are thin, transparent, semi-permeable polymeric dressings that permit the exchange of gases, prevent bacterial contamination, and protect the wound against external factors [217]. As transparent materials, they are highly useful for visualising the wound progression. However, they lack high absorbency and moisture absorption, which can result in fluid accumulation beneath the dressing, requiring frequent changes. Furthermore, due to their

adhesive nature, they can cause damage to the wound when removed, and may be unsuitable for individuals with fragile skin. These films are optimal for superficial wounds, which typically involve only the epidermis and are not highly exudative [226]. However, they are contraindicated for use on infected wounds due to their limited absorptive capacity.

1.5.1.3.- Bioactive products

1.5.1.3.1.- Hydrogels: Hydrogels are water-soluble polymer networks that can absorb and retain large amounts of water, rendering them suitable for moisturising dry wounds [207], [227], [228]. In addition, they are non-adherent materials, which reduce pain during dressing changes and provide a cooling sensation due to their high water content [207]. Furthermore, they can be employed to deliver drugs, antimicrobial agents, or growth factors to the wound site. Hydrogels are particularly useful for pressure ulcers, as they maintain a soft consistency, thereby facilitating the removal of necrotic debris. However, it is not recommended for use on infected or exuding wounds due to poor absorption [217].

1.5.1.3.2.- Foams: Foams are popular dressings due to their ease of handling, versatility and low cost. Foams are typically composed of three distinct layers: an absorbent non-adherent porous inner layer, a fluid-retaining middle layer, and a semi-permeable hydrophobic outer layer. The soft material protects the wound from trauma, while the non-adherent inner layer prevents adherence to granulation tissue. Furthermore, the foam rapidly absorbs wound exudate. However, this characteristic necessitates more frequent dressing changes, making them suitable for the treatment of infected and non-infected wounds, surgical wounds, and graft donor sites with moderate exudate. Conversely, they are contraindicated for use on dry wounds or pressure ulcers, as they tend to dry out, [213].

1.5.1.3.3.- Hydrocolloids: Hydrocolloids are moisture-retaining dressings composed of compounds, such as carboxymethylcellulose, gelatine and pectins. In general, hydrocolloids comprise two distinct layers: an inner hydrophilic layer that maintains moisture balance and an outer semipermeable membrane that allows for gas exchange while preventing the passage of bacteria. They effectively retain fluid, thereby allowing for extended wear without the necessity for replacement, which in turn reduces trauma and costs. Consequently, these dressings are employed in the treatment of dry wounds, including abrasions, superficial pressure ulcers, surgical wounds, grafts and burns [213], [217], [229].

1.5.1.3.4.- Composites: Composite dressings are versatile, multi-layered products designed for use on moderately exuding, non-infected superficial wounds. The inner layer is adhesive and porous, facilitating the transfer of moisture to the absorbent second layer, which may be composed of hydrogel, alginate, foam, or hydrocolloid. The outer layer is elastic, semipermeable, allowing for gas exchange and protecting against bacterial contamination and possesses high mechanical

strength. These dressings are durable and require less frequent replacement, as they do not dry out as quickly. Furthermore, they can be employed in isolation or in conjunction with other dressings or topical medications to enhance their efficacy. Despite their efficacy on non-infected wounds, their multi-layered design renders them a more expensive option than other types of dressing [213].

1.5.2.- Biomaterials for wound dressings

The design and creation of matrices composed of innovative biomaterials must exhibit two fundamental characteristics: biodegradability and biocompatibility, which denotes their minimal toxicity and immunogenicity [230]. Furthermore, these biomaterials must interact with the biological environment and regulate the cellular response [231].

Biomaterials can be classified according to their source, including animal, human, plant, or synthetic. However, they can be broadly divided into two categories: synthetic and natural biomaterials [232]. Table 4 provides an overview of the advantages and disadvantages associated with different types of biomaterials employed in skin regeneration. In the field of tissue engineering, natural biomaterials derived from living and plant sources, are widely explored due to their biocompatibility, bioactivity, structural similarity to native ECM tissue, tuneable degradation, and lack of toxic residues, as well as their ability to promote cell adhesion and function [232], [233]. Among the most commonly used biomaterials that are sources of proteins and polysaccharides include gelatine, fibrin, elastin, collagen, cellulose, and chitosan [234].

1.5.2.1.- Synthetic polymers

In recent times, the synthetic biomaterials that mimic ECM systems, which are manufactured from hydrocarbon [232] building blocks, can be produced on a large scale with controlled properties, including degradation time and molecular weight. Furthermore, these materials offer the advantage of being more readily adaptable in terms of shape, architecture and chemistry, which makes them a promising option for applications in skin regeneration [230]. Nevertheless, the absence of cell recognition signals and the production of acid in their degradation products restrict their use in therapeutic tissue reconstruction. The most commonly utilised synthetic polymers for the formation of matrices are polyglycolic acid (PGA), polylactic acid (PLA), polycaprolactone (PCL), polyethylene glycol and related copolymers such as polylactic-co-glycolic acid (PLGA) [232].

1.5.2.1.1.- Polylactic acid (PLA): PLA is a polyester derived from rice and corn and has been approved by the US Food and Drug Administration (FDA) for use in medical applications [230]. Although it has some limitations, such as a lack of cell interaction, slow degradation, low elasticity and hydrophobicity, which can cause inflammation, PLA is frequently used in the production of tissue-engineered scaffolds to transport cells to the site of injury [235].

1.5.2.1.2.- Polycaprolactone (PCL): In contrast to PLA and PLGA, PCL exhibits a slower degradation rate [230], making it an optimal candidate for the fabrication of resorbable sutures, drug delivery systems, and structures for tissue regeneration [236]. Moreover, due to its slow degradation time and non-toxic degradation products, it is considered a good option for modifying natural biomaterials with slower degradation and improved mechanical properties [237].

1.5.2.1.3.- Polyglycolic acid (PGA): PGA is a crystalline polymer that dissolves with difficulty in organic solvent and has a hydrophilic nature that contributes to a rapid loss of mechanical strength allowing it to be resorbed by the body [230], [234], [238]. Nevertheless, it can be modified with different fractions in order to enhance its capacity to adhere to cells, to accelerate its short-term degradation and to reduce inflammation.

1.5.2.2.- Natural polymers

The intrinsic biological signals/cell binding motifs, biocompatibility and biodegradation properties of natural polymer matrices contribute to their generally well-tolerated nature. Nevertheless, a certain degree of loss of mechanical and degradation properties has been documented.

1.5.2.2.1.- Collagen: Collagen, a biodegradable and biocompatible protein, is primarily located in connective tissue and is essential for skin structural integrity. As a result, it is a widely used in the skin regeneration and wound healing. However, it is susceptible to degradation by enzymes and affected by cross-linking and sterilisation processes [230]. Collagen-based formulations are currently employed in numerous biomedical applications in various forms, including hydrogels and sponges, with the objective of restoring haemostasis and promoting wound healing in the form of dressings [234], [239]–[241]. Additionally, collagen is employed in electrospun nanofibrous scaffolds as a skin substitute or coating for alternative materials, such as gold nanoparticles, to improve their biocompatibility [242].

1.5.2.2.2.- Gelatine: Gelatine, a partially hydrolysed form of collagen, retains many of its physicochemical properties and functions [230], although it exhibits poor mechanical properties. Gelatine-based dressings incorporate the RGD sequence, which enhances cell adhesion [243] and has been demonstrated to facilitate healing in patients with diabetic foot ulcers [244]. Gelatine represents a less expensive alternative to collagen and also has a higher solubility and a lower antigenicity, which renders it an appropriate material for the treatment of wounds at high risk of infection [245].

Table 4: Synthetic and natural biomaterials used in skin tissue engineering and their advantages and disadvantages.

Types	Advantages	Disadvantages	Key properties in wound healing	Papers
Synthetic biomaterials				
PLA	Easy modification with other biomaterials and bioactive compounds	Poor cell interaction, low elongation, and hydrophobicity	Exhibit high mechanical properties, reasonable wetting time, preferred surface morphology, low moisture absorption, prolonged swelling behaviour and strong antibacterial properties against Staphylococcus aureus and *Escherichia coli*	[230][235]
PCL	Biocompatible with relatively slow degradation time	Poor cell attachment due to hydrophobicity	Demonstrate desirable electroactivity, biocompatibility, free radical scavenging capacity and antibacterial activity; promote collagen deposition and granulation tissue thickness during the wound healing process	[230][236][237]
PGA	Highly biocompatible and biodegradable	Rapid loss of mechanical strength	Exhibit adequate wetting time, desirable surface morphology, low moisture uptake and prolonged swelling behaviour	[230][234][238]
Natural biomaterials				
Collagen	Appropriate mechanical properties and biocompatibility	Sensitive to cross-linking and any sterilization process	Triple helix conformation of collagen type I promotes cell adhesion and migration; pore sizes for 5 and 8 mg/mL collagen type I scaffolds ranged from 126-188 μm; promotes connective tissue regeneration	[230][239][240] [241][242]
Gelatine	Low antigenicity and high solvent solubility	Lack of high mechanical resistance	Porous gelatine matrices absorb wound exudate, maintaining a moist environment essential for wound healing	[230][243][245]
Alginate	Shape retention due to low viscosity and zero shear viscosity	Inert material and suitable for in vitro assays only, requires crosslinking due to low bioactivity	Porous, good absorption, biocompatible and biodegradable nature promotes wound healing, resulting in less scarring, minimal bacterial infection, and the creation of a moist wound environment	[246][247][248] [249][250]
Chitosan	Antibacterial, antifungal, mucoadhesive and analgesic properties	Slightly soluble in aqueous solutions except in acidic medium	Interact with negatively charged molecules (protein, fatty acid, bile acid, polysaccharide, phospholipids); chelate metal ions (iron, copper, magnesium); stimulate haemostasis and accelerate tissue regeneration	[252][253][254] [255][256][257]
Cellulose	Flexibility of shape, ease of processing, good mechanical strength, and biodegradability	Insoluble in water and many organic solvents	Hydrophilic nature, purity, ability to maintain proper moisture balance and flexibility form a tight barrier between the wound and the environment, preventing bacterial infection	[259][260][261] [262]
Fibroin	Biocompatible with high mechanical properties	High brittleness	Porous template supports cell proliferation, differentiation, and ECM production	[263][264][265]
Elastin	High elasticity	Poor mechanical strength and availability	Half-life > 70 years and the monomer can reversibly stretch up to eight times its resting length; fibre orientation positively affects cell phenotype, adhesion, and proliferation	[84][266][277]

1.5.2.2.3.- Alginate: Alginates, a natural polysaccharide derived from marine algae, form gels when exposed to calcium ions [246]. The calcium in the dressing reacts with the sodium in the exudate to produce a soluble sodium-calcium gel on contact, which retains and balances moisture in the wound bed, thereby promoting the proper healing process and reducing the healing time [247]. Alginates have the capacity to absorb more than 20 times their weight in fluid, making them an optimal candidate for use in heavily exuding wounds and allowing for prolonged use. Nevertheless, it is less suitable for dry wounds due to the potential challenges in removal, and the necessity for a secondary dressing to provide structural reinforcement, which increases the final cost [248]–[250]. The distinctive characteristics of alginate permit its manufacture into a variety of wound dressings, including hydrogels, films, foams, sponges, and nanofibres [251].

1.5.2.2.4.- Chitosan: Chitosan, derived from chitin, can be employed in isolation or in combination with other materials, including gelatine, fibrin, and collagen, to generate a variety of scaffolds, such as films, sponges, hydrogels, fibres, powders and micro/nanoparticles [252], [253]. Chitosan has been demonstrated to be an effective treatment for wounds and burns due to its haemostatic, antifungal, antibacterial, mucoadhesive and analgesic properties, which do not cause inflammation or infection [230], [254] and it may accelerate the formation of fibroblasts and enhance early-phase responses associated with healing [255]. Despite its low toxicity and its biocompatibility with blood and tissues [256], [257], chitosan has low mechanical strength and is highly susceptible to degradation [232], with variable properties across different batches [258].

1.5.2.2.5.- Cellulose: Cellulose, a natural biopolymer found in plants and some bacteria, is highly biocompatible, flexible, easy to process, mechanically strong, and biodegradable, making it a promising scaffold for the treatment of skin wounds [259]. It facilitates autolytic debridement, reduces pain and accelerates the granulation process [260]. A cellulose/collagen hybrid dressing has been demonstrated to improve tissue re-epithelialisation in diabetic foot ulcers [261]. Furthermore, the functionality of cellulose dressings can be enhanced through the incorporation of enzymes, antioxidants, vitamins, hormones, or antimicrobial agents, thereby creating a bioactive dressing [262].

1.5.2.2.6.- Fibroin: Fibroin, a biomaterial characterised by a high degree of amino acid repeatability, exhibits considerable potential for wound healing due to its biocompatibility, biodegradability, flexibility, adhesion and exudate absorption, in conjunction with a minimal inflammatory response [263], [264]. Silk fibroin, a semi-crystalline protein, exhibits high mechanical strength (exceeding that of collagen) [265], which enables the formation of nanofibres that facilitate the adhesion of fibroblasts and keratinocytes cells [251]. In addition, fibroin gels can release growth factors, such as cytokines, which regulate the healing process [230]. Conversely, one of the principal disadvantages of these materials is that they can induce allergic reactions and release tumour necrosis factor due to the presence of sericin [265].

1.5.2.2.7.- Elastin: Elastin is a biomaterial that has been employed extensively in the fabrication of skin substitutes, either in a monolayer or bilayer configuration [266] due to its elasticity, making up 2 and 4 % of natural skin [267]. Elastin plays a role in skin repair, including the attenuation of wound contraction and the stimulation of protease production, along with cell migration and proliferation [84]. Furthermore, the natural process of elastin formation can take up to 4-5 years in damaged tissue, which may result in compromised distribution and morphology and, consequently, impaired normal functionality [266]. The majority of skin substitutes currently available on the market are composed of collagen alone, lacking elastin. This results in reduced elasticity, high shrinkage, and the formation of scar tissue during the healing process [230].

In conclusion, it can be posited that wounds treated with biopolymers and biomaterials demonstrate accelerated healing. Furthermore, natural biopolymers are demonstrably more efficacious as wound healing accelerators than synthetic polymers [222].

1.6.- Elastin-like recombinamers (ELRs)

Due to the interesting properties of tropoelastin, numerous researchers began to explore potential synthesis possibilities and attempted to artificially produce a multitude of polypeptides that could mimic it [268], [269], thus obtaining a novel group of biomaterials, known as elastin-like polypeptides (ELPs). The most repeated amino acid sequence in ELPs is the polypeptide, $(VPGVG)_n$ ($n \leq 150$), which is capable or undergoing reversible phase separation analogous to that observed in the native tropoelastin molecule in aqueous solution. Consequently, the self-assembly process of ELPs is similar to that described above for tropoelastin chains and is thermodynamically favourable, as the increase in order within ELP chains (decrease in entropy) is compensated by the decrease in order within water (increase in entropy) [270].

The initial synthesis of these elastin-like polymers (ELPs) was conducted chemically in accordance with the established protocol developed by Urry, Prasad and co-workers [271]–[273]. However, these procedures were highly complex and numerous complications arose during purification, resulting in low yields of the final product with high polydispersity [274]. Consequently, in the late 1980s, the advent of recombinant DNA technology enabled the development of novel methodologies for the design and bioproduction of artificial proteins, which overcame the limitations of chemical synthesis. These new approaches yielded end products with greater control over their amino acid sequence and less or no polydispersity. In addition, the thermo-responsive behaviour of these polymers was exploited to achieve easier purification. Specifically, this purification process involved the application of several cooling and heating cycles above and below the transition temperature (T_t), a process known as the inverse transition cycle (ITC), which is allowed by the intrinsic property of ELPs [275], [276]. This method avoids the addition of compounds that have to be removed later and reduces waste or by-products, as well as costs [277]. In order to emphasise the recombinant nature of these elastin-like polymers (ELPs), Rodriguez-Cabello's group proposed the nomenclature elastin-like recombinamers (ELRs) and this will be the term used to refer to these biomaterials in this work [278], [279].

The previously described repetitive sequences of the mammalian elastic protein, elastin, have been found to form the basic repetitive structure of ELRs, which is the pentapeptide $(VPGXG)_n$, where X can be any amino acid, with the exception of L-proline, which has been identified as destabilising the β-turn due to steric reasons [111], [280]. The possibility to select the host amino acid, X, enables to modulate the physicochemical properties of the ELRs obtained. The most distinctive property of ELRs is their thermosensitivity, which results in a reversible alteration of the spatial conformation of these polypeptides as a function of T_t. Two

intrinsic factors, namely the choice of the amino acid host and the chain length (n-value), are of significant importance in determining T_t. Typically, T_t increases in conjunction with an elevated average ELR polarity and decreases in correlation with an augmented overall hydrophobicity [281]. Similarly, an increase in the length of the ELRs also results in a reduction in T_t. Conversely, there are a number of extrinsic factors that can influence T_t, including pH, the oxidation state of a side chain or functional group, ionic strength, pressure, light or chemical modifications [282], [283]. Therefore, the addition of chaotropic anions (anions with a low hydration level) can increase T_t even at low concentrations, whereas kosmotropic anions (anions with a high hydration level) can decrease T_t because they interact directly with the water molecules, thereby weakening their interaction with the polymers [284]. The specific T_t of each polymer can be quantified by employing a range of experimental techniques, such as turbidity and calorimetric methods, but the T_t values obtained by different means often differ due to the influence of several factors [285].

The importance of ELRs lies in the fact that, in addition to their mechanical performance, these polymers exhibit a wide and versatile range of interesting properties that are not easily found all together in other materials, such as high flexibility, strength and elasticity, stimuli-responsive behaviour and the ability to self-assemble. Furthermore, their degradation products (natural amino acids) are non-toxic [286]–[289] and have the additional property of high biocompatibility [273], allowing these bio-inspired peptide polymers to be used in advanced biomedical applications such as controlled drug release, tissue engineering and regenerative medicine.

1.6.1.- Design of ELRs. Genetic engineering

ELRs are biological polymers, of protein origin, and produced biosynthetically using genetic engineering techniques, with a well-defined sequence thanks to recombinant DNA technology. This technique has enabled the synthesis of proteins using heterologous hosts, with the bacterium *Escherichia coli* being a notable example due to its ease of manipulation, rapid growth, and well-known genetics [290]. Thus, the process of ELR biosynthesis can be described in four basic steps: 1) the design of a synthetic gene encoding for the desired protein; 2) the obtaining of the monomeric gene to construct the multiblock; 3) the transformation of the gene into a bacterial strain to express the desired recombinant proteins; and 4) the bioproduction of the recombinant polypeptide in a fermenter and its subsequent purification. The aforementioned process in depicted in Figure 7.

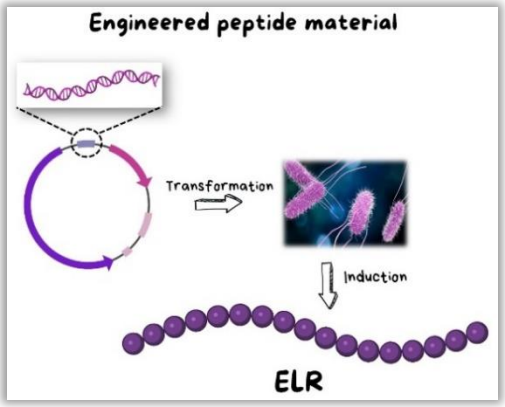

Figure 7: ***Schematic representation of the design of the sequence and production of an elastin-like recombinamer.*** *Created with BioRender.*

In this work, the iterative-recursive directional ligation (IRDL) method proposed by Meyer and Chilkoti [291] was used for the synthesis of highly repetitive recombinant proteins. The method achieves precise control of block size and distribution by oligomerising monomeric genes in a continuous, unidirectional manner, overcoming the limitations of previously proposed methods that relied on concatemerisation to achieve the desired gene length and constructed the gene randomly [105], [277], [279]

The IRDL method thus permits the synthesis of long genes through the controlled ligation of small genes, following a series of well-established individual steps. This is based on the use of restriction enzymes that leave cohesive ends, allowing the insertion of DNA fragments into a plasmid of interest [291]. To initiate the process, the monomeric DNA segment of interest (monomeric gene) must be designed and must be flanked at both ends by specific non-palindromic restriction sites. This approach allows for the facile isolation of the fragments by enzymatic digestion with IIS-type restriction enzymes, which can then be subjected to oligomerisation by enzymatic ligation, as is illustrated in Figure 8A and Figure 8B. These IIS enzymes have the capacity to cleave DNA away from its recognition sequences, at a defined distance from them, thereby facilitating the process of "seamless" cloning of genes. This approach avoids the incorporation of unwanted nucleotide residues in the final construction and self-ligation by leaving non-complementary ends. The utilization of type II enzymes may result in the incorporation of terminally manipulated restriction sites within the gene sequence, which may subsequently lead to the generation of unwanted nucleotide residues within the final gene construct [292].

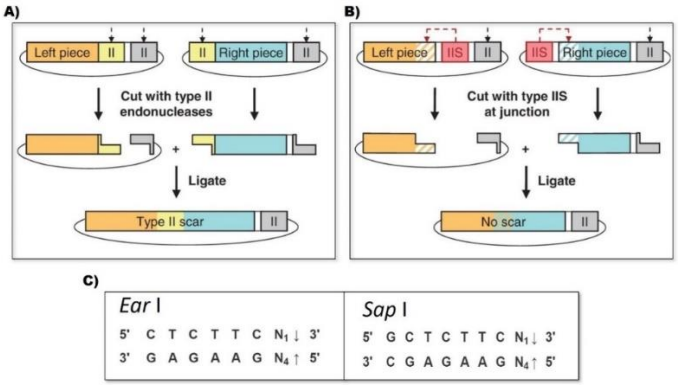

Figure 8: ***Ligation-based DNA assembly using restriction endonucleases. A)*** *The use of conventional type II endonucleases for DNA assembly necessitates the presence of a type II recognition site at the connection point between the two initial DNA fragments. The junction is retained in the final product, thereby preventing the creation of arbitrary DNA sequences.* ***B)*** *The use of type IIS endonucleases in DNA assembly enables the creation of overhangs with any arbitrary sequence, thus allowing for sequence-independent construction. Reproduced from* [293]. ***C)*** *Recognition and cutting sequences of EarI and SapI endonucleases.*

Among the most commonly used endonucleases of the IIS-type in the IRDL method are *EarI* and *SapI*, which can be utilised in combination to yield the desired gene fragment. It is noteworthy that these enzymes exhibit a distinctive property: while *EarI* is capable of recognizing and cleaving *SapI* sites, the reverse is not true, as the *SapI* recognition sequence contains an additional nucleotide, as illustrated in Figure 8C. In addition, the asymmetric ends produced by their digestion can be interchanged [293].

In order to employ the IRDL method with *EarI* and *SapI* enzymes, it is necessary to use a single restriction site for *SapI,* and two sites for *EarI*. This configuration allows *SapI* to facilitate linearisation of the cloning vector, while *EarI* enables the isolation of the gene segment of interest. Furthermore, the shrimp alkaline phosphatase enzyme is utilised to prevent self-ligation of the receptor plasmid. Consequently, the deliberate positioning of both restriction sites thus allows the vector to be linearised using *SapI* to obtain protruding ends to which the gene of interest isolated using *EarI* is then added with compatible ends. The result of this linkage between a vector and an insert is a circular plasmid. It is crucial to highlight that the plasmid vector has been designed in a manner that preserves the restriction sites throughout each cloning step. This allows for the sequential insertion of distinct genes, employing these enzymes in succession, to yield a gene encoding the ELR of interest [294].

1.6.2.- ELRs with more advanced and complex functionalities

To enhance tissue specificity, the ELR backbone can be modified and biofunctionalized to incorporate biological signals, such as cell adhesion domains, protease sequences or growth factors that promote adhesion, cell proliferation, migration, differentiation, ECM degradation, angiogenesis or regeneration, thus providing a suitable environment for cell survival and proper tissue growth [295]. For instance, the incorporation of the RGD (arginine-glycine-aspartic acid)

sequence, which is found in fibronectin and other extracellular matrix proteins, promotes the adhesion of various cell types to ELRs via α5β1 and α5β3 integrins, as is illustrated in Figure 9A [296]. Another specific example of enhanced endothelial cell adhesion is the REDV (arginine-glutamic acid-aspartic acid-valine) sequence, which is found in the alternatively spliced IIICS-5 domain of human plasma fibronectin. This motif is involved in cell adhesion and spreading via the α4β1 integrin in endothelial cells, but not in smooth muscle cells or fibroblasts [297]. Additionally, the aforementioned AASIKVAVSADR and PPFLMLLLKGSTR sequences in laminin, as is shown in Figure 9B, have been demonstrated to promote angiogenesis and anchor epidermal keratinocytes to the dermal-epidermal junction, respectively [62], [64].

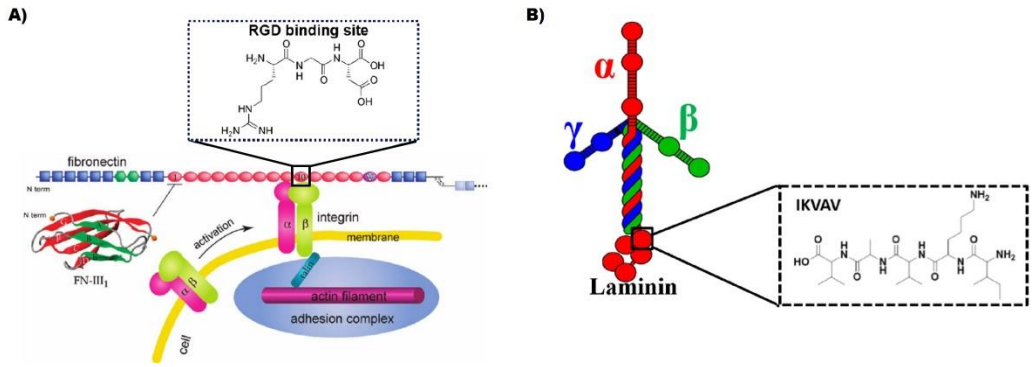

Figure 9: ***Examples of cell adhesion domains that improve the functionality of ELR polymers****. Schematic representation of* ***A)*** *RGD binding domain in fibronectin and* ***B)*** *IKVAV binding domain in laminin. Adapted from* [298] *and* [71].

Similarly, the inclusion of enzymatic degradation sequences assists ELRs in the undergoing degradation during the process of tissue regeneration, thereby enabling host cells to grow and form new tissue by depositing ECM [299],[300]. For example, the hexapeptide VGVAPG (valine-glycine-valine-alanine-proline-glycine) is recognised by elastase. The degradation rate of ELRs can be adjusted by incorporating specific protease recognition sites in the amino acid sequence, such as active domains (GTAR and DRIR, which facilitate fast and slow degradation, respectively). These sites can be cleaved by *uPA* (urokinase plasminogen activator) enzymes, which have with different kinetics and sensitivities [301]–[304].

In addition, ELRs have also been combined with growth factors for more specific applications, such as bone morphogenetic protein-2 (BMP), which can promote the regeneration of damaged bone tissue, thereby conferring osteoinductive properties to ELRs [273], or vascular endothelial growth factor (VEGF) or the angiogenic peptide QK, which mimics the VEGF receptor binding domain, which are widely used in angiogenic processes, including the promotion of functional capillary formation [303]–[308].

Finally, ELRs have also been employed in combination with other protein polymers, such as silk, collagen, and resilin, with the objective of enhancing or modifying their properties. For instance, silk-like domains are derived from the GAGAGS hexapeptide repeat found in the silk fibroin *Bombyx mori*, which is known

to self-assemble into β-sheet secondary structures, conferring the material high strength, toughness and ductile elongation [309]–[311].

1.7.-Scaffolds for tissue engineering

Despite the advances that have been made, two-dimensional environments are unable to adequately capture the complexity of living systems, as they lack the ability to mimic cell-cell and cell-extracellular interactions that occur in a three-dimensional environment, as is depicted in Figure 10. In these tissue models, cells in a monolayer have unlimited access to the components of the medium, such as nutrients, oxygen, metabolites and signalling molecules. However, this does not reflect the natural environment of tissues, where nutrient uptake is often more complex. Furthermore, the morphology of cells is altered in two-dimensional systems, which affects their native function [312], organisation of internal structures, secretion and signalling [313]. Consequently, the development of new artificial tissues must consider the environment in which the real tissue functions [314], [315], including other cell types, ECM components and bioactive molecules.

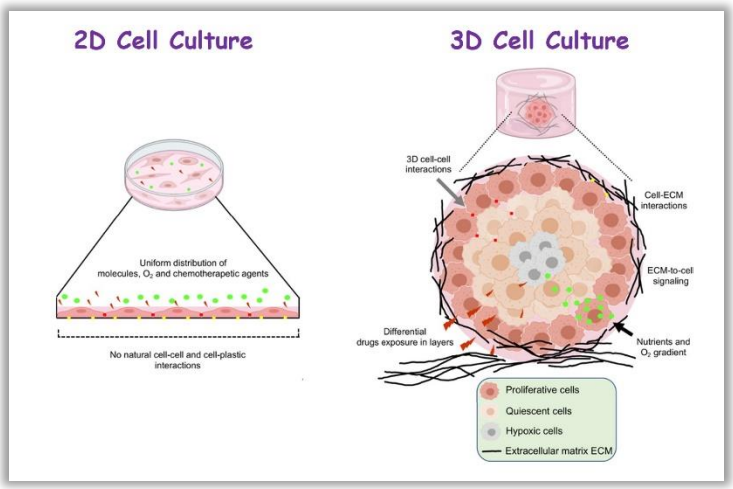

Figure 10: ***Schematic illustration of the cell microenvironment in two-dimensional (2D) and three-dimensional (3D) cell cultures****. In traditional two-dimensional (2D) cell culture, cells are grown in a flattened monolayer at the bottom of plastic plates. These cultures are constrained by the absence of cell-cell interactions and the unlimited exposure of cells to nutrients, oxygen, and drugs. In contrast, three-dimensional (3D) cell culture systems facilitate enhanced cell-cell and cell-extracellular matrix interactions, restricted access to nutrients and oxygen, and heterogeneous drug interactions, which more closely resemble the real microenvironment observed in vivo. Reproduced from* [316].

The new scaffolds must exhibit mechanical properties analogous to those of the tissues to be simulated, in addition to an appropriate external geometry, macrostructure, microstructure and interconnectivity [314], [317]. Furthermore, they must provide a structural support in which cells can properly grow, migrate, proliferate and differentiate properly in order to form a three-dimensional tissue-like construct. The principal challenges associated with three-dimensional structures are the supply of oxygen and nutrients, which is limited by the intricate diffusion processes within them. It is evident that larger and more structurally and functionally complex human tissues cannot be maintained by simple diffusion. Instead, a network of vascularisation is required to promote the exchange of nutrients, oxygen and waste, thus maintaining cellular function [318].

To overcome this problem and ensure proper functionality, porosity and pore size have currently been proposed as key parameters in the design of scaffolds for tissue engineering and regenerative medicine [317], [319]. In this context, it is widely acknowledged that scaffolds necessitate high porosity and interconnectivity to facilitate homogeneous cell distribution, cell proliferation and adequate nutrition to support tissue expansion [320]. Indeed, internal porosities greater than 90 % are regarded as optimal for tissue engineering applications [321]. The optimal pore size is dependent upon the intended application or target tissue [322], with values ranging from tens to hundreds of micrometres. Moreover, porosity and pore size have been shown to influence the vascularisation process [322], which is a crucial event in tissue regeneration. In addition to pore size, the shape and structure of the pore network are of critical importance in guiding and promoting the formation of new tissue, thus achieving the correct mechanical properties and biological signals [323]. Finally, the porosity of the scaffold surface is also of great importance, as it influences cell adhesion and anchorage between the scaffolds and the surrounding tissue, which improves the cleavage and mechanical stability of the implants [317], [324].

Consequently, a plethora of techniques have been devised to alter the pore architecture (size, shape and porosity) and mechanical properties of diverse scaffolds, thereby facilitating the desired tissue-cell interaction [319], including freeze-drying, moulding, solvent casting, gas foaming, salt leaching, electrospinning, phase separation, and 3D printing [325]–[327].

1.7.1.-Elastin-like recombinamer hydrogels

ELRs are highly similar to natural elastin and therefore exhibit high elasticity, biocompatibility, biodegradability, thermo-responsiveness and an absence of immunogenicity [289], [328]. In addition, their recombinant nature allows for precise control over the amino acid sequence and molecular weight, which is not easily achievable in synthetic polymers. Furthermore, the high yield in the production of these polypeptides when expressed in *Escherichia coli* bacteria (approximately 500 mg/L growth) and their simple purification based on their transition temperature, a simple and less costly procedure than other protein purification protocols [276], allows the production of large quantities of polymer for later use in the final application as regenerative medicine [329].

Finally, as previously mentioned, the recombinant nature of these ELRs allows for the modulation of their physicochemical properties by the introduction of amino acids or cross-linking sequences. Furthermore, numerous new functionalities can be incorporated, including cell recognition domains (RGD or REDV), which enhance cell adhesion [330]–[336], sequences that induce biomineralization [337]–[339], sequences that promote angiogenesis [307] or neurogenesis [303], non-thrombogenic coatings [308], [340], [341], selective cell harvesting or antimicrobial coatings that are either chemically or recombinantly incorporated [342]–[344] Depending on the final application, ELRs can generate a variety of structures such as micelles, nanoparticles, hydrogels, films and nanofibres. Consequently, ELRs represent a potential source for the fabrication of

highly porous, hydrated and biocompatible three-dimensional (3D) scaffolds [345], which are promising for regenerative medicine and tissue engineering, particularly in the form of hydrogels, as they provide mechanical and biochemical properties resembling those of living tissues. In addition to providing basic structural support, hydrogels can also mediate specific cellular responses such as cell migration and differentiation, support host tissue integration and ultimately promote matrix synthesis [346].

ELR hydrogels can be obtained through physical or chemical cross-linking. On the one hand, the self-assembly of physical ELR hydrogel networks is mediated by the sum of physical interactions that collectively stabilise an entire three-dimensional architectural network, including hydrogen bonding, Van der Waals interactions, hydrophobic and electrostatic interactions [347]. As the hydrogels obtained by these ionic or hydrophobic interactions are typically weak and fragile, reinforcing sequences have been incorporated to strengthen the intermolecular forces. Specifically, two distinct sequences have been incorporated into the ELR chain with the objective of achieving this purpose. The first of these is the silk-like motif (GAGAGS) [348], which is a sequence that favours a supramolecular rearrangement ending, which results in the formation of β-sheet structures. Additionally the human liver leukaemia factor (HLF), also known as the leucine zip motif [349], which is a sequence that consists of the repetition of the heptadic periodicity, which is usually designated 'abcdefg' with hydrophobic residues at positions 'a' and 'd'. Furthermore, charged residues are located at positions 'e' and 'g' [350], where the interaction between hydrophobic and ionic intermolecular forces between the charged residues in the zip motifs results in the formation of coiled-coil dimers that enhance the gelation of an amphiphilic ELR block.

Conversely, chemical cross-linking results in the production of hydrogels with enhanced mechanical properties. While there are various approaches to chemical cross-linking ELRs, nearly all of them necessitate the presence of an amino group on the side chain of lysine amino acids. Among the various cross-linking options, the use of chemicals is the most prevalent [351]. Recently, one of the most widely used chemical reactions is Huisgen's 1,3-dipolar cycloaddition between azides and alkynes as illustrated in Figure 11. This is an example of catalyst-free click chemistry and therefore has advantages as a rapid, high-yield cross-linking process because it is stereospecific, biocompatible and cell-friendly, allowing it to be carried out in aqueous solution in mild physiological environments without the release of toxic by-products [352]–[354]. To achieve this, ELRs are chemically modified to hold cross-linkable azide or cyclooctyne groups by exploiting the ε-amino group present on the side chain of the lysine residues. Once the ELRs have undergone modification, both groups react orthogonally to form an irreversible covalent bond between the ELR molecules, in the form of a triazole ring, resulting in the formation of a stable hydrogel [302]. Moreover, the mechanical properties and pore size of these hydrogels can be readily modified by simply varying the density of azide and cyclooctyne groups in the ELR chains, which will consequently alter the final cross-linking density of the network. Similarly, the presence of these lysine groups in the ELR chains can be exploited to introduce various bioactive compounds, such as peptides to modify the functionality of the polymer [303].

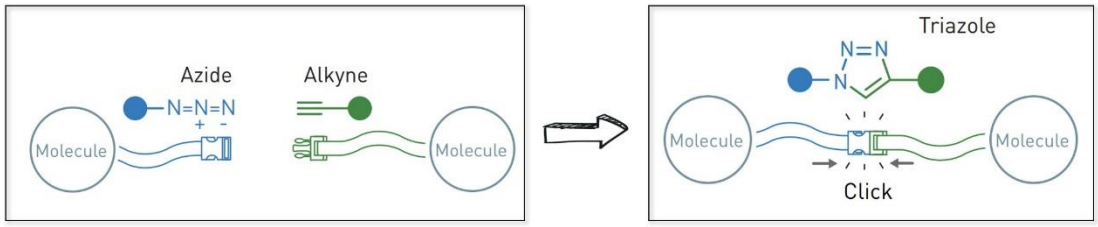

*Figure 11: **Click reaction**. Azides and alkynes react orthogonally to form an irreversible covalent bond. Adapted from The Royal Swedish Academy of Sciences.*

ELR hydrogels have been demonstrated to be extremely beneficial in biomedical applications due to their high-water content and elastic nature, which is comparable to that of natural tissues. Furthermore, the facile tunability in terms of specific mechanical, chemical and biological properties enables the design of specific scaffolds for cell growth and proliferation in a multitude of applications, including skin substitutes, cartilage or bone repair, vascular grafts or heart valves, among others [308], [355]–[357].

1.8.-Elastin-based wound dressings for skin

As previously stated, a number of underlying molecular and cellular pathophysiological mechanisms can contribute to the development of chronic wounds. These include poor vascularisation, excessive degradation of the extracellular matrix, degradation by proteases, reduced growth factor activity and bacterial infection. Furthermore, these wounds frequently result in severe tissue contraction, which further compromises the structure and appearance of the scar. Consequently, the most efficacious therapies for these wounds will need to address one or more of these mechanisms in order to make a significant advance in wound care. The utilisation of elastin-based materials may represent a promising therapeutic avenue for the management of chronic wound healing. These materials exhibit excellent biocompatibility and can be engineered to possess multiple functionalities, including the capacity for drug delivery, modulation of mechanical properties, and ECM mimicking properties. Additionally, elastin can be employed to create intricate, multifunctional structures that can accommodate the varying dimensions and contours of chronic wounds. Furthermore, the presence of elastin dressings has been demonstrated to reduce wound contraction, as it suppresses the differentiation of fibroblasts into contractile myofibroblasts, thereby modulating scar tissue formation [160], [358], [359]. Furthermore, tissue elasticity exerts a modulatory influence on cellular physiology, thereby offering the potential to constrain wound contraction. The contractile forces of cells are influenced by the elasticity of the underlying substrate, and therefore, elastin dressing may be used as a novel means of reducing wound contraction [360]. The mechanical nature of elastin regulates cellular properties. For example, nanofibres incorporating elastin within their material show an improvement in the shape and organisation of epithelial tissue compared to elastin-coated nanofibres, highlighting the influence of mechanical stretch on cell morphology and alignment [361], [362]. Moreover, cells

within the elastin matrix generate reciprocal mechanical forces, which provide additional signalling cues. It is not straightforward for cells to adhere to substrates that are excessively flexible or excessively rigid, as they are unable to adequately deform these surfaces [363]. Consequently, matrix stiffness can regulate a number of important aspects of cell behaviour, including cell migration, adhesion, spreading, proliferation and ECM deposition [363], [364]. Thus, engineered materials with appropriate elasticity and stiffness can be designed to guide regenerative cellular responses. Oriented fibres are associated with elasticity and contractility, whereas randomly oriented fibres are associated with stiffness and load-bearing properties [365]. Furthermore, the incorporation of elastin into these materials also affects their geometry, porosity and morphological structure, which in turn influences the mechanical properties [366]. The architecture of the elastin matrix defines the shape, distribution, alignment and arrangement of cells within tissues by providing cell-to-cell contact orientation and spatially modulating cell infiltration and clustering [367]. Therefore, elastin biomaterials facilitate cellular organisation [362], [368], [369].

There are several advanced methods of wound healing, including negative pressure therapies, the use of bioengineered skin substitutes or hyperbaric oxygen. However, these approaches do not achieve complete healing due to the significant variability in wound size and location between individuals, and they only partially address the relevant biological mechanisms [370]–[372]. Elastin-based materials can address the critical need to develop better treatments that target multiple mechanisms in chronic wounds. Chronic wounds are characterised by being stuck in the inflammatory phase, which impairs healing through the following mechanisms: loss of endogenous ECM, impaired growth factor activity and bacterial infection. These issues can potentially be addressed with elastin-based materials, as the fundamental components are derived from natural peptides and can emulate the ECM by providing a matrix that replaces damaged or lost tissue in wounds by conferring elasticity and functionality. This can be achieved by replacing the missing elastic network or by signalling the positive regulation of elastic tissue biosynthesis. In chronic wounds, the presence of excess metalloproteinases results in the degradation of endogenous growth factors and bioactive peptides, thereby inhibiting cell proliferation, differentiation, and migration. In such instances, elastin-based materials can be employed as drug delivery vehicles to protect bioactive compounds from degradation [373]. Finally, chronic wounds and burns are prone to infection and bacterial colonisation, a growing problem due to the emergence of antibiotic-resistant pathogens. In such cases, the use of elastin-based materials may be beneficial, either by virtue of their antibacterial properties or by allowing the sustained and controlled release of antibiotics [374].

A number of complex multifunctional structures based on elastin in the form of as fibres [352], [375]–[377], coacervates [378], sponges [379], [380], particles [381]–[383] or hydrogels have been developed by different research groups to meet all the requirements mentioned above, such as mechanical properties and adequate stiffness, porosity or morphology. Nevertheless, the use of fibres, coacervates, sponges and particles derived from natural biomaterials is constrained by a number

of significant limitations in their application to tissue engineering. Despite their notable mechanical strength, fibres present significant challenges in terms of manipulation and precise engineering for specific applications. Furthermore, they can exhibit long-term structural integrity issues. Coacervates, despite their utility in encapsulating bioactive agents, frequently exhibit limitations in stability, reproducibility, and cellular integration. Sponges, due to their porous structure, facilitate the diffusion of nutrients. However, they often lack the elasticity and adaptability necessary to follow the dynamic movements of living tissue. Furthermore, they present problems of uniformity in cellular distribution and vascularisation. Despite the high specific surface area offered by the particles, there is a risk of heterogeneous distribution, which can impede the formation of uniform and functional tissues and may result in the onset of unwanted inflammatory responses. Consequently, hydrogels represent the optimal choice as they exhibit the most suitable properties for chronic wound healing. These include a high-water content due to their porous, three-dimensional structure, biocompatibility and bioadhesiveness. Hydrogels are hydrophilic polymeric networks that exhibit the property of swelling and deflating in aqueous solutions. This moisture exchange provides an optimal microclimate between the dressing and the wound bed, thereby promoting the wound healing process more effectively [384].

As hydrogels are applied directly to the wound, it is imperative that the dressings are non-toxic and do not cause a foreign body reaction. Therefore, it is essential that these materials are biocompatible. Furthermore, hydrogels must adhere sufficiently to the wound to protect the wound microenvironment from external factors and bacterial infection, as well as to prevent fluid leakage. These materials ensure complete coverage by rapidly conforming to the shape of the wound, even in the case of irregular wounds [385], [386]. Finally, some hydrogels have the capacity to self-repair, maintaining their structural stability and intrinsic integrity even after mechanical disruption. Consequently, these dressings offer a number of advantages, including prolonged life, prevention of secondary injury and the ability to maintain their shape through a variety of self-repair mechanisms [387].

Furthermore, hydrogel dressings provide a cooling and soothing effect, as well as reducing the pain associated with dressing changes due to their high moisture content. They are easily removed from the wound site without causing any additional tissue damage [388]. In addition, some hydrogels are transparent, which facilitates clinical assessment of the wound healing process without the need to remove them from the site of application. Finally, some hydrogels exhibit additional properties, such as stimuli-responsiveness, which enables them to release and diffuse charged bioactive molecules in a controlled manner to promote wound healing [389]–[391]. Figure 12 schematically illustrates some of the key properties of hydrogels that make them an ideal wound dressing. These include biocompatibility, biodegradability, and good bioadhesiveness. It is also of great importance that these wound dressings have a high capacity to adsorb wound exudate and maintain the correct humidity, which is conducive to the healing process. Furthermore, it is important that they present tuneable properties, such as

mechanical properties or porosity, as well as the ability to be injected, which would facilitate the placement of the hydrogel in the wound. Finally, it is advantageous if these hydrogels possess additional properties, including antibacterial or antioxidant characteristics or the capacity to release drugs [176].

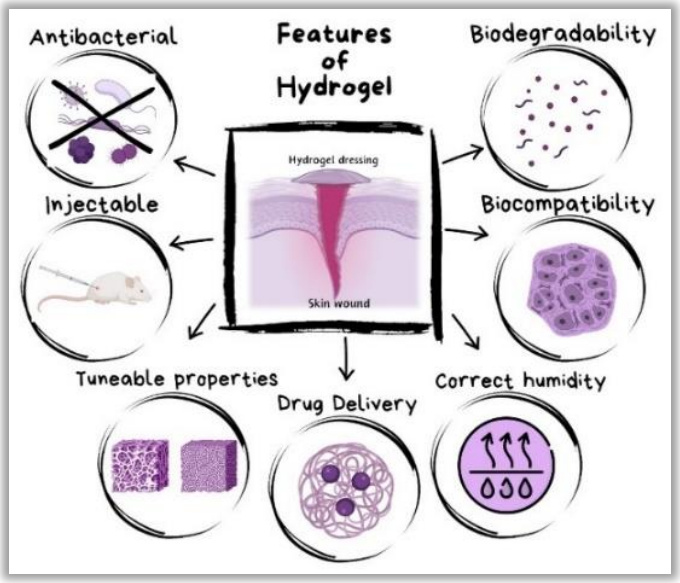

Figure 12 : ***Biological and structural features of hydrogels to enhance wound healing****. Created with BioRender.*

Consequently, numerous researchers have turned their attention to tropoelastin- and elastin-derived hydrogels in their constant search for innovative solutions in wound management. The authors have investigated the potential benefits of these bioactive materials, with the objective of developing more effective and advanced therapies for tissue regeneration and the restoration of normal skin function. In comparison to other natural materials, which are often associated with disadvantages such as collagen-based hydrogel dressings, which are commonly used for ulcers and burns, these materials have been found to exhibit poor biostability and inadequate mechanical properties. Hyaluronic acid, which is effective in promoting cell proliferation and protecting against microorganisms, suffers from low mechanical stability and rapid degradation. This necessitates the frequent replacement of the material, which can cause new lesions and increase the risk of infection. Silk fibroin, renowned for its mechanical strength and biocompatibility, degrades at a relatively slow rate, which may result in encapsulation, granuloma formation, and allergic responses. Finally, chitosan, which is valued for its biodegradability, haemostatic activity, and antibacterial properties, degrades rapidly in acidic environments, which complicates its use in wound healing, given that the pH of wounds is often altered. Consequently, numerous researchers have conducted studies on the use of tropoelastin or elastin, which has the potential to facilitate effective wound treatment and healing. In this context, **Mithieux** *et al.* [392] presented a novel approach for the production of adjustable amounts of elastic fibres. For this purpose, human dermal fibroblasts from donors of varying ages were seeded onto *Integra*® hydrogels for a period of 33 days, with recombinant human tropoelastin added on alternate days. As controls, they had

Integra® cultured with cells but without tropoelastin, and *Integra*® without cells but with tropoelastin. It was observed that the addition of tropoelastin to fibroblasts resulted in the formation of fibres that initially aligned in the direction of the cells, thereby creating a broadly branched elastic fibre network, regardless of the age of the cell donor. However, the fibre architecture undergoes changes with age, with a reduction in the number of fibres observed in cells derived from older age groups, accompanied by an increase in fibre thickness and a reduction in branching. Furthermore, it was demonstrated that the incorporation of exogenous tropoelastin is a prerequisite for the synthesis of elastic fibres, with the absence of synthesis observed in the absence of this addition. Consequently, a hybrid biomaterial was developed that was capable of providing sufficient and detectable levels of elastin in full-thickness wounds, which had previously lacked this elastic underlayer. Following on from this, a year later, the same authors, **Mithieux** *et al.* [393], developed a synthetic heat-treated tropoelastin (HeaTro) construct that promotes the repair of full-thickness skin wounds in pigs through the formation of new blood vessels and the recruitment of adjacent cells. This novel system is based on a novel form of heat-stabilised human tropoelastin, which is subjected to a thermosetting process at 160 °C. The resulting construct, HeaTro, was found to become increasingly stable with prolonged heating times. Subsequently, the scaffolds are implanted into the dermal wound bed, where they are hydrated to form a hydrogel. This dressing has been demonstrated to generate an environment that demonstrates significant benefits in dermal repair, epithelial regeneration and wound healing compared to sterile dressings, commercial hydrogels and dermal regeneration products. Using the same tropoelastin type as described in the two preceding papers, **Rnjak** *et al.* [394] constructed a matrix based on synthetic human elastin that was cross-linked with bis-sulfosuccinimidyl suberate (BS3) at a final concentration of 10 mM. The formed synthetic elastin (SE) hydrogel matrix was observed to promote adhesion and proliferation of primary human dermal fibroblasts for at least 14 days, accompanied by the deposition of extracellular matrix proteins, fibronectin and type I collagen. To facilitate further cellular infiltration, the electrospun ES was transformed into fibrous scaffolds that closely resemble the fibrous nature of the skin dermis, exhibiting an elasticity comparable to that of natural elastin. Additionally, they obtained three-dimensional structures of SE that retained the ability to interact with fibroblasts, forming a monolayer that spans the entire surface of the scaffold and infiltrates into the interior of the scaffold by presenting larger spaces between individual fibres with larger fibre diameters, which resemble dermal elastic fibres. Finally, **Annabi** *et al.* [395] also employed recombinant human tropoelastin in their work, substituting it with methacryloyl (MeTro), which undergoes visible light-induced cross-linking with gelatine methacryloyl (GelMA) to form a novel composite hydrogel. The physical properties, tensile strength, and elastic moduli of this composite hydrogel can be readily modified by varying the concentration of MeTro. Furthermore, GelMA comprises a modified form of denatured collagen, which provides protease-sensitive degradation and cell-binding sites. These properties may be complementary to the interactions exhibited by tropoelastin. The compound is biocompatible, elastic, and sprayable, and exhibits antimicrobial activity against both gram-positive and gram-

negative bacteria through conjugation of Tet213 AMP. The system was demonstrated to support the proliferation and migration of mouse embryonic fibroblast cells in two- or three-dimensional (3D) culture systems *in vitro*. Subcutaneous implantation of hydrogels in Wistar rats confirmed the biocompatibility and *in vivo* biodegradation of the material. Furthermore, the potential of MeTro/GelMA-AMP hydrogels for sutureless wound closure was documented, with the aim of preventing infections and promoting the healing of chronic wounds. Furthermore, in a paper published in the same year, **Annabi** *et al.* [396] proved that recombinant methacryloyl-substituted human tropoelastin (MeTro) can serve as a surgical sealant in the absence of sutures or staples. In a subsequent study, **Tian** *et al.* [397] also used methacrylated gelatine (GelMA) in a different manner. They created a *in situ* hydrogel through the visible light cross-linking of methacrylated gelatine (GelMA) with acryloyl-(polyethylene glycol) N-hydroxysuccinimide ester-modified elastin, which was designed to mimic the dermal microenvironment. This elastin/gelatine composite hydrogel is capable of recruiting and modulating the behaviour of innate immune cells and accelerating angiogenesis at the wound site, thereby promoting healing. The regenerative capacity of these elastin-based hydrogels was therefore studied in a full-thickness skin defect model in mice. It was observed that a predominance of neutrophils and M2 macrophages was present at the wound site, in addition to a high infiltration of the hydrogel. Consequently, the immunoregulatory effect of elastin-based hydrogels enhances angiogenesis, collagen deposition and dermal regeneration, thereby accelerating the wound healing process.

Elastin-based hydrogels have been subjected to more extensive study. A number of authors have dedicated their research efforts to investigating the unique properties of elastin when associated with silk, with the aim of developing biomimetic materials with significant potential for wound treatment. These materials exhibit enhanced mechanical properties and the capacity to facilitate cell adhesion. From this approach, **Kawabata** *et al.* [398] described the development of a flexible silk-elastin sponge that is capable of absorbing wound exudate at physiological temperatures. This is achieved using a recombinant silk elastin protein polymer consisting of a silk-derived sequence (GAGAGS) and a human elastin-derived sequence (GVGVP). This polymer has the ability to self-assemble from liquid to gel on contact with the wound. The efficacy of the silk-elastin sponge was examined *in vivo* using 8 mm full-thickness wounds on the back of guinea pigs. It was found that after administration, the silk-elastin sponge was absorbed and dissolved by the exudate itself. Furthermore, these innovative sponges can be readily applied at a density of 12.5 or 25 mg/cm^3 to a skin wound, thereby encouraging the formation of granulation tissue and facilitating stable wound healing. In a subsequent paper, the same authors, **Kawabata** *et al.* [399], further demonstrated that when the same silk elastin polymer (with GAGAGS and GVGVP sequences) is applied to a severe and intractable full-thickness skin ulcer in a diabetic mouse in an aqueous state, the silk elastin spreads over the wound area, forming a hydrogel layer and maintaining a moist condition without inflammation. This resulted in the wound being protected from external bacterial exposure, which

in turn facilitated the acceleration of healing and the formation of granulation tissue and epithelialisation. Furthermore, the efficacy of the silk-elastin hydrogels was compared with that of conventional products on the market, such as carboxymethylcellulose gel. The results demonstrated that the silk-elastin hydrogels exhibited significantly higher epithelialisation rates and larger areas of granulation tissue. Finally, **Vasconcelos** *et al.* [400] were the first to successfully synthesise a silk fibroin/elastin (SF/EL) scaffold for burn wound treatment using genipin as a cross-linking agent. This resulted in a conformational transition from a random coil to a β-sheet of SF chains. To achieve the desired physical properties, the SF/EL ratio was varied to produce hydrogels with varying pore sizes, expansion ratios and release rates. Furthermore, *in vitro* degradation studies demonstrated that cross-linking with genipin significantly reduced the susceptibility to degradation. The SF/EL scaffolds exhibited reduced cytotoxicity and enhanced cell proliferation of human skin fibroblasts *in vitro*. Finally, a dermal burn healing experiment using human skin equivalents showed that wounds treated with silk fibroin/elastin scaffolds containing a higher amount of elastin induced keratinocyte and fibroblast migration, resulting in accelerated re-epithelialisation and wound closure.

A multitude of studies have yielded hybrid hydrogels comprising elastin in conjunction with other compounds, including chitosan, collagen, gelatine, and hyaluronic acid. These hybrid hydrogels have been demonstrated to be capable of harbouring antibacterial and antimicrobial agents, or even stem cells, and of being released in a controlled manner in the wound area. The objective of this approach is to effectively reduce infections and thus accelerate wound healing. In this regard, the aforementioned work by **Vasconcelos** *et al.* [400] introduced gentamicin as a highly effective antibacterial agent, which stimulated the migration of keratinocyte and fibroblast and accelerated re-epithelialisation and wound closure. Similarly, **Abdel-Aty** *et al.* [401] made a bovine elastin (E) and tannic acid (T) scaffold using a simple conjugation method. This was then combined with polyethylene glycol (PEG) to create a gel, facilitating its placement on the wound. The incorporation of tannic acid into these systems significantly enhanced the wetting, swelling and solubility properties. A micromorphological study confirmed the deposition of tannic acid on elastin fibres, which improved the thermal stability of the assembly and the controlled release of T in various media. Tannic acid also exhibited potent antibacterial activity. Finally, an *in vivo* study was conducted in which burns were performed on the dorsal side of Wistar rats using a heated plate of boiling water. The wounds were treated daily with the E/T conjugate. The results demonstrate that this E/T conjugate accelerates the wound healing process, reducing the wound closure time by reducing the infiltration of inflammatory cells and increasing fibroblast proliferation. Furthermore, it favours the disappearance of the scar by completely restoring both the epidermis and the dermis of the damaged skin. Under this same premise, in a recent work, **Ramzan** *et al.* [402] developed a porous scaffold composed of chitosan, sodium alginate and elastin for the repair of chronic skin wounds. Furthermore, variable concentrations of zinc oxide nanoparticles (ZnO-NP) were incorporated into this hydrogel, which are released in a controlled

manner and act as an antimicrobial agent against *Escherichia coli* and *Staphylococcus aureus* by producing reactive oxygen species that increase lipid peroxidation of the bacterial cell membrane. The *in vitro* cytocompatibility of the composite hydrogel was investigated using human adipose-derived stem cells (ADSC), which demonstrated a high cell proliferation capacity and a uniform distribution of cells within the scaffold. These composite hydrogels can be employed in a variety of wound types, including those with excessive exudate or infected wounds, due to their high porosity and ability to absorb large quantities of fluid. Furthermore, they exhibit potent antimicrobial activity against a wide range of bacteria. From the perspective of charged hydrogels that allow the release of factors that promote healing, **Choi** *et al.* [403] studied the potential of elastin-like polypeptide (ELP) containing, at regular intervals of its skeleton, the cell adhesive ligand RGD (TGPG[VGRGD(VGVPG)$_6$]$_{20}$WPC, termed REP) to enhance cell attachment and proliferation in the treatment of a chronic wound. When REP is co-administered with mouse adipose stem cells (ASCs), a hydrogel-like ASC/REP composite forms *in situ* under physiological conditions. The ASC/REP hydrogels were implanted into full-thickness excisional wound defects in mice together with ASCs. No inflammation or immune response was observed, and neovascularisation and the viability of the transplanted ASCs were significantly enhanced. These effects significantly promoted wound closure and wound re-epithelialisation. Therefore, REP is not only an alternative matrix to replace damaged or lost natural ECM compounds in a wound, but also has the therapeutic potential to enhance stem cell-based therapy with increased *in vivo* viability of transplanted ASCs, which improves wound healing. Finally, **Bergonzi** *et al.* [404] developed a film based on the combination of alginate (ALG) and a biomimetic elastin-derived polypeptide (Human Elastin-Like Polypeptide, HELP), resulting in a composite with improved properties. Furthermore, the ALG/HELP composite films were loaded with curcumin, a natural hydrophobic antioxidant and antimicrobial agent, which is released in a controlled manner over 10 days. The *in vitro* cytocompatibility of these composite films with different concentrations of HELP was studied with human dermal fibroblasts (hDFs), with the results indicating that the films were not toxic to the cells and that they promoted cell proliferation due to HELP. Consequently, the antioxidant activity of curcumin was found to correlate with an increased HELP content, which suggested the applicability of these compounds as smart biomaterials with potential application in the healing process.

The combination of elastin hydrogels with alginate has emerged as a promising option in the field of wound healing. For example, the aforementioned work of **Bergonzi** *et al.* [404] and the work of **Hashimoto** *et al.* [405] where they developed an alginate dressing covalently linked to a hybrid peptide, SIRVXVXPG (X: A or G), consisting of a laminin-derived peptide, SIKVAV, and an elastin-derived peptide, VGVAPG. Initially, the efficacy of the hybrid peptides was examined by studying the binding and proliferation of normal human dermal fibroblasts (NHDF) *in vitro*. The results demonstrated that these peptides exhibited significantly stronger NHDF proliferative activity compared to the control peptides (Ac-KSIKVAV and Ac-KVGVAPG). Subsequently, an alginate dressing incorporating the hybrid

peptide was created and its efficacy on wound healing was evaluated in an *in vivo* model of a rabbit ear skin defect. After nine days, the wounds exhibited significantly greater epithelialisation compared to controls (alginate dressings with SIKVAV alone, VGVAPG alone and no peptides), as well as a greater volume of regenerated tissue.

An alternative method for the production of elastin-based materials for the creation of hydrogels is through the utilisation of recombinant technology, whereby proteins or peptides are specifically engineered to replicate the characteristics of biological tissues. Their capacity to self-assemble and form a three-dimensional matrix provides an optimal environment for tissue regeneration. In this context, **Stojic** *et al.* [406] tested how the mechanical, elastic and biological properties of plasma-derived fibrin hydrogels are improved by adding an ELR network consisting of two ELRs (one modified with azide (SKS-N_3) and one with complementary cyclooctyne (SKS-cc)) at three different SKS concentrations of 1, 3 and 5 wt %. In order to study the biological properties of these novel hydrogels, the researchers employed both primary human fibroblasts (hFBs) and primary human keratinocytes (hKCs). The findings indicated enhanced mechanical properties and augmented elasticity when the SKS content was equivalent to or greater than 3 % and a reduction in the shrinkage of the hydrogel. However, the viability of the 3D model is dependent on the concentration of ELR. Consequently, when the SKS concentration was 1 %, an improvement in hFB proliferation was observed, whereas no such improvement was observed with hKCs. In contrast, when the SKS concentration was 5 %, hKC proliferation was increased, but hFB proliferation was decreased, in comparison to the plasma hydrogel control. The authors propose that these plasma-ELR hydrogels, which possess adjustable properties, could serve as *in vitro* dermoepidermal skin models for the testing of pharmaceutical products used in chronic wounds and even cosmetics.

Furthermore, in a recent paper, **Sarangthem** *et al.* [407] proposed the use of human elastin-derived materials with controlled biological properties, which play an important role in the regulation of molecular signalling, including proliferation, migration, differentiation and tissue repair. To this end, they genetically synthesised a heat-sensitive ELR and cell adhesins containing ECM domains, such as RGD (integrin-binding ligand) and YIGSR (laminin-selective receptor-binding ligand). Three cell types were employed in a series of experiments to assess the impact of these novel ELR polymers: murine fibroblasts (NIH3T3), human umbilical vein endothelial cells (HUVEC) and human keratinocytes (HaCaT). The results demonstrated an enhanced cellular response in terms of cell-cell or cell-matrix integration, motility and proliferation. In particular, these engineered fusion ELRs facilitated rapid and robust fibroblast adhesion, as well as enhanced keratinocyte migration and HUVEC cell tube formation. These processes are essential in the wound healing process, as they favour epithelialisation, dermal repair and blood vessel formation, which are crucial for tissue regeneration. Finally, **Del Prado-Audelo** *et al.* [408] reported the synthesis of a novel composite hydrogel using elastin and polyvinylpyrrolidone (ELT-PVP) via gamma radiation-induced cross-linking. The hydrogel exhibited a porous morphology with interconnected pores,

which permitted a pseudoplastic fluid rheological behaviour. Furthermore, to assess the biological characteristics of these novel ELT-PVP hydrogels, viability and proliferation analyses were conducted with human dermal fibroblasts, which exhibited high biocompatibility and demonstrated higher cell viability in the hydrogel compared to ELT. This suggests that cross-linking ELT with PVP by gamma irradiation in aqueous solution allows the production of a hydrogel with an appropriate morphology for use as a wound dressing.

Other studies have combined elastin with other components, such as collagen and gelatine, which are generally cross-linked with the help of genipin to form hybrid hydrogels that simulate skin substitutes. In this regard, **Sallehuddin** *et al.* [409] developed an acellular hydrogel based on collagen, gelatine and elastin (CollaGee) for use in full-thickness skin wounds and added genipin flavonoids (GNP) as a cross-linker to improve mechanical strength, degradation rate and thermal properties. The physicochemical, mechanical and biocompatibility properties were studied with and without the GNP cross-linker (0.1 % w/v), and it was found that the GNP cross-linked CollaGee exhibited superior physicochemical (increased porosity and swelling ratio) and mechanical (higher strength and degree of cross-linking) properties compared to the non-cross-linked CollaGee groups. In addition, the samples were observed to be compatible with cells and human dermal fibroblasts demonstrated a viability of at least seven days. Additionally, in a recent paper, **Kamaruzaman** *et al.* [410] constructed hybrid scaffolds of collagen (derived from sheep tendon type I) and elastin (derived from chicken skin) that they cross-linked with 0.1 % (w/v) genipin, thereby mimicking the extracellular matrix of skin matrices. The scaffolds exhibited a uniform and interconnected porous structure with a porosity greater than 60 % and a high-water absorption capacity. Furthermore, the biodegradation rate of the 5 % elastin-containing gel was found to be lower than that of the collagen-only control. The biocompatibility of these scaffolds was evaluated *in vitro* using human dermal fibroblasts (HDFs) extracted directly from abdominoplasty or facelift skin. No toxic effects were identified, and the hybrid scaffolds demonstrated significant support for the adhesion and viability of human skin cells, suggesting their potential use as acellular matrices in wound treatment.

Finally, in recent years, there has been a significant increase in the use of 3D printers to generate complex scaffolds for tissue regeneration. Consequently, the development of biocompatible and functionally active bioinks for 3D printing has become a crucial area of research for various applications aimed at the formation of new tissues, organ regeneration and the restoration of normal function of damaged tissue. These bioinks permit the fabrication of customised three-dimensional structures that emulate the intricacy and functionality of natural tissues, thereby offering an innovative approach to tissue regeneration. Nevertheless, despite the considerable advances that have been made in the field of 3D scaffold bioprinting, the availability of elastin-based bioinks that are capable of reducing scar contraction, facilitating the healing process and restoring elasticity to regenerated skin remains limited. This is due to the limitations of current printing methodologies, which prevent the printing of elastic and highly vascularised tissues.

The scientific literature on elastin-based bioinks is limited. They are typically composed of natural tropoelastin or recombinant elastin (ELRs) [411], [412]. From this perspective, **Derr** *et al.* [413] developed a bioink for three-dimensional printing of skin-equivalent hydrogels based on collagen, gelatine, fibrin and elastin. The addition of gelatine to the bio-ink facilitated the extrusion process by increasing its viscosity. Fibrin was included to prevent matrix shrinkage by strengthening the collagen matrix. Elastin conferred elasticity to the bio-ink. Finally, collagen was added as an extracellular matrix (ECM) component to enhance cell adhesion, maintain tissue thickness, and reduce the maturation time of the tissue. This distinctive hydrogel formulation enables the fabrication of a human-like artificial skin with minimal tissue shrinkage, which can be bioprinted with high throughput, rapid printing times and short incubation periods. To develop the dermal compartment, they employed a bioink loaded with neonatal human dermal fibroblasts (HDFn), which simulated the basal layer. To develop the epidermal compartment, they used a bioink loaded with neonatal normal human epithelial keratinocytes (NHEK). Consequently, these advances in bioprinting functional artificial skin with these novel hydrogels pave the way for new avenues of research in the field of chronic wound healing, as well as in the creation of skin disease models for the evaluation of drugs and cosmetics. This line of reasoning was subsequently followed by **Tayebi** *et al.* [414]. Rheology analysis was employed to identify the optimal composition for the development of a printable bioink for use in 3D-printed guided tissue regeneration. The resulting composition consisted of 8 % gelatine, 2 % elastin, and 0.5 % w/v sodium hyaluronate. The soft membranes were composed of six layers with a gradient structure, allowing the generation of small pores on one side and large pores on the other. This structure was designed to accommodate different cells, such as fibroblasts and keratinocytes, on different sides. *In vitro* tests showed that this structure allowed for the complete separation of the epithelial layer from the underlying tissues. Finally, in a more recent study, **Cadamuro** *et al.* [415] described a procedure that relies on a biocompatible click reaction between elastin and hyaluronic acid to obtain 3D bioprintable hydrogels. To achieve this, the elastin and hyaluronic acid were functionalised with linkers ending in maleimide groups and cross-linked with a dithiol PEG linker. The biocompatibility of these 3D hydrogels was evaluated through *in vitro* studies, in which fibroblasts and epithelial cells were exposed to the hydrogels and observed for survival and proliferation. Furthermore, ELHA hydrogels have been demonstrated to exert functional biological effects on both fibroblasts and epithelial cells. These effects include increased expression of CD44 and αvβ3 integrin and modulation of metalloproteinase transcription levels.

A summary of the published work to date on elastin-containing hydrogels applied to promote wound healing is presented in Table 5.

Table 5: A summary of published work on elastin-containing hydrogels used to promote wound healing.

Polymer/sequence	Structure type	Release of bioactive products	*In vitro* experiments (types of cells)	*In vivo* experiments (Types of wounds and animal model)	Year	Paper
*Recombinant human tropoelastin isoform SHELΔ26A (synthetic human elastin without domain 26A) *Integra	Hydrogel	-	*Human Dermal Fibroblast (HDFs) from neonatal, 10, 31 burned, 51- and 92-year-old males	-	2016	[392]
*Recombinant human tropoelastin isoform SHELΔ26A (synthetic human elastin without domain 26A)	Heat-Based Formation of Stabilized Tropoelastin (HeaTro) Hydrogel	-	*Human Dermal Fibroblast (HDFs)	*Murine Model: Four square full-thickness skin wounds (1 × 1 cm) on the back of 12 mice (Balb/c, male) at 10 weeks of age. *Porcine Model: Six full-thickness skin wounds on the back of 12 pigs.	2018	[393]
*Recombinant human tropoelastin isoform SHELD26A (Synthetic Human Elastin without domain 26A) * Bis-sulfosuccinimidyl suberate (BS3)	*Electrospun scaffolds * Hydrogels	-	*Primary Human Dermal Fibroblast	-	2009	[394]
*Methacryloyl-substituted recombinant human tropoelastin (MeTro) *Gelatin methacryloyl (GelMA)	Composite hydrogels: MeTro/GelMA MeTro/GelMA-AMP MeTro/GelMA-ZnO	Antimicrobial peptide (Tet213)	* Mouse Embryonic Fibroblast cells (NIH-3T3)	*Murine model: Eight 1-cm incisions on the posterior dorsomedial skin of male Wistar rats for subcutaneous implantation	2017	[395]
* Acryloyl-(polyethylene glycol)-N-hydroxysuccinimide ester elastin (Elastin-PEG-AC) • Gelatin methacryloyl (GelMA)	*In-situ* Visible-light cross-linking hydrogel	-	*Primary Human Umbilical Vein Endothelial cells (HUVECs) *Human Foreskin Fibroblast (HFF-1) *Monocyte/Macrophage-like Raw 264.7 cells	*Murine model: Full-thickness skin wounds of 10 mm diameter on the back of female C57BL/6J mice weighing about 20 g and 8 weeks age	2022	[397]
* Silk-fibroin (GAGAGS) * Elastin (GVGVP) (MDPVVLQRRDWENPGVTQLNRLAAHPPFASDPMGAGSGAGAGS [(GVGVP)4 GKGVP (GVGVP)3 (GAGAGS)4]12 (GVGVP)4 GKGVP (GVGVP)3 (GAGAGS)2 GAGAMDPGRYQDLRSHHHHHH)	Silk-elastin sponge hydrogel	-	-	*Guinea Pig Model: Full-thickness wounds of 8 mm in diameter on the backs of female guinea pigs at 7 weeks of age * Diabetic Murine Model: Pressure ulcers wound on the backs of BKS.Cg-+Leprdb/+Leprdb/Jcl) diabetic mice at 9 weeks of age	2017	[398]
* Silk-fibroin (GAGAGS) * Elastin (GVGVP) (MDPVVLQRRDWENPGVTQLNRLAAHPPFASDPMGAGSGAGAGS [(GVGVP)4 GKGVP (GVGVP)3 (GAGAGS)4]12 (GVGVP)4 GKGVP (GVGVP)3 (GAGAGS)2 GAGAMDPGRYQDLRSHHHHHH)	Silk-elastin sponge hydrogel	-	-	*Guinea Pig Model: Four full-thickness wounds of 8 mm in diameter on the backs of female guinea pigs at 7 weeks of age * Diabetic Murine Model: Full-thickness skin defect on the backs of C57BLKS/J Iar+Lepr db/+Leprdb female diabetic mice at 9 weeks of age	2018	[399]
* Silk-fibroin: Silk cocoons from Bombyx mori * Elastin: Elastin soluble from bovine neck ligament • Genipin (GNP)	Silk fibroin-elastin (SF/EL) hydrogels	Gentamicin (antibacterial agent)	*Human Normal Skin Fibroblasts (BJ5ta telomerase-immortalized cell line)	* EpidermFT- Human full-thickness skin equivalents: Two burn wounds with a cautery on top of the tissue for 10 s.	2012	[400]
*Elastin: Elastin soluble from bovine neck ligament * Tannic acid * Polyethylene glycol (PEG)	Elastin/tannic acid (E/T) Conjugate Hydrogel	Tannic acid (antibacterial agent)	-	* Rat Model: Burn wound with a hot plate (diameter 5 cm × 2.5 cm) on the dorsal of twenty-five male Wistar rats	2023	[401]

Polymer/sequence	Structure type	Release of bioactive products	*In vitro* experiments (types of cells)	*In vivo* experiments (Types of wounds and animal model)	Year	Paper
* **Elastin**: Elastin soluble from bovine neck ligament * **Chitosan**: High molecular weight: 310.000–375.000 Da * **Sodium-alginate** * **ZnO-NPs**	Chitosan sodium alginate- elastin/ ZnO-NPs composite hydrogels	Zinc oxide nanoparticles (ZnO-NPs) (antimicrobial agent)	*Human Adipose Stem Cells (ADSCs)	-	2023	[402]
* **RGD-containing elastin-like polypeptide (REP):** TGPG[VGRGD(VGVPG)6]20 WPC * **Adipose stem cells (ASC)**	ASC/REP composite hydrogel	Adipose stem cells (ASC)	*Adipose stem cells (ASC) from C57BL/6J-GFP mice *Human Epidermal Keratinocytes	*Murine model: Full-thickness excisional skin wounds on the back of male C57BL/6J or nude mice weighing about 20 g and 8 weeks age	2016	[403]
* **Human elastin-like polypeptide (HELP)** * **Alginate:** Sodium alginate	ALG/HELP Composite films	Curcumin (antimicrobial agent)	*Human Dermal Fibroblasts (hDF)	-	2020	[404]
***Hybrid peptide:** SIRVXVXPG (X: A or G), fashioned from a laminin-derived peptide, SIKVAV, and an elastin-derived peptide, VGVAPG ***Alginate**	Hydrogel	-	*Normal Human Dermal Fibroblasts (NHDFs)	*Rabbit model: One 10 mm-diameter circular skin defect in each ear with a scalpel to the depth of bare cartilage of sixty-six young adult male Japanese white rabbits	2004	[405]
* **Elastin-like recombinamer (ELR):** MESLLP [(VPGVG VPGSG VPGVG VPGKG VPGVG VPGSG VPGVG)2 VAVTGRGDSP ASSGGGGSGGGGSGGGGS (VPGVG VPGSG VPGVG VPGKG VPGVG VPGSGVPGVG)2]6-V * **Plasma-derived fibrin: Fresh frozen human platelet-poor plasma**	Hybrid-plasma-derived fibrin-ELR hydrogels	-	*Human Primary Fibroblasts (hFBs) * Human Primary Keratinocytes (hKCs)	-	2021	[406]
* **Elastin-like recombinamer (ELR):** containing ECM domains: - RGD (Arg-Gly-Asp) integrin binding ligand -YIGSR (Tyr-Ile-Gly-Ser-Arg) laminin-selective receptor binding ligand	Hydrogel	-	*Murine Fibroblast cell (NIH3T3) * Human Umbilical Vein Endothelial cell (HUVEC) * Human Keratinocytes cells (HaCat)	-	2022	[407]
* **Elastin:** Alpha fraction hydrolyzed elastin (ELT) (70,000 Da) * **Polyvinylpyrrolidone (PVP)**	*In-situ* gamma irradiation cross-linking ELT-PVP hydrogel	-	* Human Dermal Fibroblasts (HDFs)	-	2021	[408]
* **Elastin:** From poultry skin * **Collagen type I:** From ovine tendon * **Gelatin** * **Genipin (GNP)**	Hybrid CollaGee/ GNP hydrogel (Skin substitute)	-	* Human Dermal Fibroblasts (HDFs)		2022	[409]
* **Elastin:** From poultry skin * **Collagen type I**: From ovine tendon * **Genipin (GNP)**	Hybrid hydrogel (Skin substitute)	-	* Human Dermal Fibroblasts (HDFs)	-	2023	[410]
* **Elastin** * **Collagen type I** * **Gelatin** * **Fibrinogen**	Hydrogel (Skin substitute) (Bioink)	-	*Neonatal Human Dermal Fibroblasts (HDFN) *Neonatal Normal Human Epithelial Keratinocytes (NHEKN)	-	2019	[413]

Polymer/sequence	Structure type	Release of bioactive products	*In vitro* experiments (types of cells)	*In vivo* experiments (Types of wounds and animal model)	Year	Paper
* **8% Gelatin**: from porcine skin * **2% Elastin**: molecular weight 60 KDa * **0.5% Sodium hyaluronate** molecular weight 500 KDa-749 KDa	Hybrid membrane-hydrogel (Bioink)	-	* Normal Oral Fibroblasts (NOF) * Normal Oral Keratinocytes (NOK)	-	2018	[414]
* **Elastin:** α-elastin with maleimide-PEG2-succinimidyl ester (EL-PEG-MA) * **Hyaluronic acid:** hyaluronic acid with 2-maleimidoethylamine (HA-MA)	Click ELHA Hydrogel (Bioink)	-	* Human lung fibroblast cell (CCD-19Lu) * Human Endothelial cells (HUVEC) * Human Bronchial Epithelial cells (HBEC-1cells)	-	2023	[415]

Consequently, the objective of chronic skin wound management is not merely wound closure; it is also the prevention of scar contracture following wound healing. However, in light of the aforementioned research findings, no currently available dressing material or ointment is simultaneously effective in preventing infection in chronic ulcers and reducing wound contracture in acute ulcers. Furthermore, none of these materials meets all the requirements for an ideal dressing, including being biodegradable, having a good injectability, being antimicrobial, or enhancing keratinocytes adhesion and proliferation. Consequently, the objective of this thesis is to develop a dressing based exclusively on elastin that promotes the healing of chronic wounds. By using a recombinantly synthesised elastin, the precise composition of the material can be modulated and designed to support the recruitment and proliferation of both fibroblasts and keratinocytes. Furthermore, the use of elastin in the formulation of this dressing exploits its biocompatible and biodegradable nature, which reduces the risk of adverse reactions or side effects on the skin. Additionally, its elastic capacity to reduce wound contraction and subsequent visible scarring is beneficial. Besides, the bioactive properties of elastin are leveraged to modulate cell migration, adhesion, and proliferation at the wound site. Moreover, the tuneable mechanical properties facilitate the formation of new tissue, thereby accelerating the healing process. In addition, it can be predicted that the elastin-only dressing will have a high capacity to regulate moisture, taking into account its swelling capacity. This will promote an optimal environment for wound healing, as a moist environment promotes cell proliferation and new tissue formation.

MATERIALS AND METHODS

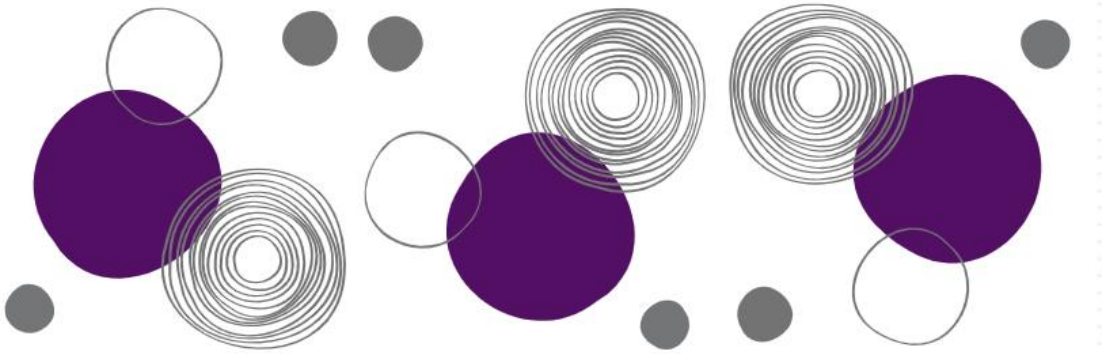

2.- Materials and Methods

2.1.- Materials

2.1.1.- Chemical Reagents

The reagents utilized in this thesis are catalogued in Table 6, organized according to their intended use. The chemicals purchased are of synthetic or analytical quality. The reagents were obtained from commercial sources and utilized without any prior purification or procedure.

Table 6: Chemical reagents.

Reagents (Abreviation)	Brand
Molecular biology	
Acrylamide	Amresco LLC
Ampicillin	Apollo Scientific
Bacto™ Agar	BD/Difco Biosciences
Bromophenol Blue	Sigma-Aldrich
DNA marker (1kb Plus DNA Ladder)	Invitrogen
DNA staining (SimplySafe)	Eurx
Kanamycin	Apollo Scientific
Plasmid Purification Kit (NucleoSpinPlasmid)	Macherey-Nagel
PureLink® Quick Gel Extration Kit for purifying DNA fragments from agarose gels	Invitrogen
Quantum Prep Plasmid Miniprep Kit for purifying plasmid DNA from bacteria	Biorad
Seakem Agarose	Cambrex
Production and purification	
Ammonium sulfate ($(NH_4)_2SO_4$)	Sigma-Aldrich
Antifoam 204	Sigma-Aldrich
Auto-induction culture medium (Terrific Broth, TB)	Formedium
4-(2-Aminoethyl) benzenesulphonyl fluoride hydrochloride (AESBF)	Apollo Scientific
Chloroform	Sigma-Aldrich
Coomassie Brillant-blue	Sigma-Aldrich
Copper chloride ($CuCl_2$)	Sigma-Aldrich
Disodium hydrogen phosphate (Na_2HPO_4)	Fisher Scientific
E-64	Apollo Scientific
Ethylenediaminetetraacetic acid (EDTA)	Sigma-Aldrich
Glucose	Panreac Chemistry
Glycerol	ThermoFisher Scientific
Hydrochloric acid (HCl)	ThermoFisher Scientific
Isopropanol	Invitrogen
Leupeptin	Apollo Scientific
Lysogeny culture medium (Luria Bertani, LB)	Conda-Pronadisa
Pepstatina A	Apollo Scientific
Phenylmethylsulfate fluoride (PMSF)	Apollo Scientific
Protein marker (Unstained Protein Ladder (MUNS))	ThermoFisher Scientific
SOC medium	Sigma-Aldrich
Sodium chloride (NaCl)	ThermoFisher Scientific
sodium dodecyl sulfate (SDS)	Sigma-Aldrich
Sodium hydroxide (NaOH)	ThermoFisher Scientific
Tetramethylethylenediamine (TEMED)	Sigma-Aldrich
Tris(hydroxymethyl)aminomethane (Tris-base)	Sigma-Aldrich
β-Mercaptoethanol	Sigma-Aldrich

Chemical modification	
(1R,8S,9S)-bicyclo[6.1.0]non-4-yn-9-ylmethyl succinimidyl carbonate (cyclooctyne)	SynAffix BV
2-azidoethyl (2,5-dioxopyrrolidin-1-yl) carbonate (azide)	GalChimia
Acetone	Sigma-Aldrich
Diethyl ether (Et_2O)	Sigma-Aldrich
Dimethyl sulfoxide (DMSO)	ThermoFisher Scientific
Dimethylformamide (DMF)	Sigma-Aldrich
Ethanol	Panreac Chemistry
N -butanol	Sigma-Aldrich
Cells	
Alamar Blue	Invitrogen
Bovine serum albumin (BSA)	Sigma-Aldrich
CellTiter 96® Aqueous One Solution (Cell Proliferation Assay)	Promega
Culture media (DMEM 4.5g/L glucose, Medium 200)	Gibco
CytoTox 96® Non-Radioactive (Cytotoxicity Assay)	Promega
Fetal Bovine Serum (FBS)	Gibco
LIVE/DEAD ® Viability/Cytotoxicity Kit	Invitrogen
Penicillin/Streptomycin	Gibco
Phosphate buffer saline (PBS)	Gibco
Triton X-100	Sigma-Aldrich
Trypan Blue	Sigma-Aldrich
Trypsin Enzyme/ EDTA 0.05%	Gibco

Peptide synthesis	
Dichloromethane (DMC)	Sigma-Aldrich
Fmoc-protected amino acid	Novabiochem
Fmoc-Rink Amide-linker	Iris Biotech
HBTU	Sigma-Aldrich
N,N-Diisopropylethylamine	Sigma-Aldrich
Piperidine	Sigma-Aldrich
TentaGel S NH2	Iris Biotech
Trichloroacetic Acid (TFA)	Sigma-Aldrich
Ex vivo	
Biopsy punches (2 and 8 mm)	Sigma Aldrich
Fungizone	Sigma Aldrich
In vivo	
3M™ Tegaderm™ transparent film roll	3M Science. Applied to Life
Isoflurane	Sigma Aldrich
Pain killer	MSD
Others	
Deuterated dimethyl sulfoxide(DMSO-d_6)	Sigma-Aldrich
Hematoxylin-eosin staining	Sigma-Aldrich
Masson's Trichrome staining	Sigma-Aldrich
Nitrocellulase filter 0.22μm	Millipore Sigma
Paraffin	Sigma-Aldrich
Paraformaldehyde	Sigma-Aldrich
Ultrapure water type I	Millipore Sigma
Ultrapure water type II	Millipore Sigma
Xylol	Sigma-Aldrich

2.1.2.- Buffers

The research presented in this doctoral study employed a variety of buffers, the characteristics of which are outlined in Table 7. All solutions were prepared using ultrapure deionised water. Where appropriate, sterilisation was carried out by autoclaving, as previously mentioned. Those solutions that do not support autoclaving were sterilised by filtration through nitrocellulose membranes with a pore size of 0.22 µm.

Table 7: Buffers.

Buffer	pH	Composition
PBS 1X	7.4	5 mM Na_2HPO_4 and 140 mM NaCl
TAE 1X	8.0	40 mM Tris-acetate and 1 mM EDTA
TE (sonication buffer)	8.0	10 mM Tris-base, 1 mM EDTA and 1 mM PMSF
TBS (washing buffer)	8.0	20 mM Tris-base and 140 mM NaCl
SDS-PAGE Running Buffer	8.3	25 mM Tris-base, 192 mM glycine and 0.1% (w/v) SDS
DNA loading buffer	-	30% (v/v) glycerol, 0.1% (w/v) SDS, 0.05% (w/v) bromophenol blue, 50 mM Tris-base and 0.05 mM EDTA
Protein loading buffer	-	0.3 M Tris-base pH 6.5, 10% (w/v) SDS, 50% (v/v) glycerol, 2% (w/v) bromophenol blue and 25% (v/v) β-mercaptoethanol

2.1.3.- Enzymes

The enzymes employed can be categorised into two distinct types, depending on their intended use:

- **Restriction enzymes**: These are employed in restriction mapping of genes. These enzymes can be classified according to the time of their action, resulting in either rapid digestion or normal digestion. The former category includes enzymes such as *EarI, EcoRI, SspI* and NdeI (Thermo Fisher), while the latter encompasses enzymes such as *Eam1104I (EarI)* and *LguI (SapI)* (Fermentas). Each enzyme is utilised in conjunction with its corresponding buffer, in accordance with the instructions provided by the manufacturer.

-**Other enzymes employed in the modification of DNA**: Other enzymes employed in the modification of DNA included FastAP (Thermo Fisher) and Shrimp Alkaline Phosphate (SAP) (Fermentas) phosphatases, which were used to dephosphorylate the phosphate groups of the linearised plasmids. T4 DNA ligase (ThermoFisher Scientific) was employed as a polynucleotide binding enzyme. Each of these enzymes was utilised with its corresponding buffer and in accordance with the instructions of the manufacturer.

2.1.4.- Cloning and expression vectors

2.1.4.1.- Cloning plasmid

The pDriveAll cloning vector is derived from the commercial cloning vector pDrive (Qiagen), in which the recognition targets of the type II endonucleases *SapI* and *EarI* have been mutated to flank the vector, as illustrated in Figure 13. This mythology permits the construction of genes in a controlled and directional manner by leaving cohesive ends that facilitate the insertion of DNA fragments into the plasmid of interest [416], [417]. Additionally, the cloning vector should not contain any endogenous *SapI* restriction sites [416].

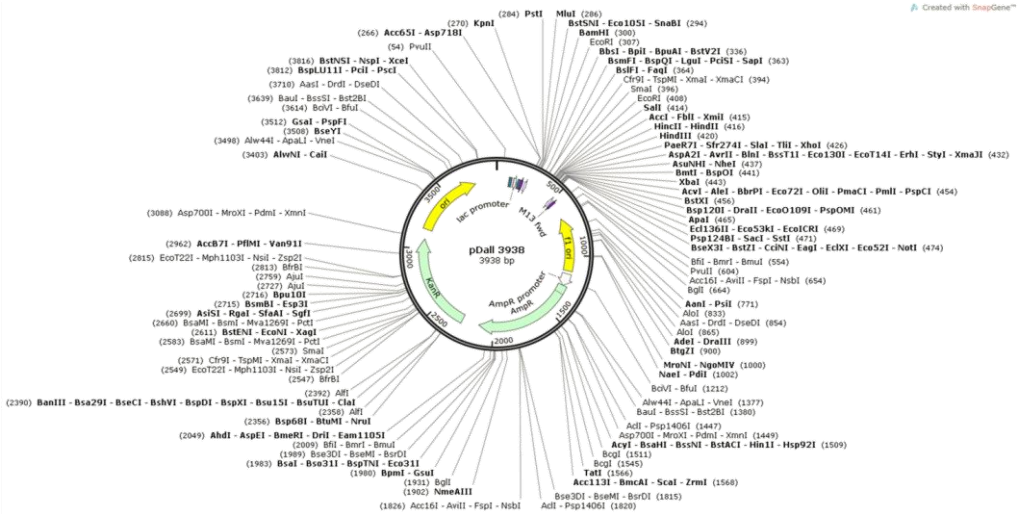

Figure 13: ***Restriction map with all enzymes of the pDrive All cloning plasmid****. Created with SnapGene® software.*

2.1.4.2.- Expression plasmid

The p7RARE expression vector, represented in Figure 14, was employed to express the designed recombinant polymers. The p7RARE expression plasmid was also developed by the Bioforge group from the commercial vector pET25(+) (Novagen) [294]. This expression vector contains recognition sequences for overexpression in *E. coli* strains using an expression system based on the RNA polymerase of phage T7 [418]. Consequently, the mutation occurs within the N-terminal domain and is manifested by a distinct codon choice for translation of the N-terminal amino acid sequence Met-Glu-Ser-Ser-Leu-Pro, with the objective of enhancing ELR expression:

p7: ATGGAA**TCCCTGCTGCCG** (→MESSLP)

p7 RARE: ATGGAA**TCACTACTACCC** (→MESSLP)

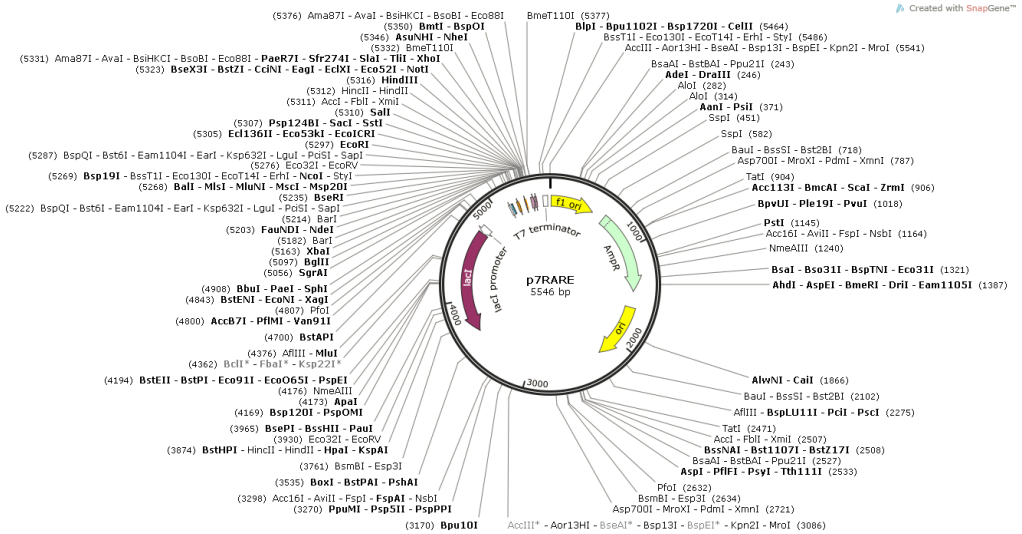

Figure 14: ***Restriction map with all enzymes of the p7RARE expression plasmid.*** *Created with SnapGene® software.*

2.1.5.- Biological materials

2.1.5.1.- Bacterial strains

The various bacterial strains of *Escherichia coli* employed in genetic engineering as hosts for cloning and as expression systems for the genes designed for the production of biomaterials are presented in Table 8.

Table 8: Bacterial strains.

Essay	Bacterial Strain	Competence	Brand
Cloning			
	XL-1 Blue competent cells (*Escherichia coli*)	Transformation efficiencies ≥ 1×10^8 transformants/µg of DNA cloning vector	Agilent Technologies
Subcloning			
	XL-1 Blue subcloning cells (*Escherichia coli*)	Transformation efficiencies ≥ 1×10^6 transformants/µg of DNA cloning vector	Agilent Technologies
Recombinant production			
	BLR (DE3) (*Escherichia coli*)	Transformation efficiencies ≥ 2×10^6 transformants/µg of DNA for protein expression	ThermoFisher Scientific
Recombinant production			
	BL21 (DE3) (*Escherichia coli*)	Transformation efficiencies ≥ 2×10^6 transformants/µg of DNA for protein expression	Novagen

2.1.5.2.- Cell lines

The Table 9 provides a comprehensive list of all cell lines used in this thesis for all *in vitro* tests. In particular, two cell types that are relevant to the process of wound healing, namely fibroblasts and keratinocytes, were employed for the purpose of biologically characterization.

Table 9: Cell lines.

Cell Line	Passage	Brand
Human primary foreskin fibroblastic cells (**HFF-1**)	Early stage (2-15)	ATCC®
Immortal human adult skin keratinocytes (**HaCaT**)	Early stage (2-15)	ATCC®

2.1.5.3.- Animal models

Finally, the animal models employed in this study for *in vivo* investigations, both to assess the biocompatibility of elastin membranes and to examine the regenerative capacity in full-thickness excision wounds, are presented in Table 10.

Table 10: Animal models.

Animal model	Gender	Purchased	Housed	Experiment
Healthy Swiss C57 mice	Female	Chares River Laboratory	Animal Research and Welfare Service (SIBA) of the University of Valladolid	To assess *in vivo* biocompatibility and stability of elastin membranes
Healthy C57BL/6J (JAX™ Mice strain) mice	Male	Chares River Laboratory	Center for Molecular Medicine, Karolinska University Hospital Solna (Stockholm)	To investigate the use of elastin membranes in full-thickness excision wounds

2.1.6.- Culture media

2.1.6.1.- Culture media for bacteria growth

The following culture media were employed throughout this work for gene construction, bacterial growth, transformation and biomaterial production:

-**LB-Agar:** solid-state culture medium for the coating of culture plates. Experimental procedure: 25 g/L LB medium and 15 g/L Bacto™ agar were weighed and reconstituted with distilled water and sterilised in an autoclave for 20 minutes at 121 °C. Once the temperature had been reduced to a level that would not degrade the antibiotic, 100 µg/mL sterile ampicillin and 1 % (w/v) glucose were added to the medium and subsequently plated in Petri dishes (approximately 30 mL).

-**Luria-Bertani Broth medium (LB):** liquid medium used to obtain bacterial growth without protein overexpression. Experimental procedure: 25 g/L LB medium is reconstituted with distilled water and sterilised by autoclaving for 20 minutes at 121 °C. When this medium is to be used, it should be supplemented with 1 % (w/v) sterile glucose and antibiotics as required (100 µg/mL ampicillin or 30 µg/mL kanamycin).

-**Self-inductive Terrific Broth medium (TB):** liquid culture medium that induces protein expression due to its lactose content. Experimental procedure: 55.85 g/L TB medium is reconstituted with distilled water and supplemented with 8 mL/L glycerol and 100 µg/mL antifoam. The medium is then autoclaved for 20 minutes at 121 °C. Once the temperature had reached a sufficiently low level to prevent the antibiotic from being degraded, 100 µg/mL sterile ampicillin was added to the medium.

2.1.6.2.- Culture media for cell lines

The following media were employed to cultivate the respective cell lines, in accordance with the specifications outlined by the suppliers for each case.

-**Human foreskin fibroblastic cells (HFF-1)** were cultured in Dulbecco's Modified Eagle's Medium (DMEM) supplemented with 2 nM L-glutamine, 4.5 g/L glucose, 15 % fetal bovine serum (FBS) and 1 % penicillin/streptomycin solution. HFF-1 cells were incubated in 75 cm^2 tissue culture flask at 37 °C in a humidified air atmosphere with 5 % CO_2, with the medium renewed every 2 days. Cell cultures were subcultured when cells reached 80-90 % confluency. To detach adherent cells

for subculturing and plating, trypsin-EDTA (0.25 % solution) was used and fresh FBS-containing cell culture medium was added in order to neutralize the trypsin. The resulting cell suspension was centrifuged for 5 minutes at 240 g and the supernatant was discarded. Fresh medium was added to obtain a new cell suspension which was loaded into an automated cell counter for cell concentration estimation. Subsequently, specific concentrations of fibroblasts were drop-seeded according to the requirements of each experiment.

-**Immortal human adult skin keratinocytes cells (HaCaT)** were cultured in Dulbecco's modified Eagle's medium (DMEM), containing 2nM L-glutamine and 4.5 g/L glucose, and then supplemented with 10 % (v/v) fetal bovine serum (FBS) and 1 % (v/v) penicillin/streptomycin solution. HaCaT cells were incubated in a 75 cm^2 tissue culture flask at 37 °C in a humidified air atmosphere with 5 % CO_2, and medium was replaced every 2 days. Cell subcultures were made when confluence reached values close to 80-90 %. Upon detachment of adherent cells with 0.25 % (w/v) trypsin-EDTA solution, fresh cell culture medium containing FBS was added to neutralise the trypsin. After centrifugation at 240 g for 5 minutes, the supernatant was discarded and fresh medium was used to prepare a new cell suspension. The cell suspension was loaded into an automated cell counter to determine cell concentration. Subsequently, specific concentrations of keratinocytes were drop-seeded according to the requirements of each experiment.

2.1.7.- RT-qPCR

The material (PCR microtubes and tips) used for PCR is purchased in a sterile state and free from DNases and RNases. Table 11 lists the reagents and TaqMan probes used for qPCR.

Table 11: qPCR material.

Material	Brand
High-Capacity cDNA Reverse Transcription Kits	Applied Biosystems
Maxima Probe qPCR Master Mix (2X)	Thermo Scientific
MicroAmp™ EnduraPlate™ Optical 96-Well Fast Multicolor Reaction Plates	ThermoFisher
MicroAmp™ Splash-Free 96-Well Base	ThermoFisher
Phasemaker™ Tubes	Invitrogen
TRIzol™ Plus RNA Purification Kit	Invitrogen
TRIzol™ Reagent	Invitrogen
TaqMan Probe	
ACTA2, Hs00909449_m1	ThermoFisher
CDH1, Hs01023895_m1	ThermoFisher
VCL, Hs00419715_m1	ThermoFisher
KRT10, Hs00166289_m1	ThermoFisher
KRT14, Hs00265033_m1	ThermoFisher
PTK2, Hs01056457_m1	ThermoFisher
RPL18, Hs00965812_g1	ThermoFisher

2.1.8.- Antibodies

Table 12 provides a detailed description of the antibodies utilised in this thesis.

Table 12: Antibodies.

Antibody	Brand
Alexa Fluor® 488 Phalloidin	Sigma-Aldrich
Anti-Actin, α-Smooth Muscle antibody, Mouse monoclonal (**α-SMA**)	Sigma-Aldrich
Anti-FAK antibody produced in rabbit	Sigma-Aldrich
Anti-VE-Cadherin Antibody (**CD144**), clone BV9 Monoclonal antibody	Sigma-Aldrich (Millipore Corp)
Cytokeratin 14 Monoclonal Antibody (**LL002**)	ThermoFisher (Invitrogen)
Diamidino-2-phenylindole dihydrochloride (**DAPI**)	Lonza
Rhodamin phalloidin 540	Sigma-Aldrich
Vinculin Monoclonal Antibody (**VLN01**)	ThermoFisher (Invitrogen)

2.1.9.- Glass and plastic material

The glassware was subjected to a preliminary cleaning process, followed by sequential rinsing with distilled water, acetone, and again distilled water and ultrapure water type II. Sterilisation was then carried out by autoclaving at 121 °C and 1 atmosphere pressure for a period of 20 minutes in an Autoester E-75 autoclave of the Selecta brand, based in Spain. In contrast, the single-use plastic materials employed, including pipette tips, well plates, centrifuge tubes, and Petri dishes, were purchased in sterile condition or underwent the identical sterilisation process by autoclaving at 121 °C and 1 atmosphere pressure for 20 minutes.

2.1.10.- Materials used in this thesis

2.1.10.1.- ELR Polymers

Table 13 provides a detailed description of the ELR polymers employed in this thesis, including the amino acid sequence and molecular weight.

Table 13: ELR polymers used in this thesis.

ELR Abbreviation	Amino acid sequence	Molecular Weight (Mw)
VKV	MESLLP VG VPGVG [VPGKG (VPGVG)$_5$]$_{23}$ VPGKG (VPGVG)$_3$ VPGV	60462 Da
		
SKS	MESLLP {[VPGVG VPGSG VPGVG VPGKG VPGVG VPGSG VPGVG]$_2$ VAVTGRGDSPASSGGGGSGGGGSGGGGS [VPGVG VPGSG VPGVG VPGKG VPGVG VPGSG VPGVG]$_2$}$_6$ V	82487 Da
		
SKS-IKVAV	MESLLP {[VPGVG VPGSG VPGVG VPGKG VPGVG VPGSG VPGVG]$_2$ AASIKVAVSADR [VPGVG VPGSG VPGVG VPGKG VPGVG VPGSG VPGVG]$_2$}$_6$V	75946 Da
		
SKS-PPFLM	MESLLP {[VPGVG VPGSG VPGVG VPGKG VPGVG VPGSG VPGVG]$_2$ PPFLMLLKGSTR [VPGVG VPGSG VPGVG VPGKG VPGVG VPGSG VPGVG]$_2$}$_6$V	76980 Da
		
SKS-IKVAV-PPFLM	MESLLP {[VPGVG VPGSG VPGVG AASIKVAVSADR VPGVG VPGSG VPGVG]$_2$ VAVTGRGDSPASSGGGGSPPFLMLLKGSTRGGGGS [VPGVG VPGSG VPGVG VPGKG VPGVG VPGSG VPGVG]$_2$}$_6$ V	96744 Da
		

2.1.10.2.- Peptides

Table 14 presents the laminin peptides that were chemically synthesised in this thesis.

Table 14: Laminin peptides synthesised in this thesis.

Peptide Abbreviation	Amino acid sequence	Molecular Weight (Mw)
IKVAV	KAASIKVAVSADR	1358 Da
	N_2—KAASIKVAVSADR	
PPFLM	KPPFLMLLKGSTR	1530Da
	N_2—KPPFLMLLKGSTR	

2.1.10.3.- Dermal substitute – Integra®

One of the most commonly utilised artificial skin grafts in clinical settings is the Integra® Matrix for dermal regeneration, depicted in Figure 15. This matrix is manufactured from a three-dimensional porous structure comprising bovine tendon type I collagen fibres, which are cross-linked with glycosaminoglycans, specifically chondroitin 6-sulphate. The matrix has been designed with a controlled porosity and a defined degradation rate, with the objective of facilitating wound healing. This complex matrix, comprising cross-linked fibres, serves as a scaffold for the regeneration of dermal skin cells, facilitating the growth of a new functional dermal layer in cases of full or partial thickness defects, where autograft is not available in sufficient quantity or is not desirable due to the physiological conditions of the patient.

Although the matrix is designed to mimic the structure of the dermis, the use of a temporary acellular polymeric acellular base does not ensure adequate regeneration of the basal layer. Consequently, dermal grafts have significant limitations, all of which stem from the absence of a substitute epidermal layer. Additionally, it is important to note that Integra® Matrix is not suitable for use in infected wounds.

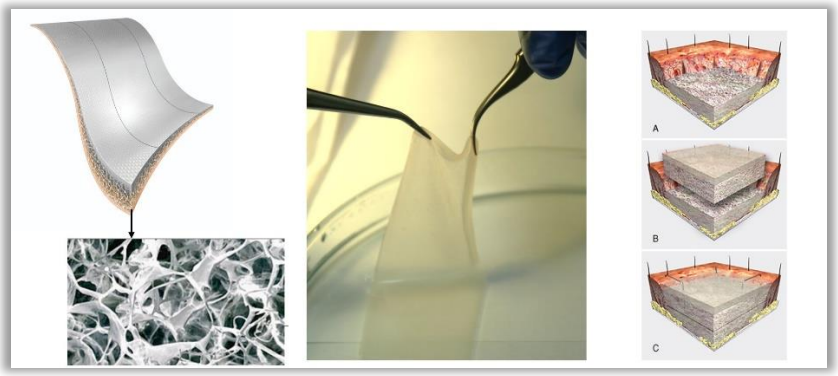

Figure 15: ***Single layer thin Integra® dermal regeneration template.***

2.1.10.4.- Pluronic® Hydrogel

Pluronic F-127 is a thermo-reversible hydrogel that has been recognised and approved by the US Food and Drug Administration (FDA). Its composition is based on a polyoxyethylene - polyoxypropylene - polyoxyethylene (PEO-PPO-PEO) triblock copolymer, which is characterised by the hydrophilic nature of the PEO block and the hydrophobicity of the PPO block. At physiological temperatures (~37 °C), this copolymer undergoes a phase transition where the hydrophobic PPO block dehydrates and cross-links with the hydrophilic PEO block, leading to the formation of spherical microgels, as illustrated in Figure 16. These three-dimensional porous cross-linked gels can revert to the solution phase at temperatures close to 4 °C.

The Pluronic F127 hydrogel displays temperature sensitivity, rendering it injectable. Furthermore, it is biodegradable, non-toxic and compatible with biological tissues. Given these properties, it has become a subject of intense research for its application as a dressing for both acute and chronic wounds, with the aim of promoting healing of skin lesions [419]–[421].

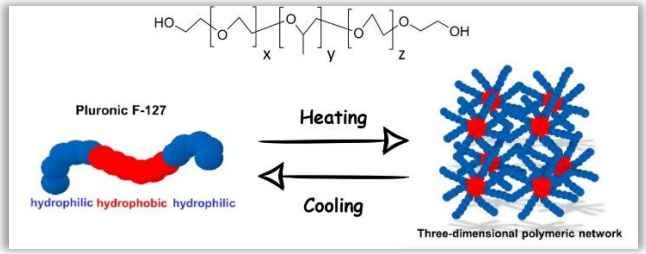

*Figure 16: **Pluronic F-127**. Changes in the morphology of Pluronic F-127 at different temperatures.*

2.2.- Methods

2.2.1.- Molecular Biology

All ELRs utilised in this thesis were produced recombinantly and exclusively for this purpose. As previously mentioned in the introduction, the ELR coding genes were constructed using genetic engineering, employing the iterative-recursive method [416]. The initial coding genes for the ELR sequences were developed by an external company (NZYTech, Portugal). The genes were cloned into the pDriveAll cloning plasmid using XL-1 Blue competent cells as the cloning strain. *E. coli* is a commonly used as a bacterial host for the production of recombinant proteins due to its rapid growth rate, ease of manipulation, and ability to grow at different temperatures and nutrient sources [422]. In addition, this plasmid has the recognition targets of the type II endonucleases *SapI* and *EarI,* which leave cohesive ends that allow the insertion of DNA fragments into the plasmid of interest [416], [417]. Accordingly, the ELR gene sequences must be flanked by two *EarI* restriction sites to facilitate the excision of cloning vector inserts and by a *SapI* restriction site for vector linearisation. Once the final construct has been created, it is inserted into the p7RARE expression plasmid.

In general, hyperproducing strains are typically screened using electrophoresis under denaturing conditions (SDS-PAGE) and the strain with the highest expression is then used to inoculate a fermenter. Fermentation is conducted under controlled conditions of pH, temperature, agitation, and O_2 concentration for a period of 16-18 hours. Then, after washing the bacteria with saline buffer, the biomaterial is extracted using a mechanical disruptor and purified by inverse transition cycling (ITC). This process involves a consecutive heating (40 °C) and cooling (4 °C) cycles, taking advantage of the temperature-dependent reversible phase separation of the ELRs. In all stages of the process, water is used as the solvent, and a 1.5 M concentration of salt is added to contribute to the hot precipitation of the biomaterials. Following three to four purification cycles, the ELRs are subjected to SDS-PAGE analysis to verify their complete purity. Subsequently, the samples are then dialysed against distilled water (3 changes) and ultrapure water (1 change), with the objective of removing all salts, and filtered through a 0.22 µm filter (Nalgene), thus obtaining a sterile product. Finally, the product is freeze-dried (FreeZone 1, LABCONCO) and stored at a temperature of -20 °C until use. The observed yield of purified ELR per litre of bacterial culture ranges from 400 to 600 mg/L.

The following sections will provide a detailed account of the synthesis steps involved in the recombinant production of polymers. Figure 17 illustrates the general strategy employed to obtain the recombinant polymers SKS-IKVAV, SKS-PPFLM, and SKS-IKVAV-PPFLM.

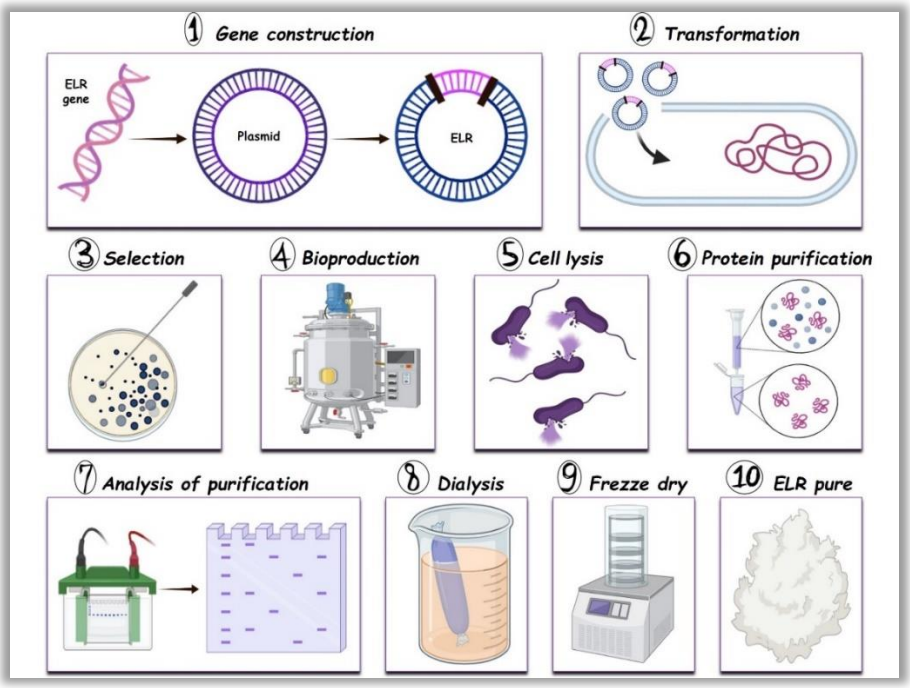

Figure 17: ***Strategy for the recombinant protein production in E. coli****. Created with BioRender.*

2.2.1.1.- DNA digestion with restriction enzymes

The digestion of DNA using restriction enzymes is performed in accordance with the specifications provided by the manufacturer for each used enzyme, including the specific conditions for the reaction, such as temperature, reaction time, concentration, and buffer. Two types of digestion are typically conducted: analytical digestions using FastDigest enzymes, which require incubation of the digestion solution for 15 minutes at 37 °C, and preparative digestions, which require incubation for 1 hour at 37 °C or overnight at 4 °C. The results of both digestions are confirmed through DNA agarose electrophoresis.

The fast digestion process employed enzymes from the FastDigest range, including *EarI, EcoRI, NdeI,* and *SspI*. *Ear I* was the most commonly used enzyme, given that the ELR gene sequences were flanked by two *EarI* restriction sites. In preparative digests, the enzymes *EarI* and *SapI* are typically employed.

2.2.1.2.- DNA dephosphorylation

When a plasmid is treated with restriction enzymes *EarI* and *SapI*, the enzymes create complementary sticky ends. Subsequently, a dephosphorylation step is necessary to prevent the plasmid from closing without the insertion of the desired fragment. The manufacturer of the phosphatase provides the conditions for the dephosphorylation reaction, including temperature, reaction time, and buffer. In preparative digestions, the dephosphorylation process involves two consecutive steps that use two different phosphatases to ensure effective processing. The FastAP enzyme is employed subsequent to preparative digestion, while the shrimp alkaline

phosphatase (SAP) enzyme is applied after purifying the linearised plasmid from the agarose gel.

2.2.1.3.- DNA agarose gel electrophoresis

In order to guarantee the correct insertion of DNA fragments into the plasmid, the size of the fragments resulting from enzymatic digestion with endonucleases is analysed using analytical DNA agarose gel electrophoresis. Analytical electrophoresis is used to rapidly verify the linkages between the insert of interest and the plasmid. Preparative electrophoresis is employed to separate DNA fragments following preparative digestion, with the objective of isolating the gene fragments of interest. The concentration of agarose in TAE 1X buffer is selected based on the expected size of the DNA fragment to be isolated on the gel, as shown in Table 15.

Table 15: Relation between the fragment size and the final concentration of agarose in TAE 1X buffer.

Fragment size (bp)	Agarose final % in 1X TAE (w/v)
800-10000	0.8
400-8000	1.0
300-7000	1.2
200-4000	1.5
100-2000	2.0

In order to prepare agarose gels, the appropriate quantity of agarose must be dispersed in a 30 mL volume of TAE 1X buffer in an Erlenmeyer flask. Prior to the melting of the agarose, the flask is weighed. Subsequently, the agarose is melted by heating it in a microwave to a temperature close to the boiling point, taking care to avoid boiling. After that, ultrapure water is added to the solution until the initial weight is reached, thus maintaining the initial concentration. The solution is cooled until it can be poured into a horizontal mould and a comb is then used to create wells for loading the DNA sample. The gel must be fully hardened before use. Once the gel has formed correctly, it is placed in the reaction cuvette, and the comb is removed, leaving wells where DNA samples can be loaded carefully to avoid damaging the gel. Prior to loading, the DNA sample is mixed with the loading buffer (0.20 volumes of 5X DNA loading buffer). A fixed voltage, ranging from 2 to 7 V/cm, depending on the sample, is applied. The progress of the electrophoresis is monitored using the bromophenol blue-coloured marker as a reference, as shown in Table 16. In analytical electrophoresis, the general conditions are 90 V constant and 400 mA for 60 minutes. In preparative electrophoresis, the general conditions are 60 V constant and 400 mA for 120 minutes.

Table 16: Relation between linear DNA migration and bromophenol blue (BFB) according to agarose concentration.

1X TAE-BPB (bp)	% Agarose final gel (w/v)
2900	0.30
1650	0.50
1000	0.75
500	1.00
370	1.25
200	1.75
150	2.00

After electrophoresis, the plasmid bands are stained with SimplySafe™ DNA stain (20000x solution; 0.005 % (v/v) in TAE 1X buffer) for 30 minutes at room temperature. The stain utilises an intercalating dye that binds between the nitrogen pairs of the DNA. Subsequently, the DNA bands are visualised and recorded by exposing them to UV light in a Gel Doc™ Imager (BioRad) using Image Lab 6.0 software (BioRad). The size of DNA fragments is determined by comparing them with a commercial marker with known weight sizes, such as the 1 Kb Plus ladder (Invitrogen) shown in Figure 18A. The obtained images are then compared to the theoretical restriction map of the samples, which is generated using SnapGene® software.

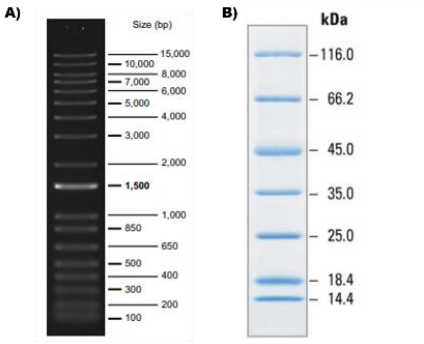

Figure 18: ***Markers. A)*** *1 kb Plus Ladder for determination of DNA fragments.* ***B)*** *Unstained Protein Pierce™ MW marker for determination of protein fragments.*

2.2.1.4.- DNA fragments purification from an agarose gel

After acquiring the corresponding image of the characteristic bands of the DNA fragments resulting from preparative digestion, the preparative agarose gel is subjected to analysis on a TFX-20M transilluminator (Vilber Lourmat). The DNA bands of interest are then extracted using a scalpel. The recovered bands are then weighed, and the DNA within them is purified using the commercial PureLink™ gel extraction kit, in accordance with the instructions provided by the manufacturer.

Finally, the concentration (µg/mL) and purity of the DNA are evaluated using a NanoDrop 2000c spectrophotometer (Thermo Scientific). The absorbance of the DNA sample is measured at 230, 260, and 280 nm using the NanoDrop2000 software. The purity of the samples is determined by calculating the ratio of A260 nm to A280 nm. If the A260 nm/A280 nm ratio is equal to or greater than 1.8, it can be concluded that the DNA is pure and free from protein contaminants and aromatic compounds. The A260 nm/A230 nm ratio is also employed to detect the presence of salt, phenol, and carbohydrate contaminants, with a value of less than 1.5.

2.2.1.5.- Ligation reaction

The ligation reaction involves the use of the T4 ligase enzyme in conjunction with its corresponding buffer, in accordance with the specifications of the manufacturer. The DNA insert with the sequence of interest (sticky end) is ligated

with the linear plasmid (vector) after obtaining the dephosphorylated vector and gene fragments with compatible sticky ends. The ligation reaction occurs when two DNAs are combined in a solution with a molar ratio of 1:5 (vector : insert). Subsequently, the T4 DNA ligase and the respective reaction buffers are then added to the solution, which is then brought to a final volume of 10 µl (with the addition of ultrapure water when necessary). The reaction is then carried out for 1 hour at room temperature. T4 DNA ligase is then inactivated by incubating the mixture for 10 minutes at 65 °C. After incubation, 5 µl of the aforementioned solution is used to transform XL1 blue competent cells.

2.2.1.6.- Transformation of competent cells

2.2.1.6.1.- Transformation of XL1 blue competent cells and XL1 blue subcloning grade competent cells

The transformation of competent cells was performed on XL1-Blue competent *E. coli* strains and XL1-Blue subcloning competent *E. coli* strains. These strains have different transformation efficiencies, with ≥ 1 x 10^8 and ≥ 1 x 10^6 transformants per microgram of DNA, respectively and they are frequently used for gene cloning and manipulation. The XL1-Blue competent cells are employed to amplify a ligation product, whereas the subcloning competent cells are utilized to amplify the quantity of plasmid DNA of interest by cloning. In both cases, the protocol specified by the supplier is followed. To transform XL1-Blue competent cells, 5 µl of the ligation reaction solution is added to 50 µl of bacteria and 1.7 µl of β-mercaptoethanol in a pre-chilled 14 ml BD Falcon polypropylene round-bottom tube (Stratagene). The solution is then incubated on ice for a period of 30 minutes. Subsequently, the cells are subjected to a thermal shock at 42 °C for 45 seconds and then placed them on ice for 2 minutes. Subsequently, pre-warmed SOC medium at 42 °C is added to the cells and incubate and the solution is incubated at 37 °C and 250 rpm for 1 hour. Finally, the cells are plated on Petri dishes containing LB-Agar medium and glucose, and supplemented with kanamycin or ampicillin, depending on the plasmid used (pD or p7, respectively). The plates are then incubated overnight at 37 °C to allow for the growth of colonies with the plasmid of interest. In order to transform XL1-Blue subcloning competent cells, certain modifications are made, including the use of only 10 µL of *E. coli* and 1 µL of plasmid DNA. The initial incubation on ice should last for 20 minutes, followed by a thermal shock at 42 °C for 30 seconds.

2.2.1.6.2.- Transformation of BLR (DE3) competent cells y BL21 (DE3) competent cells

The *E. coli* strain BLR is utilised in the transformation of expression plasmids, such as p7RARE or p10, using the TSS (Transformation and Storage Solution) method to produce ELR polymers. The BLR strain exhibits a transformation efficiency of ≥ 2 x 10^6 transformants per microgram of DNA for protein expression. Briefly, an isolated colony is selected and grown on an LB-Agar plate. Subsequently,

10 mL of LB medium, supplemented with 1 % tetracycline antibiotic, is inoculated for bacterial growth and incubated at 37 °C with shaking at 250 rpm. Once the absorbance of the solution reaches an optical density (OD_{600}) value of 0.3-0.4, cell growth is stopped by incubation on ice for 5 minutes. Cell suspension is then centrifuged at 3000 rpm (1100 g) for 10 minutes at 4 °C. The supernatant is then discarded, and the cell pellet is resuspended in 1 mL of cold 1X TSS solution. Subsequently, the selected plasmid (1-10 ng, 1-10 µL) is added to the mixture. The suspension is maintained on ice for 1 hour, after which thermal shock at 42 °C for 2 minutes is applied. The thermal shock process is terminated by placing the solution on ice for 2 minutes. Following this, 1 mL of warm LB medium (instead of SOC medium) is added, and the suspension is incubated for 1 hour at 37 °C with shaking (250 rpm). Finally, 50-200 µl of the transformation mixture is plated in LB-Agar Petri dishes with the appropriate antibiotic, depending on the plasmid, and incubated for 16-20 hours at 37 °C.

In situations where the expression of the polypeptide in BLR bacteria is challenging, it can be expressed in the bacterial strain BL21 using the protocol provided by the manufacturer, which is analogous to the procedure described in the preceding paragraph. The BL21 strain contains the recombinase recA, which is absent in the BLR strain.

2.2.1.7.- Plasmid purification from bacteria

Following the transformation of the *E. coli* strains and incubation in LB medium with the appropriate antibiotic overnight, based on the plasmid used (kanamycin for the cloning vector and ampicillin for the expression vector), the plasmids are purified using the Quantum Prep Plasmid Mini, Midi or Maxi commercial kit, in accordance with the instructions provided by the manufacturer. The DNA is then eluted in ultrapure water and its concentration and purity are evaluated using a NanoDrop 2000c spectrophotometer (Thermo Scientific) by measuring the absorbance of the DNA sample with NanoDrop2000 software. After purification of the plasmids and bacterial gene fragments, the samples are then sequenced in order to compare the DNA sequences with the theoretical sequences obtained with SnapGene® software. The genes cloned in the pD plasmid were sequenced using primers T7 and Sp6, while the genes cloned in the p7RARE vector were sequenced using primers T7 and T7ter.

2.2.1.8.- Analysis of protein fractions

BLR bacteria that have been transformed with the plasmid of interest contain an expression vector that promotes protein expression. The total fraction of bacterial proteins is quantified using protein gel electrophoresis (SDS-PAGE electrophoresis). In brief, the bacteria are grown overnight in 5 mL TB medium (per colony) supplemented with 1 % antibiotic. In order to evaluate the final protein composition expressed by each bacterial colony, 1 mL of the grown bacterial culture is extracted into an Eppendorf tube and centrifuged at 13400 rpm for 45 seconds at RT. Subsequently, the resulting cell pellet is washed with 1 mL of ultrapure water,

repeating the cycle twice more. After the final centrifugation cycle, the bacterial pellet is resuspended in 100 µL of ultrapure water by vortexing. From this solution, a 20 µl aliquot of the sample is then taken and 5 µl of electrophoresis loading buffer is added. Prior to their loading into the acrylamide gel, the samples are boiled for 5 min and then centrifuged for 5 min at 13400 rpm at RT for subsequent analysis by SDS-PAGE electrophoresis.

2.2.1.9.- Denaturing polyacrylamide gel electrophoresis (SDS-PAGE)

The expression of ELR proteins is analysed using polyacrylamide gel electrophoresis with the addition of the anionic detergent sodium dodecyl sulphate (SDS-PAGE). In the presence of SDS and denaturing agents, proteins are completely denatured and dissociate from each other. Denaturation occurs when the non-covalent bonds that maintain the secondary structure are broken by the effect of the anionic detergent SDS. Additionally, the inclusion of β-mercaptoethanol, a reducing agent, facilitates the breakdown of disulphide bonds present within the proteins. Moreover, the non-covalent binding of SDS to the protein chain confers a negative charge on the polypeptides, which masks their inherent charge and leads to migration that is dependent on size. The protocol used to estimate molecular weight was first reported by Laemmli [423]. In order to achieve better resolutions, various acrylamide ratios (denoted as % T) can be used in accordance with the molecular weight of the polypeptide to be separated. Consequently, the gel resolution was 10 % as the SKS-IKVAV protein has a theoretical molecular weight of 75946 Da, the SKS-PPFLM protein has a theoretical molecular weight of 76980 Da, and the SKS-IKVAV-PPFLM protein has a theoretical molecular weight of 96744 Da. Table 17 presents the optimal acrylamide ratios (% T) for a given size range.

Table 17: Optimal % T according to the size range in which the molecular weight of the polypeptide is encountered.

Size range (kDA)	% T in Resolving gel
24-205	7.5
14-205	10.0
14-66	12.5
14-45	15.0

Table 18 provides a detailed description of the methodology employed for the preparation of resolving and stacking gels at varying acrylamide concentrations.

Table 18: SDS-PAGE resolving and stacking gel composition (one gel).

	Resolving gel				Stacking gel
One gel	7.5 %	10.0 %	12.5 %	15.0 %	4.0 %
Tris 1.5 M (pH = 8.8)	1.88 mL	1.88 mL	1.88 mL	1.88 mL	-
Tris 0.5 M (pH = 6.8)	-	-	-	-	0.63 mL
Acrylamide 40%	1.40 mL	1.88 mL	2.25 mL	2.81 mL	250 µL
SDS 10%	75 µL	75 µL	75 µL	75 µL	18.75 µL
APS 10%	37. 5 µL	37. 5 µL	37. 5 µL	37. 5 µL	18.75 µL
TEMED	3.75 µL	3.75 µL	3.75 µL	3.75 µL	2.35 µL
Ultrapure water	4.10 mL	3.63 mL	3.25 mL	2.69 mL	1.59 mL
Total Volumen	7.5 mL	7.5 mL	7.5 mL	7.5 mL	2.5 mL

The sample preparation process involves heating to a temperature close to boiling point for 5 minutes, which induces denaturation of the proteins, thus adopting their linearized conformation. The protein samples are then loaded onto a polyacrylamide gel and immersed completely in 1X running buffer inside an electrophoresis chamber to ensure current flow. Polyacrylamide electrophoresis is performed using a Hoefer MiniVE vertical electrophoresis system (Amersham Pharmacia Biotech). The regulated direct current power supply allows for the control of voltage, current, or power. A constant electric current of 25 mA per gel was applied to the electrophoresis chamber for 80 to 120 minutes, causing negatively charged proteins (due to the presence of SDS) to migrate towards the anode. Once the bromophenol blue in the loading buffer has reached the end of the polyacrylamide gel, electrophoresis is ceased.

2.2.1.9.1.- Protein marker

In order to ascertain the molecular weight of the proteins present in the sample, a reference ladder containing proteins of known molecular weight must be used. The ladder should move under the same conditions as the sample during electrophoresis. The marker used is a combination of seven native proteins, known as Unstained Protein Pierce™ MW marker (Thermo Scientific), with a size range of 14.4-116 kDa, as illustrated in Figure 18B. The molecular weight of the protein is determined by comparison with the marker.

2.2.1.9.2.- SDS-PAGE Staining

Once electrophoresis has been completed, the gel is stained in order to reveal the separated proteins present in the sample. Two distinct staining methodologies may be employed: the use of copper chloride and Coomassie Brilliant Blue.

2.2.1.9.2.1.- Copper chloride

Staining with copper (II) chloride ($CuCl_2$) is a negative staining technique. This implies that the detergent molecules attached to the proteins prevent the precipitation of metal ions in protein bands, thereby enabling the gel to be stained instead of the proteins. To achieve this, the gel is immersed in a 0.3 M solution of $CuCl_2$ in distilled water and left for 10 minutes in agitation at RT. Subsequently, the gel is then washed with distilled water, and the separated protein bands are visualised on the Gel Doc™ Imager (BioRad), by applying negative contrast for better visualisation, using Image Lab 6.0 software (BioRad).

2.2.1.9.2.2.- Coomassie Brilliant Blue

Proteins are stained using Coomassie Brilliant Blue dye, which interacts with the amino and carboxyl groups of proteins through electrostatic interactions. The negatively charged acid of the dye forms ionic bonds with the positively charged proteins. To achieve this, the gel is immersed in a solution containing 0.125 % (w/v) Coomassie Brilliant Blue, 40 % methanol (v/v), 10 % acetic acid (v/v), and 50 % distilled water, and heated for 30 seconds to enhance the staining process. The gel is then agitated for 30 minutes at room temperature and washed with distilled

water. The expression pattern, represented by protein bands, is visualised using the Gel Doc™ Imager (BioRad) and Image Lab 6.0 software (BioRad).

2.2.1.10.- Glycerol stock preparation

Following the analysis of the results of the expression screening, the clones exhibiting the highest levels of ELR polymer expression after SDS-PAGE electrophoresis are selected and stored as glycerol stocks for future production. To prepare the glycerol stock, the selected colony is grown in 5 mL of LB medium supplemented with 1 % glucose and 1 % antibiotic at 37 °C with shaking at 250 rpm. Once the bacterial solution reaches an optical density of 0.6-0.8 at a wavelength of 600 nm (OD_{600nm}), 0.9 mL is transferred to a cryovial and 0.1 mL of sterile 80 % glycerol is added. The solution is stored at a temperature of -80 °C in order to ensure complete preservation.

2.2.2.- ELRs Bioproduction and purification

2.2.2.1.- Expression screening

Prior to large-scale production it is necessary to screen the expression colonies to identify the optimal producer, as target protein expression can vary between clones derived from a single bacterial transformation. Bacteria containing the ELR polymer are seeded on an LB-Agar plate with 1 % of the appropriate antibiotic and 1 % glucose from the bacterial stock. Isolated colonies are observed after one day of incubation. Eight of these colonies are randomly selected and each one is inoculated in 5 ml of TB expression medium and cultured for 16 hours. Subsequently, the total protein fraction is analysed on an SDS-PAGE gel. The colony that exhibits the highest level of recombinamer expression is selected as the producer colony and used for large-scale production.

2.2.2.2.- Recombinamer bioproduction

In order to screen bacteria carrying the plasmid of interest, a depletion seeding procedure is performed on Petri dishes containing LB-Agar. The colony exhibiting the greatest expression level is then selected. Subsequently, a pre-inoculum is prepared by pouring 5 mL of LB medium containing 1 % ampicillin and 1 % glucose into a 50 mL centrifuge tube. To initiate the bacterial culture, a sterile stick that has been in contact with the selected isolated colony of bacteria is inserted into the tube and incubated at 37 °C and 250 rpm for 10-15 hours. Subsequently, 100 µL of the cultured bacteria are inoculated into a 500 mL Erlenmeyer flask containing 30 mL of fresh LB medium with antibiotics and 1 % glucose. The bacterial culture is incubated at 37 °C and 250 rpm for 4-5 hours. Then, 15 mL (X2) of this culture is transferred to two additional Erlenmeyer flasks (2L), each containing 500 mL of fresh LB medium with antibiotics and 1 % glucose. This ensures that the bacteria always grow in a fresh medium and are in optimal conditions for maximal protein expression. After 2-3 hours, the contents of both Erlenmeyer flasks are used

as an inoculum and poured into the 15 L bioreactor (Applikon Biotechnology). The fermenter contains 14 L of TB medium, 112 mL of glycerol, 1 mL of antifoam, and antibiotics are also added. The culture conditions are programmed to remain constant at 37 °C, 500 rpm, and an air flow of 10 L/min, as well as a pH of 7.2. To prepare negative controls, an inoculum is grown in 5 mL of TB medium supplemented with ampicillin at 37 °C with constant shaking (250 rpm) overnight in an incubator. Following a period of incubation between 14 and 16 hours, the bacteria have grown and have expressed the proteins of interest. To determine the end of bacterial growth and thus the conclusion of the culture, samples are taken to measure the absorbance and determine the stationary phase in the bacterial culture [424]. These samples are also used for subsequent electrophoretic analysis.

2.2.2.3.- Bacteria disruption

Once bacterial growth has ceased, the bacteria in suspension are extracted from the fermenter and centrifuged at 4 °C and 4000 rpm for 12 minutes, resulting in a two-phase separation. The supernatant, comprising the medium, is discarded, leaving only the sediment, which contains the bacteria. To wash the bacterial sediment, multiple resuspension and centrifugation steps with washing buffer at 4 °C and 4000 rpm for 12 minutes are performed, until a clear, translucent supernatant is obtained. Typically, three washing steps are sufficient. Finally, the bacteria that sedimented during the washing process are resuspended in sonication buffer. The volume is calculated by multiplying the final absorbance measured during fermentation by the volume (in L) of the culture and then multiplying by a factor of 5 (in mL). The solution is preheated to 100 °C to denature any proteins or enzymes that could potentially damage the ELR. However, to prevent the degradation of the ELR during subsequent steps, protease inhibitors are added to the suspension. The inhibitors employed are 1 ml of PMSF at 6 µM, 0.5 ml of EDTA at 0.8, 0.5 ml of E-64 at 6 µM, 0.5 ml of pepstatin A at 6 µM, and/or 0.5 ml of AESBF at 0.46 mM. Then, proteins are extracted through mechanical disruption of the bacterial membrane using a GEA Lab PandaPLUS2000 homogeniser (GEA Farm Technologies) with an attached cooling system that maintains the process temperature at 4 °C. The resulting lysate is then centrifuged at 13000 rpm for 90 minutes at 4 °C, resulting in the separation of a supernatant containing the biosynthesised recombinamer, although not in a pure form, as it may contain cell debris.

2.2.2.4.- Purification

The supernatant obtained following the lysis process contains the recombinant of interest, which must be separated from other proteins. Purification of the elastin-like recombinamer is achieve through the use of the inverse transition cycle (ITC) [425], which takes advantage of the intelligent nature based on the inverse temperature transition (ITT) [115], [426]. This process involves a successive cycles of precipitation (by heating) and resuspension (by cooling) of the ELR-containing solution, as illustrated in Figure 19.

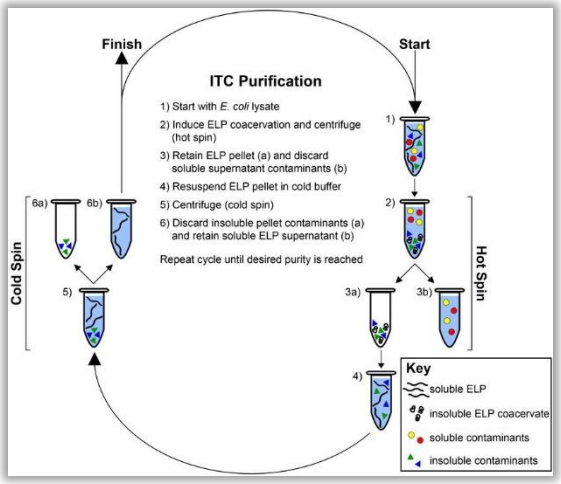

Figure 19: ***Inverse transition cycling process (ITC), involves the purification of the ELR through the exploitation of the inverse temperature transition (ITT).*** *Figure reproduced from* [427].

The purification protocol commences with the heating of the sample at 42 °C for 2.5 hours to precipitate all proteins. Subsequently, the ELRs are subjected to cold solubilisation through overnight agitation at 4 °C and 250 rpm. The solution is then centrifuged at 4 °C and 14000 rpm for 30 minutes. After removing the precipitate by centrifugation, $(NH_4)_2SO_4$ is added in several steps to decrease the T_t, a process known as salting-out [428]. This is followed by a 15-minute incubation at room temperature to facilitate the separation of the recombinamer. The solution is then centrifuged at room temperature at 7000 rpm for 1.5 hours, with the objective of removing any residual salts. Following this, the pellet is resolubilised in cold ultrapure water through overnight agitation at 4 °C. Inhibitors are replenished at each purification step to prevent polymer degradation. Finally, centrifugation is performed at 4 °C and 14000 rpm for 15 minutes. The purification process is cyclic and is monitored by SDS-PAGE electrophoresis. Once the desired purity is achieved, a final reverse osmosis (dialysis) process is performed using distilled water (3 changes) and ultrapure water (1 change) to remove any remaining salts. The recombinamers are then filtered through a 0.22 µm filter (Nalgene) to obtain a sterile product, which is then freeze-dried using a FreeZone 1 (LABCONCO) and stored at -20 °C until use. The quality of the final product is verified using a range of physico-chemical techniques, as described in the subsequent sections.

2.2.3.- Chemical functionalization of ELRs

2.2.3.1.- Catalyst-free click chemistry

The recombinant nature of ELRs enables the inclusion of specific motifs in their peptide chain, which in turn facilitates further chemical modification to functionalise the polymers. Cross-linking domains can be incorporated to obtain covalently cross-linked hydrogels through rapid, orthogonal, and biocompatible catalyst-free click chemistry reactions.

Briefly, the ε-amino groups on the lysine amino acid side chains of each ELR can be modified by the introduction of cross-linkable groups, such as azide or cyclooctyne. Figure 20A illustrates the introduction of cyclooctyne, while Figure 20B displays the introduction of azide. The two groups are complementary and react orthogonally when mixed, forming an irreversible covalent bond between ELR chains, which results in a stable hydrogel.

The chemical hydrogels in question are obtained through the use of the strain-promoted [3+2] azide-alkyne cycloaddition (SPAAC) chemical reaction [429]–[431]. This reaction is a catalyst-free click chemistry reaction that is promoted by the tension of its rings, as presented in Figure 20C. The reaction is dependent on the higher reactivity of the conformationally unfavourable geometry of the deformed cyclooctynes (activated alkyne groups). The deformation of the ring structure facilitates a rapid reaction in the absence of a catalyst [432]. Therefore, the success of SPAAC is contingent upon the molecular structure of the cyclooctyne, which was subjected a series of optimisations over time, culminating in the (1R,8S,9S)-bicyclo[6.1.0]non-4-in-9-ylmethylsuccinimidyl carbonate compound used in this thesis, due to its commercial availability and in addition to its favourable stability and solubility.

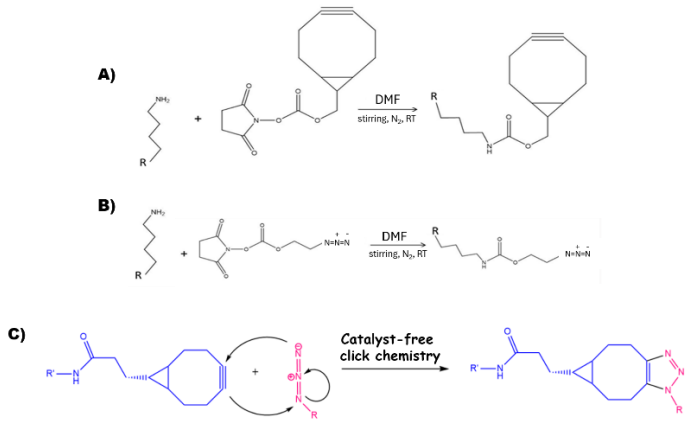

*Figure 20: **Cross-linkable groups**. **A)** Scheme of an ELR modification with the activated alkyne. **B)** Scheme of an ELR modification with an azide group. **C)** Scheme of the SPAAC click reaction between two modified ELRs.*

The 1,3-dipolar Huisgen cycloaddition of azides and alkynes has been demonstrated to be stereospecific, offering several advantages. These include high yields, rapidity, and the ability to achieve chemical cross-linking under physiological conditions (aqueous solvent and near-physiological pH and temperature) without the release of any intermediate products that could be cytotoxic, thus promoting biocompatibility [433], [434].

The degree of modification of lysines can be confirmed using a variety of techniques, such as NMR spectroscopy, ATR (only for azide groups), and mass spectrometry (MALDI-TOF). Additionally, the cross-linking density can be adjusted by varying the density of azide and cyclooctyne groups. This enables control over the mechanical properties and pore size of the network. ELRs can be chemically modified through lysine groups and chemical click reactions, thereby allowing for

tailoring of ELR chains with different bioactive compounds. This makes ELR-based hydrogels a promising candidate for various tissue engineering and regenerative medicine applications [435].

2.2.3.2.- Cyclooctyne-bearing ELRs

In this thesis, ELRs that have been chemically modified to carry a cyclooctyne group on the side chain of the lysine residues are designated as ELR-cyclooctyne or ELR-cc.

-VKV-cc: VKV polymer contains 24 lysines, of which 60 % are modified, therefore approximately 14 lysine side chains will be modified with cyclooctyne groups.

In order to prepare the reaction mixture, 2000 mg of lyophilised VKV was dissolved in anhydrous DMF, followed by the addition of (1R,8S,9S)-bicyclo[6.1.0]non-4-in-9-ylmethylsuccinimidyl carbonate (SynAffix BV), which had been previously dissolved in DMF. The mixture was stirred at room temperature in an inert atmosphere of N_2 for 48 hours. After this time, the product was precipitated by the addition of diethyl ether and centrifugation at 12500 g, 4 °C for 15 minutes. The supernatant was removed, and the white precipitate was washed three times with acetone by centrifugation at 12500 g, 4 °C for 15 minutes. The solvents were then removed, and the precipitate was dried under reduced pressure overnight. The precipitate was resuspended in ultrapure water at 4 °C and dialysed against ultrapure water at 4 °C (3 x 25 L). The pH of the solution was adjusted to 7. The polymer was sterilised by filtration (0.22 µm) and freeze-dried to produce a fluffy white recombinamer.

2.2.3.3.- Azide-bearing ELRs

In this thesis, ELRs that have been chemically modified to carry an azide group on the side chain of the lysine residues are referred to as ELR-azide or ELR-N_3.

-SKS-N_3: SKS polymer also contains 24 lysines, of which 75 % are modified. Consequently, approximately 18 lysines of the side chains will be modified with azide groups.

In order to modify the SKS polymer with azide, the ε-amine group on the lysine side chain was transformed, in a manner analogous to the modification of ELR with alkyne, as previously described. A quantity of 2000 mg of lyophilised SKS was dissolved in anhydrous DMSO. Subsequently, 2-azidoethyl (2,5-dioxopyrrolidin-1-yl) carbonate (GalChimia), which had been previously dissolved in DMSO, was added. The resulting mixture was stirred at room temperature and in an inert atmosphere of N_2 for 48 hours. After this time, the product was precipitated by adding diethyl ether and centrifuging at 12500 g and 4 °C for 15 minutes. The supernatant was removed, and the white precipitate was washed three times with acetone by centrifugation at 12500 g, 4 °C, for 15 minutes. The solvents were then removed, and the drying process was carried out under reduced pressure overnight.

The precipitate was then resuspended in ultrapure water at 4 °C and dialysed against ultrapure water at 4 °C (3 x 25 L). The pH of the solution was adjusted to 7, and the polymer was sterilised by filtration (0.22 µm) and freeze-dried to produce a fluffy white recombinamer.

-SKS-IKVAV-N_3: SKS-IKVAV polymer contains 30 lysines, of which 60 % are modified. Consequently, approximately 18 lysines of the side chains will be modified with azide groups. The procedure is analogous to that previously described.

-SKS-IKVAV-PPFLM-N_3: SKS-IKVAV-PPFLM polymer also contains 30 lysines, of which 60 % are modified. Consequently, approximately 18 lysines of the side chains will be modified with azide groups. The procedure is analogous to that previously described.

-Peptide-N_3: The novel hydrogel to be prepared was a three-component system that already contained the alkyne (in the VKV-cc) and the azide (SKS-N_3). Therefore, the peptide could have been functionalised with either of the two functional groups. However, due to the presence of the RGD cell-binding sequence within the SKS polymer, which is inherently difficult to dissolve, and the necessity of using DMSO to prevent the loss of functionality, peptides were anchored to the VKV-cc. Consequently, peptides were manually synthesised by incorporating an azide group into the amino-terminal region (N_3-KAASIKVAVSADR and N_3-KPPFLMLLKGSTR) in order to tether them to VKV-cc via a click reaction between their complementary groups, thus obtaining the functionalised recombinamer, VKV-cc-peptide.

2.2.4.- Production of ELR-based membranes at a liquid-liquid interface by click chemistry

This thesis employs a chemical click reaction in the absence of a catalyst to generate elastin membranes between polymers VKV-cc and SKS-N_3, as illustrated in Figure 21A. The resulting membrane is a hydrogel with an extremely thin thickness, obtained following the protocol previously described by González-Pérez *et al.* [436]. This technology produces micrometric ELR-based membranes that are particularly effective for the regeneration of damaged soft tissue. The synthetic matrix is colonised by cells, which ensures the adequate neovascularisation and functionality of the newly formed tissue.

Briefly, the production of these ELR membranes requires the use of two ELR polymers. VKV-cc represents the structural group, which is contained in an organic phase that is immiscible with water, and SKS-N_3 exhibits the group with cell adhesion functionality, which remains dissolved in an aqueous phase. Upon contact, the two complementary groups create a liquid-liquid interface due to their respective immiscibility with one another, as depicted in Figure 21B. The polymer chains migrate to the interface in each phase, where a spontaneous cross-linking reaction occurs, leading to the formation of a thin ELR-based membrane.

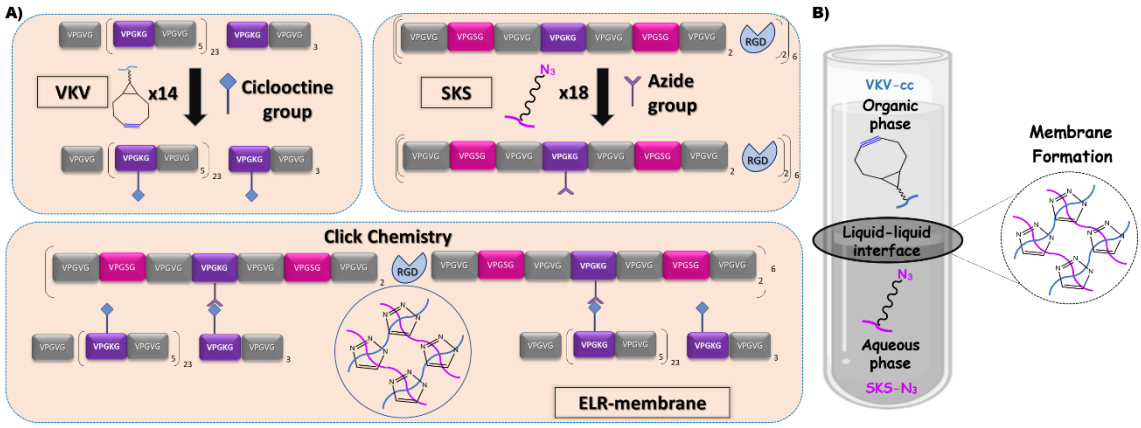

Figure 21: ***Click cross-linking reaction and formation of the ELR-based membrane at the liquid-liquid interface. A)*** *Click cross-linking reaction between the VKV-cyclooctyne (contained in the organic phase, which is composed of 23 % DMSO and 77 % butanol) and the SKS-azide (contained in the aqueous phase) results in the formation of a network via the triazole groups.* ***B)*** *Schematic representation of the cylindrical device employed for the manufacture of the ELR-based membrane.*

The VKV-SKS membranes are synthesized in a customized cylinder where the organic and aqueous phases are mixed to form a circular interface, resulting in a membrane with the same geometry. The device is equipped with a plunger seal and an orifice specifically located on the side, which facilitates the isolation of the formed membrane and the extraction of the aqueous phase. Prior to the addition of the solutions, a circular coverslip is inserted into the container in order to collect the formed membrane. Then, the SKS-N_3 polymer is dissolved in ultrapure water, whereas the VKV-cc polymer is dissolved in 23 % DMSO in butanol. Subsequently, the solutions are then combined sequentially in equal volumes (1:1 v/v), commencing with the denser aqueous phase, followed by a slow addition of the organic phase, with particular attention paid to the avoidance of disruption to the surface of the aqueous phase. The polypeptide chains are cross-linked for 50 minutes at room temperature, forming triazole groups that create the membrane at the interface. Once the reaction has been completed, the upper organic phase is removed using a pipette. The membrane is then detached from the device wall, and the aqueous phase is removed through the lower orifice. Finally, the membrane is deposited on the coverslip and removed by applying a slight force on the plunger.

This system allows the production of tuneable membranes with varying pore sizes, thicknesses, and diffusion rates by adjusting the concentration of polymers in the initial solutions. The thesis will concentrate on the preparation of VKV-SKS membranes at concentrations of 5, 10, 25, and 50 mg/mL for further analysis.

2.2.5.- Synthesis of peptidomimetics by SPPS

Peptides are shorter amino acid chains than proteins, but they play an essential role in protein function. In order to synthesize peptides that mimic natural proteins, it is necessary to control the sequence, composition, and length of the amino acid chain.

A number of techniques are available for the synthesis of peptides, including recombinant deoxyribonucleic acid technology, enzymatic synthesis, transgenesis,

and chemical synthesis [437]. In this thesis, the synthesis of peptides was achieved through the use of organic chemistry, employing the solid phase peptide synthesis (SPPS) method, which was first described by Merrifield [438]. This methodology is faster, more efficient, and more economical than other available techniques. SPPS is a technique that involves covalently bonding an insoluble polymeric support (resin) to the nascent peptide chain. Subsequently, the anchored peptide is then extended through a series of addition cycles using expensive reagents for the efficient coupling and protection of amino acid. These steps are necessary to ensure sequence specificity, eliminate by-products and prevent racemisation. Once chain elongation is complete, the peptide is released from the support.

The SPPS method offers several advantages over other peptide synthesis methods. For instance, it provides high yields since the peptide is bound to a solid support, which allows for the use of excess reagents that can be easily removed through simple washing and filtering processes. Additionally, there is no mechanical loss of the peptide as the solid support to which the peptide is bound remains in the same container throughout the process. Furthermore, the process is easily automated, and the utilisation of this method for synthesis and purification results in a considerable reduction in time [439], [440].

The general process for synthesising peptides in solid phase involves the covalent bonding of the carboxy-terminal (C-terminal) residue, present in an insoluble resin, with the amino group of the given amino acid. The peptide chain is then extended by sequentially coupling specific amino acids until the desired peptide is complete. In order to achieve high specificity and prevent amino acid polymerisation, a series of temporary protectors are used for the α-amino group. These protectors are removed at each deprotection step prior to the binding of the subsequent amino acid. Additionally, permanent protection is employed for the reactive groups on the amino acid side chains, which are removed at the end of the synthesis [441]. The peptide bond is formed by the attachment of the next amino acid, following activation, to the preceding amino acid, once the α-amino group is free. The coupling process requires the activation of the α-carboxyl group of the incoming amino acid, thereby enabling it to react with the amino group of the growing peptide chain. After the amino acid is attached, the resin is filtered and washed to remove any by-products and excess reagents. Subsequently, the protecting group is removed through a deprotection process, and the resin is washed to eliminate by-products and excess reagents. The next amino acid is then attached to the residue. This cycle of deprotection and attachment is repeated until the desired peptide sequence is complete. Once the peptide chain has been synthesized, it is separated from the polymeric support, and the protective groups are removed from the amino acid side chains, typically in a single step. Figure 22 depicts the general process of solid phase peptide synthesis.

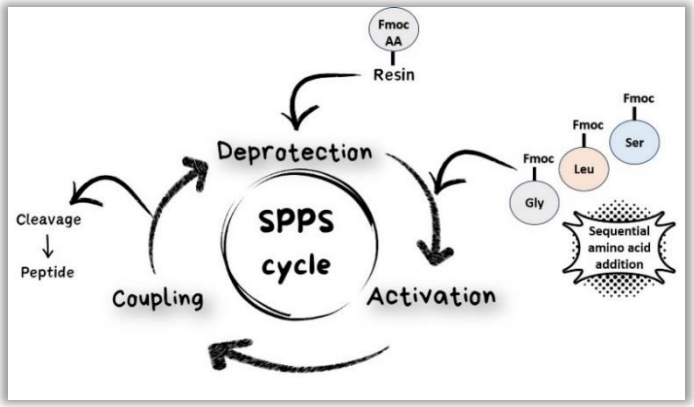

Figure 22: ***General Solid Phase Peptide Synthesis (SPPS) cycle.***

The length of peptide fragments is of great importance in determining the methodology to be employed in SPPS. Consequently, in this thesis, the synthesis of a peptide with a length of less than 40 amino acids (exactly 13) is performed in steps, as illustrated in Figure 22 [442].

2.2.5.1.- Solid support

In recent years, numerous polymeric matrices or resins have been developed for solid-phase peptide synthesis. These matrices must be inert, mechanically stable, and completely insoluble in the solvents used during synthesis. Additionally, they must be suitably functionalised to bind the amino acid or connector.

The peptides chosen for this thesis were synthesized using commercial TentaGel® S NH_2 resins (Iris Biotech). The chemical structure is displayed in Figure 23A. These resins are composed of low cross-linked polystyrene beads with grafted polyethylene glycol (PEG) having a molecular weight of 3000 Da. The PEG spacer is attached to the polymer matrix by an ether bond, which exhibits high stability against acid treatment and minimizes PEG leaching. The commercial resins used have a loading range of 0.2-0.35 mmol (reactive group) per g (carrier), and the beads have a particle size between 90 and 130 µm.

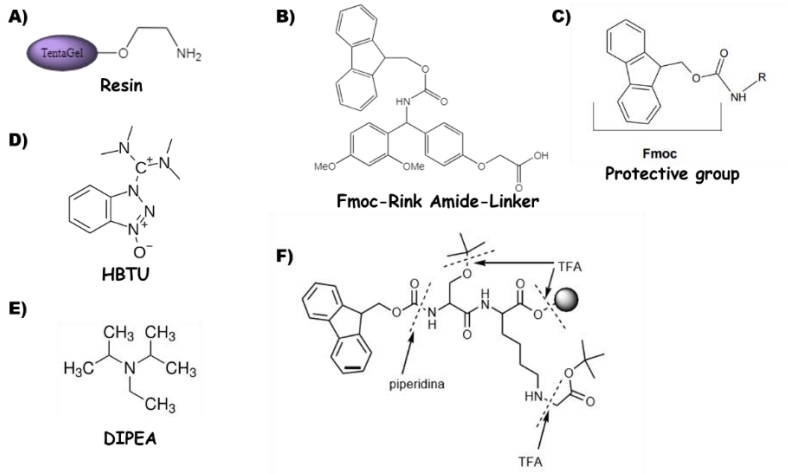

Figure 23: ***Reagents for solid phase peptide synthesis (SPPS). A)*** *Commercial TentaGel® S NH_2 resin composes of polystyrene beads with grafted polyethylene glycol (PEG).* ***B)*** *Fmoc-Rink amide linker.* ***C)*** *The 9-*

fluoromethoxycarbonyl (Fmoc) group to temporarily protect the α-amino group. ***D) - E)*** *Coupling agents (HBTU and DIPEA).* ***F)*** *Scheme for deprotection of the Fmoc/tBu group and cleavage from resin. Chemical structure of compounds from commercial establishments.*

It is important to note that the resins tend to increase in volume when in contact with solvents, which is key for the successful development of the synthesis. The swelling of the polystyrene material with organic solvents is crucial for efficient chain assembly during solid-phase synthesis [438].

2.2.5.2.- Linker

Linkers are chemical units used to attach an amino acid to a resin bead for solid-phase growth of the molecule. The type of chemistry that can be performed and the conditions under which the products can be cleaved from the resin are determined by the nature of the linker. A wide variety of linkers exist for polystyrene core resins, but the most commonly used are Wang, Rink, and derivatives of each. Wang linkers produce COOH products, and Rink linkers produce amide products. In this thesis, a Fmoc-Rink amide linker (Iris Biotech) was employed as it is recommended for the routine synthesis of peptide amides and its chemical structure is displayed in Figure 23B.

2.2.5.3.- N-terminal amino acid protecting group

In SPPS, the protection of functional groups in amino acids is crucial in order to prevent unwanted side reactions involving the α-amino group and side chains [443], [444]. The Fmoc strategy was selected for this thesis because it can be removed under mild basic conditions, thus avoiding peptide instability in acidic environments. Its chemical structure is displayed in Figure 23C [445]. Fmoc chemistry also supports orthogonal protection, which involves eliminating protective groups in a different order, thus achieving deprotection [446]. Piperidine in 20 % DMF was used as the base for the deprotection process, as it captures the Fmoc group.

2.2.5.4.- Coupling agents

To achieve efficient peptide bond formation and minimize racemisation processes, it is necessary to activate the α-carboxyl group of the incoming amino acid. This thesis employs onium salts (aminium/uronium and phosphonium), specifically the N-Hexafluorophosphate salts of [(1H-benzotriazol-1-yl) (dimethylamino)-methylene]-N-methylmethanaminium (HBTU), to achieve this activation. In the presence of a base, typically N,N-diisopropylethylamine (DIPEA), most of these salts can convert the carboxylate of the protected amino acid into an activated species [447]. The chemical structures of HBTU and DIPEA are displayed in Figure 23D and Figure 23E, respectively.

2.2.5.5.- Cleavage from Resin

After the synthesis was completed, the α-amino Fmoc group was removed, and the peptide was fully deprotected and released from the resin through

acidolysis with TFA [448]. The scheme for deprotecting the Fmoc/tBu group and cleavage from resin is shown in Figure 23F.

2.2.5.6.- Synthesis Process

The N_3-KAASIKVAVSADR and N_3-KPPFLMLLKGSTR peptides were synthesized using solid-phase peptide synthesis (SPPS) with the conventional Fmoc protection/deprotection strategy on TentaGel® S NH_2 resin (0.1 mmol equivalent) and DMF as the reaction solvent. The TentaGel® resin was incubated with 7 mL of DMF for 30 minutes with slow stirring to complete the swelling and solvation process. The peptides were synthesized by attaching a Fmoc-Rink amide connector, followed by sequential amino acid coupling and deprotection steps according to the peptide sequence. In order to facilitate the attachment of the peptide to the elastin polymer via click chemistry, a final amino acid containing an azide group (Fmoc-L-Lys (N_3)-OH) was incorporated. This addition does not affect the functionality of the peptide. The coupling reaction was conducted using HBTU and DIPEA at concentrations of one and two times that of the amino acids, respectively, at room temperature for 30 minutes, twice. For the deprotection process, 20 % (v/v) piperidine in DMF was used for 2 minutes, three times. In all preparations, the resin, connector, and amino acids were added in a molar ratio of 1:4:4, respectively. After each coupling or deprotection step, the mixture was washed three times with DMF. After the final deprotection step, the resin underwent washing with 10 ml of DMF (x3), dichloromethane (x4), methanol (x4), and diethyl ether (x4). Then, peptides were dried in a vacuum oven at room temperature until a constant weight was achieved, which took approximately 2 hours. Subsequently, the samples were then stored at 4 °C until their release. To release the peptides, the resin was incubated in a cleavage solution (95 % TFA, 5 % H_2O) for 3 hours at room temperature, resulting in the formation of two distinct phases: one comprising the resin and the other the peptide. The cleaved peptides were then filtered through glass wool, and then precipitated. The isolation of the peptides was achieved through washing and centrifugation in cold diethyl ether (≤ 4 °C) and washed again with acetone. The samples were dried overnight in a desiccator and stored at -20 °C until further analysis.

2.2.6.- Laminin Peptide-Functionalized Click Hydrogel

This thesis presents the development of a three-dimensional, tricomponent scaffold using orthogonal and highly selective chemical cross-linking of azide-alkyne click without catalyst to obtain ELR hydrogels with specific bioactivities achieved through the inclusion of peptides. The VKV-cc polymer is employed as a structural group, while the SKS-N_3 polymer serves as a group with specific cell adhesion functionality. Additionally, both groups included cross-linkable components to enhance structural stability. Furthermore, this system incorporates the attachment of the laminin-derived peptides N_3-KAASIKVAVSADR and N_3-KPPFLMLLKGSTR to stimulate and facilitate wound healing.

The tricomponent ELR hydrogel is obtained through a sequential chemistry process involving two consecutive click reactions. Firstly, the VKV polymer is functionalised with laminin peptides (VKV-cc + peptide-N_3) prior to gelation. Subsequently, a second click reaction occurs between the VKV-peptide with free cyclooctyne groups and SKS-N_3 polymer, resulting in the formation of peptide-functionalised hydrogels (VKV-peptide-SKS). It is important to highlight that the VKV-cc polymer contains 24 lysines, of which approximately 14 undergone modifications with cyclooctynes. The cyclooctynes serve two purposes: firstly, to anchor the synthesised laminin peptides, and secondly, to form the gel when reacting with the SKS-N_3 polymer. Consequently, it is important to meticulously optimise the stoichiometric amounts of peptides in order to guarantee that an adequate quantity of cyclooctynes remains unoccupied, thus enabling the correct formation of the hydrogels.

In addition to the synthesis of the new hydrogels, the impact of conjugated peptide functionalisation on their application with keratinocytes and fibroblasts is also investigated. Hydrogels with increasing peptide concentrations (2X, 4X, and 6X) will be constructed in order to determine which construction exhibits superior properties.

2.2.6.1.- Binding of VKV-cc with peptides-N_3

As previously stated, VKV-cc is initially conjugated to azide-functionalised peptides. In order to achieve this, it is necessary to calculate the mass to be reacted, taking into account the molecular weight of the components (ELR polymer and peptide) and the number of peptides to be included. Therefore, mass will vary depending on the type of peptide (KAASIKVAVSADR or KPPFLMLLKGSTR) and the specific concentration of peptides to be anchored (2X, 4X, and 6X).

Consequently, the N_3-KAASIKVAVSADR peptide is dissolved in DMSO, as it is insoluble in water. Similarly, VKV-cc is also dissolved in DMSO at room temperature overnight with stirring. Once both components are completely dissolved, they are mixed and then allowed to react for 24-48 hours at RT to ensure that all correct binding of all peptide has occurred. In contrast, the N_3-KPPFLMLLKGSTR peptide is dissolved in ultrapure water, which is similar to the VKV peptide with which it will react. Therefore, a temperature of 4 °C is required for dissolution, and the same procedure as that previously described is followed, but in a cold chamber. Once the reaction is complete, the functionalised polymers are dialysed three times against ultrapure water at 4 °C (25 L each time), sterilised by filtration (0.22 µm), and freeze-dried to obtain the white fluffy functionalised polymer, which is ready for use.

Prior to the utilisation of the polymer, the success of the conjugation was confirmed utilizing various experimental techniques, including MALDI-TOF, FTIR, HPLC, NMR, and turbidimetry.

2.2.6.2.- Binding of VKV-peptide to SKS-N_3 to obtain functionalised click hydrogel

The final hydrogels with increasing peptide concentrations will be obtained by reacting all VKV polymers with their respective modifications (VKV-2X-KAASIKVAVSADR, VKV-4X-KAASIKVAVSADR, VKV-6X-KAASIKVAVSADR and VKV-2X-KPPFLMLLKGSTR, VKV-4X-KPPFLFLMLLKGSTR, VKV-6X-KPPFLMLLKGSTR) with SKS-N_3.

To create the new hydrogels with a concentration of 50 mg/mL, the number of cyclooctynes used to introduce the peptides need to be considered. It is important to maintain a stoichiometric ratio of 1:1 between cyclooctynes and azides for proper cross-linking through the click reaction. Therefore, the mass of each VKV-cc and SKS-N_3 polymer in the reaction must be readjusted. It is crucial to have knowledge of the available cyclooctyne-containing lysines. Based on the given specifications, the mass of the VKV-peptide polymer and SKS-N_3 is calculated to be dissolved for each condition, and the volume required to react with each other to form a 400 µl hydrogel is determined. The volume will vary depending on the number of peptides introduced in order to maintain a 1:1 stoichiometry between azides and cyclooctynes. Both polymers, VKV-peptide and SKS-N_3, are dissolved separately in ultrapure water at the final concentration by incubating the solution at 4 °C for at least 24 hours. Once the polymers have been completely dissolved, they are brought into contact and left to react at 4 °C for approximately 30 minutes (below the T_t of each ELR used) to allow the chains with functional groups to meet and form covalent bonds, resulting in a homogeneous three-dimensional network. The reaction is then left to complete for 2 hours at room temperature. During this period, all azide and cyclooctyne functional groups are consumed, resulting in the formation of stable hydrogels (VKV-peptide-SKS). A control VKV-SKS hydrogel with a concentration of 50 mg/mL, excluding the peptides of interest, is used to serve as a reference point for comparison against the novel functionalised three-dimensional network.

The properties of the VKV-peptide-SKS hydrogels will be characterised based on their properties, including transparency, mechanical properties, and internal structure through porosity to determine whether the degree of peptide functionalisation has a direct impact on the network structure, mechanics, and cell behaviour.

2.2.7.- Physico-chemical characterisation techniques

2.2.7.1.- General characterisation techniques

A plethora of physico-chemical techniques are currently available for the study and characterisation of polymer-based materials for biomedical applications. These techniques encompass spectroscopy, microscopy, thermodynamics and

electrochemical measurements, among others. A concise overview of the principal characteristics of these techniques is presented in Table 19. Correlations between surface parameters and structure with the final material properties are of great importance for the application, as many properties depend on them. These include roughness, porosity, swelling, hydrophobicity and biocompatibility. Surface properties of materials forming interfaces with biological organisms essentially determine the biocompatibility of the corresponding systems and treatments [449]. Surface characterisation of polymers varies greatly depending on whether the polymers are in bulk or structured as hydrogels or membranes. Furthermore, these general physico-chemical properties can be modified by varying the concentration of the polymers, the pH, or the ion concentration. However, they are also strongly influenced by the processing conditions, the presence of additives and stabilisers, as well as by the sterilisation techniques employed [449].

The determination of different categories of properties depends on the type of information obtained. These categories include: a) chemical properties (elemental and molecular composition); b) physical properties (porosity, roughness, specific surface area, domain structure); c) physico-chemical properties (the ability of the surface to interact with well-defined test media, including biomedically relevant substances); and d) biological properties (the pattern of interaction with complex biological systems) [449].

Table 19: A summary of the most commonly used methods for characterising biomedical polymer devices.

Characterisation techniques				
Method of analysis	**Nature of information**	**Depth of analysis**	**Lateral resolution**	**Medium**
Attenuated Total Reflectance Fourier-Transform Infrared Spectroscopy (ATR-FTIR)	Molecular composition	300 nm	mm	air, liquids
Mass spectrometry	Molecular composition	Uppermost surface layer	< mm	UHV (Ultra High vaccumm)
X-ray photoelectron spectroscopy (XPS)	Elemental composition	1-5 nm	5 mm	UHV
Wetting measurements	Wettability, Hydrophilicity/Hydrophobicity, Interfacial free energy, Mobility of molecule groups	Uppermost surface layer	mm	air, liquids
Scanning electron microscopy (SEM)	Morphology	Uppermost surface layer	nm	UHV
Atomic force microscopy (AFM)	Morphology, Adhesion	Uppermost surface layer	< nm	air, liquids, UHV
Electrokinetic measurements	Zeta potential, Interfacial charge density, Surface site pk values , Non-electrostatic adsorption free energy of ions	Hydrodynamic boundary	cm	aqueous solutions
Potentiometric and Conductometric measurements	Surface charge density caused by dissociated surface groups (dispersed solids)	Water-assessable surface volume	m^2	aqueous solutions
Ellipsometry	Optical properties, Layer thickness	nm	mm	air, liquids

2.2.7.2.- Physico-chemical characterisation techniques

The purity, molecular weight, amino acid composition and other features of the final product were characterized by a range of analytical techniques, including SDS-PAGE, high-performance liquid chromatography (HPLC), Fourier-transform

infrared spectroscopy (ATR-FTIR), matrix-assisted laser desorption/ionization time-of-flight (MALDI-TOF) and nuclear magnetic resonance (NMR).

2.2.7.2.1.- Proton nuclear magnetic resonance spectroscopy (^{1}H-NMR)

Proton Nuclear Magnetic Resonance (^{1}H-NMR) spectroscopy was used to assess the molecular structure of the polymers and their purity, as well as to accurately and reliably determine the degree of chemical modification of the ELR compounds after a SPAAC click chemical reaction to introduce azides or cyclooctynes, as these molecules cause the appearance of new predictable peaks in the NMR spectrum. Finally, this technique was employed to verify the successful functionalisation of the VKV polymer with the laminin peptides.

In this thesis, we employed a solution of 25 mg/mL of ELR dissolved in deuterated DMSO on a 500 MHz NMR (Agilent Technologies) belonging to the Laboratory of Instrumental Techniques (LTI-University of Valladolid). The spectrum obtained was optimised using the MestReNova programme, correcting the phase so that the baseline was straight and referencing with respect to deuterated DMSO, which corresponds to the highest peak (chemical shift around 2.5 ppm). Once referenced, the area of the peaks corresponding to the different types of hydrogens present in the structure is integrated based on the theoretical prediction of the chemical shift provided by the ChemDraw program.

2.2.7.2.2.- Mass Spectrometry

2.2.7.2.2.1.- Matrix-assisted laser desorption/ionization time-of-flight mass spectrometry (MALDI-TOF)

Matrix-assisted laser desorption/ionization time-of-flight (MALDI-TOF) mass spectrometry is a technique employed to ascertain the precise molecular weight and purity of recombinamers. The molecules are ionised to a gaseous state and filtered based on their m/z for detection. MALDI-TOF is considered to be more precise than SDS-PAGE, and can be used as a complementary technique. This technique can be used to determine the degree of chemical modification of ELR compounds subsequent to a SPAAC click reaction, which introduces azides or cyclooctynes. In this thesis, MALDI-TOF was also employed to corroborate the correct functionalisation of the VKV-cc polymer with varying concentrations (2X, 4X, and 6X) of the laminin peptides (KAASIKVAVSADR and KPPFLMLLKGSTR).

The Laboratory of Instrumental Techniques (LTI-University of Valladolid) conducted the analysis using a Bruker Autoflex Speed instrument (Bruker Daltonics). The sample was prepared by adding approximately 1 µl of matrix consisting of 2,5-dihydroxyacetophenone (DHAP), to a metal MALDI target with 1 µl of dissolved ELR solution (1 mg/mL in DMSO or ultrapure water). The plate was dried with air, and mass spectra were acquired using an Autoflex Speed MALDI-TOF mass spectrometer with a Smartbeam™ laser as the ionisation source. In order to ensure the correct interpretation of the spectra, it is necessary to locate the peak corresponding to the single-charged molecular ion (z=1), which represents the

molecular weight of the polymer. This value can be compared with the theoretical value obtained using ExPASy and the ProtParam tool.

2.2.7.2.2.2.- Ultra-high performance liquid chromatography with quadrupole time-of-flight mass spectrometry (UPLC-ESI-qTOF)

Ultra-high performance liquid chromatography (UPLC) is employed to separate and identify analytes. This technique is often coupled with mass spectrometry (MS-qTOF) in order to enhance the results, thereby enabling the detection of components based on their mass/charge ratio (m/z). Furthermore, molecular fragmentation spectra can assist in the identification of components by comparison with specific software databases. The Laboratory of Instrumental Techniques (LTI-University of Valladolid) employs the ESI-qTOF model Maxis Impact (Bruker) equipment with an electrospray ionisation (ESI) source in positive mode to perform this technique. In this thesis, the UPLC-ESI-qTOF was employed to validate the successful synthesis of the laminin peptides, KAASIKVAVSADR and KPPFLMLLKGSTR, by quantifying their experimental molecular weight.

2.2.7.2.3.- High performance liquid chromatography (HPLC) amino acid analysis

A quantitative analysis of the amino acid composition of the ELRs produced was conducted using high-performance liquid chromatography (HPLC). HPLC was also employed to confirm the correct synthesis of the peptides and the functionalisation of the VKV-cc polymer with the laminin peptides at different concentrations (2X, 4X, and 6X). The Laboratory of Instrumental Techniques (LTI-University of Valladolid) was responsible for carrying out this technique using high-performance liquid chromatography (HPLC) with ultraviolet (UV) detection. The WATERS600 HPLC gradient system (Marshall Scientific) was coupled to a WATERS2487 detector (Waters).

To analyse each component individually, 4 mg of pure polymer underwent acid hydrolysis (6 M HCl, 1 % phenol, and 2.5 hours at 155 °C in an inert atmosphere) to break the bonds between the amino acids. The experimental value obtained from this technique can be compared to the theoretical values calculated from the amino acid sequence.

2.2.7.2.4.- Attenuated Total Reflectance Fourier-Transform Infrared spectroscopy (ATR-FTIR)

Attenuated Total Reflectance Fourier-Transform Infrared Spectroscopy (ATR-FTIR) was employed to identify the functional groups present in the molecules of the compounds of interest, in this case the recombinamers in the freeze-dried solid state, without the necessity for any pre-treatment. The apparatus used was a Bruker Tensor 27 spectrometer (Bruker Corporation) equipped with a Golden Gate ATR accessory (Bruker), with data acquisition and analysis software provided by OPUS (version 4.2).

Prior to commencing analysis of the sample of interest, a background measurement is recorded with the sample holder empty. Once obtained, the lyophilised sample is placed in the ATR equipment and compressed against the ATR crystal until a satisfactory signal-to-noise ratio is achieved. Subsequently, the acquisition scans are conducted at room temperature with a wavelength sweep between 600 and 4000 cm^{-1}, comprising 256 scans with a resolution of 4 cm^{-1}. It is necessary to carry out the correction and normalisation of the signals obtained using the OPUS spectroscopy software. Some signals are challenging to distinguish due to potential signal overlap, given that the polymer in question has a high molecular weight.

2.2.7.3.- Thermal behaviour characterization

The thermal behaviour of ELR polymers can be determined by two techniques: differential scanning calorimetry (DSC) and turbidimetry.

2.2.7.3.1.- Differential scanning calorimetry (DSC)

In this thesis, Differential Scanning Calorimetry (DSC) was employed to ascertain the transition temperature (T_t) of ELRs. The characterisation of hydrogels by DSC allows for the determination of the amount of free and bound water present in the scaffold. The experiments were conducted in a DSC822e (Mettler Toledo) coupled to a liquid nitrogen refrigerator. The temperature and enthalpy were calibrated using standard samples of indium, zinc and n-octane. To determine the transition temperature of the polymers, VKV-cc and SKS-azide, a 50 mg/mL solution was prepared in ultrapure water at pH 7. Subsequently, 20 µL of the ELR solution was placed in a standard 40 µL aluminium pan and hermetically sealed. The same volume of the solvent used to dissolve the ELR was added as a reference. Both the sample and the reference are subjected to the same experimental temperature cycle, which consists of an initial isothermal step (5 minutes at 0 °C to stabilise the temperature and state of the sample), followed by a gradual increase in temperature from 0 °C to the desired temperature range at a rate of 5 °C/min. For analysis of the ELR-based membrane, 2 mg of lyophilised membrane was placed on the sample pan. Subsequently, 20 µL of ultrapure water was added and allowed to equilibrate with the sample overnight at 4 °C. The heating programme in this instance comprises an initial isothermal stage (5 minutes at 0 °C) followed by a constant rate of heating at 1 °C per minute from 0 to 100 °C. A thermogram is generated, in which exothermic processes are associated with positive enthalpy values and endothermic processes with negative enthalpy values.

2.2.7.3.2.- Turbidimetry

To characterise the thermal behaviour of ELRs at low concentrations (1 mg/mL), turbidimetry experiments were conducted in a Cary 100 UV-Vis spectrophotometer (Agilent) with a thermostated sample chamber. The Optical density (OD) is determined by the change in absorbance at 350 nm for ELR solutions in ultrapure water as a function of temperature in a heating ramp from 10 to 90 °C (at a rate of 1 °C/min). The samples are stabilised at each temperature until a

constant turbidity value is reached. This constant value is taken as the optical density of the sample at that temperature. The transition temperatures were determined by identifying the temperature at which the first derivative of the turbidity versus temperature curve reached its maximum [450].

2.2.7.4.- Topography and surface characterisation

Surface roughness is a measure of the texture of a surface. For membranes, roughness can be defined as the deviation of the actual topography of the membrane surface from an atomically smooth ideal surface [451].

An understanding of the surface properties of ELR membranes used as wound dressings is useful in determining how the membrane will interact with its environment. For example, surface roughness is important in understanding the filtration of substances such as nutrients, debris or particles of interest such as drugs, as well as the adsorption and retention of various substances such as wound exudates. In addition, surface roughness can be correlated with other material properties, such as pore size distribution and molecular weight [452].

A variety of techniques were used to characterize the surface properties of ELR membranes, including SEM, ESEM, AFM or contact angle.

2.2.7.4.1.- Scanning electron microscopy (SEM)

Scanning electron microscopy was used to determine the topography of the VKV-SKS membranes and the morphology of the internal microstructure of the elastin hydrogels with different concentrations (2X, 4X, and 6X) of the laminin peptides (KAASIKVAVSADR and KPPFLMLLKGSTR) and the novel polymers SKS-IKVAV and SKS-IKVAV-PPFLM. Two different microscopes were used. On the one hand, the membranes were only freeze-dried and an FEI Quanta 200 FEG instrument (Unidad de Microscopía Avanzada, Parque Científico, Universidad de Valladolid) equipped with a tungsten Schottky filament, an acceleration voltage of 15 kV and a BSED detector was used. These samples were coated with a 4 nm gold layer deposited in a sputter coater using an EMITECH K575X equipment to form a conductive surface. Four locations were randomly selected for image acquisition from different areas of each sample. Each image for every sample was photographed under identical conditions with an 800X of magnification. To analyse the roughness of SEM samples, we installed a special Image J plugin, called Roughness Calculation. This plugin calculates surface roughness statistics based on topographic images. The input is an image or stack where the pixel values represent the distance, z, to a surface. The calculated roughness value was provided in terms of Rq (Root Mean Square roughness) or Ra (Average roughness). Rq is defined as the square root of the sum of the squares of the individual heights and depths from the mean line, while Ra is the average of the individual heights (asperities) and depths from the arithmetic mean elevation of the profile.

On the other hand, new biofunctionalized hydrogels were frozen in liquid nitrogen, cryofractured and freeze-dried. Micrographs were obtained using a Jeol

JSM-IT500 microscope (Servicio de Microscopía de NUCLEUS, Universidad de Salamanca) equipped with a tungsten Schottky filament, an acceleration voltage of 20 kV and an ES detector to observe the internal structure of the fractured hydrogels. In this case, the samples were coated with a 5 nm gold layer using a Quorum Q15RES instrument. Morphological details, such as pore size or porosity, were quantitatively assessed using Fiji ImageJ software [453].

2.2.7.4.2.- Environmental scanning electron microscopy (ESEM)

The environmental scanning electron microscopy (ESEM) technique was employed initially, as it theoretically permitted observation under more physiologically relevant conditions, namely not fully dehydrated and not metallised. In this study, ESEM was employed to characterise the surface properties of the ELR-based membranes. Given that these membranes are intended for use as wound dressings in their hydrated state, it is essential to ascertain that the surface roughness remains consistent when compared to their freeze-dried state, which was previously characterised by SEM. In brief, the hydrated membranes were mounted directly on aluminium supports using carbon adhesive tape and observed using the same instrument as SEM, without the need for gold coating of the sample surfaces. Four locations were randomly selected to obtain images of different areas of each sample. Each image of each sample was captured under identical conditions at 3000x magnification. In order to analyse the roughness, the same procedure described in the SEM section was employed.

2.2.7.4.3.- Atomic force microscopy (AFM)

Atomic Force Microscopy (AFM) in tapping mode was employed to investigate the topography at the Surface Analysis and Fabrication Platform of the CIC biomaGUNE in San Sebastian, using a Multimode 8HR (Bruker). For membranes with a concentration of 50 mg/mL, topography images were captured in standard tapping mode using a TESPA-V2 probe (Bruker), with a nominal resonant frequency of 320 kHz and a force constant of 0.42 N/m. The scanning rate was set at 1 Hz. For membranes at concentrations of 25, 10, and 5 mg/mL, the PeakForce tapping mode was employed with SCANASYST-AIR probes with a nominal resonant frequency of 70 kHz and a force constant of 0.4 N/m. Adjustments to the scanning rate and peak force frequency were made to optimize results. Hydrated samples were cut, and double-sided FIXO tape was used to mount them onto magnetic tabs, after removing excess water. A chamber was employed specifically to maintain a humid environment and prevent dehydration of the sample. The topography of the surface area (10 µm x 10 µm) is represented by height profiles. The images were analysed using the roughness routine Nanoscope Analysis 2.0 software (Bruker). To characterise the surface topography of membranes, the root-mean-square roughness (Rq) is the most commonly parameter used and can be calculated by using Equation 1:

$$R_q = \sqrt{\frac{1}{L}\int_0^L |Z^2(x)|dx}$$

Equation 1: Root-mean-square roughness (Rq)

where L is defined as the surface profile measure in terms of height (Z) and position (x) of the sample over the evaluation length (L). Other definitions can also be used to characterise the roughness, such as the mean roughness (the mean value of the surface relative to the centre plane) or the peak-to-valley distance (the distance between the highest data point and the lowest data points on the surface). However, these definitions are less accurate than the Rq roughness. All experiments were performed in triplicate.

To assess the membrane recovery study, a thin scalpel was used to manually create a scratch in the 50 mg/mL membrane. Images were captured at time zero, after 30 minutes, and after the membrane was rehydrated with 5 µl of water. The scratched area was imaged using SCANASYST-AIR probes in tapping mode, with a scan area of 100 µm x 100 µm. Samples were cut and fixed onto magnetic tabs with double-sided FIXO tape, removing any excess water. Image analysis was conducted using the sectioning routine in Nanoscope Analysis 2.0 software (Bruker). Furthermore, three-dimensional illustrations were generated to enhance the visibility of the self-renewing process using the Nanoscope Analysis 2.0 software (Bruker).

Finally, AFM is a standard technique utilised for evaluating the Young´s modulus of soft materials at the nanoscale using nanoindentation. To assess the quantitative nanomechanical measurements, the PeakForce QNM module was implemented for mapping the topography of the sample and recording nanomechanical properties, such as Young´s modulus, adhesion, dissipation and deformation. The distribution was obtained by bearing analysis, while the average values were obtained by roughness routine. The probe employed for this study was a SCANASYST-AIR (Bruker). Prior to use, the spring constant rate and deflection sensitivity were calibrated on a sapphire sample. The tip radius was determined by the absolute method, which involved measuring a rough titanium reference sample and utilizing the tip qualification tool in the Nanoscope Analysis 2.0 software (Bruker). The estimated value for the radius was 3.7 ± 0.1 µm. The Hertzian model was applied to calculate Young´s modulus. After numerous attempts, it was unfeasible to acquire measurements that match the results from the previously published paper [436]. This was due to the high viscosity of the samples, which causes them to adhere to the tip of the cantilever, making it unattainable to obtain accurate measurements.

2.2.7.4.4.- Contact angle. Wettability

The analysis of the surface energy and affinity of the liquid to the solid substrate represents a simple and effective approach to obtaining surface properties. In particular, the wettability or hydrophilicity of a membrane has a significant influence on the flux rate, adsorption, type of fouling, efficiency and

lifetime of the membrane [454]. The composition of the membrane material and the chemistry of its surface both influence the interaction between the material and water molecules, which in turn affects the wettability of the material.

The surface tension of a material can be used to determine the wettability of a substrate by certain liquids by measuring the contact angle between a solid surface and a liquid droplet on the surface in a three-phase system (solid/liquid/air). The angle formed by the intersection of the liquid-vapour and liquid-solid interfaces (geometrically integrated by drawing a tangent line from the point of contact along the liquid-vapour interface of the droplet) is called the contact angle and is determined by Young's equation:

$$\cos\theta = \frac{\gamma_{SG} - \gamma_{SL}}{\gamma_{LG}}$$ *Equation 2: Young's equation*

where θ is the contact angle, γ_{LG}, γ_{SG} and γ_{SL} are the liquid-vapour, solid-vapour and solid-liquid interfacial tensions, respectively, as is shown in Figure 24A.

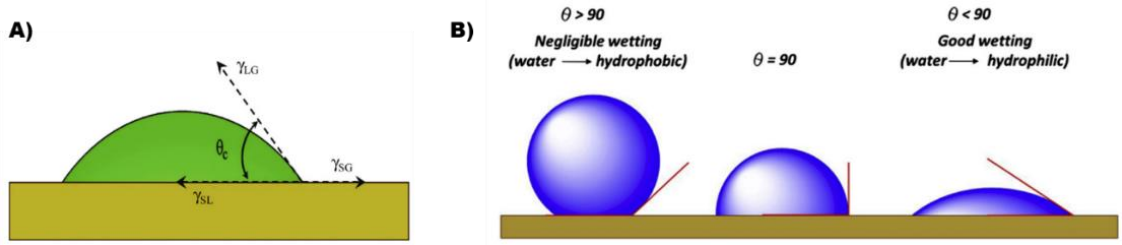

*Figure 24: **Contact angle. A)** Contact angle formed by the liquid spreading over the surface. **B)** The effect of the contact angle on the analysis of hydrophilicity and hydrophobicity. Image adapted from* [454].

A lower contact angle value indicates the hydrophilic nature of the material, i.e. a high affinity of water molecules towards the hydrophilic substrate and such materials readily absorbs water molecules due to the presence of polar active functional groups. A larger contact angle indicates the hydrophobic nature of the surface. Hydrophobic materials have little tendency to interact with water and tend to form 'beads' on their surface, as is shown in Figure 24B.

Measurements were made at room temperature using the sessile drop method with an OCA20 (Data Physics) instrument equipped with a CCD camera. The tip of the stainless-steel needle was always kept at the top of the sessile drop and immersion of the needle in the drop was avoided during the measurements to prevent the needle from distorting the shape of the drop. Contact angles were measured by analysing the deposition of 0.5 µl water droplets on the sample surface. For each membrane condition tested (5, 10, 25 and 50 mg/mL), two different samples were used and five measurements were taken on each sample at different locations on the film surface. Data are presented as SD averaged over the left and right angles. Both hydrated and freeze-dried membranes were imaged after a 15 s stabilisation of the droplet and it was not possible to image the hydrated membranes by this method as they are very hydrophilic.

2.2.7.5.- Other characterizations

2.2.7.5.1.- Swelling ratio and water content percentage (WCP)

The swelling ratio and the water content percentage (WCP) in hydrogels are important parameters that define the mechanical properties on which the final application of the material for biomedical purposes will depend. In addition, the swelling of materials in the presence of fluids is essential to enable absorption and transfer of nutrients or metabolites throughout the film structure in a physiological environment. The degree of swelling or hydration was determined by the gravimetric method. On the one hand, membranes with concentrations of 5, 10, 25 and 50 mg/mL were prepared, lyophilised to remove all water from their structure and weighed to obtain the initial scaffold weight (W_i). They were then immersed in phosphate buffered saline (PBS) or ultrapure water at 37 °C and weighed to obtain the final weight (W_f) of the hydrated scaffold. This process was repeated at various time intervals until the membrane reached physicochemical equilibrium. The equilibrium swelling ratio of membranes is the swelling ratio when the membranes swell to constant weight.

The swelling ratio was calculated using the following Equation 3:

$$Swelling\ ratio\ (w/w) = \frac{Wf - Wi}{Wi}$$

Equation 3: Swelling ratio

On the other hand, to determine the WCP, new membranes were prepared with concentrations of 5, 10, 25 and 50 mg/mL, immersed in ultrapure water at 37 °C until the membranes were completely swollen and weighed when they reached a constant final weight (W_f) of the hydrated scaffold. They were then lyophilized and dried at 50 °C for 2 hours to obtain the constant dry weight of the membranes (W_i) [455], [456]. Additionally, the WCP of hydrogels containing varying concentrations (2X, 4X, and 6X) of the laminin peptides (KAASIKVAVSADR and KPPFLMLLKGSTR) and the new hydrogels, SKS-IKVAV and SKS-IKVAV-PPFLM, were also studied.

The WCP value was calculated according to the following Equation 4:

$$WCP\ (\%) = \frac{Wf - Wi}{Wf} x100$$

Equation 4: Water content percentage

2.2.7.5.2.- Porosity

The porosity of the ELR-based membranes was estimated by measuring their swelling in water and applying the subsequent Equation 5 [435], [457]:

$$Porosity\ (\%) = \frac{Wf - Wi}{\rho_{water}}\ x\ \frac{100}{V_{memb}}$$

Equation 5: Porosity

where W_f and W_i represent the weight of the wet and dry states of membranes, respectively, ρ_{water} is the density of pure water at 20 °C and V_{memb} refers to the volume of the membrane in the wet state ($V_{memb} = \Pi r^2 h$, where r and h are the radius and height of the cylindrical sample, respectively). All measurements were taken 24 hours after soaking the hydrogel in water at the appropriate temperature. Excess surface water was removed with a filter paper before each measurement. All experiments were performed in triplicate.

2.2.7.5.3.- In vitro enzymatic degradation

In general, biodegradability refers to the capacity of materials to decompose over time once implanted in host bodies [458]. The degradation rate of ELR membranes was studied *in vitro* using elastase from porcine pancreas enzyme. The enzyme activity and optimal conditions are detailed in the enzyme data sheet (E1250- Sigma Aldrich). Degradation experiments were performed in triplicate by incubating each membrane with concentrations of 5, 10, 25, and 50 mg/mL in a non-enzymatic solution – phosphate-buffered saline (PBS) to evaluate the stability of biomaterials. The membrane was also incubated in elastase enzymatic solution at a concentration of 24 nM to evaluate the degradation rate in contact with the wound environment. To begin the process, the elastin-based membranes were immersed in PBS for 12 hours until they reached an equilibrium state, then each membrane was placed in 1.5 mL of elastase solution after removing the surface liquid using filter paper. Next, the samples were incubated for 25 days at 37 °C with mild shaking at 80 rpm, and the solution was replaced every 2 days with a fresh portion of elastase solution. The remaining weight of the membranes was measured at specific time points (12 hours, daily from 1 to 25 days) after drying at room temperature. They were then further dried in a desiccator until a constant weight (W_d) was reached. The residual weight (W_r) of the scaffolds is determined by the following equation:

$$Wr(\%) = \frac{Wd}{Wi}\ x\ 100$$

Equation 6: Remaining weight (%) of membranes after immersion with elastase solution

where W_i represents the weight of the membrane after swelling. The rate of membrane degradation was also calculated using the following formula:

$$Dr(\%) = \frac{Wi - Wd}{Wi}\ x\ 100$$

Equation 7: Degradation rate (%) of membranes after immersion with elastase solution

2.2.7.5.4.- Rheological properties

Rheology is a branch of physics that studies the ability of materials to flow and deform. Consequently, this methodology is employed to assess the viscoelastic properties of hydrogels, which enables the determination of their stiffness and hardness, thereby indicating their mechanical characteristics. Oscillating shear measurements were conducted on elastin hydrogels with varying concentrations (2X, 4X, and 6X) of the laminin peptides (KAASIKVAVSADR and KPPFLMLLKGSTR) and hydrogels of the new SKS-IKVAV polymer using a non-porous stainless steel

circular parallel geometry with a diameter of 12 mm on an AR2000ex rheometer (TA Instruments). The measurements were conducted at a temperature of 37 °C, which is representative of the physiological conditions observed in biological systems.

Each ELR hydrogel was prepared in a 12 mm diameter cylindrical mould at a concentration of 50 mg/mL with a volume of 400 µL. The hydrogel was maintained at 4 °C for a period of two hours, during which time the polymer chains underwent cross-linking. Following this, the hydrogel was incubated at room temperature for a further four hours, during which time the cross-linking process was completed. Finally, the hydrogel was equilibrated overnight at 37 °C in a saturated water atmosphere. The VKV-SKV hydrogel was employed as a control. Three replicates were analysed for each hydrogel condition.

After calibrating the equipment, the hydrogel is placed on the thermostated plate and adjust the distance between plates by applying a normal force of 0.01 N to prevent slippage. To determine the range of strain amplitudes for which hydrogels have a linear viscoelasticity range (LVR), conduct oscillatory shear measurements. To achieve this, a dynamic strain sweep was conducted at a constant angular frequency of 1 Hz, with strain amplitudes ranging from 0.01 % to 20 % at 37 °C. Once the linear range of viscoelastic behaviour was established, a frequency sweep was performed. The frequency sweep range was set between 0.1 and 10 Hz at a fixed strain of 1 % (within the LVR region of the hydrogel) at 37 °C. The data were recorded using the Rheology Advantage software, version 4.1 [433].

Rheological measurements provide the storage or elastic modulus (G') and the loss or viscous modulus (G") as a function of stress or frequency at a fixed temperature. The elastic modulus, or storage modulus, indicates the elastic component of the material up to a maximum value, beyond which it is purely elastic. Conversely, the viscous or loss modulus indicates the energy dissipated in the material during deformation. These two moduli are related by the loss tangent ($tan\delta = G" / G'$), which determines the ratio of energy lost in relation to the energy stored.

2.2.8.- Biological characterisation

2.2.8.1.- *In vitro* characterisation

A number of tests are available to assess the *in vitro* cytotoxicity and compatibility of VKV-SKS membranes. These include studies of cell proliferation using the MTS assay, assessment of cell membrane damage using the LDH assay, evaluation of cell viability using the Alamar Blue or LIVE/DEAD assay, gene expression analysis using qPCR, and protein expression analysis using immunostaining. Furthermore, cell growth is evaluated using the colony formation assay, while cell migration is assessed by the transwell migration assay and *in vitro* scratch assay. Additionally, the biocompatibility of hydrogels containing varying concentrations (2X, 4X, and 6X) of the laminin peptides (KAASIKVAVSADR and

KPPFLMLLKGSTR) and the new hydrogels, SKS-IKVAV and SKS-IKVAV-PPFLM, were also investigated.

2.2.8.1.1.- Cell culture in vitro

Two cell types, fibroblasts and keratinocytes, were employed in a biological characterisation of VKV-SKS membranes, which are relevant to the process of wound healing. In particular, human foreskin fibroblasts (HFF-1) and immortal human adult skin keratinocytes (HaCaT) were used for this purpose.

2.2.8.1.2.- Membrane sterilization

Prior to their use with cells, the VKV-SKS membranes underwent a process of washing and sterilisation. This process involved immersion in a range of organic reagents, including acetone (5 minutes), methanol (3 times at 5 minutes each interval), ethanol in varying concentrations (5 minutes each), followed by deionised water and phosphate-buffered saline (PBS) to eliminate any residual organic solvent. Subsequently, the membranes were immersed in PBS for sterilisation through exposure to ultraviolet radiation for a period of two hours in a cell flow hood. Subsequently, following sterilisation, the membranes were immersed in culture medium (DMEM) at 37 °C in a humid atmosphere with 5 % CO_2 overnight in order to achieve equilibrium.

2.2.8.1.3.- MTS cell proliferation assay

Cell viability and proliferation of cells on VKV-SKS membranes were assessed using the MTS colorimetric assay (CellTiter 96 Aqueous assay, Promega). The MTS assay is based on the activity of NAD(P)H-dependent dehydrogenase enzymes present in metabolically active cells that reduce tetrazolium salt (MTS) in the presence of an electron coupling reagent (PES), resulting in the formation of a coloured formazan product that is soluble in cell culture media and has a maximum absorbance at 490 nm.

For the purpose of this experiment, HaCaT and HFF-1 cells were seeded onto ELR membranes in 24-well culture plates at a density of 2 x 10^4 cells/well and then grown at 37 °C in a humidified atmosphere containing 5 % CO_2 for 48 hours. The low cell densities were used to investigate cell proliferation, as there is greater surface area available for cell growth while avoiding premature confluence. Additionally, cells were also seeded in tissue culture plates (TCP) and on a glass coverslip as a positive control for full metabolic activity. The distinct experimental groups were then exposed to the MTS reagent, with the addition of 100 µl of MTS solution to each well containing 500 µl of serum-free medium. Subsequently, cells were then incubated for two hours at 37 °C in a humidified atmosphere containing 5 % CO_2 in the absence of light. To determine the coloured product of MTS reduction, 200 µl of the supernatant was transferred to a 96-well plate and analysed using a spectrophotometric microplate reader (SpectraMax iD3, Molecular Devices) to measure absorbance at 490 nm.

2.2.8.1.4.- Cytotoxicity by a lactate dehydrogenase (LDH) colorimetric assay

The cytotoxicity of ELR membranes was evaluated in HFF-1 and HaCaT cells using the lactate dehydrogenase (LDH) colorimetric assay. LDH is a stable cytosolic enzyme that can be detected following cell lysis, and its release therefore signifies cell membrane damage. The detection was conducted using the cytotoxicity assay kit (CytoTox 96® Non-Radioactive Cytotoxicity Assay, Promega). The kit enables the quantification of LDH in the supernatant of culture media through a coupled enzymatic assay. This process involves the conversion of tetrazolium salt (iodonitrotetrazolium violet, INT) to produce a red formazan product by the action of diaphorases or electron acceptors, with a maximum absorbance at 490 nm.

A significant proportion of culture media contain lactate dehydrogenase (LDH) derived from animal serum, which can contribute to the background absorbance when using the Cytotox 96 kit. The levels of LDH in animal serum vary based on a variety of factors, including the species and the health or treatment of the animal before serum collection. For instance, human serum has a comparatively low level of LDH activity, whereas calf serum has a relatively high level. Consequently, prior to commencing the experiment, a calibration curve is performed in order to determine the optimal amount of fetal bovine serum (FBS) that can be used without affecting the measurement of LDH released by the cells, as illustrated in Figure 25.

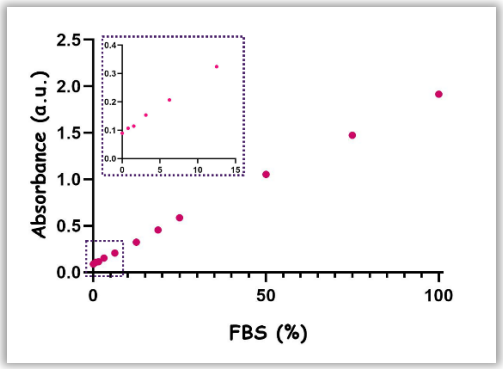

*Figure 25: **Calibration curve of the LDH assay**. A calibration curve to determine the optimal amount of fetal bovine serum (FBS) that can be used in the cell cultures without affecting the measurement of LDH release from cells.*

The results of the calibration curve indicate that the sensitivity of the LDH measurement is lost when 10 % or more FBS is used in the medium. In order to prevent any interference of the LDH released from the FBS with that released by the cells, it is necessary to work within the linear range. Consequently, the cytotoxicity test for VKV-SKS membranes is performed using DMEM medium supplemented with 5 % FBS. A reduction in serum concentration to this level has the effect of considerably decreasing background interference while preserving cell viability. The absorbance value of the control sample is employed to standardise the absorbance values of the other samples.

In order to conduct this experiment, HaCaT and HFF-1 cells were seeded onto ELR membranes in 24-well culture plates at a density of 2 x 10^4 cells/well. Subsequently, the cells were grown at 37 °C in a humidified atmosphere with 5 % CO_2 for 24 hours. Furthermore, cells were seeded in TCP to serve as a negative control and to determine the amount of LDH release in healthy cells. Additionally, they are used as a positive control, indicating the maximum amount of LDH that can be released by the cells when they are all dead. This is achieved by adding 10 µl of the 10X lysis solution from the kit to 100 µl of medium to lyse the positive controls, which are then incubated for 45 minutes. Following that, 50 µl of the supernatant from each experimental type group is collected and transferred to a 96-well plate in triplicate. Subsequently, 50 µl of Cytotox 96 reagent is added to each well, and the plate is incubated in darkness for 30 minutes at room temperature. After incubation, 50 µl of stop solution was added, and the absorbance was measured at 490 nm using a spectrophotometric microplate reader (SpectraMax iD3, Molecular Devices).

2.2.8.1.5.- Cell viability assay using AlamarBlue reagent

In order to complete the cytotoxicity analysis of cells seeded on VKV-SKS membranes, the AlamarBlue bioassay was employed to observe their metabolic activity and cellular health. AlamarBlue is a cell viability indicator dye that utilizes an oxidation-reduction (redox) reaction, which fluoresces and changes colour in response to the chemical reduction of resazurin (a non-fluorescent blue colour) to resorufin (a fluorescent pink colour) due to the activity of mitochondrial enzymes and other redox enzymes caused by cell proliferation [459].

The quantity of resorufin produced is directly proportional to the number of surviving cells and correlates with cellular metabolic activity. The percentage of viable cells can be determined by observing the change in colour solution qualitatively or quantitatively measuring the absorbance of the solution in the ultraviolet-visible (UV-Vis) range at 570 nm or by fluorescence with a 560 nm excitation/590 nm emission filter set using a plate reader. While both methods are suitable for this purpose, fluorescence-based methods are more sensitive than absorbance-based methods. Non-viable and damaged cells exhibit a reduction in inherent metabolic activity, which results in a correspondingly weak or absent signal.

To assess the metabolic activity of HFF-1 and HaCaT on the ELR membranes, 1.5 x 10^4 cells were seeded per well on both membranes and controls. In order to establish positive and negative controls, cells were seeded in a TCP and wells were treated with bovine serum albumin (BSA), respectively. The metabolic activity of cells was measured using the AlamarBlue assay (Invitrogen) at four experimental points (1, 7, 14, and 21 days), in accordance with the instructions of the manufacturer. For this purpose, after reaching the experimental time, the experimental groups were rinsed thrice with PBS. Then, a DMEM solution containing 10 % AlamarBlue (v/v) was added in place of the culture medium, followed by incubation of the cells in darkness for four hours at 37 °C and 5 % CO_2 humidity. Subsequently, 70 µL of the reduced medium was transferred to an opaque 96-well plate in order to quantify fluorescence. Fluorescence was quantified at an

excitation wavelength of 560 nm and an emission wavelength of 590 nm using a multimode plate reader (SpectraMax iD3, Molecular Devices). The membranes and all experimental wells were washed three times with PBS, after which the corresponding growth medium was added and incubated one more in order to determine metabolic activity at different time points.

Furthermore, this method was also utilised to evaluate metabolic activity of HFF-1 and HaCaT on the newly peptide-biofunctionalised hydrogels and the novel polymers, SKS-IKVAV and SKS-IKVAV-PPFLM. In order to achieve this, 200 µL of hydrogels of each peptide concentration were directly prepared on a 96-well plate, and 8000 cells per well were subsequently seeded onto them. The procedure was similar to that used for the ELR membranes.

2.2.8.1.6.- LIVE/DEAD fluorescence cell viability assay

Fluorescence imaging was utilised as an additional and complementary approach to evaluate cell viability, with the aim of observing cell morphology, cell progression within membranes, and cell viability at various intervals using LIVE/DEAD staining. The experiment employed two fluorescent dyes, namely calcein AM and ethidium homodimer (EthD-1), to label live and dead cells simultaneously. The intracellular esterase activity of living cells facilitated the conversion of the cell-permeable, non-fluorescent calcein AM into the significantly fluorescent calcein. The polyanionic calcein dye persists in viable cells, producing an intense and uniform green fluorescence (excitation/emission = 494/517 nm). EthD-1 penetrates cells with impaired membranes, resulting in a 40-fold increase in fluorescence upon association with nucleic acids. This results in a bright red fluorescence within dead cells (excitation/emission = 528/617 nm). EthD-1 is excluded by intact plasma membranes of viable cells.

To conduct the experiment, 1.5 x 10^4 cells were seeded per well onto the membranes and allowed them to grow for varying experimental times (1, 7, 14, and 21 days). The reagents were prepared in accordance with the instructions of manufacturer. Next, the membranes were rinsed with PBS and treated with the reagent assay kit, followed by a 30-minute incubation at room temperature in a dark environment. After staining, the cover with the membrane was inverted carefully (but quickly) using fine-tipped forceps and mounted with a coverslip on the microscope slide. The coverslip was sealed to the glass slide using clear nail polish to prevent evaporation. The stained HaCaT and HFF-1 cells on membrane were observed and representative images were taken with a Nikon Eclipse Ti-SR fluorescence microscope (Japan). In the LIVE/DEAD assay, live cells were stained green, while dead cells were stained red.

Furthermore, this staining was utilised to assess cell viability, morphology, and progression within the newly peptide-biofunctionalised hydrogels. For this purpose, 200 µL hydrogels of each peptide concentration were prepared directly on an 8-well glass chamber slide, and 8000 cells per well were seeded onto them. The procedure was analogous to that used for the ELR membranes. The stained HaCaT

cells were observed under a Leica TCS SP8 lightning confocal microscope (Leica Microsystems).

2.2.8.1.7.- Colony formation assay (CFA)

To examine the survival of single cells *in vitro* and their clonogenicity, the colony formation assay (CFA) was employed. This experimental method is based on the ability of an individual cell to proliferate and form a colony within VKV-SKS membranes. In accordance with the specifications outlined in [460], a colony is defined as a minimum of 50 cells. Essentially, the technique assesses each cell in the cohort, evaluating its potential for unlimited division. The clonogenic assay is the preferred method for determining the cell reproductive death of cells following contact with a substance or a treatment. Only a proportion of the seeded cells retain the capacity to generate colonies. Both the HaCaT and HFF-1 cell types were placed on the ELR membranes at an extraordinarily low density (1,5 x 10^3 cells per well) in order to enable colony formation within a period of 1 to 3 weeks. Following an approximate period of fifteen days, colonies have developed to a sufficient size for the observation of cellular growth. To facilitate this, the cells were fixed with 4 % PFA and stained with 0.5 % (w/v) crystal violet (Sigma-Aldrich), before being photographed with a stereoscopic microscope to allow for subsequent manual quantification. To determine the plating efficiency (PE), it is necessary to ascertain the accurate number of cells that were initially seeded. Consequently, this step must be performed with the greatest possible care. It should be noted that the plating efficiency of each cell line is different. When cells were seeded on protein membranes at low densities, they grow to form colonies. The PE is defined as the ratio of the number of colonies to the number of cells seeded [460].

2.2.8.1.8.- Cell adhesion assay

A 96-well plate was coated with different VKV-peptide (2X, 4X and 6X) and VKV-cc or the new polymers, SKS-IKVAV and SKS-IKVAV-PPFLM, at 4 °C overnight. The plates were then washed twice with PBS, after which the uncoated surfaces were blocked with 1 % BSA for 30 minutes at 37 °C. A total of 5 × 10^4 HaCaT and HFF-1 cells were seeded on the protein-coated plate and incubated for 3 hours at 37 °C. The unattached cells were removed by washing three times with PBS, and the attached cells were fixed with 4 % paraformaldehyde for 15 minutes at room temperature. The plates were then washed twice with PBS. Subsequently, the cells were stained with 0.5 % crystal violet (Sigma-Aldrich) in methanol for 10 minutes. The excess stain was removed by repeated washing with PBS [461]. The attached cells were observed under a magnifying glass (Leica DMS1000 BTL5000).

2.2.8.1.9.- Immunofluorescent staining

VKV-SKS membranes were seeded with 1.5 x 10^4 HFF-1 and HaCaT cells in 24-well plates on sterile glass coverslips. The cells were cultured for 7 and 14 days in accordance with the standard procedure. Immunostaining was conducted to evaluate cell morphology at the junction between the cells and the elastin biomaterial, as well as their capacity to express various proteins. The anti-vinculin

antibody was employed to investigate the formation of focal contacts between cells and the extracellular matrix. Additionally, anti-focal adhesion kinase was utilized to examine the interaction of cells with the material, anti-cadherin to investigate the interaction between cells, anti-alpha smooth muscle actin to assess the degree of fibroblast differentiation, and anti-cytokeratin 14 to explore the degree of keratinocyte differentiation. Meanwhile, rhodamine phalloidin was used to stain the cell actin cytoskeletons, while DAPI was utilised to stain the cell nuclei.

Each membrane was placed in conjunction with its respective cover slip on a slide and encircled with a liquid barrier marker. All procedures were conducted within a dark, humid chamber to prevent desiccation of the samples. Following a period of 7 or 14 days, the cells attached to the membranes were fixed with 4 % (w/v) PFA in PBS for 10 minutes. Following the removal of PFA, a subsequent PBS washing is carried out, after which 0.1 % (w/v) Triton X-100 is added to induce cell permeabilization for 10 minutes at room temperature. Subsequently, the non-specific binding sites were blocked by incubation with 1 % (w/v) BSA for one hour. The primary antibodies were diluted in 0.1 % (w/v) BSA in PBS at the concentration recommended by the manufacturer and incubated for one hour at room temperature. After washing with PBS twice, the secondary antibodies were diluted in 1 % (w/v) BSA in PBS at the intended concentration (1:500) and incubated at 4 °C overnight in darkness. Finally, samples were washed and mounted, using an aqueous mounting medium containing DAPI (Abcam) to stain cell nuclei in blue, prior to sealing with a cover glass. Representative images were obtained using an inverted Nikon Eclipse Ti-E epifluorescence microscope (Nikon) and a Leica TCS SP8 lightning confocal microscope (Leica Microsystems). The specifications of the primary and secondary antibodies used in this section are summarised in Table 20. Due to the high autofluorescence of the elastin membrane in the green field, it is preferable to prioritize the use of red fluorophores.

Table 20: The specifications of the primary and secondary antibodies employed for protein expression.

Antibody	Abbrev.	Dilution	Ref.	Action
Primary antibodies				
Rabbit anti-Focal Adhesion Kinase	FAK	1:200	Sigma-Aldrich SAB4502498	Interaction Cells-material (FB&KC)
Mouse anti-Vinculin Monoclonal	VCL01	1:100	ThermoFisher (Invitrogen) MA5-11690	Interaction Cells-ECM (FB&KC)
Mouse anti-VE-Cadherin, clone BV9 Monoclonal	CD144	1:200	Sigma-Aldrich (Millipore Corp) MABT129	Interaction Cell-Cell (FB&KC)
Mouse anti-α-Smooth Muscle Actin monoclonal	αSMA	1:100	Sigma-Aldrich A5228	Differentiation Fibroblasts
Mouse anti-Cytokeratin 14 Monoclonal	CK14	1:200	ThermoFisher (Invitrogen) MA5-11599	Differentiation keratinocytes
Secondary antibodies				
Goat Anti-Mouse IgG1-Alexa Fluor 488®		1:500	ThermoFisher (Invitrogen) a21121	Green staining
Goat Anti-Mouse IgG (H+L) CF™ 594		1:500	Sigma-Aldrich SAB460032	Red staining
Goat Anti-Rabbit IgG(H+L)-Alexa Fluor 568®		1:500	Abcam ab175471	Red staining

2.2.8.1.10.- RNA isolation, Reverse Transcription (RT) and quantitative real-time Polymerase Chain Reaction (q-PCR)

Quantitative real-time PCR is a technique that is widely used for the detection and quantification of gene expression levels. This method involves measuring the quantity of DNA present in a sample at the conclusion of each cycle, using fluorescent dyes that generate a signal in direct proportion to the amount of PCR product produced.

For the real-time qPCR assay, 1.5 x 10^5 HFF-1 and HaCaT were seeded on VKV-SKS membranes and incubated for different experimental times (0, 3, 7, 14 and 21 days). Total RNA was extracted from cells using Trizol™ reagent (Invitrogen), and a scalpel was used for cutting the membrane in order to facilitate complete cell extraction. To obtain a greater number of cells, each experimental sample was composed of two elastin membranes. Samples in Trizol™ reagent were transferred to Phasemarker™ tubes for manual nucleic acid separation using chloroform (Merk). The Trizol™ Plus RNA purification kit (ThermoFisher) was then used to obtain purified RNA following the protocol provided by the manufacturer. The quality of the extracted RNA was analysed using a spectrophotometer NanoDrop 2000C (Thermo Scientific) to measure the optical density at 260 and 280 nm, which yielded the purity ratio (OD 260/280) and concentration.

A two-step real-time qRT-PCR was conducted using total RNA, which was first transcribed into complementary DNA (cDNA) by reverse transcriptase. The resulting cDNA was then utilized as a template for the qPCR reaction. The High-capacity cDNA reverse transcription kit (ThermoFisher) was employed for the RNA reverse transcription (RT) reaction to obtain cDNA. One microgram of total RNA was reverse transcribed using a Master Mix that included MultiScribe™ reverse transcriptase enzyme, 10X PCR buffer, random primers, and mixed dNTPs. The reaction was conducted in a Mastercycler Pro thermal cycler (Eppendorf) using a program comprising a 25 °C incubation for 10 minutes, a 37 °C incubation for 120 minutes, and an 85 °C incubation for 5 minutes.

The procedure was performed using the TaqMan® gene expression assay (Applied Biosystems). The RT reaction cDNA products were amplified using TaqMan® probes as primers for specific genes and the Maxima Probe qPCR Master Mix kit (ThermoFisher), according to the protocol provided by the manufacturer. The qPCR 7500 Fast Real Time PCR system (Applied Biosystems) was utilised for the procedure. In summary, the amplifications were conducted in a final volume of 20 µl, comprising 10 µl of Maxima probe qPCR Master Mix, 8 µl of endonuclease-free water, 1 µl of TaqMan® probe, and 1 µl of cDNA. A not template control (NTC) was employed as a negative control, comprising all components except the cDNA template. For each sample, qPCR reactions were made in triplicate. The following protocol was implemented in a thermal cycler: after an initial general denaturation step at 95 °C for 10 minutes, 40 cycles were performed, with DNA denaturation executed at 95 °C for 15 seconds, followed by 60 °C for 1 minute for the annealing and extension process. These amplifications were utilized for the purpose of

comparing different samples. Real-time qPCR was carried out using the MicroAmp™ Splash-Free 96-Well Base (ThermoFisher) to simultaneously quantify the expression of six genes in each sample.

The study investigated the specific genes involved in fibroblasts, which include VCL, PTK2 and ACTA2, as well as those in keratinocytes, which consist of VCL, PTK2, CDH1, KRT10, and KRT14. The 18S ribosomal RNA (RP18) was used as an endogenous control gene (housekeeping gene). The following TaqMan® gene expression assay probes were employed in the research: RP18, Hs0096585812_g1; VCL, Hs00419715_m1; PTK2, Hs01056457_m1; CDH1, Hs01023895_m1; ACTA2, Hs00909449_m1; KRT10, Hs00166289_m1 and KRT14, Hs00265033_m1.

The data were acquired using the 7500 software Fast-Real Time v2.3. The point at which the PCR product was first detected above a fixed threshold, termed as the threshold cycle (C_t), was determined for each sample. Subsequently, expression levels were examined utilising the relative quantification method ($\Delta\Delta C_t$), as previously described by Livak and Schmittgen [462]. The comparative Ct was calculated using the formula $2^{(-\Delta\Delta Ct)}$, which denotes the difference in C_t between a gene of interest and the housekeeping gene (RP18) for a sample in comparison to a calibrator, which is the zero day of the experiment for each cell type in this research. In the event that gene expression was undetectable in any of the conditions, a C_t value of 40 was assigned for comparisons.

2.2.8.1.11.- Transwell migration assay

The transwell migration assay is a quantitative method for determining the number of cells that have migrated through inserts coated with ELR membranes and into a chemoattractant (comprising either complete culture medium or a supplemented culture medium with agents including growth factors). This migratory mechanism is relevant to the movement of keratinocytes across and above the provisional matrix of granulation tissue during the growth phase of wound healing.

To perform the migration assay, cell culture inserts with an 8 µm pore size, made of a polycarbonate membrane (Costar), were used. These inserts were placed in 24-well culture plates, thus creating both upper and lower compartments for the assay. Subsequently, VKV-SKS membranes were placed on top of the transwell membranes and allowed to dry for 24 hours to facilitate adhesion. Following this, 3 x 10^4 HFF-1 and HaCaT cells were seeded in serum-free medium into the inner chamber of the insert on the ELR membranes. The outer chamber was supplemented with complete medium as a chemoattractant. Following a fifteen-day incubation period, cells that had migrated through the membrane were fixed using 4 % PFA and stained with 0.1 % (w/v) crystal violet for subsequent manual quantification under a stereoscopic microscope.

2.2.8.1.12.- Scratch assay

Cell migration is of great importance in multiple intricate physiological and pathological processes. The wound healing assay is a straightforward technique for

studying cell migration *in vitro*. The method is based on the observation that, upon creating an artificial gap in a confluent cell monolayer, cells located at the wound edge will begin to migrate until new cell-cell contacts are established, leading to the closure of the wound. The *in vitro* scratch assay is ideal method for exploring the influence of cell-matrix, cell-material, and cell-cell interactions on cell migration, simulating the *in vivo* wound healing process. Accordingly, this approach was utilized to investigate the migratory capacity of HaCaT cells in the presence of VKV-SKS membranes.

The creation of a scratch is a crucial step in this wound healing assay. Several techniques have been developed to establish a gap in a cell monolayer. These techniques include scraping with a needle or pipette tip, placing an insert or template, chemical surface treatment or the use of electricity. In order to prevent damage to the elastin membrane during the formation of a scratch in the cell layer, the 24-well culture insert (Ibidi) was used in this thesis. The insert was then positioned on the 24-well plate, and 3.5 x 10^4 HaCaT cells were seeded into each well, using 70 µl of complete media. The used insert comprises two independent cell culture wells, with a well-defined cell-free space of 500 µm between them. Once the cells have reached confluence after 24 hours, the insert was removed with sterile forceps, and the cell layer was washed with PBS to eliminate any cell debris and unattached cells. The elastin membrane was then placed over the cells, which were subsequently incubated with serum-free media at 37 °C and 5 % CO_2 until the desired experimental time. To eliminate any potential interference caused by cell proliferation, cells are maintained in a serum-free environment and their migration is analysed over shorter time periods than those required for cell division. Additionally, cell proliferation can be inhibited by the administration of a proliferation inhibitor, such as mitomycin or actinomycin C.

The most characteristic measure of a migration assay is the alteration in the area of cell coverage (scratch closure) over time, which is used to quantify the wound closure rate and determine the cell migration rate. Based on the area of concern, microscopy may be utilised to generate a video or capture images at various time intervals. In this instance, the use of a phase contrast microscope to observe cell migration in real-time is not viable due to the opacity of the elastin membrane. Consequently, the use of non-toxic live cell staining with CellTracker™ Green CMFDA fluorescent probes is necessary to follow cell migration. At each designated experimental time point, the plates are removed from the incubator for imaging using the inverted Nikon Eclipse Ti-E epifluorescence microscope (Nikon). Subsequently, the plates are returned to the incubator and incubated for the remaining duration of the experiment, which must be completed within 16 hours. To ensure precise analysis, it is of great importance to maintain the same spacing position throughout the experiment.

The acquired images are utilised to assess *in vitro* re-epithelialisation, with the cell migration rate being quantitatively analysed using the Image J software. The scratched wound recovery index (SWRI) percentage was calculated according to the following Equation 8:

$$SWRI\ (\%) = \frac{Total\ wound\ area - Actual\ wound\ area}{Total\ wound\ area} x100$$

Equation 8: Scratched wound recovery index percentage

2.2.8.2.- *Ex vivo* characterisation

2.2.8.2.1.- Human ex vivo wound culture model

This model was employed in this thesis to investigate the efficacy of elastin membranes in wound healing via partial-thickness excision wound healing in *ex vivo* human skin. These experiments were conducted as a visiting student at the Center for Molecular Medicine, Karolinska University Hospital Solna (Stockholm, Sweden), under the guidance of Dra. Ning Xu Landén.

Human skin was acquired with full informed consent from patients undergoing brachioplasty at Nordiska Kliniken in agreement with Karolinska University Hospital (Stockholm, Sweden). Skin samples that were discarded after surgery were transported in retaining media and processed immediately upon arrival at the laboratory. Subsequently, the samples were then placed in culture within five hours or less of surgical excision. All experimental procedures utilizing unfixed human tissue were conducted within a Biosafety Level-2 (BSL-2) setting, using a class II laminar flow biosafety cabinet.

Partial-thickness wounds were generated on *ex vivo* human skin and cultured throughout the healing process. To achieve this, the tissue was sterilized with 70 % ethanol, rinsed thrice using fungizone-containing saline solution (Gibco), and partial-thickness surface wounds were created using a sterile 2 mm biopsy punch by carefully removing only the epidermis layer with sterile forceps and surgical scissors, and then excised from the skin using a sterile 6 mm biopsy punch. Subcutaneous fat was then carefully detached with sterile scissors before placement of the tissues, with the epidermis facing upwards, in a 12-well cell culture plate. Any explants exhibiting inconsistent wound size or depth were excluded prior to culture. Subsequently, the wounds were then treated with different biomaterials, including the elastin VKV-SKS membrane, elastin hydrogel, Pluronic hydrogel, and a dermal substitute, referred to as Integra®. Some wounds are left uncovered to investigate the re-epithelialisation behaviour in the absence of biomaterials. Elastin membrane and dermal substitutes were cut using a 2 mm biopsy punch, while hydrogels were applied to each wound at a volume of 5 µl. High-glucose DMEM medium (Gibco) was supplemented with 10 % FBS (Gibco) and antibiotics (1x penicillin and streptomycin, Gibco) (800 µl per well) to create a surrounding environment of the tissue. This allowed the epidermal surface to be exposed to a liquid-air interface facilitating complete wound healing through epithelialisation. The samples were cultured at 37 °C in a humidified atmosphere containing 5 % CO_2. The medium was replaced every two days. The complete procedure is illustrated in Figure 26.

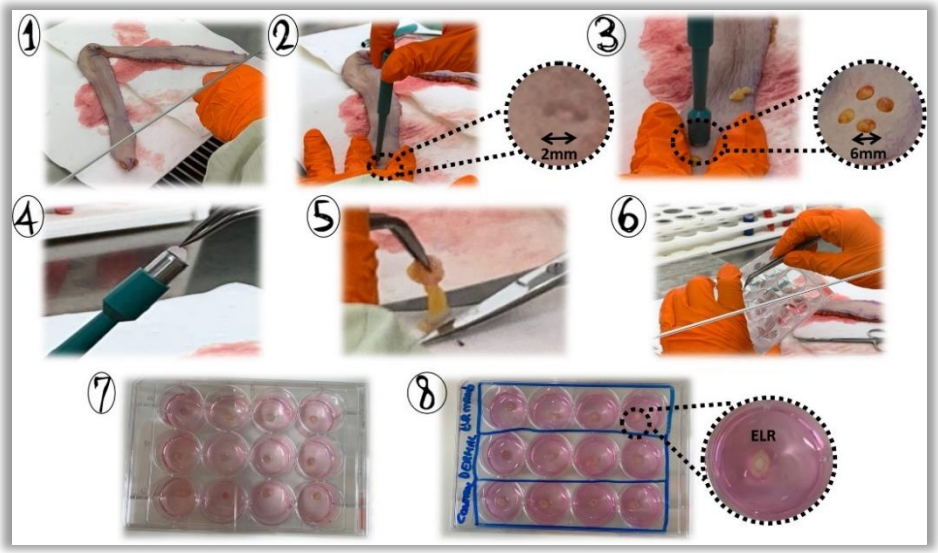

Figure 26: ***The surgical procedure for creating a partial-thickness excision wound in an ex vivo human skin model. 1)*** *Intact human arm skin is obtained from surgery.* ***2)*** *A partial-thickness wound is created using a 2 mm biopsy punch.* ***3)*** *A full-thickness wound is created to obtain an explant using a 6 mm biopsy punch.* ***4)*** *The explant is then extracted from the punch using forceps.* ***5)*** *The adipose tissue layer is excised from the explant with scissors.* ***6)*** *The explant is then placed in a 12-well plate.* ***7)*** *Complete medium is added in order to cover only the dermis, without affecting the epidermis.* ***8)*** *The wounds are then treated with the application of distinct materials.*

The use of an intravital fluorescent dye, CellTracker™ Green CMFDA Dye (Invitrogen), enables the real-time monitoring of *ex vivo* wound closure through non-invasive technology. In order to achieve this, 4 µl of CMFDA dye (50 µM) was added to each wound surface and incubated at 37 °C with 5 % CO_2 for 30 minutes. After rinsing the tissue with PBS drops, the wound was imaged daily in a perpendicular manner using a Nikon Eclipse Ni-E fluorescence microscope. Tissue from two separate donors was employed, with each treatment involving three to four explants per donor.

Furthermore, wound samples were also collected at representative time points, (days 3 and 6 post-injury) for the purpose of enabling histomorphometry analysis. The collected tissue samples were subsequently fixed with 4 % PFA for 24 hours, subjected to dehydration using an ethanol-xylene series, and processed for embedding in paraffin. Subsequently, tissue samples were sliced in consecutive 5 µm increments until the wound was visible under a microscope. The samples were then treated with xylene and water and stained with haematoxylin and eosin (H&E) using a standard protocol. Images were captured using a Nikon Eclipse Ni-E brightfield microscope.

Fluorescence and H&E images of the skin wound areas were analysed using the Image J software. The epidermis, dermis and migrating epithelium present in the wound bed can be identified in fluorescence images in order to obtain measures such as wound contraction, re-epithelialisation and percentage of wound closure. A drawing of the wound closure can be generated by marking the contour of the advancing epidermis at each experimental time point in each fluorescence photo, and then superimposing all experimental time. To ensure the accuracy of the

measurements, it is necessary to define specific parameters, including the initial wound-edge area at day 0 (IW_0), the wound-edge area at each experimental time point (IW_n), and the remaining open wound area at each experimental time point (OW_n). These parameters are illustrated in Figure 27A.

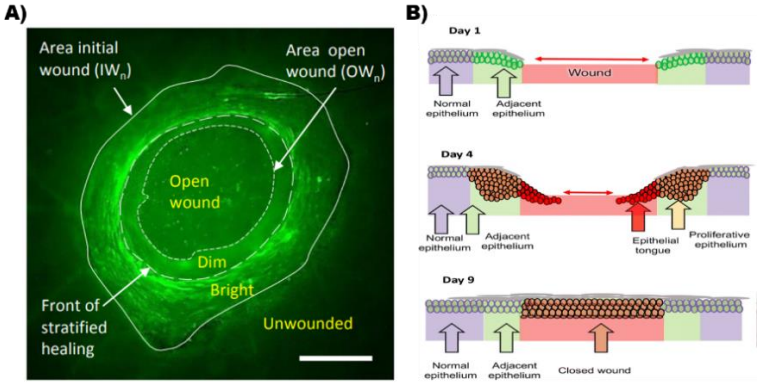

*Figure 27. **Skin wound area images**. **A)** Fluorescence images permit the evaluation of specific parameters. The initial wound-edge area (white line without interruption), the remaining open wound area (white dotted line), and sections of weakly fluorescent regions (i.e. unstratified epidermis that has recently formed) and bright areas of epidermis can be defined (white dashed line). Image from* [463]. ***B)** Schematic representation of the progression of wound healing over the course of days 1, 4, and 9. On day 1, a thin layer of adjacent epithelium can be observed near the open wound. On day 4, an epithelial tongue is observed migrating beneath the wound scab accompanied by the presence of a thick layer of proliferative epithelium, consisting of proliferative epithelial cells. By day 9, the wound has successfully closed through re-epithelization. The restored epidermis displays a dense layer of epithelial cells that envelopes the wound (box), in contrast to the regular epidermis (arrow). Image from* [464].

The extent of wound re-epithelialisation was quantified by measuring the wound-edge area and the remaining open wound area at the same experimental time point. The calculation was then expressed as a percentage of wound re-epithelialisation per day, as shown in Equation 9:

$$Re - epithelialisation\ (\%) = \frac{IW_n - OW_n}{IW_n} x100$$

Equation 9: Re-epithelialisation in percentage

Tissue contraction was calculated by evaluating modifications within the initial wound-edge (IW *time point*) over time during the wound healing period as shown in Equation 10:

$$Wound\ contraction\ (\%) = \frac{IW_0 - IW_n}{IW_0} x100$$

Equation 10: Wound contraction in percentage

The extent of epithelial wound closure was assessed by measuring the area of the initial wound-edge, and the remaining open wound area at each time point. The results were expressed in two ways: either as the percentage of wound closure on each day or as the area of healing achieved on each day in square millimetres, as shown in Equation 11:

$$Wound\ Healing\ (\%) = \frac{IW_0 - OW_n}{IW_0} x100$$

$$Area\ healed\ (mm^2) = IW_0 - OW_n$$

Equation 11: Epithelial wound closure in percentage and area of healing achieved on each day

For H&E histological examination, paraffin sections were prepared by capturing the tissue at a thickness of 80 µm from the beginning of the paraffin block containing wound tissue to the middle of the wound at its widest point of diameter. Subsequently, frontal images of the wounds were captured. In the H&E images, the epidermis, dermis, neo-epidermis, and epidermal tongue are identifiable in Figure 27B. Various measurements can be obtained, including wound re-epithelialisation, the distance between the epithelial wound margins (i.e. the open wound), and the number of cell layers of the newly formed tissue. Re-epithelialisation was quantified by measuring the neo-epidermis formed over the wound on both sides of the wound margins.

2.2.8.3.- *In vivo* characterisation

2.2.8.3.1.- Subcutaneous implantation in vivo mouse model

Experimental procedures involving the use of animals were approved by the Ethical Committee on Animal Care and Use of the University of Valladolid in accordance with the European Union Directive 2010/63/EU and the Spanish Royal Decree RD 53/2013. Animals were housed at the Animal Research and Welfare Service (S.I.B.A.) at the University of Valladolid.

To assess the *in vivo* biocompatibility and stability of elastin membranes, 9-week-old, pathogen-free Swiss female mice weighing an average of 400 g were used. In order to minimise inter-mouse variability, each mouse is subjected to two random experimental conditions. The study will examine cell-free VKV-SKS membranes and VKV-SKS hydrogels samples, with the commercial Integra®, dermal substitute which is commonly used in hospitals for treating burn patients, acting as a control. A total of 18 animals were used in the study, with four replicates utilised for every experimental group at each designated time point (1, 3, and 7 weeks). The number of animals used in the experiments was determined in accordance with the 3R principles of replacement, reduction, and refinement, as formulated by Russell and Burch, in order to ensure the ethical and humane treatment of animals whilst promoting animal welfare [465].

The mice were subjected to surgical procedures in a sterile operating room and anaesthetised via inhalation of 3 % isoflurane. The sterile ELR membranes and dermal substitute were implanted subcutaneously in the dorsal area by creating a small subcutaneous pouch using a sterile surgical scalpel, into which the scaffolds were carefully placed. The wound was subsequently closed using absorbable sutures. The hydrogels were subcutaneously injected. Prior to injection, sterile ELRs were dissolved in PBS and mixed in an Eppendorf tube. They were injected subcutaneously without cells using a 1-ml syringe with a 20-gauge needle forming an instantly chemically cross-linked hydrogels, that could be seen as a small lump under the skin. Mice were kept in a 12-hour light-dark cycle and provided with food and water *ad libitum*. Animals were euthanized using CO_2 at three different time points (1, 3, and 7 weeks) post-implantation in order to evaluate the

biocompatibility of the material and the long-term stability of the scaffold histologically.

2.2.8.3.2.- Murine excisional wound model

Excisional wounds are a frequently used model for the study of wound healing, as they are considered to mimic acute clinical wounds by removing the different layers of skin (epidermis, dermis, and subcutaneous fat). Although this model has been tested in a variety of animal species, including mice, rats, rabbits, guinea pigs and pigs, in an effort to replicate human skin repair, these models are influenced by anatomical and physiological variations. Injured mice and rats heal through the contraction of the subcutaneous muscle (panniculus carnosus), rather than re-epithelialisation, which is observed in humans. Furthermore, the thickness of the skin and the time required for healing may vary between species, as small animals tend to heal more rapidly than humans. Consequently, the utilization of an *in vivo* animal model necessitates a significant quantity of replicates for each treatment situation to minimise the impact of intraspecies differences and ensure the reproducibility of the experiments, thereby yielding dependable outcomes. Nevertheless, animal-based *in vivo* models remain the most predictive way of studying wound healing due to their capacity to reflect realistically the wound environment by simulating various cell types, environmental signals and paracrine interactions, as well as embodying the complexity of a complete organ and its interactions with other organs, as the host vascular and immune systems are active, in a way that more closely mirrors clinical scenarios than the *ex vivo* model [466]–[468]. Accordingly, this thesis will employ this model to investigate the utilisation of elastin membranes in full-thickness excision wound healing *in vivo* murine skin. These experiments were conducted as a visiting student at the Center for Molecular Medicine, Karolinska University Hospital Solna (Stockholm, Sweden), under the guidance of Dra. Ning Xu Landén. The protocols for the murine experiments were approved by the North Stockholm Ethical Committee for the Care and Use of Laboratory Animals (Stockholm, Sweden). The number of mice selected was based on the 3R principle (replacement, reduction, and refinement) to ensure ethical and humane treatment of animals, while respecting animal welfare.

For the study of murine skin wound healing, sixteen 9-week-old male C57BL/6J (JAX™ Mice strain) mice were individually housed in cages one week prior to the commencement of *in vivo* wound experiments, in order to allow the mice to become acclimatized to the facilities [469]. General anaesthesia was administered with 3 % isoflurane (Abbott). Prior to the surgical procedure, the hair on the dorsal region was shaved with an electric razor, followed by the application of depilatory cream to ensure that there were no residual hairs which could potentially interfere with the process of wound healing. The skin was then cleansed with 70 % alcohol. Two full-thickness excisional wounds, which extended through the fleshy panniculus on the dorsum, were produced by using a 4-mm biopsy punch. Sterile biomaterials (VKV-SKS membrane, VKV-SKS hydrogel, and Pluronic hydrogel) were used to cover the excision wounds. Subsequently, scaffolds were then fixed in place with medical adhesive tape, Tegaderm®, in order to prevent their damage.

Tegaderm® adhesive tape also serves to avoid wound contraction by creating a mechanical fixation of the skin, which stimulates healing through re-epithelialisation and granulation tissue formation in the murine model, which closely mimic the process in humans. The complete procedure is illustrated in Figure 28.

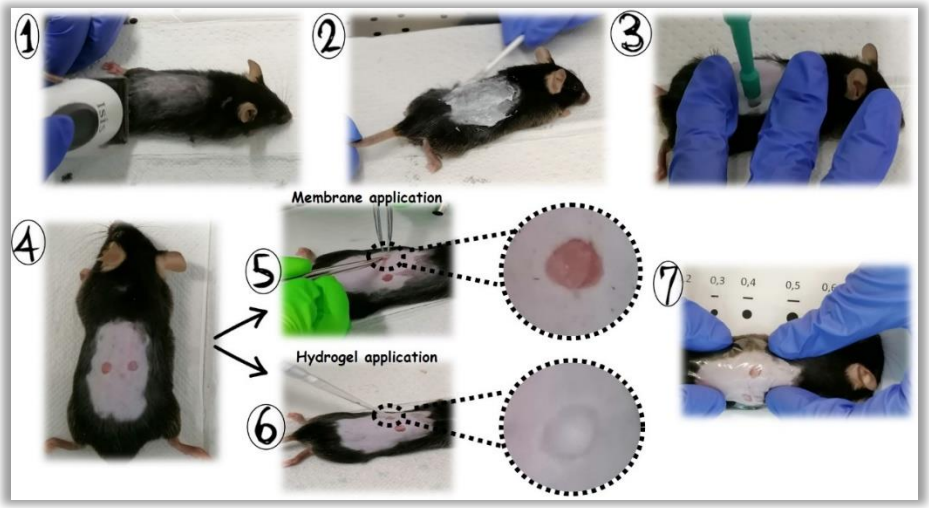

Figure 28: ***The surgical procedure for the generation of full-thickness excisional skin wounds in mice. 1)*** *Hair from the dorsal side of the mice is shaved with an electric clipper.* ***2)*** *Hair removal depilatory cream is applied to remove the remaining fur.* ***3)*** *Wound is generated with a 4 mm-biopsy punch.* ***4)*** *The skin is lifted with forceps and removed with scissors until a perfect circle wound is formed.* ***5)*** *ELR membrane is placed on the skin wound with forceps.* ***6)*** *ELR hydrogel is placed on the skin wound with a pipette.* ***7)*** *Sterile scaffolds were then fixed in place and covered with medical adhesive tape, Tegaderm®. The wound alongside with a circular reference is photographed daily using a digital camera.*

In order to serve as a control for the normal healing process in mice, wounds were left uncovered. The treatment assignment was randomised based on wound location to prevent anatomical differences. For the initial 48 hours, animals were administered analgesics via intraperitoneal injection of buprenorphine (0.03 mg/kg) twice daily to mitigate any pain and distress that might arise from the surgical procedure. Subsequently, the animals were housed individually and maintained in 12-hour light/dark cycles, with food and water were provided *ad libitum*. Daily observations were recorded of the body weights of the animals, and the wound area was photographed every day until approximately 90 % of the wound had healed. A circular reference was placed in close proximity to the wound for the purpose of quantitative analysis. To ensure accuracy, the wound area was measured using ImageJ software and then standardized to the area of the circular reference in the same image. The wound healing rate is calculated by comparing the current wound size to its original dimensions, as demonstrated in Equation 12:

$$Wound\ Healing\ (\%) = \frac{W_0 - W_t}{W_0} x100$$

Equation 12: Wound Healing rate (%)

where the wound area on the wounding day is designated as W_0, while the wound area on each respective day is named as W_t.

Eight days following the injury, the mice were euthanized via carbon dioxide asphyxiation and skin biopsies were obtained by placing the epidermis upwards on a Whatman filter paper. The collected tissue was processed for subsequent histological analysis.

2.2.8.3.3.- Sample processing and histology

Following extraction, the samples were fixed in 4 % PFA for at least 24 hours at 4 °C. Subsequently, the specimens were dehydrated by immersing them in ethanol solutions of increasing concentration (30 %, 50 %, 70 %, 95 % and 100 %), with two subsequent changes in xylene solution (Sigma-Aldrich). Samples were then embedded in paraffin for approximately six hours and sectioned at a thickness of 6 µm using a rotary microtome (Leica). The obtained samples were then collected onto slides prior to being subjected to deparaffinization. Subsequently, they underwent immersion in solutions comprising of xylene and ethanol, with the concentration gradually decreasing (100 %, 70 %, 50 % and 30 %). Finally, the specimens were fully rehydrated with distilled water.

Haematoxylin-eosin staining (Sigma-Aldrich) was performed using the method previously described [470]. In brief, the slides were immersed in haematoxylin stain for 30 seconds and then washed in water for one minute. A 1 % eosin solution was applied for a 30-second staining period with shaking. Subsequently, samples were dehydrated through immersion in ethanol and xylene solutions. Finally, the sample on the slide was covered using a microscope coverslip and a mounting medium (Sigma-Aldrich). Images were obtained using a Nikon Eclipse Ni-E bright-field microscope with various magnifications. The interpretation of the H&E staining is as follows: the nuclei are observed as blue, the cytoplasm is pink or red, and the red blood cells appear as dark red.

In addition, the samples were also stained with Masson's trichrome in order to assess the presence of collagen after biomaterial implantation, in accordance with the protocol of manufacturer. All kit components were purchased from Sigma-Aldrich. Briefly, the samples were initially deparaffinised, followed by immersion in xylene and ethanol solutions of decreasing concentration (100 %, 70 %, 50 % and 30 %), and finally rehydrated completely with distilled water. The slides were placed in a preheated solution of Bouin's (56 °C) for one hour in an oven and subsequently cooled to room temperature via a tap water wash. The nuclei were then stained with Weigert's iron haematoxylin solution for a period of five minutes, followed by tap water washes and rinses with ultrapure water. Afterwards, Biebrich's Scarlet-acid Fuchsin was used to stain the slides for five minutes followed by a rinse in ultrapure water. Subsequently, the sample was immersed in a phosphotungstic/phosphomolybdic acid working solution for five minutes, after which, an additional Aniline Blue staining was carried out for five minutes. Then, the sample was treated with a 1 % acetic acid solution for two minutes and dehydrated through immersion in ascending ethanol and xylene solutions. Finally, the sample on the slide was covered using a microscope coverslip and a mounting medium (Sigma-Aldrich). Images were obtained with a bright-field optical microscope (Nikon Eclipse 80i) equipped with a colour camera (Nikon Digital Sight DS-Fi1),

using the NIS-Elements AR software (Nikon Corporation) with various magnifications. The analysis of the samples treated with Masson's Trichrome revealed the following: the nuclei are dark brown to black; the cytoplasm appears light red, collagen is blue, and muscle fibres are red.

2.2.9.- Statistical analysis

The GraphPad Prism version 8.0 software was employed for the statistical analysis of the data. The data presented in this thesis is presented as the mean ± standard deviation. The specific statistical analyses employed in this study were contingent upon the data group collected in each experiment. A one-way analysis of variance (ANOVA) was applied followed by a *post hoc* Tukey test when only one factor was observed. However, for the purpose of conducting multiple comparisons between groups, a two-way ANOVA is employed, followed by a *post hoc* Tukey test.

The resulting values were represented by according to their respective significance levels, as follows:

No significant difference (ns) → $P > 0.05$

* → $P < 0.05$

** → $P < 0.01$

*** → $P < 0.001$

**** → $P < 0.0001$

RESULTS

Elastin-Like Recombinamer Membranes

3.- Results

3.1.- Elastin-Like Recombinamer Membranes

3.1.1.- Controlled production of ELR-based membrane at liquid-liquid interface by click chemistry

The elastin membranes used in this thesis were produced in accordance with the previously outlined protocol by González-Pérez *et al.* [436]. Elastin membranes are produced using the click chemical reaction without catalyst between the polymers VKV-cc and SKS-N_3, which act as a structural group and a group with RGD cell adhesive domains, respectively, at the interface of two immiscible liquids. Upon contact between the two complementary groups, the polymer chains migrate to the interface in each phase. A spontaneous cross-linking reaction occurs at the interface, resulting in the formation of a thin ELR-based membrane, as shown in Figure 29A. The contact of the complementary aqueous and organic ELR solutions triggers a series of events at the liquid-liquid interface. According to González-Pérez *et al.* [436], the ELR chains cross-linked in separate regions along the liquid surface, resulting in the nucleation and growth of independent entities over time. During the reaction, violent collisions between protomembranes occur, leading to the interconnection of cross-linked networks and the formation of a continuous matrix across the entire surface. This process results in the evolution of dense fibre-like clusters across the membrane surface, as illustrated in Figure 29B.

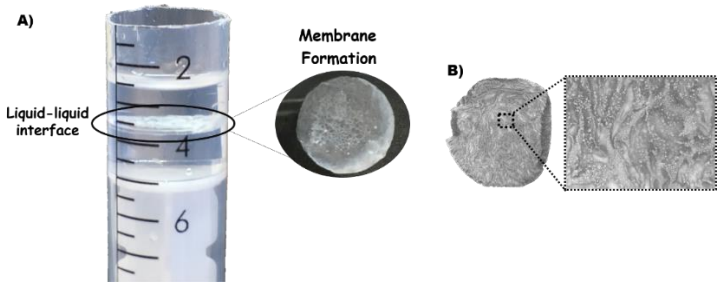

Figure 29: ***Click cross-linking reaction and formation of the ELR-based membrane at the liquid-liquid interface. A)*** *Scheme of the cylindrical device employed to manufacture the ELR-based membrane.* ***B)*** *Representative images of hydrated ELR-based membranes with dense fibre-like clusters across the membrane surface.*

González-Pérez *et al.* [436] conducted an initial physicochemical characterization, which revealed a direct correlation between the concentrations employed and the resulting thickness, porosity, mechanical, and diffusion

properties. An increase in the concentration of used recombinamers resulted in an increase in membrane thickness and a reduction in the size of pore distributions. Moreover, the capacity of the membranes to selectively regulate the diffusion rate of fluorescein isothiocyanate (FITC)-labelled dextrans with molecular weights ranging from 4 to 150 kDa was also investigated. The findings indicated that larger particles exhibited reduced permeation through the membrane, resulting in lower diffusion rates for the same membrane concentration.

Consequently, this system enables the production of tuneable membranes with varying pore sizes, thicknesses, and diffusion rates by adjusting the concentration of polymers in the initial solutions. The thesis will focus on the preparation of VKV-SKS membranes at concentrations of 5, 10, 25, and 50 mg/mL for in-depth analysis of their physicochemical properties, biocompatibility, and ability to promote cell adhesion and proliferation in a specific application, namely skin regeneration.

3.1.2.- Physico-chemical characterization of ELR membranes

3.1.2.1.- Chemical characterisation

Infrared spectroscopy (FTIR) is a valuable analytical technique that offers a straightforward approach to identifying the presence of specific functional groups in biomaterials. Each functional group exhibits characteristic vibrational frequencies that can be utilized to distinguish it from other groups. Figure 30A shows the ATR-FTIR spectra of the individual freeze-dried modified polymers, VKV-cc and SKS-azide, prior to cross-linking, and the freeze-dried cross-linked membrane, consisting of the same polymers at varying concentrations (5, 10, 25 and 50 mg/mL), with a wavelength sweep between 600 and 4000 cm^{-1}, in which the characteristic functional groups were contained.

The spectra of the VKV-cc and SKS-azide polymers and the VKV-SKS membrane showed the characteristic peptide-binding vibrational bands of the proteins corresponding to amide I and amide II [471]. The absorption associated with amide I gives rise to a high-intensity peak in the spectrum around 1600 cm^{-1}, whose signal is attributed to the stretching vibrations of the carbonyl group bond (C=O), related to the secondary structure of the proteins. On the other hand, the one associated with amide II gives rise to bending vibrations of the N-H bond, as indicated by the signal at 3400 cm^{-1}. The bands at 1450 cm^{-1} are attributed to the C-H bending of the methyl group of the alkane from amino acids such as valine, at 1200 cm^{-1} to the C-N stretching of the amine from amino acids such as lysine, and at 1000 cm^{-1} to the C-O stretching of the primary alcohol from amino acids such as serine [471].

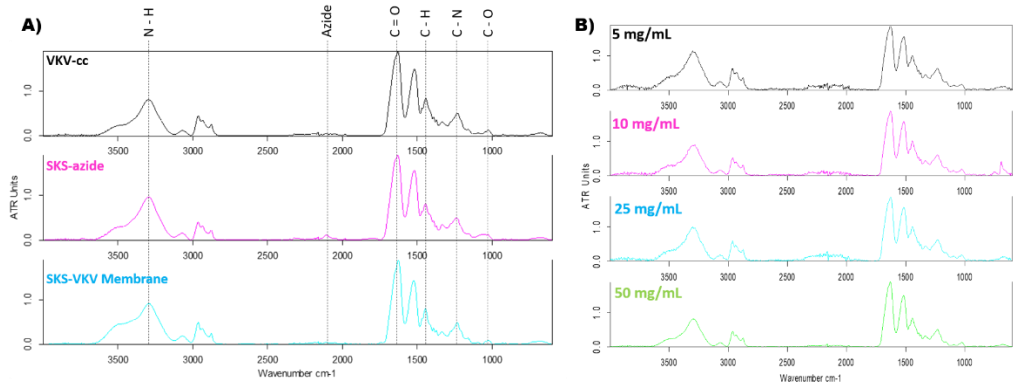

Figure 30: ***Chemical characterisation. A)*** *ATR-FTIR spectra of VKV-cc, SKS-azide and VKV-SKS membrane.* ***B)*** *ATR-FTIR of the VKV-SKS membrane as a function of concentration (5, 10, 25, 50 mg/mL).*

In addition, ATR-FTIR analysis permits the identification of the azide-reactive tethered-click group. Thus, the presence of azide groups in the SKS polymer is confirmed by a peak in the infrared region centred at 2100 cm^{-1}. However, this technique cannot identify the signal indicating the chemical modification of VKV with cyclooctyne due to the symmetry of the compound, which makes the IR absorption inactive and the triple bond invisible around 2200 cm^{-1}. Upon formation of VKV-SKS membrane, the complementary cyclooctyne and azide groups cross-link orthogonally, resulting in the disappearance of the azide signal at 2100 cm^{-1} in the spectrum of the membranes disappears as it is consumed to form the bond. As expected, the ATR-FTIR spectrum of the VKV-SKS membranes is independent of the polymer concentration and exhibits a comparable profile as depicted in Figure 30B. Consequently, this technique enables the identification of the principal functional groups that constitute ELR membranes. Furthermore, it demonstrates the correct synthesis of the ELR membrane, as the azide signalling disappears when consumed during the process of obtaining the membrane.

3.1.2.2.- Thermal behaviour characterization

Thermal characterization enables the identification of transition temperature (T_t) values associated with the endothermic phase transition of ELR polymers in aqueous solution. Furthermore, this technique allows for the observation of the effect of the inclusion of cross-linkable groups, such as azide and cyclooctyne, on the transition temperature. This introduction leads to a change in the overall polarity of the molecule, which in turn results in a change in the final transition temperature. The thermal properties of the complementary and modified polymers, VKV-cc and SKS-azide, as well as the 50 mg/mL VKV-SKS membrane, were evaluated by differential scanning calorimetry (DSC) in a nitrogen atmosphere by determining the respective transition temperature. This technique has been widely employed in the study of hydrogels, as it permits the measurement of changes in mass, water and thermal effects in hydrogels as a function of temperature. Thus, the significance of elucidating the nature of the internal water in hydrogels lies in the potential critical influence of polymer-solvent interactions on the microscopic and macroscopic properties of hydrogels, such as phase transitions, diffusion in the

vicinity of polymer chains or the stability of drugs incorporated in hydrogels [472]–[475].

Figure 31A displays the DSC thermograms obtained at temperatures ranging from 15 to 75 °C, with a heating rate of 5 °C/min for the individual polymers and 1 °C/min for the VKV-SKS membrane at a concentration of 50 mg/mL. The thermograms demonstrate the presence of endothermic peaks with negative enthalpy values, which indicates that the inverse transition with temperature of the ELR is preserved, and therefore, the thermosensitivity of the hydrogels.

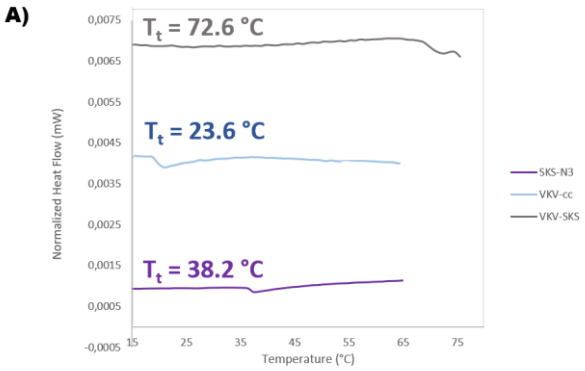

Figure 31: ***Thermal behaviour characterization. A)*** *The transition temperature of the individual polymers, namely SKS-N_3 and VKV-cc, as well as the membrane VKV-SKS at a concentration of 50 mg/mL in water at pH 7, is defined as T_t.*

The endothermic peaks indicating the transition temperatures in ultrapure water at pH 7 of the VKV-cc and SKS-N_3 polymers are 23.6 °C and 38.2 °C, respectively. On the one hand, the compositional differences between the two ELR polymers result in slight variations in their thermosensitive behaviour. The SKS polymer shows an increase in T_t, which can be attributed to the β-hydroxyl groups of the serine with polar side chains that increase the overall hydrophilicity of the polymer and prevent the characteristic hydrophobic folding of the ELR chain in aqueous media below 70 °C [436], [476]. In addition, the incorporation of azide and cyclooctyne groups into ELR polymers leads to the partial disappearance of the positively charged primary amines, thereby reducing the hydrophilicity of the ELR and causing a reduction in the T_t peak in both cases. The high transition temperatures facilitate the handling of these polymers relatively easily at room temperature and enable the formation of the VKV-SKS membrane through cross-linking. The transition temperature of the cross-linked membrane exhibits a sharp increase to 72.6 °C. This phenomenon can be attributed to the formation of a dense cross-linked network within the membrane, which results in a reduction in chain mobility and a partial loss of the conformational freedom, hindering the chain folding that occurs when the ELR is heated above its T_t. This hindered chain mobility also causes a significant broadening of the endothermic peak [433], [477]. Furthermore, the membranes exhibit a greater degree of rigidity due to the presence of a higher number of cross-links within the network, which impedes the mobility of water molecules. This, in turn, favours the interaction of associated water, as this water is structurally forced to remain within the network [478]. It is of note that the

inverse transition temperature of monomeric ELR solutions can vary by more than 30 °C, depending on the molecular weight of the ELRs. In contrast, the majority of the contraction of ELR gels occurs over a similar temperature range, regardless of the molecular weight of the ELRs from which they were constructed. This suggests that the gels are more chemically similar than are the polymers from which they were derived. Regardless of composition and molecular weight of the initial material, cross-linking results in a reduction of the difference between the ELRs by consuming charged lysine groups and producing polymer networks of essentially infinite molecular weight. The only differentiating factors between the gels are the total protein content and the segment length between cross-links [479]. Thermal analyses were also conducted for concentrations of 5, 10 and 25 mg/mL, however, no endothermic peaks were observed due to the limitations of the technique in detecting low energy exchanges associated with these transitions.

3.1.2.3.- Topography and surface characterisation

The surface properties of materials are of paramount importance, as they determine their interactions with body fluids. Thus, the roughness parameter is crucial in the context of wound dressings, as each roughness has a distinct retention and adhesion behaviour of substances. A significant number of researchers concur that increased surface roughness equates to a larger surface area in contact with water, which consequently results in greater adhesion of substances, such as chemical pollutants or cells [480].

Furthermore, the wetting properties of the membrane surface are of critical importance in wound healing applications, as they influence the process of permeate flux and the adsorption of molecules or cells. A number of factors, including pH, temperature, charge density and surface energy, influence the interaction between the membrane surface and liquid macromolecules [454].

Consequently, a variety of techniques were employed to ascertain the surface topology of ELR membranes, including SEM, ESEM, AFM and contact angle, given that this has an impact on the behaviour of the biomaterial in its surrounding environment. For instance, this can be observed in terms of adhesion.

In order to investigate the surface uniformity of ELR membranes with varying concentrations of ELR polymers (5, 10, 25 and 50 mg/mL), electron micrographs of the surface were taken upon samples are lyophilisation and coating with gold, as shown in Figure 32 (A, B, C and D). Subsequently, the roughness of the different samples is then calculated using the roughness calculation plugin of the ImageJ software. The root mean square roughness values (Rq) obtained from the top surfaces of four different membranes are presented in Figure 32E. The Rq value is preferable to the Ra value, which is the roughness average for the determination of roughness. This is because the formula described previously in the Methodology chapter for the calculation of these parameters incorporates squared terms, thereby affording greater weight to large deviations from the average height than is the case with the Ra value. The Rq value for a surface that is perfectly smooth surface would be 0 nm.

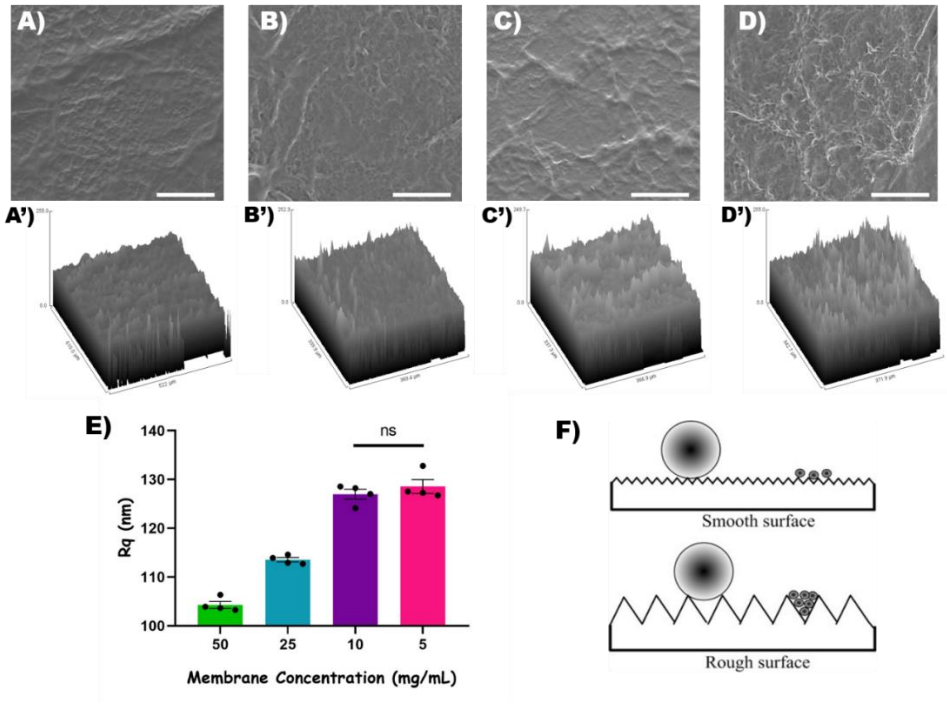

Figure 32: ***Evaluation of the roughness of ELR membranes through the use of SEM images. A, B, C and D)*** *SEM surface micrographs of membrane samples showing different roughness as a function of concentration (**A** = 50 mg/mL; **B** = 25 mg/mL; **C** = 10 mg/mL; **D** = 5 mg/mL). Magnification of 800x and scale bar = 100 µm.* ***A', B', C' and D')*** *Surface profile of the membranes (**A'** = 50 mg/mL; **B'** = 25 mg/mL; **C'** = 10 mg/mL; **D'** = 5 mg/mL).* ***E)*** *Roughness values (Rq) as a function of membrane concentration.* ***F)*** *Schematic representation of the importance of roughness for different-sized particles adhering to the membrane surface. Image from* [481].

The data indicates that surface roughness increases with decreasing ELR polymer concentration, with no statistically significant differences in roughness between the 5 and 10 mg/mL membranes, which have similar roughness. However, the remaining samples demonstrate a statistically significant change in roughness with significance, with a p-value of less than 0.0001. The reduction in surface roughness observed on the top surface of the sample can be attributed to the fact that as the polymer concentration increases, the average pore size decreases. This results in a greater number of junction points between the chains, which in turn leads to the formation of a more homogeneous surface. Consequently, the surface becomes more uniform, and thus obtaining a reduction in surface roughness. These changes in the roughness of the Rq parameter are consistent with the SEM images in Figure 32, and the average Rq value is provided in Table 21. Figure 32 (A', B', C' and D') also displays a surface plot generated with ImageJ tools, which enables the visual identification of the surface roughness of the sample. However, this plot does not provide any information about the depth or high dimensions in micrometres.

Table 21: Average roughness measurements of different membrane concentrations from SEM images.

	5 mg/mL	10 mg/mL	25 mg/mL	50 mg/mL
Rq (nm)	128.6 ± 2.8	126.9 ± 2.1	113.5± 0.9	104.3 ± 1.4

Moreover, electron microscopy was employed to ascertain the thickness of ELR-based membranes, which were found to be thicker than 3-4 µm. This was

achieved by cryo-fracturing the membranes in liquid nitrogen and subsequently freeze-drying them to determine the thickness in the cross-section [436].

Therefore, the roughness parameter is crucial for membranes used as wound dressings, as rougher surfaces exhibit greater adhesion to nanometric particles than smooth surfaces [436], as illustrated in Figure 32F. The efficacy of engineered scaffolds for skin regeneration is contingent upon the surface texture, microstructure, and morphology of the porous architecture, including porosity, pore size, pore shape, and interconnectivity between pores. Consequently, the measurement of these parameters with SEM in the membranes is of paramount importance for the subsequent success of their use.

As these membranes are to be used as wound dressings in their hydrated state, it is necessary to verify that the surface roughness does not change compared to their freeze-dried state, which was previously characterised by SEM. Ideally, the sample should be maintained at a stable hydration state, as dehydration during the measurement could result in a change in the apparent roughness, particularly if the data acquisition is prolonged.

In order to study the surface topography of hydrated ELR-based membranes with different concentrations of polymers (5, 10, 25 and 50 mg/mL), electronic images of the surface were taken in the ambient state, as shown in Figure 33 (A, B, C and D). Subsequently, the roughness of the different samples is then calculated using the roughness calculation plugin of the ImageJ software. The average roughness values (Rq) obtained from the upper surfaces of four distinct membranes are plotted in Figure 33E.

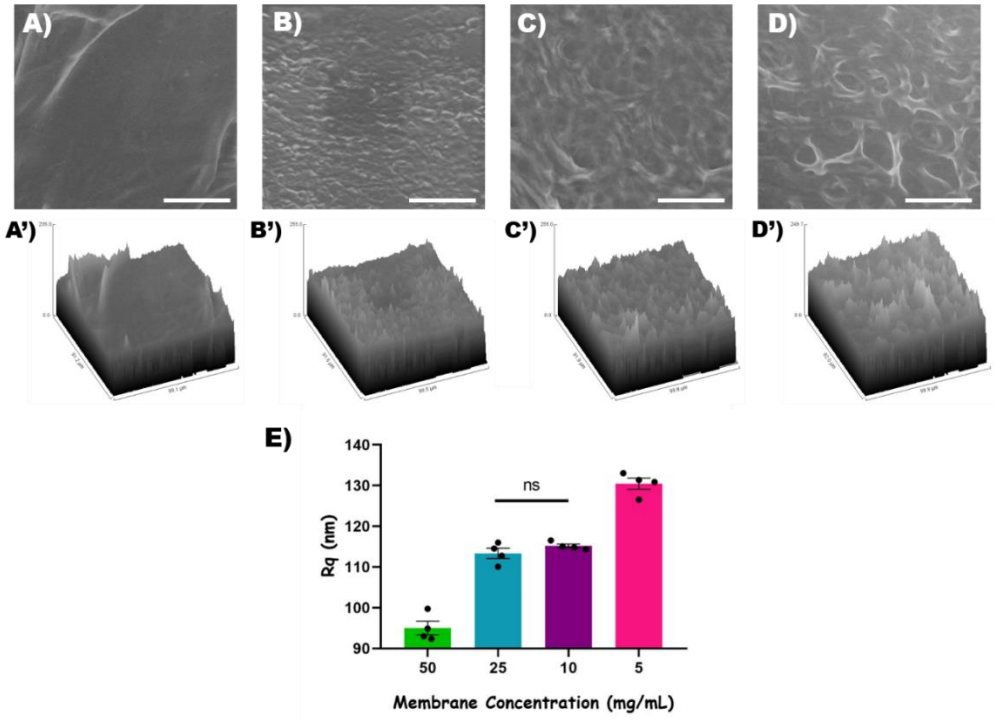

Figure 33: ***Evaluation of the roughness of ELR membranes through the use of ESEM images. A, B, C and D)*** *ESEM surface micrographs of membrane samples demonstrate a correlation between roughness and concentration (**A** = 50 mg/mL; **B** = 25 mg/mL; **C** = 10 mg/mL; **D** = 5 mg/mL). Magnification of 3000X and scale bar*

*= 30 µm. **A', B', C' and D')** Surface profile of the membranes (**A'** = 50 mg/mL; **B'** = 25 mg/mL; **C'** = 10 mg/mL; **D'** = 5 mg/mL). **E)** Relationship between membrane concentration and roughness values (Rq).*

The data indicates that the surface appearance is similar regardless of the technique used, namely ESEM and SEM. However, it seems that the definition of the images is slightly better when gold coating is performed. In addition, it is observed that they follow the same pattern of surface roughness, with a decrease in value with increasing ELR polymer concentration, finding no statistically significant differences in roughness between the 10 and 25 mg/mL membranes, which therefore have a similar roughness. However, the remaining samples exhibited a statistically significant change in roughness, with a significance of $p < 0.0001$. The observed increase in surface roughness of the sample can be related to the fact that as the polymer concentration decreases, the average pore size increases, resulting in a reduction in the number of junction points between the chains, forming a more heterogeneous surface, which reduces the uniformity and thus results in a higher roughness. The changes in roughness of the Rq parameter are corroborated by the ESEM images in Figure 33. The average Rq value is presented in Table 22, which illustrates that the roughness trajectory is consistent between ESEM and SEM. Figure 33 (A', B', C' and D') also shows a surface plot generated with ImageJ tools, which enables the visual identification of the surface roughness of the sample, but this plot does not give any information about the depth or high dimensions in micrometres.

Table 22: Average roughness measurements of different membrane concentrations from ESEM images.

	5 mg/mL	10 mg/mL	25 mg/mL	50 mg/mL
Rq (nm) ESEM	130.4 ± 2.8	115.2 ± 0.9	113.3 ± 2.5	95.0 ± 3.3
Rq (nm) SEM	128.6 ± 2.8	126.9 ± 2.1	113.5± 0.9	104.3 ± 1.4

Additionally, atomic force microscopy (AFM) is commonly utilised to characterise membranes due to its capacity to generate nanometre-resolution images of material surfaces through mechanical interaction between a small tip mounted on a cantilever and sample surfaces [482]. AFM has been employed in a multitude of studies on the roughness of polymeric and ceramic membranes, yielding not only measurements of roughness, but also the dimensions and morphology of pores on the surface [483].

In order to achieve uniform results, it is of the most importance to capture images using the same scan range to facilitate the comparison of the surface roughness of various samples. It has been demonstrated that deviations in scan size can result in differing surface topographies, which in turn can lead to distinct roughness values [483]. Consequently, the roughness of ELR-membranes of varying concentrations was scanned within an identical 10 x 10 μm^2 area.

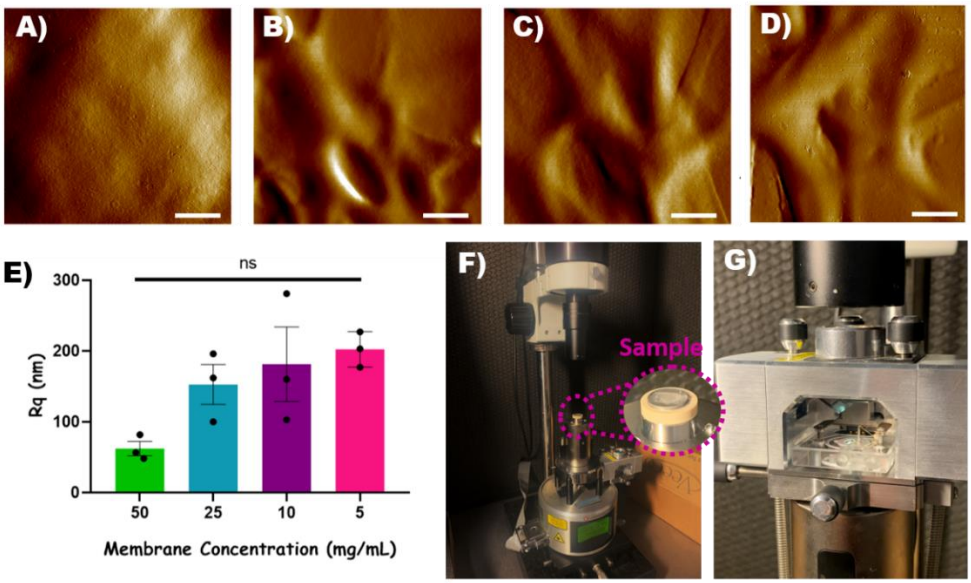

Figure 34: ***Evaluation of the roughness of ELR membranes through the use of AFM images. A, B, C and D)*** *AFM surface micrographs of membrane samples demonstrate a correlation between roughness and concentration (**A** = 50 mg/mL; **B** = 25 mg/mL; **C** = 10 mg/mL; **D** = 5 mg/mL). Scale bar = 2 µm.* ***E)*** *Roughness values (Rq) as a function of membrane concentration.* ***F)*** *Image of the device used for atomic force microscopy (AFM) with a magnification depicting the membrane placement within the system.* ***G)*** *Detail of the specific system for working in humid environments.*

Figure 34 depicts the AFM images of the surface nanomorphology of ELR membranes with four varying concentrations (A = 50 mg/mL; B = 25 mg/mL; C = 10 mg/mL; D = 5 mg/mL) manifesting a three-dimensional network structure. The morphology of the membrane with a concentration of 50 mg/mL exhibits a relatively smooth surface with a roughness of 62 nm. As the polymer concentration is reduced, the resulting membranes gradually exhibit an increase in roughness, reaching a value of 202 nm at a concentration of 5 mg/mL. The reduction in roughness, as the concentration increases may be attributed to the final roughness, which is influenced by the size and thickness of the pores. Thus, an increase in concentration leads to the formation of smaller pore sizes, which facilitates greater interconnectivity between polypeptide chains and enhances binding, resulting in the formation of a denser matrix with a lower roughness [484]. These values are clearly evident when studying the Rq of the samples, as shown in Figure 34E. However, no significant differences are observed between the roughness at the different concentrations. Although the surface roughness has varied, this variation has a minimal impact on the overall transparency of the membranes. Figure 34F illustrates the importance of correctly positioning the sample within the system in order to obtain accurate measurements. Meanwhile, Figure 34G displays the chamber system that preserves a humid environment within the sample to prevent dehydration, which may adversely impact on the final results.

The surface roughness can be identified by analysing the AFM images, where valleys are represented by darker colours and ridges by brighter ones [485]. The results of the roughness measurements acquired utilizing tapping mode AFM are presented in Table 23, which provides an average of three sets of data. These findings indicate that the concentration of the ELR-membrane has a significant

effect on the increase in surface roughness as its concentration decreases. These conclusions are consistent with the hypotheses derived from previous SEM and ESEM techniques.

Table 23: Average roughness measurements (nm) obtained using tapping mode AFM for different concentrations (5, 10, 25 and 50 mg/mL).

	5 mg/mL	10 mg/mL	25 mg/mL	50 mg/mL
Rq (nm)	202.3 ± 25.0	181.3 ± 90.8	152.6 ± 48.6	62.2 ± 17.4

The AFM technique can determine scaffold thickness. However, in this thesis, electron microscopy was necessary to determine the value for ELR membranes which are thicker than 3-4 µm, exceeding the detection limit of the AFM technique.

In conclusion, the utilisation of the aforementioned techniques, including SEM, ESEM, and AFM, has demonstrated that ELR membranes possess adequate surface roughness to facilitate cell adhesion, thus aiding in the healing process. This surface roughness increases the surface area in contact with water, thereby enhancing the adhesion of cells and other substances. Consequently, ELR membranes with lower concentrations may be more suitable for cellular applications, as their higher surface roughness facilitates better cell adhesion [454].

The new scaffolds should exhibit mechanical properties that correspond to those of the simulated tissues, in addition to an appropriate external geometry, macrostructure, microstructure, and interconnectivity. In the human body, cells exist in an extremely complex microenvironment, which is exposed to both exogenous and endogenous forces. The cytoskeleton is subjected to these forces via the extracellular matrix and integrins. Therefore, the mechanical properties of the extracellular matrix exert a profound influence on cell morphology, proliferation and differentiation [486]–[488]. The mechanical properties of various tissues differ depending on their location and composition. Hence, to replicate the physiological microenvironment during wound healing, soft and flexible materials such as ELR membranes are essential. To assess the mechanical properties of ELR membranes, the AFM technique may be employed to measure Young's modulus, adhesion, dissipation, and deformation. Nevertheless, despite the numerous attempts, obtaining accurate measurements was unfeasible due to the many complexities of the technique, particularly with ELR membranes. These membranes are highly viscous, very fine and sticky, which renders the PeakForce QNM mode unsuitable for topography mapping. The tip of the cantilever adheres to the membrane surface, preventing it from separating adequately to take readings, thus making accurate measurements unfeasible.

In a previous study, Gonzalez *et al.* [436] determined the elastic modulus (Young's modulus) and strength and strain at break of ELR-based membranes by conducting a uniaxial test to failure. In general, a reduction in the concentration of ELR-based membranes resulted in a progressive decline in their mechanical properties. Consequently, the ELR-based membrane with a concentration of 50 mg/mL (0.6 MPa) exhibited a doubled elastic modulus compared to the membrane with a concentration of 5 mg/mL (0.3 MPa). In contrast, the modulus of the

membranes with concentrations of 10 and 25 mg/mL displayed an intermediate modulus between them, being 0.35 and 0.5 MPa, respectively. An identical pattern was noticed when tensile strength was assessed the at the breaking point. The membranes, with concentrations of 25 and 50 mg/mL, demonstrated a tensile strength of approximately 2-2.5 MPa prior to fracturing. In contrast, the membranes with concentrations of 10 and 5 mg/mL exhibited a considerable decrease in strength, with values of 1.5 MPa and 1.2 MPa, respectively. Furthermore, the tensile strain at the breaking point was analysed. While the 10, 25, and 50 mg/mL membranes exhibited a value of approximately 400 %, the 5 mg/mL membranes exhibited a notably lower value of approximately 250 %. The values for the elastic modulus are comparable to those obtained from native elastin (0.3-0.6 MPa), while the values for the strain at rupture are double that of the natural substance (100-220 %). It can therefore be concluded that the mechanical properties of these membranes are also suitable for application as patches on skin wounds, since they can be easily handled and placed without fear of breakage. However, membranes with a concentration of 5 mg/mL are unsuitable for use, as they are of a soft consistency and prone to breakage when handled.

Finally, the study of membrane surface characterisation will be completed with an investigation into wettability. This property is directly related to biological interactions, which in turn affect the biocompatibility of biomaterials used in regenerative medicine. The surface properties of a material placed in the area of damaged tissue will determine the interactions with body fluids on contact. Furthermore, surface energy, which is closely related to wettability, correlates with biological interactions and determines cell adhesion, cell growth and overall implant stability. In general, biomaterial surfaces with moderate hydrophilicity facilitate cell growth and exhibit greater biocompatibility [454].

In addition to influencing cell adhesion and differentiation, surface topography also affects wettability. It is well established that surface wettability is a function of both surface chemistry and surface roughness. Consequently, wettability of the surface of ELR membranes is quantified by means of contact angle measurements. In the majority of cases, the contact angle of membranes is typically measured in their dry state, as shown in Figure 35A, using the sessile drop technique [454]. However, membranes employed as wound dressings are in a wet state, and therefore, in order to understand the surface properties of the membrane under working conditions, contact angle analysis of the membranes must also be carried out in their wet state, as illustrated in Figure 35B. For this reason, the water contact angle (WCA) of the membranes was measured in both states. The results are presented in Figure 35C, which demonstrates that the hydrophobicity of the samples undergoes a significant change when hydrated or dry. On the one hand, the freeze-dried membranes presented values exceeding 90 degrees, indicating a hydrophobic character due to the composition of the polypeptide chains, predominantly $-CH_2$ and $-CH_3$ groups, and no statistically significant differences were observed between the different polymer concentrations. The hydrophobicity of the membranes radially changes when they are maintained in their hydrated state, becoming more polar due to the presence of hydroxyl groups (-OH) of the

amino acid serine, which can form hydrogen bonds with water. This technique has the disadvantage that the lower contact angle values (below 20 degrees) cannot be measured with great accuracy due to the uncertainty in assigning a tangent line when the liquid drop profile is almost flat. For this reason, and in accordance with to the literature, we accept the value of these contact angles as 0 degrees. The hydrophilic hydrated membranes exhibit no statistically significant differences between the different polymer concentrations. It is noteworthy that there are clear statistically significant differences between the hydrophobicity values of the membranes in their wet state (0 °) and their dry state (> 90 °).

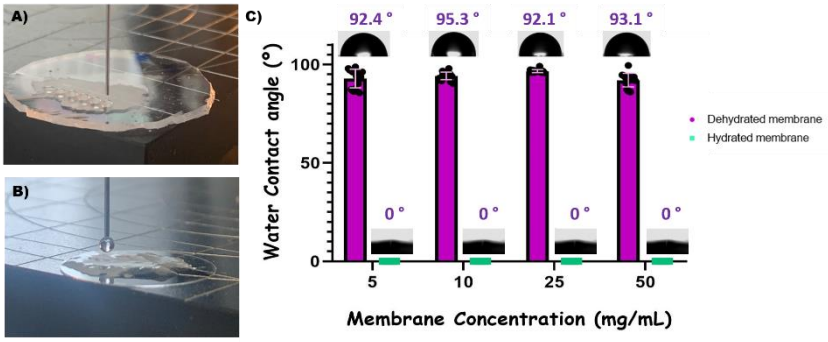

Figure 35: ***Evaluation of the wettability of the membrane surface. A)*** *Image of water contact angle (WCA) measurement of dried membranes.* ***B)*** *Image of water contact angle (WCA) measurement of hydrated membranes.* ***C)*** *Effect of polymer concentration on the water contact angle of a dried and hydrated ELR-based membrane.*

As previously mentioned, the hydrophilicity of the hydrated membranes is an essential factor in their suitability for use as wound dressings, as it provides an adequate level of moisture in the wound, which promotes uniform re-epithelialisation, facilitates the absorption of exudate and also provides good bioadhesion to the wound surface.

Consequently, the efficacy of scaffolds designed for skin regeneration is highly dependent on texture, microstructure, pore architecture morphology (including porosity, pore size, pore shape and pore interconnections) and wettability of the material, as these factors can be employed to enhance the material-host response. In light of the comprehensive characterisation of the membrane surface, it can be concluded that the physicochemical properties of the surface in terms of wettability and roughness are optimal for subsequent successful cell adhesion, migration, proliferation and differentiation processes.

3.1.2.4.- Self-healing behaviour

Currently, a considerable quantity of research is focused on the development of self-healing hydrogels for use in wound healing. The majority of these materials employ dynamic cross-linking, specifically Schiff bases, in addition to ionic interactions and hydrogen bonding [489]–[492].

The primary limitation of using membranes to treat wounds is often attributed to their integrity, so in order to evaluate the recovery potential of membranes, an AFM technique was used and a fine scalpel was employed to

manually create a scratch on the surface of the membrane, as schematically presented in Figure 36C. Figure 36A presents AFM images captured at the initial stage, after 30 minutes, and after rehydration of the membrane with 5 µl of water, with the objective of assessing its potential for regaining functionality. The images permit the measurement of different points along the horizontal distance of the scratch edges, thereby enabling the tracking of their evolution over time. The corresponding results are presented in Table 24. Therefore, it is possible to observe the wound progression and note a slight closure after 30 minutes. However, if the sample is rehydrated, it is possible to verify that the scratch has been completely closed. This quick and autonomous self-healing process of the membrane can be explained by the methodology employed in obtaining the samples. The SKS and VKV polymers are modified using complementary groups that react orthogonally upon contact. The membranes are obtained at the interface of two immiscible liquids, where only the reactive chains located at the interface can be chemically cross-linked. Thus, there may be some azide or cyclooctyne groups that did not undergo the requisite chemical reaction during the membrane formation process. Upon rehydration, the peptide chains with reactive groups can move and form a covalent bond with the free complementary groups, resulting in the closure of the scratch. To enhance the visibility of this self-renewing process, the Nanoscope Analysis 2.0 software (Bruker) is used to generate the three-dimensional illustrations depicted in Figure 36B.

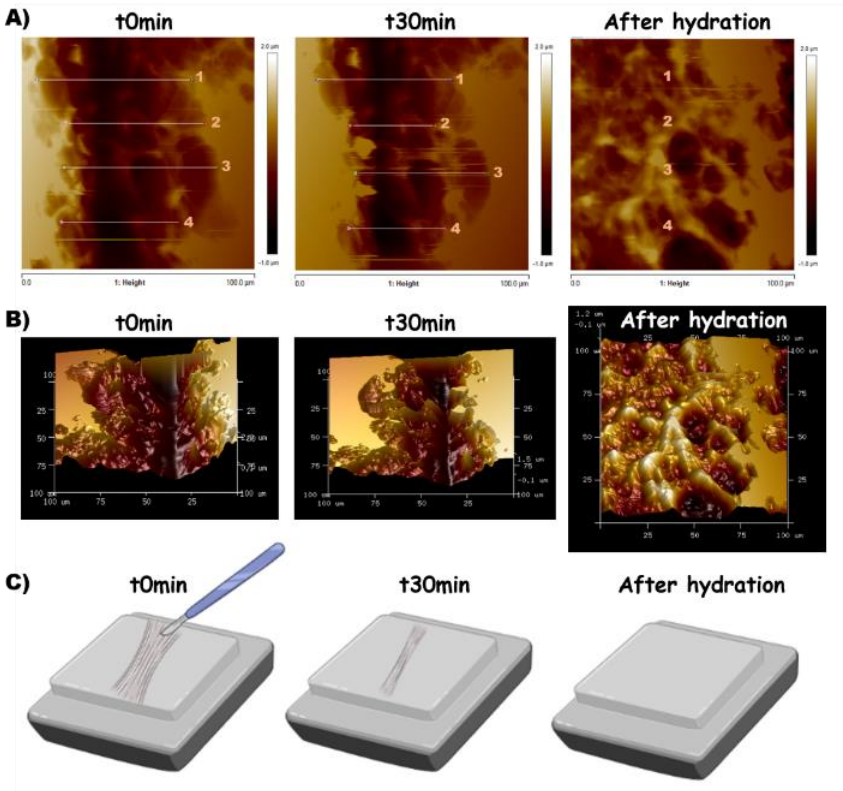

Figure 36: ***Evaluation of self-healing capacity of ELR membranes. A)*** *The use of AFM to scan planar images of the membrane surface allows for the observation of the progress of self-healing after a scratch at different time points. The numbers indicate horizontal distances and are presented in the Table 24.* ***B)*** *3D AFM images of the membrane surface demonstrate the evolution of self-healing after a scratch at different time points.* ***C)*** *Schematic representation of the self-healing process following a scratch.*

Table 24: The horizontal distances between the points of contact on the surface of the material after the creation of a scratch at different intervals of time.

Points	Horizonal distance t = 0 min (µm)	Horizonal distance t = 30 min (µm)	Horizonal distance After hydration (µm)
1	66.7	56.9	0
2	60.8	36.5	0
3	65.5	56.9	0
4	49.8	40.8	0

It is therefore possible to obtain membranes that are capable of self-healing *in situ* and restoring their properties after scratching are obtained. This feature is of great significance at the application level, as any physical damage to the membrane structure during implantation in the wound could be regenerated by the circulating water without the need for any external intervention. This property is of great interest, as hydrogel wound dressings demonstrating self-healing capability may extend the durability and provide enhanced wound protection, thereby making them safer for users [493].

3.1.2.5.- Swelling ratio and water content percentage (WCP)

The determination of the percentage of water content is of paramount importance in the characterisation of a hydrogel, as it is intimately related to a number of other properties. In general, hydrogels with higher water retention are more suitable for medical applications, as they indicate better permeability and biocompatibility [494]. Nevertheless, high water absorption results in a reduction of mechanical properties, thus necessitating the identification of an optimal balance. Moreover, measuring the swelling of the membrane is useful for determining the dimensional changes in the network. This is heavily dependent on the hydrophilicity of the membrane and is limited by the degree of cross-linking of the polymer chains and the porosity. Consequently, when hydrogels are in contact with an aqueous solution, they reach a level of equilibrium swelling that is primarily dependent on the type of polymer, as well as the type and density of their cross-linking. An increase in the content of hydrophilic monomer results in an augmented number of affinity groups for water molecules, thereby enhancing the interaction between the hydrogel and aqueous solutions [495]. Conversely, an increase in the amount of hydrophobic monomer causes a reversal of this behaviour, resulting in an increase in interactions between the polymer chains due to a decrease in their interaction with water molecules. Therefore, a reduction in the hydrophilicity of the polymer and an increase in the cross-link density led to a reduction in water absorption [496].

In their dry state, membranes are solid and relatively hard materials. However, when immersed in an aqueous solution, they exhibit an inward diffusion of water. Consequently, the membranes absorb a considerable volume of water until they reach a state of equilibrium, as illustrated in Figure 37A. In this diffusion

process, water migrates into either pre-existing or dynamically formed spaces between the hydrogel chains.

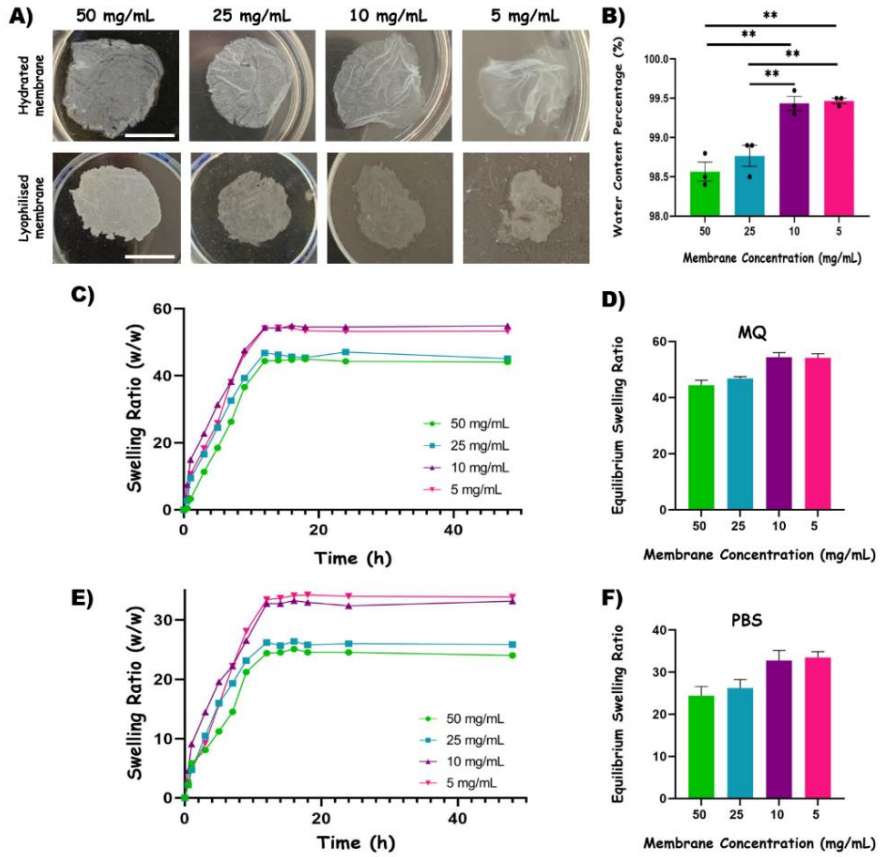

Figure 37: ***Swelling behaviour and water content percentage. A)*** *Representative images of the typical appearance of both dry and swollen membranes. Scale bar = 1cm.* ***B)*** *Water content percentage of an elastin-based membrane according to concentration.* ***C)*** *Swelling profile of elastin-based membranes in ultrapure water within 48 hours at 37 °C.* ***D)*** *Equilibrium swelling ratio of the elastin-based membranes in ultrapure water.* ***E)*** *Swelling profile of elastin-based membranes in PBS within 48 hours at 37 °C.* ***F)*** *Equilibrium swelling ratio of the elastin-based membranes in PBS.*

Figure 37C and Figure 37E illustrate the absorption isotherms of the membranes at varying concentrations in ultrapure water and PBS solution. The swelling behaviour of the membranes varied depending on the conditions under which they were tested. The study revealed that the membranes exhibited a reduced degree of swelling in PBS compared to ultrapure water. The degree of swelling and water content percentage are influenced by the duration of immersion, with longer immersions result in higher water percentages and swelling values until the equilibrium hydration values are reached, as shown in Table 25. The initial immersion period for all elastin-based membranes demonstrated a rapid increase in swelling, with equilibrium swelling being reached at approximately 12 hours for both ultrapure water (Figure 37C) and PBS (Figure 37E).

Table 25: Equilibrium Swelling ratio and water content of ELR-based membranes in PBS and ultrapure water after reaching equilibrium.

Membrane concentration (mg/mL)	Water Content (%)	Equilibrium Swelling ratio (w/w)	
	MQ	MQ	PBS
5	99.43 ± 0.04	54.2 ± 2.5	33.4 ± 2.5
10	99.42 ± 0.14	54.4 ± 2.9	32.8 ± 4.1
25	98.76 ± 0.22	46.8 ± 1.2	26.2 ± 3.5
50	98.57 ± 0.17	44.5 ± 3.0	24.4 ± 3.7

The concentration of the membrane produces an influence on its absorption regardless of the solvent, as presented in Figure 37C and Figure 37E. The degree of equilibrium swelling is observed to decrease with an increase in concentration, in accordance with the findings of other ELR hydrogels documented in the literature [479], [497], [498]. Consequently, the membrane with a concentration of 5 mg/mL exhibited the highest swelling percentage, with a value comparable to that observed at a concentration of 10 mg/mL concentration, which was 54 (w/w) in ultrapure water and 34 (w/w) in PBS. The membranes with a concentration of 25 mg/mL showed values of 46 (w/w) in ultrapure water and 26 (w/w) in PBS. Finally, the membrane with a concentration of 50 mg/mL presented the lowest degree of swelling, with values of 45 (w/w) in ultrapure water and 24 (w/w) in PBS. An increase in concentration results in an increase in the number of polymer chains and cross-linking density, which in turn leads to a stiffer polymer network. Consequently, the chains are unable to expand fully as water enters into the hydrogel network, causing a significant decrease in free volume within the polymeric network, and thereby a reduction in the swelling ability of the hydrogel [499], [500].

The equilibrium fluid absorption is a balance between the osmotic forces generated by the water entering the macromolecular network and the cohesive forces exerted by the macromolecular chains that resist expansion. The results presented in Table 25 indicate significant differences in the values of equilibrium swelling ratios between membranes with a concentration of 10 mg/mL and those with 50 and 25 mg/mL, as well as between membranes with a concentration of 5 mg/mL and those with 50 and 25 mg/mL when immersed in water, as shown in Figure 37D. In contrast, no statistically significant differences were observed when membranes were immersed in PBS, as depicted in Figure 37F. However, it is observed that there is an analogous behaviour between water and PBS with the concentrations. In both cases, the value of the swelling equilibrium rate is observed to increase as the membrane concentration decreases. This phenomenon can be attributed to an increase in concentration, which results in a reduction in pore size, thereby leading to a decrease in the maximum water content that hydrogels can retain [501].

According to the literature, the final equilibrium value reached by ELR membranes was determined by the temperature at which they swell [456], [479], [497]. At lower temperatures, ELR hydrogels exhibit a higher degree of swelling in aqueous solvents. This phenomenon can be attributed to the gradual increase in hydrophobicity of the elastin material, which results in a reduction in the degree of

swelling and water content as the temperature rises. The experiments were conducted at 37 °C, as this is the standard body temperature and the membranes are intended for use in the treatment of wounds.

In ultrapure water at 37 °C, the water content of the membranes after reaching equilibrium was found to be over 98 % regardless of the concentration, as shown in Figure 37B. This characteristic highlights their ability to absorb body exudates, rendering the membranes an appropriate material for use as an artificial wound healing dressing [456]. Moreover, ELR membranes display a degree of swelling ranging from 34 to 24 (w/w), dependent on the concentration, when immersed in PBS at 37 °C. These values do not result in material shrinkage, which in turn will promote homogeneous skin regeneration.

The results suggest that ELR membranes are suitable wound dressings for promoting the healing process. ELR membranes possess the ideal features of a wound dressing, including the regulation of wound hydration, the prevention of dehydration through the creation of an appropriate moist environment, the effective absorption of exudate, and the adhesion to the wound surface. The moist environment enhances cell migration, thereby promoting enhanced new skin regeneration.

3.1.2.6.- Morphological properties

An increase in scaffold porosity is associated with a reduction in mechanical properties, emphasising the importance of maintaining an optimal balance between scaffold porosity and mechanical properties. The porosity of a scaffold can be modified in order to achieve the desired mechanical properties. Consequently, by modifying the porosity distribution on intricate structures, optimal interconnecting channels can be designed based on functional gradients with the objective of enhancing permeability and fluid transport through the structure. The dimensions, shape, orientation, connectivity, and composition of the channel surface collectively determine the nature of nutrient transport. Furthermore, the interconnectivity of channels enables the natural expansion of cells and tissue. The efficient connectivity of biomaterials allows for the transmission of fluids to deeper regions, thereby facilitating the diffusion within scaffolds, which in turn forms a permeable structure for tissue engineering. Furthermore, the pore size exerts a significant influence on cell growth, with the optimal size for cell permeation varying according to the cell type in question. The ECM is a mesh-like network comprising pores that facilitate the transport of nutrients, growth factors, and gases. Consequently, porosity assumes a pivotal role in biomimetic hydrogels. This is of particular relevance in cell-encapsulated three-dimensional gels, as it facilitates the supply of nutrients from the medium, removal of waste products, and gas exchange. Porosity can be quantified as the maximum size of solute that can diffuse into the hydrogel. This is determined by the mesh size, which is dependent on the cross-link density of the polymer chains [502].

The porosity of the membranes can be estimated in accordance with a previously published study by the group [457], using the previously measured

swelling rate in water. This is achieved by combining the values of the membranes in their dry and wet states, the density of pure water at 20 °C and the volume of the membranes as described in the methodology chapter. Figure 38A depicts cross-sectional images of the membranes, with the thickness values for the distinct membrane concentrations delineated and presented in Table 26. The value of the membrane volume can be calculated by applying the aforementioned thickness value derived from the SEM images and the known diameter of the membrane, which is 15 mm. This allows the determination of the porosity value. Consequently, Figure 38B illustrates the percentage porosity of the ELR membranes for varying polymer concentrations.

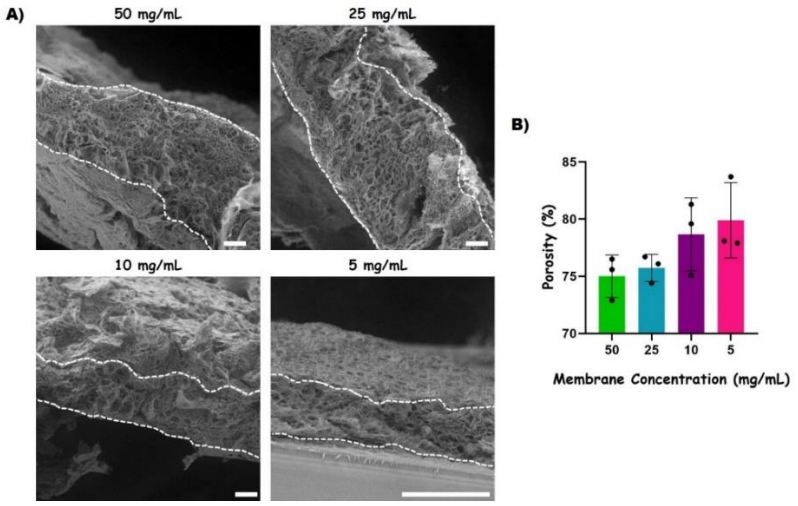

*Figure 38: **Evaluation of the porosity of ELR membranes. A)** Representative SEM images of the freeze-dried and cryo-fractured ELR-based membranes. The cross-section borders are highlighted by a white dashed line, which determines the thickness of the membrane for each concentration. Scale bar = 50 µm. Images from* [436]. ***B)** Percentage of porosity for each concentration of ELR-membrane.*

The ELR membranes exhibit a high degree of porosity, with values ranging from 75 to 80 %. Additionally, the porosity of these membranes is concentration-dependent, with lower concentrations resulting in higher porosity. The results presented in Table 26 indicate that there are no significant differences in porosity values between membranes with varying concentrations. These results are consistent with those of a previously reported study by the group [457], which was demonstrated that porosity decreases with increasing concentration. Furthermore, a direct correlation was observed between the porosity of the membranes and their swelling capacity, indicating that a decrease in porosity leads to a reduction in the membrane swelling process.

*Table 26: Comparison of the morphological properties of distinct concentrations of ELR-membranes. * Values collected from the article* [436].

Membrane concentration (mg/mL)	Thickness (µm)*	Porosity (%)	Average pore size (µm)*
5	6	79.9 ± 3.3	5.0
10	19	78.6 ± 3.2	4.1
25	23	75.7 ± 1.2	3.0
50	25	75.0 ± 1.9	2.2

The internal microstructure of the membranes was previously described by Gonzalez *et al.* [436] after freeze drying using SEM images and Table 26 presents a summary of the values. It was observed that an interconnected and porous morphology dominates the interior of the structures. Furthermore, it was demonstrated that higher polymer concentrations resulted in smaller pore size distributions and higher thicknesses. Therefore, cross-sectional imaging revealed that the average pore size was 5.0, 4.1, 3.0 and 2.2 μm for the concentrations of 5, 10, 25 and 50 mg/mL, respectively. This effect is related to the formation process, as higher concentrations should increase the binding sites used by the ELR chains to interconnect, thus forming a denser matrix with smaller pore size. Furthermore, an increase in membrane thickness was observed with increasing concentration, with values of 6, 19, 23 and 25 μm for concentrations of 5, 10, 25 and 50 mg/mL, respectively. The authors hypothesise that an increase in the quantity of material will result in an acceleration of the growth stage, thereby impeding the horizontal alignment of the developing independent networks and facilitating the reaction-melting process in a direction perpendicular to the liquid-liquid interface.

As previously stated, porosity and average pore size are crucial factors in the design of specific scaffolds that provide 3D spaces for cell attachment and the development of complex structures such as vascularisation, innervation and extracellular matrix. Consequently, the degree of control over scaffold characteristics, including pore size and porosity, should be adjustable based on various scaffold fabrication parameters, such as temperature, polymer solvent, solute concentration and cross-linking type. Given the considerable diversity in extracellular matrix composition within and between different tissues, it is essential to adjust the physicochemical features of biomaterials or biomaterial surfaces in order to recreate the local cellular surroundings and satisfy the anticipated applications (i.e. tissue or organ function).

Another relevant feature observed in the images of Figure 38A is the absence of the phenomenon known as "skin effect," which occurs in hydrogels produced by alternative methodologies. This phenomenon involves the formation of a superficial layer with distinct characteristics in comparison with the internal portion of the hydrogel [503], [504]. In this instance, the observed porosity is identical on the external faces as it is within the membrane, which will further facilitate cell invasion since they will not encounter a barrier upon contacting the membrane surfaces. This advantageous feature is a consequence of the novel methodology employed in the production of these membranes.

A number of research have demonstrated that scaffolds with a porosity of between 60 and 90 % are well-suited to applications in wound healing. These scaffolds provide sufficient space for cellular activity, oxygen and nutrient exchange, and the production of new extracellular matrix [505], [506]. Both low and high porosity scaffolds facilitate the initial attachment, spreading and proliferation of primary dermal fibroblasts. However, only high porosity scaffolds promote migration and infiltration of active cells [507]. Consequently, in the specific case under consideration, the high values of porosity observed in the membrane

(between 75 and 80 %) indicate that elastin-based membranes are suitable for use in regenerative medicine, and in particular as wound dressings.

3.1.2.7.- *In vitro* enzymatic degradation

The ELR-based membranes were evaluated with an *in vitro* degradation test to assess their stability (non-enzymatic PBS solution) and degradability under the influence of an elastase solution, which simulates the conditions present in a chronic wound environment [508]. The wound healing process involves MMPs, including collagenases, gelatinases, stromelysins, and elastases, which catalyse the hydrolysis of essential ECM components such as collagen, laminin, elastin, and fibronectin [509] through peptide bond cleavage [510], which plays a crucial role in ECM remodelling. Chronic wounds are also characterised by the persistence of infections and a prolonged inflammatory phase. As a result, the human immune system produces high levels of lysozyme, which combats bacterial infections [511]. Consequently, peptide-based materials may degrade in the presence of cell-produced enzymes, which are present in chronic wounds at elevated levels, and this may negatively impact the stability of the scaffolds [512], [513]. However, the degradation process of biomaterials is necessary to facilitate cell growth and proliferation, thereby enabling the generation of new tissue. In order to guide the ingrowth of lax connective tissue, the proliferation of fibroblasts and epithelial cells, and the formation of blood vessels, skin dressings must be both biodegradable and stable enough to maintain their composite structures for a minimum of three weeks before subsequently degrading and restoring the new tissue [514], [515].

A simple method to monitor the degradation process of ELR membranes is to evaluate their weight loss after a specified incubation time, which can also determine the degradation rate. The results of the enzymatic degradation test *in vitro* are presented as the remaining weight for each time point and as the degradation rate. Figure 39A illustrates the temporal evolution of the ELR membrane (50 mg/mL) when immersed in a proteolytic elastase solution or in PBS. In the first case, the membrane undergoes a process of degradation over time, with a complete disappearance occurring approximately 22 days after immersion. In contrast, when submerged in PBS, the membrane maintains its integrity and is not susceptible to degradation for at least 22 days. The two graphs demonstrate a notable difference in the rate of degradation between samples that were exclusively exposed to PBS, which exhibited minimal degradation, with approximately 90 % of the mass remaining consistent after 25 days, regardless of the concentration of the membrane. In contrast, samples that were exposed to elastase in PBS exhibited complete degradation within the same period of time.

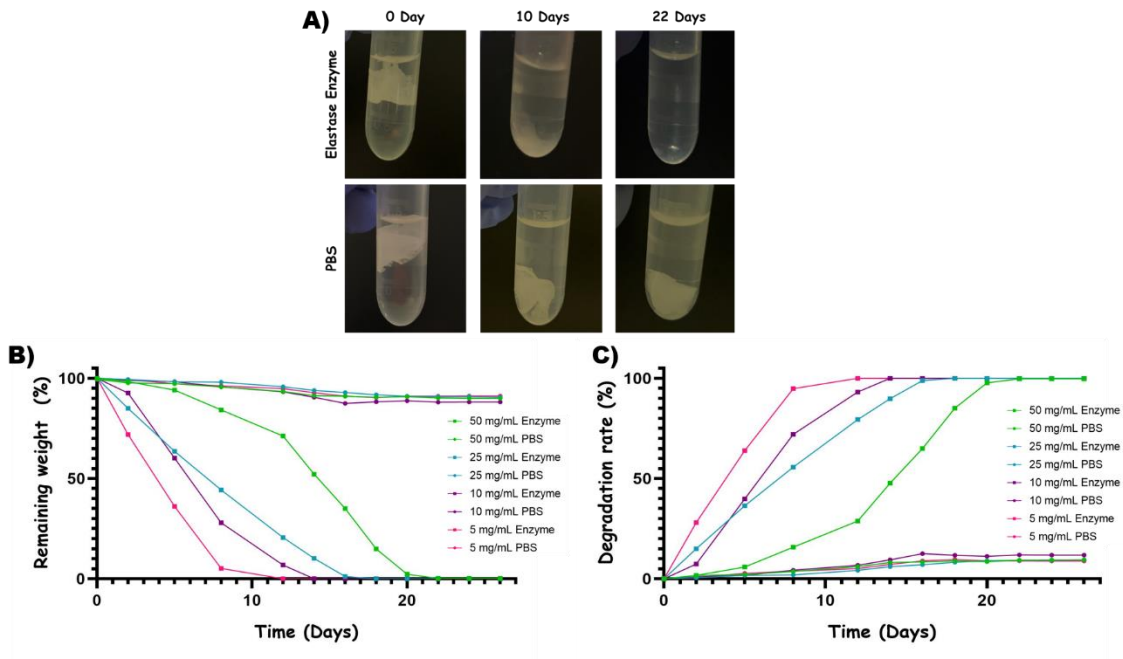

Figure 39: ***Evaluation of enzymatic degradation of ELR membranes in vitro****.* ***A)*** *Representative images of the degradation process of membranes in PBS and in elastase solution.* ***B)*** *Remaining weight profile of different concentrations of membrane samples immersed in either PBS alone or in an elastase solution, is expressed as a mass percentage.* ***C)*** *The degradation rate profile of elastin-based membranes in either PBS alone or elastase solution within 25 days.*

Figure 39B and Figure 39C demonstrate that the ELR membranes exhibited minimal weight loss following incubation in a PBS solution, indicating their high stability under the specified conditions. However, the elastin-based membranes showed degradation in the presence of elastase, with a concentration-dependent response observed. The lower the concentration of the membrane, the faster its enzymatic degradation, which is logical, given that it contains less protein material. Consequently, the 5 mg/mL membrane exhibited the highest rate of degradation among all groups, with complete degradation occurring in just 12 days. Both the 10 mg/mL and 25 mg/mL membranes completely degraded within a period of approximately two weeks, specifically in 14 and 17 days, respectively. Conversely, the 50 mg/mL membranes showed the slowest degradation rate, with a complete degradation occurring over a period of 22 days.

The existing literature emphasises the importance of materials used in regenerative medicine exhibiting slow degradation. This is especially important in the context of wound dressings, which must remain stable for a minimum of three weeks (21 days) in order to facilitate the gradual replacement of damaged tissue by newly formed healthy tissue [516]. The results clearly demonstrate that the developed ELR membranes exhibit high stability and slow degradation in enzymatic solution, thus satisfying the criteria for being a candidate wound dressing. Moreover, the degradation rate *in vivo* can be modulated by adjusting the concentration of the ELR membranes to maintain them in the wound for the desired duration [517]. However, it is crucial to consider additional factors when evaluating the degradability of dressings, as it is not solely dependent on the concentration of the material, but is also influenced by the composition of the material, which may

contain enzyme cleavage sites, as well as the pH and temperature of the wound site, the use of external additives, and the local enzyme concentrations [518]. Furthermore, the new scaffolds used as wound dressings should replicate the properties of the tissues they are meant to simulate, including external geometry, microstructure, interconnectivity, and mechanical properties. Additionally, the scaffolds must provide structural support for cells to grow, migrate, proliferate and differentiate, thus enabling the formation of three-dimensional, tissue-like construct.

In light of the findings presented in this section, it is evident that the developed VKV-SKS membranes exhibit favourable physicochemical properties, making them optimal candidates as dressings for skin regeneration and wound healing. Firstly, the membranes possess a porous structure, comprising interconnected pore spaces that are crucial for nutrient exchange, cell migration, and cell proliferation within the scaffold, thereby facilitating the creation of functional neotissues.

On the other hand, the slow dynamics of chronic wound healing requires a gradual degradation of the scaffold, which must remain stable for a minimum of two to three weeks to facilitate the replacement of damaged tissue by newly formed, healthy tissue [516]. The developed ELR membranes exhibit high stability and a slow degradation rate in enzymatic solutions, thus meeting the requirements for a possible wound dressing. Furthermore, the ELRs can be broken down into peptides and amino acids, which can be easily removed from the body ensuring that the degradation products do not elicit an immune response [458].

In addition, other characteristics of the membranes are contingent upon the porosity of the materials, including their mechanical properties. The control of the porous structure of the scaffold allows for the adjustment of these properties to match those of native tissues. Therefore, the tensile strength, Young's modulus, and strain at break values are crucial parameters for assessing the suitability of the mechanical properties of the scaffold. In the present study, the elastic modulus values are similar to those observed in native elastin, with a range of 0.3 to 0.6 MPa. Moreover, the strain at break is twice as high as that of the natural elastin. Furthermore, these membranes exhibit an appropriate degree of roughness, which makes them suitable for use as wound dressings, as rough surfaces exhibit better adhesion to wounds in comparison to smooth surfaces. In this sense, it can be concluded that lower concentration membranes would be more advantageous for cell cultures, since the rougher surfaces would encourage cell adhesion. Furthermore, these membranes exhibit strong hydrophilicity in their hydrated state and a high swelling ratio, which is ideal for absorbing wound exudate, providing an appropriate level of moisture to facilitate uniform re-epithelialization and promoting good bioadhesion to the wound surface. Finally, the capacity to manipulate these ELR-derived membranes increases their versatility, as their low probability of rupturing ensures their durability over the long term in hostile environments. If any injuries occur, the membranes are capable of self-regeneration.

From the preceding analysis, it can be reasonably inferred that VKV-SKS membranes have the potential to serve as dressings for the treatment of wounds, as they meet the aforementioned criteria. To investigate further at the cellular level and *in vivo*, the membranes with a concentration of 10 mg/mL will be selected for further analysis. Consequently, all subsequent experiments will employ this membrane concentration.

3.1.3.- Biological characterisation of ELR membranes

3.1.3.1.- Biocompatibility and cytotoxicity

The biocompatibility is a crucial factor in the development of novel dressings for chronic wound healing. Materials utilized for this application, such as scaffolds, films, and coating/functionalization surfaces, must exhibit nil toxicity towards cells and not produce any toxic degradation products that may adversely affect the ability of the host to regenerate skin [497]. A number of tests are available to assess the *in vitro* cytotoxicity and compatibility of VKV-SKS membranes. These include studies of cell proliferation using the MTS assay, assessment of cell membrane damage using the LDH assay, evaluation of cell viability using the Alamar Blue or LIVE/DEAD assay, gene expression analysis using qPCR, and protein expression analysis using immunostaining. Furthermore, cell growth is evaluated using the colony formation assay, while cell migration is assessed by the transwell migration assay and *in vitro* scratch assay.

For the purpose of cell proliferation assay, HaCaT and HFF-1 cells were seeded onto ELR membranes in 24-well culture plates at a density of 2 x 10^4 cells/well and then grown at 37 °C in a humidified atmosphere containing 5 % CO_2 for 48 hours. The results of the MTS assay for fibroblasts and keratinocytes are presented in Figure 40A. The viability of the cells seeded on the TCP is considered as a control (100 %) for comparison. Upon analysis of the aforementioned graphs, it can be inferred that the presence of ELR membranes does not restrict the viability and proliferation of HFF-1 and HaCaT cells. This is evidenced by the fact that cell viability was above 85 % for both cases following 48 hours of incubation. Therefore, according to the internationally recommended guidelines for *in vitro* cytotoxicity (International Organization for Standardization ISO-10993-5: Cytotoxicity and Biocompatibility testing), it can be concluded that our protein membranes are not toxic to cells as cell viability is above 70 % post-exposure. The data were evaluated using analysis of variance (ANOVA) and *post hoc* Tukey tests, with each type of cell being considered separately. Significant variations were observed in the cell proliferation between the cells cultivated on the membranes and those grown on the TCP and glass coverslip among HFF-1 cells. Conversely, a statistically significant difference was noted between the TCP and the membranes and the glass coverslip for HaCaT cells. The aforementioned results demonstrate that the VKV-SKS membranes, when cells were grown on them, were non-toxic. Furthermore, a 10

mg/mL concentration was found to be suitable for the *in vitro* growth and proliferation of fibroblasts and keratinocytes, which are necessary for wound healing.

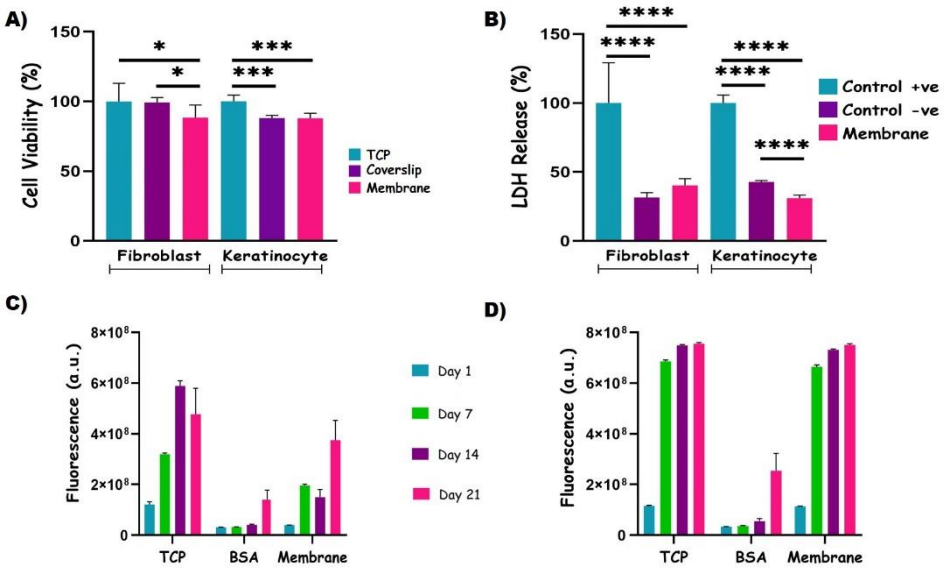

Figure 40: ***Biocompatibility and Cytotoxicity. A)*** *Cell viability values obtained from an MTS assay conducted on HFF-1 and HaCaT cells seeded onto a VKV-SKS membrane and cultured for 48 hours.* ***B)*** *Effect of the ELR membrane on LDH release after 24 hours of culturing.* ***C)*** *The reduction of AlamarBlue in HFF-1 cells seeded onto ELR membranes was measured at different time points.* ***D)*** *The reduction of AlamarBlue in HaCaT cells seeded onto ELR membranes was measured at different time points.*

The determination of the cytotoxic effect of the protein materials used in these novel wound healing dressings is a crucial parameter as the materials should not elicit a harmful reaction in the body or cause cell death within surrounding tissue. For this reason, a lactate dehydrogenase (LDH) colorimetric assay was performed. Prior to commencing the experiment, it is essential to calibrate the optimal quantity of FBS to be employed in this assay, in order to prevent interference with the absorbance of LDH released by the cells, as previously demonstrated in the methodology chapter. Consequently, the cytotoxicity of the membranes is evaluated utilising DMEM medium supplemented with 5 % FBS. In order to assess the cytotoxicity of the ELR membranes, HaCaT and HFF-1 cells were seeded onto ELR membranes in 24-well culture plates at a density of 2 x 10^4 cells/well. Subsequently, the cells were incubated at 37 °C in a humidified atmosphere with 5 % CO_2 for 24 hours. The outcomes of the lactate dehydrogenase release assay, conducted on fibroblasts and keratinocytes, which were seeded in direct contact with the cell membranes, are presented in Figure 40B.

This assay assesses the irreversible damage caused to cell membranes in culture media. The positive control for each cell type is represented by the cytotoxicity of the cells seeded in the TCP and then lysed, which corresponds to the maximum LDH release value (100 %). The optical density (OD) at a wavelength of 490 nm was measured to quantify the LDH release profile of all groups under investigation. From the graphs obtained, it can be observed that the LDH levels in the membranes are less than 40 % after 24 hours of incubation. Furthermore, the

release of LDH from living cells seeded on the TCP (negative control) exhibits a relative LDH concentration similar to that of the cells in contact with the materials. Consequently, there was no evidence to suggest that the membranes were accelerating the rate of cell death. The data were evaluated using analysis of variance (ANOVA) and *post hoc* Tukey tests, with each type of cell being considered separately and individually for each cell type. Statistically significant differences in LDH release were observed between the positive control and membranes with both HFF-1 and HaCaT cells. Therefore, the aforementioned results demonstrate that VKV-SKS membranes do not exhibit any cytotoxic effects on cells, possibly due to the purity of the material during preparation and the subsequent sterilisation process prior to use.

In order to complete the cytotoxicity analysis of the VKV-SKS membranes, a non-toxic technique, namely AlamarBlue, was employed to assess metabolic activity and long-term cell health. For this purpose, 1.5 x 10^4 HFF-1 and HaCaT cells were seeded onto both membranes and controls. In order to establish positive and negative controls, cells were seeded in a tissue culture plate (TCP) and wells were treated with bovine serum albumin (BSA), respectively. The BSA coating impedes cell adhesion, rendering it a negative control with minimal adhesion. In contrast, TCP, which promotes cell adhesion, will serve as the positive control, representing the optimal adhesion scenario. A series of time points (1, 7, 14, and 21 days) were selected to record assay data and gain a deeper insight into the cellular metabolism of HFF-1 and HaCaT in a static culture. The analysis of cell viability indicates an increase in fluorescence intensity that directly correlates with heightened metabolic activity for all conditions at various time points, as presented in Figure 40C for fibroblasts and Figure 40D for keratinocytes. While cell viability appears to be initially lower in cells cultivated on the membranes compared to those seeded on the TCP, the cells grown on the membranes exhibit the ability to proliferate over time and ultimately achieve favourable levels of cell viability after 21 days in culture.

The aforementioned statement indicates that the membranes encourage adhesion and promote the growth and proliferation of both HFF-1 and HaCaT cells. The biocompatibility demonstrated by the ELR-based membranes aligns with analogous cross-linked hydrogels that have been previously analysed [519]. The viability assay curve conforms to the standard cell growth patterns, exhibiting an exponential increase in cell number during the initial culture phase, followed by a more constant value. However, fibroblasts seeded in the TCP after 21 exhibited a slight decrease in cellular activity. This may be attributed to the cells reaching confluence after a prolonged period, resulting in their demise due to a lack of adequate space for further proliferation. Nevertheless, this phenomenon is not apparent in keratinocytes, which are capable of proliferating in multilayers.

LIVE/DEAD staining was employed to provide additional insight into the results of the cell viability analysis conducted on the protein membranes. To conduct the experiment, 1.5 x 10^4 HFF-1 and HaCaT cells were seeded per well onto the VKV-SKS membranes and allowed to grow for varying experimental times (1, 14, and 21 days). Figure 41 displays fluorescence microscopy images that demonstrate an

increase in the number of cells within the membranes over time for both cell lines, HFF-1 and HaCaT.

In addition, throughout the observation period, predominantly live cells (stained green) were observed which confirms a typical appearance in terms of cell size and morphology. Live cells were identified both on the surface of the membranes and within the internal structure, as illustrated in the magnification of day 21, where cells remained viable within the internal part of the structure. The observed results indicate that nutrients are transported freely throughout the scaffold, thereby ensuring the viability of the cells.

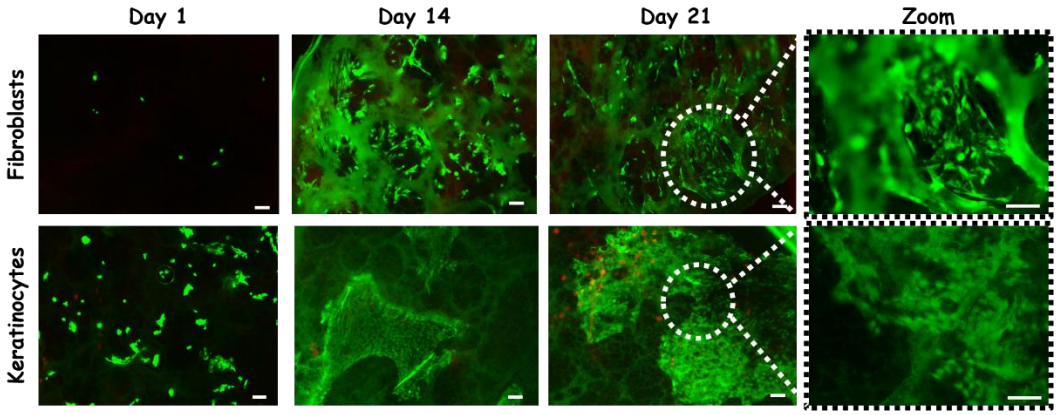

*Figure 41: **Fluorescence images**. Fluorescence microscope images of stained fibroblasts (HFF-1) and keratinocytes (HaCaT) cells, seeded onto VKV-SKS membranes, during a 21-day culture period. Green staining distinguished live cells, while red staining revealed cell death. A slight autofluorescence was detected on membranes in the green channel. Scale bar: 100 μm.*

The fluorescent images are consistent with the previously obtained viability results. The cell proliferation (MTS) and cell viability (AlamarBlue) assays verified an increase in the proliferation rate, with a peak observed at day 21 of the experiment, as also evidenced through the fluorescent images. Additionally, the images also illustrate that the cells exhibit a rounded morphology on day 1, while as the culture evolves, they adopt an expanded morphology. This behaviour is to be expected, given that both cell types are adherent cells. Adherent cells require a surface to adhere to in order to grow and proliferate and achieve their characteristic morphology. In fibroblasts, this morphology is extended with filopodia, which facilitate growth and interaction with adjacent cells. In contrast, keratinocytes grow as clustered cells, forming colonies that grow until they unite with adjacent colonies to form a monolayer. This behaviour is commonly observed in porous hydrogels [475], [520], and may be the reason why they take more days to reach values similar to those obtained when seeded in the TCP. Furthermore, the LIVE/DEAD images corroborate the findings of the cytotoxicity assay (LDH) results, which indicate a minimal presence of dead cells in samples in contact with membranes.

Based on the results, it can be concluded that ELR membranes have the capacity to support a range of cell types with great versatility, thereby enhancing cell proliferation, viability, and metabolic activity over an extended period. This confirms the biocompatibility of VKV-SKS membranes, rending them a potential

choice for wound healing dressings, as they promote the adhesion and growth of fibroblasts and keratinocytes, which are essential cell types in the healing process.

3.1.3.2.- Cell growth

In contrast to the cell numbers employed in previous experiments, which were in the range of 2-1.5 x 10^4 cells per well, this experiment utilises a significantly lower cell concentration, in the range of 1.5 x 10^3 cells per well. The colony formation assay enables the determination of cell reproductive death after exposure to substances or treatments and their clonogenic potential. This is achieved by testing the ability of an individual cell to proliferate and form colonies within the VKV-SKS membranes. Figure 42A depicts crystal violet colony staining images of fibroblasts cultured on the membranes, while Figure 42B shows crystal violet colony staining images of keratinocytes. In both cases, the images demonstrate that colonies can be formed even when the initial seeding concentration is very low. However, only a small proportion of the seeded cells possess the ability to generate colonies.

Following a 15-day incubation period, fibroblasts were observed to have formed approximately 18 colonies on the VKV-SKS membranes. Similarly, keratinocytes formed approximately 26 colonies on the protein membranes, as illustrated in Figure 42C. In this experiment, the incubation period is excessively long for the HaCaT cells, which complicates the counting of their colonies when several are joined together. However, if a shorter incubation period is selected, it becomes impossible to observe the colonies formed by fibroblasts. Consequently, in order to facilitate a comparison between the two cell types, an intermediate time period was selected that was optimal for both cell types, given that they exhibit different growth rates. In any case, the presence of membranes does not impede the colony-forming ability of cells, which is conducive to the regeneration of skin following the application of the dressing to the wound.

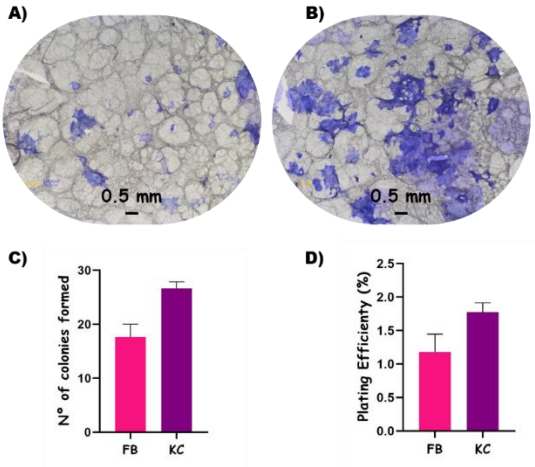

Figure 42: ***Cell growth was tested using a colony formation assay. A)*** *Representative crystal violet staining images of cell culture on membranes for fibroblasts.* ***B)*** *Representative crystal violet staining images of cell culture on membranes for keratinocytes.* ***C)*** *Number of colonies formed within ELR membranes.* ***D)*** *Plating efficiency refers to the ratio of the number of colonies to the number of cells seeded.*

Plating efficiency is defined as the ratio of the number of colonies to the number of cells seeded [460]. The results are illustrated in Figure 42D. The data indicates that there is variation in plating efficiency among the different cell lines, with differences of approximately 0.5 %. Nevertheless, although the plating efficiencies of fibroblasts and keratinocytes on membranes are relatively similar, with values of 1.2 % and 1.8 % respectively, there is a significant difference between them. Both cell types are capable of adhesion and colony formation, with this process being further facilitated by the RGD cell adhesion sequences present on the ELR membrane. However, the keratinocytes cell line is the most favoured.

3.1.3.3.- Expression of cells in membranes

More traditional techniques, such as the use of immunofluorescent markers to stain cells, can be combined with more advanced molecular biology methods like quantitative real-time polymerase chain reaction (qRT-PCR) in order to accurately determine gene expression levels. This combination of techniques can provide insight into how cells respond to and interact with their environment in the presence of a scaffold. The interactions between a biomaterial and the biological environment that surrounds it are of significant importance when considering the effects of implanted biomaterials within the human body. These interactions are recognized to exert an impact on the dynamics of the tissue interface. Accordingly, it is imperative to investigate the interactions between the surface of the biomaterial and the cell surface.

The assessment of biocompatibility in relation to a surface is contingent upon the consideration of cell adhesion, which is influenced by the surface properties of the implanted material. The focal contact is the primary subcellular structure that regulates the effects of cell adhesion. These macromolecular complexes facilitate the attachment of cells to the extracellular matrix (ECM) by connecting integrin receptors to the contractile actin cytoskeleton, concurrently aligning and organising numerous structural and signalling proteins at integrin binding and clustering locations [521]. Consequently, in a culture environment, the majority of cells adhere to their underlying growth surface through focal contacts. Focal contacts can be identified by the presence of vinculin, a protein that binds to actin filaments. Therefore, in this instance, the antibody against vinculin serves as a marker to evaluate the effectiveness of cell adhesion and spreading of fibroblasts and keratinocytes to membranes *in vitro*, as demonstrated in Figure 43. On elastin membranes, elongated, bright spots at cell peripheries, which are characteristic of focal contacts, exhibited vinculin-specific immunoreactivity. Additionally, the formation of these focal contacts occurs rapidly following surface coating. Moreover, another molecule that is characteristic of focal adhesions is focal adhesion kinase (FAK). As a scaffolding protein recruited to integrin cluster sites, it illustrates the cell-material interactions. Thus, an FAK antibody was employed to determine the adhesion of HFF1 and HaCaT cells to the material, resulting in the formation of focal adhesions, as shown in Figure 43. Similarly, FAK is also distributed evenly in proximity to the cell periphery, in a manner analogous to that of vinculin.

Immunofluorescence staining of fibroblasts and keratinocytes was also conducted to confirm the presence of cell-cell junctions, using an antibody against E-cadherin. The protein has been reported to act as a mediator of cell-cell adhesion within tissues, as visually demonstrated in Figure 43. Hence, cadherins are adhesion proteins that play a significant role in developmental processes, wound healing, and tissue homeostasis. This superfamily of calcium-dependent transmembrane proteins forms adherent junctions between adjacent cells, establishing homotypic zipper-like interactions. These junctions link to the cell cytoskeleton, allowing cadherins to sense forces and activate mechanotransduction signalling cascades that drive processes such as proliferation, differentiation and migration, among others. In the skin, E-cadherin-mediated adherent junctions play a vital role in maintaining the epidermal barrier. Therefore, visualisation of these junctions demonstrates that cell behaviour is appropriate for the development of a new tissue by mediating cell-cell adhesion.

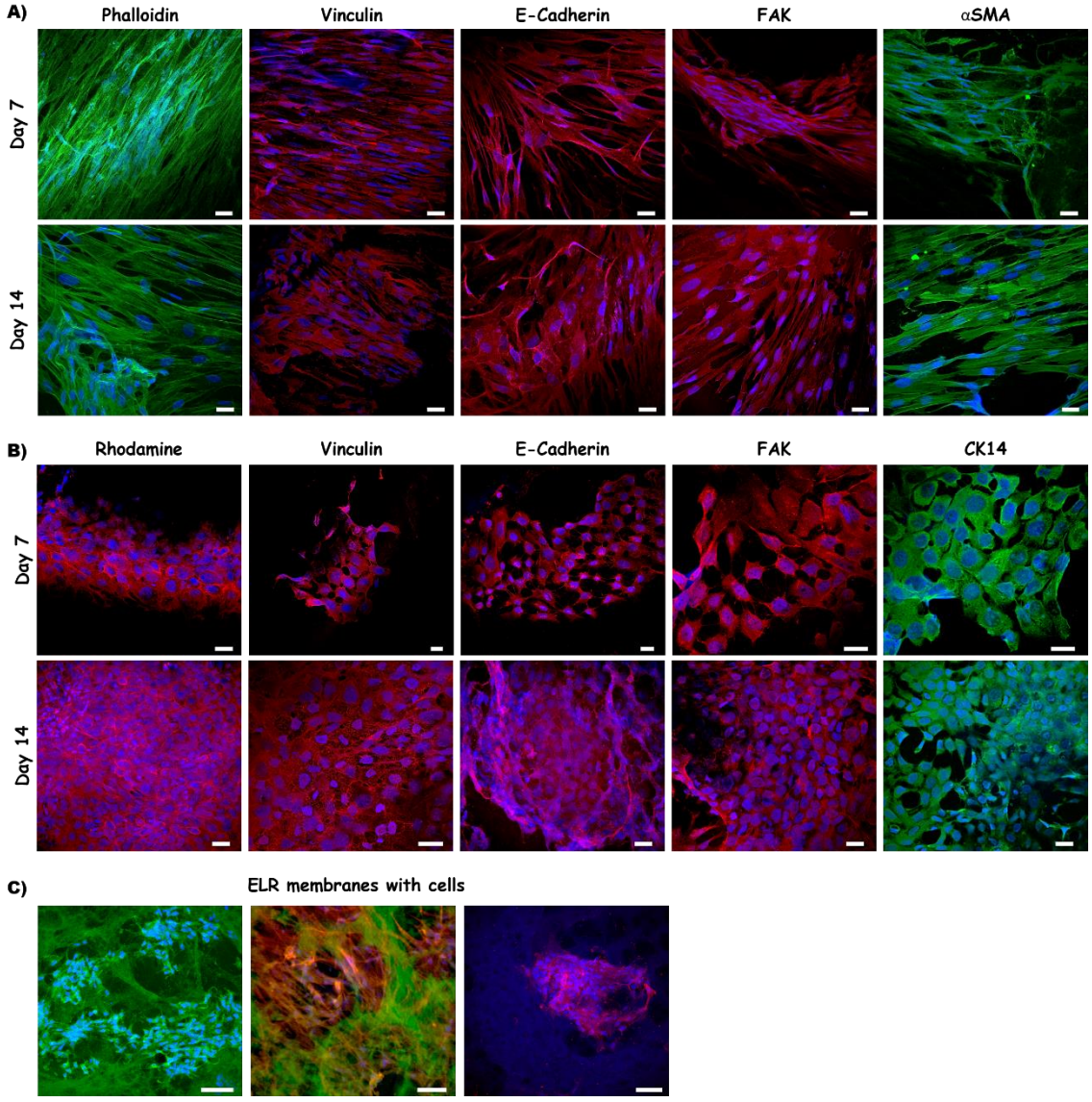

Figure 43: ***Immunofluorescence staining of fibroblasts and keratinocytes on an elastin-based membrane for 7 and 14 days. A)*** *Expression of multiple markers relevant for fibroblasts. Scale bar = 25 μm.* ***B)*** *Expression of multiple markers pertinent to keratinocytes. Scale bar = 25 μm,* ***C)*** *Examples of cell invasion inside*

membrane (in green and blue). The initial two images pertain to fibroblasts, whereas the final image corresponds to keratinocytes. Scale bar = 50 μm.

The morphology, extension, spatial arrangement, and cytoskeletal reorganization of HFF-1 and HaCaT cells were assessed *in vitro* following cell adhesion. This was achieved by staining the cytoskeletal actin and cell nucleus specifically after a 7- and 14-day of the culture period, as illustrated in Figure 43. On the seventh day of the culture period, both HFF-1 and HaCaT cells exhibited an elongated, fibrous shape on the surface of the membranes, distributed in cell islands. Over time, they were observed to gradually infiltrate the scaffold. Following 14-day culture period, the cells had colonised the majority of the material. The cells possessed distinct, regular nuclei and exhibited a longitudinal profile with cytoplasmic extensions that formed junctions with adjacent cells, thereby creating aggregates along the scaffold. Therefore, cells grown on the membrane exhibited remarkable adhesion and established a complex three-dimensional structure with widely spread cells. Based on the findings, it can be concluded that the scaffold facilitates the delivery of nutrients and provides support for cells, both internally and externally.

Furthermore, the invasion of cells into the membrane can be observed using the green autofluorescence of the elastin-based materials, as demonstrated by the examples depicted in Figure 43C. In order to optimize the visualization of cells, dyes in the red field have been given priority due to the autofluorescence of the membranes.

Finally, markers specific to each cell type were employed to assess the extent of cell differentiation. For fibroblasts, the analysis of alpha smooth muscle actin (α-SMA) antibody expression was conducted, as illustrated in Figure 43A, which is a critical feature of the transformation of fibroblasts into myofibroblasts, which are responsible for wound repair. A considerable number of cells were observed to stain positively for α-SMA. Fibroblasts play a critical role in the wound healing process, particularly during the initial inflammatory phase after biomaterial implantation. The initial adhesion, subsequent spreading and proliferation, and growth of fibroblasts are essential for the wound healing. For the analysis of keratinocytes, the expression of cytokeratin 14 was examined, as illustrated in Figure 43B. Cytokeratins (CK) serve as cell markers in human stratified squamous epithelium and play an active role in the process of wound healing.

To complete the aforementioned study, cells were examined by real-time quantitative PCR, using probes to assess their capacity to express specific genes during proliferation on the surface of VKV-SKS membranes. The expression of the desired genes indicates the capacity of cells to adhere, proliferate, and migrate on the material, establishing new connections with neighbouring cells. The wound healing process is accompanied by the expression of various cytokines in epithelial cells, namely KRT14, KRT10 and VCL. Furthermore, the expression of several genes related to cell adhesion and proliferation was also investigated, including PTK2, CDH1 and ACTA2. In order to normalize gene expression data, the 18S ribosomal

RNA (RP18) was utilized as an endogenous control gene. Consequently, the relative gene abundance is expressed as $2^{(-\Delta Ct)}$, where $\Delta C_t = Ct_{gene} - Ct_{RP18}$.

The relative abundance of genes in fibroblast and keratinocyte cells is presented in Figure 44A and Figure 44B, respectively. The graphs illustrate the expression of genes in elastin membranes at various experimental times (1, 3, 7, 14, and 21 days), with data being normalized to an endogenous control, ribosomal protein RP18. Upon examination of the cellular expression profile of the membranes, it becomes evident that the KRT14 and CDH1 genes are the most abundant in keratinocytes, whereas the VCL gene is the most abundant in fibroblasts. Additionally, the VCL gene displays high levels of abundance in keratinocytes, with the KRT10 gene being minimally represented. Furthermore, the expression of the ACTA2 and PTK2 genes is observed in fibroblasts.

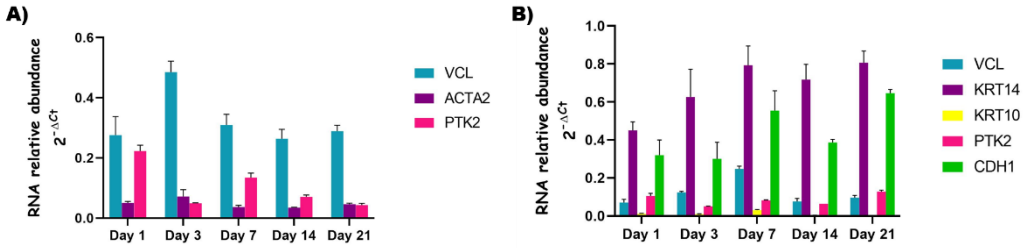

*Figure 44: **Gene expression in cells on the VKV-SKS membrane. A)** The expression of VCL, ACTA2 and PTK2 genes in fibroblasts (HFF-1) and **B)** VCL, KRT14, KRT10, PTK2 and CDH1 genes in keratinocytes (HaCaT) were quantified by qRT-PCR. The relative RNA expressions were normalized to RP18.*

Cytokines, in particular KRT14 and KRT10, act as markers expressed within epithelial cells to denote the differentiation status of keratinocytes. In addition to proliferation, differentiation is a crucial cellular function of keratinocytes in achieving and maintaining the integrity and homeostasis of epithelial tissue [522]. During the 21-day experiment, cultured keratinocytes on elastin membranes exhibited extensive expression of KRT14, indicative of basal keratinocytes characterised by continuous cell proliferation and renewal [523]. However, the expression of KRT10 is minimal and virtually absent after seven days of incubation. Keratin 10 expression is commonly observed in cells of the keratinized stratified epithelial layer, which indicates a withdrawal from the cell cycle. The findings are consistent with the use of the immortalized keratinocyte cell line (HaCaT), which is unable to differentiate into highly keratinized cells, unless factors are added to stimulate the process, such as the presence of Ca^{2+}, resulting in minimal KRT10 expression throughout the study period [524].

In cell culture, the majority of cells adhere to their underlying growth surface through focal contacts, which can be distinguished by the presence of the vinculin protein [525], [526]. Consequently, both fibroblasts and keratinocytes are able to bind to the ELR membrane, as the VCL gene is expressed in both cell types. Although the expression levels of the VCL gene in fibroblasts are slightly higher than those in keratinocytes, the levels remain constant throughout the incubation period, with the exception of day 3, which shows a slight increase. This indicates that the efficacy of cell adhesion is maintained throughout the incubation period [527].

Integrins constitute a family of extracellular matrix transmembrane receptors, which are present in cell adhesions. The α6β4 integrin is considered to be as specific to the epithelium and is responsible for the formation of tight adhesive junctions between cells and the basement membrane [528]. Focal adhesion kinase (FAK) has been identified as a crucial mediator of integrin-triggered intracellular signalling. Hence, the aggregation of FAK with integrins and cytoskeletal proteins in focal contacts is responsible for the activation and autophosphorylation of FAK by integrins in cell adhesion, thereby demonstrating the interaction between cells with surrounding substrates [529]. Consequently, the expression of the PTK2 gene is evident in both fibroblast and keratinocytes cells, with a higher abundance on the first day of incubation in both cases, followed by a slight reduction on the remaining days. This suggests that the cells are capable of adhering to elastin membranes.

The formation of cell-cell contacts is a fundamental process in the maintenance of epithelial cell structural integrity and the regulation of their adhesion, proliferation, and differentiation. The mature organization and function of epithelial tissues rely on the establishment of stable junctions between neighbouring cells, which are controlled by adherents and tight junctions where E-cadherin plays a crucial role as a main component [530]. The data revealed a slight increase in CDH1 gene expression in keratinocytes from day 7, which can be attributed to the elevated cell density, which in turn enhances the formation of stronger connections between adjacent cells.

Finally, the expression of α-actin was investigated, which performs a vital function in numerous cellular processes, including cell division, cell motility, and contractile force generation. The expression of smooth muscle α-actin (ACTA 2) is predominantly limited to smooth muscle cells, pericytes, and specialised fibroblasts, also referred to as myofibroblasts. α-SMA expression begins when fibroblasts differentiate into myofibroblasts, and acquire a contractile phenotype that enhances wound closure [531]. The findings indicate that the expression of ACTA2 is present in fibroblasts and remains relatively constant over time. This may be attributed to the possibility that some of the fibroblasts employed in this specific experiment may have undergone differentiation into myofibroblasts.

It can be inferred from representative immunofluorescence staining images and gene expression results of fibroblasts and keratinocytes that the membranes are non-toxic and promote normal cell adhesion, growth, proliferation, and metabolic activity by expressing various markers relevant to both cell types. In particular, focal cell-cell contacts have been identified through the vinculin protein and the VCL gene itself, where cell-cell interactions have been demonstrated, with good cell adhesion and proliferation of fibroblasts and keratinocytes. Furthermore, the interactions between the cells and the material were also confirmed through another molecule present in the focal adhesions, namely focal adhesion kinase (FAK), at both the immunostaining and PTK2 gene level. This demonstrated that the cells were adequately adhered to the VKV-SKS membranes. Finally, the degree of differentiation of both cell types was determined by studying the smooth muscle α-actin and its gene ACTA2 for fibroblasts, and cytokeratins as markers of the degree

of differentiation of epithelial cells, through cytokeratins 10 and 14 and their respective genes KRT10 and KRT14. It can be concluded that a small degree of differentiation from fibroblasts to myofibroblasts has occurred, which is responsible for generating the contractile force that favours wound closure. While keratinocytes express predominantly 14, indicating the presence of basal cells that are characterised by a continuous proliferation, this is thought to favour the renewal of damaged tissue.

3.1.3.4.- Cell migration

During the proliferative phase of wound healing, cells initiate the process of reproduction and migration towards the damaged area, with the objective of reconstructing the destroyed tissue. In the case of chronic wounds, cells at the injury site experience premature senescence as a result of unremitting inflammation and stress, thereby resulting in a reduction in migratory capacity and alterations to the microenvironment that affect nearby cells. The application of biomaterials in the healing process is essential, as they interact with biological systems and accelerate the healing process. Dressings provide structural support and facilitate cell adhesion and migration. Hence, the *in vitro* scratch assay and transwell migration assay are conducted to investigate the cell motility of fibroblasts and keratinocytes on elastin membranes, given that this plays a vital role in the re-epithelialisation of wounds.

The results of the transwell migration assay demonstrate that the membrane does not impede cell motility, as some cells can be observed in the well of the culture plate. Figure 45A (fibroblasts) and Figure 45B (keratinocytes) display representative images of cells that have migrated through both the elastin and transwell membranes and have been stained with crystal violet after fifteen days of culture. The results demonstrate that migrated cells are capable of proliferating within the fifteen-day culture period, with evidence of cell clusters, particularly in keratinocytes. Additionally, a schematic diagram in Figure 45C presents an objective overview of the experimental setup and cell flow in the transwell assay. Finally, Figure 45D illustrates the complete coverage of the insert using the elastin membrane for the experiment.

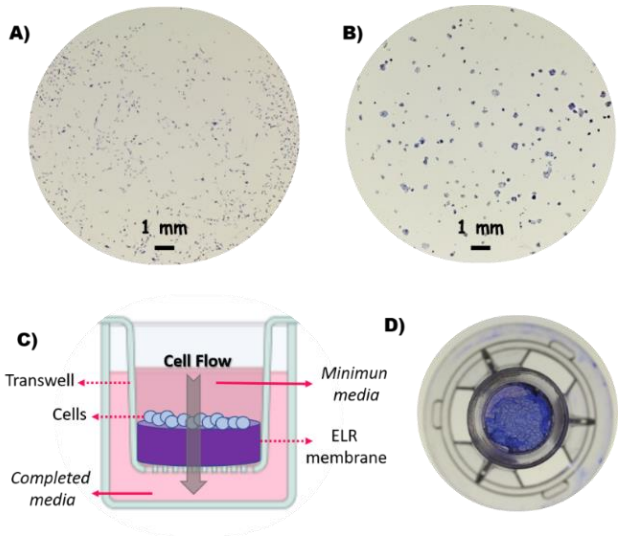

*Figure 45: **Transwell migration assay**. **A)** Representative image of HFF-1 cells migrating through the VKV-SKS membrane after fifteen days. **B)** Representative image of HaCaT cells migrating through the VKV-SKS membrane after fifteen days. The findings indicate that migrating cells have the ability to undergo proliferation during the fifteen-day incubation period, as evidenced by the formation of cell clusters. **C)** Diagram outlines the procedure for conducting the experiment. **D)** Real image of the transwell with an elastin membrane.*

In a previous examination of these membranes, it was demonstrated that certain molecules are capable of passing through them. To substantiate this, Gonzalez *et al* [436] performed diffusion studies in which ELR-based membranes were clamped between the donor and acceptor compartments of a Franz cell glass device. Phosphate-buffered saline (PBS) was added to the recipient compartment, and the donor compartment was filled with a fluorescent dextran solution of distinct molecular weights (4, 20, 40, 70, and 150 kDa). The outcomes indicated that the membranes were capable of diffusing the molecules and demonstrated that the concentration of the selected membrane affected the diffusion process.

Furthermore, in order to ascertain the efficacy of the membranes in facilitating *in vitro* cell migration, a second assay is conducted. This involves the creation of an artificial gap in a confluent cell monolayer, whereby cells located at the wound edge will begin to migrate until new cell-cell contacts are established, thus leading to the closure of the wound. The results of the *in vitro* scratch assay indicate that ELR membranes do not impede the movement of HaCaT cells. It is crucial to ensure that the gap sizes in all wells are consistently and homogeneously identical throughout the experiments, in order to reduce any potential variations caused by differences in scratch width and to improve the reproducibility of the results. The inserts were employed in accordance with the protocol outlined in Figure 46C. Figure 46D displays a real insert seeded with keratinocytes in both reservoirs, separated by a 500 µm gap.

In the conventional scratch experiment, phase contrast microscopes are utilised to observe the cells. Nevertheless, the use of these microscopes in this particular case is precluded due to the presence of opaque elastin membranes, which hinder the passage of light and, thereby restrict the visualisation of cells. Consequently, an alternative approach was employed to track cell migration, using non-toxic live cell staining via CellTracker™ Green CMFDA fluorescent probes. It is

imperative to ensure that the fluorescence intensity does not cause damage to the cells. Prolonged illumination of the same area for image acquisition can result in the production of sufficient heat to damages the cells. In order to protect the cells, it is advisable to reduce the light intensity or utilise a shutter that opens solely when the image is acquired. Figure 46A presents two images captured at the same location on the 24-well plate. The image on the left was captured using a phase contrast microscope, while the image on the right was captured using a fluorescence microscope. The image comparison reveals that the cells are not visible in the former due to the presence of the elastin membrane, whereas the latter exhibits clear cell observations.

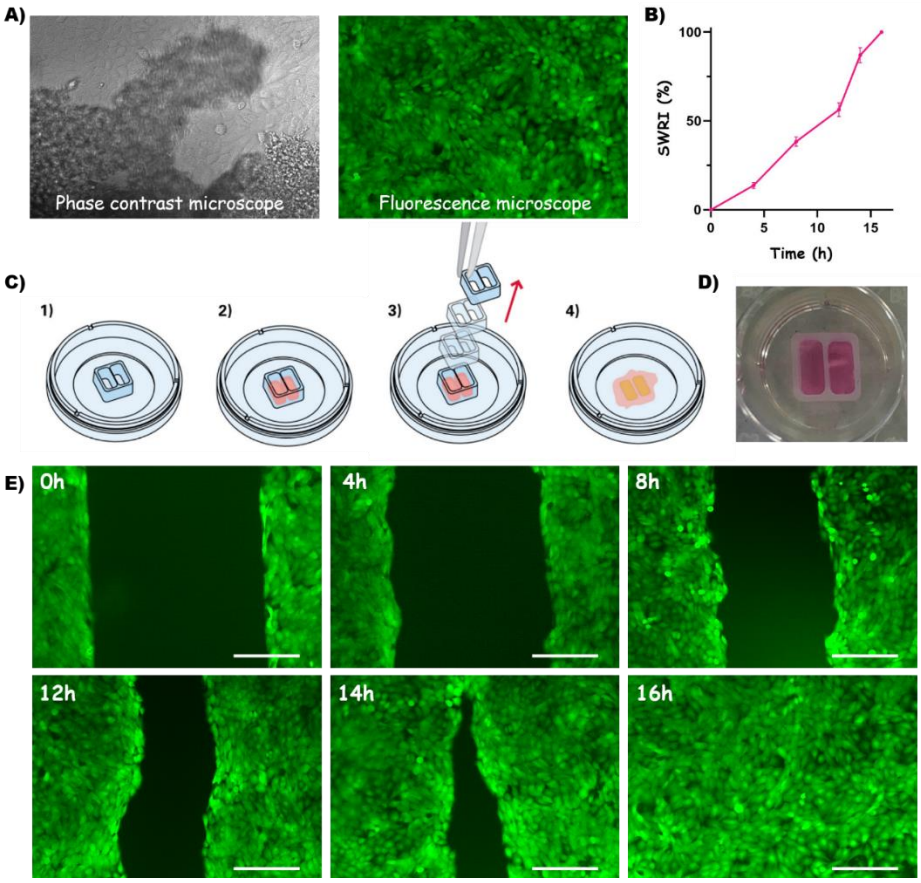

Figure 46: ***In vitro scratch wound assay on keratinocytes****.* ***A)*** *Two images were captured at the same location on a 24-well plate. The image on the left was captured using a phase contrast microscope, and it is notable that no cells are visible due to the presence of the elastin membrane. Conversely, the image on the right, obtained via fluorescence microscopy, displays clear cell observations.* ***B)*** *Quantitative analysis of the scratch wound recovery index (SWRI) widths at the indicated time points by measuring the area of the scratched region.* ***C)*** *A uniform gap size was achieved by employing a specific protocol involving the use of inserts.* ***D)*** *A real insert seeded with keratinocytes in both reservoirs, separated by a 500 µm gap.* ***E)*** *Representative photographs of the migration of serum-free keratinocytes in the presence of VKV-SKS membranes for wound closure at the indicated time points following the scratch. Scale bar = 200 µm.*

The observation of the change in the cell-free region over time is the primary measure of a migration assay, which is used to determine the rate of wound closure and cell migration. Figure 46E presents representative fluorescence images acquired with inverted microscopy of confluent cells forming an artificial wound at various time points until closure completion. To eliminate any potential interference caused by cell proliferation, the cells are maintained in a serum-free

environment. Consequently, the migration of cells from the edges of the gap to the centre can be monitored until the wound is completely closed and new cell-to-cell contacts are established. It is important to note that this experiment exclusively utilises keratinocytes, as they are crucial cells for effectively migrating over the ELR membrane and re-epithelializing chronic wounds [532], [533]. A quantitative analysis was conducted to evaluate the impact of migration on the scratch wound recovery index (%), as determined by fluorescent imaging. Figure 46B displays the results obtained, indicating a slower *in vitro* re-epithelialization rate during the initial hours after the wound scratch, which reaches approximately 50 % after 11 hours. Subsequently, the percentage of mobility increases gradually until it reaches a full recovery of 100 % after 16 hours.

The findings indicate that the VKV-SKS membrane, acting as a temporary scaffold, preserves cellular mobility *in vitro*. The implementation of these membranes in chronic wounds is anticipated to enhance the movement of cells in the senescent cell population with reduced mobility. The utilization of biomaterials will facilitate adhesion and subsequent mobility from the wound margins towards the injured site, thus promoting re-epithelialization of the wounds.

3.1.4.- Human skin wound healing of ELR membranes

3.1.4.1.- Assessment of wound regeneration capacity of ELR membranes using a human *ex vivo* wound culture model

Chronic non-healing wounds represent a significant unmet clinical need, with preclinical models inadequately predicting the clinical effectiveness of novel therapies. The most commonly employed model for studying wound repair is that of acute wounds in mice. Despite the general similarities observed between mouse and human healing, interspecies differences in skin structure and healing dynamics persist. Thus, rodent skin is distinct in that it possesses a layer of subcutaneous muscle (panniculus carnosus), which causes rapid wound contraction following injury. In contrast, in humans, wounds heal through re-epithelialisation and granulation tissue formation [468]. This discrepancy between species makes it challenging to extrapolate *in vivo* rodent wound research to clinical settings, and thus, there has been a growing emphasis on the development of *ex vivo* human models with broad applicability and translatability [534], [535]. Consequently, the *ex vivo* model provides significant advantages by incorporating all skin cell types, maintains the native architecture of skin, and ensures the basement membrane, Langerhans cells, pigment cells, and nerve endings remain intact [466]. Nevertheless, the differentiation of keratinocytes and the epidermis-dermis junction remain inadequately characterised in this model [466]. Additionally, it is essential for this model to replicate the processes of wound healing in humans. This

should include a re-epithelialisation procedure that is comparable to the re-epithelialisation observed *in vivo* in human skin, where keratinocytes migrate, proliferate and differentiate from the wound margin to cover the complete wound region [536]. Moreover, the model exhibits gene expression patterns comparable to those observed in *in vivo* models, thereby enhancing the potential for translating *ex vivo* data to clinical applications [537]. Finally, an additional significant benefit is that a considerable number of wounds can be obtained from a single donor, thus reducing experimental variability. In conclusion, the *ex vivo* human skin culture model represents a valuable tool for investigating and comprehending the fundamental mechanisms of human wound healing, identifying potential wound-healing agents to devise novel strategies for wound healing [536], and assessing the efficacy of potential new treatments to enhance the healing process [538]–[540].

As previously mentioned, chronic wounds do not heal in a typical process; therefore, biomaterials can facilitate the healing process. In humans, re-epithelialisation and granulation tissue formation play a significant role in wound healing, and *ex vivo* human skin models are a suitable starting point for testing elastin-based biomaterials in these processes. In order to conduct these experiments, surplus skin from arm reduction surgeries (brachioplasty) is utilised. Punch biopsies are used to create small 2-mm partial-thickness excisional wounds on healthy donor skin, penetrating to the level of the papillary dermis. Subsequently, the excised skin is maintained viable at the air-liquid interface. Biomaterials are placed over the wound to investigate complete healing by epithelialisation, whereby progress is evaluated through fluorescence and histology between days 0 and 6. One of the key advantages of this methodology over *in vitro* studies is that skin explants utilise primary human cells that are derived directly from living human tissue. In contrast, *in vitro* studies employ immortalised lines that do not accurately reflect the environment of real human tissue. Consequently, the *ex vivo* technique more closely resembles the living conditions of human skin.

To track the real-time healing progression of wounds, a macroscopic evaluation was conducted employing a non-invasive fluorescent dye (CMFDA), which is absorbed by viable cells in culture to trace the epidermal cell lineage [541]. In addition, dye absorption can be easily visualised using an upright fluorescent microscope. Tissue-native molecules emitting fluorescence upon light excitation can also indicate cellular activity and protein structure [536].

Figure 47A presents representative fluorescent images for the longitudinal monitoring of *ex vivo* wounds over the period of six days. The images demonstrate the daily changes in re-epithelialization, demonstrating the presence of the epidermis, dermis and migrating epithelium in the wound bed. This evidence suggests that *ex vivo* human wound repair employs an extended shield mechanism of collective migration. A comprehensive interpretation of these images is presented in the chapter of methodology. This technique distinguishes the neoepidermis and areas of open wound and surrounding unwounded tissue. The resulting images produced with cellular tracking allow for the qualitative assessment of tissue characteristics and pathology, as well as quantitative measurements such as wound

re-epithelialization, tissue contraction, and epidermal maturation being able to identify alterations in healing.

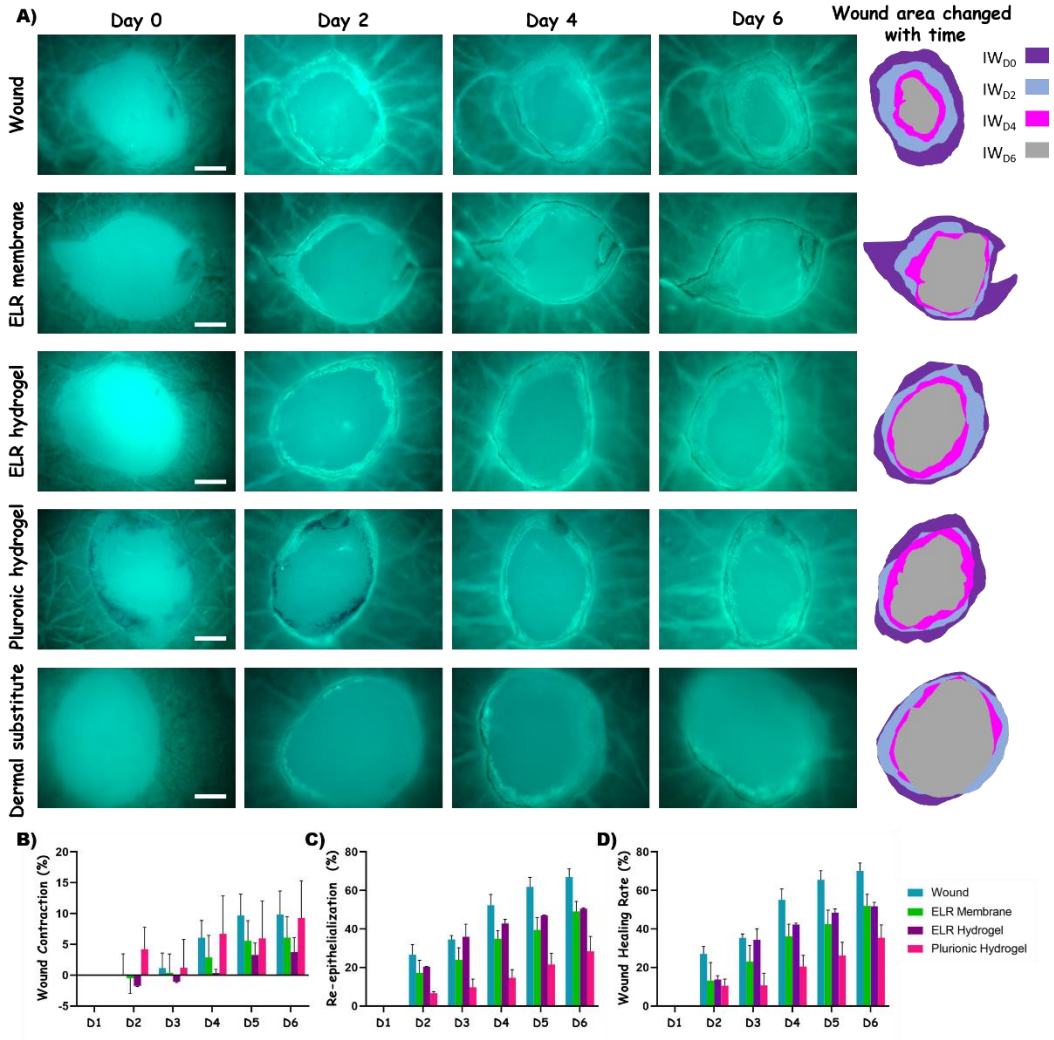

Figure 47: ***Fluorescent images of wound healing ex vivo****.* ***A)*** *Daily fluorescent imaging was used to monitor the epithelial migration of ex vivo wounds over the period of six days following the injury. The size and shape of the initial wound, as well as the progression of the migrating epithelium, were observed at various time points in the same wound for different experimental samples, including an ELR membrane, an ELR hydrogel, a Pluronic hydrogel, an Integra dermal substitute and an uncovered wound. Scale bar = 500 µm. A figure in the right panel displays the changes in wound area over time, indicating the degree of re-epithelialisation following injury.* ***B)*** *Quantification of wound contraction (%). A slight contraction was observed in the wounds in culture after six days.* ***C)*** *Quantification of the area of re-epithelialization (%).* ***D)*** *Wound healing rate (%).*

One advantage of *ex vivo in situ* wound assessment is that it is non-invasive, thereby eliminating any detrimental effects and therefore obviating the need to waste skin tissue in order to collect data. Consequently, this methodology permits the longitudinal acquisition of visual data on the same wound over several time points, thereby reducing variability by studying the entire wound evolution on the same sample. Thus, Figure 47A illustrates the initial wound size and shape, as well as the progression of the migrating epithelium at various time points in the same wound for different experimental samples, including an ELR membrane, an ELR hydrogel, a Pluronic hydrogel, an Integra® dermal substitute, and an uncovered wound. With regard to the ELR materials, the objective is to ascertain whether the structure and thickness of the scaffold influence the regeneration process. The ELR

membrane is thinner than a slightly thicker ELR hydrogel, which would presumably facilitate cell proliferation and nutrient diffusion due to its thinner nature. In addition, Pluronic hydrogel and Integra® dermal substitute are employed as positive controls, as they are materials that are routinely used in clinical wound healing. The Integra® dermal substitute is an artificial skin graft comprising a high concentration of collagen, bound with chondroitin-6-sulphate. The Pluronic hydrogel is a triblock copolymer comprising hydrophilic groups (PEO) and hydrophobic groups (PPO), which present a temperature-dependent behaviour. Daily imaging revealed the presence of clearly defined areas of epidermal restoration, with a faint CMFDA expression band visible towards the epidermal front with brighter regions closer to the margin, indicating longer-lived cells that have been previously labelled several times, while the darker regions indicated newly formed tissue [463], [542]. Hence, through this technique, the epidermis and dermis were identifiable in every *ex vivo* wound analysed, regardless of the degree of wound closure. Furthermore, Figure 47A presents a graph that depicts the variation in wound area over time, measuring the extent of re-epithelialisation following injury. The graph illustrates a reduction in the wound area as keratinocyte cells cover the exposed dermis. Furthermore, it has been discovered that the process of wound healing is not uniform across the various regions of a single wound. In fact, certain areas exhibit a significant inward migration. The underlying cause of this phenomenon can be attributed to the disparities in the microenvironment of the wound bed at the cellular level [542].

In all cases, it is evident that the wound area decreases gradually over time as a result of the re-epithelialisation process. However, after six days of the experiment, the wound did not close entirely. As indicated in the literature, the excisional wound of healthy human skin without biomaterial should close entirely between days three and five after injury [466]. Fluorescent staining must be conducted every day to obtain images, which necessitates the samples being outside the incubator. This delay may impede the healing process. The rate of epithelialisation of *ex vivo* samples is slower than that of healthy *in vivo* skin, as evidenced by literature. Furthermore, the duration of the cultured skin experiment was constrained by the limited lifespan of the skin samples. Following six days, the capacity of keratinocyte to proliferate in response to injury is reduced, and cell apoptosis may occur, making it challenging to correlate with *in vivo* behaviour [466].

Upon examination of the images, it is evident that the edge of the wound cannot be observed when treated with Integra® dermal substitute, as the biomaterial is of considerable thickness, so when placed on the wound, the material protrudes from the top and reflects the light, as illustrated in Figure 47A. For this reason, this material has been excluded from the subsequent quantitative analyses, as it is not possible to measure the requisite values from the image. This technique is not suitable for this biomaterial.

The measurements of the explants every day display that the wound experiences some contraction over time, as demonstrated in Figure 47B. Fluorescence images indicate that the outer edge of the wound is not always

constant, undergoing periodic changes. Following the wound, there may be a slight initial increase, which is particularly noticeable with the ELR hydrogel. However, over time, a shrinkage process typically occurs, which can reach up to 10 % after 6 days of treatment with the Pluronic hydrogel or in the wound alone without biomaterials. It has been observed that the utilization of elastin materials, including both hydrogels and membranes, significantly reduces the phenomenon of contraction. This indicates that the use of these biomaterials facilitates healing without causing contraction, which is the main cause of visible scars. This is a problem particularly relevant in the context of severe burns.

Re-epithelialization is a crucial process in the healing of wounds, as it delineates the reconstruction of the stratified squamous epithelium. It is therefore used as a criterion for defining success, with the absence of re-epithelialization precluding the classification of wound as healed. Moreover, epithelialization is affected in all types of chronic wounds [536]. Figure 47C therefore evaluates the wound re-epithelialization process. In partial-thickness epidermal wounds, re-epithelialisation arises predominantly at the wound edges from viable epidermal cells that undergo behavioural changes, such as cell migration, proliferation and keratinocyte differentiation at the wound margins [543]. Both elastin membranes and hydrogels demonstrate superior re-epithelialisation compared to the Pluronic hydrogel, which is frequently utilised in hospitals for burn wounds. The *ex vivo* samples were obtained from healthy patients, and the wound without materials progressed rapidly, resulting in the quickest case. It would be of interest to conduct experiments using skin explants derived from diabetic or burn patients, who face a pronounced hurdle in wound closure rate. Such experiments would provide a reliable assessment of the efficacy of employing biomaterials in wound management. However, obtaining these samples is challenging due to the potential for biopsies of chronic wounds to impede healing [463].

The quantification of the epithelial closure rate during the process of skin wound healing can be illustrated in Figure 47D. To measure this rate, the outer edge of the wound on the initial day is compared to the edge of the newly formed epithelium in subsequent days. The results resemble those of re-epithelialisation, where the wound healing process of elastin materials is more effective than that of the commonly used commercial Pluronic hydrogel in hospitals.

Comparisons are made between assessments of wound spaces observed in fluorescence and histological images, as presented in Figure 48A, in order to gain insight into their relationship. The fluorescence images display similar identifying features of traditional histological techniques, such as the initial wound edges and the migrating epithelial tongue. The epithelial tongue that migrates is composed of a uniform layer composition of keratinocytes, typically one or two layers of cells. It extends without any disruptions from the wound edge, positioned parallel to the more disorganized dermis. Figure 48A presents a fluorescence image on the left and an H&E histology image of a wound at the same experimental stage (3 days) on the right. The use of different coloured arrows serves to indicate the same areas in both types of images. The white arrows indicate undamaged normal epithelium within

the wound with a typical skin structure. The black arrows reveal the presence of activated cells in the adjacent epithelium, which are proliferative and facilitate wound closure. Finally, the purple arrows illustrate the epithelial tongue, which comprises the cells responsible for wound closure.

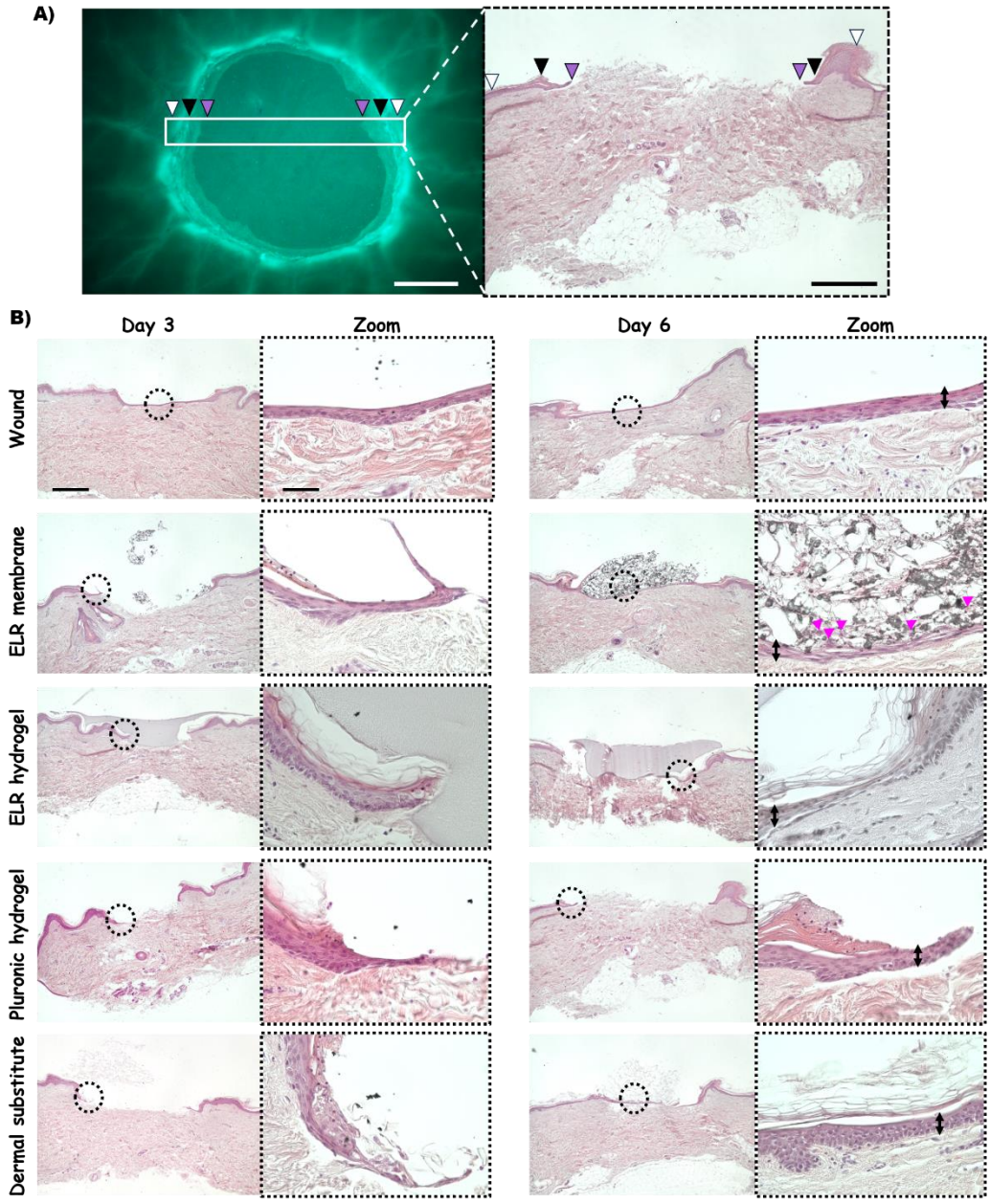

Figure 48: ***H&E images of ex vivo wound healing process. A)*** *A comparison between fluorescence and histological quantification methods on day 3. The white arrows indicate undamaged normal epithelium within the wound with typical skin structure. The black arrows identify activated cells in the adjacent epithelium that are proliferative and support of wound closure. Additionally, the purple arrows indicate the epithelial tongue, which consists of cells responsible for wound growth and closure. Scale bar = 500 µm.* ***B)*** *Representative images of ex vivo human wounds at 3- and 6-days post-injury, stained using H&E method, display the epidermis and dermis following biopsy. Epithelial migration at different time points was observed for several experimental samples, including an ELR membrane, an ELR hydrogel, a Pluronic hydrogel, an Integra® dermal substitute, and an untreated wound. Samples collected on day 4 demonstrate the presence of an epithelial tongue migrating beneath the wound scab, accompanied by a thick proliferative epithelium consisting of proliferating epithelial cells. Conversely, samples collected on day 6 reveal the presence of a thick layer of epithelial cells covering the wound in the repaired epidermis. Scale bar standard image (4X) = 500 µm. Scale bar zoomed image (40X) = 50 µm.*

For the purposes of data collection, tissue sacrifice for histological analysis is required at selected experimental times, specifically days 3 and 6. Hence, tissue samples were acquired for morphological analysis by haematoxylin and eosin staining at the characteristic wounding times of day 3 and day 6 in order to examine epithelialisation. Figure 48B illustrates the epidermis, dermis, and epidermal tongue observed in these images. From these frontal images of wounds, a plenty of quantitative data can be extracted, including the level of re-epithelialisation, which can be identified by measuring the distance between the wound margins and the number of cell layers in the newly formed tissue. Moreover, comparisons of the morphology and size of newly formed cells can be performed.

In partial-thickness excisional epidermal wounds, epithelial cells enter a proliferation stage and undergo cell migration as early as days 3 to 4 post-injury. Viable epidermal cells at the wound edge exhibit behavioural transformations, including migration, proliferation and keratinocyte differentiation. The initial event, migration, involves the movement of suprabasal cells, which is then succeeded by a mitotic process. Upon the closure of the wound, epithelial cells cease migration and proliferation due to contact inhibition. The process of differentiation of the newly formed epidermis commences shortly after the migrating tips, preceding the completion of wound re-epithelialization. This process results in the formation of epidermal layers and the consolidation of a new epithelial barrier [543].

The wound healing process can be categorised into three distinct phases: the latent phase (early phase), the proliferative phase, and the remodelling phase. Although various cell types work together in an organised manner to orchestrate the healing process, it is the re-epithelialisation process that provides the protective barrier to the wound. The timeline commences on the day of the injury. The size of the wound has a direct impact on the duration of each stage of the healing timeline. The Figure 48B demonstrates the wound area (day 3) and the surface area of the re-epithelialized wound (day 6) in both standard (4X magnification) and zoomed (40X magnification) images. The images illustrate that on the third day, the wound without biomaterials has completely closed. In the other samples, re-epithelialisation is becoming apparent as neoformed epidermis migrates over granulation tissue of the open wound, carrying proliferative cells that can close the wound. Nevertheless, a gap persists between the two edges of the wound. After six days of incubation, all samples, with the exception of the Pluronic hydrogel, achieved full wound closure, thereby completing the process of re-epithelialisation. Furthermore, the regenerated epidermis was indistinguishable from the surrounding uninjured tissue. Morphologically, the keratinocytes in samples with elastin biomaterials displayed no significant differences compared to fresh human skin. The number of cell layers that are able to form is a crucial aspect of the wound healing process, indicating keratinocyte proliferation. The cell layers are displayed in Figure 48B, with black arrows indicating their respective positions. After a period of six days of culturing, keratinocyte layers between four and five cells thick were observed in the wound that had not received any biomaterial. Similarly, the wounds that were treated with the ELR membrane and ELR hydrogel showed the presence of these layers, indicating the involvement of proliferation and migration in the

wound closure process. On the other hand, the Pluronic hydrogel resulted in the formation of three to four layers of cells, which was comparable to the dermal substitute. As illustrated in Figure 48B with pink arrows, it is evident that keratinocyte infiltration occurs within the elastin membrane. This is particularly important in chronic wounds that do not heal spontaneously and necessitate the use of biomaterials. The elastin membranes promote the adhesion, proliferation, and migration of keratinocytes, thereby aiding in the complete closure of the wound and potentially reducing the visible scarring resulting from certain types of wounds.

As previously stated, the fluorescence images indicate that the wound remained incompletely healed throughout the six-day period following injury. Conversely, the H&E images demonstrate re-epithelialisation of all samples, with the exception of the Pluronic hydrogel. This finding is consistent with the literature, which indicates that healthy human skin wounds should fully close within 3-5 days. The prolonged period of time required for samples to be kept outside of the incubator for fluorescent imaging may result in a delay in the normal healing process. In contrast, the samples used for histology remain within the incubator and exhibit normal healing. Consequently, the H&E staining technique provides more accurate results that more closely reflect the actual healing process. However, fluorescence images offer a comprehensive daily evaluation of the wound, while histological images only offer a brief picture showcasing the wound, which may vary slightly contingent on the wound region being evaluated.

The results demonstrate that the *ex vivo* model provides significant advantages by incorporating a realistic environment of natural skin architecture. Furthermore, it is crucial for this model accurately replicates the features of wound healing in humans in order to demonstrate a re-epithelialisation procedure that is comparable to that observed in wound re-epithelialisation in skin *in vivo*. In this process, keratinocytes migrate, proliferate and differentiate from the wound margin, gradually covering the entire wound region. The rate of epithelialization is slower for all biomaterials than that of healthy skin *in vivo* [536]. Nevertheless, these ELR membranes are employed when a critical defect or non-healing wound necessitates the use of a biomaterial to stimulate cell regeneration, which is not the case when the skin is healthy and capable of healing independently [544], [545].

Furthermore, it has been demonstrated that the elastin membranes exhibit adequate elasticity, allowing them to adapt to the dynamics of the wound environment without suffering initial degradation. This is due to the fact that the elastin membranes are a more elastic material than those used as controls, namely the Pluronic hydrogel and the Integra® dermal substitute. This property, in conjunction with the favourable porosity of the scaffold, contributes to the biocompatibility of the membranes, which exhibit good migration and proliferation of keratinocytes. This phenomenon is facilitated by the adequate diffusion of nutrients and gases. Furthermore, it is observed that the cells are able to grow within the elastin membrane, since it presents the RGD cell adhesion sequences that favour cell infiltration. Another crucial factor in this experiment is the thickness of the materials employed. Both the hydrogels (ELR and Pluronic) and the Integra®

dermal substitute have a thickness greater than that of the elastin membranes, rendering this thinner thickness highly suitable for skin regeneration. This is because the cells can proliferate more easily, and the diffusion of nutrients is also favoured. Furthermore, although the natural process of skin healing involves re-epithelialisation, a minor degree of contraction can be observed due to the presence of myofibroblasts, which possess contractile properties that facilitate the approximation of wound edges. The findings indicate that elastin materials significantly reduce excessive wound contraction, exhibiting notable improvements in comparison to Pluronic hydrogels and the Integra® dermal substitute. This suggests that the utilisation of these biomaterials facilitates healing without inducing contraction, which is the predominant factor contributing to the formation of visible scars.

These characteristics render ELR membranes a highly promising option as dressings for the treatment of chronic wounds, offering a solution that could improve the speed and quality of healing. The combination of mechanical strength, elasticity, and biocompatibility suggests that they have potential for use in clinical applications for the regeneration of complex and difficult-to-treat wounds. Nevertheless, it is important to note that this *ex vivo* human skin culture model is subject to inherent limitations. Further testing of elastin-based biomaterials *in vivo* is necessary to observe their toxicity and assess their effect on the wound healing process in living animals.

3.1.5.- *In vivo* behaviour of ELR membranes

3.1.5.1.- Assessment of *in vivo* biocompatibility and long-term stability of ELR membranes via subcutaneous implantation

It is crucial to conduct biological evaluations of materials that come into contact with tissues and fluids through animal implantation. In addition to non-toxicity, the material must also meet functional requirements whilst eliciting the appropriate host response, a property referred to as biocompatibility [546]. Moreover, achieving a balance between neotissue formation and scaffold biodegradation remains a significant challenge in biomedical applications, with controlling the biodegradation rate of biological surrogates [547], [548]. It is therefore important to determine the degree of biocompatibility of biomaterials, particularly their propensity to induce innate immunity, inflammation, fibrosis, and foreign body response. Furthermore, a comprehensive preliminary investigation of *in vivo* cytotoxicity, cell survival, cell infiltration, and degradability of these biomaterials is required. Such inquiries are crucial for the optimal utilisation of these materials in the biomedical field.

A multitude of previous studies have corroborated the *in vivo* biocompatibility of ELRs, demonstrating that they have no influence on cytotoxicity

or inflammatory response following subcutaneous placement, and remain stable over time [549], [550]. In order to assess the biocompatibility, stability, cell invasion of the support, as well as the degradation rate and neovascularisation potential of the VKV-SKS membranes, they were implanted subcutaneously in the dorsal area of Swiss mice. The 3R principle was followed to minimize the number of experimental animals and all experimental procedures were approved by the Ethical Committee on Animal Care and Use of the University of Valladolid, in accordance with the European Union Directive 2010/63/EU and the Spanish Royal Decree RD 53/2013. In addition to the membranes, the VKV-SKS hydrogels and commercial Integra® dermal substitute were also included. A comparison was made between the elastin membrane and hydrogel, with Integra® serving as a control, which is routinely utilized in hospitals for skin issues. The sterile ELR membranes and dermal substitute were implanted subcutaneously in the dorsal area by creating a small subcutaneous pouch using a sterile surgical scalpel, into which the scaffolds were carefully placed while the hydrogels were subcutaneously injected. The experimental times selected for analysis were 1, 3 and 7 weeks, with the objective of evaluating the biocompatibility of the material and the long-term stability of the scaffold histologically.

Figure 49A illustrates the macroscopic appearance of the implant materials and surrounding tissue seven weeks post-operation. A solid material is present at all post-operative stages (1, 3 and 7 weeks), and a slight reduction in the dimensions of the implanted materials is discernible, particularly observed in the ELR hydrogels following seven weeks. The materials exhibited complete integration into the tissue, as evidenced by slight adhesion to the hypodermis in all mice across each group and time point. This highlights the excellent stability of the materials upon subcutaneous implantation *in vivo*, which correlates with the previously obtained *in vitro* [433], [551]. Furthermore, there is no evidence of inflammation or fibrotic tissue in the implantation area, indicating non-toxicity in the surrounding tissue. The elastin scaffolds, comprising both membrane and hydrogel, exhibit the formation of functional blood vessels, whereas the dermal substitutes do not present the same outcome.

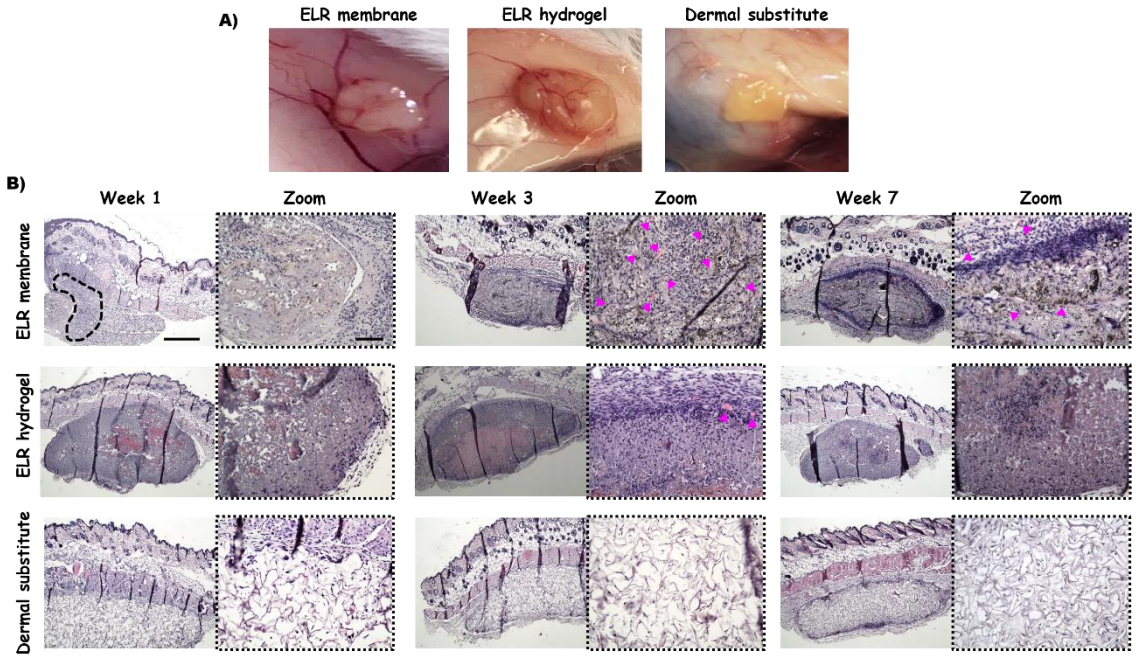

Figure 49: ***In vivo biocompatibility of ELR subcutaneously implanted in mice. A)*** *Representative images of the materials implanted in mice subcutaneously seven weeks after operation.* ***B)*** *Representative H&E staining images of ELR-membrane, ELR hydrogel and Integra® dermal substitute at 1-, 3- and 7-weeks post-injury. Columns correspond to different time points, while rows indicate different materials. The pinks arrows identify newly formed capillaries and the dashed circle indicates the granulomatous inflammatory reaction in the samples of elastin membrane. Scale bar standard image (5X) = 500 µm. Scale bar zoomed image (20X) = 100 µm.*

In order to gain a better understanding of the cellular behaviour of the ELR membrane, histological staining using H&E was conducted. Figure 49B displays cross-sectional images of the elastin membranes, elastin hydrogels, and Integra® dermal substitute at varying magnifications (5X and 20X) over three experimental intervals (1, 3 and 7 weeks). The H&E staining provides a detailed analysis of the cell types present in the implant and their morphology. The cells appear blue-violet in hue, while the materials exhibit a slightly greyish tone, which facilitates their identification, in contrast to the surrounding pinkish muscle fibres.

From the first week following surgery, it is noticeable that all materials are fully integrated into the tissue, as they adhere to the hypodermis of the mice. A small number of cell nuclei have begun an initial cellular infiltration within the scaffold area. It has been observed that cells of the animal invade the material by starting from the edge in contact with the tissue, where there is a higher predominance of cells in the first week. Subsequently, cells gradually colonise the interior of the material, where cell density is higher, after several weeks. The integration of the material into the surrounding host tissue is particularly evident in the case of elastin-based materials, while it is somewhat lower in Integra® due to the fact that fewer cells are observed inside the scaffold. This indicates that the elastin materials are highly compatible with the surrounding tissue, as evidenced by the infiltration of various cell types within the material after seven weeks of implantation, with differences become more evident in the enlarged images from weeks 3 and 7, as shown in Figure 49B. The presence of cell adhesion domains (RGD) in the elastin membrane and hydrogel, due to the SKS polymer which contains this sequence is

likely to enhanced cell colonisation. Consequently, it encourages the recruitment of cells from surrounding tissue to infiltrate the material, thereby facilitating the regeneration of injured tissue by accelerating the rate of cell migration. The histological examination revealed a higher cellular density in the ELR membrane compared to the hydrogels and dermal substitute. The thinness of the elastin membrane may facilitate the migration of cells through it and their complete colonisation of the structure due to the suitability of the pore size of the structure. The pore size, porosity and elasticity of the materials regulate cell behaviour and tissue remodelling *in vivo*. Furthermore, the volume of the material structure determines the time required for cells to colonise the construct [552].

The images demonstrate the structural integrity of scaffolds, which remain stable with a reduction in size visible after seven weeks. This can be attributed to the longevity of protein polymers (VKV and SKS) with no degradation sequences, which allows for the extended preservation of scaffold integrity. Similar results have been observed in other elastin materials employed in diverse [307], [435], [553], [554]. As these materials degrade slowly, an increasing number of cells accumulate in the border region of the structure. This process of cell infiltration occurs simultaneously with the degradation of the biomaterial. The existing literature highlights the importance of materials used in regenerative medicine to degrade slowly. This is of particular importance in the context of wound dressings, which must remain stable for a minimum of three weeks (21 days) to facilitate the gradual replacement of damaged tissue with newly formed healthy tissue [516]. The results obtained clearly demonstrate that the developed ELR membranes show good long-term *in vivo* stability, thus fulfilling this requirement. The initial cells that infiltrate the tissue not only release cytokines to stimulate the recruitment of more cells, but also secrete proteases that degrade the matrix and enhance cell penetration. As this degradation proceeds, an increasing number of cells infiltrate the scaffolds, accelerating their deterioration and simultaneously restoring damaged tissue.

Upon close examination of the H&E-stained elastin samples reveals that the newly formed capillaries are distributed uniformly, as depicted in Figure 49B with pink arrows. An increased vascularisation is observed within the elastin membranes, with the formation of more pink blood cells forming vessel-like structures. This indicates a compatible interaction between the organism and the membranes. Conversely, these formations are not observed in the Integra® samples. This does not imply that they cannot form vessels, but rather it suggests that they may require additional time for the full colonisation and organisation of the endothelial cells [555]. Consequently, the incorporation of elastin into tissue regeneration scaffolds promotes wound angiogenesis, leading to the formation of abundant neovascularisation. The microstructural evaluation thus corresponds favourably with the macroscopic analysis, which reveals the presence of vascular structures within the materials.

A histological assessment of the different structures, conducted one week post subcutaneous implantation *in vivo* and stained with haematoxylin-eosin, revealed the presence of a certain degree of granulomatous inflammatory reaction,

as illustrated in Figure 49B. This reaction was clearly observed in the samples of elastin membrane, as indicated by the dashed circle. It is evident that inflammatory cells play a pivotal role in the biodegradation process of biomaterials, as they are the initial colonisers of the surface of material following implantation [556] and they possess mechanisms that help reduce the pH of the microenvironment [557]. Inflammatory cells have been shown to play a significant role in the restoration of vascular networks through the ECM reconstruction, endothelial cell fusion, and increased collagen synthesis. Macrophages and fibroblasts have been observed to degrade scaffold networks and generate type I collagen, thereby leading to the gradual replacement of the construct with regenerated tissue [558]. Samples taken seven weeks after implantation demonstrate that the biomaterials do not induce a cellular immune response, as there is an absence of macrophages or giant cells within or around them. Furthermore, histological analysis revealed the presence of a thin layer of connective tissue surrounding the structures, which is interpreted as a non-harmful reaction whereby the materials interact with the cells in a biocompatible way, rather than resulting in encapsulation or fibrosis due to a foreign body response. As anticipated, the Integra® dermal substitute, which is commonly used in clinical settings, did not exhibit toxicity in the sample, as no macrophages were observed. The scaffold also demonstrated stability over time, although there appeared to be less cellular infiltration within the scaffold after seven weeks. Inflammation is a physiological response of the body to damage. The presence of macrophages is necessary and beneficial in the early stages of healing. However, if this situation persists over time, the wound will not progress to the subsequent stage of the healing process, as it will prevent proliferation and become chronic. Macrophages initially exhibit an M1 phenotype, which enables them to act as microbicides and facilitate cell migration. Subsequently, they adopt an anti-inflammatory M2 phenotype, which promotes neovascularisation, re-epithelialisation and fibroblast migration. Consequently, persistent hyperinflammation represents a defining feature of chronic wounds, with macrophage malfunction serving as a significant contributing factor [152], [153].

Based on the outcomes, it can be concluded that neither of these substances is toxic since all the mice used in this experiment survived without any abnormal behaviour, such as dull, bristly fur or pain. Furthermore, *in vivo* subcutaneous implantation experiments in mice demonstrate the *in vivo* stability over time and excellent biocompatibility of both elastin membranes and elastin hydrogels as they do not elicit cytotoxicity or an aggressive inflammatory response after subcutaneous placement. Additionally, the appropriate porosity of the scaffolds facilitates optimal cell invasion without a foreign body reaction and superior neovascularisation in comparison to Integra®, a commercially available dermal substitute that is routinely administered in hospitals. The presence of RGD cell adhesion sequences also contributes to the enhanced cell adhesion observed, in conjunction with the inherent properties of the elastin, including adequate mechanical properties and excellent biocompatibility. In addition, the thinner elastin membranes facilitate cell proliferation against elastin hydrogels, and also enhance the diffusion of nutrients and gases. Nevertheless, while cell invasion and degradation of the synthetic matrix

are important for tissue regeneration, they cannot guarantee sufficient repair. Consequently, we will perform specific experiments on mouse skin wounds to validate the efficacy of ELR membranes in improving wound healing. The aforementioned models permit the simulation of realistic wound conditions.

3.1.5.2.- Assessment of wound regeneration capacity of ELR membranes using a murine excisional wound model

After studying the biocompatibility of protein materials through subcutaneous implantation in mice, it was observed that they exhibited low immunogenicity, no toxicity, high biocompatibility, and low inflammation and fibrosis. Therefore, it is necessary to evaluate the efficacy of elastin membranes in facilitating the total excision wound healing process to determine their potential use as a dressing for chronic wounds.

As in the aforementioned biocompatibility study, the 3R principle was also considered to optimize and minimize the number of experimental animals. Figure 50A shows that the most commonly used model to mimic clinical wounds is the formation of full-thickness excisional wounds in the dorsal region of C57BL/6J mice. Prior to the surgical procedure, the hair on the dorsal region was shaved with an electric razor, followed by the application of depilatory cream. Subsequently, the skin was then cleansed with 70 % alcohol, and two full-thickness excisional wounds, which extended through the fleshy panniculus on the dorsum, were produced by using a 4-mm biopsy punch. In order to evaluate the effectiveness of the biomaterials in the healing process, VKV-SKS membranes are placed over the wounds. In addition to the membranes, the study also included the use of VKV-SKS hydrogels, Pluronic hydrogels, and wounds without biomaterials. A comparison was made between the membrane and elastin hydrogel with the uncovered wound and the Pluronic hydrogel, which is commonly used for skin healing studies. The materials were then covered with Tegaderm® medical adhesive tape in order to hold them in place during the healing process and to avoid wound contraction by mechanically fixing the skin. This process promotes re-epithelialisation healing, which more closely resembles the process that occurs in humans. The tape used in the experiment is air-permeable, thereby facilitating the delivery of oxygen to the healing site. Tegaderm® tape was not changed during the experiment to avoid causing additional damage to the wound, given the difficulty in removing it. To alleviate discomfort, buprenorphine was injected intradermally for the first 48 hours. A total of eight experimental samples were obtained for each of the four experimental conditions, with four mice per condition. All mice survived the experiment without experiencing pain, although some sustained skin wounds while attempting to remove the Tegaderm® plastic covering the wounds and biomaterials. Following the sacrifice of the animals, skin biopsies were collected from the wound site eight days after the injury.

Figure 50B and Figure 50C illustrate the macroscopic appearance of the total excision wounds in mice and the application of the biomaterials: (B) the use of ELR membranes and (C) the use of ELR hydrogels, which completely covered the wounds. A schematic for the collection of wound samples for histological analysis is presented in Figure 50D. A sample can be collected from either a fresh wound (I) or from a healed wound. In the former case, the normal skin adjacent to the wound should be collected and a 30-40 mm rectangle cut around the wound (dashed box). In order to ensure the collection of accurate and reliable information from the samples, the skin should be mounted on Whatman filter paper with the epidermis facing upwards (III) and then cut into sagittal sections for histological processing (dashed lines) (II).

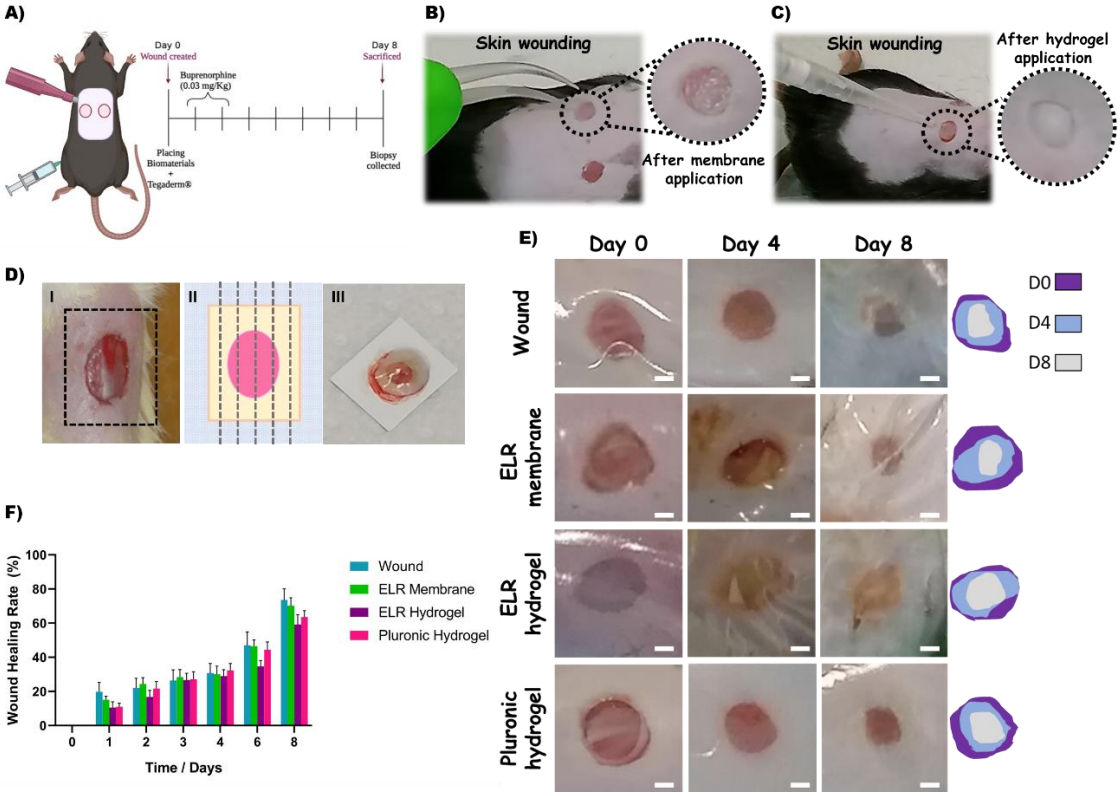

Figure 50: ***Assessment of wound healing process in a full-thickness excisional wound murine model****.* ***A)*** *Schematic illustration of the study design.* ***B)*** *Macroscopic appearance of the excision wounds in mice and the application of the ELR membranes, which completely cover the wounds.* ***C)*** *Macroscopic appearance of the excision wounds in mice and the application of the ELR hydrogels, which completely cover the wounds.* ***D)*** *Schematic for the collection of wound samples for histological analysis. A sample can be collected from a fresh wound* ***(I)*** *by first collecting the normal skin adjacent to the wound and cutting a rectangle measuring 30-40 mm around the wound (dashed box). In order to ensure the accuracy and reliability of the information obtained from the samples, the skin should be mounted on Whatman filter paper with the epidermis facing upwards* ***(III)*** *and then cut into sagittal sections for histological processing (dashed lines)* ***(II)****.* ***E)*** *Daily representative macroscopic images of in vivo wounds on days 0, 4 and 8 post-injuries. The size and shape of the initial wound, as well as the progression of wound healing, were observed at various time points in the same wound for different experimental samples, including an ELR membrane, an ELR hydrogel, a Pluronic hydrogel, and an uncovered wound. Scale bar = 0.5 mm. A figure in the right panel displays the temporal evolution of wound area.* ***F)*** *Quantification of the wound healing rate (%).*

To monitor the wound healing process in real-time, photographs of the wound surface were taken daily throughout the experiment, as illustrated in Figure 50E. The results indicate that the biomaterials were fully integrated into the surrounding tissue, emphasising the significance of scaffold hydrophilicity in

biomaterial-tissue integration [559]. Figure 50E also displays representative images of the longitudinal monitoring of wound healing progress with different treatments on days 0, 4, and 8. Additionally, a graph representing the temporal variation in wound area is presented at the end of each sequence. In all cases, the images demonstrate a gradual reduction in size over time, indicative of the healing process. Nevertheless, after eight days, no wound has reached a state of complete closure. According to the literature, a total excision wound in a healthy mouse should close completely within seven days after injury [560]. It is possible that the use of Tegaderm® adhesive tape may result in a delay in the healing process. However, the use of adhesive tape is imperative because the biomaterials must be retained *in situ* to prevent their disappearance when the animals scratch. Furthermore, the application of this Tegaderm® to the skin mechanically fixes it, thereby preventing the skin from healing by contraction and facilitating the re-epithelialisation process that occurs in human skin.

The images permit a quantitative assessment of the rate of epithelial closure during skin wound healing, as shown in Figure 50F, using the ImageJ software. The wound healing rate was calculated by comparing the wound size at each time point with the original wound size on day 0. Over time, the wound size decreased progressively, with no significant difference observed between empty wounds (controls) and wounds treated with biomaterials. All materials employed were found to maintain wound moisture and promote healing. However, the closure rate of wounds treated with elastin membrane (approximately 70 %) is slightly higher than those treated with Pluronic hydrogels (approximately 60 %), which are commonly used in wound healing. It has been observed that the ELR membrane exhibits a slightly higher tendency towards closure, in comparison to the ELR hydrogel. This may be attributed to the fact that the membrane is thinner and therefore presents a higher oxygen permeability. Furthermore, the thinness of the membrane may facilitate the adhesion and proliferation of adjacent tissue cells more easily through it, thereby making it easier the reconstruction of the three-dimensional network of new tissue.

It is important to note that sometimes it is difficult to define the edge of the wound, either because of the biomaterial, because the Tegaderm® tape slightly interferes with the sharpness of the image, or because the size of the wound also depends on the perspective from which images are taken, always trying to get a representative and adequate image to take and compare data.

In order to analyse the morphology and progression of wound healing, samples were stained with H&E, in a manner analogous to the aforementioned biocompatibility assay. Additionally, Masson's trichrome staining was also employed in a full-thickness excisional wound samples in mice. Figure 51 presents cross-sectional images of elastin VKV-SKS membranes, elastin hydrogels, Pluronic hydrogels, and untreated wounds, stained with H&E and observed at various magnifications (4X, 10X, and 40X) after eight days of healing. The information that can be provided by H&E staining is similar to that obtained through the *ex vivo* assay, including detailed views of the epidermis, dermis, and epidermal tongue, which

highlight cell types and morphology. The violet hue of the cells contrasts with the pinkish-grey materials, which aids in the identification process. The frontal images of the wounds provide extensive information, including the level of re-epithelialisation, which is measured by the distance between wound margins and the number of cell layers in the newly formed tissue. Furthermore, the images also permit comparisons of the morphology and size of new cells with that of the surrounding undamaged tissue.

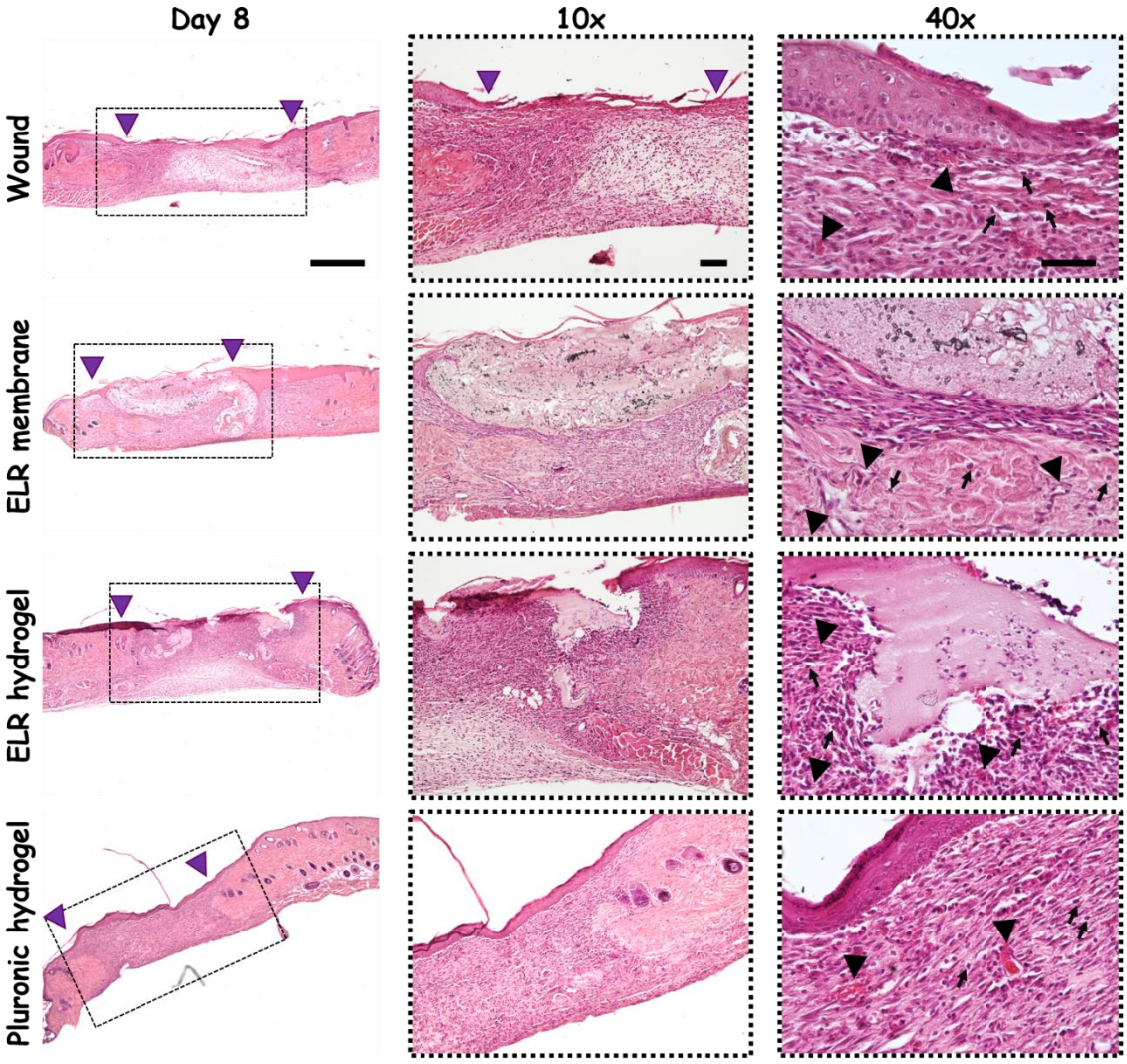

Figure 51: ***Haematoxylin and Eosin staining of full-thickness excisional wounds in mice****. Representative H&E staining images of wounds without material, with ELR-membrane, ELR hydrogel, and Pluronic hydrogel at 8 days post-injury. Columns correspond to different magnifications, while rows indicate different materials. The black arrows identify newly formed capillaries, while the purple arrows indicate the distance between the edges of the epidermis forming the epithelial gap. The small black arrows indicate the presence of neutrophils in the dermis. Scale bar standard image (4X) = 500 µm. Scale bar zoomed image (10X) = 100 µm and (40X) = 50 µm.*

As animal sacrifice is a requisite for obtaining tissue samples for histological analysis, only data collected at the experimental point, eight days after surgery, is utilized. The obtained images, as shown in Figure 51, demonstrate that the elastin materials are well integrated into the tissue, with cell nuclei present within the scaffold. When Tegaderm® medical adhesive tape is used to secure the edges and

prevent shrinkage, it is observed that animal cells invade the material from the edge in contact with the tissue. This process is analogous to the re-epithelialisation of human skin, which was investigated in the previous chapter with the *ex vivo* experiments.

The images reveal that cell mobility is superior when working with elastin membranes compared to hydrogels. Both materials have cell adhesion domains (RGD) that facilitate the recruitment of cells from the surrounding tissue. However, the thinner and more porous structure of the membranes allows for easier access to the interior, promoting cell proliferation and complete colonization of the structure, which facilitates tissue reconstitution and accelerates the healing process. In addition, the thinner membrane exhibits greater permeability to oxygen, allowing for easier exchange of nutrients and debris, which promotes wound healing through fibroblast proliferation and collagen synthesis [561]. Keratinocytes proliferate below the membrane, reconstituting the epidermis with several layers of ordered cells. However, they can also grow above and within it, as evidenced by the detailed images (40X). In contrast, the elastin hydrogels display a disorganized population of undifferentiated and unordered cells.

In addition, both the membrane and the hydrogels permit the retention of moisture within the wound, thus preventing direct exposure to air, which would result in the cells becoming dehydrated and leading to their demise. This situation would result in the formation of a scab over the wound, which would impede the healing process. It is therefore demonstrated that these three-dimensional networks act as an extracellular matrix for cells to incorporate into their structure, increasing epithelial cell migration and further promoting wound healing while reducing scarring. This is in accordance with the findings presented in the bibliography [456], [562]. The Pluronic hydrogel is also capable of maintaining moisture in the wound, and the formation of scabs is also not observed in these samples.

The assessment of wound healing included an evaluation of the inflammatory response, re-epithelialisation, and granulation tissue formation. The initial response to skin injury is the inflammatory reaction, which can influence the quality of tissue repair [563]. Innate immune cells, such as neutrophils and macrophages, are recruited to the wound site to eliminate pathogens and wound debris. Additionally, they produce proangiogenic growth factors and bioactive cytokines that accelerate angiogenesis and attract regenerative cells to the injury site [564]–[569]. In addition, these cells play a crucial role in the biodegradation process of biomaterials. They are the first colonisers of the material surface after implantation and possess mechanisms that help to lower the pH of the microenvironment, facilitating biomaterial degradation. Recent studies have reported that ELR hydrogels may be capable of recruiting and modulating macrophages, thereby being biologically active and highly desirable materials for wound healing, facilitating tissue regeneration [570]. In the *in vivo* murine wound model, all experimental samples demonstrated the ability to attract a significant number or neutrophils and macrophages to the wound site, facilitating their infiltration into the wound. As the healing process

progresses, the proportion of inflammatory cells at the wound site is expected to decline gradually. H&E-stained images revealed a moderate inflammatory response after eight days, characterized mainly by neutrophils in all experimental samples. This is illustrated by the small black arrows (40X) in Figure 51, observing a massive infiltration of neutrophils in the dermis, which are recognised for small circular purple cells [571]. However, wounds treated with ELR membranes exhibited a lower density of violet-stained inflammatory cells, resulting in less wound exudate [572].

Proliferation occurs subsequent to the resolution of inflammation, leading to re-epithelialisation, granulation tissue formation, and the restoration of the vascular network. This process restores the structure and function of the wounded skin by replacing the provisional wound matrix formed during haemostasis. The histological examination of the H&E images reveals that during the process of re-epithelialisation, the epidermal keratinocytes of the basal layer at the wound edge undergo proliferation and migration towards the centre of the wound. This process is illustrated in Figure 51, where the new epithelial layer and the restoration of the skin barrier are observed [573]. As previously described, the epithelial gap is the distance between the edges of the epidermis (purple arrows). Epithelial tongues advance to close the epithelial gap and form the new epidermis until complete closure, as depicted in the detailed image of the wounds without biomaterials (40X). Epithelial thickness is another crucial parameter that determines the degree of epithelialisation. The histological examination of the samples containing the Pluronic hydrogel revealed the presence of a well-structured and formed epithelium, comprising distinct layers of keratinocytes. Furthermore, there is evidence of cell proliferation above and below the membranes, which appears to form a new epithelial layer, thus reducing the epithelial gap. Samples without the material exhibited visible epithelial tongues. However, complete healing of the epidermis is not observed for ELR hydrogels, as there is no observed keratinocyte cell organization.

The proliferation stage of wound healing requires the formation of new blood capillaries, which ensure the supply of oxygen and nutrients to growing tissues [574]. During this stage, new capillaries grow rapidly, resulting in a dense network of blood vessels with denser capillaries than normal tissue. Wound angiogenesis is gradually suppressed when tissue hypoxia is restored. This is due to a decrease in the level of growth factors in the granulation tissue and a subsiding of inflammation [575]. Consequently, assessing wound angiogenesis can often correlate with the progression of healing. The formation of small blood vessels (black arrows) can be observed in samples with ELR membranes, as illustrated in Figure 51, which is similar to samples with ELR hydrogels. Furthermore, these vessels are observed in the samples devoid of materials and in the Pluronic hydrogels.

In the later stages of the wound healing process, accelerated angiogenesis can promote the synthesis of collagen fibres at the wound site. This process assists in the maturation of granulation tissue, which is an important indicator of tissue remodelling [576]. Collagen acts as a primary structural protein in the extracellular

matrix, and its presence at wound sites is indicative of efficient tissue regeneration [575]. Histological samples were stained with Masson's trichrome, as displayed in Figure 52, to illustrate cross-sectional images of elastin membranes, elastin hydrogels, Pluronic hydrogels, and wounds without biomaterial treatment at different magnifications (5X, 10X, and 20X) after 8 days of healing. The cytoplasm of epidermal and dermal cells was stained red, similar to that observed in muscle fibres or keratin. In contrast, collagen fibres in the dermis were stained blue, and cells and components of the surrounding connective tissues were distinguishable. The scaffolds were not stained and appeared greyish in colour.

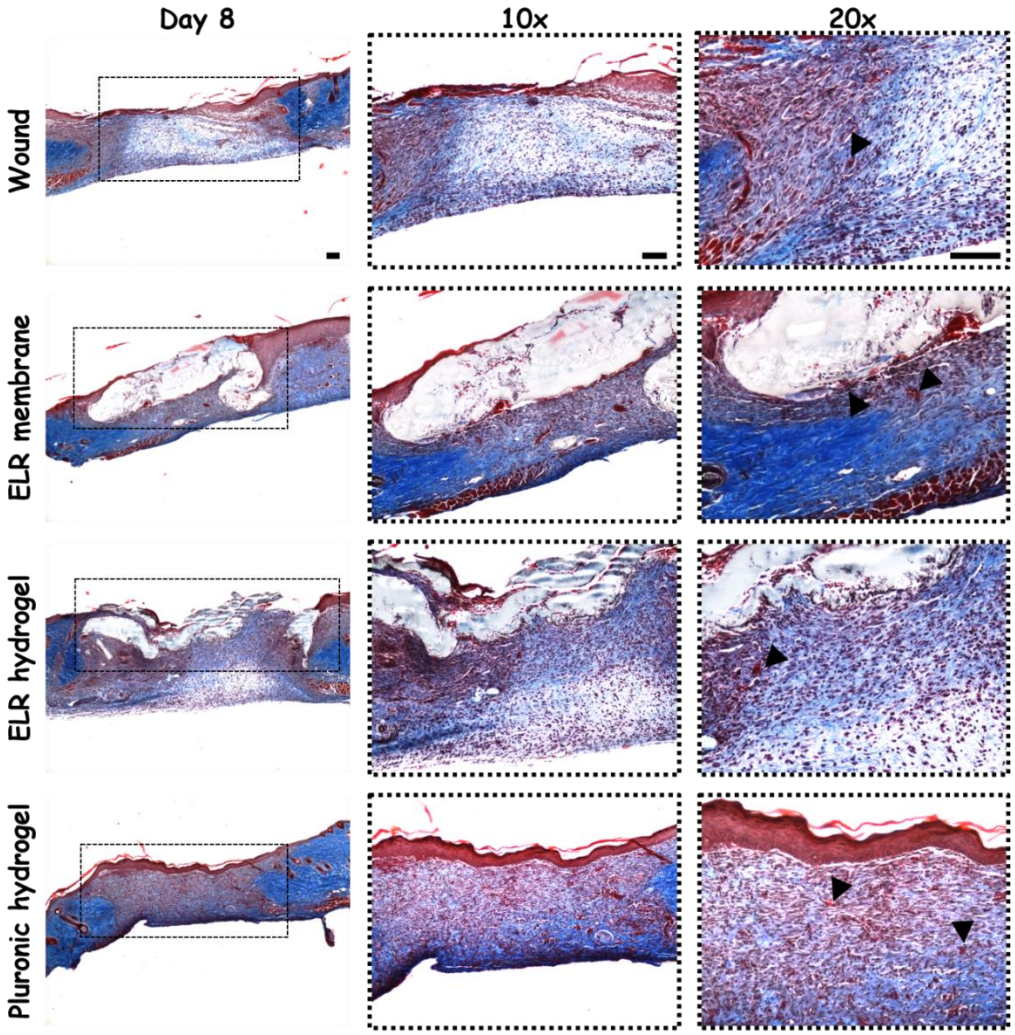

Figure 52: ***Masson's Trichrome staining of full-thickness excisional wounds in mice****. Representative Masson's Trichrome staining images of wounds without material, with ELR-membrane, ELR hydrogel, and Pluronic hydrogel at eight days post-injury. Columns correspond to different magnifications, while rows indicate the different materials. The black arrows identify the presence of newly formed capillaries. Scale bar standard image (5X) = 100 µm. Scale bar zoomed image (10X) = 100 µm and (20X) = 100 µm.*

The use of ELR membranes resulted in a smaller granulation tissue space between the healthy dermis on both sides of the wound compared to the control groups (wound without biomaterial and Pluronic hydrogel). Furthermore, ELR membrane treatment led to increased collagen deposition, resulting in thicker, more organized and packed fibre bundles. Furthermore, the fibroblasts located beneath the granulation tissue area exhibited a more developed morphology, being arranged

horizontally in sheet-like patterns. Conversely, the fibres and fibroblasts in the remaining experimental groups exhibited a reticular pattern with both vertical and horizontal orientations [572], [577]. The orientation of collagen in scar tissue is of significance, as it can lead in the formation of stiff and inflexible tissue. Furthermore, the excessive production of collagen can result in the loss of tissue elasticity, which may give rise to hypertrophic or keloid scars [578]. Consequently, the presence of an elastin membrane appears to enhance the structural organisation of scar tissue by facilitating the formation of more organised collagen fibres. Moreover, in the preceding chapter, *ex vivo* experiments demonstrated that the use of elastin membranes reduced wound contraction, because it is a highly elastic material that may also influence collagen production and organisation, preventing the formation of visible contracted scars.

The present study employed an *in vivo* full-thickness excisional mouse wound model to validate the efficacy of elastin biomaterials in accelerating wound healing rates. It has been demonstrated that the speed of wound healing is higher in membranes than in both elastin and Pluronic hydrogels. This may be attributed to the thinner dimensions of the membranes, which makes it easier the proliferation and migration of cells, thereby reconstituting the epidermis with several layers of ordered cells. In addition, the reduced thickness and high porosity of the membrane facilitate the exchange of nutrients and oxygen, which improves the wound healing process. Furthermore, elastin-based biomaterials retain moisture in the wound, thereby preventing the formation of scabs that impede the healing process. The histological examination of the samples using H&E staining revealed that wounds treated with VKV-SKS membranes exhibited a lower density of inflammatory cells, resulting in a reduction in wound exudate. Moreover, a re-epithelialisation process can be observed from the edges of the wounds, where keratinocytes proliferate and migrate towards the interior of the wound to close it, thereby restoring the skin barrier. Additionally, samples treated with ELR membranes revealed the formation of small new blood vessels, a phenomenon also observed in samples with hydrogels. Finally, to evaluate the maturation of granulation tissue, through collagen synthesis, Masson's trichrome staining is used as an indicator of this tissue remodelling. The results demonstrate that elastin membranes facilitate the alignment of collagen fibres, thereby preventing the formation of rigid tissue with limited flexibility. Additionally, the elasticity of these materials reduces wound contraction, promoting healing that prevents the formation of visible contracted scars. The preceding analysis leads to the conclusion that elastin membranes offer some advantages over Pluronic hydrogels, including a faster healing speed, the formation of more new blood vessels, and the organisation of the collagen formed. These membranes, therefore, appear to be promising candidates for use as wound dressings for the treatment of challenging wounds.

The study was conducted on healthy mice using a conventional model, and the results were found to be promising. It would be worthwhile to test more complex models, such as diabetic mice with impaired normal healing, in order to simulate chronic wounds and evaluate the effect of biomaterials on the healing process. Additionally, pigs could be also utilised as a model, as their skin exhibits

characteristics similar to those of humans, including the process of re-epithelialisation and granulation tissue formation. The objective of these experiments is to assess the efficacy of biomaterials in the treatment of chronic wounds and burns.

Despite the favourable results obtained with elastin membranes, the process of optimising their synthesis is arduous and complex. This is due to the necessity of obtaining two immiscible phases through the mixing of multiple organic solvents. For this reason, in the subsequent chapter, in which new functionalities will be incorporated into elastin polymers, we will develop new hydrogels, as their synthesis is more straightforward and this preliminary stage of optimisation of the ideal condition is sufficient to determine if these new sequences improve the properties of the ELR polymers.

Development of advanced biomaterials functionalized with laminin mimetic peptides

3.2.- Development of advanced biomaterials functionalized with laminin mimetic peptides to enhance the wound healing process

3.2.1.- Synthesis and characterisation of biofunctionalized hydrogels using click reaction chemically grafted laminin peptides

3.2.1.1.- Synthesis of laminin mimetic peptides

3.2.1.1.1.- Peptide sequence selection

The literature search resulted in the selection of the laminin mimetic peptides AASIKVAVSADR and PPFLMLLKGSTR for the functionalisation of elastin polymers. These sequences support the adhesion and growth of fibroblasts and keratinocytes, thereby favouring the wound healing process through the application of potential wound dressings that can assist in the treatment of chronic wounds. On the one hand, the peptide with the amino acid sequence AASIKVAVSADR is located in the globular region of the long α-chain of laminin 1. This sequence has been shown to promote various functions, including cell adhesion, differentiation, and migration, by binding to α3β1, α4β1, and α6β1 integrins [579]. Additionally, this peptide enhances endothelial cell mobilisation, capillary branching, and vessel formation, thereby promoting angiogenesis, a process essential for tissue healing [580]. On the other hand, the peptide PPFLMLLKGSTR is present in the globular domain (LG3) of the α3-chain of laminin 5. This sequence regulates a number of cellular functions, such as cell adhesion, spreading, and motility [581]. Laminin-5 regulates the adhesion of epithelium to underlying connective tissue and interacts with cell surface receptors, such as α3β1 integrins, to form focal adhesions, which are associated with actin-containing stress fibres and promote keratinocyte motility, accelerating re-epithelialisation and aiding wound healing [582]. In a series of experiments conducted on rats and rabbits with full-thickness wounds, the active peptide was found to significantly promote wound healing. These outcomes were achieved by accelerating re-epithelialisation, reducing inflammatory cell infiltration, and enhancing fibroblast proliferation [71].

The peptides selected for their functionality are AASIKVAVSADR and PPFLMLLKGSTR. In order to attach the peptides to the polypeptide chain of the polymer, an extra lysine amino acid is added to the N-terminal end with a coupled

azide (K-N_3), resulting in the N_3-KAASIKVAVSADR and N_3-KPPFLFLMLLKGSTR peptides, as illustrated in Figure 53. In this manner, the elastin polymer containing cyclooctynes can be functionalised by a click reaction with the azide-containing synthetic peptides.

3.2.1.1.2.- Peptide synthesis

Peptides were synthesised manually using the solid phase peptide synthesis (SPPS) with Fmoc strategy. This technique involves the sequential addition of amino acids to a growing resin, whereby the linear peptide chain is extended through repetitive cycles of coupling, washing, deprotection, and washing. The amino-terminal end of a peptide bound in a solid phase is coupled to a single N-protected amino acid unit. The unit becomes unprotected, thereby revealing a new amino-terminal end where another amino acid can bind. SPPS progresses from the C-terminal to the N-terminal end, in contrast to protein synthesis carried out by ribosomes. Figure 53 presents a schematic representation of the assembly of AASIKVAVSADR and PPFLMLLKGSTR peptides by SPPS. The amino acid N-terminal of monomers is protected by Fmoc groups and added to an unprotected amino acid chain. The coupling cocktail for each amino acid comprises the corresponding side-chain protected amino acid, N,N-diisopropylethylamine (DIPEA) as the base, and [(1H-benzotriazol-1-yl) (dimethylamino)-methylene]-N-methylmethanaminium (HBTU) as the coupling agent. The deprotection of the side-chain protecting groups and cleavage of the peptide from the resin were performed under acidic TFA conditions.

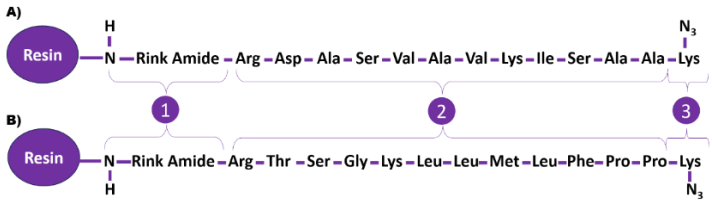

Figure 53: ***Schematic representation of the peptide assembly process via SPPS. A)*** *N_3-KAASIKVAVSADR and* ***B)*** *N_3-KPPFMLLKGSTR. Numbered sections indicate the order of assembly. The numbers used refer to the following:* ***(1)*** *the attachment of a rink amide linker;* ***(2)*** *the coupling of the amino acids in the order specified by the peptide sequence;* ***(3)*** *the coupling of one lysine with azide to provide a click reaction.*

In the synthesis of these two peptides, an azide-tethered lysine was introduced at the end of the peptide chain. This modification does not affect the functionality of the peptide, but enables it to bind and functionalise the elastin polymers through a click reaction.

The Expasy program was employed to calculate the atomic composition and molecular weight of the peptides. The peptide N_3-KAASIKVAVSADR has a molecular weight of 1340.96 g/mol and an atomic composition of $C_{56}H_{100}N_{20}O_{18}$. The peptide N_3-KPPFLMLLKGSTR has a molecular weight of 1513.69 g/mol and an atomic composition of $C_{69}H_{116}N_{20}O_{16}S_1$.

The two-dimensional (2D) structure was generated using the ChemDraw program and is depicted in Figure 54A. The three-dimensional (3D) structure was

predicted and modelled using the PEPFOLD3 program [583] based on the amino acid sequences and is illustrated in Figure 54B.

In order to calculate the hydrophilicity profiles of the peptides, in addition to the net charge, the Bachem peptide calculator was used (https://www.bachem.com/knowledge-center/peptide-calculator). Figure 54C displays the hydrophilicity profiles generated by the aforementioned program. For the peptide N_3-KAASIKVAVSADR, the predicted net charge at pH 7 is 2, and its average hydrophilicity is 0.45. For the peptide N_3-KPPFLMLLKGSTR, the predicted net charge at pH 7 is 3, and its average hydrophilicity is -0.02.

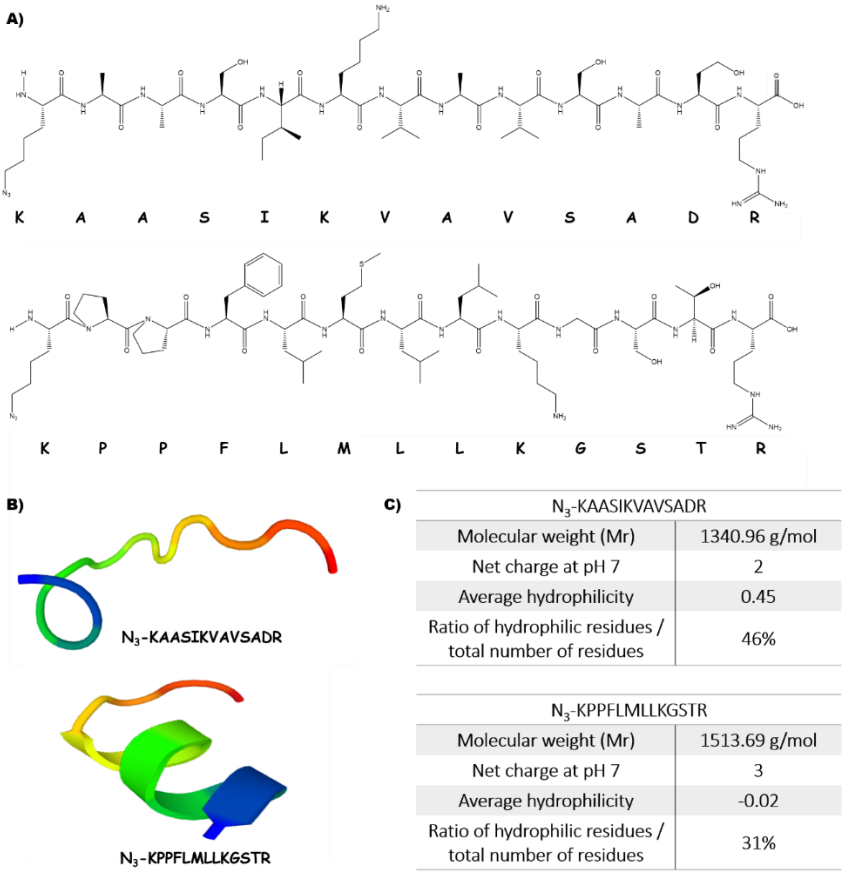

N_3-KAASIKVAVSADR	
Molecular weight (Mr)	1340.96 g/mol
Net charge at pH 7	2
Average hydrophilicity	0.45
Ratio of hydrophilic residues / total number of residues	46%

N_3-KPPFLMLLKGSTR	
Molecular weight (Mr)	1513.69 g/mol
Net charge at pH 7	3
Average hydrophilicity	-0.02
Ratio of hydrophilic residues / total number of residues	31%

*Figure 54: **2D and 3D structures of the synthesised peptides. A)** 2D structures of laminin peptides using the ChemDraw program. **B)** 3D structures of laminin peptides were generated using the PEPFOLD3 program. **C)** Summary table of hydrophilicity characteristics, as determined by the Bachem peptide calculator.*

The solubility of a peptide can be predicted based on its amino acid composition, as it is related to the hydrophobicity of peptide. The sequence KPPFLFLFLLKGSTR contains numerous hydrophobic residues (W, L, I, F, M, V, Y, P, A), which renders it generally insoluble in aqueous solutions and typically soluble in organic solvents such as DMSO or DMF. The IKVAV sequence is also hydrophobic due to the uncharged amino acids and has low solubility in water [584], [585]. To enhance its solubility, polar and charged amino acid residues are introduced into the peptide sequence, resulting in the sequence KAASIKVAVSADR, which is more soluble in aqueous solvents and can also dissolve in organic solvents.

3.2.1.2.- Physico-chemical characterisation of laminin mimetic peptides

In order to guarantee the correct synthesis of peptides, a series of general characterisation techniques are employed prior to their utilisation. These techniques include amino acid analysis with HPLC, NMR spectroscopy to provide peptide fingerprint data, as well as mass spectrometry (UPLC-ESI-qTOF) to determine the purity and molecular weight of the final products.

Firstly, the amino acid composition of the synthesised peptides was verified. Figure 55A presents the theoretical numerical values (Theor.) calculated with the Expasy program and the experimental values (Exp.) of the amino acids composing each peptide. The experimentally determined number of residues closely matched the theoretical values calculated from the peptide sequence, thereby confirming the accuracy and purity of the synthesised peptides (KAASIKVAVSADR and KPPFLMLLKGSTR). Any slight variations were within the experimental error associated with the technique. Furthermore, this technique also serves to confirm the absence of any unwanted contaminants.

A)

	KAASIKVAVSADR		KPPFLMLLKGSTR	
Amino Acid	Theoretical	Experimental	Theoretical	Experimental
Ala (A)	4	4.22	0	-
Arg (R)	1	1.24	1	1.16
Asn (N)	0	-	0	-
Asp (D)	1	1.14	0	-
Cys (C)	0	-	0	-
Gln (Q)	0	-	0	-
Glu (E)	0	-	0	-
Gly (G)	0	-	1	1.23
His (H)	0	-	0	-
Ile (I)	1	0.77	0	-
Leu (L)	0	-	3	2.95
Lys (K)	2	1.75	2	1.74
Met (M)	0	-	1	0.99
Phe (F)	0	-	1	0.84
Pro (P)	0	-	2	2.02
Ser (S)	2	1.98	1	1.11
Thr (T)	0	-	1	1.12
Trp (W)	0	-	0	-
Typ (Y)	0	-	0	-
Val (V)	2	1.91	0	-

B)

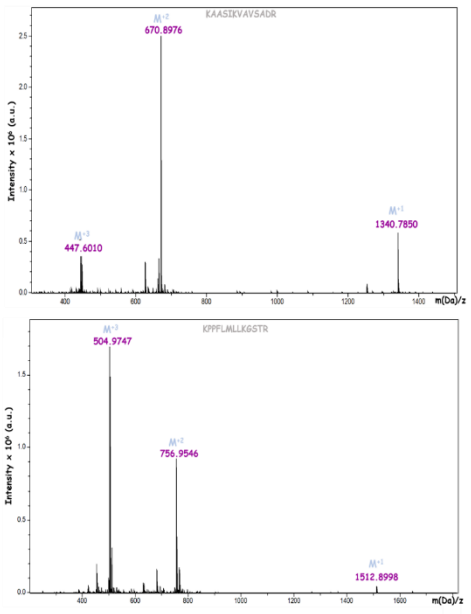

C)

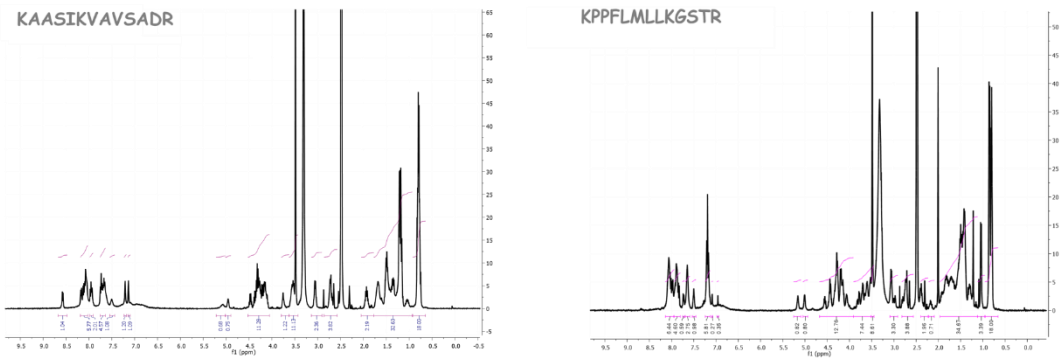

Figure 55: ***Physico-chemical characterisation of laminin mimetic peptides. A)*** *Predicted and measured amino acid compositions for the KAASIKVAVSADR and KPPFLMLLKGSTR peptides using HPLC following acid hydrolysis.* ***B)*** *The UPLC-ESI-qTOF spectra of the KAASIKVAVSADR and KPPFLMLLKGSTR peptides. Marked*

peaks correspond to the third, second, and first charged ions, respectively. The samples were dissolved in DMSO at a concentration of 1 mg/mL. ***C)*** *^{1}H-NMR spectra of the KAASIKVAVSADR and KPPFLMLLKGSTR peptides.*

To further verify the successful synthesis of peptides using the SPPS strategy, ultra-high performance liquid chromatography (UPLC) coupled in tandem with a quadrupole time-of-flight mass spectrometer (MS-qTOF) is employed to accurately determine the experimental molecular weight (M_w) [586]. The MS acquisition for the synthesized peptides is performed in full scan mode using ESI-qTOF positive ion mode, providing an overview of the products. Figure 55B presents the mass spectra of the KAASIKVAVSADR and KPPFLMLLKGSTR peptides, respectively. The spectra permit the precise determination of the molecular mass of compounds, thereby confirming the correct peptide synthesis. The abscissa axis displays the mass-to-charge ratios (m/z) of the ions detected with mass in Dalton, while the ordinate axis shows the relative intensities of the ions produced. Figure 55B illustrates the first ionisation of the analyte $(M+H)^{+}$, which enables precise determination of the peptide weight (m/z = m/1 = m). Additionally, second ionisation $(M+2H)^{+2}$ and third ionisation $(M+3H)^{+3}$ are also displayed. For the KAASIKVAVSADR peptide, the value of the first ionisation (M^{+}) is 1340.79 Da, which is in agreement with the theoretical molecular weight. Moreover, the second ionisation (M^{+2}) has a value of 670.90 Da, while the third ionisation (M^{+3}) is 447.60 Da. For the peptide KPPFLMLLKGSTR, first ionisation (M^{+}) reveals a value of 1512.90 Da, which is similar to its theoretical molecular weight. Furthermore, the second ionisation (M^{+2}) has a value of 756.95 Da, while the third ionisation (M^{+3}) has a value of 504.97 Da. The theoretical mass-to-charge ratio (m/z) of peptides and their respective fragment ions were generated using the MS product tool of the ProteinProspector online program. The experimental molecular weights are in close agreement with the theoretical values, which indicates that the peptide synthesis was successful. Table 27 provides a summary of these values.

Table 27: Predicted and measured molecular weights (Mw) for peptides (KAASIKVAVSADR and KPPFLMLLKGSTR) were determined using UPLC-ESI-qTOF.

	Theor. (Da)	Exp. (Da)
KAASIKVAVSADR	1340.96	1340.79
KPPFLMLLKGSTR	1513.69	1512.90

Furthermore, the chemical composition of each peptide is determined by analysing the spectra with the Compass IsotopePattern application (Bruker), and confirming the empirical molecular formula through total atom content calculations. The elemental analysis of the KAASIKVAVSADR peptide reveals an empirical formula of $C_{56}H_{100}N_{20}O_{18}$, with an elemental composition of 50.14 % C, 7.51 % H, 20.88 % N, and 21.47 % O. Similarly, the elemental analysis of the KPPFLMLLKGSTR peptide shows an empirical formula of $C_{69}H_{116}N_{20}O_{16}S_{1}$, with an elemental composition of 54.74 % C, 7.72 % H, 18.50 % N, 16.91 % O, and 2.12 % S. Both peptides are confirmed to have been synthesised correctly, as the experimental mass is similar to the theoretical mass predicted in the Expasy program.

Finally, the correct synthesis of the peptides is confirmed by analysing the ^{1}H-NMR spectra. To achieve this, the different types of protons present in the

peptides are theoretically studied using the ChemDraw programme, with the resulting values then being compared with the experimental results of the signal integrals for each corresponding region. Figure 55C illustrates the NMR spectra with the corresponding integrals of the laminin mimetic peptides, KAASIKVAVSADR and KPPFLMLLKGSTR. In addition, a detailed description of each proton types observed in the spectrum is provided in the appendix to this chapter.

The NMR spectrum of the KAASIKVAVSADR peptide displays signals in six characteristic areas. The first zone, between 0.7 and 0.9 ppm, exhibits signals from methyl groups of valine and isoleucine. The second zone, between 0.9 and 3.1 ppm, displays three multiplets, corresponding to the amino groups of lysine, the methyl groups of alanine and isoleucine, the methylene groups of lysine, aspartic acid, arginine and isoleucine, and the methine groups of isoleucine and valine. In the 3.4-4.5 ppm region, the principal resonance is from the methine groups adjacent to the amido group, in addition to the methylene group of serine and the methylene group in the alpha position to the guanidinium group of arginine. Two broad singlet signals corresponding to the protons of the hydroxyl groups of the serines are observed at 5.1 and 5.2 ppm. Additionally, three singlets corresponding to the protons of the guanidinium group of arginine are observed between 7.1 and 7.5 ppm. The final zone of characteristics, ranging from 7.7 to 8.6 ppm, comprises four multiplets that correspond to the protons of the amido group of all the amino acids present.

The KPPFLMLLKGSTR peptide exhibits the same six characteristic zones of the spectrum as the KAASIKVAVSADR peptide, although some signals correspond to protons of different amino acids. The first zone of the spectrum corresponds to a range of 0.7-0.9 ppm, wherein the methyl groups of leucine resonate. In the second zone of the spectrum, between 0.9 and 3.1 ppm, there are three multiplets. These correspond to the amino groups of lysine, the methine groups of leucine, and the methyl groups of leucine, methionine, arginine, proline, and lysine. Furthermore, the more unshielded methyl groups of methionine and threonine are present. In the zone corresponding to 3.4-4.5 ppm, the majority of the resonances are attributed to methylenes and methines adjacent to the amido group. At 5.0 and 5.2 ppm, two broad singlet signals are observed, corresponding to the protons of the hydroxyl groups of serine and threonine. Between 7.1 and 7.5 ppm, two multiplets are observed, corresponding to the aromatic protons of phenylalanine and the protons of the guanidinium group of arginine. The last characteristic zone, in the range of 7.6 to 8.2 ppm, comprises two multiplets corresponding to the amido group protons of all amino acids, with the exception of proline.

In both cases, the synthesis of the KAASIKVAVSADR and KPPFLMLLKGSTR peptides was confirmed as correct, as the experimentally obtained values of the integrals of the signals of each corresponding region matched the theoretically planned values. Consequently, based on the results of all the experimental techniques employed, it can be concluded that both peptides have been successfully synthesised and are suitable for use in the formation of biofunctionalized hydrogels.

3.2.1.3.- Laminin peptide-functionalized click hydrogel

3.2.1.3.1.- Binding of VKV-cc with peptides-N_3

The synthesis of this tricomponent ELR hydrogel is achieved through the application of two consecutive click chemistry reactions. Prior to gelation, the VKV polymer is functionalised with laminin peptides (VKV-cc + peptide-N_3). Subsequently, a second click reaction occurs between the VKV-peptide with free cyclooctyne groups and the SKS-N_3 polymer, resulting in the formation of peptide-functionalised hydrogels (VKV-peptide-SKS). In order to achieve this, the required mass must be calculated by considering the molecular weight of the components (ELR polymer and peptide) and the number of peptides to be included. Consequently, the mass will vary depending on the specific peptide type (KAASIKVAVSADR or KPPFLMLLKGSTR) and the concentration of peptides to be anchored (2X, 4X, and 6X). Table 28 presents a summary of the mass ratios used to obtain 150 mg of VKV-cc polymer at each of the increasing peptide concentrations.

Table 28: Summary of the mass ratios used to functionalise the VKV-cc polymer with increasing peptide concentrations.

	VKV-cc + 2X peptide	VKV-cc + 4X peptide	VKV-cc + 6X peptide
	mass (mg)	mass (mg)	mass (mg)
VKV-cc	150	150	150
KAASIKVAVSADR	6.7	13.5	21.2
KPPFLMLLKGSTR	7.6	15.2	23.7

In order to ascertain the efficacy of peptide anchoring to the ELR polymer at varying concentrations (2X, 4X, and 6X), the VKV-cc polymer with peptides was characterised using several techniques. These included amino acid analysis with HPLC, NMR spectroscopy to provide peptide fingerprint data, mass spectrometry (specifically MALDI-TOF) to determine the purity and molecular weight of the final products, as well as ATR-FTIR spectroscopy.

3.2.1.3.2.- Physico-chemical characterisation of the VKV-peptide anchoring

Once the anchoring reaction of the peptide to the VKV-cc polymer has been completed, the effectiveness of the attachment process is evaluated through the use of a range of experimental techniques. Consequently, Table 29 displays the amino acid composition analysis for the modification of the VKV-cc polymer with peptides at varying concentrations (2X, 4X, and 6X). The table presents both the theoretical numerical values (Theor.) calculated using the Expasy program and the corresponding experimental values (Exp.) of the amino acids comprising each system.

In order to guarantee the correct attachment of peptides to the VKV-cc polymer, it is necessary to analyse the amino acids derived from the peptide and observe their evolution as the concentration varies. Table 29A presents the study of the KAASIKVAVSADR peptide, with the amino acids of interest highlighted by a dotted rectangle. The amino acids alanine (A), arginine (R), isoleucine (I), and serine

(S) exhibit increasing values as the number of peptides anchored to the VKV-cc peptide chain increases, thereby confirming their correct anchoring at all concentrations. Table 29B presents the study of the KPPFLMLLKGSTR peptide, with the amino acids of interest highlighted by a dotted rectangle. The amino acids arginine (R), leucine (L), methionine (M), and threonine (T) exhibit an increase in values as the number of peptides anchored to the peptide chain of VKV-cc increases, thereby confirming their correct anchoring at all concentrations. In all cases, the experimentally determined number of residues was found to be in close agreement with the theoretical values calculated from the peptide sequence, thereby confirming the accuracy and purity of the compounds formed from VKV-peptides. The slight variations were within the experimental error associated with the technique.

Table 29: Predicted and measured amino acid composition for VKV-cc + peptides using HPLC following acid hydrolysis. ***A)*** *Results for the KAASIKVAVSADR peptide and* ***B)*** *Results for the KPPFLMLLKGSTR peptide.*

A)

	VKV-cc		Pept		VKV-cc+2Xpept		VKV-cc+4Xpept		VKV-cc+6Xpept	
Amino Acid	Theor.	Exp.	Theor.	Exp.	Theor.	Exp.	Theor.	Exp.	Theor.	Exp.
Ala (A)	0	-	4	4.22	8	9.94	16	13.53	24	28.57
Arg (R)	0	-	1	1.24	2	2.92	4	3.71	6	8.87
Asn (N)	0	-	0	-	0	-	0	-	0	-
Asp (D)	0	-	1	1.14	2	4.35	4	4.17	6	8.46
Cys (C)	0	-	0	-	0	-	0	-	0	-
Gln (Q)	0	-	0	-	0	-	0	-	0	-
Glu (E)	1	1.63	0	-	1	2.05	1	1.46	1	1.06
Gly (G)	288	291.17	0	-	288	272.78	288	318.01	288	279.01
His (H)	0	-	0	-	0	-	0	-	0	-
Ile (I)	0	-	1	0.77	2	1.79	4	2.75	6	5.27
Leu (L)	2	2.52	0	-	2	2.42	2	2.87	2	2.07
Lys (K)	24	21.54	2	1.75	28	28.19	32	27.65	36	34.46
Met (M)	1	1.19	0	-	1	1.32	1	1.01	1	0.85
Phe (F)	0	-	0	-	0	-	0	-	0	-
Pro (P)	145	144.79	0	-	145	145.86	145	146.51	145	144.33
Ser (S)	1	1.22	2	1.98	5	5.07	9	7.19	13	11.72
Thr (T)	0	-	0	-	0	-	0	-	0	-
Trp (W)	0	-	0	-	0	-	0	-	0	-
Typ (Y)	0	-	0	-	0	-	0	-	0	-
Val (V)	265	264.44	2	1.91	269	270.15	273	261.27	277	276.82

B)

	VKV-cc		Pept		VKV-cc+2Xpept		VKV-cc+4Xpept		VKV-cc+6Xpept	
Amino Acid	Theor.	Exp.	Theor.	Exp.	Theor.	Exp.	Theor.	Exp.	Theor.	Exp.
Ala (A)	0	-	0	-	0	-	0	-	0	-
Arg (R)	0	-	1	1.16	2	2.28	4	4.48	6	6.54
Asn (N)	0	-	0	-	0	-	0	-	0	-
Asp (D)	0	-	0	-	0	-	0	-	0	-
Cys (C)	0	-	0	-	0	-	0	-	0	-
Gln (Q)	0	-	0	-	0	-	0	-	0	-
Glu (E)	1	1.63	0	-	1	1.85	1	1.58	1	1.53
Gly (G)	288	291.17	1	1.23	290	287.40	292	302.54	294	295.01
His (H)	0	-	0	-	0	-	0	-	0	-
Ile (I)	0	-	0	-	0	-	0	-	0	-
Leu (L)	2	2.52	3	2.95	8	9.65	14	14.92	20	19.87
Lys (K)	24	21.54	2	1.74	28	28.22	32	25.34	36	36.20
Met (M)	1	1.19	1	0.99	3	3.16	5	5.06	7	6.83
Phe (F)	0	-	1	0.84	2	1.98	4	3.53	6	4.69
Pro (P)	145	144.79	2	2.02	149	149.55	153	152.72	157	157.02
Ser (S)	1	1.22	1	1.11	3	3.55	5	4.90	7	6.99
Thr (T)	0	-	1	1.12	2	2.45	4	4.24	6	6.38
Trp (W)	0	-	0	-	0	-	0	-	0	-
Typ (Y)	0	-	0	-	0	-	0	-	0	-
Val (V)	265	264.44	0	-	265	260.63	265	264.81	265	264.44

Figure 56 shows the ATR-FTIR spectra of VKV-cc polymer modifications with peptides at varying concentrations (2X, 4X, and 6X). Figure 56A represents the KAASIKVAVSADR peptide, while Figure 56B indicates the KPPFLMLLKGSTR peptide. The spectra were obtained by scanning wavelengths between 600 and 4000 cm^{-1}, which encompassed the characteristic functional groups.

The spectra of the VKV-cc polymers and VKV-cc with peptide modification, exhibit characteristic vibrational bands of proteins corresponding to amide I and amide II [471]. The absorption associated with amide I produces a high-intensity peak in the spectrum around 1600 cm^{-1}, whose signal is attributed to the stretching vibrations of the carbonyl group bond (C=O), which is related to the secondary structure of the proteins. Conversely, the amide II band is indicative of bending vibrations of the N-H bond, which is signalled at 3400 cm^{-1}. Additionally, the bands at 1450 cm^{-1} correspond to the C-H bending of the methyl group of the alkane, at 1200 cm^{-1} to the C-N stretching of the amine, and at 1000 cm^{-1} to the C-O stretching of the primary alcohol [471].

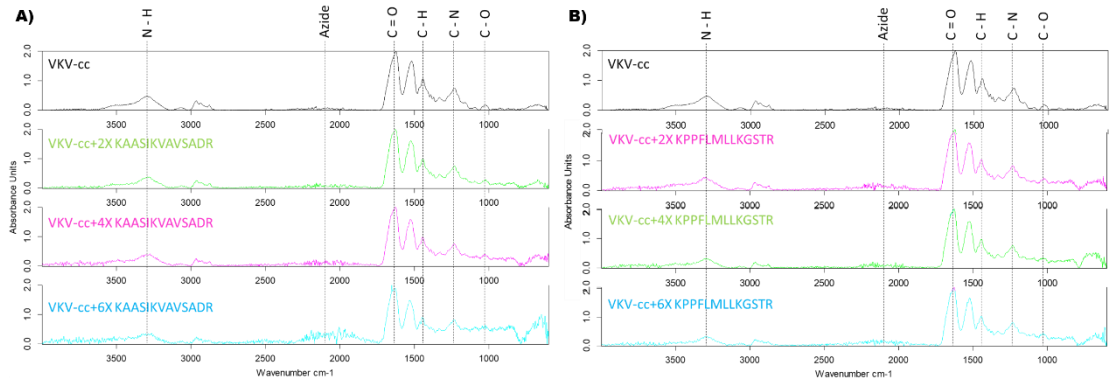

Figure 56: ***ATR-FTIR spectra. A)*** *ATR-FTIR spectra of VKV-cc with different concentrations of the KAASIKVAVSADR peptide (2X, 4X and 6X).* ***B)*** *ATR-FTIR spectra of VKV-cc with different concentrations of the KPPFLMLLKGSTR peptide (2X, 4X and 6X).*

Furthermore, ATR-FTIR analysis is employed to identify the reactive tethered click groups. The presence of azide groups on the peptides is indicated by the appearance of a peak at 2100 cm^{-1} in the infrared region. However, this technique is unable to detect the chemical modification signal of VKV with cyclooctyne due to the symmetry of the compound, rendering the IR absorption inactive and the triple bond invisible around 2200 cm^{-1}. The signal at 2100 cm^{-1} is not present in the spectra shown in Figure 56 because the azide groups, which are supported by the synthesised peptides, cross-link orthogonally with the cyclooctyne groups of VKV to bind and functionalize the polymer with laminin-specific peptides that promote wound regeneration.

The experimental molecular weights (M_w) were determined using matrix-assisted laser desorption/ionization time-of-flight (MALDI-TOF) mass spectrometry. The mass spectra of the VKV-cc polymer modification with peptides at different concentrations (2X, 4X and 6X) are presented in Figure 57. Figure 57A depicts the KAASIKVAVSADR peptide, while Figure 57B displays the KPPFLMLLKGSTR peptide. These spectra permit the precise determination of the molecular mass of the compounds, thereby confirming the correct introduction of the peptides into the VKV-cc polymer chain. The abscissa axis displays the mass-to-charge ratios (m/z) of the detected ions, as the mass in Daltons (Da), while the ordinate axis shows the intensities, which reflect the number of ions of a given m/z ratio that have impacted the detector during the analysis. Figure 57 displays the first ionisation of the analyte (M^{+1}), which has the highest intensity band, allowing for the

precise determination of the weight of the polymer (m/z = m/1 = m). Furthermore, the second ionisation (forming the dication, M^{+2}) is half the mass of the polymer (m/z = m/2).

In order to conduct the study, an initial VKV polymer modified with cyclooctynes was used with an initial mass of a) 63125 Da and b) 62970 Da. The study examines the number of peptides introduced in each modification (2X, 4X and 6X). To ascertain the number of peptides introduced by the click reaction of the azides of the peptides with the cyclooctynes of VKV, the amount of mass incorporated into the initial polymer is studied. It is crucial to highlight that each individual peptide of KAASIKVAVSADR has a mass of 1340.96 Da, while the individual peptide of KPPFLMLLKGSTR has a mass of 1513.96 Da. It can be observed that the molecular mass increases as the number of peptides included in the reaction increases. This is evidenced by the characteristic band of the first and second ionisation, which shifts to the right on the abscissa axis.

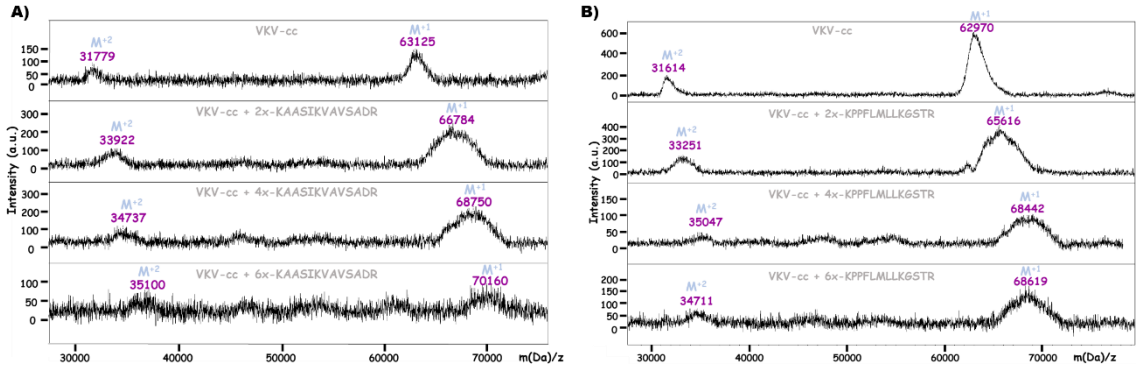

*Figure 57: **MALDI-TOF spectra. A)** MALDI-TOF spectra of VKV-cc with varying concentrations of the KAASIKVAVSADR peptide (2X, 4X and 6X). **B)** MALDI-TOF spectra of VKV-cc with different concentrations of the KPPFLMLLKGSTR peptide (2X, 4X and 6X). Marked peaks correspond to the doubly and singly charged ions, respectively. The samples were dissolved in DMSO at a concentration of 1 mg/mL.*

Table 30 exhibits the theoretical masses for 2, 4, and 6 peptides, along with their corresponding experimental values. The results indicate a satisfactory concordance between the anticipated experimental and theoretical molecular weights, within the expected experimental errors. The only exception is the VKV-cc polymer with six KPPFLMLMLLKGSTR peptides, where only four peptides were detected instead of the expected six. Nevertheless, alternative methodologies verify the correct anchoring of six peptides.

Table 30: Predicted and measured molecular weight (Mw) for VKV-cc + peptides (KAASIKVAVSADR and KPPFLMLLKGSTR) was determined using MALDI-TOF. The experimental peptide concentration was calculated according to the observed mass changes.

	KAASIKVAVSADR			KPPFLMLLKGSTR		
ELR	**Theor.**	**Exp. (Da)**	**Exp. peptide concentration**	**Theor. (Da)**	**Exp. (Da)**	**Exp. peptide concentration**
VKV-cc		63125			62970	
VKV-cc + 2X peptide	65806	66784	≈ 2.5	65974	65616	≈ 1.9
VKV-cc + 4X peptide	68488	68750	≈ 4.2	69000	68442	≈ 3.7
VKV-cc + 6X peptide	71170	70160	≈ 5.3	72028	68619	≈ 3.9

The mass spectra are useful for assessing the purity of the ELRs. In this instance, it can be confirmed that the VKV-cc polymers modified with varying concentrations of peptides are pure, as only the bands of interest are observed.

To complete the study on the proper anchoring of peptides to the VKV-cc polymer, ^{1}H-NMR spectra are analysed to determine how the proton environment varies under different conditions. Figure 58 shows the NMR spectra for a series of increasing peptide concentrations (2X, 4X, and 6X), with a magnified view of the areas where a clear change in protons is observed. Figure 58A displays the results for the KAASIKVAVSADR peptide, whereas Figure 58B represents the results for the KPPFLMLLKGSTR peptide.

In order to analyse the NMR spectra of polymers, the ChemDraw programme is employed to study the different types of protons theoretically. These values are then compared to the experimental results of the integrals of the signals of each corresponding region. The appendix of this chapter presents all the spectra of the VKV-cc polymer with different peptide concentrations (2X, 4X and 6X) and their experimental integrals. Additionally, a detailed description of the proton types present in the spectrum is provided.

The NMR spectra of both VKV-cc and VKV-peptide exhibit signals primarily in four characteristic zones of the spectrum, as described in their respective NMR spectra. In the case of the KAASIKVAVSADR peptide, a first zone is identified between 0.5 and 1.0 ppm, in which only signals from the methyl groups of valines are observed. This zone is comparable in both VKV-cc alone and in VKV-peptide. The recombinamers with grafted peptides exhibit higher levels of signals from aspartic acid methylene groups, isoleucine methylene and methylene groups, and alanine methyl groups between 1.0 and 2.2 ppm compared to VKV-cc. The increase in signals between 1.10 and 1.85 ppm upon peptide introduction is most clearly observed in a zoomed-in view in Figure 58A. In particular, the signals between 1.15 and 1.30 ppm exhibit an increase as the number of tethered KAASIKVAVSADR peptides increases.

However, the binding of peptides to the VKV-cc is most clearly observed in the region between 6.9 and 7.32 ppm. The signal of the amide proton of the cyclooctyne residue introduced into the VKV-cc appears at 7.0 ppm. Two new signals emerge at 7.16 and 7.24 ppm as the KAASIKVAVSADR peptides are grafted in, as illustrated in the magnified view in Figure 58A in the region between 6.94 and 7.32 ppm. Moreover, the integral values confirm the presence of guanidinium group protons characteristic of arginine, which are indicative of the peptide. This indicates the presence of peptides grafted onto VKV-cc at varying concentrations (2X, 4X, and 6X).

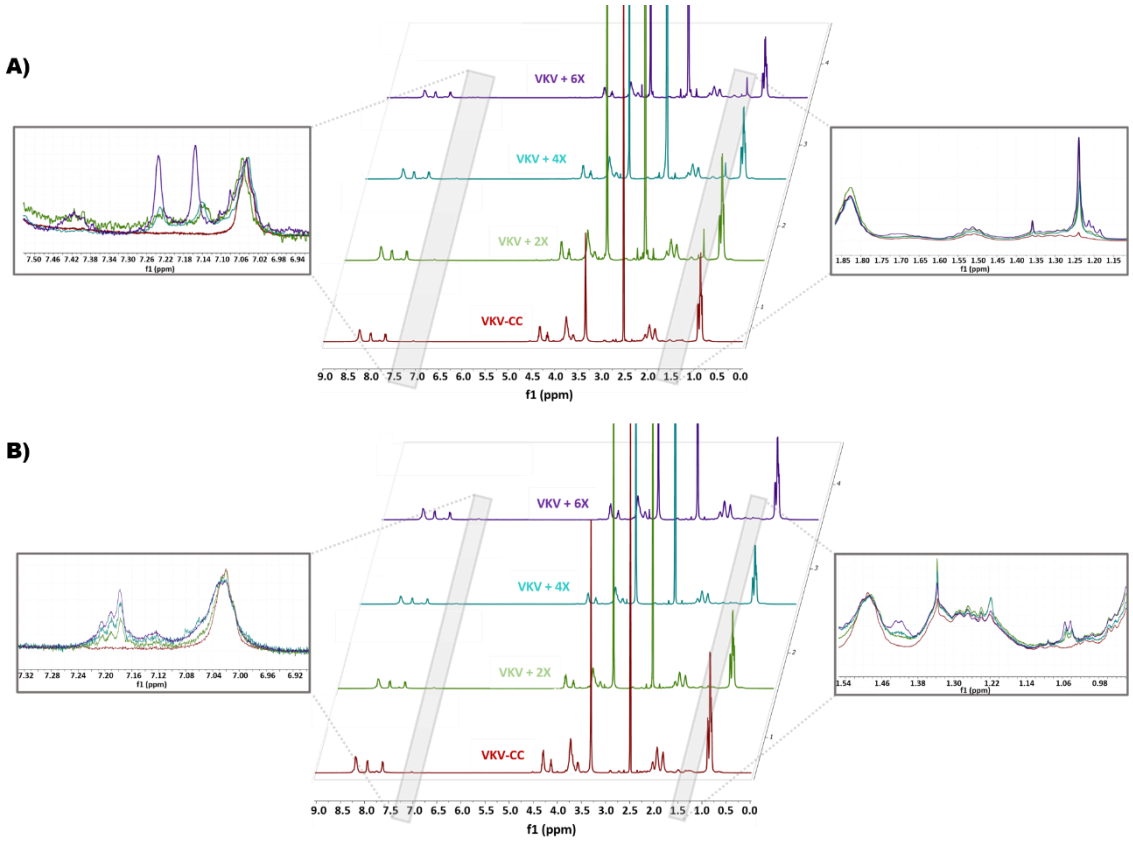

Figure 58: ***¹H-NMR spectra. A)*** *¹H-NMR spectrum of the VKV-cc polymer modified with different concentrations of the KAASIKVAVSADR peptide (2X, 4X and 6X). The zoomed-in sections indicate the impact of peptide introduction on the observed signal.* ***B)*** *¹H-NMR spectrum of the VKV-cc polymer modified with different concentrations of KPPFLMLLKGSTR peptide (2X, 4X and 6X). The zoomed-in sections indicate the impact of peptide introduction on the observed signal.*

With regard to the VKV-cc polymer with the KPPFLMLLKGSTR anchored peptide, it can also be observed the four characteristic zones of the spectrum similarly to previous spectra of the KAASIKVAVSADR peptide. Nevertheless, some signals correspond to protons of different amino acids. The first zone of the spectrum corresponds to 0.5-1 ppm, wherein the methyl groups of valines are observed in the VKV-cc polymer. In the polymers bearing the grafted peptides, methyl groups of leucine are also detected. In the second zone of the spectrum, between 1.0 and 2.2 ppm, the methylene groups of proline and leucine, as well as the methylene groups of the valines, resonate mainly for VKV-cc. In the case of the grafted peptides, the protons of the methine and methylene groups of leucine, methionine, and lysine, as well as the more unshielded methylene groups of methionine and threonine, also appear. The most pronounced increase in signals is detected between 0.94 and 1.54 ppm, as depicted in a magnified view in Figure 58B. The intensity of signals between 1.04 and 1.42 ppm increases as the number of tethered KPPFLMLLKGSTR peptides increases.

The zone between 3.5 and 4.4 ppm mainly resonates with methylene groups and methines adjacent to the amido group, both in VKV-cc and VKV-peptide. The final distinctive zone in the range of 7.6-8.2 ppm corresponds to the protons of the amido group of all amino acids, with the exception of proline. The binding of the peptides to the VKV-cc is most clearly observed in this last zone, specifically the

region between 6.0 and 7.2 ppm. In this region, at 7.0 ppm, the signal of the amide proton of the remaining cyclooctyne in VKV-cc is observed. The signal at 7.0 ppm (increase of the integral under the signal) grows in intensity and a new signal appears at 7.2 ppm as the KPPFLMLLKGSTR peptides are anchored, as depicted in Figure 58B, which has been zoomed in to show the region between 6.9 and 7.3 ppm. Moreover, the integral values provide further evidence of the presence of the phenyl group of phenylalanine, which is a characteristic of this peptide. This confirms the existence of the peptides grafted onto the VKV-cc at varying concentrations (2X, 4X and 6X).

The presence of the tethered KAASIKVAVSADR and KPPFLMLLKGSTR peptides has also been confirmed, as the experimentally obtained signal integral values match the theoretically planned values for each corresponding region.

The collective results of the complementary techniques employed to ascertain the accurate anchoring of varying peptide concentrations permits a definitive conclusion that the peptides have been effectively anchored to the VKV-cc polymer. With regard to the KAASIKVAVSADR peptide, an increase in the number of amino acids characteristic of this peptide (alanine (A), arginine (R), isoleucine (I) and serine (S)) is observed as the number of peptides anchored to the VKV-cc polymer chain increases. Furthermore, mass spectrometry demonstrates an increase in molecular weight in accordance with the observed increase in peptide concentration. Furthermore, NMR spectra corroborate an augmentation in the characteristic signals at 7.16 and 7.24 ppm concomitant with the grafting of elevated peptide concentrations, indicative of the presence of guanidinium group protons, a characteristic feature of arginine. Furthermore, the signal between 1.15 and 1.50 ppm increases in accordance with the number of anchored KAASIKVAVSADR peptides, originating from the methylene groups of aspartic acid, the methylene of isoleucine, and the methyl groups of alanine.

Conversely, while mass spectrometry indicates that the maximum molecular weight added to the polymer corresponds to four KPPFLMLLKGSTR peptides at the maximum concentration, the other two techniques confirm the correct synthesis of the VKV-cc polymer with six anchored peptides. Therefore, an increase in the number of amino acids characteristic of this peptide (arginine (R), leucine (L), methionine (M) and threonine (T)) is observed as the number of anchored peptides increases. Furthermore, the NMR spectra demonstrate an increase in the characteristic signals of this peptide between 6.9 and 7.3 ppm, thereby confirming the presence of the phenyl group of phenylalanine, which is characteristic of this peptide. Furthermore, the signal between 1.04 and 1.42 ppm increases with the number of anchored KPPFLMLLKGSTR peptides, coming from the protons of the methine and methylene groups of leucine, methionine and lysine, as well as the less shielded methylene groups of methionine and threonine, which are characteristic of this peptide.

In light of the aforementioned summary, it can be concluded that all peptide concentrations have been successfully grafted to the VKV-cc polymer (2X, 4X and 6X) for both peptides.

3.2.1.3.3.- Binding of VKV-peptide to SKS-N_3 to obtain biofunctionalized click hydrogel

3.2.1.3.3.1.- Design of biofunctionalized hydrogel network

The utilisation of a synthetic peptide cross-linker confers a significant advantage as it enables for the precise covalent coupling of a specific sequence to the hydrogel backbone, thus incorporating the desired biological functionality. The VKV-cc polymer reacts with peptides that contain azide groups to anchor to the polymer and obtain a functionalised polymer. Subsequently, the VKV-peptide is reacted with the SKS-N_3 polymer, resulting in a click reaction and cross-linking to form a multifunctional hydrogel. The stoichiometric ratio between azides and cyclooctynes is maintained at 1:1. Thus, the final hydrogels, with varying peptide concentrations, will be produced by reacting all VKV polymers with their respective modifications (VKV-2X-KAASIKVAVSADR, VKV-4X-KAASIKVAVSADR, VKV-6X-KAASIKVAVSADR, and VKV-2X-KPPFLMLLKGSTR, VKV-4X-KPPFLMLLKGSTR, VKV-6X-KPPFLMLLKGSTR) with SKS-N_3.

The polymers were selected for this study due to their favourable biocompatibility and the presence of cross-linking domains (via lysine residues) in both ELRs. These domains are subsequently modified with functional groups for hydrogel formation via catalyst-free click chemistry. The VKV polymer serves as a structural group, while the SKS polymer introduces biological functionality through the incorporation of the universal cell adhesion sequence (RGD). Finally, the system also includes the anchoring of the laminin-derived peptides KAASIKVAVSADR and KPPFLMLLKGSTR, which have been demonstrated to be involved in the adhesion and proliferation processes of keratinocytes and fibroblasts, both of which are essential for the wound healing process.

Once SKS azides are mixed with VKV-peptide cyclooctynes, cross-linking occurs spontaneously, producing a three-dimensional network. The creation of these novel hydrogels at a concentration of 50 mg/mL necessitates the consideration of the number of cyclooctynes employed to introduce the peptides. It is of paramount importance to maintain a stoichiometric ratio of 1:1 between cyclooctynes and azides for the successful cross-linking via the click reaction. To achieve this, the masses of each VKV-cc and SKS-N_3 polymer present in the reaction must be adjusted. It is crucial to be aware of the number of cyclooctyne-containing lysines that are theoretically available. Table 31 presents a summary of the theoretically lysines present in each polymer, including those that have been modified with cross-linking groups such as azides and cyclooctynes, those used for peptide anchoring, and those available for hydrogel formation.

Table 31: Summary of the theoretically lysines present in each polymer, including those that have been modified with cross-linking groups such as azides and cyclooctynes, those used for peptide anchoring, and those available for hydrogel formation.

	Lysines		Modified Lysines (*)	
ELR	Available	Modified with cross-linking groups	Used with peptides	Available for hydrogel
SKS-N_3	24	18	-	18
VKV-cc + 2X peptide	24	14	2	12
VKV-cc + 4X peptide	24	14	4	10
VKV-cc + 6X peptide	24	14	6	8

Accordingly, the mass of the VKV-peptide polymer and SKS-N_3 is calculated based on the specified conditions for dissolution of each condition and the volume required for the two substances to react and form a 400 µl hydrogel. The volume will vary depending on the number of peptides introduced, in order to maintain a 1:1 stoichiometry between azides and cyclooctynes. Table 32 summarises the volumes used for each type of hydrogel.

Table 32: Summary of the volume of material required to obtain a functionalised VKV-peptide-SKS hydrogel with increasing peptide concentrations.

	2X peptides	4X peptides	6X peptides
	Volume (µl)	Volume (µl)	Volume (µl)
SKS-N_3	178.4	156.0	130.0
VKV-peptide	221.6	244.0	270.0

The method of obtaining tricomponent hydrogels allows for precise control of the quantity of active peptides within the hydrogel. Moreover, previous studies on cross-linked hydrogels comparable to the new hydrogels [457] indicate that it is reasonable to anticipate that elastin hydrogels could easily modify their mechanical properties by simply adjusting the final gel concentration, as well as by varying the degree of functionalisation with the peptides. Consequently, the new hydrogels will be characterised in terms of their properties, including transparency and internal structure, through porosity. Furthermore, the impact of varying degrees of peptide functionalisation within the hydrogel will be investigated on both mechanical properties and cellular activity to ascertain whether this enhances the regenerative capacity.

3.2.1.3.3.2.- Macroscopic properties

Biofunctionalized tricomponent hydrogels (VKV-peptide-SKS) were synthesised using the click methodology following several gelation tests and optimisation of masses and volumes between SKS-N_3 and VKV-peptides. Figure 59A confirms that hydrogels with a concentration of 50 mg/mL reveal a stable macroscopic structure in all studied systems. Upon initial inspection, it appears that hydrogels with varying peptide concentrations exhibit comparable properties, including viscosity, hardness, and malleability, regardless of peptide type. These properties are comparable to those of the control gel (VKV-SKS), as depicted in Figure 59B. However, this hypothesis will be verified in a subsequent study of the rheological properties of the scaffolds. Additionally, all scaffolds display good consistency and are easily manageable, as demonstrated in Figure 59C, which is a representative example of all the hydrogels.

The ELR polymers used in the reaction to obtain functionalised hydrogels were dissolved in ultrapure water, resulting in transparent hydrogels in all cases due to their high-water retention, as shown in Figure 59A. The transparency of these hydrogels is a crucial property for wound dressings used in wound healing, as it allows for monitoring of the healing process without the need to remove the dressing. This is a significant advantage, as removing the dressing can potentially damage the wound and impede the proper healing progress.

The stability of hydrogels is a crucial parameter for the suitability of a device for tissue engineering. Matrices must remain stable in aqueous media for an extended period, as would be the case in a normal tissue environment. The stability of the 50 mg/mL hydrogels was tested by incubating them in excess water for one week at 37 °C. Observation of the scaffold following incubation revealed that the structures remained stable without losing their initial shape, as illustrated in Figure 59D.

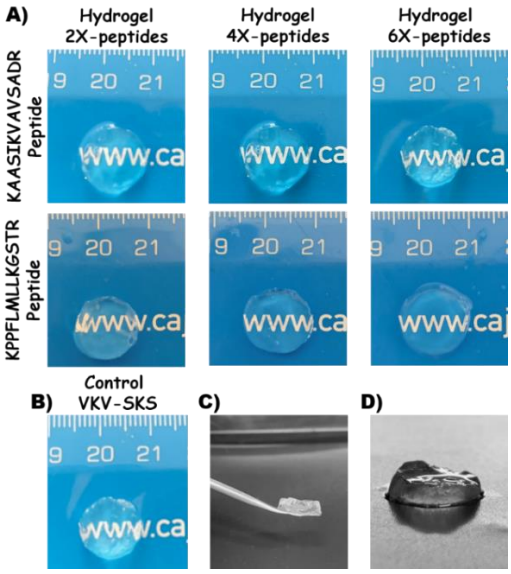

Figure 59: ***Biofunctionalized click hydrogels. A)*** *Hydrogels with varying concentrations of peptides exhibited transparency.* ***B)*** *VKV-SKS Control Hydrogel.* ***C)*** *Example of consistency and manageability of a biofunctionalized hydrogel.* ***D)*** *Example of stability of a biofunctionalized hydrogel after one week of incubation in water at 37 °C, demonstrating that the initial shape is retained.*

Furthermore, hydrogels have the additional benefit of being able to be used directly in *in vivo* systems due to the mild conditions required for the click reaction to be triggered. This implies that the hydrogel of interest can be generated *in situ* on the chronic wound, conforming to the dimensions and shape of the wound and rapidly gelling upon contact with body temperature. Once reaching a temperature of 37 °C immediately following the mixing process, the ELR transition accelerates the reaction, resulting in cross-linking that may exhibit a slightly less uniform distribution.

A transparent dressing with multiple properties, including moisture retention, self-healing, and bioadhesiveness, has been developed by forming *in situ* functionalized hydrogels to enhance the wound healing process. Moreover, the presence of particular peptides that facilitate adhesion and movement of

keratinocytes can guide cell migration to specific areas of the scaffold, thereby promoting skin regeneration [587].

3.2.1.3.3.3.- Evaluation of internal morphology of biofunctionalized click hydrogels

It is widely acknowledged that the porosity and pore size of 3D scaffolds have a direct impact on their functionality in biomedical applications. Open pores and interconnected networks are crucial for cell nutrition, proliferation, and migration, as well as for tissue vascularisation, and the formation of new tissue [320], [588]. Furthermore, the network structure of the pores plays a role in guiding and promoting the formation of new tissues [589]. Hydrogels produced using elastin-like recombinamers are typically expected to exhibit this specific internal porous structure, largely due to their high-water content.

The internal microstructure is investigated by immersing hydrogels in liquid nitrogen, cryofracturing, and freeze-drying them for SEM microscopy, thereby providing high-resolution images for microscopic morphological analysis. Figure 60A displays representative SEM micrographs of cross-sections of biofunctionalized tricomponent hydrogels of 50 mg/mL with different peptide concentrations. These include VKV-2X-KAASIKVAVSADR-SKS, VKV-4X-KAASIKVAVSADR-SKS, VKV-6X-KAASIKVAVSADR-SKS, VKV-2X-KPPFLMLLKGSTR-SKS, VKV-4X-KPPFLFLMLLKGSTR-SKS and VKV-6X-KPPFLMLLKGSTR-SKS.

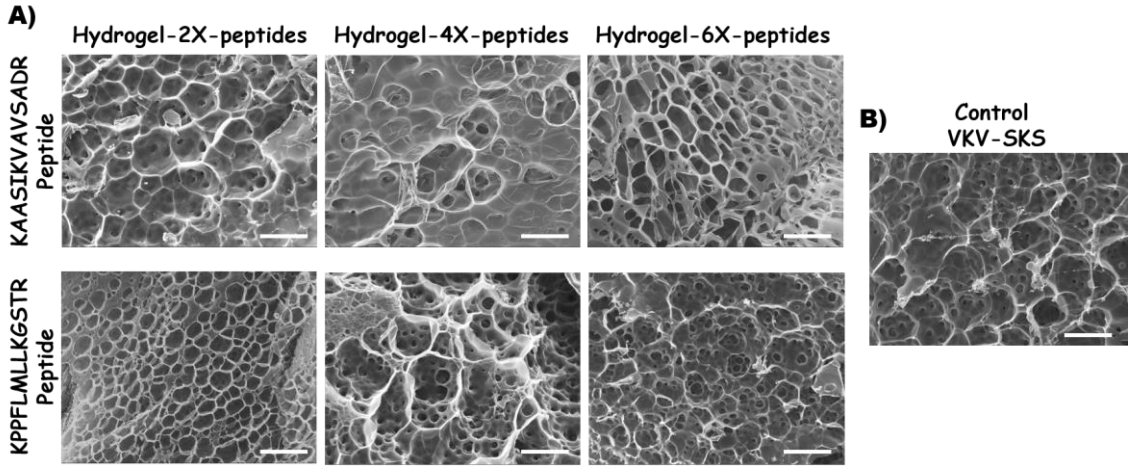

Figure 60: ***Morphological characterization. A)*** *Representative SEM images illustrate the cryo-fractured, lyophilised and gold-sputtered across sections of biofunctionalized click hydrogels with varying peptide concentrations (2X, 4X and 6X). Scale bar = 50 µm.* ***B)*** *Representative SEM images of the VKV-SKS Control Hydrogel. Scale bar = 50 µm.*

All hydrogels exhibit a highly porous internal structure, which is consistent with the appearance of covalently cross-linked ELR hydrogels that have been previously reported [433], [471], [497]. This suggests that the general properties of ELRs facilitate satisfactory exchange of liquids and nutrients both within and outside the scaffold. The pore shape is predominantly circular or ellipsoidal, with a considerable degree of heterogeneity and irregularity in pore size. From a practical perspective, the presence of heterogeneous porous surfaces on the scaffolds enhances the mechanical contact between the hydrogel and the surrounding tissue,

thereby improving the mechanical stability of the implant [590]. Additionally, the rough surfaces of the scaffolds are designed to provide anchorage points for cellular interactions, and may even induce cellular behaviour and differentiation [591].

Figure 60B presents a SEM micrograph of the VKV-SKS control hydrogel. The internal structure of the hydrogel is porous, exhibiting a configuration comparable to that observed in hydrogels with grafted peptides. These structures comprise large pores with smaller internal micropores. A quantitative analysis of the characteristics of the pore was conducted using the ImageJ software. The measured pore size exhibited considerable heterogeneity within the same samples, with the larger pores measuring approximately 30-35 μm and the smaller pores ranging from 4 to 6 μm. This observation was consistent across all hydrogel types, regardless of the number of peptides introduced. It can therefore be concluded that neovascularisation can occur in a pore structure of 5 μm, whereas fibroblast growth requires a pore size of 5 to 15 μm and keratinocyte growth requires a pore size of 10 to 20 μm. Consequently, the pore size identified in the examined samples is sufficient for cell invasion, and the microstructure is consistent with that of similar structures designed for soft tissue engineering purposes. The presented evidence provides support for the potential applicability of ELR hydrogels manufactured for the intended purpose [317], [433].

3.2.1.3.3.4.- Mechanical characterization of biofunctionalized click hydrogels by rheological measurements

The rheological properties of ELR hydrogels containing varying concentrations of laminin peptides, prepared at 50 mg/mL, are evaluated for use in tissue engineering and regenerative medicine. In order to achieve this, a strain sweep experiment is conducted on each hydrogel, with a strain amplitude ranging from 0.01 to 20 %. A strain of 1 % is selected for all subsequent rheological measurements. Figure 61A displays the evolution of the elastic modulus (G') and viscous modulus (G'') as a function of frequency (ranging from 0.01 to 10 Hz), with a strain of 1 % and a temperature of 37 °C, for hydrogels containing the KAASIKVAVSADR peptide. Figure 61B shows the evolution of the elastic modulus (G') and viscous modulus (G'') in a similar manner to that described above, but with the KPPFLMLLKGSTR peptide. Each hydrogel was subjected to a single test, which was performed in triplicate. The graph depicts the mean value of the three tests, along with the corresponding standard deviation. Although there is a frequency-dependent relationship with G', no significant relationship with G'' is observed. It is important to highlight that throughout the study, the value of G' consistently exceeded that of G'', indicating the presence of viscoelastic hydrogel behaviour.

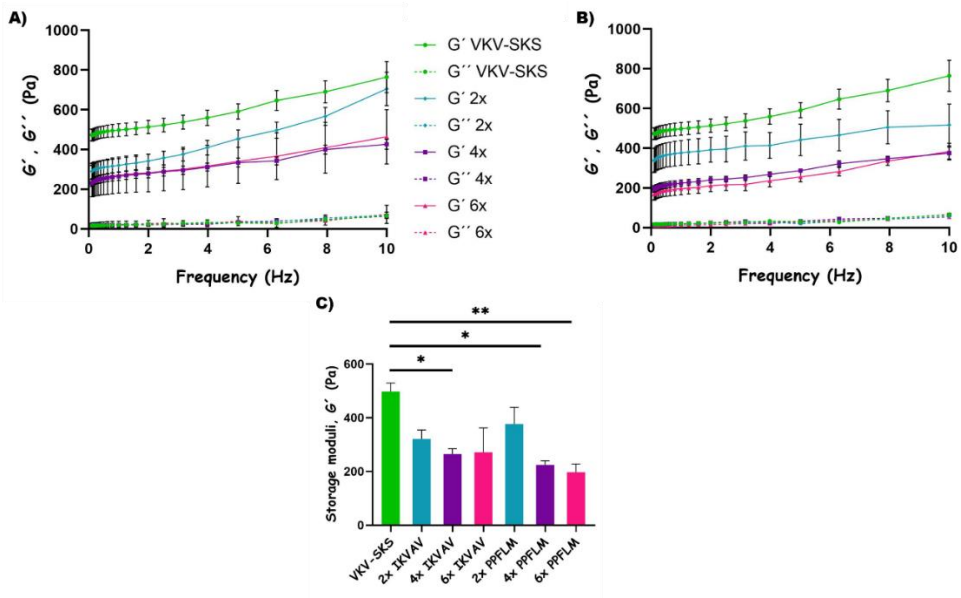

Figure 61: ***Assessment of the mechanical properties of a preformed biofunctionalized ELR hydrogel.*** ***A)*** *Evaluation of the evolution of the storage modulus (G') and loss modulus (G'') as a function of frequency of biofunctionalized click hydrogels with different KAASIKVAVSADR peptide concentrations (2X, 4X and 6X).* ***B)*** *Evaluation of the evolution of the storage modulus (G') and loss modulus (G'') as a function of frequency of biofunctionalized click hydrogels with different KPPFLMLLKGSTR peptide concentrations (2X, 4X and 6X).* ***C)*** *Average storage (G') and loss (G'') moduli measurement for different sample at a frequency of 1 Hz, a strain of 1 % and a temperature of 37 °C.*

Frequency sweep measurements are conducted at a frequency of 1 Hz, under a strain of 1 % and a temperature of 37 °C. The results indicate that the elastic modulus ranges from 200 to 350 Pa, while the viscous modulus ranges from 10 to 40 Pa, regardless of the peptide employed. These values are consistent with those obtained for the VKV-SKS hydrogels used as controls, with a value of approximately of 500 Pa. Figure 61C presents the mean values obtained for the different hydrogels under a frequency sweep condition of 1 Hz, with Table 33 providing a detailed specification of these values. The rheological properties of these hydrogels are consistent with the soft tissue engineering properties required for biomedical applications [433], [553].

Table 33: Average storage modulus (G') and loss modulus (G''), as measured on preformed biofunctionalized ELR hydrogel under frequency sweep mode at a frequency of 1 Hz and a temperature of 37 °C.

	KAASIKVAVSADR		KPPFLMLLKGSTR	
	G´ (Pa)	G´´ (Pa)	G´ (Pa)	G´´ (Pa)
VKV-SKS	497.5 ± 54.8	19.5 ± 3.0		
2X peptide	320.7 ± 58.4	21.6 ± 7.6	376.3 ± 108.1	20.4 ± 5.5
4X peptide	264.9 ± 34.8	19.6 ± 1.8	224.0 ± 27.4	19.7 ± 3.5
6X peptide	271.0 ± 158.2	23.3 ± 15.4	196.5 ± 52.9	12.7 ± 1.3

Consequently, the incorporation of both peptides at varying concentrations appears to moderately diminish the mechanical properties of the ELR hydrogels. Although the hydrogels are designed with a constant 1:1 ratio of azides to cyclooctynes for a final concentration of 50 mg/mL, the number of cyclooctynes and azides forming bonds in each type of hydrogel varies slightly, as shown in Table 31. This implies that for hydrogels comprising two grafted peptides, a total of 12 azide-cyclooctyne bonds are formed. Similarly, for hydrogels with four grafted peptides,

10 azide-cyclooctyne bonds are formed, while for hydrogels with six grafted peptides, 8 azide-cyclooctyne bonds are formed per macromolecule in all cases. Consequently, despite maintaining the ratio of azides to cyclooctynes constant, the number of available cyclooctynes for cross-linking and gel formation increases with a reduction in the number of grafted peptides. Thus, the degree of cross-linking between polymer chains diminishes as the quantity of grafted peptides increases, resulting in the formation of softer hydrogels with a reduced storage modulus. This phenomenon is clearly evident in the case of the peptide KPPFLMLLKGSTR, where the storage modulus (G') decreases as the peptide concentration increases. This indicates that the hydrogel becomes softer with an increase in peptide concentration. A similar tendency is noticed with the introduction of the KAASIKVAVSADR peptide. Conversely, as anticipated, the hydrogel with the most robust mechanical properties is the control hydrogel VKV-SKS, which exhibits the highest elastic modulus (G') among all the hydrogels studied. This is due to the hydrogel having the its highest number of cross-links, with 18 cross-linking groups, which results in the densest network. Statistically significant differences were observed in the mechanical properties of the VKV-SKS control hydrogel in comparison to the hydrogels containing four KAASIKVAVSADR peptides, four KPPFLMLLKGSTR peptides, and six KPPFLMLLKGSTR peptides.

The values obtained are comparable to those achieved with click technology, where elastic moduli in the range of 1 to 10 kPa are of great interest in tissue engineering applications, as many native tissues have moduli in this range. For example, very soft tissues, such as adipose tissue or brain, exhibit a modulus of approximately 100 Pa, whereas muscle tissue has a modulus of approximately 10000 Pa [433], [553]. As demonstrated in the aforementioned study, the mechanical properties of hydrogels can be modulated by varying their final concentration, allowing for the mimicking of diverse tissues. This mechanical performance, in conjunction with the porosity of the scaffolds, suggests potential applications of these biofunctionalized click hydrogels in skin regeneration.

3.2.1.3.3.5.- Water content percentage of biofunctionalized hydrogels

The determination of the water content percentage (WCP) is crucial for the characterisation of a hydrogel, as it is intimately related to several other properties. A higher water retention is generally more suitable for medical applications, as it indicates a greater permeability and biocompatibility of hydrogels [494]. Nevertheless, high water absorption has the effect of reducing the mechanical properties of the hydrogel, thus necessitating the identification of an optimal compromise. In ultrapure water, all hydrogels with varying peptide concentrations have a water content above 93 % after reaching equilibrium at a concentration of 50 mg/mL, as illustrated in Figure 62A. In their dry state, elastin hydrogels are solid and hard materials. However, upon immersion in an aqueous solution, water diffuses into their interior, resulting in significant water absorption by the hydrogels. This water migrates within the spaces of the hydrogel chains until a physicochemical equilibrium is reached. Moisture within these hydrogels has been demonstrated to promote wound healing by regulating the hydration of the wound,

which in turn facilitates homogeneous skin regeneration without material shrinkage.

A)

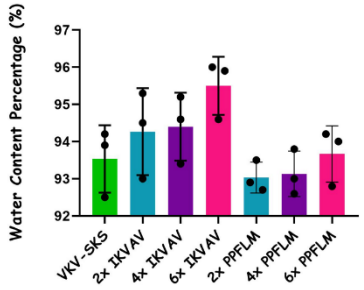

B)

	KAASIKVAVSADR	KPPFLMLLKGSTR
	WCP (%)	WCP(%)
VKV-SKS	93.5 ± 0.9	
2X peptide	94.3 ± 1.2	93.0 ± 0.4
4X peptide	94.4 ± 0.9	93.1 ± 0.6
6X peptide	95.4 ± 0.7	93.7 ± 0.8

*Figure 62: **Water content percentage (WCP). A)** Water content percentage of biofunctionalized click hydrogels with different peptide concentrations (2X, 4X and 6X). **B)** Mean values of WCP in ultrapure water following reaching equilibrium.*

As depicted in Figure 62A, there is a slight correlation between the number of peptides introduced and the water content, as it increases with an increasing number of peptides. This is reasonable and aligns with the variations in the degree of cross-linking deduced previously in each case. A higher degree of cross-linking results in greater structural rigidity and therefore a reduced capacity to retain water within its structure. However, no statistically significant differences are observed within each peptide series or with respect to the control hydrogel VKV-SKS. Figure 62B represent the mean values for the water content percentage. It is evident that the type of peptide used has a slight effect on the water content. As previously stated in this chapter, the KAASIKVAVSADR peptide has a higher average hydrophilicity than the KPPFLMLLKGSTR peptide, with values of 0.45 and -0.02, respectively. Consequently, hydrogels comprising the KAASIKVAVSADR peptide exhibit higher water content values, as the swelling of hydrogels depends on their hydrophilicity. An increase in the hydrophilic monomer content results in an enhanced affinity for water molecules, thereby facilitating the interaction between the hydrogel and aqueous solutions [495].

3.2.1.3.3.6.- In vitro characterisation of laminin mimetic peptides hydrogels

3.2.1.3.3.6.1.- Effect of laminin mimetic peptides on cell adhesion

A cell adhesion assay is conducted to investigate the role of laminin mimetic peptides, KAASIKVAVSADR and KPPFLMLLKGSTR, anchored to VKV-cc polymer, as well as their concentration, in the adhesion and proliferation process of HFF-1 and HaCaT cells according to the previously described protocol [461]. In order to achieve this purpose, the cells are seeded onto wells that have been previously coated with VKV-cc polymer functionalised with different peptide concentrations. Following a three-hour incubation period, the cells are fixed and stained with crystal violet, as illustrated in Figure 63A for HFF-1 cells and Figure 63B for HaCaT cells. The early adhesion of fibroblasts to the different functionalised surfaces indicates a slight adhesion-stimulating effect for all polymers, both those containing the KAASIKVAVSADR peptide and those containing KPPFLMLLKGSTR, in comparison to the control polymer VKV-cc. This latter polymer exhibits a lack of any adhesion

sequence and shows a reduced ability to anchor to the cells. Moreover, no consistent correlation was observed between the number of peptides anchored to VKV-cc and the degree of adhesion. With regard to the early adhesion of keratinocytes, it can be observed that the use of polymers containing the KPPFLMLLKGSTR peptide exhibits a clear stimulatory effect when compared to the VKV-cc polymer and those containing the KAASIKVAVSADR peptide. In particular, a significant improvement in HaCaT cell adhesion is noticed at concentrations of 2X and 6X. It can therefore be concluded that the presence of the KPPFLMLLKGSTR peptide enhances cell adhesion and subsequent proliferation of keratinocytes. This suggests that the peptides remain accessible for cell contact when anchored to the polymers, which facilitates the formation of an optimal cell adhesive matrix. Additionally, the development of patches comprising this peptide may facilitate the healing of chronic wounds. This is because the peptide with the ELR has the potential to attract cells from the wound margins and encourage the growth of the two cell types most relevant in the healing process: fibroblasts and keratinocytes [582].

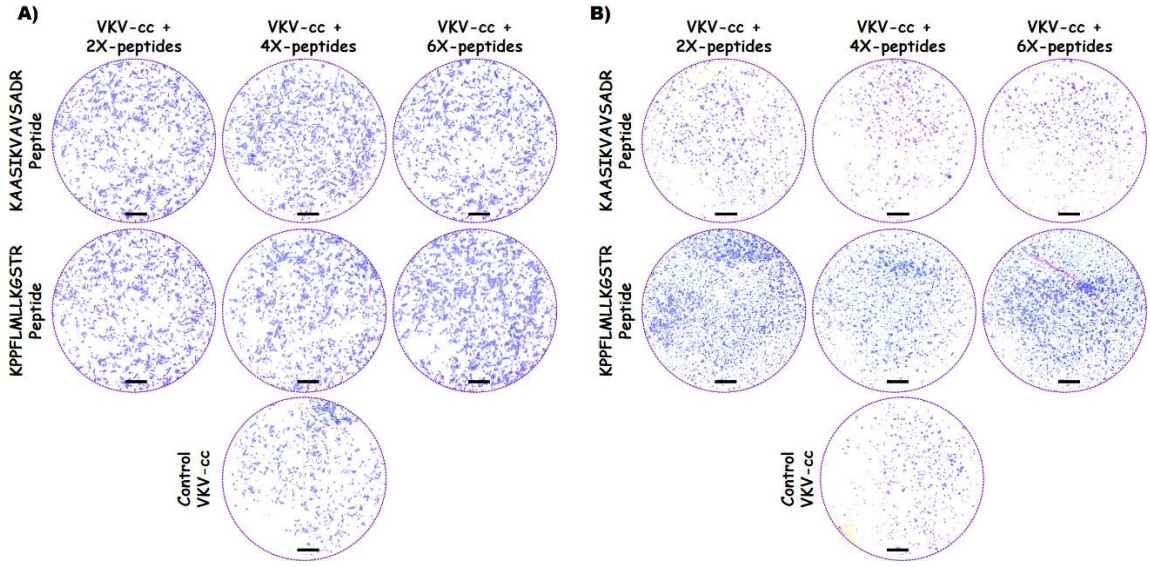

Figure 63: ***Effect of varying concentrations (2X, 4X and 6X) of adhesion domains (AASIKVAVSADR and PPFLMLLKGSTR) on cell adhesion and proliferation. A)*** *Representative images of crystal violet-stained fibroblasts adhered to a surface coated with VKV-cc with different concentrations of KAASIKVAVSADR and KPPFLMLLKGSTR peptide (2X, 4X and 6X).* ***B)*** *Representative images of crystal violet-stained keratinocytes adhered to a surface coated with VKV-cc with different concentrations of KAASIKVAVSADR and KPPFLMLLKGSTR peptide (2X, 4X and 6X). Scale bar: 0.5 mm.*

3.2.1.3.3.6.2.- Biocompatibility and cytotoxicity

The biocompatibility of novel biofunctionalized tricomponent elastin hydrogels is evaluated through the utilisation of AlamarBlue, a non-toxic cell viability indicator. The data obtained from the assay is recorded at several time points (1, 3, 7, and 14 days) in order to gain a deeper insight into the metabolic processes of the HFF-1 and HaCaT cells in a static culture. The analysis of cell viability demonstrates a direct correlation between increased metabolic activity and an increase in fluorescence intensity for all conditions at various time points. This is presented in Figure 64A for fibroblasts and Figure 64B for keratinocytes. The viability assay curve exhibits the typical pattern of cell growth, whereby the number of cells increases exponentially over time until reaching its maximum value on the

final day of culture, when the highest number of cells is present in hydrogels. The biocompatibility demonstrated by these new biofunctionalized ELR hydrogels is consistent with that observed in analogous cross-linked hydrogels that have been previously reviewed [582].

In the context of fibroblast adhesion, the initial adhesion is found to be superior in hydrogels containing varying concentrations of KPPFLMLLKGSTR, and in the control hydrogel VKV-SKS. Nevertheless, the rate of cell growth is not uniform in these hydrogels, as cell viability appears to decrease slightly on the third day in all cases. In contrast, despite a reduction in the initial adhesion of fibroblasts to hydrogels with varying concentrations of KAASIKVAVSADR, cell growth and viability remain constant over time, indicating the capacity to proliferate and ultimately reach maximum levels of cell viability after 14 days of culture. Conversely, it is evident that the KPPFLMLLKGSTR peptide exhibits specificity when working with keratinocytes, as more keratinocytes initially adhere to hydrogels containing this peptide. Of particular significance is the hydrogel comprising six anchored peptides. Moreover, keratinocytes seeded in hydrogels containing this peptide demonstrate the ability to proliferate over time and reach maximum levels of cell viability after 14 days of culture.

In conclusion, the KPPFLMLLKGSTR sequence results in a notable enhancement in keratinocyte adhesion, while fibroblast adhesion behaviour is comparable to that of the control. The KAASIKVAVSADR sequence does not appear to induce an improvement in either cell type, and its behaviour is similar to that of the control, which also contains RGD cell adhesion sequences.

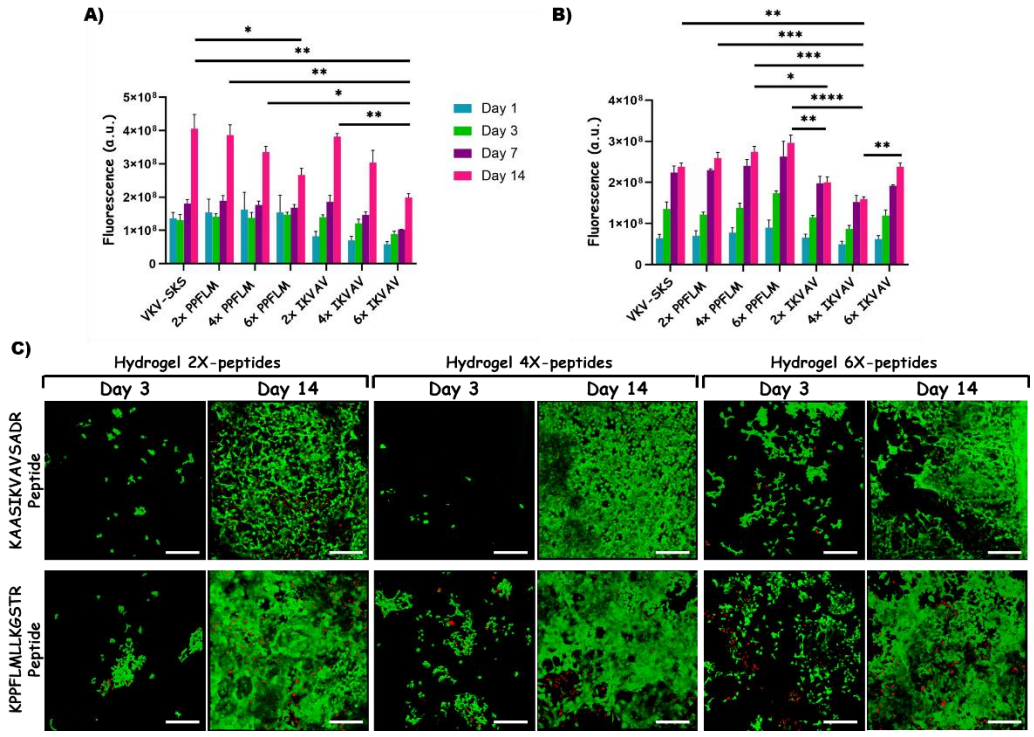

*Figure 64: **Biocompatibility and cytotoxicity**. **A)** Reduction of AlamarBlue by HFF-1 cells seeded onto biofunctionalized click hydrogels at different time points. **B)** Reduction of AlamarBlue by HaCaT cells seeded onto biofunctionalized click hydrogels at varying time points. **C)** Fluorescence L&D microscopy images of stained HaCaT*

cells, seeded on biofunctionalized click hydrogels with different peptide concentrations (2X, 4X and 6X) during a 14-day culture period. Green staining distinguished live cells, while red staining revealed cell death. Scale bar: 250 µm.

The cell viability and cytotoxicity of the novel biofunctionalized tricomponent hydrogels (VKV-peptide-SKS) were complemented through the use of LIVE/DEAD staining. Figure 64C displays projections of 3D fluorescence images captured with a confocal microscope, which confirm an increase in the number of HaCaT cells within hydrogels over time (3 and 14 days). Throughout the observation period, the majority of cells observed were alive (stained green), confirming that they were of a typical cell size and morphology. The presence of live cells was detected on both the surface and within the hydrogels, with a minimal number of dead cells (stained red). The findings suggest that the nutrients permeate the scaffold with ease, thereby ensuring the survival of the cells. The fluorescent images are in alignment with the previously obtained viability results. The cell viability assay, specifically AlamarBlue, confirmed an increase in the proliferation rate, reaching a peak on day 14 of the experiment. Furthermore, this increase is also evident in the fluorescent images.

Hydrogels containing the KPPFLMLLKGSTR peptide demonstrated a greater preference for HaCaT cells, as evidenced by the higher number of cells adhering to this type of hydrogel after three days of the experiment. Furthermore, it appears that hydrogels with the highest peptide concentration (6X) are the ones where the greatest number of cells have adhered, for both peptides. It is important to note that the KPPFLMLLKGSTR peptide plays a regulatory role in epithelial adhesion to the underlying connective tissue and enhances keratinocyte motility. It can therefore be concluded that these new hydrogels, which contain the KPPFLMLLKGSTR peptide, are capable of achieving good specificity towards keratinocytes when applied to a wound, thus accelerating re-epithelialisation and promoting wound healing [582].

In summary, this chapter presents the development of a novel tricomponent hydrogel (VKV-peptide-SKS) in which two laminin mimetic peptides, KAASIKVAVSADR and KPPFLMLLKGSTR, have been click-grafted to functionalise the elastin polymers. The results demonstrated a high affinity between HaCaT cells and ELR hydrogels, which was attributed to the inclusion of the peptide with the keratinocyte-specific adhesion sequence, KPPFLMLLKGSTR, which confers an improved adhesion of this type of cell to the hydrogels. However, the KAASIKVAVSADR peptide does not appear to confer any additional benefit in either of the two cell types, as its behaviour is similar to that of the control hydrogels, which also contain the RGD cell adhesion sequence. Additionally, the quantities of peptides that yielded the most favourable outcomes have been optimised, with the highest concentration of peptides (6X) per ELR molecule, eliciting the most pronounced benefits in terms of keratinocyte cell adhesion. Moreover, these hydrogels comprising six KPPFLMLLKGSTR peptides retain good transparency, an adequate water content, and favourable mechanical properties. These attributes, in conjunction with the inherent advantages of elastin, such as high biocompatibility, porosity, and an appropriate pore size, indicate that these novel hydrogels have the potential to serve as effective dressings for promoting the healing of challenging

wounds as they are capable of attracting cells from the wound margins and facilitating the proliferation of both fibroblasts and keratinocytes.

Nevertheless, this approach to obtaining hydrogels is highly laborious and time-consuming. This process requires the manual synthesis of peptides and the performance of numerous consecutive chemical reactions, accompanied by their corresponding purification processes. Furthermore, the degree of functionalisation of the hydrogels cannot be precisely controlled, which increases the variability of the results. Consequently, in the following chapter, the objective is to introduce the sequences of interest, AASIKVAVSADR and PPFLMLLKGSTR, via recombinant means through molecular biology. This approach will enhance productivity by facilitating the production of materials and enabling more precise control over the final sequence of the polymer, thereby reducing variability.

Appendix

KAASIKVAVSADR peptide

^{1}H NMR (400 MHz, DMSO-d6): 8.6-8.5, 8.2-8.1, 8.0-7.9, 7.8-7.7 (4 m, 12H,-NH-CO), 7.5, 7.2 and 7.1 (3s, 3H, NH-Arg), 5.1 and 5.0 (2 bs, 2H, HO-Ser), 4.5-3.4 (m, 22H, HN-CH-Val + HN-CH-Lys + HN-CH-Ala + HN-CH-Ser + CH_2-Ser + HN-CH-Ile + HN-CH-Asp + HN-CH-Arg + C*H*$_2$-NH-Arg), 3.1-3.0, 2.7-2.6 and 2.0-0.9 (three m, 44H, εCH_2-Lys, CH_2-Lys, H_2N-Lys, N*H*-CH2-Arg, C*H*$(CH_3)_2$-Val, CH_3-Ala, C*H*$(CH_3)_2$-Ile, CH_2-Ile and CH_2-Asp), 0.9-0.7 (m, 1602H, CH-C*H*$_3$-Ile, CH(C*H*$_3$)$_2$-Val).

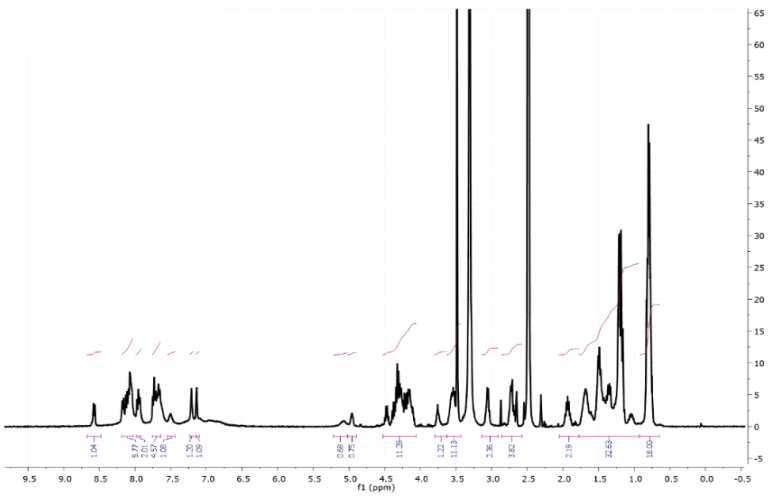

KPPFLMLLKGSTR peptide

^{1}H NMR (400 MHz, DMSO-d6): 8.2-7.8, 7.7-7.6 (2 m, 10H,-NH-CO), 7.5-7.4, 7.3-7.1 (2m, 8H, CH-arom-Phe, -NH-Arg), 5.2 and 5.0 (2 bs, 2H, HO-Ser, HO-Tre), 4.5-3.4 (m, 25H, HN-C*H*-Phe + HN-C*H*-Leu + HN-C*H*-Ser + HN-C*H*-Met + HN-C*H*-Lys + HN-C*H*-Tre + HN-C*H*-Arg + HN-C*H*$_2$-Gly + CH_2-Ser + C*H*$_2$-NH-Arg, HC-C*H*$_2$-Phe + + α-CH-Pro + δCH_2-Pro), 3.1-3.0, 2.7-2.6 and 2.0-0.9 (three m, 52H, εCH_2-Lys, CH_2-Lys, H_2N-Lys, β and γCH_2-Pro, C*H*$(CH_3)_2$-Leu, C*H*$_2$-Leu, C*H*$_2$-Met, C*H*$_2$-Arg), 0.9-0.7 (m, 18H, CH(C*H*$_3$)$_2$-Leu).

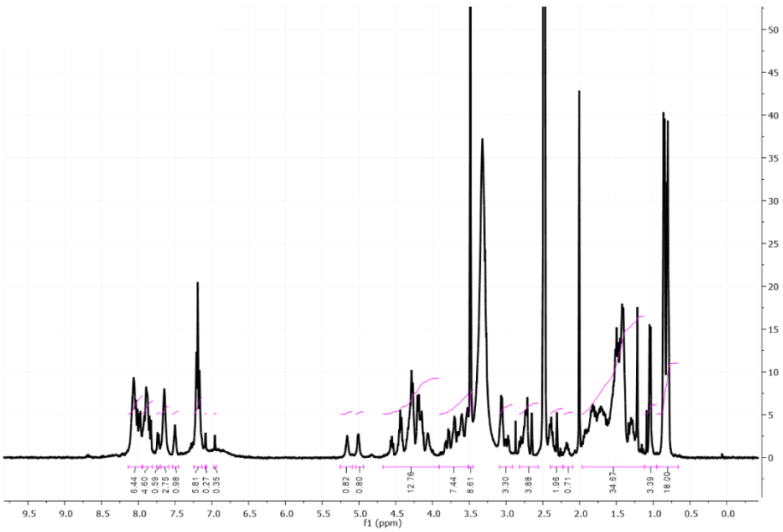

VKV-CC

^{1}H NMR (400 MHz, DMSO-d6): 8.2-7.6 (m, 582H, -NH-CO), 7.0 (s, 12H, -NH-CO-Lys), 4.4-3.5 (m, 1311H, CH-Val +α-CH-Pro + δCH_2-Pro + CH_2-Gly + CH-Lys), 2.9 and 2.7 (two m, 48H, εCH_2-Lys), 2.2-1.1 (m, 1108H, β and γCH_2-Pro, C*H*$(CH_3)_2$-Val and CH_2-Lys), 0.9-0.7 (m, 1602H, CH(C*H*$_3)_2$-Val).

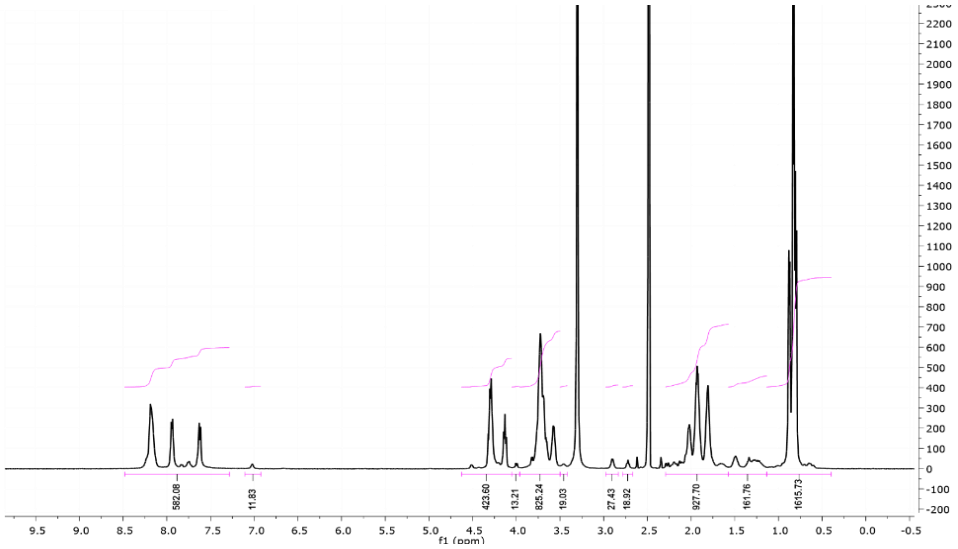

VKV-2X-KAASIKVAVSADR

^{1}H NMR (400 MHz, DMSO-d6): 8.2-7.6 (m, 606H,-NH-CO), 7.0 (s, 12H, -NH-CO-Lys), 7.4-7.0 (m, 6H, -NH-Arg), 4.4-3.5 (m, 1355H, CH-Val + α-CH-Pro + δCH_2-Pro + CH_2-Gly + CH-Lys + CH_2-Ser + C*H*$_2$-NH-Arg), 2.9 and 2.7 (two m, 48H, εCH_2-Lys), 2.2-1.1 (m, 1202H, β and γCH_2-Pro + C*H*$(CH_3)_2$-Val + CH_2-Lys + C*H*$(CH_3)_2$-Ile + CH_2-Ile + CH_2-Asp + CH_3-Ala + $(CH_2)_2$-Arg), 0.9-0.7 (m, 1632H, CH(C*H*$_3)_2$-Val).

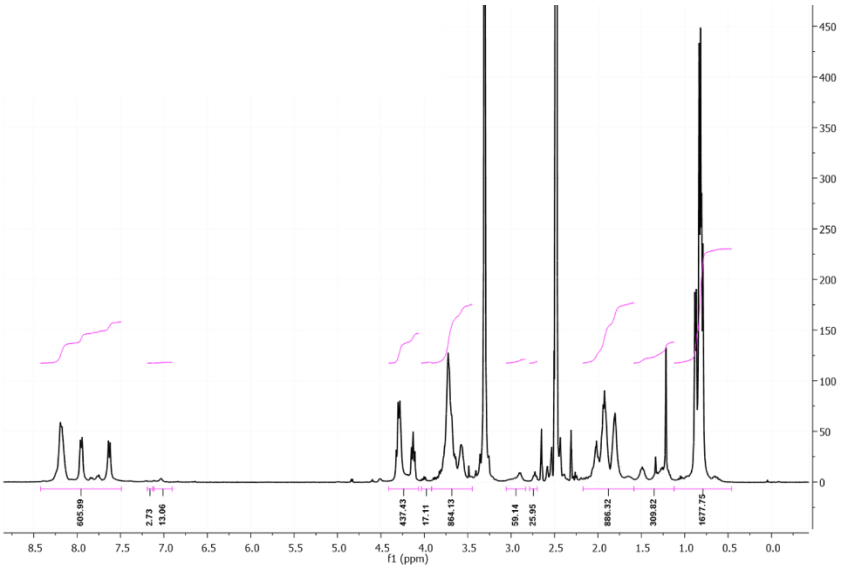

VKV-4X-KAASIKVAVSADR

^{1}H NMR (400 MHz, DMSO-d6): 8.2-7.6 (m, 630H,-NH-CO), 7.0 (s, 12H, -NH-CO-Lys), 7.4-7.0 (m, 12H, -NH-Arg), 4.4-3.5 (m, 1399H, CH-Val + α-CH-Pro + δCH_2-Pro + CH_2-Gly + CH-Lys + CH_2-Ser + C*H_2*-NH-Arg), 2.9 and 2.7 (two m, 48H, εCH_2-Lys), 2.2-1.1 (m, 1202H, β and γCH_2-Pro + C*H*$(CH_3)_2$-Val + CH_2-Lys + C*H*$(CH_3)_2$-Ile + CH_2-Ile + CH_2-Asp + CH_3-Ala + $(CH_2)_2$-Arg), 0.9-0.7 (m, 1662H, CH(C*H_3*$)_2$-Val).

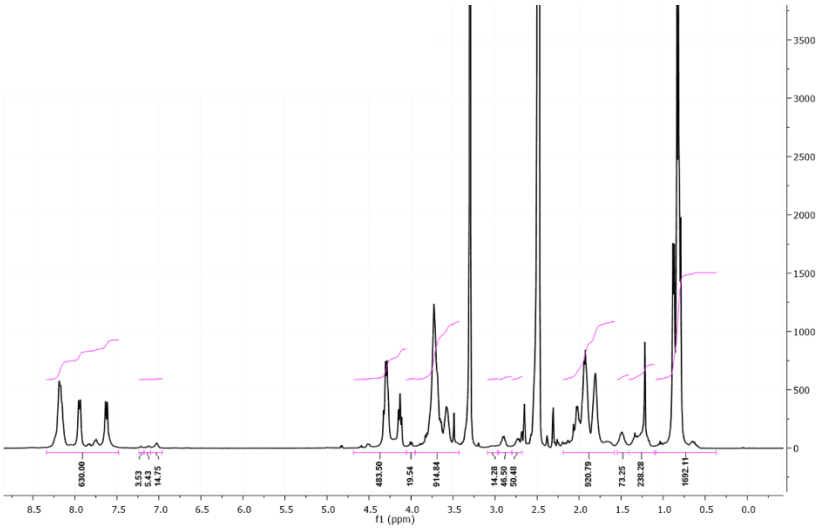

VKV-6X-KAASIKVAVSADR

^{1}H NMR (400 MHz, DMSO-d6): 8.2-7.6 (m, 654H,-NH-CO), 7.0 (s, 12H, -NH-CO-Lys), 7.4-7.0 (m, 18H, -NH-Arg), 4.4-3.5 (m, 1443H, CH-Val +α-CH-Pro + δCH_2-Pro + CH_2-Gly + CH-Lys + CH_2-Ser + C*H_2*-NH-Arg), 2.9 and 2.7 (two m, 48H, εCH_2-Lys), 2.2-1.1 (m, 1202H, β and γCH_2-Pro + C*H*$(CH_3)_2$-Val + CH_2-Lys + C*H*$(CH_3)_2$-Ile + CH_2-Ile + CH_2-Asp + CH_3-Ala + $(CH_2)_2$-Arg), 0.9-0.7 (m, 1692H, CH(C*H_3*$)_2$-Val).

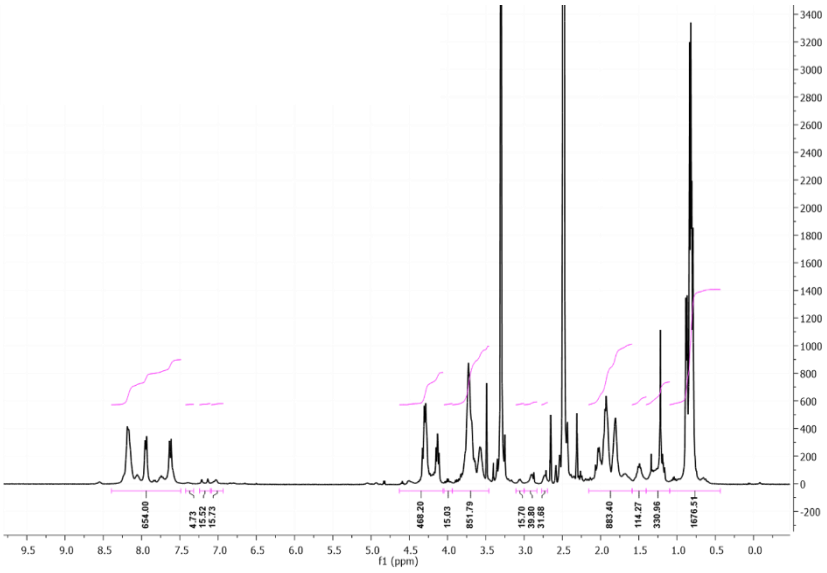

VKV-2X-KPPFLMLLKGSTR

^{1}H NMR (400 MHz, DMSO-d6): 8.2-7.6 (m, 602H,-NH-CO), 7.0 (s, 12H, -NH-CO-Lys), 7.2-6.5 (m, 16H, CH-arom-Phe and -NH-Arg) 4.4-3.5 (m, 1361H, CH-Val + α-CH-Pro + δCH_2-Pro + CH_2-Gly + CH-Lys, CH_2-Phe and C*H_2*-NH-Arg), 2.9 and 2.7 (two m, 48H, εCH_2-Lys), 2.2-1.1 (m, 1212H, β and γCH_2-Pro, C*H*$(CH_3)_2$-Val, C*H*$(CH_3)_2$-Leu, CH_2-Leu, CH_3-Thr, CH_3-Met, CH_2-Met, -$(CH_2)_2$-Leu and CH_2-Lys), 0.9-0.7 (m, 1638H, -Val, CH(C*H*$_3)_2$-Leu).

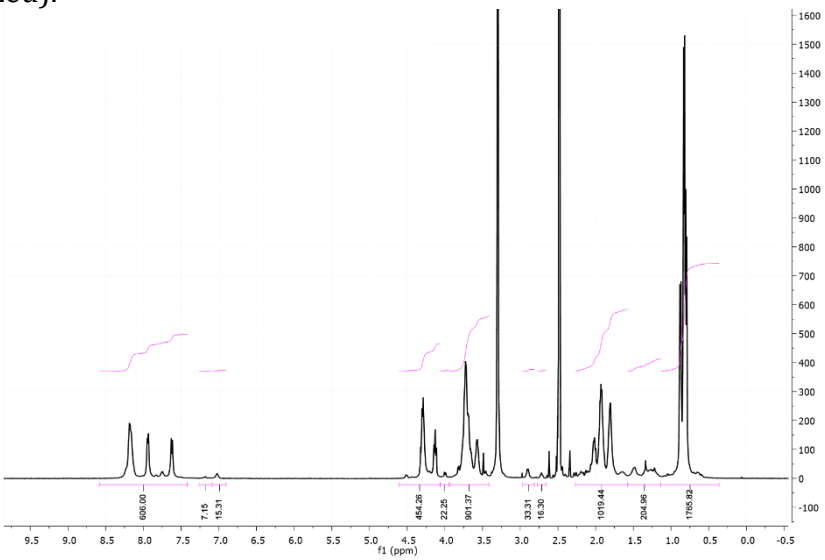

VKV-4X-KPPFLMLLKGSTR

^{1}H NMR (400 MHz, DMSO-d6): 8.2-7.6 (m, 622H,-NH-CO), 7.0 (s, 12H, -NH-CO-Lys), 7.2-6.5 (m, 32H, CH-arom-Phe and -NH-Arg) 4.4-3.5 (m, 1411H, CH-Val +α-CH-Pro + δCH_2-Pro + CH_2-Gly + CH-Lys, CH_2-Phe and C*H_2*-NH-Arg), 2.9 and 2.7 (two m, 48H, εCH_2-Lys), 2.2-1.1 (m, 1316H, β and γCH_2-Pro, C*H*$(CH_3)_2$-Val, C*H*$(CH_3)_2$-Leu, CH_2-Leu, CH_3-Thr, CH_3-Met, CH_2-Met, -$(CH_2)_2$-Leu and CH_2-Lys), 0.9-0.7 (m, 1674H, -Val, CH(C*H*$_3)_2$-Leu).

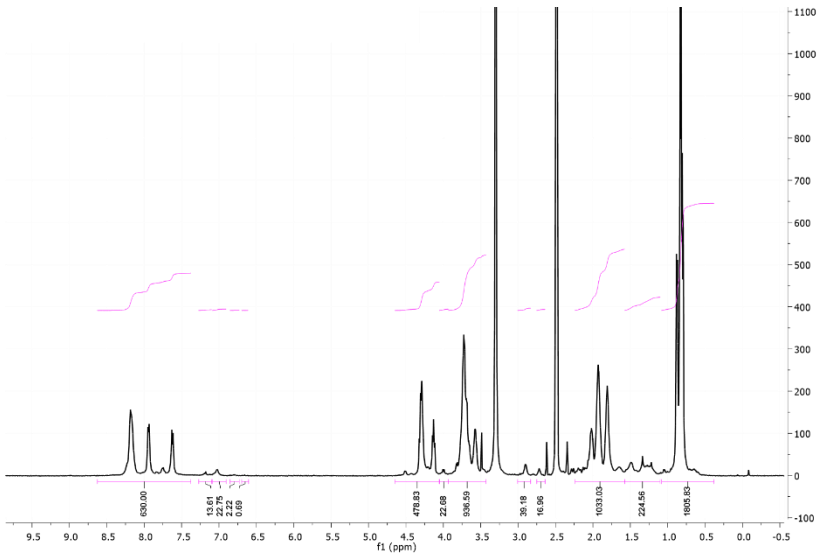

VKV-6X-KPPFLMLLKGSTR

^{1}H NMR (400 MHz, DMSO-d6): 8.2-7.6 (m, 642H,-NH-CO), 7.0 (s, 12H, -NH-CO-Lys), 7.2-6.5 (m, 48H, CH-arom-Phe and -NH-Arg) 4.4-3.5 (m, 1461H, CH-Val + α-CH-Pro + δCH_2-Pro + CH_2-Gly + CH-Lys, CH_2-Phe and C*H_2*-NH-Arg), 2.9 and 2.7 (two m, 48H, εCH_2-Lys), 2.2-1.1 (m, 1420H, β and γCH_2-Pro, C*H*$(CH_3)_2$-Val, C*H*$(CH_3)_2$-Leu, CH_2-Leu, CH_3-Thr, CH_3-Met, CH_2-Met, -$(CH_2)_2$-Leu and CH_2-Lys), 0.9-0.7 (m, 1710H, -Val, CH(C*H*$_3)_2$-Leu).

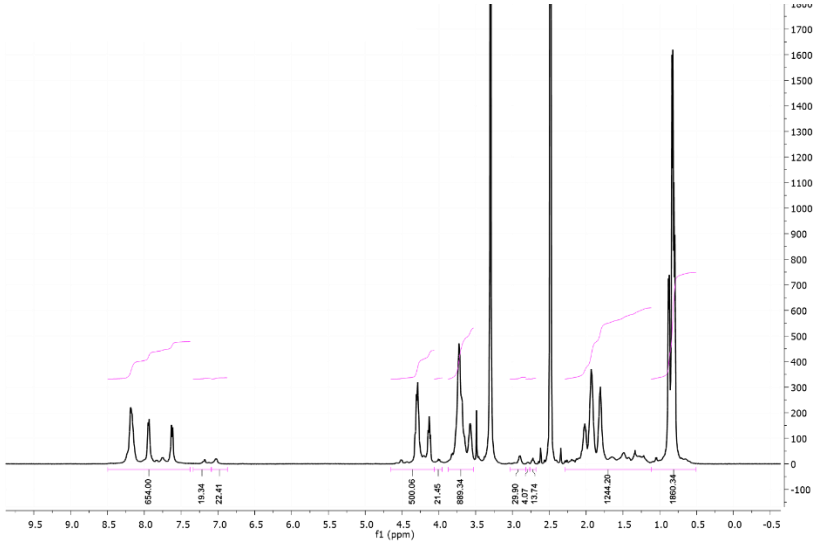

3.2.2.- Synthesis and characterisation of biofunctionalized hydrogels by inclusion of the laminin gene into the backbone of elastin polymers

3.2.2.1.- Laminin mimetic sequence selection

The studies conducted in the preceding section of this thesis have yielded a substantial amount of information regarding the capacity of the sequences AASIKVAVSADR and PPFLMLLKGSTR to facilitate the adhesion and proliferation of fibroblasts and keratinocytes, which could potentially enhance the wound healing process. As previously stated, the sequence AASIKVAVSADR is situated within the globular region of the long α-chain of laminin 1, where it performs a variety of functions, including cell adhesion, differentiation, and migration, by binding to α3β1, α4β1, and α6β1 integrins. The sequence PPFLMLLKGSTR is present in the globular domain (LG3) of the α3-chain of laminin 5 and regulates the adhesion of epithelium to underlying connective tissue and interacts with cell surface receptors such as α3β1 integrins to promote keratinocyte motility, accelerating re-epithelialisation and aiding wound healing. In the initial approach, these sequences bind to the polymer via a click reaction between the cyclooctyne group of the polymer and the azide group of the desired peptides. One of the major advantages of ELRs is their recombinant character, which allows for the modification of their sequence to substitute some of their amino acids to modulate possible cross-linking or to include specific sequences of interest in their main backbone. In this way, it can be anticipated that the incorporation of laminin sequences within the same amino acid chain of an ELR will result in a more precise final composition of the polymer, thereby enhancing the specificity for certain cells compared to grafting through a chemical reaction. Furthermore, the advantages of recombinant technology can be leveraged to improve productivity by facilitating the production of materials and reducing the time required.

In light of this hypothesis and based on the previously obtained polymer SKS [436], several novel ELR polymers have been developed with the objective of improving the specificity of adhesion and proliferation processes in keratinocytes and fibroblasts, which are the cells of interest during wound healing. In the preceding section, it was determined that the optimal concentration of these laminin-specific adhesion motifs, exhibiting the most favourable outcomes, is the highest concentration (6X). Consequently, in this section, the specific sequences AASIKVAVSADR and PPFLMLLKGSTR will be recombinantly introduced into the main chain of the initial SKS polymer at the optimised concentration in order to develop new polymers with new biological functionalities and hopefully improved properties.

The initial approach involved the independent introduction of each of the sequences in the initial SKS polymer backbone, with the aim of replacing the general cell adhesion sequence RGD with the specific sequences of interest AASIKVAVSADR and PPFLMLLKGSTR. This resulted in the generation of two independent polymers, referred to as SKS-IKVAV and SKS-PPFLM, respectively, with six repetitions of the sequence of interest, as illustrated in Figure 65A.

Figure 65: ***Amino acid composition of the novel polymers SKS-IKVAV, SKS-PPFLM and SKS-IKVAV-PPFLM.***

Conversely, a polymer is obtained that contains both sequences within the same main backbone. For this purpose, a VPGKG group from the original polymer SKS is replaced by the sequence of interest, AASIKVAVSADR, while maintaining the number of amino acids K constant. However, to introduce the sequence PPFLMLLLKGSTR, it is preferable to replace it with a GGGGS spacer, as if it were replaced by another VPGKG group, all the lysines that serve for the introduction of cross-linkable groups would be lost, and therefore the polymer would be unable to form gels. It is preferable that the two sequences, AASIKVAVSADR and PPFLMLLKGSTR, are separated in space to prevent interference with their respective functionalities. Furthermore, the functionality of the general cell adhesion RGD motif is preserved. The proposed design would result in the optimal concentration of keratinocyte-specific binding sequences, PPFLMLLLLKGSTR, with six repeats, and the addition of twice the concentration of the AASIKVAVSADR sequence with a total of 12 repeats. This would guarantee that, in the event that any of these lysines are employed for cross-linking, the complete functionality of the sequence would remain intact. The aforementioned process results in the synthesis of a novel polymer, designated SKS-IKVAV-PPFLM, as illustrated in Figure 65B.

3.2.2.2.- Gene construction

The final genes are obtained through the recursive directional ligation (RDL) technique, which involves the sequential introduction of repetitive segments of the polypeptide coding gene to form fusion genes with a controlled final composition [416], [592]. In all three cases, SKS-IKVAV, SKS-PPFLM and SKS-IKVAV-PPFLM, the initial coding genes for the ELR sequences were purchased from an external

company (NZYTech, Portugal). Subsequently, the final gene (with six repeats) encoding the polymer with the desired sequences is obtained through molecular biology. The general procedure for obtaining the desired genes following this methodology is illustrated in Figure 66. Steps A, B, C and D are conducted in succession and repeatedly using restriction enzymes that leave cohesive and complementary ends in a pDrive cloning plasmid until the final gene is obtained. Subsequently, the aforementioned gene is introduced into a p7RARE expression plasmid in order to obtain the polymer, as displayed in step E.

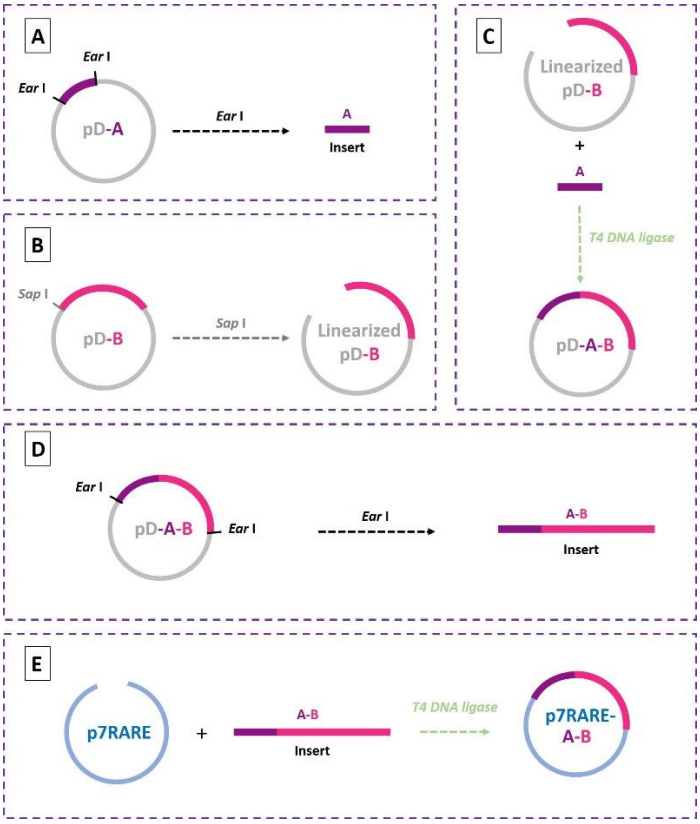

Figure 66: ***Schematic representation of the cloning strategy employed for obtaining the final gene construction****, with the actions taken outlined.* ***A)*** *The pD cloning vector, which contains the gene fragment of interest (A), is digested using EarI in order to obtain the A insert.* ***B)*** *The pD cloning vector, comprising the gene fragment of interest (B), is digested with SapI to generate the linearized pD-B plasmid.* ***C)*** *The linearized pD-B plasmid is ligated with the A insert using T4 DNA ligase to produce the new plasmid, pD-A-B.* ***D)*** *The pD-A-B plasmid is subjected to digestion with EarI, thereby yielding the A-B-ELR gene coding insert.* ***E)*** *The final gene construction is introduced into an expression vector (p7RARE) in order to achieve protein expression.*

3.2.2.3.- Gene construction of SKS-IKVAV and SKS-PPFLM

The recombinant SKS-IKVAV and SKS-PPFLM genes are synthesized in parallel at each step of the process in order to optimise the utilisation of resources. This section was carried out with the assistance of Salomé Carneiro, a Master's student.

3.2.2.3.1.- Cloning vector pDrive All

The cloning vector employed in this thesis is pDrive All, which we will refer to as pD from now on, provided by the Bioforge research group. Figure 67A shows the restriction map of the pD plasmid, indicating the cleavage points for the *EarI* and *SapI* enzymes, as well as the number of base pairs comprising this vector, which is 3938 bp.

Consequently, it is necessary to clone the pD vector in order to subsequently insert the first fragment of the SKS-IKVAV or SKS-PPFLM genes and to be able to carry out all the molecular biology steps until the desired final gene is obtained. For this purpose, the pD plasmid is inserted into competent cells by transformation into XL1-Blue subcloning cells. Following purification, the concentration and purity of several colonies are analysed. The results are presented in Table 34.

Table 34: Concentration (ng/µL) and degree of purity of pD plasmids after purification.

Sample	Concentration (ng/µL)	260/280	260/230
pD 1	534.8	1.88	1.22
pD 2	433.0	1.90	1.43
pD 3	568.7	1.89	1.32

The results confirmed that all the samples exhibit and adequate concentration and purity of DNA, as evidenced by their 260/280 ratio. Furthermore, these samples are devoid of contaminants, as the 260/230 ratio has values lower than 1.5. In order to perform the initial insertion of the gene fragments of interest, the pD3 sample with the highest DNA concentration is selected. Subsequently, the vector is subjected to a rapid digestion with the *EarI* enzyme in order to verify the characteristic bands after analytical electrophoresis in an agarose gel (1 %) as is observed in Figure 67B.

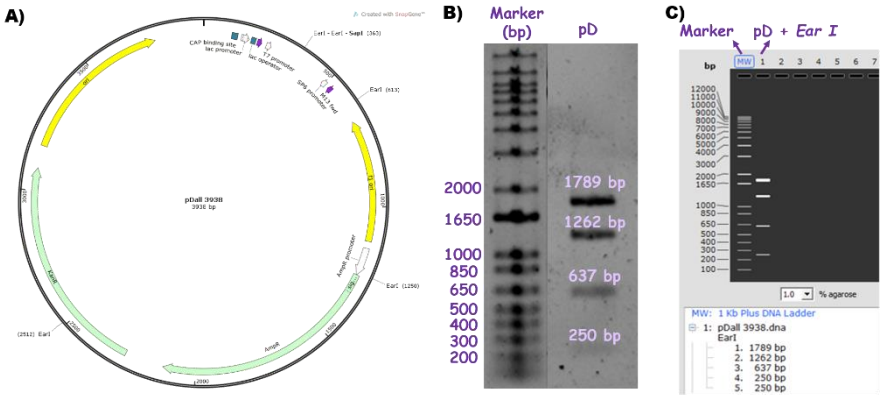

*Figure 67: **Subcloning of the pD plasmid. A)** Restriction map of the pD plasmid, where the cleavage sites for EarI and SapI enzymes are specified. **B)** Analytical agarose gel electrophoresis (1 %) of the pD vector digested with EarI endonuclease (Image Lab™). **C)** Theoretical restriction map of the pD vector, digested with EarI using the SnapGene® software.*

The selected colony exhibits all the expected bands of the pD vector when compared to the theoretical values of the restriction map obtained with the SnapGene® software after digestion with *EarI*, as is displayed in Figure 67C. This result is verified by sequencing with the primers T7 and Sp6, after which the colony is selected for the subsequent stage. The pD plasmid is linearised by preparative

digestion with *SapI* endonuclease, dephosphorylated with FastAP, and the resulting bands are observed after preparative agarose gel electrophoresis (1 %) as shown in Figure 68A. While the band corresponding to the linearised pD vector is present on the experimental agarose gel at 3938 bp, another band is observed between 2000 and 3000 bp. This band indicates that the linearisation is not complete, corresponding to one of the isoforms of the non-linearised vector. Subsequently, the plasmid digestion is compared with the theoretical value of 3938 bp of the restriction map obtained with the SnapGene® software after digestion with *SapI*, as observed in Figure 68C. Once the correct linearisation of the vector has been confirmed, the band corresponding to the linearised pD vector is excised as illustrated in Figure 68B.

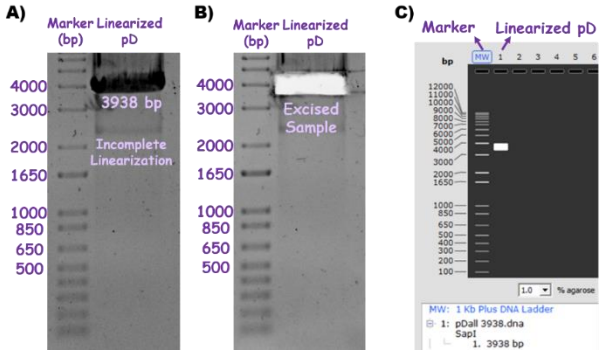

Figure 68: ***Linearisation of the pD plasmid. A)*** *Preparative agarose gel (1 %) electrophoresis of the pD vector, digested with SapI endonuclease (Image Lab™).* ***B)*** *Excision of the band corresponding to the linearized pD vector (Image Lab™).* ***C)*** *Theoretical restriction map of the pD vector, digested with SapI using the SnapGene® software.*

Following the removal of the DNA from the agarose gel, a second dephosphorylation with SAP is performed in order to prevent the ends from closing. Subsequently, the concentration and purity of the vector are then measured. The results are presented in Table 35.

Table 35: Concentration (ng/µL) and degree of purity of linearized pD plasmid.

Sample	Concentration (ng/µL)	260/280	260/230
Linearized pD	50.0	1.95	1.49

All samples were found to exhibit satisfactory levels of DNA concentration and purity. At this juncture, the pD vector is prepared for the insertion of the gene fragments of interest.

3.2.2.3.2.- SKS-IKVAV and SKS-PPFLM inserts

The initial coding genes for SKS-IKVAV and SKS-PPFLM were purchased from NZYTech with a single repeat. In order to obtain the final gene, six repeats of each amino acid sequence must be obtained. The delivery of these genes is conducted via pUC57 cloning plasmids, which exhibit ampicillin resistance and contain three *SapI* restriction sites. The coding gene of interest is situated between two of these sites. The pUC57 vector is 2710 base pairs in length.

In order to prepare the SKS-IKVAV and SKS-PPFLM inserts, the commercial plasmid pUC57-SKS-IKVAV and the commercial plasmid pUC57-SKS-PPFLM are transformed into XL1-Blue competent cells for subcloning of these vectors. Subsequently, three bacterial colonies are selected and the concentration and purity of the plasmids obtained after purification are analysed. The results are presented in Table 36.

Table 36: Concentration (ng/µL) and degree of purity of commercial plasmids with the SKS-IKVAV or SKS-PPFLM insert.

Sample	Concentration (ng/µL)	260/280
pUC57-SKS-IKVAV_1	576.1	1.89
pUC57-SKS-IKVAV_2	820.2	1.89
pUC57-SKS-IKVAV_3	658.9	1.86
pUC57-SKS-PPFLM_1	738.6	1.89
pUC57-SKS-PPFLM_2	626.1	1.86
pUC57-SKS-PPFLM_3	288.0	1.90

All samples exhibited a satisfactory degree of DNA concentration and purity. Consequently, the samples with the highest concentration are selected, namely pUC57-SKS-IKVAV_2 and pUC57-SKS-PPFLM_1. Subsequently, the plasmids are then subjected to digestion with the *SapI* endonuclease enzyme in order to extract the SKS-IKVAV and SKS-PPFLM gene inserts. This enzyme then cleaves the vector into smaller fractions, releasing the SKS-IKVAV or SKS-PPFLM gene fragment located between two *SapI* cleavage sites. This process results in an insert with a size of 456 bp for both genes. The resulting bands from this digestion are observed after preparative agarose gel electrophoresis (1 %), as shown in Figure 69A. This demonstrates the presence of the 2416 bp and 294 bp bands, which correspond to the plasmid without the insert cut with *SapI*, the 456 bp insert band and bands from the partially digested plasmid.

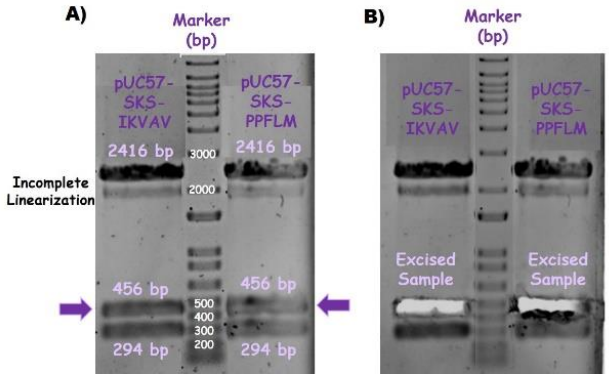

*Figure 69: **Extraction of the inserts. A)** Preparative agarose gel electrophoresis (1%) of the commercial plasmids pUC57-SKS-IKVAV and pUC57-SKS-PPFLM, digested with SapI endonuclease (Image Lab™). **B)** Excision of the bands corresponding to the SKS-IKVAV and SKS-PPFLM inserts (Image Lab™).*

Subsequently, the bands of interest are extracted from the agarose gel, as illustrated in Figure 69B, and the genes are then purified using a gel extraction microcentrifuge centrifuge column. The degree of concentration and purity of the obtained inserts is then evaluated, as displayed in Table 37.

Table 37: Concentration (ng/µL) and degree of purity of SKS-IKVAV and SKS-PPFLM inserts after purification.

Sample	Concentration (ng/µL)	260/280
SKS-IKVAV insert	11.7	1.68
SKS-PPFLM insert	8.3	2.25

3.2.2.3.3.- SKS-IKVAV and SKS-PPFLM genes insertion in the pDrive All plasmid

The ligation strategy is based on the joining of compatible adhesive ends obtained using the *SapI* enzyme for linearisation of the pD plasmid (previously dephosphorylated) and the *EarI* enzyme for obtaining ELR inserts. Ligation is performed using the enzyme DNA T4 ligase. The products of these reactions, pD-SKS-IKVAV and pD-SKS-PPFLM, are subsequently employed to transform into competent *E. coli*. A number of colonies are selected and tested to verify the introduction of the SKS-IKVAV and SKS-PPFLM inserts into the pD. In addition, the concentration and purity of the plasmids containing the inserts are evaluated, as illustrated in Table 38.

Table 38: Concentration (ng/µL) and degree of purity of the pD-SKS-IKVAV and pD-SKS-PPFLM plasmids.

Sample	Concentration (ng/µL)	260/280
pD-SKS-IKVAV_1	758.3	1.89
pD-SKS-IKVAV_2	711.4	1.90
pD-SKS-IKVAV_3	736.5	1.90
pD-SKS-IKVAV_4	688.7	1.91
pD-SKS-PPFLM_1	604.7	1.88
pD-SKS-PPFLM_2	596.4	1.89
pD-SKS-PPFLM_3	735.1	1.92
pD-SKS-PPFLM_4	705.8	1.90

All samples exhibited satisfactory levels of DNA concentration and high degrees of purity. Consequently, samples with the highest concentrations are selected, and pD-SKS-IKVAV_1 and pD-SKS-PPFLM_3 are chosen for the subsequent cloning steps. Furthermore, to ascertain the accuracy of the gene incorporation of the insert into the cloning vector, each plasmid is subjected to digestion with both the *EarI* and *EcoRI* enzymes. The resulting bands are then analysed in an analytical agarose gel (1 %), as illustrated in Figure 70A. Finally, the plasmid digestion is compared with the theoretical value of the restriction map obtained with the SnapGene® software, as presented in Figure 70B. Although bands corresponding to a repeat of the SKS-IKVAV or SKS-PPFLM genes (456 bp) and bands from the plasmid digestion with *EarI + EcoRI* (1733 bp, 1262 bp, 637 bp and 205 bp) are observed, other bands higher than 2000 bp are also found. These bands may be indicative of a non-linearised plasmid. Sequencing of the plasmids containing the genes revealed the correct insertion of the SKS-IKVAV and SKS-PPFLM genes into the pD vector.

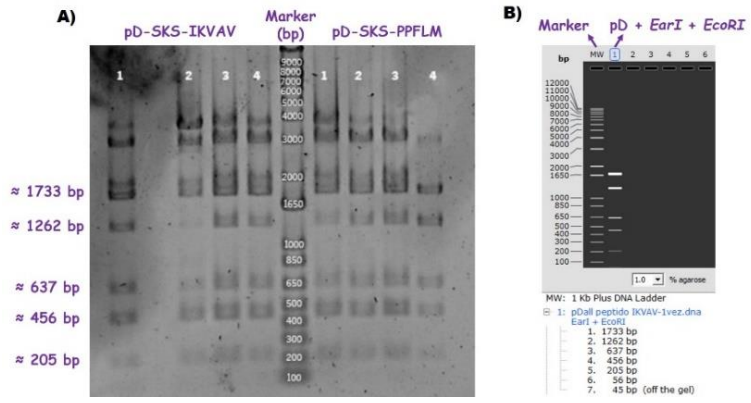

Figure 70: ***Verification of the plasmids obtained. A)*** *Analytical agarose gel electrophoresis (1 %) of the pD-SKS-IKVAV and pD-SKS-PPFLM plasmids, digested with the EarI and EcoRI endonuclease (Image Lab™).* ***B)*** *Theoretical restriction map of pD-insert vectors, digested with EarI and EcoRI using the SnapGene® software.*

Following the successful introduction of the SKS-IKVAV and SKS-PPFLM genes into the pD vector, the subsequent cloning steps entail amplifying the gene size by increasing the number of repeats until the six repeats constituting the final gene coding for the polymer of interest (SKS-IKVAV-6X and SKS-PPFLM-6X) are obtained. This is achieved in a sequential and consecutive manner through the iterative/recursive approach, which involves the steps of insert extraction with the *EarI* enzyme and subsequent introduction into a linearised and dephosphorylated plasmid treated with *SapI*.

The final constructs, pD-SKS-IKVAV-6X and pd-SKS-PPFLM-6X, are subjected to rapid digestion with *EcoRI* and *SspI* enzymes together in order to confirm the correct insertion of the inserts. The resulting bands are analysed by electrophoresis on an analytical agarose gel (1 %) as shown in Figure 71A. Finally, the plasmid digestion is compared with the theoretical value of the restriction map obtained with the SnapGene® software, as illustrated in Figure 71B. Upon analysis of the results obtained in the experimental agarose gel, all the bands of the theoretical pattern are identified, and two additional bands are observed between 3000 and 4000 bp, which may correspond to non-linearised isoforms of the samples. Subsequently, the selected plasmids are subjected to further sequencing, with the genetic sequences of the SKS-IKVAV-6X and SKS-PPFLM-6X genes being confirmed.

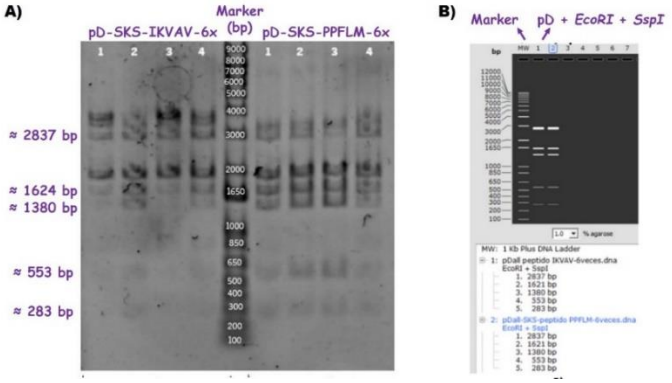

Figure 71: ***Verification of the plasmids obtained. A)*** *Analytical agarose gel electrophoresis (1 %) of the pD-SKS-IKVAV-6X and pD-SKS-PPFLM-6X plasmids, digested with the EcoRI and SspI endonuclease (Image Lab™).* ***B)*** *Theoretical restriction map of pD-insert-6X vectors digested with EcoRI and SspI using the SnapGene® software.*

3.2.2.3.4.- SKS-IKVAV-6X and SKS-PPFLM-6X genes insertion in the p7RARE plasmid

The expression vector employed in this thesis is p7RARE, which has been provided by the Bioforge research group. Once the correct sequences of the SKS-IKVAV-6X and SKS-PPFLM-6X genes in the pD cloning plasmid have been confirmed, the vector is digested with the *EarI* enzyme in such a way that the inserts, SKS-IKVAV-6X and SKS-PPFLM-6X, are obtained. In turn, the p7RARE expression plasmid is treated with the *SapI* enzyme for linearisation and subsequent dephosphorylation. The resulting bands are resolved on preparative agarose gel electrophoresis (1 %) as shown in Figure 72A. The plasmid digests are then compared with the theoretical values of the restriction maps obtained with the SnapGene® software, as illustrated in Figure 72C.

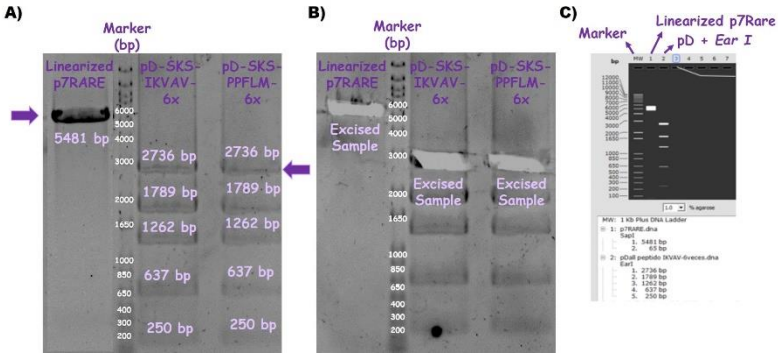

*Figure 72: **Linearisation of the p7RARE plasmid and extraction of the inserts. A)** Preparative agarose gel electrophoresis (1 %) of the expression vector, p7RARE and the pD-SKS-IKVAV-6X and pD-SKS-PPFLM-6X, digested with SapI and EarI, respectively (Image Lab™). **B)** Excision of the bands corresponding to the linearized expression vector, p7RARE and SKS-IKVAV-6X and SKS-PPFLM-6X inserts (Image Lab™). **C)** Theoretical restriction map of the p7RARE vector digested with SapI and the pD-insert-6X digested with EarI using the SnapGene® software.*

Finally, the bands of interest, namely the 5481 bp band for the linearised p7RARE and the 2736 bp band corresponding to the inserts, SKS-IKVAV-6X and SKS-PPFLM-6X, are extracted from the gel as depicted in Figure 72B. The purified genes are then evaluated for the degree of concentration and purity, as exhibited in Table 39.

Table 39: Concentration (ng/µL) and degree of purity of the p7RARE plasmid, SKS-IKVAV-6X insert and SKS-PPFLM-6X insert after purification.

Sample	Concentration (ng/µL)	260/280
Linearized p7RARE	24.3	1.63
SKS-IKVAV-6x insert	14.9	1.77
SKS-PPFLM-6x insert	17.4	1.86

The SKS-IKVAV-6X and SKS-PPFLM-6X inserts are introduced into the linearised and dephosphorylated expression plasmid p7RARE by ligation between the two fragments. The products of these reactions, p7RARE-SKS-IKVAV-6X and p7RARE-SKS-PPFLM-6X, are subsequently used to transform into competent *E. coli.* A number of colonies are selected and examined to ascertain the successful integration of the SKS-IKVAV-6X and SKS-PPFLM-6X inserts into the p7RARE. In

addition, the concentration and purity of the plasmids containing the inserts are evaluated, as illustrated in Table 40.

Table 40: Concentration (ng/µL) and degree of purity of p7RARE-SKS-IKVAV-6X and p7RARE-SKS-PPFLM-6X plasmids after purification.

Sample	Concentration (ng/µL)	260/280
p7RARE-SKS-IKVAV-6x_1	145.6	1.87
p7RARE-SKS-IKVAV-6x_2	130.4	1.90
p7RARE-SKS-IKVAV-6x_3	185.2	1.92
p7RARE-SKS-IKVAV-6x_4	138.3	1.92
p7RARE-SKS-PPFLM-6x_1	118.2	1.93
p7RARE-SKS-PPFLM-6x_2	189.7	1.91
p7RARE-SKS-PPFLM-6x_3	164.0	1.91
p7RARE-SKS-PPFLM-6x_4	177.4	1.90

Furthermore, to verify that the gene insert has been correctly inserted into the expression vector, each plasmid is subjected to co-digestion with *EcoRI* and *NdeI* enzymes, and the resulting bands are analysed on an analytical agarose gel (1 %) as depicted in Figure 73A. Finally, the plasmid digestion is compared with the theoretical value of the restriction map obtained with the SnapGene® software, as shown in Figure 73B. The appearance of the bands at 5452 bp and 2765 bp is observed, thus confirming the correct insertion of the SKS-IKVAV-6X and SKS-PPFLM-6X genes in the p7RARE expression vector. The gene sequences are subsequently validated through sequencing, thereby verifying the functionality of the plasmids for the expression of the proteins encoded by the aforementioned genes in *Escherichia coli* bacteria.

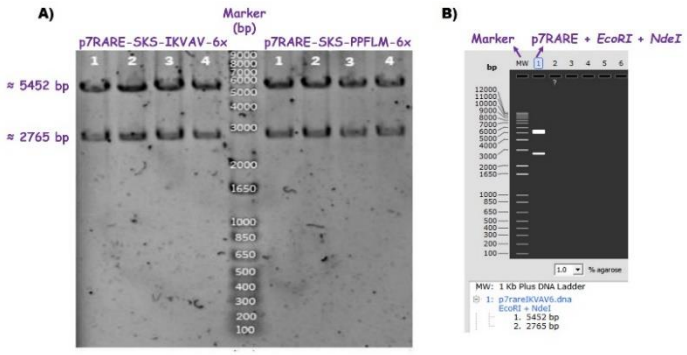

*Figure 73: **Verification of the plasmids obtained. A)** Analytical agarose gel electrophoresis (1 %) of the p7RARE-SKS-IKVAV-6X and p7RARE-SKS-PPFLM-6X plasmids, digested with the EcoRI and NdeI enzymes (Image Lab™). **B)** Theoretical restriction map of p7RARE-insert-6X vectors digested with EcoRI and NdeI using the SnapGene® software.*

3.2.2.4.- Gene construction of SKS-IKVAV-PPFLM

3.2.2.4.1.- Cloning vector pDrive All

The same cloning plasmid (pDrive all) will be used for the construction of the SKS-IKVAV-PPFLM gene as was employed for the two previous SKS-IKVAV and SKS-PPFLM polymers. Consequently, the linearised and dephosphorylated pD plasmid is now ready for use, as illustrated in Figure 68, with an optimal concentration and purity, as shown in Table 35.

3.2.2.4.2.- SKS-IKVAV-PPFLM insert

The initial coding sequences for SKS-IKVAV-PPFLM were acquired from NZYTech, and each contained a single repeat. In order to achieve the final gene construct, six repeats of each amino acid sequence must be obtained. The genes are delivered using the same pUC57 cloning plasmid as previously employed, which features identical *SapI* restriction sites. The coding gene of interest is inserted between two of the aforementioned restriction sites.

The SKS-IKVAV-PPFLM insert is prepared by transforming the commercial plasmid pUC57-SKS-IKVAV-PPFLM into XL1-Blue competent cells, which facilitates vector subcloning. Following this step, three bacterial colonies are selected, and the concentration and purity of the resulting plasmids are assessed post-purification. The results are detailed in Table 41.

Table 41: Concentration (ng/µL) and degree of purity of commercial plasmids with the SKS-IKVAV-PPFLM insert.

Sample	Concentration (ng/µL)	260/280
pUC57-SKS-IKVAV-PPFLM_1	193.0	1.96
pUC57-SKS-IKVAV-PPFLM_2	205.6	1.97
pUC57-SKS-IKVAV-PPFLM_3	199.6	1.95

All the samples exhibited satisfactory levels of DNA concentration and purity. Consequently, the sample demonstrating the highest concentration, namely pUC57-SKS-IKVAV-PPFLM_2, is selected for further analysis. The plasmid is subjected to digestion using the *SapI* endonuclease enzyme, which cleaves the vector into smaller fragments, releasing the SKS-IKVAV-PPFLM gene fragment located between two *SapI* cleavage sites, resulting in an insert of 567 bp. The resulting bands from this digestion process are visualized following preparative agarose gel electrophoresis (1 %), as illustrated in Figure 74A.

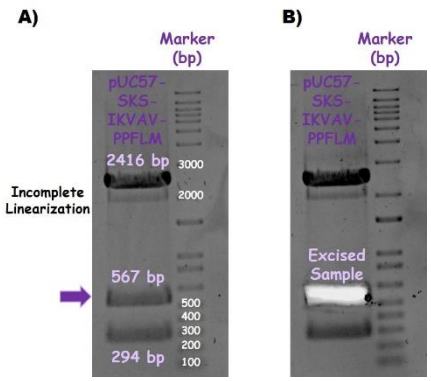

*Figure 74: **Extraction of the inserts. A)** Preparative agarose gel electrophoresis (1 %) of the commercial plasmids pUC57-SKS-IKVAV-PPFLM, digested with SapI endonuclease (Image Lab™). **B)** Excision of the band corresponding to the SKS-IKVAV-PPFLM inserts at 567 bp (Image Lab™).*

The image depicts the 2416 bp bands corresponding to the plasmid devoid of the insert, the 567 bp insert band, and bands stemming from partially digested plasmid molecules. Subsequently, the band of interest is isolated from the agarose gel, as depicted in Figure 74B, and the gene is purified. Finally, the concentration and purity of the obtained insert are assessed, as outlined in Table 42.

Table 42: Concentration (ng/µL) and degree of purity of SKS-IKVAV-PPFLM insert after purification.

Sample	Concentration (ng/µL)	260/280
SKS-IKVAV-PPFLM insert	10.5	1.97

3.2.2.4.3.- SKS-IKVAV-PPFLM gene insertion in the pDrive All plasmid

The ligation process is initiated by the T4 DNA ligase enzyme, which connects the *SapI* linearized and dephosphorylated pD plasmid with the SKS-IKVAV-PPFLM insert obtained through the *EarI* enzyme digestion. The resulting product, designated pD-SKS-IKVAV-PPFLM, is subsequently utilized for transformation into competent *E. coli* cells. Following transformation, several colonies are selected and analysed to confirm the presence and integrity of the inserted fragments. Furthermore, the concentration and purity of the insert are evaluated, with the detailed findings presented in Table 43.

Table 43: Concentration (ng/µL) and degree of purity of the pD-SKS-IKVAV-PPFLM plasmid.

Sample	Concentration (ng/µL)	260/280
pD-SKS-IKVAV-PPFLM_1	806.8	1.89
pD-SKS-IKVAV-PPFLM_2	626.6	1.89
pD-SKS-IKVAV-PPFLM_3	910.6	1.88

All samples demonstrated robust DNA concentrations and excellent purity levels. Consequently, the sample exhibiting the highest concentration, specifically pD-SKS-IKVAV-PPFLM_3, is selected for subsequent cloning procedures. Additionally, to ensure accurate insertion of the gene into the cloning vector, the plasmid undergoes digestion using either the *EcoRI* enzyme or the *EarI* enzyme independently, and the resulting bands are analysed via analytical agarose gel electrophoresis (1 %), as illustrated in Figure 75A. Finally, the plasmid digestion pattern is compared with the theoretical restriction map generated using the SnapGene® software. The observed bands in the electrophoresis aligned with the theoretical bands at 3837 bp and 668 bp when *EcoRI* was used and at 1789 bp, 1262 bp, 637 bp, 567 bp and 250 bp when *EarI* was used, as shown in Figure 75B. Following this validation, the plasmid containing the gene is subjected to further sequencing, thereby confirming the precise insertion of the SKS-IKVAV-PPFLM gene into the pD vector.

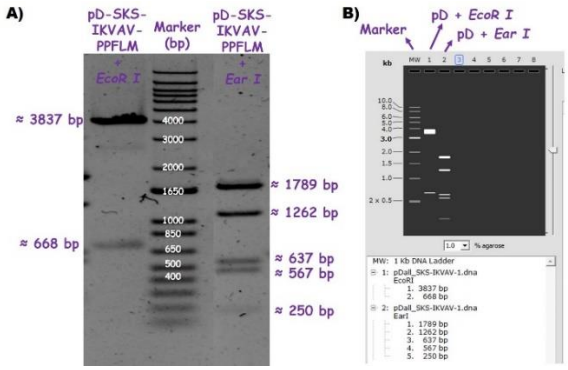

Figure 75: ***Verification of the plasmids obtained. A)*** *Analytical agarose gel electrophoresis (1 %) of the pD-SKS-IKVAV-PPFLM plasmid, digested with EcoRI or EarI endonucleases (Image Lab™).* ***B)*** *Theoretical restriction map of the pD-insert vector, digested with EcoRI or EarI using the SnapGene® software.*

Following the successful incorporation of the SKS-IKVAV-PPFLM gene into the pD vector, the subsequent cloning process involves the amplification of the size of the gene through the addition of repeats until the desired six repeats are achieved, thereby forming the final gene encoding the polymer of interest (SKS-IKVAV-PPFLM-6X). This amplification occurs sequentially and iteratively, with inserts being extracted using the *EarI* enzyme and then introduced into a linearized and dephosphorylated plasmid treated with *SapI*. While these intermediary steps are crucial, they have been omitted from the thesis in order to prevent unnecessary lengthening.

The resulting construct, pD-SKS-IKVAV-PPFLM-6X, is subjected to rapid digestion with *EcoRI* and *SspI* enzymes simultaneously in order to validate the correct insertion of the insert. The resulting bands are then analysed via electrophoresis on a 1 % analytical agarose gel, as depicted in Figure 76A. Furthermore, the plasmid digestion pattern is compared with the theoretical restriction map generated using the SnapGene® software, as illustrated in Figure 76B. The observed bands in the electrophoresis align with the bands of the theoretical pattern, thereby validating the accuracy of the cloning process. Finally, the selected plasmid is subjected to sequencing to confirm the gene sequence of the SKS-IKVAV-PPFLM-6X gene.

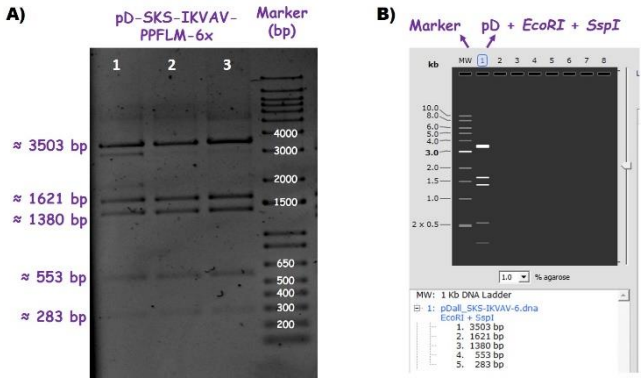

Figure 76: ***Verification of the plasmids obtained. A)*** *Analytical agarose gel electrophoresis (1 %) of the pD-SKS-IKVAV-PPFLM-6X plasmid, digested with EcoRI and SspI endonuclease (Image Lab™).* ***B)*** *Theoretical restriction map of pD-insert-6X vector digested with EcoRI and SspI using the SnapGene® software.*

3.2.2.4.4.- SKS-IKVAV-PPFLM-6X gene insertion in the p7RARE plasmid

The SKS-IKVAV-PPFLM-6X gene will be incorporated into the same expression plasmid (p7RARE) used for the two previous SKS-IKVAV and SKS-PPFLM polymers. Therefore, the linearized and dephosphorylated p7RARE plasmid is readily available for use as depicted in Figure 72, with optimal concentration and purity levels, as detailed in Table 39.

Upon confirmation of the correct sequence of the SKS-IKVAV-PPFLM-6X gene within the pD cloning plasmid, the vector is subjected to digestion with the *EarI* enzyme to isolate the insert, SKS-IKVAV-PPFLM-6X. The resulting bands are subsequently separated using a preparative agarose gel electrophoresis (1 %), as presented in Figure 77A. Subsequently, the plasmid digestion pattern is compared with the theoretical values of the restriction maps generated using the SnapGene® software, as depicted in Figure 77C.

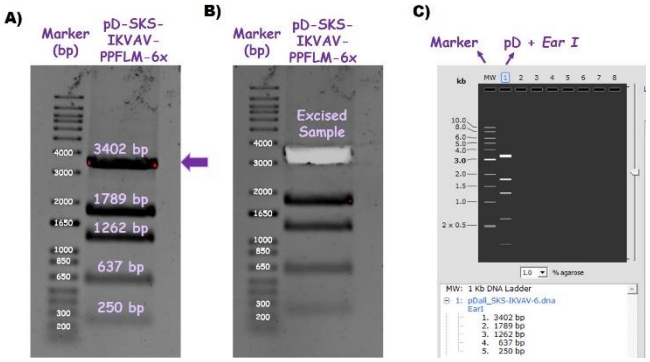

*Figure 77: **Extraction of the insert. A)** Preparative agarose gel electrophoresis (1%) of the pD-SKS-IKVAV-PPFLM-6X plasmid, digested with EarI, (Image Lab™). **B)** Excision of the band corresponding to the SKS-IKVAV-PPFLM-6X insert (Image Lab™). **C)** Theoretical restriction map of pD-insert-6X digested with EarI using the SnapGene® software.*

Finally, the band corresponding to the SKS-IKVAV-PPFLM-6X insert, specifically the 3402 bp band of interest, is carefully extracted from the gel, as illustrated in Figure 77B. The gene is purified, and the concentration and purity of the obtained insert are meticulously evaluated, with findings summarized in Table 44.

Table 44: Concentration (ng/µL) and degree of purity of the SKS-IKVAV-PPFLM-6X insert after purification.

Sample	Concentration (ng/µL)	260/280
SKS-IKVAV-PPFLM-6x insert	21.2	2.95

The final step in molecular biology involves the ligation of the SKS-IKVAV-PPFLM-6X insert onto the linearized and dephosphorylated expression plasmid, p7RARE. The resulting product, p7RARE-SKS-IKVAV-PPFLM-6X, is utilized to transform competent *E. coli* cells. Subsequently, a number of colonies are selected and examined in order to verify the successful integration of the SKS-IKVAV-PPFLM-6X inserts into the p7RARE plasmid. Moreover, the concentration and purity of the plasmids containing the inserts are evaluated, as depicted in Table 45.

Table 45: Concentration (ng/µL) and degree of purity of the p7RARE-SKS-IKVAV-PPFLM-6X plasmid following purification.

Sample	Concentration (ng/µL)	260/280
p7RARE-SKS-IKVAV-PPFLM-6x_1	143.8	1.89
p7RARE-SKS-IKVAV-PPFLM-6x_2	162.8	1.90
p7RARE-SKS-IKVAV-PPFLM-6x_3	157.2	1.87
p7RARE-SKS-IKVAV-PPFLM-6x_4	125.3	1.92

Furthermore, to ensure accurate insertion of the insert into the expression vector, the plasmid is subjected to co-digestion with *EcoRI* and *NdeI* enzymes, and the resulting bands are analysed using an analytical agarose gel electrophoresis (1 %), as shown in Figure 78A. Finally, the plasmid digestion pattern is compared with the theoretical restriction map generated using the SnapGene® software, as depicted in Figure 78B. The presence of bands at 5452 bp and 3431 bp indicates the successful insertion of the SKS-IKVAV-PPFLM-6X gene into the p7RARE expression vector. Subsequent confirmation of the genetic sequence through sequencing validates the integrity of this plasmid, rendering it suitable for protein expression in *E. coli* bacteria.

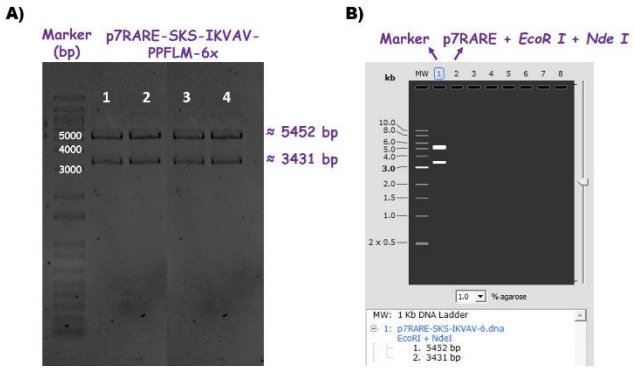

*Figure 78: **Verification of the plasmids obtained. A)** Analytical agarose gel electrophoresis (1 %) of the p7RARE-SKS-IKVAV-PPFLM-6X plasmid, digested with the EcoRI and NdeI enzymes (Image Lab™). **B)** Theoretical restriction map of the p7RARE-insert-6X vector, digested with EcoRI and NdeI using the SnapGene® software.*

3.2.2.5.- Bioproduction and purification of novel ELRs laminin mimetic polymers

3.2.2.5.1.- SKS-IKVAV and SKS-PPFLM polymers

The p7RARE plasmid, which contains the SKS-IKVAV-6X gene and produces the polymer SKS-IKVAV, and the p7RARE plasmid, which contains the SKS-PPFLM-6X gene and produces the polymer SKS-PPFLM, are transformed into the *E. coli* BLR expression strain. Given that the expression of target proteins often varies in terms of the amount of protein produced between clones derived from a single bacterial transformation, it is necessary to screen among the expression colonies in order to identify the clone that produces the greatest quantity of protein before large-scale production. This can be achieved by isolating colonies and analysing the total protein fraction on an SDS-PAGE gel (10 %), as illustrated in Figure 79. The protein expression of the SKS-IKVAV polymer is detected by the appearance of a band at

75946 Da, as shown in Figure 79A. In contrast, the SKS-PPFLM polymer is identified by the presence of a band at 76980 Da, as depicted in Figure 79B. Upon analysis of the results, it can be observed that both proteins are expressed, as evidenced by the presence of a band that closely aligns with their respective theoretical molecular weights. Additionally, a negative control is included, in which the protein of interest remains unexpressed, and the bacterial bands are observed for comparison.

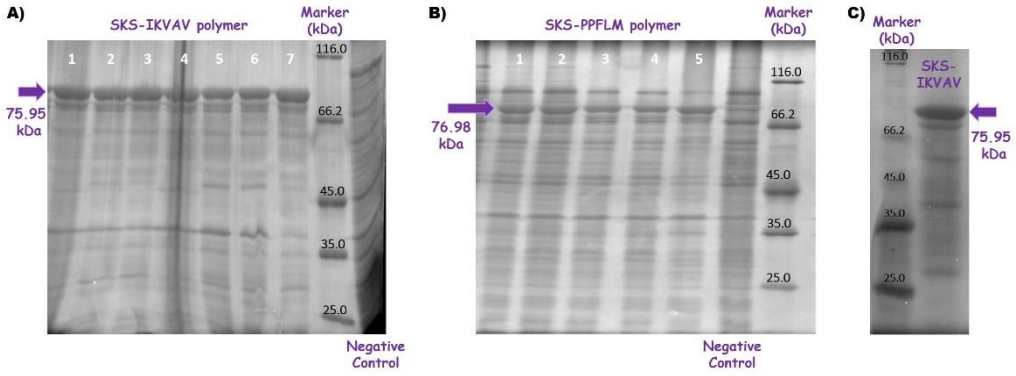

Figure 79: ***Total protein fraction analysis on an SDS-PAGE electrophoresis. A)*** *Expression screening of the SKS-IKVAV protein with a characteristic band at 75.95 kDa.* ***B)*** *Expression screening of the SKS-PPFLM protein with a characteristic band at 76.98 kDa.* ***C)*** *SKS-IKVAV-ELR recombinamer after purification. SDS-PAGE gel stained with a copper chloride (II) solution for visualization (Image Lab™).*

The subsequent step is to select the bacterial colony exhibiting the highest expression level, which is colony 7 for SKS-IKVAV and colony 1 for SKS-PPFLM, to produce the polymer in the bioreactor until the stationary phase is reached, at which point no bacterial cell growth is observed [424], following the protocol described in the methodology section, the procedure is repeated for each polymer. The purification of SKS-IKVAV and SKS-PPFLM polymers is also based on the protocol defined above in the methodology section. Due to the inverse transition temperature-dependent nature of these polymers, ELRs are easily solubilised [593]. Thus, at their transition temperature and low salinity conditions, ELR chains tend to remain hydrophobically hydrated in a disordered reversible soluble state, facilitating their extraction from the insoluble bacterial protein fraction. Taking advantage of this property, it is anticipated that when a solution containing ELRs is heated to a temperature exceeding its T_t, the recombinamer will precipitate and settle in the sediment. Conversely, when the solution is cooled below T_t, the protein will dissolve in the supernatant phase. During the disruption and purification process, various protease inhibitors (PMSF, EDTA, E-64, pepstatin A and/or AESBF) are added to prevent the degradation of the polymers, as well as to reduce the process time and to carefully control the temperature. In particular, when working with the one containing the IKVAV sequence, which is particularly sensitive and susceptible to degradation, as was already known in the group from a polymer developed with the same sequence. Consequently, purification must be conducted by reducing the transition temperature of the recombinamer through the addition of salt (ammonium sulphate).

In light of the outcomes depicted in Figure 79C, the SKS-IKVAV polymer is obtained with a minimal degree of degradation that does not impede its utilisation

for future applications. Nevertheless, the development of an optimised protocol for obtaining the pure and undegraded SKS-PPFLM polymer has not been feasible during the course of this thesis. Consequently, the project will henceforth progress solely with the SKS-IKVAV polymer.

3.2.2.5.2.- SKS-IKVAV-PPFLM polymer

The p7RARE plasmid, which contains the SKS-IKVAV-PPFLM-6X gene, is a complex polymer that is difficult to produce and purify due to the presence of several specific bioactive sequences. In order to ascertain which *E. coli* expression strain gave the best protein expression yield, the plasmid was transformed into two strains, BLR and BL21. Initially, the expression colonies are screened to identify the colony that produces the greatest quantity of protein polymer by isolating colonies and analysing the total protein fraction on an SDS-PAGE gel (10 %) as illustrated in Figure 80A for BL21 bacteria and in Figure 80B for BLR bacteria. The expression of the recombinant polymer SKS-IKVAV-PPFLM is identified by the presence of a band at 96744 Da, which proves that it is expressed in both bacterial strains by identifying a band that is close to the theoretical molecular weight. Furthermore, a negative control is included, which allows the observation of the bacterial bands but the absence of the protein of interest.

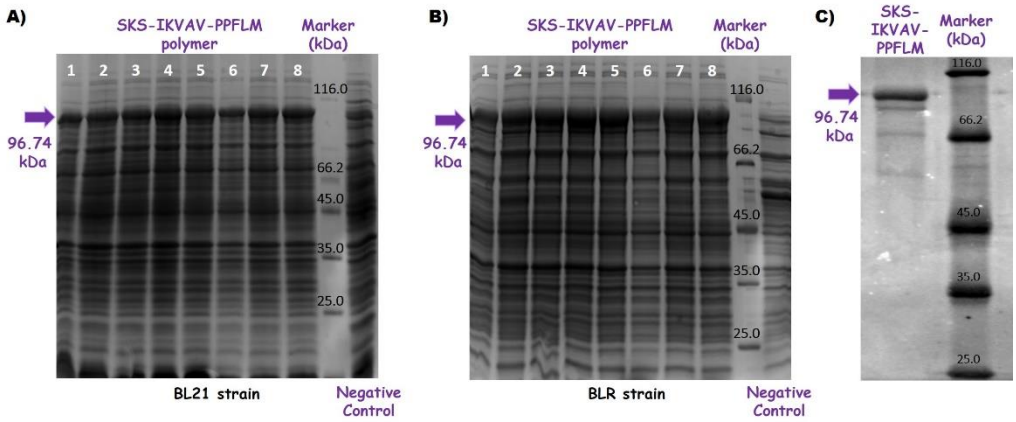

Figure 80: ***Total protein fraction analysis on an SDS-PAGE electrophoresis. A)*** *Expression screening of the SKS-IKVAV-PPFLM protein in the BL21 bacterial strain with a characteristic band at 96.745 kDa.* ***B)*** *Expression screening of the SKS-IKVAV-PPFLM protein in the BLR bacterial strain with a characteristic band at 96.745 kDa. SDS-PAGE gel was stained with a Coomassie solution for visualization (Image Lab™).* ***C)*** *The SKS-IKVAV-PPFLM-ELR recombinamer after purification.*

Subsequently, the bacterial colony exhibiting the highest level of expression, as evidenced by the widest band and the absence of aberrant or overexpressed bands, is selected. Colony 5 of strain BLR is identified as the optimal candidate for polymer production in the bioreactor, and the SKS-IKVAV-PPFLM polymer is purified in accordance with the specified methodology, which exploits its inverse transition temperature-dependent property. Consequently, a pure SKS-IKVAV-PPFLM polymer with a slight degree of degradation is obtained, as illustrated in Figure 80C. During the disruption and purification steps, a range of protease inhibitors (PMSF, EDTA, E-64, pepstatin A and/or AESBF) are added to prevent or

minimise the degradation of the polymer. This minor degree of degradation does not preclude its future use for applications.

3.2.2.6.- Physico-chemical characterisation of novel ELRs laminin mimetic polymers

The two novel polymers obtained, SKS-IKVAV and SKS-IKVAV-PPFLM, which contain laminin sequences, are characterised using a series of analytical techniques in order to confirm their accuracy in terms of molecular composition, final purity, and thermal response behaviour. In this context, the molecular composition of amino acids is corroborated by HPLC. The purity and molecular weight of the polymers are evaluated by SDS-PAGE electrophoresis and mass spectrometry (MALDI-TOF), as well as by nuclear magnetic resonance spectroscopy (^{1}H-NMR) and infrared spectroscopy (ATR-FTIR) analysis.

Initially, the amino acid composition of both polymers is verified by HPLC. The number of residues determined experimentally is found to be in close agreement with the theoretical values calculated by the Expasy program from the amino acid sequence composing each polymer. This result corroborates the accuracy and purity of the recombinamers, as evidenced in Figure 81A for the SKS-IKVAV polymer and Figure 82A for the SKS-IKVAV-PPFLM polymer. The slight observed variations are within the experimental error associated with the technique. The amino acid isoleucine exhibits the most significant variation.

Mass spectrometry (MALDI-TOF) is employed to elucidate the experimental molecular weight (Mw) of the recombinamers through the m/z ratios of the ions produced. The mass spectrum obtained for the SKS-IKVAV polymer shows the first three ionisations (M^{+1}, M^{+2} and M^{+3}), as illustrated in Figure 81B. The experimental value of M^{+1} allows for the precise determination of the weight of the polymer, which is 76401 Da. This value is in close agreement with the theoretical value. In contrast, the mass spectrum obtained for the SKS-IKVAV-PPFLM polymer shows only the first two ionisations (M^{+1} and M^{+2}), as illustrated in Figure 82B. The experimental M^{+1} value of 94938 Da is somewhat lower than the theoretical value of 96744 Da obtained with the ProteinProspector online program.

Furthermore, the purity and molecular weight of the SKS-IKVAV and SKS-IKVAV-PPFLM polymers are evaluated using SDS-PAGE gel electrophoresis, as illustrated in Figure 81C and Figure 82C, respectively. In both cases, it can be observed that there is a slight degradation of the polymer, which is a predictable consequence of the IKVAV sequence. However, this does not prevent the polymers from being used for their potential future applications.

A)

SKS-IKVAV		
Amino Acid	Theoretical	Experimental
Ala (A)	24	21.57
Arg (R)	6	6.80
Asn (N)	0	-
Asp (D)	6	5.98
Cys (C)	0	-
Gln (Q)	0	-
Glu (E)	0	-
Gly (G)	336	338.59
His (H)	0	-
Ile (I)	6	3.36
Leu (L)	0	-
Lys (K)	30	29.97
Met (M)	0	-
Phe (F)	0	-
Pro (P)	168	167.87
Ser (S)	60	61.19
Thr (T)	0	-
Trp (W)	0	-
Typ (Y)	0	-
Val (V)	276	277.09

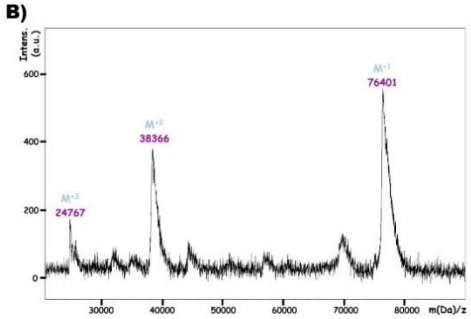

SKS-IKVAV		
	Theor. (Da)	Exp. (Da)
M +1	75946	76401
M +2	37973	38366
M +3	25315	24767

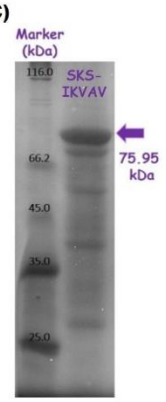

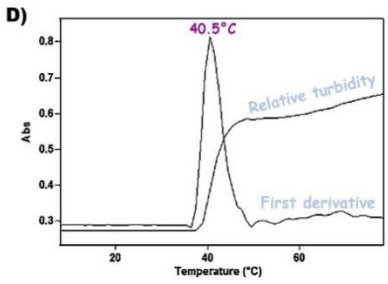

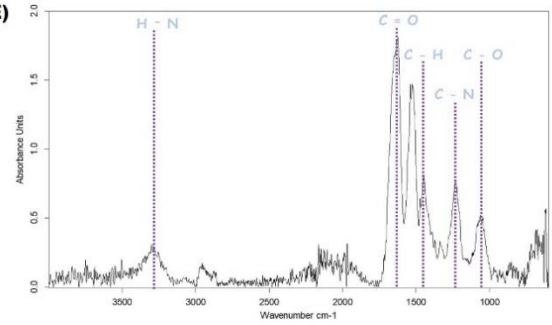

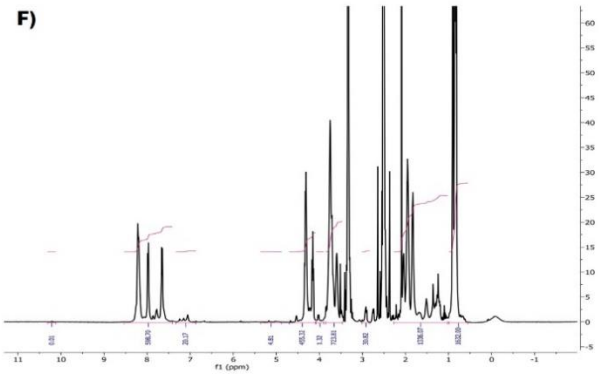

SKS-IKVAV		
Chemical shift of protons (ppm)	Theoretical Value	Experimental Value
0.7 - 1	1632	1632.0
1.1 - 2.7	1390	1336.07
3.5 - 4.5	1443	1184.45
5.0 - 5.5	12	4.81
6.5 - 7.4	18	20.17
7.5 - 8.7	654	598.70
9.5 – 12.0	12	1

*Figure 81: **Physico-chemical characterisation of SKS-IKVAV**. **A)** Predicted and measured amino acid composition using HPLC after acid hydrolysis. **B)** MALDI-TOF spectrum showing the mono- (M^{+1}), di- (M^{+2}) and tri-charged (M^{+3}) states. **C)** SDS-Page electrophoresis after copper chloride (II) staining. **D)** Thermal analysis is verified through turbidimetry, which determines the transition temperature (T_t) by calculating the first derivative of the data. **E)** ATR-FTIR spectra. **F)** ^{1}H-NMR integrated spectra.*

The thermal responsiveness of the purified biopolymers is verified through turbidimetry by providing the transition temperature (T_t) values. The SKS-IKVAV and SKS-IKVAV-PPFLM polymers are dissolved at a concentration of 1 mg/mL in ultrapure water in order to analyse their thermal behaviour after complete solubilisation after 12 hours at 4 °C with stirring. The transition temperatures are obtained by measuring the turbidity at 350 nm in the temperature range between 10 and 90 °C using a scan rate of 1 °C per minute. Furthermore, the transition temperatures are determined as the temperature corresponding to the maximum of the first derivative of the turbidity versus temperature curve [450]. Thus, Figure 81D illustrates the turbidity profile as a function of temperature obtained for the SKS-IKVAV polymer, which reveals a T_t of 40.5 °C. Figure 82D also depicts the

turbidity profile as a function of temperature obtained for the SKS-IKVAV-PPFLM polymer, which exhibits a T_t of 62.6 °C, as determined by the value of its first derivative. These temperatures are consistent with those anticipated based on the polarity of the polymers. Consequently, these temperatures can be compared with the temperature of the starting polymer SKS, which is 34.2 °C [436]. A slight increase in temperature is observed in the SKS-IKVAV polymer when the serines are kept constant and the RGD-binding groups are replaced with a DR-containing sequence. Furthermore, the incorporation of additional lysines per molecule results in a slight increase in hydrophilicity, which is reflected in an increase in T_t. Conversely, an increase in the temperature of the SKS-IKVAV-PPFLM polymer is also observed. This change is due to an increase in the number of serines and threonines containing hydroxyl groups, as well as an increase in the number of lysines, which collectively result in a globular increase in hydrophilicity, and therefore, an increase in T_t. Below this T_t, the ELRs are structurally disordered, highly solvated, and soluble. However, when the solution temperature is increased and T_t is reached, the polymers undergo a collapse and coalescence, resulting in the formation of large, micrometre-sized aggregates, as evidenced by a change in turbidity of sufficiently concentrated solutions [436]. The study of the thermal behaviour of ELRs is essential in order to establish the thermal conditions that should be maintained during their use in biomedical applications.

The infrared spectra of the SKS-IKVAV and SKS-IKVAV-PPFLM polymers evident characteristic protein vibrational bands corresponding to amide I and amide II, as illustrated in Figure 81E for the SKS-IKVAV polymer and Figure 82E for the SKS-IKVAV-PPFLM polymer. The absorption associated with amide I produces a high intensity peak in the spectrum around 1600 cm^{-1}, whose signal is attributed to the stretching vibrations of the carbonyl group bond (C=O). This is related to the secondary structure of the proteins. In contrast, the amide II band corresponds to bending vibrations of the NH bond, which is signalled at 3400 cm^{-1}. Furthermore, the bands at 1450 cm^{-1} correspond to the CH bending of the methyl group of the alkane, at 1200 cm^{-1} to the CN stretching of the amine, and at 1000 cm^{-1} to the CO stretching of the primary alcohol [436]. Consequently, both polymers exhibit the characteristic bands of ELR polymers, thereby confirming the correct molecular composition.

A)

SKS-IKVAV-PPFLM		
Amino Acid	Theoretical	Experimental
Ala (A)	60	65.88
Arg (R)	24	22.76
Asn (N)	0	-
Asp (D)	18	17.34
Cys (C)	0	-
Gln (Q)	0	-
Glu (E)	0	-
Gly (G)	378	374.82
His (H)	0	-
Ile (I)	12	8.19
Leu (L)	18	20.90
Lys (K)	30	29.17
Met (M)	6	6.87
Phe (F)	6	6.10
Pro (P)	174	183.03
Ser (S)	108	107.24
Thr (T)	12	10.57
Trp (W)	0	-
Typ (Y)	0	-
Val (V)	289	283.24

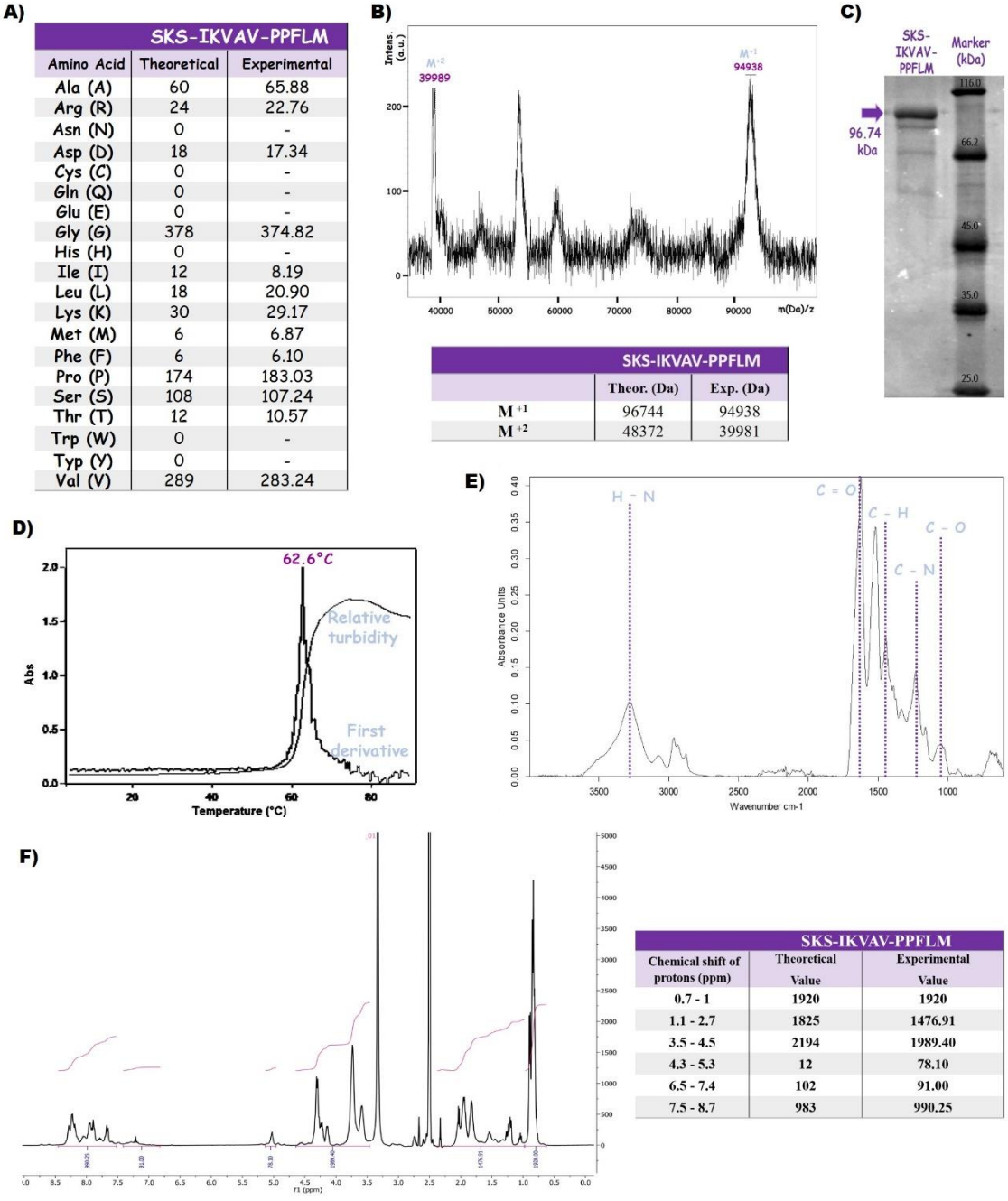

SKS-IKVAV-PPFLM		
	Theor. (Da)	Exp. (Da)
M^{+1}	96744	94938
M^{+2}	48372	39981

SKS-IKVAV-PPFLM		
Chemical shift of protons (ppm)	Theoretical Value	Experimental Value
0.7 - 1	1920	1920
1.1 - 2.7	1825	1476.91
3.5 - 4.5	2194	1989.40
4.3 - 5.3	12	78.10
6.5 - 7.4	102	91.00
7.5 - 8.7	983	990.25

*Figure 82: **Physico-chemical characterisation of SKS-IKVAV. A)** Predicted and measured amino acid composition using HPLC after acid hydrolysis. **B)** MALDI-TOF spectrum showing the mono- (M^{+1}) and di- (M^{+2}) states. **C)** SDS-Page electrophoresis after copper chloride (II) staining. **D)** Thermal analysis is verified through turbidimetry which determines the transition temperature (T_t) by calculating the first derivative of the data. **E)** ATR-FTIR spectra. **F)** ^{1}H-NMR integrated spectra.*

Finally, a nuclear magnetic resonance (^{1}H-NMR) analysis is performed to obtain information on the molecular structure of recombinamers. Theoretically, the different hydrogen-containing functional groups that comprise the ELR (mainly: -NHCO-, -CH_3, -CH_2- and -CH-) undergo different chemical shifts in parts per million (ppm) depending on the chemical environment in which they are situated. These signals can be predicted in advance using ChemDraw software. For the experimental analysis, the SKS-IKVAV and SKS-IKVAV-PPFLM polymers are dissolved in deuterated dimethyl sulfoxide (DMSO) at a concentration of 5 mg/mL. Figure 81F

for the SKS-IKVAV polymer and Figure 82F for the SKS-IKVAV-PPFLM polymer present the NMR spectra, in which the ^{1}H (δ) chemical shifts in ppm are evaluated, with the integrals corresponding to the different areas delimiting the different hydrogen types, with the -CH_3 peak, located at 1 ppm, serving as a reference for the evaluation of the integrals. A table is also provided, which compares the experimental values obtained after integrating the signals of each region with the planned theoretical values. This serves to corroborate the accuracy of the molecular structures of both polymers.

3.2.2.7.- Laminin Biofunctionalized Click Hydrogel

The potential for improved cell specificity and binding of the recombinantly incorporated laminin sequences within the ELR amino acid chain, in comparison to those sequences grafted by click chemistry, are evaluated by obtaining hydrogels using the newly developed polymers SKS-IKVAV and SKS-IKVAV-PPFLM. This process involves the modification of 18 lysine residues with azides, out of the 30 available, in a manner analogous to that previously employed with the SKS base polymer.

Subsequently, the VKV-cc polymer is combined with the SKS-IKVAV-N_3 or SKS-IKVAV-PPFLM-N_3 polymers, resulting in a cross-linking click reaction that generates a multifunctional hydrogel. The VKV polymer serves as a structural group, while the SKS-IKVAV and SKS-IKVAV-PPFLM polymers provide additional biological functionalities. These include the universal cell adhesion sequence (RGD) and/or laminin-derived sequences (KAASIKVAVSADR and KPPFLMLLKGSTR), which play a crucial role in the adhesion and proliferation processes of keratinocytes and fibroblasts, which are essential in wound healing. The stoichiometric ratio between azides and cyclooctynes is maintained at a constant 1:1 throughout the formation of these new hydrogels. By combining the azides of SKS-IKVAV-N_3 or SKS-IKVAV-PPFLM-N_3 with the cyclooctynes of VKV-cc, cross-linking occurs spontaneously, resulting in the formation of a three-dimensional network. The biophysical properties of the gel can be adjusted by varying the initial concentrations of the polymers and changing the degree of cross-linking. Gels are then characterised in terms of transparency, mechanical properties and internal structure by assessing porosity, as well as their regenerative capacity with cells.

3.2.2.7.1.- Macroscopic properties

A concentration of 50 mg/mL was selected for the formation of the hydrogels based on the previous experience of the Bioforge group with numerous hydrogels of a similar nature to those obtained with these new polymers [435], [553]. Figure 83A corroborates the structural stability of the novel hydrogels at a concentration of 50 mg/mL for the two polymers (SKS-IKVAV and SKS-IKVAV-PPFLM), as evidenced at the macroscopic level. Upon initial observation, the new hydrogels appear to exhibit similar properties to the control gel (VKV-SKS), as displayed in Figure 83B, including viscosity, hardness, and malleability which is anticipated due

to the consistent 1:1 ratio of azides to cyclooctynes. However, this assumption will be further substantiated by analysing the rheological properties of the scaffolds.

Furthermore, all scaffolds reveal adequate consistency and are easily handled, as illustrated in Figure 83C, which depicts a representative example of all hydrogels formed. The stability of hydrogels is a critical parameter for their suitability in tissue engineering. These matrices must retain their integrity in aqueous media for extended periods of time, as in normal tissue conditions. Consequently, to assess the stability of hydrogels at 50 mg/mL, an incubation in excess water at 37 °C for one week is performed. Subsequent inspection revealed that the structures remained stable without altering their initial shape, as shown in Figure 83D.

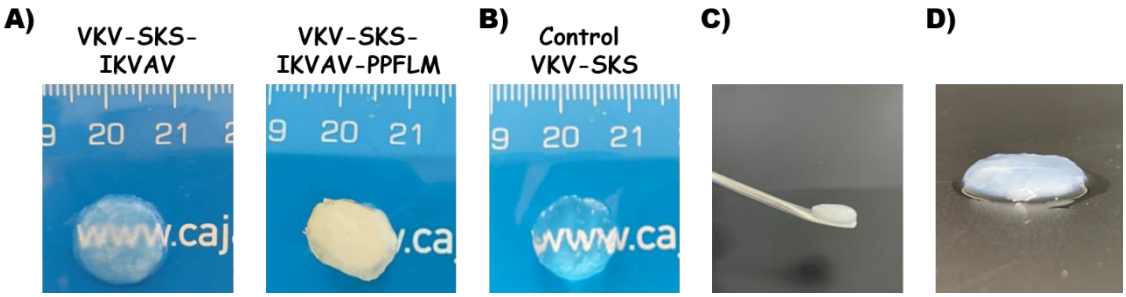

Figure 83: ***Biofunctionalized click hydrogels. A)*** *Novel hydrogels for both polymers (SKS-IKVAV and SKS-IKVAV-PPFLM) showing low transparency with a noticeable whiteness.* ***B)*** *VKV-SKS Control hydrogel showing transparency.* ***C)*** *Example of consistency and manageability of a biofunctionalized hydrogel.* ***D)*** *Example of stability of a biofunctionalized hydrogel after one week of incubation with water at 37 °C without losing its initial shape.*

One distinguishing feature between the hydrogels containing grafted peptides and the novel hydrogels comprising the polymers SKS-IKVAV and SKS-IKVAV-PPFLM is their differing levels of transparency. As illustrated in Figure 83A, the latter form hydrogels with a lower transparency, exhibiting a noticeable whiteness. Thus, the reference VKV-SKS hydrogel is practically transparent, while the VKV-SKS-IKVAV hydrogel shows a gradual decrease in transparency, up to the VKV-SKS-IKVAV-PPFLM hydrogel, which is characterised by being completely opaque, preventing the clear visualisation of objects through it.

However, a common feature of hydrogels containing grafted peptides is their ability to form *in situ* on wounds, adapting to their size and shape, and gelling rapidly on contact with body temperature. This ability facilitates the production of dressings with a wide range of characteristics, including moisture retention, biological adhesion capacity, and enhanced adhesion and movement of cells such as keratinocytes and fibroblasts, which can direct the migration to specific areas of the structure to support the skin regeneration process.

3.2.2.7.2.- Evaluation of internal morphology of biofunctionalized click hydrogels

An investigation of the internal microstructure is conducted by immersing the hydrogels in liquid nitrogen, followed by cryofracture and freeze-drying for subsequent analysis by scanning electron microscopy (SEM), which provides high-

resolution images for morphological evaluation. Figure 84A displays representative SEM micrographs of cross-sections of VKV-SKS-IKVAV and VKV-SKS-IKVAV-PPFLM hydrogels, while Figure 84B presents the corresponding micrographs for the VKV-SKS control.

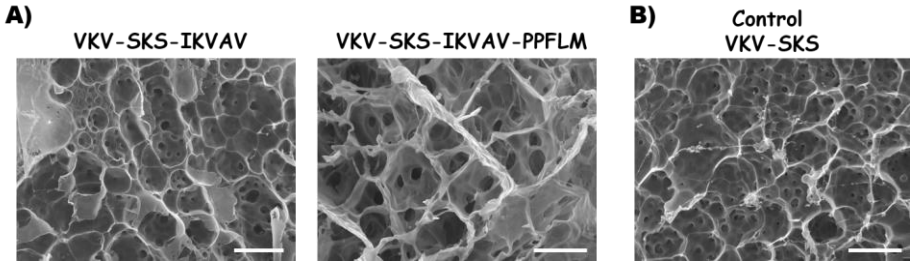

Figure 84: ***Morphological characterization. A)*** *Representative SEM images of cryo-fractured, lyophilised and gold-sputtered across sections of biofunctionalized click hydrogels (VKV-SKS-IKVAV and VKV-SKS-IKVAV-PPFLM). Scale bar = 50 µm.* ***B)*** *Representative SEM images of VKV-SKS Control Hydrogel. Scale bar = 50 µm.*

All hydrogels exhibit a porous internal structure, comprising internal pores within pores of larger diameter. This is consistent with the reference hydrogel and those covalently cross-linked ELRs previously reported [433], [434], [497]. Furthermore, all hydrogels are obtained at an optimum concentration of 50 mg/mL, suggesting similar morphological characteristics. This suggests that the inherent characteristics of the ELRs promote a fluid transfer of liquids and nutrients in and out of the scaffold. Furthermore, the rough textures are designed to provide attachment points for material-cell interactions, which may influence cell behaviour and differentiation [591]. The pore shape is predominantly circular or ellipsoidal, with a considerable degree of heterogeneity in pore size. In both the new hydrogels, VKV-SKS-IKVAV and VKV-SKS-IKVAV-PPFLM, and in the control hydrogels, VKV-SKS, larger pores are observed, with several smaller pores situated within them. The pore size of the control hydrogel is slightly smaller than that of the recently developed new hydrogels. Thus, for the VKV-SKS control hydrogel, the pore size is approximately 32 µm for the large pore and 5 µm for the small pore. In contrast, the pore size of the VKV-SKS-IKVAV hydrogel is approximately 34 µm large pore and 6 µm small pore, while that of the VKV-SKS-IKVAV-PPFLM hydrogel is approximately 39 µm large pore and 10 µm small pore.

3.2.2.7.3.- Mechanical characterization of biofunctionalized click hydrogels by rheological measurements

In order to assess the regenerative potential of these novel hydrogels in the context of regenerative medicine, it is essential to investigate their rheological properties. Therefore, VKV-SKS-IKVAV hydrogels and VKV-SKS control hydrogels are prepared at a concentration of 50 mg/mL. A strain sweep experiment is conducted on each hydrogel to study their rheological properties. The amplitude of the strain for all subsequent rheological measurements was set at 1 %. This value was selected as it is within the linear viscoelastic range (LVR) of the hydrogels, as established in the methodology section. Figure 85A illustrates the evolution of the elastic modulus (G') and viscous modulus (G'') as a function of frequency (in the range from 0.01 to 10 Hz), with a strain of 1 % and a temperature of 37 °C, for VKV-

SKS-IKVAV hydrogels compared to VKV-SKS control hydrogels. Each hydrogel is subjected to a single test, which is performed in triplicate. The graph presents the average of the three tests, together with the respective standard deviation. Although a frequency-dependent relationship with G' is observed, no significant relationship with G'' is evident. It is noteworthy to mention that, throughout the study, the value of G' was persistently higher than G'', indicating the presence of viscoelastic behaviour in hydrogels under investigation.

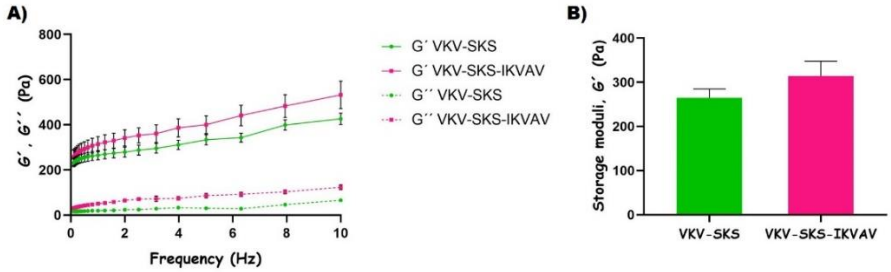

Figure 85: ***Assessment of mechanical properties of preformed VKV-SKS-IKVAV and VKV-SKS hydrogels. A)*** *Evolution of the storage modulus (G'), and loss modulus (G'') as a function of frequency for new click hydrogels.* ***B)*** *Average storage (G´) and loss (G´´) moduli measurement for each sample at a frequency of 1 Hz, a strain of 1 %, and a temperature of 37 °C.*

The results indicate that the elastic modulus of the VKV-SKS-IKVAV hydrogel ranges between 250 and 500 Pa, while the viscous modulus varies between 20 and 100 Pa. These values are consistent with those obtained for the VKV-SKS hydrogels used as control. Consequently, this novel polymer retains the morphological and mechanical characteristics inherent to ELR hydrogels, probably, due to the design of the hydrogels with a constant 1:1 ratio of azides to cyclooctynes, resulting in a final concentration of 50 mg/mL, which ensures uniform mechanical properties among all types of hydrogels. Nevertheless, it is observed that both the storage modulus (G') and the loss modulus (G'') values are slightly higher in the VKV-SKS-IKVAV hydrogels compared to the VKV-SKS control, indicating a higher stiffness in the new hydrogels. This can be attributed to a reduction in the water content of the new hydrogels, as evidenced by the subsequent section, which also aligns with the transparency images in Figure 83. Consequently, VKV-SKS-IKVAV hydrogels with more compact chains may retain fewer water molecules, resulting in higher stiffness and a colour change towards a whiter shade.

Figure 85B presents the mean values obtained for the different hydrogels under a sweep frequency of 1 Hz, while Table 46 provides further detail on these values, demonstrating the absence of statistically significant differences in the mechanical properties between the two types of hydrogels.

Table 46: Average storage modulus (G´) and loss modulus (G´´), as measured on preformed VKV-SKS-IKVAV and VKV-SKS hydrogels under frequency sweep mode at 1 Hz at 37 °C.

	G´ (Pa)	G´´ (Pa)
VKV-SKS	264.9 ± 34.8	19.5 ± 3.0
VKV-SKS-IKVAV	314.3 ± 57.9	50.5 ± 9.5

These findings are consistent with those obtained using the previously described click technology, which achieve elastic moduli in the range of 1 to 10 kPa, in line with the characteristics required for biomedical applications in soft tissue engineering [433]. Moreover, previous studies on hydrogels with comparable cross-links to the new hydrogels [457] indicate that it is reasonable to anticipate that VKV-SKS-IKVAV hydrogels could readily modify their mechanical properties by simply adjusting the final gel concentration. This adaptability renders them suitable for a wide range of applications and allows the simulation of the mechanical properties of various tissues.

3.2.2.7.4.- Water content percentage of biofunctionalized hydrogels

Although elastin hydrogels, in their dry state, exhibit a solid consistency and remarkable hardness, when immersed in an aqueous solution, water penetrates into the spaces of the hydrogel chains until it reaches a physicochemical equilibrium upon swelling. Consequently, in ultrapure water and at a concentration of 50 mg/mL, the hydrogels VKV-SKS-IKVAV and VKV-SKS-IKVAV-PPFLM exhibit a water content percentage of 92.2 % and 91.9 %, respectively, after reaching equilibrium, as illustrated in Figure 86A. It can be observed that the water content of both samples is slightly lower than that of the control hydrogel VKV-SKS. However, no statistically significant differences are identified.

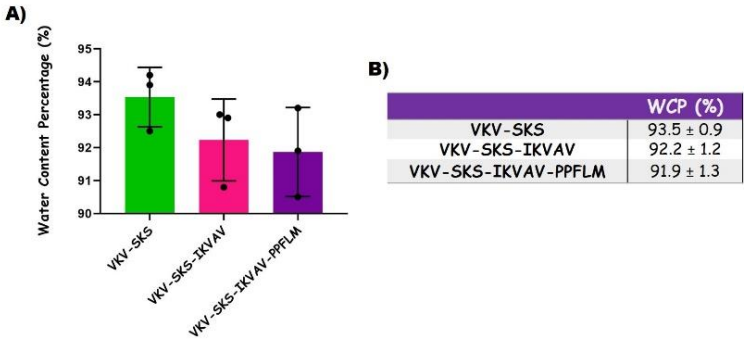

Figure 86: ***Water content percentage (WCP). A)*** *Water content percentage of VKV-SKS-IKVAV and VKV-SKS-IKVAV -PPFLM hydrogels.* ***B)*** *Average values of WCP in ultrapure water after reaching equilibrium.*

Figure 86B presents the averages of the percentage of water content, which demonstrate that the AASIKVAVSADR sequence exhibits a higher hydrophilicity in comparison to the PPFLMLLKGSTR sequence. Consequently, due to the trend of the results, the hydrogel incorporating only the AASIKVAVSADR sequence should exhibit a slightly higher water content than the hydrogel including both sequences. Moreover, as previously indicated, the new gels reveal a slightly higher stiffness compared to the control hydrogel, due to a lower presence of water. This is also reflected in their transparency. Thus, both the VKV-SKS-IKVAV hydrogel and the VKV-SKS-IKVAV-PPFLM hydrogel display a higher opacity compared to the transparent VKV-SKS control hydrogel.

3.2.2.7.5.- In vitro characterisation of Laminin mimetic hydrogels

3.2.2.7.5.1.- Effect of laminin mimetic sequences on cell adhesion

A cell adhesion assay was conducted to ascertain the role of the adhesion domains AASIKVAVSADR and PPFLMLLKGSTR incorporated into the newly developed polymers in the adhesion and proliferation of various cell types, including HFF-1 and HaCaT cells. The methodology employed was in accordance with the previously described protocol in [494]. For this purpose, cells are seeded onto the polymer-coated wells and, after a period of three hours, cells are fixed and stained with crystal violet, as illustrated in Figure 87A. The early adhesion of fibroblasts to the different functionalised surfaces reveals a slight increase in adhesion for the SKS-IKVAV-PPFLM polymer, with a greater number of cells observed. The adhesion to the SKS-IKVAV polymer also appears to be slightly superior to that of the control SKS polymer, which also contains cell adhesion sequences (RGD) that facilitate good adhesion to the cells. The SKS-IKVAV-PPFLM polymer demonstrate a stimulatory effect on keratinocyte adhesion, with a pronounced increase in early adhesion observed after 3 hours in comparison to the other two polymers, where HaCaT cells also adhere, but to a lesser extent. It can therefore be confirmed that the SKS-IKVAV-PPFLM polymer has enhanced cell adhesion and induces cell proliferation of keratinocytes. Despite the sequences being integrated into the main structure of the polypeptide chain, the polymer acquires a suitable conformation to form an optimal cell adhesive matrix.

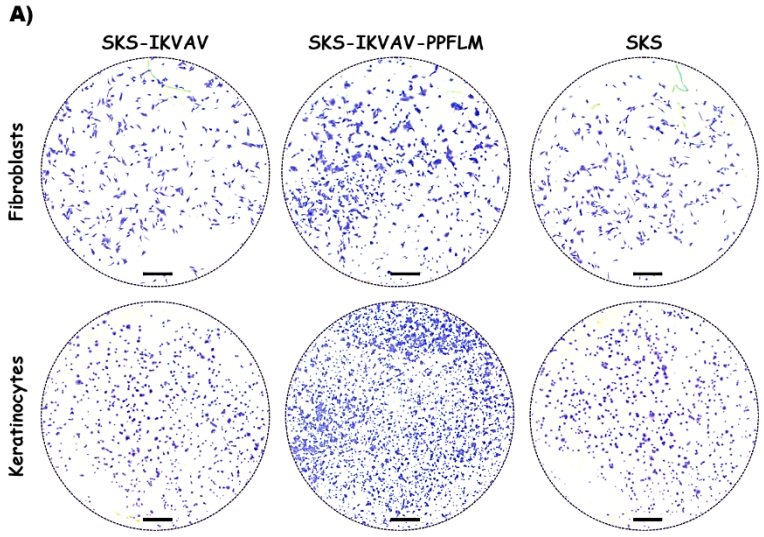

Figure 87: ***Effect of the incorporation of the adhesion domains, AASIKVAVSADR and PPFLMLLKGSTR, into the new polymers on cell adhesion and proliferation. A)*** *Representative images of crystal violet-stained cells adhered to the surface coated with the SKS-IKVAV and SKS-IKVAV-PPFLM polymers, in comparison to the SKS control. Adhesion time of 3 hours. Scale bar: 0.5 mm.*

3.2.2.7.5.2.- Biocompatibility and cytotoxicity

The evaluation of the biocompatibility of the new elastin hydrogels, VKV-SKS-IKVAV and VKV-SKS-IKVAV-PPFLM, is evaluated using AlamarBlue at different experimental times (1, 3, 7 and 14 days), with the aim of understanding the metabolism of HFF-1 and HaCaT cells in the presence of hydrogel. The results of the

cell viability analysis demonstrate a direct correlation between the increase in metabolic activity and an increase in fluorescence intensity for all conditions over different periods. The aforementioned findings are presented in Figure 88A and Figure 88B for fibroblasts and keratinocytes, respectively. The cell viability curve follows the typical pattern of cell growth, exhibiting an exponential increase in cell number over time until reaching a maximum on the final day of culture. In general terms, therefore, it can be stated that these novel biofunctionalized ELR hydrogels demonstrate biocompatibility consistent with previous studies on similar cross-linked elastin hydrogels [519].

The newly developed elastin hydrogels have been found to be non-cytotoxic when used with fibroblasts. Furthermore, an increase in the fluorescent signal is observed with increasing days of culture, which is reasonable as there are more cells in the hydrogels. Initially, there are no significant differences in the adhesion of the new hydrogels compared to the control hydrogel VKV-SKS during the first days of culture. However, after 14 days of culture, statistically significant differences were observed between the new VKV-SKS-IKVAV-PPFLM hydrogel in comparison to the VKV-SKS control. These findings indicate that these hydrogels provide a favourable environment for cell growth by favouring cell proliferation.

Conversely, the hydrogel comprising the PPFLMLLKGSTR sequence evidences a higher degree of specificity in keratinocyte adhesion. These findings are consistent with those of a previous study of early adhesion, which demonstrated enhanced keratinocyte adhesion when the well was coated with the SKS-IKVAV-PPFLM polymer. Moreover, keratinocytes show the highest proliferation capacity and cell viability after 14 days in the VKV-SKS-IKVAV-PPFLM hydrogels, in contrast to the VKV-SKS-IKVAV hydrogels. Notably, the VKV-SKS control hydrogels also demonstrate good cell adhesion capacity due to the presence of the general adhesion sequence (RGD).

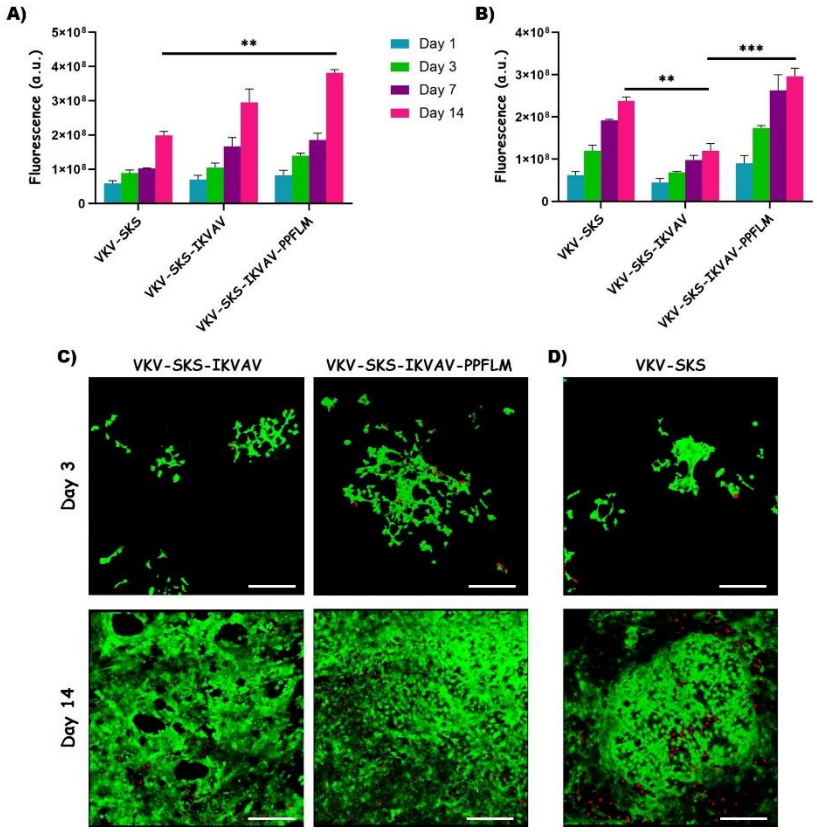

*Figure 88: **Biocompatibility and cytotoxicity**. **A)** Reduction of AlamarBlue in HFF-1 cells seeded onto new functionalised click hydrogels (VKV-SKS-IKVAV and VKV-SKS-IKVAV-PPFLM) at different time points. **B)** Reduction of AlamarBlue in HaCaT cells seeded onto new functionalised click hydrogels (VKV-SKS-IKVAV and VKV-SKS-IKVAV-PPFLM) at different time points. **C)** Fluorescence L&D microscopy images of stained HaCaT cells, seeded on new functionalised click hydrogels (VKV-SKS-IKVAV and VKV-SKS-IKVAV-PPFLM) during a 14-day culture period. **D)** Fluorescence L&D microscopy images of stained HaCaT cells, seeded on a control hydrogel (VKV-SKS). Green staining distinguished live cells, while red staining revealed cell death. Scale bar: 250 µm.*

The new hydrogels are subjected to cell viability and cytotoxicity analysis using LIVE/DEAD staining, which provided additional insight into the results obtained. Figure 88C displays projections of 3D fluorescence images obtained with a confocal microscope. The images reveal an increase in the number of HaCaT cells within the hydrogels over time, with the number of cells increasing from 3 to 14 days. Figure 88D shows fluorescence images of the VKV-SKS control hydrogels. Throughout the observation period, the majority of cells observe on the surface and within the hydrogels are alive, as indicated by green staining. The minimal red staining observed suggest that the cells maintain their characteristic morphology and size, and that nutrients are able to circulate freely through the scaffold, thus ensuring cell viability. These findings are consistent with those obtained through the AlamarBlue viability assessment, which demonstrate a significant increase in the rate of cell proliferation, reaching a maximum at 14 days. This is also reflected in the fluorescence images.

Hydrogels incorporating the PPFLMLLKGSTR sequence demonstrate a clear preference for HaCaT cells, as evidenced by the higher number of cells adhering to this type of hydrogel in biocompatibility experiments with AlamarBlue and cytotoxicity experiments with L&D, as well as higher early adhesion after three

hours in contact with the SKS-IKVAV-PPFLM polymer. The efficacy of the PPFLMLLKGSTR sequence when is introduced into the ELR chain against keratinocytes is therefore corroborated. Consequently, these novel hydrogels incorporating the PPFLMLLKGSTR sequence are likely to be capable of regulating epithelial adhesion to the underlying connective tissue and enhancing keratinocyte motility, thus facilitating the re-epithelialisation process and promoting wound healing.

The outcomes of the study indicated that hydrogels comprising recombinantly inserted laminin sequences exhibited comparable results to hydrogels with chemically grafted laminin sequences. This was evidenced by the observation of similar adhesion values for both fibroblasts and keratinocytes. Consequently, the efficacy of the PPFLMLLKGSTR sequence at the optimised concentration of six repeats for keratinocyte cell adhesion is demonstrated. Furthermore, the incorporation of this sequence into the recombinant chain offers several advantages, including the precise control of the final sequence, which reduces variability in the results. Additionally, the recombinant technology enables a more efficient and rapid production process.

It can therefore be concluded that these innovative biofunctionalized hydrogels, developed with specific laminin sequences, concretely PPFLMLLKGSTR, have the potential to serve as candidates for wound dressings for difficult-to-heal wounds, as they exhibit favourable mechanical properties and an appropriate water content to maintain the adequate moisture. Furthermore, the inherent properties of elastin, including high biocompatibility and porosity, in addition to the added functionalities, will favour adhesion and proliferation of keratinocytes from the wound edge, thereby improving the healing process.

CONCLUSION AND FUTURE DIRECTIONS

Conclusions and future directions

4.1.- Conclusions

The presented thesis successfully demonstrated that elastin-based recombinamers (ELRs) are an optimal candidate for the development of wound dressings. In this context, ELRs dressings with tailored bioactivity for the purpose of skin regeneration were prepared in the form of membranes and hydrogels. Subsequently, a comprehensive evaluation was conducted, in which the scaffolds were examined in relation to their mechanical characteristics, biocompatibility and bioactivity. These properties are crucial for the effective promotion of skin regeneration and enhancement of the healing of challenging wounds. Moreover, the innovative multifunctional elastin-based hydrogels with incorporated laminin sequences were demonstrated to markedly enhance wound healing by delivering targeted bioactivities. Two distinct methodologies were employed in order to achieve this objective. The first approach entailed chemical synthesis with click chemistry for peptide anchoring, whereas the second utilised genetic engineering techniques with recombinant expression in *Escherichia coli*, resulting in the biosynthesis of polymers with the desired bioactive properties. The distinctive characteristics of ELRs, including their thermosensitivity, biocompatibility, bioactivity, and mechanical strength, as well as the incorporation of new functionalities, were pivotal in eliciting these favourable biological responses, thereby reinforcing their potential in the development of tailored wound dressings for skin regeneration.

Consequently, the methodologies developed and employed to procure these novel ELR dressings may be classified into two categories:

1.- The synthesis of elastin membranes with a high degree of porosity and minimal thickness was achieved by the dissolution of two distinct ELRs in two immiscible liquid phases.

- Two ELRs were employed in the controlled production of an elastin-like recombinamer polymer-based membrane in a liquid-liquid interface of immiscible solvents via click chemistry. Both polymers (VKV and SKS) contain 24 lysine residues distributed evenly along the polypeptide structure, which facilitates the formation of click cross-linkable groups. In addition, the serine amino acid was selected as a host residue in the SKS polymer, responsible for increasing T_t by increasing polarity and maintaining the ELR in an aqueous phase. Complementarily, the cell adhesion sequence RGD was included in the protein backbone, thereby confirming the ability to tailor the bioactivity of the engineered membrane.

- A comprehensive characterisation of the ELR membranes was conducted, employing multiple characterisation techniques to elucidate their structure and suitability for potential practical applications. The ATR-FTIR technique

corroborates the correct formation of the membranes, as evidenced by the disappearance of the azide signal at 2100 cm^{-1} upon consumption to form the orthogonal bond with the cyclooctyne. Furthermore, the investigation of the thermal behaviour of the membranes using differential scanning calorimetry (DSC) revealed that the elevated transition temperature of the SKS polymer renders it to be relatively straightforward to handle at room temperature.

- The application of a set of analytical techniques to the surface of ELRs at different concentrations (5, 10, 25 and 50 mg/mL) yielded information regarding the surface topography (SEM, ESEM and AFM) and material properties at the interface (based on contact angle measurements). It was thus demonstrated that the surface roughness increases with decreasing ELR polymer concentration, regardless of the technique employed and the state of the membrane (dry or hydrated). These findings confirm that the topography and surface roughness of ELR membranes can facilitate the interaction between cells and the material, and promote the adhesion of the membrane to the wound, resulting in an efficient dressing. Furthermore, the SEM cross-section of the membrane demonstrated that the scaffolds possess a porous structure with values ranging from 5 to 2 μm depending on the membrane concentration, which facilitates cell colonization and improves fluid exchange when applied *in vivo*. Finally, contact angle measurements revealed that the hydrated membranes exhibited high hydrophilicity, which is essential for their use as wound dressings. This property enables the membranes to maintain moisture content and promote uniform re-epithelialization, as well as facilitating exudate absorption.

- The self-healing capacity of the ELR membranes was evaluated following the creation of a scratch and subsequent rehydration. The results demonstrated that a completely closed surface was attained, as evidenced by the AFM data. It was thus determined that following a period of 30 minutes from the commencement of the scratch, the wound exhibited a closure rate of approximately 15 %. Furthermore, upon rehydration through the addition of water, the wound exhibited a complete closure.

- The results of the membrane swelling measurements in both water and PBS solution provided evidence that water diffuses within the three-dimensional network of the ELR membrane. The study revealed that the membranes exhibited a reduction in swelling in PBS compared to ultrapure water. Furthermore, a correlation was observed between the degree of swelling and the concentration of the membrane, with a higher concentration resulting in a lower degree of swelling. Finally, the amount of water in the membranes was found to be between 98.5 % and 99.4 % for membranes with a concentration of 50 mg/mL and 5 mg/mL, respectively. This is advantageous for the permeability and biocompatibility of the scaffolds, as well as for the absorption of wound exudates.

- The biodegradation of ELR membranes was assessed through *in vitro* enzymatic digestion with elastase, which corroborated the complete disappearance of the membrane after 22 days of incubation. The results demonstrated that the rate of enzymatic degradation was concentration-dependent, with accelerated enzymatic degradation resulting in a reduced concentration of the membrane. Materials used for wound dressings must remain stable for a minimum of three weeks (21 days) to allow for the gradual replacement of the dressing by newly formed healthy tissue. Our elastin membranes thus satisfy this condition.

- The biocompatibility and lack of cytotoxicity of membranes based on chemically cross-linked ELRs were evaluated in this work using a range of methods, both *in vitro* and *in vivo*. In particular, it was demonstrated that fibroblasts (HFF-1) and keratinocytes (HaCaT) were able to adhere and proliferate on ELR membranes over a period of 21 days. The presence of cell adhesion motifs (RGD) in the matrix of the materials was found to induce an improvement in cell-material interaction and promote a favourable cellular response in tissue regeneration. Furthermore, the majority of cells exhibited good viability after 21 days of experimentation, displaying typical dimensions and morphology (elongated and expanded) and adapting to the membranes both on their surface and within.

- The capacity of cells to undergo growth and maturation, as well as their migratory potential, was investigated in the presence of ELR membranes through the utilisation of a series of assays. The clonogenic potential of fibroblasts (HFF-1) and keratinocytes (HaCaT) was evaluated by testing their ability to form colonies on ELR membranes after 15 days. Furthermore, immunofluorescent markers were employed to stain the cells, in addition to more sophisticated techniques such as quantitative real-time polymerase chain reaction (qRT-PCR), which enabled the determination of the expression of specific genes. This provided insights into the manner in which cells interact with their surroundings in the presence of a scaffold. Consequently, based on this information, it was concluded that the biomaterial facilitates the adhesion, proliferation, and maturation of cells, thereby enabling the expression of genes characteristic of the cells. Finally, the motility of fibroblasts and keratinocytes was investigated through two assays: a transwell migration assay and an *in vitro* scratching assay. Both cell types play a vital role in wound re-epithelialisation, and thus this study was conducted to ascertain their motility. In both instances, it was demonstrated that the presence of the membrane does not impede or hinder cell motility. Moreover, the implementation of these membranes in chronic wounds is expected to improve cell migration within the senescent cell population, which exhibits reduced motility. This is achieved by favouring the adhesion and subsequent motility of healthy cells from the wound margins to the injured site, thus promoting wound re-epithelialisation.

- The regenerative capacity of ELR membranes was evaluated in an *ex vivo* partial-thickness excision human skin wound model. The results demonstrated that the presence of elastin membranes significantly reduced wound shrinkage compared to other treatments, such as the use of Pluronic hydrogel or dermal substitutes. This finding suggests that wound healing without shrinkage, which is a significant contributor to visible scarring, can be achieved with the use of elastin materials. Furthermore, elastin materials exhibited superior re-epithelization compared to Pluronic hydrogel. Furthermore, histological analysis revealed that keratinocytes in samples containing elastin biomaterials formed a new epidermis with no discernible differences compared to fresh human skin after six days of healing. Additionally, the newly formed epidermis was observed to have a thickness of four to five cells, which was comparable to that of intact skin.

- Finally, animals were used to elucidate the interaction between ELR-based membranes and living tissues. Initially, Swiss mice were employed for *in vivo* evaluation of the biocompatibility and long-term stability of these membranes by subcutaneous implantation. The subcutaneous placement of ELR-based membranes did not result in an excessive inflammatory response, foreign body rejection, or fibrotic tissue formation in the area of implantation upon macroscopic and histological observation of these materials. Furthermore, the elastin scaffolds exhibited the formation of functional blood vessels, in contrast to the dermal substitute. Additionally, the membranes demonstrated high stability following seven weeks of *in vivo* experimentation, accompanied by evidence of cell infiltration and colonization within the membranes, reinforced by the presence of RGD cell adhesion domains, which substantiates their high biocompatibility. On the other hand, the subsequent performance of elastin membranes in full-thickness excision wound healing processes was evaluated using a C57BL/6J murine model. The study demonstrated that elastin membranes were effectively integrated into *de novo* tissue and promoted the formation of all skin layers, particularly the epidermis, indicating active re-epithelialisation, with several layers of ordered keratinocytes observed. The membranes demonstrated superior wound healing rates (approximately 70 %) in comparison to elastin and Pluronic hydrogels (approximately 60 %), which can be attributed to their thin, porous structure, which facilitated cell proliferation, migration, and nutrient/oxygen exchange. Furthermore, they retained moisture, thereby preventing the formation of a scab. The histological analysis revealed a reduction in inflammatory processes, the formation of new blood vessels, and the alignment of collagen fibres in a more efficient manner, which prevented the formation of fibrosis. This was in comparison with the misplaced fibres observed in other samples studied, such as Pluronic hydrogels. The elastin membranes contributed to the formation of thicker, more organised collagen bundles, a reduction in wound contraction, and a promotion of healing without the formation of visible scars.

2.- The creation of a novel advanced hydrogel with enhanced bioactivity was achieved through the incorporation of laminin-specific adhesion domains, AASIKVAVSADR and PPFLMLLKGSTR, which could facilitate cell adhesion to fibroblasts and keratinocytes. This innovation has the potential to accelerate the wound healing process. Two distinct strategies were employed to successfully obtain the novel hydrogels.

The initial approach entails the chemical synthesis of laminin mimetic peptides and their subsequent anchoring by click chemistry to the main chain of the ELR polymer.

- The chemical synthesis of two novel laminin mimetic peptides (KAASIKVAVSADR and KPPFLMLLKGSTR) was successfully accomplished via the solid phase peptide synthesis (SPPS) technique. The peptides were designed to contain the cross-linkable azide group, which allowed subsequent binding to an ELR polymer for the purpose of biofunctionalization. Prior to binding, the peptides were characterised by amino acid analysis, elemental analysis (UPLC-ESI-qTOF) and nuclear magnetic resonance, thereby corroborating the correct synthesis prior to use.

- A comprehensive physico-chemical characterisation was conducted to ascertain the efficacy of the anchoring of the laminin peptides to the ELR polymer for functionalisation via a click reaction between the cross-linkable groups of both the peptides and the ELR polymer, which were azides and cyclooctynes, respectively. A variety of physicochemical techniques were employed, including amino acid analysis with HPLC, NMR spectroscopy to generate peptide fingerprint data, mass spectrometry (specifically MALDI-TOF) to determine the purity and molecular weight of the final products, as well as ATR-FTIR spectroscopy.

- A novel tricomponent hydrogel (VKV-peptide-SKS) was developed by taking advantage of the modularity of the catalyst-free SPAAC click reaction chemistry, whereby the reactions were performed consecutively. Consequently, the VKV-cc polymer was initially reacted with peptides containing azide groups in order to be functionalised. Subsequently, maintaining the 1:1 stoichiometric ratio between azides and cyclooctynes, the VKV-peptide polymer reacted with the SKS-azide polymer to successfully form a multifunctional hydrogel with improved adhesion, which has the potential to facilitate enhanced wound healing. Furthermore, the synthesis of these tricomponent hydrogels represents a significant advancement, as it marks the first successful creation of ELRs gels with medium-sized grafted peptides.

- The new hydrogels were extensively characterised in order to ascertain their macroscopic properties, internal morphology, water content, and mechanical properties. All hydrogels with different peptide concentrations

(2X, 4X, and 6X) were found to be stable, manageable, and transparent, thus facilitating the observation of wound healing without the need to remove the dressing. The internal morphology analysis revealed a porous matrix with pore sizes varying significantly within the same samples. The larger pores were approximately 30-35 μm, while the smaller pores ranged from 4 to 6 μm. There was no clear relationship between the pore size and the peptide concentration. The water content of the hydrogels increased with higher peptide concentrations, from 94.3 % for 2X to 95.4 % for 6X in hydrogels with the KAASIKVAVSADR peptide, and from 93.0 % for 2X to 93.7 % for 6X with the KPPFLMLLKGSTR peptide. The enhanced porosity and high-water content facilitated improved nutrient and oxygen exchange, which in turn promoted cell proliferation and tissue formation. The results of the rheological studies indicated that the storage modulus exhibited a slight decline with an increase in peptide concentration. However, this did not preclude its suitability for soft tissue regeneration applications.

- The biocompatibility and absence of cytotoxicity of the novel multifunctional tricomponent mimetic ELR hydrogels were confirmed by *in vitro* methods. The study concluded that hydrogels with the KPPFLMLLKGSTR peptide exhibited similar initial fibroblast adhesion in comparison with the control VKV-SKS. In contrast, hydrogels with the KAASIKVAVSADR peptide demonstrated consistent cell growth and viability over time, with a maximum in cell viability achieved after 14 days. Conversely, it is evident that the KPPFLMLLKGSTR peptide exhibited enhanced specificity for keratinocyte adhesion and proliferation, particularly in hydrogels with six anchored peptides, which also reached maximum viability after 14 days. The KAASIKVAVSADR sequence did not appear to induce an improvement in either cell type, and its behaviour was similar to that of the control, which also contains RGD cell adhesion sequences. In conclusion, the results of this approach corroborated those of the KPPFLMLLKGSTR sequence, indicating a notable enhancement in keratinocyte adhesion in contrast to fibroblast adhesion behaviour, which was comparable to that of the control. This allowed us to determine the optimal concentration of peptides anchoring to the hydrogel for promoting adhesion and proliferation of keratinocytes, especially at high peptide concentrations (6X), which is expected to facilitate the wound healing process.

It has been successfully demonstrated that an alternative approach to incorporating the same keratinocyte-specific sequences is possible. Three genes encoding elastin-like polymers that include the desired highly selective complementary specific bioactivities within the polymer backbone have been biosynthesized using genetic engineering techniques and recombinant DNA expression in *Escherichia coli*. This technology enables the production of polymer hydrogels with a more reproducible composition.

- The gene constructs for the expression of the new polymers (SKS-IKVAV, SKS-PPFLM and SKS-IKVAV-PPFLM) were successfully

obtained and verified through the use of agarose gel electrophoresis and DNA sequencing. Furthermore, the ELRs (SKS-IKVAV and SKS-IKVAV-PPFLM) were expressed in *Escherichia coli* as a heterologous host for bioproduction, and purified by ITC, resulting in yields of 80 to 150 mg/L culture medium. Nevertheless, the SKS-PPFLM polymer could not be obtained in a pure form. The characterisation techniques, including SDS-PAGE and MALDI-TOF, demonstrated a satisfactory agreement between the experimental and theoretical or expected molecular weight, as well as a high degree of purity. However, a slight initial degradation remained, even after the application of various protease inhibitors. The results of the HPLC analysis confirmed the correct amino acid composition, and the T_t of the ELRs was verified by aqueous phase turbidimetry measurements. Finally, additional characterisation techniques, including ^{1}H-NMR and FTIR, yielded favourable outcomes, confirming the purity of all batches of the distinct ELRs and validating that the ELRs exhibited the intended structure and the subsequent requisite chemical modifications.

- Both ELRs (SKS-IKVAV and SKS-IKVAV-PPFLM) were successfully modified at the ε-amine of the lysine residues within the macromolecule to carry an azide group, which allow the subsequent cross-linking of the hydrogel by binding with a complementary group carried by the other polymer. The modification rate was approximately 60 %, indicating that the recombinamer was functionalised with approximately 18 azide groups. Similarly, VKV was modified to carry an activated alkyne group (cyclooctyne), with a modification rate of 60 % and approximately 14 cyclooctyne groups. Subsequently, maintaining the stoichiometric ratio of 1:1 between azides and cyclooctynes, the VKV-cc polymer is combined with SKS-IKVAV-azide or SKS-IKVAV-PPFLM-azide polymers, resulting in a cross-linking click reaction that successfully generates chemically cross-linked bioactive ELRs hydrogels with improved adhesion. Such hydrogels will facilitate interactions with cells, thereby promoting skin regeneration in chronic wounds or burns following implantation in the affected area.

- The novel biofunctionalized hydrogels were characterised through a series of macroscopic properties, internal morphology, water content and mechanical properties. Thus, the two obtained hydrogels were found to be stable and easy to handle, although they exhibited a certain degree of opacity compared to the control hydrogel VKV-SKS. The internal morphology of the hydrogels revealed a porous three-dimensional matrix, with water contents of 92.2 % and 91.9 % for SKS-IKVAV and SKS-IKVAV-PPFLM, respectively. Finally, rheological studies were conducted on the VKV-SKS-IKVAV hydrogel, which exhibited rheological properties consistent with those observed in soft tissues.

- The biocompatibility and lack of cytotoxicity of the new ELR hydrogels with enhanced bioactivities (VKV-SKS-IKVAV and VKV-SKS-IKVAV-PPFLM) were confirmed by *in vitro* methods. In particular, hydrogels comprising the PPFLMLLKGSTR sequence exhibited a pronounced preference for HaCaT cells, as evidenced by enhanced cell adhesion and viability in biocompatibility and cytotoxicity assays conducted after 14 days of culture. Moreover, the outcomes of the early adhesion experiments illustrate the effectiveness of this sequence in enhancing keratinocyte adhesion when compared to the control hydrogels, which also contained RGD adhesion sequences. It can therefore be concluded that these new hydrogels have the potential to regulate epithelial adhesion to connective tissue and enhance keratinocyte motility, thus facilitating re-epithelialisation and promoting wound healing. Moreover, these results are comparable to those obtained with hydrogels containing the same chemically grafted peptides, but with the advantage of greater precision in sequence and ease of production due to the recombinant production of the polymer.

4.2.- Future prospects

In the long history of biomaterials development, ELRs have been extensively researched due to their remarkable versatility and potential to create customised solutions in a range of biomedical fields. One illustration of their versatility is the variety of their designs, which may include cell adhesion domains (such as RGD and REDV), controlled degradation capacity, self-assembly into vesicles or micelles to encapsulate vaccines or gene delivery, among others. This thesis presents new ELRs and ELR membranes obtained by an innovative technology, which show promising prospects for improving the wound healing process. Both VKV-SKS membranes and ELRs designed with specific adhesion sequences, AASIKVAVSADR and PPFLMLLKGSTR, which are present in the main polymer chain or anchored as peptides, have been demonstrated to possess the requisite mechanical and biological properties to be considered as promising dressings for the treatment of chronic wounds facilitating cell adhesion and proliferation of keratinocytes.

Consequently, the research conducted throughout this thesis constitutes a modest contribution to scientific progress, serving more as a starting point than an end point. It establishes the initial foundations for future research with considerable potential for further development. Upon the conclusion of this study, new challenges emerge for the refinement of the polymer system employed as a dressing, particularly with regard to sequence optimisation, which build upon years of expertise in ELR development. Although the *in vitro* behaviour of the polymer system with cells has been demonstrated to be satisfactory, one of the key points that needs to be implemented for *in vivo* systems is the control of matrix bioresorption in line with tissue remodelling. Therefore, an initial improvement could be the integration of specific enzymatic degradation domains into the polymer sequence, which would allow more precise spatiotemporal control over cell infiltration and material remodelling. This would enable cells to digest the materials and invade and propagate within such a system while creating their own ECM. This approach involves the synthesis of ELRs containing proteolytic target sites with different degradation rates (fast-GTAR and slow-DRIR). These ELRs belong to the plasminogen activator system, specifically the enzyme uPA, which is encoded in their backbone [302]. This approach allows for the temporal and spatial control of cellular infiltration, as well as the structural transformation of the infiltrated tissue through the use of adapted and controlled degradation, and can be employed as a provisional support for soft tissues until the functional native tissue is obtained [587], [594].

Furthermore, it is possible to introduce a final intrinsic functionality into the dressing polymer in the form of an antimicrobial capacity to prevent infectious processes that are prevalent in chronic wounds or severe burns. This approach involves the synthesis of ELRs containing sequences of the antimicrobial peptide, GL13K, derived from the parotid secretory protein, which is known for its high

bactericidal potential [343], [595]. This addition aims to prevent bacterial invasion of the area, thus contributing to the prevention of infectious processes.

Consequently, dressings with tailored degradation kinetics and antimicrobial resistance may be obtained, depending on patient-specific variabilities, which will ultimately result in the generation of a scaffold that will faithfully replicate healthy native tissue and assist in the current need for suitable substitutes in clinics.

Additionally, the selection of an appropriate animal model for the testing of biomaterials is crucial in biomedical research, particularly in the development of therapies for clinical applications in humans. While mice, rats and rabbits are commonly employed in preclinical studies due to their availability, cost and ease of handling, there is a growing recognition of the limitations of this model in predicting the human biological response, particularly with regard to wound healing. In contrast, pigs are considered more relevant models for these studies due to their anatomical, physiological and metabolic similarities to humans. In particular, the skin structure (epidermal thickness and dermal-epidermal thickness ratios) as well as the wound healing process in pigs is more similar to that in humans than in mice, as it occurs through a process of re-epithelialisation rather than contraction. In addition, their skin contains dermal hair follicles analogous to those found in humans, which influence the healing process. Furthermore, the speed and quality of wound healing in pigs are more comparable to those observed in humans, thereby providing more relevant and translational results that can be applied to the clinic. It would therefore be of interest to test both ELR membranes and the novel ELR hydrogels, which have been designed with specific adhesion sequences (AASIKVAVSADR and PPFLMLLKGSTR), in this pig model with partial thickness and full thickness wounds [468], [596]–[598].

Finally, due to the high cost of pig experimentation, another interesting alternative could be diabetic mice. This model is relevant in the study of chronic wounds, which have poor wound healing. Diabetic mice provide a valuable experimental model as they reproduce many of the characteristics of chronic wounds observed in diabetic patients including an altered inflammatory response, decreased collagen formation and compromised vascularisation. The assessment of biomaterials in diabetic mice allows for the evaluation of their capacity to enhance chronic wound healing by providing an optimal environment conducive to cell migration, angiogenesis and extracellular matrix synthesis. This is crucial, as chronic wounds in diabetic patients represent a significant clinical challenge due to their tendency to fail to heal properly, which increases the risk of serious complications such as infections, ulcers and amputations. Consequently, the objective of testing both ELR membranes and the novel ELR hydrogels, in diabetic mice is to develop effective therapies that address this issue and improve the quality of life of patients with chronic wounds by promoting more effective and complete wound healing [577], [599].

The ideas presented in this section are intended to stimulate the curiosity of future researchers, who may develop new projects using existing and future techniques.

REFERENCES

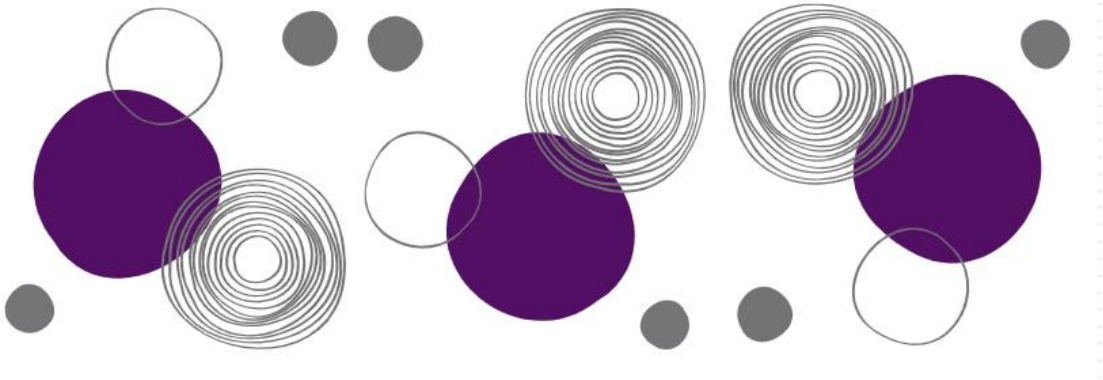

References

[1] S. Gupta, S., Sagar, S., Maheshwari, G., Kisaka, T., & Tripathi, "Chronic wounds: magnitude, socioeconomic burden and consequences," *Wounds Asia*, vol. 4(1), pp. 8-14., 2021.

[2] M. B.-D. Cristina López-Alayeto, Sandra Alexandre-Lozano , Iraida Gimeno-Pi , Carme Marquilles-Bonet, "Prevalencia de heridas crónicas y lesiones cutáneas relacionadas con la dependencia en atención primaria de la provincia de Lleida en 2022," *Gerokomos*, vol. 34 (2), pp. 134-137-Helcos, 2023.

[3] M. C. F. Simões, J. J. S. Sousa, and A. A. C. C. Pais, "Skin cancer and new treatment perspectives: A review," *Cancer Lett.*, vol. 357, no. 1, pp. 8–42, Feb. 2015, doi: 10.1016/j.canlet.2014.11.001.

[4] J. Koller, "EFFECTS OF RADIATION ON THE INTEGRITY AND FUNCTIONALITY OF AMNION AND SKIN GRAFTS," in *Sterilisation of Tissues Using Ionising Radiations*, Elsevier, 2005, pp. 197–220. doi: 10.1533/9781845690779.3.197.

[5] J. R. Yu *et al.*, "Current and Future Perspectives on Skin Tissue Engineering: Key Features of Biomedical Research, Translational Assessment, and Clinical Application," *Adv. Healthc. Mater.*, vol. 8, no. 5, Mar. 2019, doi: 10.1002/adhm.201801471.

[6] R. F. Pereira and P. J. Bártolo, "Traditional Therapies for Skin Wound Healing," *Adv. Wound Care*, vol. 5, no. 5, pp. 208–229, May 2016, doi: 10.1089/wound.2013.0506.

[7] J. Ho, C. Walsh, D. Yue, A. Dardik, and U. Cheema, "Current Advancements and Strategies in Tissue Engineering for Wound Healing: A Comprehensive Review," *Adv. Wound Care*, vol. 6, no. 6, pp. 191–209, Jun. 2017, doi: 10.1089/wound.2016.0723.

[8] K. Changi *et al.*, "Biocompatibility and immunogenicity of elastin-like recombinamer biomaterials in mouse models," *J. Biomed. Mater. Res. Part A*, vol. 106, no. 4, pp. 924–934, Apr. 2018, doi: 10.1002/jbm.a.36290.

[9] J. C. Rodríguez-Cabello, S. Escalera ☆, D. Juanes-Gusano ☆, M. Santos, and A. Girotti, "Designing Elastin-Like Recombinamers for Therapeutic and Regenerative Purposes," in *Multifunctional Hydrogels for Biomedical Applications*, Wiley, 2022, pp. 37–62. doi: 10.1002/9783527825820.ch3.

[10] J. Kanitakis, "Anatomy, histology and immunohistochemistry of normal human skin," *Eur. J. dermatology*, vol. 12, no. 4, pp. 390–401, 2002.

[11] R. Nejati, D. Kovacic, and A. Slominski, "Neuro-immune-endocrine functions of the skin: an overview," *Expert Rev. Dermatol.*, vol. 8, no. 6, pp. 581–583, Dec. 2013, doi: 10.1586/17469872.2013.856690.

[12] W. Z. Mostafa and R. A. Hegazy, "Vitamin D and the skin: Focus on a complex relationship: A review," *J. Adv. Res.*, vol. 6, no. 6, pp. 793–804, 2015.

[13] A. A. E. Ibrahim, N. Bagherani, B. Smoller, N. Bagherani, and C. Reyes-Barron,

"Anatomy and Organization of Human Skin," in *Atlas of Dermatology, Dermatopathology and Venereology*, Cham: Springer International Publishing, 2022, pp. 109–132. doi: 10.1007/978-3-319-53811-2_3.

[14] J. A. McGrath, R. A. J. Eady, and F. M. Pope, "Anatomy and organization of human skin," *Rook's Textb. dermatology*, vol. 1, pp. 2–3, 2004.

[15] P. A. J. Kolarsick, M. A. Kolarsick, and C. Goodwin, "Anatomy and physiology of the skin," *J. Dermatol. Nurses. Assoc.*, vol. 3, no. 4, pp. 203–213, 2011.

[16] W. D. Losquadro, "Anatomy of the skin and the pathogenesis of nonmelanoma skin cancer," *Facial Plast. Surg. Clin.*, vol. 25, no. 3, pp. 283–289, 2017.

[17] F. M. Watt, M.-D. Kubler, N. A. Hotchin, L. J. Nicholson, and J. C. Adams, "Regulation of keratinocyte terminal differentiation by integrin-extracellular matrix interactions," *J. Cell Sci.*, vol. 106, no. 1, pp. 175–182, 1993.

[18] F. M. Watt, "Role of integrins in regulating epidermal adhesion, growth and differentiation," *EMBO J.*, vol. 21, no. 15, pp. 3919–3926, 2002.

[19] L. A. Goldsmith, S. I. Katz, B. A. Gilchrest, A. S. Paller, D. J. Leffell, and K. Wolff, "Fitzpatrick's Dermatology in General Medicine, 8e," *McGrawHill Med.*, pp. 2421–2429, 2012.

[20] R. Moll, M. Divo, and L. Langbein, "The human keratins: biology and pathology," *Histochem. Cell Biol.*, vol. 129, pp. 705–733, 2008.

[21] S. Nithya, T. Radhika, and N. Jeddy, "Loricrin–an overview," *J. oral Maxillofac. Pathol. JOMFP*, vol. 19, no. 1, p. 64, 2015.

[22] H. Yousef, M. Alhajj, and S. Sharma, "Anatomy, Skin (Integument), Epidermis. 2021," *Treasure Isl. StatPearls Publ. https//www. ncbi. nlm. nih. gov/books/NBK470464*, 2022.

[23] L. Eckhart, S. Lippens, E. Tschachler, and W. Declercq, "Cell death by cornification," *Biochim. Biophys. Acta (BBA)-Molecular Cell Res.*, vol. 1833, no. 12, pp. 3471–3480, 2013.

[24] T. Matsui and M. Amagai, "Dissecting the formation, structure and barrier function of the stratum corneum," *Int. Immunol.*, vol. 27, no. 6, pp. 269–280, 2015.

[25] E. Candi, R. Schmidt, and G. Melino, "The cornified envelope: a model of cell death in the skin," *Nat. Rev. Mol. cell Biol.*, vol. 6, no. 4, pp. 328–340, 2005.

[26] J. Q. Del Rosso and J. Levin, "The clinical relevance of maintaining the functional integrity of the stratum corneum in both healthy and disease-affected skin," *J. Clin. Aesthet. Dermatol.*, vol. 4, no. 9, p. 22, 2011.

[27] D. E. Elder, *Lever's Histopathology of the Skin*. Lippincott Williams & Wilkins, 2014.

[28] M. Cichorek, M. Wachulska, A. Stasiewicz, and A. Tymińska, "Skin melanocytes: biology and development," *Adv. Dermatology Allergol. Dermatologii i Alergol.*, vol. 30, no. 1, pp. 30–41, 2013.

[29] S. Maksimovic *et al.*, "Epidermal Merkel cells are mechanosensory cells that tune mammalian touch receptors," *Nature*, vol. 509, no. 7502, pp. 617–621, 2014.

[30] D. Chomiczewska, E. Trznadel-Budźko, A. Kaczorowska, and H. Rotsztejn, "The role of Langerhans cells in the skin immune system," *Pol. Merkur. Lek. organ Pol. Tow. Lek.*, vol. 26, no. 153, pp. 173–177, 2009.

[31] A. Arjonen, R. Kaukonen, and J. Ivaska, "Filopodia and adhesion in cancer cell motility," *Cell Adh. Migr.*, vol. 5, no. 5, pp. 421–430, 2011.

[32] R. O. Hynes, "The extracellular matrix: not just pretty fibrils," *Science (80-.).*, vol. 326, no. 5957, pp. 1216–1219, 2009.

[33] F. Gattazzo, A. Urciuolo, and P. Bonaldo, "Extracellular matrix: a dynamic microenvironment for stem cell niche," *Biochim. Biophys. Acta (BBA)-General Subj.*, vol. 1840, no. 8, pp. 2506–2519, 2014.

[34] R. V Iozzo, J. J. Zoeller, and A. Nyström, "Basement membrane proteoglycans: modulators Par Excellence of cancer growth and angiogenesis," *Mol. Cells*, vol. 27, pp. 503–513, 2009.

[35] R. Jayadev and D. R. Sherwood, "Basement membranes," *Curr. Biol.*, vol. 27, no. 6, pp. R207–R211, 2017.

[36] V. S. LeBleu, B. MacDonald, and R. Kalluri, "Structure and function of basement membranes," *Exp. Biol. Med.*, vol. 232, no. 9, pp. 1121–1129, 2007.

[37] F. M. Watt, "Mammalian skin cell biology: at the interface between laboratory and clinic," *Science (80-.).*, vol. 346, no. 6212, pp. 937–940, 2014.

[38] D. Breitkreutz, N. Mirancea, and R. Nischt, "Basement membranes in skin: unique matrix structures with diverse functions?," *Histochem. Cell Biol.*, vol. 132, no. 1, pp. 1–10, Jul. 2009, doi: 10.1007/s00418-009-0586-0.

[39] G. J. Tortora and B. Derrickson, *Principles of anatomy and physiology: volume 1, organization, support and movement, and control systems of the human body.*, no. Ed. 13. John Wiley & Sons, 2011.

[40] M. Paulsson, "Basement membrane proteins: structure, assembly, and cellular interactions.," *Crit. Rev. Biochem. Mol. Biol.*, vol. 27, no. 1–2, pp. 93–127, 1992.

[41] D. M. Noonan *et al.*, "The complete sequence of perlecan, a basement membrane heparan sulfate proteoglycan, reveals extensive similarity with laminin A chain, low density lipoprotein-receptor, and the neural cell adhesion molecule.," *J. Biol. Chem.*, vol. 266, no. 34, pp. 22939–22947, 1991.

[42] H. Merker, "Morphology of the basement membrane," *Microsc. Res. Tech.*, vol. 28, no. 2, pp. 95–124, Jun. 1994, doi: 10.1002/jemt.1070280203.

[43] A. Bardhan *et al.*, "Epidermolysis bullosa," *Nat. Rev. Dis. Prim.*, vol. 6, no. 1, p. 78, Sep. 2020, doi: 10.1038/s41572-020-0210-0.

[44] M. Xue, R. Zhao, L. March, and C. Jackson, "Dermal fibroblast heterogeneity and its contribution to the skin repair and regeneration," *Adv. Wound Care*, vol. 11, no. 2, pp. 87–107, 2022.

[45] J. M. Sorrell and A. I. Caplan, "Fibroblast heterogeneity: more than skin deep," *J. Cell Sci.*, vol. 117, no. 5, pp. 667–675, Feb. 2004, doi: 10.1242/jcs.01005.

[46] J. Cracowski and M. Roustit, "Human Skin Microcirculation," in *Comprehensive Physiology*, Wiley, 2020, pp. 1105–1154. doi: 10.1002/cphy.c190008.

[47] A. Stunova and L. Vistejnova, "Dermal fibroblasts—A heterogeneous population with regulatory function in wound healing," *Cytokine Growth Factor Rev.*, vol. 39, pp. 137–150, 2018.

[48] K. Kabashima, T. Honda, F. Ginhoux, and G. Egawa, "The immunological anatomy of the skin," *Nat. Rev. Immunol.*, vol. 19, no. 1, pp. 19–30, Jan. 2019, doi: 10.1038/s41577-018-0084-5.

[49] A. V. Nguyen and A. M. Soulika, "The Dynamics of the Skin's Immune System," *Int. J. Mol. Sci.*, vol. 20, no. 8, p. 1811, Apr. 2019, doi: 10.3390/ijms20081811.

[50] S. X. Chen, L.-J. Zhang, and R. L. Gallo, "Dermal white adipose tissue: a newly recognized layer of skin innate defense," *J. Invest. Dermatol.*, vol. 139, no. 5, pp. 1002–1009, 2019.

[51] V. Feisst, S. Meidinger, and M. B. Locke, "From bench to bedside: use of human adipose-derived stem cells," *Stem cells cloning Adv. Appl.*, pp. 149–162, 2015.

[52] L. V Trevor, K. Riches-Suman, A. L. Mahajan, and M. J. Thornton, "Adipose tissue: a source of stem cells with potential for regenerative therapies for wound healing," *J. Clin. Med.*, vol. 9, no. 7, p. 2161, 2020.

[53] A. Domogatskaya, S. Rodin, and K. Tryggvason, "Functional diversity of laminins," *Annu. Rev. Cell Dev. Biol.*, vol. 28, pp. 523–553, 2012.

[54] E. Hohenester and P. D. Yurchenco, "Laminins in basement membrane assembly," *Cell Adh. Migr.*, vol. 7, no. 1, pp. 56–63, 2013.

[55] K. M. Mak and R. Mei, "Basement membrane type IV collagen and laminin: an overview of their biology and value as fibrosis biomarkers of liver disease," *Anat. Rec.*, vol. 300, no. 8, pp. 1371–1390, 2017.

[56] R. Timpl, D. Tisi, J. F. Talts, Z. Andac, T. Sasaki, and E. Hohenester, "Structure and function of laminin LG modules," *Matrix Biol.*, vol. 19, no. 4, pp. 309–317, 2000.

[57] M. Yamada *et al.*, "Ile-Lys-Val-Ala-Val (IKVAV)-containing laminin α1 chain peptides form amyloid-like fibrils," *FEBS Lett.*, vol. 530, no. 1–3, pp. 48–52, 2002.

[58] S. Kasai, Y. Ohga, M. Mochizuki, N. Nishi, Y. Kadoya, and M. Nomizu, "Multifunctional peptide fibrils for biomedical materials," *Pept. Sci. Orig. Res. Biomol.*, vol. 76, no. 1, pp. 27–33, 2004.

[59] D. Thid *et al.*, "Issues of ligand accessibility and mobility in initial cell attachment," *Langmuir*, vol. 23, no. 23, pp. 11693–11704, 2007.

[60] J. E. Frith, R. J. Mills, J. E. Hudson, and J. J. Cooper-White, "Tailored integrin–extracellular matrix interactions to direct human mesenchymal stem cell differentiation," *Stem Cells Dev.*, vol. 21, no. 13, pp. 2442–2456, 2012.

[61] M. Nomizu *et al.*, "Identification of Cell Binding Sites in the Laminin α1 Chain Carboxyl-terminal Globular Domain by Systematic Screening of Synthetic Peptides (∗)," *J. Biol. Chem.*, vol. 270, no. 35, pp. 20583–20590, 1995.

[62] D. S. Grant *et al.*, "Interaction of endothelial cells with a laminin A chain peptide (SIKVAV) in vitro and induction of angiogenic behavior in vivo," *J. Cell. Physiol.*, vol. 153, no. 3, pp. 614–625, 1992.

[63] J.-M. Kim, W. H. Park, and B.-M. Min, "The PPFLMLLKGSTR motif in globular domain 3 of the human laminin-5 α3 chain is crucial for integrin α3β1 binding and cell adhesion," *Exp. Cell Res.*, vol. 304, no. 1, pp. 317–327, 2005.

[64] C. M. Niessen *et al.*, "The α6β4 integrin is a receptor for both laminin and kalinin," *Exp. Cell Res.*, vol. 211, no. 2, pp. 360–367, 1994.

[65] P. Rousselle and M. Aumailley, "Kalinin is more efficient than laminin in promoting adhesion of primary keratinocytes and some other epithelial cells and has a different requirement for integrin receptors.," *J. Cell Biol.*, vol. 125, no. 1, pp. 205–214, Apr. 1994, doi: 10.1083/jcb.125.1.205.

[66] W. M. Longmate and C. M. DiPersio, "Integrin Regulation of Epidermal Functions in Wounds," *Adv. Wound Care*, vol. 3, no. 3, pp. 229–246, Mar. 2014, doi: 10.1089/wound.2013.0516.

[67] K. Zhang and R. H. Kramer, "Laminin 5 Deposition Promotes Keratinocyte Motility," *Exp. Cell Res.*, vol. 227, no. 2, pp. 309–322, Sep. 1996, doi: 10.1006/excr.1996.0280.

[68] C. M. DiPersio, S. Shah, and R. O. Hynes, "α3aβ1 integrin localizes to focal contacts in response to diverse extracellular matrix proteins," *J. Cell Sci.*, vol. 108, no. 6, pp. 2321–2336, Jun. 1995, doi: 10.1242/jcs.108.6.2321.

[69] T. H. Barker, "The role of ECM proteins and protein fragments in guiding cell behavior in regenerative medicine," *Biomaterials*, vol. 32, no. 18, pp. 4211–4214, Jun. 2011, doi: 10.1016/j.biomaterials.2011.02.027.

[70] A. M. Mercurio, I. Rabinovitz, and L. M. Shaw, "The α6β4 integrin and epithelial cell migration," *Curr. Opin. Cell Biol.*, vol. 13, no. 5, pp. 541–545, Oct. 2001, doi: 10.1016/S0955-0674(00)00249-0.

[71] S.-K. Min, S.-C. Lee, S.-D. Hong, C.-P. Chung, W. H. Park, and B.-M. Min, "The effect of a laminin-5-derived peptide coated onto chitin microfibers on re-epithelialization in early-stage wound healing," *Biomaterials*, vol. 31, no. 17, pp. 4725–4730, Jun. 2010, doi: 10.1016/j.biomaterials.2010.02.045.

[72] J. Uitto, "Biochemistry of the Elastic Fibers in Normal Connective Tissues and its Alterations in Diseases," *J. Invest. Dermatol.*, vol. 72, no. 1, pp. 1–10, Jan. 1979, doi: 10.1111/1523-1747.ep12530093.

[73] J. Rosenbloom, W. R. Abrams, and R. Mecham, "Extracellular matrix 4: The elastic fiber," *FASEB J.*, vol. 7, no. 13, pp. 1208–1218, Oct. 1993, doi: 10.1096/fasebj.7.13.8405806.

[74] I. Pasquali-Ronchetti and M. Baccarani-Contri, "Elastic fiber during development and aging," *Microsc. Res. Tech.*, vol. 38, no. 4, pp. 428–435, Aug.

1997, doi: 10.1002/(SICI)1097-0029(19970815)38:4<428::AID-JEMT10>3.0.CO;2-L.

[75] F. W. Keeley, C. M. Bellingham, and K. A. Woodhouse, "Elastin as a self–organizing biomaterial: use of recombinantly expressed human elastin polypeptides as a model for investigations of structure and self–assembly of elastin," *Philos. Trans. R. Soc. London. Ser. B Biol. Sci.*, vol. 357, no. 1418, pp. 185–189, Feb. 2002, doi: 10.1098/rstb.2001.1027.

[76] A. Goddi, "The Role of the Extracellular Matrix Protein Laminin-α4 in Obesity and Adipocyte Beiging." The University of Chicago, 2022.

[77] J. Gosline, M. Lillie, E. Carrington, P. Guerette, C. Ortlepp, and K. Savage, "Elastic proteins: biological roles and mechanical properties," *Philos. Trans. R. Soc. London. Ser. B Biol. Sci.*, vol. 357, no. 1418, pp. 121–132, Feb. 2002, doi: 10.1098/rstb.2001.1022.

[78] B. Vrhovski and A. S. Weiss, "Biochemistry of tropoelastin," *Eur. J. Biochem.*, vol. 258, no. 1, pp. 1–18, Nov. 1998, doi: 10.1046/j.1432-1327.1998.2580001.x.

[79] L. DEBELLE, "The structures of elastins and their function," *Biochimie*, vol. 81, no. 10, pp. 981–994, Oct. 1999, doi: 10.1016/S0300-9084(99)00221-7.

[80] D. W. Urry and T. M. Parker, "Mechanics of elastin: molecular mechanism of biological elasticity and its relationship to contraction," in *Mechanics of Elastic Biomolecules*, Dordrecht: Springer Netherlands, 2003, pp. 543–559. doi: 10.1007/978-94-010-0147-2_14.

[81] D. W. Urry *et al.*, "Elastin: a representative ideal protein elastomer," *Philos. Trans. R. Soc. London. Ser. B Biol. Sci.*, vol. 357, no. 1418, pp. 169–184, Feb. 2002, doi: 10.1098/rstb.2001.1023.

[82] L. Debelle and A. M. Tamburro, "Elastin: molecular description and function," *Int. J. Biochem. Cell Biol.*, vol. 31, no. 2, pp. 261–272, 1999.

[83] K. CM, "Elastic fibres," *J Cell Sci*, vol. 115, pp. 2817–2828, 2002.

[84] J. F. Almine, S. G. Wise, and A. S. Weiss, "Elastin signaling in wound repair," *Birth Defects Res. Part C Embryo Today Rev.*, vol. 96, no. 3, pp. 248–257, 2012.

[85] M. J. Sherratt, "Tissue elasticity and the ageing elastic fibre," *Age (Omaha).*, vol. 31, no. 4, pp. 305–325, 2009, doi: 10.1007/s11357-009-9103-6.

[86] S. G. Wise and A. S. Weiss, "Tropoelastin," *Int. J. Biochem. Cell Biol.*, vol. 41, no. 3, pp. 494–497, Mar. 2009, doi: 10.1016/j.biocel.2008.03.017.

[87] L. Sabatier *et al.*, "Fibrillin Assembly Requires Fibronectin," *Mol. Biol. Cell*, vol. 20, no. 3, pp. 846–858, Feb. 2009, doi: 10.1091/mbc.e08-08-0830.

[88] J. E. Wagenseil and R. P. Mecham, "New insights into elastic fiber assembly," *Birth Defects Res. Part C Embryo Today Rev.*, vol. 81, no. 4, pp. 229–240, Dec. 2007, doi: 10.1002/bdrc.20111.

[89] E. M. Green, J. C. Mansfield, J. S. Bell, and C. P. Winlove, "The structure and micromechanics of elastic tissue," *Interface Focus*, vol. 4, no. 2, p. 20130058,

Apr. 2014, doi: 10.1098/rsfs.2013.0058.

[90] T. Nakamura, "Roles of short fibulins, a family of matricellular proteins, in lung matrix assembly and disease," *Matrix Biol.*, vol. 73, pp. 21–33, Nov. 2018, doi: 10.1016/j.matbio.2018.02.003.

[91] M. Gabriela Espinosa, M. Catalin Staiculescu, J. Kim, E. Marin, and J. E. Wagenseil, "Elastic Fibers and Large Artery Mechanics in Animal Models of Development and Disease," *J. Biomech. Eng.*, vol. 140, no. 2, Feb. 2018, doi: 10.1115/1.4038704.

[92] J. Uitto, Q. Li, and Z. Urban, "The complexity of elastic fibre biogenesis in the skin–a perspective to the clinical heterogeneity of cutis laxa," *Exp. Dermatol.*, vol. 22, no. 2, pp. 88–92, 2013.

[93] L. Baumann *et al.*, "Clinical Relevance of Elastin in the Structure and Function of Skin," *Aesthetic Surg. J. Open Forum*, vol. 3, no. 3, Sep. 2021, doi: 10.1093/asjof/ojab019.

[94] B. E. Cohen, R. G. Geronemus, D. H. McDaniel, and J. A. Brauer, "The role of elastic fibers in scar formation and treatment," *Dermatologic Surg.*, vol. 43, pp. S19–S24, 2017.

[95] L. Gardeazabal and A. Izeta, "Elastin and collagen fibres in cutaneous wound healing," *Exp. Dermatol.*, vol. 33, no. 3, Mar. 2024, doi: 10.1111/exd.15052.

[96] J. F. Almine, S. G. Wise, and A. S. Weiss, "Elastin signaling in wound repair," *Birth Defects Res. Part C Embryo Today Rev.*, vol. 96, no. 3, pp. 248–257, Sep. 2012, doi: 10.1002/bdrc.21016.

[97] A. K. Baldwin, A. Simpson, R. Steer, S. A. Cain, and C. M. Kielty, "Elastic fibres in health and disease," *Expert Rev. Mol. Med.*, vol. 15, p. e8, Aug. 2013, doi: 10.1017/erm.2013.9.

[98] W. DAAMEN, J. VEERKAMP, J. VANHEST, and T. VANKUPPEVELT, "Elastin as a biomaterial for tissue engineering," *Biomaterials*, vol. 28, no. 30, pp. 4378–4398, Oct. 2007, doi: 10.1016/j.biomaterials.2007.06.025.

[99] J. F. Almine *et al.*, "Elastin-based materials," *Chem. Soc. Rev.*, vol. 39, no. 9, pp. 3371–3379, 2010.

[100] F. Antonicelli, G. Bellon, L. Debelle, and W. Hornebeck, "Elastin-elastases and inflamm-aging," *Curr. Top. Dev. Biol.*, vol. 79, pp. 99–155, 2007.

[101] P. Toonkool, D. G. Regan, P. W. Kuchel, M. B. Morris, and A. S. Weiss, "Thermodynamic and Hydrodynamic Properties of Human Tropoelastin," *J. Biol. Chem.*, vol. 276, no. 30, pp. 28042–28050, Jul. 2001, doi: 10.1074/jbc.M103391200.

[102] A. S. Tatham and P. R. Shewry, "Comparative structures and properties of elastic proteins," *Philos. Trans. R. Soc. London. Ser. B Biol. Sci.*, vol. 357, no. 1418, pp. 229–234, Feb. 2002, doi: 10.1098/rstb.2001.1031.

[103] L. Debelle *et al.*, "The secondary structure and architecture of human elastin," *Eur. J. Biochem.*, vol. 258, no. 2, pp. 533–539, Dec. 1998, doi: 10.1046/j.1432-

1327.1998.2580533.x.

[104] B. Vrhovski, S. Jensen, and A. S. Weiss, "Coacervation Characteristics of Recombinant Human Tropoelastin," *Eur. J. Biochem.*, vol. 250, no. 1, pp. 92–98, Nov. 1997, doi: 10.1111/j.1432-1033.1997.00092.x.

[105] G. C. Yeo, F. W. Keeley, and A. S. Weiss, "Coacervation of tropoelastin," *Adv. Colloid Interface Sci.*, vol. 167, no. 1–2, pp. 94–103, 2011.

[106] F. Sato *et al.*, "Distinct Steps of Cross-linking, Self-association, and Maturation of Tropoelastin Are Necessary for Elastic Fiber Formation," *J. Mol. Biol.*, vol. 369, no. 3, pp. 841–851, Jun. 2007, doi: 10.1016/j.jmb.2007.03.060.

[107] R. Ross, P. J. Fialkow, and L. K. Altman, "The Morphogenesis of Elastic Fibers," 1977, pp. 7–17. doi: 10.1007/978-1-4684-9093-0_2.

[108] H. M. Kagan and K. A. Sullivan, "[35] Lysyl oxidase: Preparation and role in elastin biosynthesis," 1982, pp. 637–650. doi: 10.1016/0076-6879(82)82092-2.

[109] H. Vindin, S. M. Mithieux, and A. S. Weiss, "Elastin architecture," *Matrix Biol.*, vol. 84, pp. 4–16, 2019.

[110] J. Xu and G.-P. Shi, "Vascular wall extracellular matrix proteins and vascular diseases," *Biochim. Biophys. Acta - Mol. Basis Dis.*, vol. 1842, no. 11, pp. 2106–2119, Nov. 2014, doi: 10.1016/j.bbadis.2014.07.008.

[111] M. Miao, C. M. Bellingham, R. J. Stahl, E. E. Sitarz, C. J. Lane, and F. W. Keeley, "Sequence and Structure Determinants for the Self-aggregation of Recombinant Polypeptides Modeled after Human Elastin," *J. Biol. Chem.*, vol. 278, no. 49, pp. 48553–48562, Dec. 2003, doi: 10.1074/jbc.M308465200.

[112] S. Rauscher and R. Pomès, "Structural Disorder and Protein Elasticity," 2012, pp. 159–183. doi: 10.1007/978-1-4614-0659-4_10.

[113] D. W. Urry and M. M. Long, "On the Conformation, Coacervation and Function of Polymeric Models of Elastin," 1977, pp. 685–714. doi: 10.1007/978-1-4684-9093-0_59.

[114] D. W. Urry, "Physical Chemistry of Biological Free Energy Transduction As Demonstrated by Elastic Protein-Based Polymers," *J. Phys. Chem. B*, vol. 101, no. 51, pp. 11007–11028, Dec. 1997, doi: 10.1021/jp972167t.

[115] B. Li, D. O. . Alonso, and V. Daggett, "The molecular basis for the inverse temperature transition of elastin11Edited by A. R. Fersht," *J. Mol. Biol.*, vol. 305, no. 3, pp. 581–592, Jan. 2001, doi: 10.1006/jmbi.2000.4306.

[116] R. A. Pierce, C. H. Moore, and M. C. Arikan, "Positive transcriptional regulatory element located within exon 1 of elastin gene," *Am. J. Physiol. Cell. Mol. Physiol.*, vol. 291, no. 3, pp. L391–L399, 2006.

[117] L. Duca, N. Floquet, A. J. P. Alix, B. Haye, and L. Debelle, "Elastin as a matrikine," *Crit. Rev. Oncol. Hematol.*, vol. 49, no. 3, pp. 235–244, 2004.

[118] R. M. Senior, G. L. Griffin, R. P. Mecham, D. S. Wrenn, K. U. Prasad, and D. W. Urry, "Val-Gly-Val-Ala-Pro-Gly, a repeating peptide in elastin, is chemotactic

for fibroblasts and monocytes.," *J. Cell Biol.*, vol. 99, no. 3, pp. 870–874, 1984.

[119] N. Fujimoto, S. Tajima, and A. Ishibashi, "Elastin peptides induce migration and terminal differentiation of cultured keratinocytes via 67 kDa elastin receptor in vitro: 67 kDa elastin receptor is expressed in the keratinocytes eliminating elastic materials in elastosis perforans serpiginosa," *J. Invest. Dermatol.*, vol. 115, no. 4, pp. 633–639, 2000.

[120] S. Mochizuki, B. Brassart, and A. Hinek, "Signaling pathways transduced through the elastin receptor facilitate proliferation of arterial smooth muscle cells," *J. Biol. Chem.*, vol. 277, no. 47, pp. 44854–44863, 2002.

[121] A. Robinet *et al.*, "Elastin-derived peptides enhance angiogenesis by promoting endothelial cell migration and tubulogenesis through upregulation of MT1-MMP," *J. Cell Sci.*, vol. 118, no. 2, pp. 343–356, 2005.

[122] B. Brassart *et al.*, "Conformational dependence of collagenase (matrix metalloproteinase-1) up-regulation by elastin peptides in cultured fibroblasts," *J. Biol. Chem.*, vol. 276, no. 7, pp. 5222–5227, 2001.

[123] G. Faury, Y. Usson, M. Robert-Nicoud, L. Robert, and J. Verdetti, "Nuclear and cytoplasmic free calcium level changes induced by elastin peptides in human endothelial cells," *Proc. Natl. Acad. Sci.*, vol. 95, no. 6, pp. 2967–2972, 1998.

[124] A. Hinek, Y. Wang, K. Liu, T. F. Mitts, and F. Jimenez, "Proteolytic digest derived from bovine Ligamentum Nuchae stimulates deposition of new elastin-enriched matrix in cultures and transplants of human dermal fibroblasts," *J. Dermatol. Sci.*, vol. 39, no. 3, pp. 155–166, 2005.

[125] B. Cantarelli, L. Duca, C. Blanchevoye, S. Poitevin, L. Martiny, and L. Debelle, "Elastin peptides antagonize ceramide-induced apoptosis," *FEBS Lett.*, vol. 583, no. 14, pp. 2385–2391, 2009.

[126] U. R. Rodgers and A. S. Weiss, "Cellular interactions with elastin," *Pathol. Biol.*, vol. 53, no. 7, pp. 390–398, 2005.

[127] W. F. Daamen *et al.*, "A biomaterial composed of collagen and solubilized elastin enhances angiogenesis and elastic fiber formation without calcification," *Tissue Eng. Part A*, vol. 14, no. 3, pp. 349–360, 2008.

[128] M. Raghunath *et al.*, "Fibrillin and elastin expression in skin regenerating from cultured keratinocyte autografts: morphogenesis of microfibrils begins at the dermo-epidermal junction and precedes elastic fiber formation," *J. Invest. Dermatol.*, vol. 106, no. 5, pp. 1090–1095, 1996.

[129] T. P. Amadeu, A. S. Braune, L. C. Porto, A. Desmoulière, and A. M. A. Costa, "Fibrillin-1 and elastin are differentially expressed in hypertrophic scars and keloids," *Wound repair Regen.*, vol. 12, no. 2, pp. 169–174, 2004.

[130] N. A. Coolen, K. C. W. M. Schouten, E. Middelkoop, and M. M. W. Ulrich, "Comparison between human fetal and adult skin," *Arch. Dermatol. Res.*, vol. 302, pp. 47–55, 2010.

[131] A. Aloysius, "Tissue regeneration: Fetal to adult transition," in *Tissue Engineering*, Elsevier, 2022, pp. 77–100. doi: 10.1016/B978-0-12-824064-

9.00020-4.

[132] R. A. F. Clark, K. Ghosh, and M. G. Tonnesen, "Tissue engineering for cutaneous wounds," *J. Invest. Dermatol.*, vol. 127, no. 5, pp. 1018–1029, 2007.

[133] G. C. Gurtner, S. Werner, Y. Barrandon, and M. T. Longaker, "Wound repair and regeneration," *Nature*, vol. 453, no. 7193, pp. 314–321, 2008.

[134] H. D. Zomer and A. G. Trentin, "Skin wound healing in humans and mice: Challenges in translational research," *J. Dermatol. Sci.*, vol. 90, no. 1, pp. 3–12, Apr. 2018, doi: 10.1016/j.jdermsci.2017.12.009.

[135] G. C. Gurtner, S. Werner, Y. Barrandon, and M. T. Longaker, "Wound repair and regeneration," *Nature*, vol. 453, no. 7193, pp. 314–321, May 2008, doi: 10.1038/nature07039.

[136] J. Li, J. Chen, and R. Kirsner, "Pathophysiology of acute wound healing," *Clin. Dermatol.*, vol. 25, no. 1, pp. 9–18, 2007.

[137] T. Velnar, T. Bailey, and V. Smrkolj, "The wound healing process: an overview of the cellular and molecular mechanisms," *J. Int. Med. Res.*, vol. 37, no. 5, pp. 1528–1542, 2009.

[138] A. J. Singer and R. A. F. Clark, "Cutaneous wound healing," *N. Engl. J. Med.*, vol. 341, no. 10, pp. 738–746, 1999.

[139] J. M. Reinke and H. Sorg, "Wound repair and regeneration," *Eur. Surg. Res.*, vol. 49, no. 1, pp. 35–43, 2012.

[140] P. Martin and R. Nunan, "Cellular and molecular mechanisms of repair in acute and chronic wound healing," *Br. J. Dermatol.*, vol. 173, no. 2, pp. 370–378, 2015.

[141] T. J. Shaw and P. Martin, "Wound repair at a glance," *J. Cell Sci.*, vol. 122, no. 18, pp. 3209–3213, 2009.

[142] M. Rodrigues, N. Kosaric, C. A. Bonham, and G. C. Gurtner, "Wound healing: a cellular perspective," *Physiol. Rev.*, vol. 99, no. 1, pp. 665–706, 2019.

[143] S. Pradhan, T. Khatlani, A. C. Nairn, and K. V. Vijayan, "The heterotrimeric G protein Gβ1 interacts with the catalytic subunit of protein phosphatase 1 and modulates G protein–coupled receptor signaling in platelets," *J. Biol. Chem.*, vol. 292, no. 32, pp. 13133–13142, 2017.

[144] R. F. Diegelmann and M. C. Evans, "Wound healing: an overview of acute, fibrotic and delayed healing," *Front biosci*, vol. 9, no. 1, pp. 283–289, 2004.

[145] N. X. Landén, D. Li, and M. Ståhle, "Transition from inflammation to proliferation: a critical step during wound healing," *Cell. Mol. Life Sci.*, vol. 73, pp. 3861–3885, 2016.

[146] T. A. Wilgus, S. Roy, and J. C. McDaniel, "Neutrophils and wound repair: positive actions and negative reactions," *Adv. wound care*, vol. 2, no. 7, pp. 379–388, 2013.

[147] C. L. Baum and C. J. Arpey, "Normal cutaneous wound healing: clinical

correlation with cellular and molecular events," *Dermatologic Surg.*, vol. 31, no. 6, pp. 674–686, 2005.

[148] L. Sorokin, "The impact of the extracellular matrix on inflammation," *Nat. Rev. Immunol.*, vol. 10, no. 10, pp. 712–723, 2010.

[149] S. J. Galli, N. Borregaard, and T. A. Wynn, "Phenotypic and functional plasticity of cells of innate immunity: macrophages, mast cells and neutrophils," *Nat. Immunol.*, vol. 12, no. 11, pp. 1035–1044, 2011.

[150] S. Willenborg *et al.*, "CCR2 recruits an inflammatory macrophage subpopulation critical for angiogenesis in tissue repair," *Blood, J. Am. Soc. Hematol.*, vol. 120, no. 3, pp. 613–625, 2012.

[151] R. J. Snyder, J. Lantis, R. S. Kirsner, V. Shah, M. Molyneaux, and M. J. Carter, "Macrophages: a review of their role in wound healing and their therapeutic use," *Wound Repair Regen.*, vol. 24, no. 4, pp. 613–629, 2016.

[152] M. Li, Q. Hou, L. Zhong, Y. Zhao, and X. Fu, "Macrophage Related Chronic Inflammation in Non-Healing Wounds," *Front. Immunol.*, vol. 12, Jun. 2021, doi: 10.3389/fimmu.2021.681710.

[153] K. Raziyeva, Y. Kim, Z. Zharkinbekov, K. Kassymbek, S. Jimi, and A. Saparov, "Immunology of Acute and Chronic Wound Healing," *Biomolecules*, vol. 11, no. 5, p. 700, May 2021, doi: 10.3390/biom11050700.

[154] N. Jain *et al.*, "Conditional knockout of N-WASP in mouse fibroblast caused keratinocyte hyper proliferation and enhanced wound closure," *Sci. Rep.*, vol. 6, no. 1, p. 38109, 2016.

[155] J. Li, Y. Zhang, and R. S. Kirsner, "Angiogenesis in wound repair: angiogenic growth factors and the extracellular matrix," *Microsc. Res. Tech.*, vol. 60, no. 1, pp. 107–114, 2003.

[156] M. Marx, R. A. Perlmutter, and J. A. Madri, "Modulation of platelet-derived growth factor receptor expression in microvascular endothelial cells during in vitro angiogenesis.," *J. Clin. Invest.*, vol. 93, no. 1, pp. 131–139, 1994.

[157] T. Kalebic, S. Garbisa, B. Glaser, and L. A. Liotta, "Basement membrane collagen: degradation by migrating endothelial cells," *Science (80-.).*, vol. 221, no. 4607, pp. 281–283, 1983.

[158] I. Pastar *et al.*, "Epithelialization in wound healing: a comprehensive review," *Adv. wound care*, vol. 3, no. 7, pp. 445–464, 2014.

[159] P. Rousselle, M. Montmasson, and C. Garnier, "Extracellular matrix contribution to skin wound re-epithelialization," *Matrix Biol.*, vol. 75, pp. 12–26, 2019.

[160] I. A. Darby and T. D. Hewitson, "Fibroblast differentiation in wound healing and fibrosis," *Int. Rev. Cytol.*, vol. 257, pp. 143–179, 2007.

[161] I. Darby, O. Skalli, and G. Gabbiani, "Alpha-smooth muscle actin is transiently expressed by myofibroblasts during experimental wound healing.," *Lab. Invest.*, vol. 63, no. 1, pp. 21–29, 1990.

[162] S. Porter, "The role of the fibroblast in wound contraction and healing," *WOUNDS UK*, vol. 3, no. 1, p. 33, 2007.

[163] S. Werner, T. Krieg, and H. Smola, "Keratinocyte–fibroblast interactions in wound healing," *J. Invest. Dermatol.*, vol. 127, no. 5, pp. 998–1008, 2007.

[164] B. Hinz, "Formation and function of the myofibroblast during tissue repair," *J. Invest. Dermatol.*, vol. 127, no. 3, pp. 526–537, 2007.

[165] G. Majno, "The story of the myofibroblasts," *Am. J. Surg. Pathol.*, vol. 3, no. 6, pp. 535–542, 1979.

[166] M. P. Welch, G. F. Odland, and R. A. Clark, "Temporal relationships of F-actin bundle formation, collagen and fibronectin matrix assembly, and fibronectin receptor expression to wound contraction.," *J. Cell Biol.*, vol. 110, no. 1, pp. 133–145, 1990.

[167] B. A. Booth, K. L. Polak, and J. Uitto, "Collagen biosynthesis by human skin fibroblasts. I. Optimization of the culture conditions for synthesis of type I and type III procollagens," *Biochim. Biophys. Acta (BBA)-Nucleic Acids Protein Synth.*, vol. 607, no. 1, pp. 145–160, 1980.

[168] L. Cañedo-Dorantes and M. Cañedo-Ayala, "Skin acute wound healing: a comprehensive review," *Int. J. Inflam.*, vol. 2019, 2019.

[169] G. Wernig *et al.*, "Unifying mechanism for different fibrotic diseases," *Proc. Natl. Acad. Sci.*, vol. 114, no. 18, pp. 4757–4762, 2017.

[170] M. Takeo, W. Lee, and M. Ito, "Wound healing and skin regeneration," *Cold Spring Harb. Perspect. Med.*, vol. 5, no. 1, p. a023267, 2015.

[171] D. T. Corr, C. L. Gallant-Behm, N. G. Shrive, and D. A. Hart, "Biomechanical behavior of scar tissue and uninjured skin in a porcine model," *Wound Repair Regen.*, vol. 17, no. 2, pp. 250–259, 2009.

[172] N. Lebonvallet, B. Laverdet, L. Misery, A. Desmoulière, and D. Girard, "New insights into the roles of myofibroblasts and innervation during skin healing and innovative therapies to improve scar innervation," *Exp. Dermatol.*, vol. 27, no. 9, pp. 950–958, 2018.

[173] M. V Plikus *et al.*, "Regeneration of fat cells from myofibroblasts during wound healing," *Science (80-.).*, vol. 355, no. 6326, pp. 748–752, 2017.

[174] M. A. Fonder, G. S. Lazarus, D. A. Cowan, B. Aronson-Cook, A. R. Kohli, and A. J. Mamelak, "Treating the chronic wound: A practical approach to the care of nonhealing wounds and wound care dressings," *J. Am. Acad. Dermatol.*, vol. 58, no. 2, pp. 185–206, 2008.

[175] A. C. Tricco *et al.*, "Seeking effective interventions to treat complex wounds: an overview of systematic reviews," *BMC Med.*, vol. 13, no. 1, pp. 1–23, 2015.

[176] D. Solanki, P. Vinchhi, and M. M. Patel, "Design Considerations, Formulation Approaches, and Strategic Advances of Hydrogel Dressings for Chronic Wound Management," *ACS Omega*, vol. 8, no. 9, pp. 8172–8189, Mar. 2023, doi: 10.1021/acsomega.2c06806.

[177] V. Falanga *et al.*, "Chronic wounds," *Nat. Rev. Dis. Prim.*, vol. 8, no. 1, p. 50, 2022.

[178] C. Dealey *et al.*, "Challenges in pressure ulcer prevention," *Int. Wound J.*, vol. 12, no. 3, pp. 309–312, 2015.

[179] S. A. Eming, P. Martin, and M. Tomic-Canic, "Wound repair and regeneration: mechanisms, signaling, and translation," *Sci. Transl. Med.*, vol. 6, no. 265, pp. 265sr6-265sr6, 2014.

[180] S. A. Eming, P. Martin, and M. Tomic-Canic, "Wound repair and regeneration: Mechanisms, signaling, and translation," *Sci. Transl. Med.*, vol. 6, no. 265, Dec. 2014, doi: 10.1126/scitranslmed.3009337.

[181] V. Falanga *et al.*, "Chronic wounds," *Nat. Rev. Dis. Prim.*, vol. 8, no. 1, p. 50, Jul. 2022, doi: 10.1038/s41572-022-00377-3.

[182] A. Sindrilaru *et al.*, "An unrestrained proinflammatory M1 macrophage population induced by iron impairs wound healing in humans and mice," *J. Clin. Invest.*, vol. 121, no. 3, pp. 985–997, 2011.

[183] L. F. S. Gushiken, F. P. Beserra, J. K. Bastos, C. J. Jackson, and C. H. Pellizzon, "Cutaneous wound healing: An update from physiopathology to current therapies," *Life*, vol. 11, no. 7, p. 665, 2021.

[184] R. G. Frykberg and J. Banks, "Challenges in the treatment of chronic wounds," *Adv. wound care*, vol. 4, no. 9, pp. 560–582, 2015.

[185] S. A. Eming, M. Hammerschmidt, T. Krieg, and A. Roers, "Interrelation of immunity and tissue repair or regeneration," in *Seminars in cell & developmental biology*, 2009, vol. 20, no. 5, pp. 517–527.

[186] S. al Guo and L. A. DiPietro, "Factors affecting wound healing," *J. Dent. Res.*, vol. 89, no. 3, pp. 219–229, 2010.

[187] G. G. Walmsley *et al.*, "Scarless wound healing: chasing the holy grail," *Plast. Reconstr. Surg.*, vol. 135, no. 3, pp. 907–917, 2015.

[188] A. M. Misic, S. E. Gardner, and E. A. Grice, "The wound microbiome: modern approaches to examining the role of microorganisms in impaired chronic wound healing," *Adv. wound care*, vol. 3, no. 7, pp. 502–510, 2014.

[189] I. Pastar *et al.*, "Interactions of methicillin resistant Staphylococcus aureus USA300 and Pseudomonas aeruginosa in polymicrobial wound infection," *PLoS One*, vol. 8, no. 2, p. e56846, 2013.

[190] G. Zhao *et al.*, "Biofilms and inflammation in chronic wounds," *Adv. wound care*, vol. 2, no. 7, pp. 389–399, 2013.

[191] G. Lauer *et al.*, "Expression and proteolysis of vascular endothelial growth factor is increased in chronic wounds," *J. Invest. Dermatol.*, vol. 115, no. 1, pp. 12–18, 2000.

[192] E. Makrantonaki, M. Wlaschek, and K. Scharffetter-Kochanek, "Pathogenesis of wound healing disorders in the elderly," *JDDG J. der Dtsch. Dermatologischen Gesellschaft*, vol. 15, no. 3, pp. 255–275, 2017.

[193] I. B. Wall *et al.*, "Fibroblast dysfunction is a key factor in the non-healing of chronic venous leg ulcers," *J. Invest. Dermatol.*, vol. 128, no. 10, pp. 2526–2540, 2008.

[194] J.-I. Jun and L. F. Lau, "The matricellular protein CCN1 induces fibroblast senescence and restricts fibrosis in cutaneous wound healing," *Nat. Cell Biol.*, vol. 12, no. 7, pp. 676–685, 2010.

[195] N. Buchstein *et al.*, "Alternative proteolytic processing of hepatocyte growth factor during wound repair," *Am. J. Pathol.*, vol. 174, no. 6, pp. 2116–2128, 2009.

[196] S. Barrientos, H. Brem, O. Stojadinovic, and M. Tomic-Canic, "Clinical application of growth factors and cytokines in wound healing," *Wound repair Regen.*, vol. 22, no. 5, pp. 569–578, 2014.

[197] H. N. Wilkinson and M. J. Hardman, "The role of estrogen in cutaneous ageing and repair," *Maturitas*, vol. 103, pp. 60–64, 2017.

[198] A. D. Maderal, A. C. Vivas, W. H. Eaglstein, and R. S. Kirsner, "The FDA and designing clinical trials for chronic cutaneous ulcers," in *Seminars in cell & developmental biology*, 2012, vol. 23, no. 9, pp. 993–999.

[199] G. Sawicki, Y. Marcoux, K. Sarkhosh, E. E. Tredget, and A. Ghahary, "Interaction of keratinocytes and fibroblasts modulates the expression of matrix metalloproteinases-2 and-9 and their inhibitors," *Mol. Cell. Biochem.*, vol. 269, pp. 209–216, 2005.

[200] R. Langer and J. P. Vacanti, "Tissue engineering. Science [Internet]. 1993 [cited 2020 Sep 22]; 260 (5110): 920–6."

[201] M. Fossum and A. Nordenskjöld, "Tissue-engineered transplants for the treatment of severe hypospadias," *Horm. Res. Paediatr.*, vol. 73, no. 2, pp. 148–152, 2010.

[202] R. E. Horch, J. Kopp, U. Kneser, J. Beier, and A. D. Bach, "Tissue engineering of cultured skin substitutes," *J. Cell. Mol. Med.*, vol. 9, no. 3, pp. 592–608, 2005.

[203] P. R. Cavanagh, B. A. Lipsky, A. W. Bradbury, and G. Botek, "Treatment for diabetic foot ulcers," *Lancet*, vol. 366, no. 9498, pp. 1725–1735, 2005.

[204] C. Pang, A. Ibrahim, N. W. Bulstrode, and P. Ferretti, "An overview of the therapeutic potential of regenerative medicine in cutaneous wound healing," *Int. Wound J.*, vol. 14, no. 3, pp. 450–459, 2017.

[205] X. Li, "The Roles of MicroRNAs in Skin Wound Healing." Karolinska Institutet (Sweden), 2019.

[206] R. E. Jones, D. S. Foster, and M. T. Longaker, "Management of chronic wounds—2018," *Jama*, vol. 320, no. 14, pp. 1481–1482, 2018.

[207] A. Sood, M. S. Granick, and N. L. Tomaselli, "Wound dressings and comparative effectiveness data," *Adv. wound care*, vol. 3, no. 8, pp. 511–529, 2014.

[208] M. Balasubramani, "Skin substitutes: a review," *Burns*, vol. 27, pp. 534–544, 2001.

[209] J. G. Powers, L. M. Morton, and T. J. Phillips, "Dressings for chronic wounds," *Dermatol. Ther.*, vol. 26, no. 3, pp. 197–206, 2013.

[210] I. Jones, L. Currie, and R. Martin, "A guide to biological skin substitutes," *Br. J. Plast. Surg.*, vol. 55, no. 3, pp. 185–193, 2002.

[211] K. Vowden and P. Vowden, "Wound dressings: principles and practice," *Surg.*, vol. 35, no. 9, pp. 489–494, 2017.

[212] G. D. Winter and J. T. Scales, "Effect of air drying and dressings on the surface of a wound," *Nature*, vol. 197, pp. 91–92, 1963.

[213] Z. Obagi, G. Damiani, A. Grada, and V. Falanga, "Principles of wound dressings: a review," *Surg Technol Int*, vol. 35, pp. 50–57, 2019.

[214] D. Okan, K. Woo, E. A. Ayello, and G. Sibbald, "The role of moisture balance in wound healing," *Adv. Skin Wound Care*, vol. 20, no. 1, pp. 39–53, 2007.

[215] V. Jones, J. E. Grey, and K. G. Harding, "Wound dressings," *Bmj*, vol. 332, no. 7544, pp. 777–780, 2006.

[216] G. Han and R. Ceilley, "Chronic wound healing: a review of current management and treatments," *Adv. Ther.*, vol. 34, pp. 599–610, 2017.

[217] G. Dabiri, E. Damstetter, and T. Phillips, "Choosing a wound dressing based on common wound characteristics," *Adv. wound care*, vol. 5, no. 1, pp. 32–41, 2016.

[218] S. Sarabahi, "Recent advances in topical wound care," *Indian J. Plast. Surg.*, vol. 45, no. 02, pp. 379–387, 2012.

[219] B. S. Atiyeh, S. N. Hayek, and S. W. Gunn, "New technologies for burn wound closure and healing—review of the literature," *Burns*, vol. 31, no. 8, pp. 944–956, 2005.

[220] M. Kapoor and I. Appleton, "Wound healing: abnormalities and future therapeutic targets," *Curr. Anaesth. Crit. Care*, vol. 16, no. 2, pp. 88–93, 2005.

[221] D. Selvaraj, V. P. Viswanadha, and S. Elango, "Wound dressings-a review," *BioMedicine*, vol. 5, p. 22, 2015.

[222] A. D. Sezer and E. Cevher, "Biopolymers as wound healing materials: challenges and new strategies," *Biomater. Appl. nanomedicine*, pp. 383–414, 2011.

[223] S. A. Naimer and F. Chemla, "Elastic adhesive dressing treatment of bleeding wounds in trauma victims," *Am. J. Emerg. Med.*, vol. 18, no. 7, pp. 816–819, 2000.

[224] T. S. Stashak, E. Farstvedt, and A. Othic, "Update on wound dressings: Indications and best use," *Clin. Tech. Equine Pract.*, vol. 3, no. 2, pp. 148–163, 2004.

[225] R. D. Price, V. Das-Guptaf, J. D. Frame, and H. A. Navsaria, "A study to evaluate primary dressings for the application of cultured keratinocytes," *Br. J. Plast. Surg.*, vol. 54, no. 8, pp. 687–696, 2001.

[226] S. Dhivya, V. V. Padma, and E. Santhini, "Wound dressings–a review," *BioMedicine*, vol. 5, no. 4, p. 22, 2015.

[227] A. Jones and D. Vaughan, "Hydrogel dressings in the management of a variety of wound types: A review," *J. Orthop. Nurs.*, vol. 9, pp. S1–S11, 2005.

[228] J. S. Boateng, K. H. Matthews, H. N. E. Stevens, and G. M. Eccleston, "Wound healing dressings and drug delivery systems: a review," *J. Pharm. Sci.*, vol. 97, no. 8, pp. 2892–2923, 2008.

[229] S. Thomas, "Hydrocolloids," *J. Wound Care*, vol. 1, no. 2, pp. 27–30, 1992.

[230] M. Sheikholeslam, M. E. E. Wright, M. G. Jeschke, and S. Amini-Nik, "Biomaterials for skin substitutes," *Adv. Healthc. Mater.*, vol. 7, no. 5, p. 1700897, 2018.

[231] G. C. Gurtner and M. A. Chapman, "Regenerative medicine: charting a new course in wound healing," *Adv. Wound Care*, vol. 5, no. 7, pp. 314–328, 2016.

[232] F.-M. Chen and X. Liu, "Advancing biomaterials of human origin for tissue engineering," *Prog. Polym. Sci.*, vol. 53, pp. 86–168, 2016.

[233] P. Aramwit, "Introduction to biomaterials for wound healing," in *Wound healing biomaterials*, Elsevier, 2016, pp. 3–38.

[234] A. A. Chaudhari *et al.*, "Future prospects for scaffolding methods and biomaterials in skin tissue engineering: a review," *Int. J. Mol. Sci.*, vol. 17, no. 12, p. 1974, 2016.

[235] J. M. Ferri, J. Jordá, N. Montanes, O. Fenollar, and R. Balart, "Manufacturing and characterization of poly (lactic acid) composites with hydroxyapatite," *J. Thermoplast. Compos. Mater.*, vol. 31, no. 7, pp. 865–881, 2018.

[236] D. Mondal, M. Griffith, and S. S. Venkatraman, "Polycaprolactone-based biomaterials for tissue engineering and drug delivery: Current scenario and challenges," *Int. J. Polym. Mater. Polym. Biomater.*, vol. 65, no. 5, pp. 255–265, 2016.

[237] M. Li, J. Chen, M. Shi, H. Zhang, P. X. Ma, and B. Guo, "Electroactive anti-oxidant polyurethane elastomers with shape memory property as non-adherent wound dressing to enhance wound healing," *Chem. Eng. J.*, vol. 375, p. 121999, Nov. 2019, doi: 10.1016/j.cej.2019.121999.

[238] S. Chhabra, N. Chhabra, A. Kaur, and N. Gupta, "Wound healing concepts in clinical practice of OMFS," *J. Maxillofac. Oral Surg.*, vol. 16, pp. 403–423, 2017.

[239] Z. Ruszczak, "Effect of collagen matrices on dermal wound healing," *Adv. Drug Deliv. Rev.*, vol. 55, no. 12, pp. 1595–1611, 2003.

[240] S.-N. Park, H. J. Lee, K. H. Lee, and H. Suh, "Biological characterization of EDC-crosslinked collagen–hyaluronic acid matrix in dermal tissue restoration," *Biomaterials*, vol. 24, no. 9, pp. 1631–1641, 2003.

[241] S.-N. Park, J. K. Kim, and H. Suh, "Evaluation of antibiotic-loaded collagen-hyaluronic acid matrix as a skin substitute," *Biomaterials*, vol. 25, no. 17, pp. 3689–3698, 2004.

[242] O. Akturk *et al.*, "Collagen/gold nanoparticle nanocomposites: a potential skin wound healing biomaterial," *J. Biomater. Appl.*, vol. 31, no. 2, pp. 283–301, 2016.

[243] M. M. A. Arif, M. B. Fauzi, A. Nordin, Y. Hiraoka, Y. Tabata, and M. H. M. Yunus, "Fabrication of bio-based gelatin sponge for potential use as a functional acellular skin substitute," *Polymers (Basel).*, vol. 12, no. 11, p. 2678, 2020.

[244] I. N. Amirrah, M. F. Mohd Razip Wee, Y. Tabata, R. Bt Hj Idrus, A. Nordin, and M. B. Fauzi, "Antibacterial-integrated collagen wound dressing for diabetes-related foot ulcers: An evidence-based review of clinical studies," *Polymers (Basel).*, vol. 12, no. 9, p. 2168, 2020.

[245] A. B. Bello, D. Kim, D. Kim, H. Park, and S.-H. Lee, "Engineering and functionalization of gelatin biomaterials: From cell culture to medical applications," *Tissue Eng. Part B Rev.*, vol. 26, no. 2, pp. 164–180, 2020.

[246] C. H. Goh, P. W. S. Heng, and L. W. Chan, "Cross-linker and non-gelling Na+ effects on multi-functional alginate dressings," *Carbohydr. Polym.*, vol. 87, no. 2, pp. 1796–1802, 2012.

[247] M. Kurakula, G. S. N. K. Rao, V. Kiran, M. S. Hasnain, and A. K. Nayak, "Alginate-based hydrogel systems for drug releasing in wound healing," in *Alginates in Drug Delivery*, Elsevier, 2020, pp. 323–358.

[248] S. Thomas, "Alginate dressings in surgery and wound management—Part 1," *J. Wound Care*, vol. 9, no. 2, pp. 56–60, 2000.

[249] S. Thomas, "Alginate dressings in surgery and wound management: Part 3," *J. Wound Care*, vol. 9, no. 4, pp. 163–166, 2000.

[250] S. Thomas, "Alginate dressings in surgery and wound management: Part 2," *J. Wound Care*, vol. 9, no. 3, pp. 115–119, 2000.

[251] S. Ullah and X. Chen, "Fabrication, applications and challenges of natural biomaterials in tissue engineering," *Appl. Mater. Today*, vol. 20, p. 100656, 2020.

[252] S. Ahmed and S. Ikram, "Chitosan based scaffolds and their applications in wound healing," *Achiev. life Sci.*, vol. 10, no. 1, pp. 27–37, 2016.

[253] R. A. A. Muzzarelli *et al.*, "Chitin nanofibrils/chitosan glycolate composites as wound medicaments," *Carbohydr. Polym.*, vol. 70, no. 3, pp. 274–284, 2007.

[254] E. Khor and L. Y. Lim, "Implantable applications of chitin and chitosan," *Biomaterials*, vol. 24, no. 13, pp. 2339–2349, 2003.

[255] W. Paul and C. P. Sharma, "Chitosan and alginate wound dressings: a short review," *Trends Biomater Artif Organs*, vol. 18, no. 1, pp. 18–23, 2004.

[256] W. Tan, R. Krishnaraj, and T. A. Desai, "Evaluation of nanostructured composite collagen–chitosan matrices for tissue engineering," *Tissue Eng.*, vol. 7, no. 2, pp. 203–210, 2001.

[257] F. Mi *et al.*, "Control of wound infections using a bilayer chitosan wound dressing with sustainable antibiotic delivery," *J. Biomed. Mater. Res. An Off. J.*

Soc. Biomater. Japanese Soc. Biomater. Aust. Soc. Biomater. Korean Soc. Biomater., vol. 59, no. 3, pp. 438–449, 2002.

[258] E. M. Tottoli, R. Dorati, I. Genta, E. Chiesa, S. Pisani, and B. Conti, "Skin wound healing process and new emerging technologies for skin wound care and regeneration," *Pharmaceutics*, vol. 12, no. 8, p. 735, 2020.

[259] D. Zhao, Y. Zhu, W. Cheng, W. Chen, Y. Wu, and H. Yu, "Cellulose-based flexible functional materials for emerging intelligent electronics," *Adv. Mater.*, vol. 33, no. 28, p. 2000619, 2021.

[260] G. M. de Olyveira, L. M. Manzine Costa, P. Basmaji, and L. Xavier Filho, "Bacterial nanocellulose for medicine regenerative," *J. Nanotechnol. Eng. Med.*, vol. 2, no. 3, 2011.

[261] R. Naomi and M. B. Fauzi, "Cellulose/collagen dressings for diabetic foot ulcer: A review," *Pharmaceutics*, vol. 12, no. 9, p. 881, 2020.

[262] J. M. Rajwade, K. M. Paknikar, and J. V Kumbhar, "Applications of bacterial cellulose and its composites in biomedicine," *Appl. Microbiol. Biotechnol.*, vol. 99, pp. 2491–2511, 2015.

[263] J. Boateng and O. Catanzano, "Advanced therapeutic dressings for effective wound healing—a review," *J. Pharm. Sci.*, vol. 104, no. 11, pp. 3653–3680, 2015.

[264] G. H. Altman *et al.*, "Silk-based biomaterials," *Biomaterials*, vol. 24, no. 3, pp. 401–416, 2003.

[265] T. P. Nguyen *et al.*, "Silk fibroin-based biomaterials for biomedical applications: A review," *Polymers (Basel).*, vol. 11, no. 12, p. 1933, 2019.

[266] J. M. Aamodt and D. W. Grainger, "Extracellular matrix-based biomaterial scaffolds and the host response," *Biomaterials*, vol. 86, pp. 68–82, 2016.

[267] J. C. R. Cabello, I. G. De Torre, F. Cipriani, and L. Poocza, "Elastin-like materials for tissue regeneration and repair," in *Peptides and proteins as biomaterials for tissue regeneration and repair*, Elsevier, 2018, pp. 309–327.

[268] D. W. Urry, "Entropic elastic processes in protein mechanisms. I. Elastic structure due to an inverse temperature transition and elasticity due to internal chain dynamics," *J. Protein Chem.*, vol. 7, no. 1, pp. 1–34, Feb. 1988, doi: 10.1007/BF01025411.

[269] H. Reiersen, A. R. Clarke, and A. R. Rees, "Short elastin-like peptides exhibit the same temperature-induced structural transitions as elastin polymers: implications for protein engineering," *J. Mol. Biol.*, vol. 283, no. 1, pp. 255–264, Oct. 1998, doi: 10.1006/jmbi.1998.2067.

[270] D. W. Urry, M. M. Long, B. A. Cox, T. Ohnishi, L. W. Mitchell, and M. Jacobs, "The synthetic polypentapeptide of elastin coacervates and forms filamentous aggregates," *Biochim. Biophys. Acta - Protein Struct.*, vol. 371, no. 2, pp. 597–602, Dec. 1974, doi: 10.1016/0005-2795(74)90057-9.

[271] D. W. Urry, "Entropic elastic processes in protein mechanisms. II. Simple

(passive) and coupled (active) development of elastic forces," *J. Protein Chem.*, vol. 7, no. 2, pp. 81–114, Apr. 1988, doi: 10.1007/BF01025240.

[272] D. W. Urry and K. U. Prasad, "In DW Williams (Ed.), Biocompatibility of Tissue Analogues." CRC Press Inc., Boca Raton, Florida, 1985.

[273] D. W. Urry, T. M. Parker, M. C. Reid, and D. C. Gowda, "Biocompatibility of the Bioelastic Materials, Poly(GVGVP) and Its γ-Irradiation Cross-Linked Matrix: Summary of Generic Biological Test Results," *J. Bioact. Compat. Polym.*, vol. 6, no. 3, pp. 263–282, Jul. 1991, doi: 10.1177/088391159100600306.

[274] D. T. McPherson, C. Morrow, D. S. Minehan, J. Wu, E. Hunter, and D. W. Urry, "Production and purification of a recombinant elastomeric polypeptide, G-(VPGVG)19-VPGV, from Escherichia coli," *Biotechnol. Prog.*, vol. 8, no. 4, pp. 347–352, Jul. 1992, doi: 10.1021/bp00016a012.

[275] D. T. McPherson, J. Xu, and D. W. Urry, "Product purification by reversible phase transition FollowingEscherichia coliExpression of genes encoding up to 251 repeats of the elastomeric pentapeptide GVGVP," *Protein Expr. Purif.*, vol. 7, no. 1, pp. 51–57, 1996.

[276] D. E. Meyer and A. Chilkoti, "Purification of recombinant proteins by fusion with thermally-responsive polypeptides," *Nat. Biotechnol.*, vol. 17, no. 11, pp. 1112–1115, Nov. 1999, doi: 10.1038/15100.

[277] W. Hassouneh, T. Christensen, and A. Chilkoti, "Elastin-Like Polypeptides as a Purification Tag for Recombinant Proteins. vol. 2. Hoboken." NJ, USA: John Wiley & Sons, Inc, 2001.

[278] J. C. Rodríguez-Cabello, L. Martín, M. Alonso, F. J. Arias, and A. M. Testera, "'Recombinamers' as advanced materials for the post-oil age," *Polymer (Guildf).*, vol. 50, no. 22, pp. 5159–5169, Oct. 2009, doi: 10.1016/j.polymer.2009.08.032.

[279] J. C. Rodríguez-Cabello, A. Girotti, A. Ribeiro, and F. J. Arias, "Synthesis of genetically engineered protein polymers (recombinamers) as an example of advanced self-assembled smart materials," *Nanotechnol. Regen. Med. methods Protoc.*, pp. 17–38, 2012.

[280] J. C. Rodriguez-Cabello, A. Ibáñez Fonseca, M. Alonso, L. Poocza, F. Cipriani, and I. González de Torre, "Elastin-Like Polymers: Properties, Synthesis, and Applications," in *Encyclopedia of Polymer Science and Technology*, Hoboken, NJ, USA: John Wiley & Sons, Inc., 2017, pp. 1–36. doi: 10.1002/0471440264.pst656.

[281] F. Aladini, C. Araman, and C. F. W. Becker, "Chemical synthesis and characterization of elastin-like polypeptides (ELPs) with variable guest residues," *J. Pept. Sci.*, vol. 22, no. 5, pp. 334–342, May 2016, doi: 10.1002/psc.2871.

[282] B. Li, D. O. V Alonso, and V. Daggett, "The molecular basis for the inverse temperature transition of elastin," *J. Mol. Biol.*, vol. 305, no. 3, pp. 581–592, 2001.

[283] N. K. Li, F. G. Quiroz, C. K. Hall, A. Chilkoti, and Y. G. Yingling, "Molecular Description of the LCST Behavior of an Elastin-Like Polypeptide," *Biomacromolecules*, vol. 15, no. 10, pp. 3522–3530, Oct. 2014, doi: 10.1021/bm500658w.

[284] J. Reguera, D. W. Urry, T. M. Parker, D. T. McPherson, and J. C. Rodríguez-Cabello, "Effect of NaCl on the Exothermic and Endothermic Components of the Inverse Temperature Transition of a Model Elastin-like Polymer," *Biomacromolecules*, vol. 8, no. 2, pp. 354–358, Feb. 2007, doi: 10.1021/bm060936l.

[285] J. C. Rodríguez-Cabello, J. Reguera, A. Girotti, M. Alonso, and A. M. Testera, "Developing functionality in elastin-like polymers by increasing their molecular complexity: the power of the genetic engineering approach," *Prog. Polym. Sci.*, vol. 30, no. 11, pp. 1119–1145, 2005.

[286] D. W. Urry, "Elastic molecular machines in metabolism and soft-tissue restoration," *Trends Biotechnol.*, vol. 17, no. 6, pp. 249–257, 1999.

[287] H. Zhang *et al.*, "Human amniotic cell sheet harvest using a novel temperature-responsive culture surface coated with protein-based polymer," *Tissue Eng.*, vol. 12, no. 2, pp. 391–401, 2006.

[288] D. W. Urry, A. Pattanaik, J. Xu, T. Cooper Woods, D. T. McPherson, and T. M. Parker, "Elastic protein-based polymers in soft tissue augmentation and generation," *J. Biomater. Sci. Polym. Ed.*, vol. 9, no. 10, pp. 1015–1048, 1998.

[289] S. R. MacEwan and A. Chilkoti, "Elastin-like polypeptides: Biomedical applications of tunable biopolymers," *Pept. Sci.*, vol. 94, no. 1, pp. 60–77, Jan. 2010, doi: https://doi.org/10.1002/bip.21327.

[290] J. C. Rodriguez-Cabello, A. Ibáñez Fonseca, M. Alonso, L. Poocza, F. Cipriani, and I. González de Torre, "Elastin-Like Polymers: Properties, Synthesis, and Applications," *Encycl. Polym. Sci. Technol.*, pp. 1–36, 2002.

[291] D. E. Meyer and A. Chilkoti, "Genetically encoded synthesis of protein-based polymers with precisely specified molecular weight and sequence by recursive directional ligation: examples from the elastin-like polypeptide system," *Biomacromolecules*, vol. 3, no. 2, pp. 357–367, 2002.

[292] S. M. Lippow, P. M. Aha, M. H. Parker, W. J. Blake, B. M. Baynes, and D. Lipovšek, "Creation of a type IIS restriction endonuclease with a long recognition sequence," *Nucleic Acids Res.*, vol. 37, no. 9, pp. 3061–3073, 2009.

[293] S. M. Lippow, P. M. Aha, M. H. Parker, W. J. Blake, B. M. Baynes, and D. Lipovšek, "Creation of a type IIS restriction endonuclease with a long recognition sequence," *Nucleic Acids Res.*, vol. 37, no. 9, pp. 3061–3073, May 2009, doi: 10.1093/nar/gkp182.

[294] A. Girotti, "Desarrollo de una nueva plataforma biotecnológica para la obtención de polímeros recombiantes tipo elastina," 2007.

[295] E. Ruoslahti, "RGD and other recognition sequences for integrins," *Annu. Rev. Cell Dev. Biol.*, vol. 12, no. 1, pp. 697–715, 1996.

[296] M. J. Humphries, "Peptide recognition motifs involved in the binding of integrins to their ligands," *Kidney Int.*, vol. 41, no. 3, pp. 645–649, 1992.

[297] H. Tan and K. G. Marra, "Injectable, biodegradable hydrogels for tissue engineering applications," *Materials (Basel).*, vol. 3, no. 3, pp. 1746–1767, 2010.

[298] M. Gao, M. Sotomayor, E. Villa, E. H. Lee, and K. Schulten, "Molecular mechanisms of cellular mechanics," *Phys. Chem. Chem. Phys.*, vol. 8, no. 32, p. 3692, 2006, doi: 10.1039/b606019f.

[299] D. E. Meyer and A. Chilkoti, "Quantification of the effects of chain length and concentration on the thermal behavior of elastin-like polypeptides," *Biomacromolecules*, vol. 5, no. 3, pp. 846–851, 2004.

[300] D. J. Coletta *et al.*, "Bone Regeneration Mediated by a Bioactive and Biodegradable Extracellular Matrix-Like Hydrogel Based on Elastin-Like Recombinamers," *Tissue Eng. Part A*, vol. 23, no. 23–24, pp. 1361–1371, Apr. 2017, doi: 10.1089/ten.tea.2017.0047.

[301] K. S. Straley and S. C. Heilshorn, "Independent tuning of multiple biomaterial properties using protein engineering," *Soft Matter*, vol. 5, no. 1, pp. 114–124, 2009.

[302] T. Flora, I. G. De Torre, M. Alonso, and J. C. Rodríguez-Cabello, "Use of proteolytic sequences with different cleavage kinetics as a way to generate hydrogels with preprogrammed cell-infiltration patterns imparted over their given 3D spatial structure," *Biofabrication*, vol. 11, no. 3, p. 35008, 2019.

[303] F. González-Pérez, M. Alonso, I. G. D. Torre, M. Santos, and J. C. Rodríguez-Cabello, "Laminin-Derived Peptide Sequences within Elastin-Like Recombinamer Scaffolds Provide Spatiotemporally Synchronized Guidance of Angiogenesis and Neurogenesis," *Adv. Heal. Mater*, vol. 11, p. 2201646, 2022.

[304] F. González-Pérez *et al.*, "Biohybrid elastin-like venous valve with potential for in situ tissue engineering," *Front. Bioeng. Biotechnol.*, vol. 10, p. 988533, 2022.

[305] A. N. N. Hoeben, B. Landuyt, M. S. Highley, H. Wildiers, A. T. Van Oosterom, and E. A. De Bruijn, "Vascular endothelial growth factor and angiogenesis," *Pharmacol. Rev.*, vol. 56, no. 4, pp. 549–580, 2004.

[306] L. Cai, C. B. Dinh, and S. C. Heilshorn, "One-pot synthesis of elastin-like polypeptide hydrogels with grafted VEGF-mimetic peptides," *Biomater. Sci.*, vol. 2, no. 5, pp. 757–765, 2014.

[307] T. Flora, I. G. de Torre, M. Alonso, and J. C. Rodríguez-Cabello, "Tethering QK peptide to enhance angiogenesis in elastin-like recombinamer (ELR) hydrogels," *J. Mater. Sci. Mater. Med.*, vol. 30, no. 2, p. 30, Feb. 2019, doi: 10.1007/s10856-019-6232-z.

[308] I. G. de Torre *et al.*, "Elastin-like recombinamer-covered stents: Towards a fully biocompatible and non-thrombogenic device for cardiovascular diseases," *Acta Biomater.*, vol. 12, pp. 146–155, 2015, doi: https://doi.org/10.1016/j.actbio.2014.10.029.

[309] J. Cappello *et al.*, "Genetic engineering of structural protein polymers," *Biotechnol. Prog.*, vol. 6, no. 3, pp. 198–202, 1990.

[310] A. Bracalello *et al.*, "Design and production of a chimeric resilin-, elastin-, and collagen-like engineered polypeptide," *Biomacromolecules*, vol. 12, no. 8, pp. 2957–2965, 2011.

[311] S. Salinas-Fernández, M. Santos, M. Alonso, L. Quintanilla, and J. C. Rodríguez-Cabello, "Genetically engineered elastin-like recombinamers with sequence-based molecular stabilization as advanced bioinks for 3D bioprinting," *Appl. Mater. Today*, vol. 18, p. 100500, 2020, doi: https://doi.org/10.1016/j.apmt.2019.100500.

[312] G. Mahmud *et al.*, "Directing cell motions on micropatterned ratchets," *Nat. Phys.*, vol. 5, no. 8, pp. 606–612, Aug. 2009, doi: 10.1038/nphys1306.

[313] C. M. Nelson and M. J. Bissell, "Of Extracellular Matrix, Scaffolds, and Signaling: Tissue Architecture Regulates Development, Homeostasis, and Cancer," *Annu. Rev. Cell Dev. Biol.*, vol. 22, no. 1, pp. 287–309, Nov. 2006, doi: 10.1146/annurev.cellbio.22.010305.104315.

[314] S. J. Hollister, E. E. Liao, E. N. Moffitt, C. G. Jeong, and J. M. Kemppainen, "Defining design targets for tissue engineering scaffolds," in *Fundamentals of tissue engineering and regenerative medicine*, 2009, pp. 521–537.

[315] B. M. Baker and C. S. Chen, "Deconstructing the third dimension–how 3D culture microenvironments alter cellular cues," *J. Cell Sci.*, vol. 125, no. 13, pp. 3015–3024, 2012.

[316] Y. M. Salinas-Vera *et al.*, "Three-Dimensional 3D Culture Models in Gynecological and Breast Cancer Research," *Front. Oncol.*, vol. 12, May 2022, doi: 10.3389/fonc.2022.826113.

[317] L. Mbundi, M. González-Pérez, F. González-Pérez, D. Juanes-Gusano, and J. C. Rodríguez-Cabello, "Trends in the Development of Tailored Elastin-Like Recombinamer–Based Porous Biomaterials for Soft and Hard Tissue Applications," *Front. Mater.*, vol. 7, Jan. 2021, doi: 10.3389/fmats.2020.601795.

[318] L. G. Griffith and G. Naughton, "Tissue Engineering--Current Challenges and Expanding Opportunities," *Science (80-.).*, vol. 295, no. 5557, pp. 1009–1014, Feb. 2002, doi: 10.1126/science.1069210.

[319] M. A. Morelli, M. DeBiasi, A. DeStradis, and A. M. Tamburro, "An aggregating elastin-like pentapeptide.," *J. Biomol. Struct. Dyn.*, vol. 11, no. 1, pp. 181–190, 1993.

[320] S. J. Hollister, "Porous scaffold design for tissue engineering," *Nat. Mater.*, vol. 4, no. 7, pp. 518–524, Jul. 2005, doi: 10.1038/nmat1421.

[321] L. E. Freed *et al.*, "Biodegradable Polymer Scaffolds for Tissue Engineering," *Nat. Biotechnol.*, vol. 12, no. 7, pp. 689–693, Jul. 1994, doi: 10.1038/nbt0794-689.

[322] S. Yang, K.-F. Leong, Z. Du, and C.-K. Chua, "The Design of Scaffolds for Use in

Tissue Engineering. Part I. Traditional Factors," *Tissue Eng.*, vol. 7, no. 6, pp. 679–689, Dec. 2001, doi: 10.1089/107632701753337645.

[323] A. Gleadall, D. Visscher, J. Yang, D. Thomas, and J. Segal, "Review of additive manufactured tissue engineering scaffolds: relationship between geometry and performance," *Burn. trauma*, vol. 6, 2018.

[324] V. Karageorgiou and D. Kaplan, "Porosity of 3D biomaterial scaffolds and osteogenesis," *Biomaterials*, vol. 26, no. 27, pp. 5474–5491, 2005.

[325] H. P. Wiesmann and L. Lammers, "Scaffold structure and fabrication," *Fundam. Tissue Eng. Regen. Med.*, pp. 539–549, 2009.

[326] Q. L. Loh and C. Choong, "Three-dimensional scaffolds for tissue engineering applications: role of porosity and pore size," 2013.

[327] D. W. Hutmacher, B. Tandon, and P. D. Dalton, "Scaffold design and fabrication," in *Tissue engineering*, Elsevier, 2023, pp. 355–385.

[328] C. D. Spicer, "Hydrogel scaffolds for tissue engineering: the importance of polymer choice," *Polym. Chem.*, vol. 11, no. 2, pp. 184–219, 2020, doi: 10.1039/C9PY01021A.

[329] D. C. Chow, M. R. Dreher, K. Trabbic-Carlson, and A. Chilkoti, "Ultra-High Expression of a Thermally Responsive Recombinant Fusion Protein in E. coli," *Biotechnol. Prog.*, vol. 22, no. 3, pp. 638–646, Jun. 2006, doi: 10.1021/bp0503742.

[330] J. C. Liu and D. A. Tirrell, "Cell Response to RGD Density in Cross-Linked Artificial Extracellular Matrix Protein Films," *Biomacromolecules*, vol. 9, no. 11, pp. 2984–2988, Nov. 2008, doi: 10.1021/bm800469j.

[331] E. R. Welsh and D. A. Tirrell, "Engineering the Extracellular Matrix: A Novel Approach to Polymeric Biomaterials. I. Control of the Physical Properties of Artificial Protein Matrices Designed to Support Adhesion of Vascular Endothelial Cells," *Biomacromolecules*, vol. 1, no. 1, pp. 23–30, Mar. 2000, doi: 10.1021/bm0002914.

[332] M. I. Castellanos *et al.*, "Biofunctionalization of REDV elastin-like recombinamers improves endothelialization on CoCr alloy surfaces for cardiovascular applications," *Colloids Surfaces B Biointerfaces*, vol. 127, pp. 22–32, 2015.

[333] E. Salvagni *et al.*, "A bioactive elastin-like recombinamer reduces unspecific protein adsorption and enhances cell response on titanium surfaces," *Colloids Surfaces B Biointerfaces*, vol. 114, pp. 225–233, 2014, doi: https://doi.org/10.1016/j.colsurfb.2013.10.008.

[334] C. García-Arévalo, M. Pierna, A. Girotti, F. J. Arias, and J. C. Rodríguez-Cabello, "A comparative study of cell behavior on different energetic and bioactive polymeric surfaces made from elastin-like recombinamers," *Soft Matter*, vol. 8, no. 11, pp. 3239–3249, 2012.

[335] R. R. Costa *et al.*, "Stimuli-responsive thin coatings using elastin-like polymers for biomedical applications," *Adv. Funct. Mater.*, vol. 19, no. 20, pp. 3210–3218,

2009.

[336] K. S. Straley and S. C. Heilshorn, "Design and adsorption of modular engineered proteins to prepare customized, neuron-compatible coatings," *Front. Neuroeng.*, vol. 2, p. 519, 2009.

[337] Y. Li *et al.*, "Hybrid Nanotopographical Surfaces Obtained by Biomimetic Mineralization of Statherin-Inspired Elastin-Like Recombinamers," *Adv. Healthc. Mater.*, vol. 3, no. 10, pp. 1638–1647, Oct. 2014, doi: https://doi.org/10.1002/adhm.201400015.

[338] M. Vila *et al.*, "3D silicon doped hydroxyapatite scaffolds decorated with Elastin-like Recombinamers for bone regenerative medicine," *Acta Biomater.*, vol. 45, pp. 349–356, 2016.

[339] E. Tejeda-Montes *et al.*, "Mineralization and bone regeneration using a bioactive elastin-like recombinamer membrane," *Biomaterials*, vol. 35, no. 29, pp. 8339–8347, Sep. 2014, doi: 10.1016/j.biomaterials.2014.05.095.

[340] M. Putzu, F. Causa, V. Nele, I. G. de Torre, J. C. Rodriguez-Cabello, and P. A. Netti, "Elastin-like-recombinamers multilayered nanofibrous scaffolds for cardiovascular applications," *Biofabrication*, vol. 8, no. 4, p. 45009, 2016.

[341] K. A. Woodhouse *et al.*, "Investigation of recombinant human elastin polypeptides as non-thrombogenic coatings," *Biomaterials*, vol. 25, no. 19, pp. 4543–4553, 2004.

[342] S. Atefyekta, M. Pihl, C. Lindsay, S. C. Heilshorn, and M. Andersson, "Antibiofilm elastin-like polypeptide coatings: functionality, stability, and selectivity," *Acta Biomater.*, vol. 83, pp. 245–256, Jan. 2019, doi: 10.1016/j.actbio.2018.10.039.

[343] S. Acosta, L. Quintanilla, M. Alonso, C. Aparicio, and J. C. Rodríguez-Cabello, "Recombinant AMP/Polypeptide Self-Assembled Monolayers with Synergistic Antimicrobial Properties for Bacterial Strains of Medical Relevance," *ACS Biomater. Sci. Eng.*, vol. 5, no. 9, pp. 4708–4716, Sep. 2019, doi: 10.1021/acsbiomaterials.9b00247.

[344] S. Acosta, A. Ibañez-Fonseca, C. Aparicio, and J. C. Rodríguez-Cabello, "Antibiofilm coatings based on protein-engineered polymers and antimicrobial peptides for preventing implant-associated infections.," *Biomater. Sci.*, vol. 8, no. 10, pp. 2866–2877, May 2020, doi: 10.1039/d0bm00155d.

[345] D. L. Nettles, A. Chilkoti, and L. A. Setton, "Applications of elastin-like polypeptides in tissue engineering," *Adv. Drug Deliv. Rev.*, vol. 62, no. 15, pp. 1479–1485, 2010.

[346] K. Y. Lee and D. J. Mooney, "Hydrogels for tissue engineering," *Chem. Rev.*, vol. 101, no. 7, pp. 1869–1880, 2001.

[347] A. Ibáñez-Fonseca *et al.*, "Biocompatibility of two model elastin-like recombinamer-based hydrogels formed through physical or chemical cross-linking for various applications in tissue engineering and regenerative medicine," *J. Tissue Eng. Regen. Med.*, vol. 12, no. 3, pp. e1450–e1460, 2018.

[348] F. G. Omenetto and D. L. Kaplan, "New opportunities for an ancient material," *Science (80-.).*, vol. 329, no. 5991, pp. 528–531, 2010.

[349] D. N. Woolfson, "The design of coiled-coil structures and assemblies," *Adv. Protein Chem.*, vol. 70, pp. 79–112, 2005.

[350] J. Moitra, L. Szilák, D. Krylov, and C. Vinson, "Leucine is the most stabilizing aliphatic amino acid in the d position of a dimeric leucine zipper coiled coil," *Biochemistry*, vol. 36, no. 41, pp. 12567–12573, 1997.

[351] A. M. Testera *et al.*, "Biocompatible elastin-like click gels: design, synthesis and characterization," *J. Mater. Sci. Mater. Med.*, vol. 26, pp. 1–13, 2015.

[352] I. G. de Torre, A. Ibáñez-Fonseca, L. Quintanilla, M. Alonso, and J.-C. Rodríguez-Cabello, "Random and oriented electrospun fibers based on a multicomponent, in situ clickable elastin-like recombinamer system for dermal tissue engineering," *Acta Biomater.*, vol. 72, pp. 137–149, 2018.

[353] R. Huisgen, "1, 3-dipolar cycloadditions. Past and future," *Angew. Chemie Int. Ed. English*, vol. 2, no. 10, pp. 565–598, 1963.

[354] N. J. Agard, J. A. Prescher, and C. R. Bertozzi, "A strain-promoted [3+ 2] azide–alkyne cycloaddition for covalent modification of biomolecules in living systems," *J. Am. Chem. Soc.*, vol. 126, no. 46, pp. 15046–15047, 2004.

[355] A. Mahara, K. L. Kiick, and T. Yamaoka, "In vivo guided vascular regeneration with a non-porous elastin-like polypeptide hydrogel tubular scaffold," *J. Biomed. Mater. Res. Part A*, vol. 105, no. 6, pp. 1746–1755, 2017.

[356] E. M. Brey, *Vascularization: regenerative medicine and tissue engineering*. CRC Press, 2014.

[357] F. González-Pérez, A. Ibáñez-Fonseca, M. Alonso, and J. C. Rodríguez-Cabello, "Combining tunable proteolytic sequences and a VEGF-mimetic peptide for the spatiotemporal control of angiogenesis within Elastin-Like Recombinamer scaffolds," *Acta Biomater.*, vol. 130, pp. 149–160, 2021.

[358] H. J. C. De Vries, E. Middelkoop, J. R. Mekkes, R. P. Dutrieux, C. H. R. Wildevuur, and W. Westerhof, "Dermal regeneration in native non-cross-linked collagen sponges with different extracellular matrix molecules," *Wound Repair Regen.*, vol. 2, no. 1, pp. 37–47, 1994.

[359] J. L. Walden, H. Garcia, H. Hawkins, J. R. Crouchet, L. Traber, and D. C. Gore, "Both dermal matrix and epidermis contribute to an inhibition of wound contraction.," *Ann. Plast. Surg.*, vol. 45, no. 2, pp. 162–166, 2000.

[360] A. M. Kloxin, J. A. Benton, and K. S. Anseth, "In situ elasticity modulation with dynamic substrates to direct cell phenotype," *Biomaterials*, vol. 31, no. 1, pp. 1–8, 2010.

[361] M. H. van Marion *et al.*, "Behavior of CMPCs in unidirectional constrained and stress-free 3D hydrogels," *J. Mol. Cell. Cardiol.*, vol. 87, pp. 79–91, 2015.

[362] Z. I. Foraida, T. Kamaldinov, D. A. Nelson, M. Larsen, and J. Castracane, "Elastin-PLGA hybrid electrospun nanofiber scaffolds for salivary epithelial cell self-

organization and polarization," *Acta Biomater.*, vol. 62, pp. 116–127, 2017.

[363] M. Floren and W. Tan, "Three-dimensional, soft neotissue arrays as high throughput platforms for the interrogation of engineered tissue environments," *Biomaterials*, vol. 59, pp. 39–52, 2015.

[364] M. Klaas *et al.*, "The alterations in the extracellular matrix composition guide the repair of damaged liver tissue," *Sci. Rep.*, vol. 6, no. 1, pp. 1–12, 2016.

[365] J. M. Gluck *et al.*, "Biochemical and biomechanical properties of the pacemaking sinoatrial node extracellular matrix are distinct from contractile left ventricular matrix," *PLoS One*, vol. 12, no. 9, p. e0185125, 2017.

[366] J. Skopinska-Wisniewska, J. Kuderko, A. Bajek, M. Maj, A. Sionkowska, and M. Ziegler-Borowska, "Collagen/elastin hydrogels cross-linked by squaric acid," *Mater. Sci. Eng. C*, vol. 60, pp. 100–108, 2016.

[367] P. Kuppan, S. Sethuraman, and U. M. Krishnan, "Interaction of human smooth muscle cells with nanofibrous scaffolds: effect of fiber orientation on cell adhesion, proliferation, and functional gene expression," *J. Biomed. Mater. Res. Part A*, vol. 103, no. 7, pp. 2236–2250, 2015.

[368] S. Minardi *et al.*, "Biomimetic collagen/elastin meshes for ventral hernia repair in a rat model," *Acta Biomater.*, vol. 50, pp. 165–177, 2017.

[369] G. C. Yeo, S. M. Mithieux, and A. S. Weiss, "The elastin matrix in tissue engineering and regeneration," *Curr. Opin. Biomed. Eng.*, vol. 6, pp. 27–32, 2018.

[370] P. Krzyszczyk, R. Schloss, A. Palmer, and F. Berthiaume, "The role of macrophages in acute and chronic wound healing and interventions to promote pro-wound healing phenotypes," *Front. Physiol.*, vol. 9, p. 419, 2018.

[371] G. FrykbergRobert, "Challenges in the treatment of chronic wounds," *Adv. wound care*, 2015.

[372] S. R. Nussbaum *et al.*, "An economic evaluation of the impact, cost, and medicare policy implications of chronic nonhealing wounds," *Value Heal.*, vol. 21, no. 1, pp. 27–32, 2018.

[373] A. Yeboah, R. I. Cohen, C. Rabolli, M. L. Yarmush, and F. Berthiaume, "Elastin-like polypeptides: A strategic fusion partner for biologics," *Biotechnol. Bioeng.*, vol. 113, no. 8, pp. 1617–1627, 2016.

[374] H. J. Kang, N. Chen, B. C. Dash, H. C. Hsia, and F. Berthiaume, "Self-assembled nanomaterials for chronic skin wound healing," *Adv. Wound Care*, vol. 10, no. 5, pp. 221–233, 2021.

[375] J. Rnjak-Kovacina *et al.*, "Tailoring the porosity and pore size of electrospun synthetic human elastin scaffolds for dermal tissue engineering," *Biomaterials*, vol. 32, no. 28, pp. 6729–6736, 2011.

[376] C. Chong, Y. Wang, A. Fathi, R. Parungao, P. K. Maitz, and Z. Li, "Skin wound repair: Results of a pre-clinical study to evaluate electropsun collagen–elastin–PCL scaffolds as dermal substitutes.," *Burns*, vol. 45, no. 7, pp. 1639–

1648, 2019.

[377] A. Da Costa *et al.*, "Single step fabrication of antimicrobial fibre mats from a bioengineered protein-based polymer," *Biomed. Mater.*, vol. 12, no. 4, p. 45011, 2017.

[378] J. Devalliere, K. Dooley, Y. Hu, S. S. Kelangi, B. E. Uygun, and M. L. Yarmush, "Co-delivery of a growth factor and a tissue-protective molecule using elastin biopolymers accelerates wound healing in diabetic mice," *Biomaterials*, vol. 141, pp. 149–160, 2017.

[379] K. Noda *et al.*, "Clinical Utility of Silk-Elastin Sponge in Patients with Chronic and Acute Skin Ulcers: Study Protocol of a Multicenter Clinical Trial," *Dermatol. Ther. (Heidelb).*, vol. 12, no. 1, pp. 243–252, 2022.

[380] K. Noda *et al.*, "Safety of silk-elastin sponges in patients with chronic skin ulcers: A phase I/II, single-center, open-label, single-arm clinical trial," *Plast. Reconstr. Surg. Glob. Open*, vol. 9, no. 4, 2021.

[381] A. Yeboah, T. Maguire, R. Schloss, F. Berthiaume, and M. L. Yarmush, "Stromal cell-derived growth factor-1 alpha-elastin like peptide fusion protein promotes cell migration and revascularization of experimental wounds in diabetic mice," *Adv. wound care*, vol. 6, no. 1, pp. 10–22, 2017.

[382] A. Yeboah, R. I. Cohen, R. Faulknor, R. Schloss, M. L. Yarmush, and F. Berthiaume, "The development and characterization of SDF1α-elastin-like-peptide nanoparticles for wound healing," *J. Control. release*, vol. 232, pp. 238–247, 2016.

[383] P. Koria *et al.*, "Self-assembling elastin-like peptides growth factor chimeric nanoparticles for the treatment of chronic wounds," *Proc. Natl. Acad. Sci.*, vol. 108, no. 3, pp. 1034–1039, 2011.

[384] F. Fan, S. Saha, and D. Hanjaya-Putra, "Biomimetic hydrogels to promote wound healing," *Front. Bioeng. Biotechnol.*, vol. 9, p. 718377, 2021.

[385] T. A. Debele and W.-P. Su, "Polysaccharide and protein-based functional wound dressing materials and applications," *Int. J. Polym. Mater. Polym. Biomater.*, vol. 71, no. 2, pp. 87–108, 2022.

[386] H. Yao *et al.*, "Design strategies for adhesive hydrogels with natural antibacterial agents as wound dressings: Status and trends," *Mater. Today Bio*, p. 100429, 2022.

[387] P. Bertsch, M. Diba, D. J. Mooney, and S. C. G. Leeuwenburgh, "Self-healing injectable hydrogels for tissue regeneration," *Chem. Rev.*, 2022.

[388] C. Huang *et al.*, "Anti-inflammatory hydrogel dressings and skin wound healing," *Clin. Transl. Med.*, vol. 12, no. 11, p. e1094, 2022.

[389] A. B. Sousa, A. P. Águas, M. A. Barbosa, and J. N. Barbosa, "Immunomodulatory biomaterial-based wound dressings advance the healing of chronic wounds via regulating macrophage behavior," *Regen. Biomater.*, vol. 9, 2022.

[390] D. Solanki, P. Vinchhi, and M. M. Patel, "Design Considerations, Formulation

Approaches, and Strategic Advances of Hydrogel Dressings for Chronic Wound Management," *ACS omega*, vol. 8, no. 9, pp. 8172–8189, 2023.

[391] D. Massella *et al.*, "Bio-functional textiles: Combining pharmaceutical nanocarriers with fibrous materials for innovative dermatological therapies," *Pharmaceutics*, vol. 11, no. 8, p. 403, 2019.

[392] S. M. Mithieux and A. S. Weiss, "Design of an elastin-layered dermal regeneration template," *Acta Biomater.*, vol. 52, pp. 33–40, 2017.

[393] S. M. Mithieux *et al.*, "Tropoelastin implants that accelerate wound repair," *Adv. Healthc. Mater.*, vol. 7, no. 10, p. 1701206, 2018.

[394] J. Rnjak, Z. Li, P. K. M. Maitz, S. G. Wise, and A. S. Weiss, "Primary human dermal fibroblast interactions with open weave three-dimensional scaffolds prepared from synthetic human elastin," *Biomaterials*, vol. 30, no. 32, pp. 6469–6477, 2009.

[395] N. Annabi *et al.*, "Engineering a sprayable and elastic hydrogel adhesive with antimicrobial properties for wound healing," *Biomaterials*, vol. 139, pp. 229–243, 2017.

[396] N. Annabi *et al.*, "Engineering a highly elastic human protein–based sealant for surgical applications," *Sci. Transl. Med.*, vol. 9, no. 410, p. eaai7466, 2017.

[397] D.-M. Tian *et al.*, "In-situ formed elastin-based hydrogels enhance wound healing via promoting innate immune cells recruitment and angiogenesis," *Mater. Today Bio*, vol. 15, p. 100300, 2022.

[398] S. Kawabata *et al.*, "The development of a novel wound healing material, silk-elastin sponge," *J. Biomater. Sci. Polym. Ed.*, vol. 28, no. 18, pp. 2143–2153, 2017.

[399] S. Kawabata *et al.*, "The utility of silk-elastin hydrogel as a new material for wound healing," *Plast. Reconstr. Surg. Glob. Open*, vol. 6, no. 5, 2018.

[400] A. Vasconcelos, A. C. Gomes, and A. Cavaco-Paulo, "Novel silk fibroin/elastin wound dressings," *Acta Biomater.*, vol. 8, no. 8, pp. 3049–3060, 2012.

[401] A. M. Abdel-Aty, A. Z. Barakat, H. M. Abdel-Mageed, and S. A. Mohamed, "Development of bovine elastin/tannic acid bioactive conjugate: physicochemical, morphological, and wound healing properties," *Polym. Bull.*, pp. 1–21, 2023.

[402] A. Ramzan *et al.*, "Freeze gelation (chitosan-elastin-sodium alginate)/zinc oxide nanocomposite gel with enhanced adipose stem cell proliferation and antibacterial properties.," *Int. J. Biol. Macromol.*, p. 123519, 2023.

[403] S.-K. Choi *et al.*, "Integrin-binding elastin-like polypeptide as an in situ gelling delivery matrix enhances the therapeutic efficacy of adipose stem cells in healing full-thickness cutaneous wounds," *J. Control. Release*, vol. 237, pp. 89–100, 2016.

[404] C. Bergonzi, G. G. d'Ayala, L. Elviri, P. Laurienzo, A. Bandiera, and O. Catanzano, "Alginate/human elastin-like polypeptide composite films with antioxidant

properties for potential wound healing application," *Int. J. Biol. Macromol.*, vol. 164, pp. 586–596, 2020.

[405] T. Hashimoto, Y. Suzuki, M. Tanihara, Y. Kakimaru, and K. Suzuki, "Development of alginate wound dressings linked with hybrid peptides derived from laminin and elastin," *Biomaterials*, vol. 25, no. 7–8, pp. 1407–1414, 2004.

[406] M. Stojic *et al.*, "Elastin-plasma hybrid hydrogels for skin tissue engineering," *Polymers (Basel).*, vol. 13, no. 13, p. 2114, 2021.

[407] V. Sarangthem *et al.*, "Application of elastin-like polypeptide (ELP) containing extra-cellular matrix (ECM) binding ligands in regenerative medicine," *Int. J. Biol. Macromol.*, vol. 207, pp. 443–453, 2022.

[408] M. L. Del Prado-Audelo *et al.*, "Radiation-induced graft polymerization of elastin onto polyvinylpyrrolidone as a possible wound dressing," *Cell. Mol. Biol.*, vol. 67, no. 1, pp. 64–72, 2021.

[409] N. Sallehuddin *et al.*, "Characterization and Cytocompatibility of Collagen–Gelatin–Elastin (CollaGee) Acellular Skin Substitute towards Human Dermal Fibroblasts: In Vitro Assessment," *Biomedicines*, vol. 10, no. 6, p. 1327, 2022.

[410] N. Kamaruzaman, M. B. Fauzi, Y. Tabata, and S. M. Yusop, "Functionalised Hybrid Collagen-Elastin for Acellular Cutaneous Substitute Applications," *Polymers (Basel).*, vol. 15, no. 8, p. 1929, 2023.

[411] S. Salinas-Fernandez, M. Santos, M. Alonso, L. Quintanilla, and J. C. Rodríguez-Cabello, "Genetically engineered elastin-like recombinamers with sequence-based molecular stabilization as advanced bioinks for 3D bioprinting," *Appl. Mater. Today*, vol. 18, p. 100500, 2020.

[412] J. C. Rodríguez-Cabello, I. G. de Torre, A. Ibañez-Fonseca, and M. Alonso, "Bioactive scaffolds based on elastin-like materials for wound healing," *Adv. Drug Deliv. Rev.*, vol. 129, pp. 118–133, 2018.

[413] K. Derr *et al.*, "Fully three-dimensional bioprinted skin equivalent constructs with validated morphology and barrier function," *Tissue Eng. Part C Methods*, vol. 25, no. 6, pp. 334–343, 2019.

[414] L. Tayebi, M. Rasoulianboroujeni, K. Moharamzadeh, T. K. D. Almela, Z. Cui, and H. Ye, "3D-printed membrane for guided tissue regeneration," *Mater. Sci. Eng. C*, vol. 84, pp. 148–158, 2018.

[415] F. Cadamuro, S. Sampaolesi, G. Bertolini, L. Roz, F. Nicotra, and L. Russo, "Click Chemistry Protocol for 3D Bioprintable Elastin– Hyaluronic Acid Hydrogels," *ChemNanoMat*, vol. 9, no. 2, p. e202200508, 2023.

[416] J. C. Rodríguez-Cabello, A. Girotti, A. Ribeiro, and F. J. Arias, "Synthesis of Genetically Engineered Protein Polymers (Recombinamers) as an Example of Advanced Self-Assembled Smart Materials," 2012, pp. 17–38. doi: 10.1007/978-1-61779-388-2_2.

[417] D. E. Meyer and A. Chilkoti, "Genetically Encoded Synthesis of Protein-Based Polymers with Precisely Specified Molecular Weight and Sequence by

Recursive Directional Ligation: Examples from the Elastin-like Polypeptide System," *Biomacromolecules*, vol. 3, no. 2, pp. 357–367, Mar. 2002, doi: 10.1021/bm015630n.

[418] P. Goffin and P. Dehottay, "Complete Genome Sequence of Escherichia coli BLR(DE3), a recA -Deficient Derivative of E. coli BL21(DE3)," *Genome Announc.*, vol. 5, no. 22, Jun. 2017, doi: 10.1128/genomeA.00441-17.

[419] S. Li *et al.*, "Progress in Pluronic F127 Derivatives for Application in Wound Healing and Repair," *Int. J. Nanomedicine*, vol. Volume 18, pp. 4485–4505, Aug. 2023, doi: 10.2147/IJN.S418534.

[420] T. Wang *et al.*, "Pluronic F127-Lipoic Acid Adhesive Nanohydrogel Combining with Ce 3+ /Tannic Acid/Ulinastatin Nanoparticles for Promoting Wound Healing," *Biomacromolecules*, vol. 25, no. 2, pp. 924–940, Feb. 2024, doi: 10.1021/acs.biomac.3c01060.

[421] V. Kant *et al.*, "Topical pluronic F-127 gel application enhances cutaneous wound healing in rats," *Acta Histochem.*, vol. 116, no. 1, pp. 5–13, Jan. 2014, doi: 10.1016/j.acthis.2013.04.010.

[422] G. L. Rosano, E. S. Morales, and E. A. Ceccarelli, "New tools for recombinant protein production in Escherichia coli : A 5-year update," *Protein Sci.*, vol. 28, no. 8, pp. 1412–1422, Aug. 2019, doi: 10.1002/pro.3668.

[423] U. K. LAEMMLI, "Cleavage of Structural Proteins during the Assembly of the Head of Bacteriophage T4," *Nature*, vol. 227, no. 5259, pp. 680–685, Aug. 1970, doi: 10.1038/227680a0.

[424] O. Pletnev, P., Osterman, I., Sergiev, P., Bogdanov, A., & Dontsova, "Survival Guide: Escherichia coli in the stationary phase," *Acta Naturae*, vol. 7(4 (27)), pp. 22–33, 2015.

[425] A. Meyer, D. E., & Chilkoti, *Protein purification by inverse transition cycling*, Protein-Pr. 2002.

[426] D. W. Urry, "Free energy transduction in polypeptides and proteins based on inverse temperature transitions," *Prog. Biophys. Mol. Biol.*, vol. 57, no. 1, pp. 23–57, 1992, doi: 10.1016/0079-6107(92)90003-O.

[427] S. R. MacEwan, W. Hassouneh, and A. Chilkoti, "Non-chromatographic Purification of Recombinant Elastin-like Polypeptides and their Fusions with Peptides and Proteins from Escherichia coli," *J. Vis. Exp.*, no. 88, Jun. 2014, doi: 10.3791/51583.

[428] G. Pinedo-Martín, M. Santos, A. M. Testera, M. Alonso, and J. C. Rodríguez-Cabello, "The effect of NaCl on the self-assembly of elastin-like block co-recombinamers: Tuning the size of micelles and vesicles," *Polymer (Guildf).*, vol. 55, no. 21, pp. 5314–5321, Oct. 2014, doi: 10.1016/j.polymer.2014.08.053.

[429] H. C. Kolb, M. G. Finn, and K. B. Sharpless, "Click Chemistry: Diverse Chemical Function from a Few Good Reactions," *Angew. Chemie Int. Ed.*, vol. 40, no. 11, pp. 2004–2021, Jun. 2001, doi: 10.1002/1521-

3773(20010601)40:11<2004::AID-ANIE2004>3.0.CO;2-5.

[430] J. M. Baskin *et al.*, "Copper-free click chemistry for dynamic in vivo imaging," *Proc. Natl. Acad. Sci.*, vol. 104, no. 43, pp. 16793–16797, Oct. 2007, doi: 10.1073/pnas.0707090104.

[431] J. Xu, T. M. Filion, F. Prifti, and J. Song, "Cytocompatible Poly(ethylene glycol)-co -polycarbonate Hydrogels Cross-Linked by Copper-Free, Strain-Promoted Click Chemistry," *Chem. – An Asian J.*, vol. 6, no. 10, pp. 2730–2737, Oct. 2011, doi: 10.1002/asia.201100411.

[432] N. J. Agard, J. A. Prescher, and C. R. Bertozzi, "A Strain-Promoted [3 + 2] Azide–Alkyne Cycloaddition for Covalent Modification of Biomolecules in Living Systems," *J. Am. Chem. Soc.*, vol. 126, no. 46, pp. 15046–15047, Nov. 2004, doi: 10.1021/ja044996f.

[433] I. González de Torre, M. Santos, L. Quintanilla, A. Testera, M. Alonso, and J. C. Rodríguez Cabello, "Elastin-like recombinamer catalyst-free click gels: Characterization of poroelastic and intrinsic viscoelastic properties," *Acta Biomater.*, vol. 10, no. 6, pp. 2495–2505, Jun. 2014, doi: 10.1016/j.actbio.2014.02.006.

[434] A. Fernández-Colino *et al.*, "Macroporous click-elastin-like hydrogels for tissue engineering applications," *Mater. Sci. Eng. C*, vol. 88, pp. 140–147, Jul. 2018, doi: 10.1016/j.msec.2018.03.013.

[435] F. González-Pérez, A. Ibáñez-Fonseca, M. Alonso, and J. C. Rodríguez-Cabello, "Combining tunable proteolytic sequences and a VEGF-mimetic peptide for the spatiotemporal control of angiogenesis within Elastin-Like Recombinamer scaffolds," *Acta Biomater.*, vol. 130, pp. 149–160, Aug. 2021, doi: 10.1016/j.actbio.2021.06.005.

[436] M. González-Pérez, I. González de Torre, M. Alonso, and J. C. Rodríguez-Cabello, "Controlled Production of Elastin-like Recombinamer Polymer-Based Membranes at a Liquid–Liquid Interface by Click Chemistry," *Biomacromolecules*, vol. 21, no. 10, pp. 4149–4158, Oct. 2020, doi: 10.1021/acs.biomac.0c00939.

[437] P. Vlieghe, V. Lisowski, J. Martinez, and M. Khrestchatisky, "Synthetic therapeutic peptides: science and market," *Drug Discov. Today*, vol. 15, no. 1–2, pp. 40–56, Jan. 2010, doi: 10.1016/j.drudis.2009.10.009.

[438] R. B. Merrifield, "Solid Phase Peptide Synthesis. I. The Synthesis of a Tetrapeptide," *J. Am. Chem. Soc.*, vol. 85, no. 14, pp. 2149–2154, Jul. 1963, doi: 10.1021/ja00897a025.

[439] I. Coin, M. Beyermann, and M. Bienert, "Solid-phase peptide synthesis: from standard procedures to the synthesis of difficult sequences," *Nat. Protoc.*, vol. 2, no. 12, pp. 3247–3256, Dec. 2007, doi: 10.1038/nprot.2007.454.

[440] M. Amblard, J.-A. Fehrentz, J. Martinez, and G. Subra, "Methods and Protocols of Modern Solid Phase Peptide Synthesis," *Mol. Biotechnol.*, vol. 33, no. 3, pp. 239–254, 2006, doi: 10.1385/MB:33:3:239.

[441] M. Cudic and G. B. Fields, "Solid-Phase Peptide Synthesis," 2008, pp. 515–546. doi: 10.1007/978-1-60327-375-6_32.

[442] T. Bruckdorfer, O. Marder, and F. Albericio, "From Production of Peptides in Milligram Amounts for Research to Multi-Tons Quantities for Drugs of the Future," *Curr. Pharm. Biotechnol.*, vol. 5, no. 1, pp. 29–43, Feb. 2004, doi: 10.2174/1389201043489620.

[443] M. Engelhard and R. B. Merrifield, "Tyrosine protecting groups: minimization of rearrangement to 3-alkyltyrosine during acidolysis," *J. Am. Chem. Soc.*, vol. 100, no. 11, pp. 3559–3563, May 1978, doi: 10.1021/ja00479a044.

[444] L. Zervas and I. Photaki, "On Cysteine and Cystine Peptides. I. New S-Protecting Groups for Cysteine," *J. Am. Chem. Soc.*, vol. 84, no. 20, pp. 3887–3897, Oct. 1962, doi: 10.1021/ja00879a019.

[445] L. A. Carpino and G. Y. Han, "9-Fluorenylmethoxycarbonyl function, a new base-sensitive amino-protecting group," *J. Am. Chem. Soc.*, vol. 92, no. 19, pp. 5748–5749, Sep. 1970, doi: 10.1021/ja00722a043.

[446] P. Chan, W. C. W. P. D., & White, *Fmoc solid phase peptide synthesis: a practical approach*, Oxford. 1999.

[447] J. M. Palomo, "Solid-phase peptide synthesis: an overview focused on the preparation of biologically relevant peptides," *RSC Adv.*, vol. 4, no. 62, pp. 32658–32672, 2014, doi: 10.1039/C4RA02458C.

[448] M. Bodanszky, S. S. Deshmane, and J. Martinez, "Side reactions in peptide synthesis. 11. Possible removal of the 9-fluorenylmethyloxycarbonyl group by the amino components during coupling," *J. Org. Chem.*, vol. 44, no. 10, pp. 1622–1625, May 1979, doi: 10.1021/jo01324a008.

[449] C. Werner and H.-J. Jacobasch, "Surface Characterization of Polymers for Medical Devices," *Int. J. Artif. Organs*, vol. 22, no. 3, pp. 160–176, Mar. 1999, doi: 10.1177/039139889902200309.

[450] T. Christensen, W. Hassouneh, K. Trabbic-Carlson, and A. Chilkoti, "Predicting Transition Temperatures of Elastin-Like Polypeptide Fusion Proteins," *Biomacromolecules*, vol. 14, no. 5, pp. 1514–1519, May 2013, doi: 10.1021/bm400167h.

[451] P. M. Williams, "Membrane Roughness," in *Encyclopedia of Membranes*, Berlin, Heidelberg: Springer Berlin Heidelberg, 2014, pp. 1–2. doi: 10.1007/978-3-642-40872-4_999-1.

[452] W. Richard Bowen and T. A. Doneva, "Atomic force microscopy characterization of ultrafiltration membranes: correspondence between surface pore dimensions and molecular weight cut-off," *Surf. Interface Anal.*, vol. 29, no. 8, pp. 544–547, Aug. 2000, doi: 10.1002/1096-9918(200008)29:8<544::AID-SIA901>3.0.CO;2-4.

[453] J. Schindelin *et al.*, "Fiji: an open-source platform for biological-image analysis," *Nat. Methods*, vol. 9, no. 7, pp. 676–682, Jul. 2012, doi: 10.1038/nmeth.2019.

[454] R. S. Hebbar, A. M. Isloor, and A. F. Ismail, "Contact Angle Measurements," in *Membrane Characterization*, Elsevier, 2017, pp. 219–255. doi: 10.1016/B978-0-444-63776-5.00012-7.

[455] D. Rianti *et al.*, "The Characteristics, Swelling Ratio and Water Content Percentage of Chitosan-gelatin/limestone-based Carbonate Hydroxyapatite Composite Scaffold," *Int. J. Integr. Eng.*, vol. 14, no. 2, Jun. 2022, doi: 10.30880/ijie.2022.14.02.003.

[456] Y.-J. Lin, G.-H. Lee, C.-W. Chou, Y.-P. Chen, T.-H. Wu, and H.-R. Lin, "Stimulation of wound healing by PU/hydrogel composites containing fibroblast growth factor-2," *J. Mater. Chem. B*, vol. 3, no. 9, pp. 1931–1941, 2015, doi: 10.1039/C4TB01638F.

[457] T. Flora, I. González de Torre, M. Alonso, and J. C. Rodríguez-Cabello, "Use of proteolytic sequences with different cleavage kinetics as a way to generate hydrogels with preprogrammed cell-infiltration patterns imparted over their given 3D spatial structure," *Biofabrication*, vol. 11, no. 3, p. 035008, Apr. 2019, doi: 10.1088/1758-5090/ab10a5.

[458] H. K. Raut, R. Das, Z. Liu, X. Liu, and S. Ramakrishna, "Biocompatibility of Biomaterials for Tissue Regeneration or Replacement," *Biotechnol. J.*, vol. 15, no. 12, Dec. 2020, doi: 10.1002/biot.202000160.

[459] J. O'Brien, I. Wilson, T. Orton, and F. Pognan, "Investigation of the Alamar Blue (resazurin) fluorescent dye for the assessment of mammalian cell cytotoxicity," *Eur. J. Biochem.*, vol. 267, no. 17, pp. 5421–5426, Sep. 2000, doi: 10.1046/j.1432-1327.2000.01606.x.

[460] N. A. P. Franken, H. M. Rodermond, J. Stap, J. Haveman, and C. van Bree, "Clonogenic assay of cells in vitro," *Nat. Protoc.*, vol. 1, no. 5, pp. 2315–2319, Dec. 2006, doi: 10.1038/nprot.2006.339.

[461] V. Sarangthem *et al.*, "Application of elastin-like polypeptide (ELP) containing extra-cellular matrix (ECM) binding ligands in regenerative medicine," *Int. J. Biol. Macromol.*, vol. 207, pp. 443–453, May 2022, doi: 10.1016/j.ijbiomac.2022.03.018.

[462] K. J. Livak and T. D. Schmittgen, "Analysis of Relative Gene Expression Data Using Real-Time Quantitative PCR and the 2−ΔΔCT Method," *Methods*, vol. 25, no. 4, pp. 402–408, Dec. 2001, doi: 10.1006/meth.2001.1262.

[463] N. A. M. Nasir, R. Paus, and D. M. Ansell, "Fluorescent cell tracer dye permits real-time assessment of re-epithelialization in a serum-free ex vivo human skin wound assay," *Wound Repair Regen.*, vol. 27, no. 1, pp. 126–133, Jan. 2019, doi: 10.1111/wrr.12688.

[464] C. H. V. Nascimento-Filho, E. J. D. Silveira, E. M. Goloni-Bertollo, L. B. de Souza, C. H. Squarize, and R. M. Castilho, "Skin wound healing triggers epigenetic modifications of histone H4," *J. Transl. Med.*, vol. 18, no. 1, p. 138, Dec. 2020, doi: 10.1186/s12967-020-02303-1.

[465] I. A. S. Franco, N. H., & Olsson, *Scientists and the 3Rs: attitudes to animal use in biomedical research and the effect of mandatory training in laboratory animal*

science, Laboratory. 2014. doi: 10.1177/002367721349871.

[466] W. Xu, S. Jong Hong, S. Jia, Y. Zhao, R. D. Galiano, and T. A. Mustoe, "Application of a partial-thickness human ex vivo skin culture model in cutaneous wound healing study," *Lab. Investig.*, vol. 92, no. 4, pp. 584–599, Apr. 2012, doi: 10.1038/labinvest.2011.184.

[467] A. Rakita, N. Nikolić, M. Mildner, J. Matiasek, and A. Elbe-Bürger, "Re-epithelialization and immune cell behaviour in an ex vivo human skin model," *Sci. Rep.*, vol. 10, no. 1, p. 1, Jan. 2020, doi: 10.1038/s41598-019-56847-4.

[468] D. S. Masson-Meyers *et al.*, "Experimental models and methods for cutaneous wound healing assessment," *Int. J. Exp. Pathol.*, vol. 101, no. 1–2, pp. 21–37, Feb. 2020, doi: 10.1111/iep.12346.

[469] J. Wu and N. X. Landén, "Investigation of Skin Wound Healing Using a Mouse Model," 2020, pp. 239–247. doi: 10.1007/978-1-0716-0648-3_20.

[470] R. D. Cardiff, C. H. Miller, and R. J. Munn, "Manual Hematoxylin and Eosin Staining of Mouse Tissue Sections," *Cold Spring Harb. Protoc.*, vol. 2014, no. 6, p. pdb.prot073411, Jun. 2014, doi: 10.1101/pdb.prot073411.

[471] A. Barth and C. Zscherp, "What vibrations tell about proteins," *Q. Rev. Biophys.*, vol. 35, no. 4, pp. 369–430, Nov. 2002, doi: 10.1017/S0033583502003815.

[472] Z. Megeed, J. Cappello, and H. Ghandehari, "Thermal Analysis of Water in Silk–Elastinlike Hydrogels by Differential Scanning Calorimetry," *Biomacromolecules*, vol. 5, no. 3, pp. 793–797, May 2004, doi: 10.1021/bm0343491.

[473] W.-W. Song, Z.-G. Qian, H. Liu, H.-F. Chen, D. L. Kaplan, and X.-X. Xia, "On-Demand Regulation of Dual Thermosensitive Protein Hydrogels," *ACS Macro Lett.*, vol. 10, no. 4, pp. 395–400, Apr. 2021, doi: 10.1021/acsmacrolett.1c00062.

[474] M. Guillot-Ferriols *et al.*, "Effective elastin-like recombinamers coating on poly(vinylidene) fluoride membranes for mesenchymal stem cell culture," *Eur. Polym. J.*, vol. 146, p. 110269, Mar. 2021, doi: 10.1016/j.eurpolymj.2021.110269.

[475] L. Martín, M. Alonso, A. Girotti, F. J. Arias, and J. C. Rodríguez-Cabello, "Synthesis and Characterization of Macroporous Thermosensitive Hydrogels from Recombinant Elastin-Like Polymers," *Biomacromolecules*, vol. 10, no. 11, pp. 3015–3022, Nov. 2009, doi: 10.1021/bm900560a.

[476] D. W. Urry *et al.*, "Hydrophobicity scale for proteins based on inverse temperature transitions," *Biopolymers*, vol. 32, no. 9, pp. 1243–1250, Sep. 1992, doi: 10.1002/bip.360320913.

[477] S. Kripotou, E. Stefanopoulou, M. Culebras-Martínez, R. M. Morales-Román, G. Gallego Ferrer, and A. Kyritsis, "Water dynamics and thermal properties of tyramine-modified hyaluronic acid - Gelatin hydrogels," *Polymer (Guildf).*, vol. 178, p. 121598, Sep. 2019, doi: 10.1016/j.polymer.2019.121598.

[478] M. Coronado, R., Pekerar, S., Lorenzo, A., & Sabino, "Obtención y

caracterización de hidrogeles inteligentes del tipo red interpenetrada basados en Poli (N-Isopropilacrilamida).," *Supl. la Rev. Latinoam. Metal. y Mater. S*, vol. 2, pp. 65-66., 2009.

[479] K. Trabbic-Carlson, L. A. Setton, and A. Chilkoti, "Swelling and Mechanical Behaviors of Chemically Cross-Linked Hydrogels of Elastin-like Polypeptides," *Biomacromolecules*, vol. 4, no. 3, pp. 572–580, May 2003, doi: 10.1021/bm025671z.

[480] Y. Chun, D. Mulcahy, L. Zou, and I. Kim, "A Short Review of Membrane Fouling in Forward Osmosis Processes," *Membranes (Basel).*, vol. 7, no. 2, p. 30, Jun. 2017, doi: 10.3390/membranes7020030.

[481] Z. Zhong, D. Li, B. Zhang, and W. Xing, "Membrane surface roughness characterization and its influence on ultrafine particle adhesion," *Sep. Purif. Technol.*, vol. 90, pp. 140–146, Apr. 2012, doi: 10.1016/j.seppur.2011.09.016.

[482] D. Johnson and N. Hilal, "Characterisation and quantification of membrane surface properties using atomic force microscopy: A comprehensive review," *Desalination*, vol. 356, pp. 149–164, Jan. 2015, doi: 10.1016/j.desal.2014.08.019.

[483] K. Boussu, B. Van der Bruggen, A. Volodin, J. Snauwaert, C. Van Haesendonck, and C. Vandecasteele, "Roughness and hydrophobicity studies of nanofiltration membranes using different modes of AFM," *J. Colloid Interface Sci.*, vol. 286, no. 2, pp. 632–638, Jun. 2005, doi: 10.1016/j.jcis.2005.01.095.

[484] R. Oizerovich-Honig, V. Raim, and S. Srebnik, "Simulation of Thin Film Membranes Formed by Interfacial Polymerization," *Langmuir*, vol. 26, no. 1, pp. 299–306, Jan. 2010, doi: 10.1021/la9024684.

[485] S. M. Tajik, S., Moini Jazani, O., Shokrollahzadeh, S., & Latifi, "Thin film nanocomposite forward osmosis membrane prepared by graphene oxide embedded PSf substrate.," *J. Part. Sci. Technol.*, vol. 2(2), pp. 103-117., 2016, doi: 10.22104/JPST.2016.412.

[486] J. D. Humphrey, E. R. Dufresne, and M. A. Schwartz, "Mechanotransduction and extracellular matrix homeostasis," *Nat. Rev. Mol. Cell Biol.*, vol. 15, no. 12, pp. 802–812, Dec. 2014, doi: 10.1038/nrm3896.

[487] Y.-C. Yeh, J.-Y. Ling, W.-C. Chen, H.-H. Lin, and M.-J. Tang, "Mechanotransduction of matrix stiffness in regulation of focal adhesion size and number: reciprocal regulation of caveolin-1 and β1 integrin," *Sci. Rep.*, vol. 7, no. 1, p. 15008, Nov. 2017, doi: 10.1038/s41598-017-14932-6.

[488] A. M. Handorf, Y. Zhou, M. A. Halanski, and W.-J. Li, "Tissue Stiffness Dictates Development, Homeostasis, and Disease Progression," *Organogenesis*, vol. 11, no. 1, pp. 1–15, Jan. 2015, doi: 10.1080/15476278.2015.1019687.

[489] M. Li *et al.*, "Hydrogel/nanofibrous membrane composites with enhanced water retention, stretchability and self-healing capability for wound healing," *Compos. Part B Eng.*, vol. 257, p. 110672, May 2023, doi: 10.1016/j.compositesb.2023.110672.

[490] W. Zhu, J. Zhang, Z. Wei, B. Zhang, and X. Weng, "Advances and Progress in Self-Healing Hydrogel and Its Application in Regenerative Medicine," *Materials (Basel).*, vol. 16, no. 3, p. 1215, Jan. 2023, doi: 10.3390/ma16031215.

[491] K. Zhang *et al.*, "Cellulose based self-healing hydrogel through Boronic Ester connections for wound healing and antitumor applications," *Int. J. Biol. Macromol.*, vol. 230, p. 123294, Mar. 2023, doi: 10.1016/j.ijbiomac.2023.123294.

[492] J. Qu, X. Zhao, Y. Liang, T. Zhang, P. X. Ma, and B. Guo, "Antibacterial adhesive injectable hydrogels with rapid self-healing, extensibility and compressibility as wound dressing for joints skin wound healing," *Biomaterials*, vol. 183, pp. 185–199, Nov. 2018, doi: 10.1016/j.biomaterials.2018.08.044.

[493] X. Zhao, H. Wu, B. Guo, R. Dong, Y. Qiu, and P. X. Ma, "Antibacterial anti-oxidant electroactive injectable hydrogel as self-healing wound dressing with hemostasis and adhesiveness for cutaneous wound healing," *Biomaterials*, vol. 122, pp. 34–47, Apr. 2017, doi: 10.1016/j.biomaterials.2017.01.011.

[494] I. Katime and E. Mendizábal, "Swelling Properties of New Hydrogels Based on the Dimethyl Amino Ethyl Acrylate Methyl Chloride Quaternary Salt with Acrylic Acid and 2-Methylene Butane-1,4-Dioic Acid Monomers in Aqueous Solutions," *Mater. Sci. Appl.*, vol. 01, no. 03, pp. 162–167, 2010, doi: 10.4236/msa.2010.13026.

[495] T. Çaykara and M. Doğmuş, "Effects of Temperature and Surfactants on the Equilibrium Swelling Behavior of Poly[acrylamide- co -(itaconic acid)] Hydrogels," *Macromol. Mater. Eng.*, vol. 289, no. 6, pp. 548–551, Jun. 2004, doi: 10.1002/mame.200400037.

[496] Y. Shmidov, M. Zhou, G. Yosefi, R. Bitton, and J. B. Matson, "Hydrogels composed of hyaluronic acid and dendritic ELPs: hierarchical structure and physical properties," *Soft Matter*, vol. 15, no. 5, pp. 917–925, 2019, doi: 10.1039/C8SM02450B.

[497] A. M. Testera *et al.*, "Biocompatible elastin-like click gels: design, synthesis and characterization," *J. Mater. Sci. Mater. Med.*, vol. 26, no. 2, p. 105, Feb. 2015, doi: 10.1007/s10856-015-5435-1.

[498] I. Gonzalez de Torre *et al.*, "Hybrid elastin-like recombinamer-fibrin gels: physical characterization and in vitro evaluation for cardiovascular tissue engineering applications," *Biomater. Sci.*, vol. 4, no. 9, pp. 1361–1370, 2016, doi: 10.1039/C6BM00300A.

[499] I. Rojas de Gascue, B., Ramírez, M., Aguilera, R., García, A., Prin, J. L., Lias, J., ... & Katime, "Hydrogels obtained from acrylamide, maleic acid, acrylic acid and octylmonoitaconate: synthesis, absorbent capacity and pH variations in copper sulfate solutions.," *Rev. Técnica la Fac. Ing. Univ. del Zulia*, vol. 30(1), pp. 74–84, 2007.

[500] B. Singh, D. K. Sharma, and A. Gupta, "In vitro release dynamics of thiram fungicide from starch and poly(methacrylic acid)-based hydrogels," *J. Hazard. Mater.*, vol. 154, no. 1–3, pp. 278–286, Jun. 2008, doi:

10.1016/j.jhazmat.2007.10.024.

[501] T. Caykara, S. Kiper, and G. Demirel, "Thermosensitive poly(N-isopropylacrylamide-co-acrylamide) hydrogels: Synthesis, swelling and interaction with ionic surfactants," *Eur. Polym. J.*, vol. 42, no. 2, pp. 348–355, Feb. 2006, doi: 10.1016/j.eurpolymj.2005.07.006.

[502] J. R. Tse and A. J. Engler, "Preparation of Hydrogel Substrates with Tunable Mechanical Properties," *Curr. Protoc. Cell Biol.*, vol. 47, no. 1, Jun. 2010, doi: 10.1002/0471143030.cb1016s47.

[503] M. Friuli, P. Nitti, M. Madaghiele, and C. Demitri, "A possible method to avoid skin effect in polymeric scaffold produced through thermally induced phase separation," *Results Eng.*, vol. 12, p. 100282, Dec. 2021, doi: 10.1016/j.rineng.2021.100282.

[504] C. Ruan, "'Skin-Core-Skin' Structure of Polymer Crystallization Investigated by Multiscale Simulation," *Materials (Basel).*, vol. 11, no. 4, p. 610, Apr. 2018, doi: 10.3390/ma11040610.

[505] Z. Zhang, Y. Feng, L. Wang, D. Liu, C. Qin, and Y. Shi, "A review of preparation methods of porous skin tissue engineering scaffolds," *Mater. Today Commun.*, vol. 32, p. 104109, Aug. 2022, doi: 10.1016/j.mtcomm.2022.104109.

[506] T. M. Freyman, I. V. Yannas, and L. J. Gibson, "Cellular materials as porous scaffolds for tissue engineering," *Prog. Mater. Sci.*, vol. 46, no. 3–4, pp. 273–282, Jan. 2001, doi: 10.1016/S0079-6425(00)00018-9.

[507] J. Rnjak-Kovacina *et al.*, "Tailoring the porosity and pore size of electrospun synthetic human elastin scaffolds for dermal tissue engineering," *Biomaterials*, vol. 32, no. 28, pp. 6729–6736, Oct. 2011, doi: 10.1016/j.biomaterials.2011.05.065.

[508] M. P. Caley, V. L. C. Martins, and E. A. O'Toole, "Metalloproteinases and Wound Healing," *Adv. Wound Care*, vol. 4, no. 4, pp. 225–234, Apr. 2015, doi: 10.1089/wound.2014.0581.

[509] M. Xue and C. J. Jackson, "Extracellular Matrix Reorganization During Wound Healing and Its Impact on Abnormal Scarring," *Adv. Wound Care*, vol. 4, no. 3, pp. 119–136, Mar. 2015, doi: 10.1089/wound.2013.0485.

[510] V. Vivcharenko, A. Benko, K. Palka, M. Wojcik, and A. Przekora, "Elastic and biodegradable chitosan/agarose film revealing slightly acidic pH for potential applications in regenerative medicine as artificial skin graft," *Int. J. Biol. Macromol.*, vol. 164, pp. 172–183, Dec. 2020, doi: 10.1016/j.ijbiomac.2020.07.099.

[511] G. Tegl, A. Rollett, J. Dopplinger, C. Gamerith, and G. M. Guebitz, "Chitosan based substrates for wound infection detection based on increased lysozyme activity," *Carbohydr. Polym.*, vol. 151, pp. 260–267, Oct. 2016, doi: 10.1016/j.carbpol.2016.05.069.

[512] P. Krzyszczyk, R. Schloss, A. Palmer, and F. Berthiaume, "The Role of Macrophages in Acute and Chronic Wound Healing and Interventions to

Promote Pro-wound Healing Phenotypes," *Front. Physiol.*, vol. 9, May 2018, doi: 10.3389/fphys.2018.00419.

[513] R. G. Frykberg and J. Banks, "Challenges in the Treatment of Chronic Wounds," *Adv. Wound Care*, vol. 4, no. 9, pp. 560–582, Sep. 2015, doi: 10.1089/wound.2015.0635.

[514] R. Augustine, "Skin bioprinting: a novel approach for creating artificial skin from synthetic and natural building blocks," *Prog. Biomater.*, vol. 7, no. 2, pp. 77–92, Jun. 2018, doi: 10.1007/s40204-018-0087-0.

[515] H. Sekine *et al.*, "In vitro fabrication of functional three-dimensional tissues with perfusable blood vessels," *Nat. Commun.*, vol. 4, no. 1, p. 1399, Jan. 2013, doi: 10.1038/ncomms2406.

[516] H. S. Azevedo, F. M. Gama, and R. L. Reis, "In Vitro Assessment of the Enzymatic Degradation of Several Starch Based Biomaterials," *Biomacromolecules*, vol. 4, no. 6, pp. 1703–1712, Nov. 2003, doi: 10.1021/bm0300397.

[517] S. R. Ong, K. A. Trabbic-Carlson, D. L. Nettles, D. W. Lim, A. Chilkoti, and L. A. Setton, "Epitope tagging for tracking elastin-like polypeptides," *Biomaterials*, vol. 27, no. 9, pp. 1930–1935, Mar. 2006, doi: 10.1016/j.biomaterials.2005.10.018.

[518] B. K. Mann, A. S. Gobin, A. T. Tsai, R. H. Schmedlen, and J. L. West, "Smooth muscle cell growth in photopolymerized hydrogels with cell adhesive and proteolytically degradable domains: synthetic ECM analogs for tissue engineering," *Biomaterials*, vol. 22, no. 22, pp. 3045–3051, Nov. 2001, doi: 10.1016/S0142-9612(01)00051-5.

[519] M. Stojic *et al.*, "Elastin-Plasma Hybrid Hydrogels for Skin Tissue Engineering," *Polymers (Basel).*, vol. 13, no. 13, p. 2114, Jun. 2021, doi: 10.3390/polym13132114.

[520] S. Salinas-Fernández, M. Santos, M. Alonso, L. Quintanilla, and J. C. Rodríguez-Cabello, "Genetically engineered elastin-like recombinamers with sequence-based molecular stabilization as advanced bioinks for 3D bioprinting," *Appl. Mater. Today*, vol. 18, p. 100500, Mar. 2020, doi: 10.1016/j.apmt.2019.100500.

[521] A. Diener *et al.*, "Control of focal adhesion dynamics by material surface characteristics," *Biomaterials*, vol. 26, no. 4, pp. 383–392, Feb. 2005, doi: 10.1016/j.biomaterials.2004.02.038.

[522] E. Debus, K. Weber, and M. Osborn, "Monoclonal cytokeratin antibodies that distinguish simple from stratified squamous epithelia: characterization on human tissues.," *EMBO J.*, vol. 1, no. 12, pp. 1641–1647, Dec. 1982, doi: 10.1002/j.1460-2075.1982.tb01367.x.

[523] H. Alam, L. Sehgal, S. T. Kundu, S. N. Dalal, and M. M. Vaidya, "Novel function of keratins 5 and 14 in proliferation and differentiation of stratified epithelial cells," *Mol. Biol. Cell*, vol. 22, no. 21, pp. 4068–4078, Nov. 2011, doi: 10.1091/mbc.e10-08-0703.

[524] I. Colombo *et al.*, "HaCaT Cells as a Reliable In Vitro Differentiation Model to Dissect the Inflammatory/Repair Response of Human Keratinocytes," *Mediators Inflamm.*, vol. 2017, pp. 1–12, 2017, doi: 10.1155/2017/7435621.

[525] C. Burridge, K., Fath, K., Kelly, T., Nuckolls, G., & Turner, *Focal adhesions: Transmembrane junctions between the extracellular matrix and the cytoskeleton*, Annual Rev. 1988. doi: 10.17615/e5d3-6d81.

[526] W. T. Chen and S. J. Singer, "Immunoelectron microscopic studies of the sites of cell-substratum and cell-cell contacts in cultured fibroblasts.," *J. Cell Biol.*, vol. 95, no. 1, pp. 205–222, Oct. 1982, doi: 10.1083/jcb.95.1.205.

[527] L. R□is□nen *et al.*, "Expression of cell adhesion complexes in epithelial cells seeded on biomaterial surfaces," *J. Biomed. Mater. Res.*, vol. 49, no. 1, pp. 79–87, Jan. 2000, doi: 10.1002/(SICI)1097-4636(200001)49:1<79::AID-JBM10>3.0.CO;2-N.

[528] M. A. Kurpakus, V. Quaranta, and J. C. Jones, "Surface relocation of alpha 6 beta 4 integrins and assembly of hemidesmosomes in an in vitro model of wound healing.," *J. Cell Biol.*, vol. 115, no. 6, pp. 1737–1750, Dec. 1991, doi: 10.1083/jcb.115.6.1737.

[529] J.-L. Guan, "Role of focal adhesion kinase in integrin signaling," *Int. J. Biochem. Cell Biol.*, vol. 29, no. 8–9, pp. 1085–1096, Aug. 1997, doi: 10.1016/S1357-2725(97)00051-4.

[530] N. Griesche, J. Bereiter-Hahn, H. Geiger, R. Schubert, and P. C. Baer, "During epithelial differentiation of human adipose-derived stromal/stem cells, expression of zonula occludens protein-1 is induced by a combination of retinoic acid, activin-A and bone morphogenetic protein-7," *Cytotherapy*, vol. 14, no. 1, pp. 61–69, Jan. 2012, doi: 10.3109/14653249.2011.610502.

[531] R. L. Chalmers, "The evidence for the role of transforming growth factor-beta in the formation of abnormal scarring," *Int. Wound J.*, vol. 8, no. 3, pp. 218–223, Jun. 2011, doi: 10.1111/j.1742-481X.2011.00771.x.

[532] W. Li *et al.*, "Signals that Initiate, Augment, and Provide Directionality for Human Keratinocyte Motility," *J. Invest. Dermatol.*, vol. 123, no. 4, pp. 622–633, Oct. 2004, doi: 10.1111/j.0022-202X.2004.23416.x.

[533] D. P. Choma, K. Pumiglia, and C. M. DiPersio, "Integrin α3β1 directs the stabilization of a polarized lamellipodium in epithelial cells through activation of Rac1," *J. Cell Sci.*, vol. 117, no. 17, pp. 3947–3959, Aug. 2004, doi: 10.1242/jcs.01251.

[534] C. Mazio *et al.*, "Pre-vascularized dermis model for fast and functional anastomosis with host vasculature," *Biomaterials*, vol. 192, pp. 159–170, Feb. 2019, doi: 10.1016/j.biomaterials.2018.11.018.

[535] H. N. Wilkinson, S. Iveson, P. Catherall, and M. J. Hardman, "A Novel Silver Bioactive Glass Elicits Antimicrobial Efficacy Against Pseudomonas aeruginosa and Staphylococcus aureus in an ex Vivo Skin Wound Biofilm Model," *Front. Microbiol.*, vol. 9, Jul. 2018, doi: 10.3389/fmicb.2018.01450.

[536] Y. Wang, E. Gutierrez-Herrera, A. Ortega-Martinez, R. R. Anderson, and W. Franco, "UV fluorescence excitation imaging of healing of wounds in skin: Evaluation of wound closure in organ culture model," *Lasers Surg. Med.*, vol. 48, no. 7, pp. 678–685, Sep. 2016, doi: 10.1002/lsm.22523.

[537] K. Markus Roupé, M. Nybo, U. Sjöbring, P. Alberius, A. Schmidtchen, and O. E. Sørensen, "Injury Is a Major Inducer of Epidermal Innate Immune Responses during Wound Healing," *J. Invest. Dermatol.*, vol. 130, no. 4, pp. 1167–1177, Apr. 2010, doi: 10.1038/jid.2009.284.

[538] S. Olivera and M. Tomic-Canic, "Human Ex Vivo Wound Healing Model," 2013, pp. 255–264. doi: 10.1007/978-1-62703-505-7_14.

[539] J. Mendoza-Garcia, A. Sebastian, T. Alonso-Rasgado, and A. Bayat, "Optimization of an ex vivo wound healing model in the adult human skin: Functional evaluation using photodynamic therapy," *Wound Repair Regen.*, vol. 23, no. 5, pp. 685–702, Sep. 2015, doi: 10.1111/wrr.12325.

[540] T. Hodgkinson and A. Bayat, "Ex vivo evaluation of acellular and cellular collagen-glycosaminoglycan flowable matrices," *Biomed. Mater.*, vol. 10, no. 4, p. 041001, Jul. 2015, doi: 10.1088/1748-6041/10/4/041001.

[541] K. Safferling *et al.*, "Wound healing revised: A novel reepithelialization mechanism revealed by in vitro and in silico models," *J. Cell Biol.*, vol. 203, no. 4, pp. 691–709, Nov. 2013, doi: 10.1083/jcb.201212020.

[542] G. D. Glinos *et al.*, "Optical coherence tomography for assessment of epithelialization in a human ex vivo wound model," *Wound Repair Regen.*, vol. 25, no. 6, pp. 1017–1026, Nov. 2017, doi: 10.1111/wrr.12600.

[543] I. Pastar *et al.*, "Epithelialization in Wound Healing: A Comprehensive Review," *Adv. Wound Care*, vol. 3, no. 7, pp. 445–464, Jul. 2014, doi: 10.1089/wound.2013.0473.

[544] X. Zhang, W. Shu, Q. Yu, W. Qu, Y. Wang, and R. Li, "Functional Biomaterials for Treatment of Chronic Wound," *Front. Bioeng. Biotechnol.*, vol. 8, Jun. 2020, doi: 10.3389/fbioe.2020.00516.

[545] K. Las Heras, I. Garcia-Orue, F. Rancan, M. Igartua, E. Santos-Vizcaino, and R. M. Hernandez, "Modulating the immune system towards a functional chronic wound healing: A biomaterials and Nanomedicine perspective," *Adv. Drug Deliv. Rev.*, vol. 210, p. 115342, Jul. 2024, doi: 10.1016/j.addr.2024.115342.

[546] R. Sivakumar, "On the relevance and requirements of biomaterials," *Bull. Mater. Sci.*, vol. 22, no. 3, pp. 647–655, May 1999, doi: 10.1007/BF02749981.

[547] L. S. Nair and C. T. Laurencin, "Biodegradable polymers as biomaterials," *Prog. Polym. Sci.*, vol. 32, no. 8–9, pp. 762–798, Aug. 2007, doi: 10.1016/j.progpolymsci.2007.05.017.

[548] U. Jammalamadaka and K. Tappa, "Recent Advances in Biomaterials for 3D Printing and Tissue Engineering," *J. Funct. Biomater.*, vol. 9, no. 1, p. 22, Mar. 2018, doi: 10.3390/jfb9010022.

[549] A. C. Rincón *et al.*, "Biocompatibility of elastin-like polymer poly(VPAVG)

microparticles: in vitro and in vivo studies," *J. Biomed. Mater. Res. Part A*, vol. 78A, no. 2, pp. 343–351, Aug. 2006, doi: 10.1002/jbm.a.30702.

[550] R. E. Sallach *et al.*, "Long-term biostability of self-assembling protein polymers in the absence of covalent crosslinking," *Biomaterials*, vol. 31, no. 4, pp. 779–791, Feb. 2010, doi: 10.1016/j.biomaterials.2009.09.082.

[551] A. Fernández-Colino, F. J. Arias, M. Alonso, and J. C. Rodríguez-Cabello, "Self-Organized ECM-Mimetic Model Based on an Amphiphilic Multiblock Silk-Elastin-Like Corecombinamer with a Concomitant Dual Physical Gelation Process," *Biomacromolecules*, vol. 15, no. 10, pp. 3781–3793, Oct. 2014, doi: 10.1021/bm501051t.

[552] H.-I. Chang and Y. Wang, "Cell Responses to Surface and Architecture of Tissue Engineering Scaffolds," in *Regenerative Medicine and Tissue Engineering - Cells and Biomaterials*, InTech, 2011. doi: 10.5772/21983.

[553] F. González-Pérez, M. Alonso, I. González de Torre, M. Santos, and J. C. Rodríguez-Cabello, "Protease-Sensitive, VEGF-Mimetic Peptide, and IKVAV Laminin-Derived Peptide Sequences within Elastin-Like Recombinamer Scaffolds Provide Spatiotemporally Synchronized Guidance of Angiogenesis and Neurogenesis," *Adv. Healthc. Mater.*, vol. 11, no. 22, Nov. 2022, doi: 10.1002/adhm.202201646.

[554] A. Ibáñez-Fonseca *et al.*, "Biocompatibility of two model elastin-like recombinamer-based hydrogels formed through physical or chemical cross-linking for various applications in tissue engineering and regenerative medicine," *J. Tissue Eng. Regen. Med.*, vol. 12, no. 3, Mar. 2018, doi: 10.1002/term.2562.

[555] Y. Wang *et al.*, "Tropoelastin Incorporation into a Dermal Regeneration Template Promotes Wound Angiogenesis," *Adv. Healthc. Mater.*, vol. 4, no. 4, pp. 577–584, Mar. 2015, doi: 10.1002/adhm.201400571.

[556] R. S. Labow, E. Meek, L. A. Matheson, and J. P. Santerre, "Human macrophage-mediated biodegradation of polyurethanes: assessment of candidate enzyme activities," *Biomaterials*, vol. 23, no. 19, pp. 3969–3975, Oct. 2002, doi: 10.1016/S0142-9612(02)00137-0.

[557] F. Theiss *et al.*, "Biocompatibility and resorption of a brushite calcium phosphate cement," *Biomaterials*, vol. 26, no. 21, pp. 4383–4394, Jul. 2005, doi: 10.1016/j.biomaterials.2004.11.056.

[558] A. G. Arroyo and M. L. Iruela-Arispe, "Extracellular matrix, inflammation, and the angiogenic response," *Cardiovasc. Res.*, vol. 86, no. 2, pp. 226–235, May 2010, doi: 10.1093/cvr/cvq049.

[559] P. Patil *et al.*, "Reactive oxygen species–degradable polythioketal urethane foam dressings to promote porcine skin wound repair," *Sci. Transl. Med.*, vol. 14, no. 641, Apr. 2022, doi: 10.1126/scitranslmed.abm6586.

[560] M. Landén, N. X., Piipponen, M., Bian, X., Liu, Z., Sangsuwan, T., Maselli, M., ... & Halle, "Epigenetic memory of radiotherapy in dermal fibroblasts impairs wound repair capacity in cancer survivors," *Nat. Portf.*, 2023, doi:

10.21203/rs.3.rs-3242808/v1.

[561] F. Babaeijandaghi *et al.*, "Accelerated Epidermal Regeneration and Improved Dermal Reconstruction Achieved by Polyethersulfone Nanofibers," *Tissue Eng. Part A*, vol. 16, no. 11, pp. 3527–3536, Nov. 2010, doi: 10.1089/ten.tea.2009.0829.

[562] Z. Su *et al.*, "Enhancement of skin wound healing with decellularized scaffolds loaded with hyaluronic acid and epidermal growth factor," *Mater. Sci. Eng. C*, vol. 44, pp. 440–448, Nov. 2014, doi: 10.1016/j.msec.2014.07.039.

[563] E. M. Sussman, M. C. Halpin, J. Muster, R. T. Moon, and B. D. Ratner, "Porous Implants Modulate Healing and Induce Shifts in Local Macrophage Polarization in the Foreign Body Reaction," *Ann. Biomed. Eng.*, vol. 42, no. 7, pp. 1508–1516, Jul. 2014, doi: 10.1007/s10439-013-0933-0.

[564] M. Rodrigues, N. Kosaric, C. A. Bonham, and G. C. Gurtner, "Wound Healing: A Cellular Perspective," *Physiol. Rev.*, vol. 99, no. 1, pp. 665–706, Jan. 2019, doi: 10.1152/physrev.00067.2017.

[565] Q. Wen, S. M. Mithieux, and A. S. Weiss, "Elastin Biomaterials in Dermal Repair," *Trends Biotechnol.*, vol. 38, no. 3, pp. 280–291, Mar. 2020, doi: 10.1016/j.tibtech.2019.08.005.

[566] D.-M. Tian *et al.*, "In-situ formed elastin-based hydrogels enhance wound healing via promoting innate immune cells recruitment and angiogenesis," *Mater. Today Bio*, vol. 15, p. 100300, Jun. 2022, doi: 10.1016/j.mtbio.2022.100300.

[567] T. A. Wilgus, S. Roy, and J. C. McDaniel, "Neutrophils and Wound Repair: Positive Actions and Negative Reactions," *Adv. Wound Care*, vol. 2, no. 7, pp. 379–388, Sep. 2013, doi: 10.1089/wound.2012.0383.

[568] S. Jhunjhunwala, "Neutrophils at the Biological–Material Interface," *ACS Biomater. Sci. Eng.*, vol. 4, no. 4, pp. 1128–1136, Apr. 2018, doi: 10.1021/acsbiomaterials.6b00743.

[569] G. S. Selders, A. E. Fetz, M. Z. Radic, and G. L. Bowlin, "An overview of the role of neutrophils in innate immunity, inflammation and host-biomaterial integration," *Regen. Biomater.*, vol. 4, no. 1, pp. 55–68, Feb. 2017, doi: 10.1093/rb/rbw041.

[570] S. M. Staubli *et al.*, "Control of angiogenesis and host response by modulating the cell adhesion properties of an Elastin-Like Recombinamer-based hydrogel," *Biomaterials*, vol. 135, pp. 30–41, Aug. 2017, doi: 10.1016/j.biomaterials.2017.04.047.

[571] H. Kusaka, K. Nagatani, T. Sato, and S. Minota, "Increase of a wide range of bioactive substances in an active phase of neuro-Sweet disease," *BMJ Case Rep.*, vol. 13, no. 4, p. e233457, Apr. 2020, doi: 10.1136/bcr-2019-233457.

[572] N. A. Mohd Razali and W.-C. Lin, "Accelerating the excisional wound closure by using the patterned microstructural nanofibrous mats/gentamicin-loaded hydrogel composite scaffold," *Mater. Today Bio*, vol. 16, p. 100347, Dec. 2022,

doi: 10.1016/j.mtbio.2022.100347.

[573] P. Rousselle, F. Braye, and G. Dayan, “Re-epithelialization of adult skin wounds: Cellular mechanisms and therapeutic strategies,” *Adv. Drug Deliv. Rev.*, vol. 146, pp. 344–365, Jun. 2019, doi: 10.1016/j.addr.2018.06.019.

[574] G. Guan, Qizhuang Lv, S. Liu, Z. Jiang, C. Zhou, and W. Liao, “3D-bioprinted peptide coupling patches for wound healing,” *Mater. Today Bio*, vol. 13, p. 100188, Jan. 2022, doi: 10.1016/j.mtbio.2021.100188.

[575] L. A. DiPietro, “Angiogenesis and wound repair: when enough is enough,” *J. Leukoc. Biol.*, vol. 100, no. 5, pp. 979–984, Nov. 2016, doi: 10.1189/jlb.4MR0316-102R.

[576] X. Cao, Z. Zhang, L. Sun, Z. Luo, and Y. Zhao, “Multifunctional fish gelatin hydrogel inverse opal films for wound healing,” *J. Nanobiotechnology*, vol. 20, no. 1, p. 355, Dec. 2022, doi: 10.1186/s12951-022-01564-w.

[577] G. Theocharidis *et al.*, “A strain-programmed patch for the healing of diabetic wounds,” *Nat. Biomed. Eng.*, vol. 6, no. 10, pp. 1118–1133, Jul. 2022, doi: 10.1038/s41551-022-00905-2.

[578] P. P. . van Zuijlen *et al.*, “Collagen morphology in human skin and scar tissue: no adaptations in response to mechanical loading at joints,” *Burns*, vol. 29, no. 5, pp. 423–431, Aug. 2003, doi: 10.1016/S0305-4179(03)00052-4.

[579] J. E. Frith, R. J. Mills, J. E. Hudson, and J. J. Cooper-White, “Tailored Integrin–Extracellular Matrix Interactions to Direct Human Mesenchymal Stem Cell Differentiation,” *Stem Cells Dev.*, vol. 21, no. 13, pp. 2442–2456, Sep. 2012, doi: 10.1089/scd.2011.0615.

[580] D. S. Grant *et al.*, “Interaction of endothelial cells with a laminin A chain peptide (SIKVAV) in vitro and induction of angiogenic behavior in vivo,” *J. Cell. Physiol.*, vol. 153, no. 3, pp. 614–625, Dec. 1992, doi: 10.1002/jcp.1041530324.

[581] J. KIM, W. PARK, and B. MIN, “The PPFLMLLKGSTR motif in globular domain 3 of the human laminin-5 α3 chain is crucial for integrin α3β1 binding and cell adhesion,” *Exp. Cell Res.*, vol. 304, no. 1, pp. 317–327, Mar. 2005, doi: 10.1016/j.yexcr.2004.11.009.

[582] C. M. Niessen *et al.*, “The α6β4 Integrin Is a Receptor for both Laminin and Kalinin,” *Exp. Cell Res.*, vol. 211, no. 2, pp. 360–367, Apr. 1994, doi: 10.1006/excr.1994.1099.

[583] A. Lamiable, P. Thévenet, J. Rey, M. Vavrusa, P. Derreumaux, and P. Tufféry, “PEP-FOLD3: faster de novo structure prediction for linear peptides in solution and in complex,” *Nucleic Acids Res.*, vol. 44, no. W1, pp. W449–W454, Jul. 2016, doi: 10.1093/nar/gkw329.

[584] A. Farrukh, W. Fan, S. Zhao, M. Salierno, J. I. Paez, and A. del Campo, “Photoactivatable Adhesive Ligands for Light-Guided Neuronal Growth,” *ChemBioChem*, vol. 19, no. 12, pp. 1271–1279, Jun. 2018, doi: 10.1002/cbic.201800118.

[585] A. Farrukh *et al.*, "In Situ, Light-Guided Axon Growth on Biomaterials via Photoactivatable Laminin Peptidomimetic IK(HANBP)VAV," *ACS Appl. Mater. Interfaces*, vol. 10, no. 48, pp. 41129–41137, Dec. 2018, doi: 10.1021/acsami.8b15517.

[586] L. Mbundi, S. T. Meikle, R. Busquets, N. G. Dowell, M. Cercignani, and M. Santin, "Gadolinium Tagged Osteoprotegerin-Mimicking Peptide: A Novel Magnetic Resonance Imaging Biospecific Contrast Agent for the Inhibition of Osteoclastogenesis and Osteoclast Activity," *Nanomaterials*, vol. 8, no. 6, p. 399, Jun. 2018, doi: 10.3390/nano8060399.

[587] C. A. DeForest, E. A. Sims, and K. S. Anseth, "Peptide-Functionalized Click Hydrogels with Independently Tunable Mechanics and Chemical Functionality for 3D Cell Culture," *Chem. Mater.*, vol. 22, no. 16, pp. 4783–4790, Aug. 2010, doi: 10.1021/cm101391y.

[588] F. Causa, P. A. Netti, and L. Ambrosio, "A multi-functional scaffold for tissue regeneration: The need to engineer a tissue analogue," *Biomaterials*, vol. 28, no. 34, pp. 5093–5099, Dec. 2007, doi: 10.1016/j.biomaterials.2007.07.030.

[589] E. Chevalier, D. Chulia, C. Pouget, and M. Viana, "Fabrication of porous substrates: A review of processes using pore forming agents in the biomaterial field," *J. Pharm. Sci.*, vol. 97, no. 3, pp. 1135–1154, Mar. 2008, doi: 10.1002/jps.21059.

[590] V. KARAGEORGIOU and D. KAPLAN, "Porosity of 3D biomaterial scaffolds and osteogenesis," *Biomaterials*, vol. 26, no. 27, pp. 5474–5491, Sep. 2005, doi: 10.1016/j.biomaterials.2005.02.002.

[591] I. Bružauskaitė, D. Bironaitė, E. Bagdonas, and E. Bernotienė, "Scaffolds and cells for tissue regeneration: different scaffold pore sizes—different cell effects," *Cytotechnology*, vol. 68, no. 3, pp. 355–369, May 2016, doi: 10.1007/s10616-015-9895-4.

[592] A. Girotti, A. Fernández-Colino, I. M. López, J. C. Rodríguez-Cabello, and F. J. Arias, "Elastin-like recombinamers: Biosynthetic strategies and biotechnological applications," *Biotechnol. J.*, vol. 6, no. 10, pp. 1174–1186, Oct. 2011, doi: 10.1002/biot.201100116.

[593] T. Christensen, K. Trabbic-Carlson, W. Liu, and A. Chilkoti, "Purification of recombinant proteins from Escherichia coli at low expression levels by inverse transition cycling," *Anal. Biochem.*, vol. 360, no. 1, pp. 166–168, Jan. 2007, doi: 10.1016/j.ab.2006.09.020.

[594] Y. S. Zhang and A. Khademhosseini, "Advances in engineering hydrogels," *Science (80-.).*, vol. 356, no. 6337, May 2017, doi: 10.1126/science.aaf3627.

[595] S. Acosta, A. Ibañez-Fonseca, C. Aparicio, and J. C. Rodríguez-Cabello, "Antibiofilm coatings based on protein-engineered polymers and antimicrobial peptides for preventing implant-associated infections," *Biomater. Sci.*, vol. 8, no. 10, pp. 2866–2877, 2020, doi: 10.1039/D0BM00155D.

[596] M. Eldardiri, Y. Martin, J. Roxburgh, D. J. Lawrence-Watt, and J. R. Sharpe,

"Wound Contraction Is Significantly Reduced by the Use of Microcarriers to Deliver Keratinocytes and Fibroblasts in an In Vivo Pig Model of Wound Repair and Regeneration," *Tissue Eng. Part A*, vol. 18, no. 5–6, pp. 587–597, Mar. 2012, doi: 10.1089/ten.tea.2011.0258.

[597] Y. Liang *et al.*, "Application of stable continuous external electric field promotes wound healing in pig wound model," *Bioelectrochemistry*, vol. 135, p. 107578, Oct. 2020, doi: 10.1016/j.bioelechem.2020.107578.

[598] T. P. Sullivan, W. H. Eaglstein, S. C. Davis, and P. Mertz, "THE PIG AS A MODEL FOR HUMAN WOUND HEALING," *Wound Repair Regen.*, vol. 9, no. 2, pp. 66–76, Mar. 2001, doi: 10.1046/j.1524-475x.2001.00066.x.

[599] S. Narayanan *et al.*, "HypoxamiR-210 accelerates wound healing in diabetic mice by improving cellular metabolism," *Commun. Biol.*, vol. 3, no. 1, p. 768, Dec. 2020, doi: 10.1038/s42003-020-01495-y.

APPENDIX

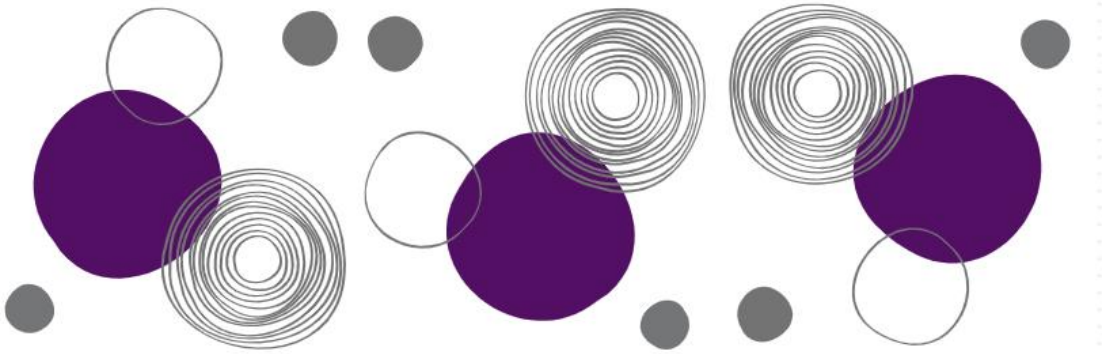

Appendix

Schematic representation of biomaterials

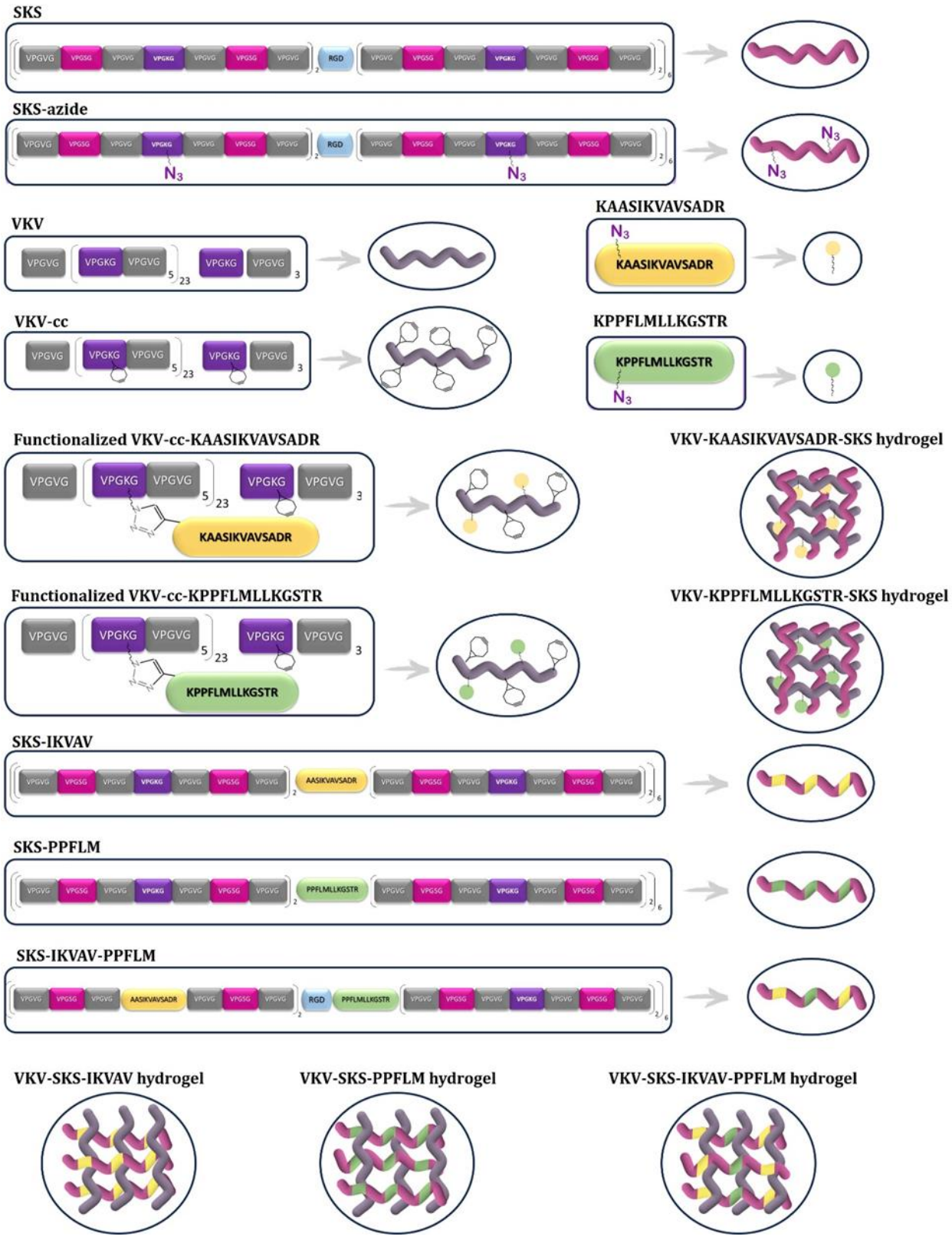

Abbreviations

List of abbreviations			
Abbrev.	**Meaning**	**Abbrev.**	**Meaning**
AB	Alamar Blue	**NTC**	Not template control (in q-RT-PCR)
AU	Arterial Ulcer	**OD**	Optical Density
BM	Basement Membrane	**PCL**	Poly(ε-Caprolactone)
Bp	Base Pair	**PCR**	Polymerase Chain Reaction
BSA	Bovine Serum Albumin	**q-PCR**	Quantitative Polymerase Chain Reaction
DNA	Deoxyribonucleic Acid	**qRT-PCR**	Quantitative Reverse Transcription Polymerase Chain Reaction
Dr	Degradation Rate	**pD**	pDrive All
DRIR	Active Domains for Slow Degradation	**PE**	Plating Efficiency
DSC	Differential Scanning Calorimetry	**PEG**	Poly(Ethylene Glycol)
DU	Diabetic Ulcer	**PFA**	Paraformaldehyde
E. coli	*Escherichia coli*	**PGA**	Polyglycolic Acid
ECM	Extracellular Matrix	**PLA**	Poly(L-Lactic Acid)
EGF	Epidermal Growth Factor	**PLGA**	Polylactic-co-Glycolic Acid
ELP	Elastin-Like Protein	**Ppm**	Parts per Million
ELR	Elastin-Like Recombamer	**PU**	Pressure Ulcer
ELRs	Elastin-Like Recombamers	**REDV**	Adhesion Sequence
FBS	Fetal Bovine Serum	**RGD**	Adhesion Sequence
FN	Fibronectin	**RT**	Reverse transcription (in qRT-PCR)
GelMA	Gelatin Methacrylated	**RT**	Room Temperature
GTAR	Active Domains for Fast Degradation	**SDS-PAGE**	Sodium Dodecyl Sulfate-Polyacrylamide Gel Electrophoresis
H&E	Haematoxylin and Eosin	**SELR**	Silk-Elastin-Like Recombamers
HaCaT	Human Adult Skin Keratinocytes Cells	**SEM**	Scanning Electron Microscopy
HFF-1	Human Foreskin Fibroblastic Cells	**SPAAC**	Strain-Promoted Azide-Alkyne Cycloaddition
HPLC	High-Performance Liquid Chromatography	**SPPS**	Solid Phase Synthesis
IDP	Intrinsically Disordered Protein	**SWRI**	Scratched Wound Recovery Index
IRDL	Iterative - Recursive Directional Ligation	**TCP**	Tissue Culture Plate
ITC	Inverse Transition Cycle	**TE**	Tissue Engineering
ITT	Inverse Temperature Transition	**TSS**	Transformation and Storage Solution
L&D	Live and Dead	**T_t**	Transition Temperature
LDH	Lactate Dehydrogenase - Colorimetric Assay	**UV**	Ultraviolet
MALDI-TOF	Matrix-Assisted Laser Desorption/Ionization-Time-of-Flight	**VEGF**	Vascular Endothelial Growth Factor
MMP	Matrix Metalloproteinase	**VU**	Venous Ulcer
MQ	MilliQ Ultra-Pure Water	**WCP**	Water Content Percentage
MTS	Tetrazolium Salt - Colorimetric Assay		
Mw	Molecular Weight		

Table of standard amino acid abbreviations

Amino acid nomenclature		
Amino acid	**3-letter code**	**1-letter code**
Alanine	Ala	A
Arginine	Arg	R
Asparagine	Asn	N
Aspartic acid	Asp	D
Cysteine	Cys	C
Glutamic acid	Glu	E
Glutamine	Gln	Q
Glycine	Gly	G
Histidine	His	H
Isoleucine	Ile	I
Leucine	Leu	L
Lysine	Lys	K
Methionine	Met	M
Phenylalanine	Phe	F
Proline	Pro	P
Serine	Ser	S
Threonine	Thr	T
Tryptophan	Trp	W
Tyrosine	Tyr	Y
Valine	Val	V

Professional achievements

Internships

- ***2022***

A three-month internship was undertaken at the laboratory of Associate Professor Ning Xu Landén at the Center for Molecular Medicine at Karolinska University Hospital in Stockholm, Sweden.

Publications

It is anticipated that three articles based on the findings of this thesis will be published in the near future. Moreover, there are several collaborative works that are currently awaiting publication.

- ***2024***

-Camal Ruggieri I.N., Aimone M., **Juanes-Gusano D.**, Ibáñez-Fonseca A., Santiago O., Stur M., Mardegan Issa J.P., Missana L.R., Alonso M., Rodriguez-Cabello J.C., and Feldman S. "*Biocompatibility and bone regeneration with Elastin-like recombinamer catalyst-free click gels*". Scientific Reports. (DOI: 10.1038/s41598-024-69658-z).

- ***2022***

- J. C. Rodríguez-Cabello, S. Escalera*, **D. Juanes-Gusano***, M. Santos, A. Girotti. "*Designing Elastin-Like Recombinamers for Therapeutic and Regenerative Purposes*". Multifunctional Hydrogels for Biomedical Applications, 37-62. First edition (Wiley-VCH) (DOI: 10.1002/9783527825820.ch3).

- ***2021***

- **D. Juanes-Gusano**, M. Santos, V. Reboto, M. Alonso, JC. Rodríguez-Cabello. "*Self-assembling Systems Comprising Intrinsically Disordered Protein Polymers like Elastin-Like Recombinamers*". Journal of Peptide Science. Special Issue "Peptides in biomaterials science: new trends and applications", 2021-e3362 (DOI:10.1002/psc.3362).

- L. Mbundi, M. González-Pérez, F. González-Pérez, **D. Juanes-Gusano**, J. C. Rodríguez-Cabello. *"Trends in the Development of Tailored Elastin-Like Recombinamer-based Porous Biomaterials for Soft and Hard Tissue Applications".* Frontiers in Materials 2021, volumen 7, article 601795 (DOI: 10.3389/fmats.2020.601795).

Participation in congresses and conferences

- ***2023***

- **D. Juanes-Gusano**, L. Mbundi, M. Santos, M. Alonso, J. C. Rodriguez-Cabello. "*Physicochemical characterization and in vitro testing of ELR-based membrane for wound healing*". Advanced Functional Polymers for Medicine (AFPM 2023). Barcelona (Spain). Poster.

- **D. Juanes-Gusano**, M. Alonso, J. C. Rodriguez-Cabello. "*Aplicación de membranas ELR como candidatos para sustitutos dérmicos*". Jornada de Seguimiento del Programa de Doctorado en Investigación Biomédica. Valladolid (Spain). Oral.

- **D. Juanes-Gusano**, L. Mbundi, M. Santos, P. Cidad, M. Alonso, J. C. Rodriguez-Cabello. "*ELR-based basement membranes analogues for wound healing applications*" European Chapter of the Tissue Engineering and Regenerative Medicine International Society (TERMIS EU-Chapter). Manchester (United Kingdom). Poster.

- **D. Juanes-Gusano**, M. Santos, M. Alonso, J. C. Rodriguez-Cabello. "*Aplicación de membranas ELR como candidatos para sustitutos dérmicos*". 2nd Bioforge Workshop "New ELRs as a key tool for the development of cell therapies in regenerative medicine". Congosto (León, Spain). Oral. **Best Oral Communication Award.**

- ***2022***

-**D. Juanes-Gusano**, M. G. Pérez, M. Santos, M. Alonso, J. C. Rodríguez-Cabello. "*Characterization of Elastin-like Recombinamer-Based Membranes produced at the*

Interface of Two Immiscible Liquids by Click Chemistry". 32st Conference of the European Society for Biomaterials (ESB). Bordeaux (France). Poster.

- **D. Juanes-Gusano**, M. G. Pérez, M. Santos, M. Alonso, J. C. Rodríguez-Cabello. "*Characterization of Elastin-like Recombinamer-Based Membranes produced at a liquid-liquid interface*". II Encuentro de Jóvenes Investigadores de la Universidad de Valladolid. Valladolid (Spain). Oral.

- VIII International Conference. Innovation Camp "*Connecting Talent Wordwide, Promoting Innovation and Excellence in Higher Education*". IMFAHE FOUNDATION. Online, Boston (Massachusetts, EE.UU.).

- **D. Juanes-Gusano**, L. Mbundi, M. G. Pérez, J. C. Rodríguez-Cabello. "*Characterization of Elastin-like Recombinamer-Based Membranes produced at a liquid-liquid interface*". XVI Reunión del Grupo Especializado de Polímeros (GEP 2022) y XVII Simposio Latinoamericano de Polímeros (SLAP 2022). San Sebastián (Spain). Oral.

- ***2021***

- **D. Juanes-Gusano**, L. Mbundi, M. G. Pérez, J. C. Rodríguez-Cabello. "*Ultra-thin ELR membranes for wound healing applications*". 31st Conference of the European Society for Biomaterials (ESB) together with the 43rd Annual Congress of the Iberian Society of Biomechanics and Biomaterials (SIBB). Online, Oporto (Portugal). Poster-Oral.

- **D. Juanes-Gusano**, M. Alonso, J. C. Rodríguez-Cabello. "*Click ELR hydrogels as advanced biocompatible scaffolds for tissue engineering*". ESAO/TERMIS-EU Winter School. Online, Jaca (Spain). Oral.

- ***2020***

- **D. Juanes-Gusano**, M. Alonso, J. C. Rodríguez-Cabello. "*Hidrogeles basados en Recombinámeros Tipo Elastina como scaffolds biocompatibles y avanzadas para ingeniería de tejidos*". Jornadas de Investigadoras de Castilla y León. Valladolid (Spain). Oral.

- ***2019***

- **D. Juanes-Gusano**, A. Ibáñez-Fonseca, M. Alonso, J. C. Rodríguez-Cabello. "*Elastin-like Recombinamers Based-Hydrogels as Advanced Scaffolds for Cardiac Tissue Engineering*". 3rd Biennial Young Researchers Workshop on Biomaterials and Applications (bioMAPP19). Leioa (Spain). Oral.

- **D. Juanes-Gusano**, A. Ibáñez-Fonseca, M. Alonso, J. C. Rodríguez-Cabello. "*Hidrogeles Recombinámeros Tipo Elastina como matrices avanzadas para Ingeniería de Tejido Cardíaco*". XLII Congreso de la Sociedad Ibérica de Biomecánica y Biomateriales (SIBB 2019). Madrid (Spain). Oral.

- **D. Juanes-Gusano,** A. Ibáñez-Fonseca, M. Alonso, J. C. Rodríguez-Cabello. "*Click ELR hydrogels as advanced biocompatible scaffolds for cardiac tissue*

engineering". X Congreso de Jóvenes Investigadores en Polímeros (JIP 2019). Burgos (Spain). Oral.

Courses and certifications

Numerous complementary training courses, with the most significant of these being:

- XVIII **Training Course on Animal Experimentation in Functions A, B and C** (Regulation ECC 566/2015) and XVIII **Training Course in Animal Experimentation in functions D** (Order ECC 566/2015). Instituto de Estudios de Ciencias de la Salud de Castilla Y León. Universidad de Salamanca. Servicio de Experimentación animal. Recognized by the General Directorate of Agriculture and Livestock of the Community of Madrid.

- **Spectral Confocal Microscopy and Super-Resolution** (Theoretical-practical). Hospital Sant Joan de Déu- Universitat de Barcelona.

-**Introduction to Fiji/Image J for fluorescence image analysis**. Hospital Sant Joan de Déu- Universitat de Barcelona.

- **New medical tools. Medical image manipulation and processing: from segmentation to 3D printing**. Instituto de Estudios de Ciencias de la Salud de Castilla y León.

-**Public speaking course and Science outreach workshop for researchers.** Universidad de Valladolid.

University teaching

- Co-direction of the TFM of the student José Ricardo Morán Cabezas at the University of Valladolid in the 2021-2022 academic year, with the work titled: "*Desarrollo de nuevos hidrogeles ELR con injertos de péptidos de la laminina mediante la tecnología Click para su aplicación en regeneración tisular*".

-Supervision of the TFG of the student David Lorenzo Calvo at the University of Valladolid in the 2018-2019 academic year, with the work titled: "*Generación y detección de ondas mecánicas en Matrices hidrogel preformado mediante elementos piezoeléctricos para su uso en mecano biología celular*" and supervision of the Erasmus Internship of the student Salomé Carneiro Neto in the 2021-2022 academic year, with the work titled "*Using elastin-like recombinamers as scaffolds for tissue engineering and regenerative medicine in the context of skin regeneration*".

- Teaching activities in the Master's programme in Physics at the University of Valladolid (2023 - 2022 - 2021 - 2020 - 2019).

- Teaching activities associated with the Degree in Biomedical Engineering at the University of Valladolid (2022 - 2021 - 2020).

-Teaching activities associated with the Degree of Mechanical Engineering and Industrial Engineering at the University of Valladolid (2022 - 2021 - 2020).